COMPUTATIONAL STUDY OF THERMODYNAMICS OF METAL CARBONATES AND CATALYTIC PROPERTIES OF GROUP IV TRANSITION METAL OXIDES

by

YIQIN HU

DAVID A. DIXON, COMMITTEE CHAIR
C. HEATH TURNER
BRAD S. PIERCE
AYANJEET GHOSH
SHANE C. STREET

A DISSERTATION

Submitted in partial fulfillment of the requirements
for the degree of Doctor of Philosophy
in the Department of Chemistry and Biochemistry
in the Graduate School of
The University of Alabama

TUSCALOOSA, ALABAMA

2023

Copyright Yiqin Hu 2023
ALL RIGHTS RESERVED

ABSTRACT

This dissertation describes computational studies of the thermodynamics of metal carbonates, the sequestration of CO_2 by group IV transition metal oxides, the reactivity of ethanol on group IV transition metal oxides as a model for biofuel conversion, and halogen atom oxidation of magnesium clusters. Gas phase heats of formation using the Feller-Peterson-Dixon (FPD) approach were predicted for carbonates, bicarbonates and hydroxides for Mg, Ca, and various first-row transition metals. These reliable FPD values were used to benchmark a range of density functional theory exchange-correlation functionals that are used in modeling larger systems and solids. None of the functionals show good chemical accuracy of ±1 kcal/mol, most likely due to issues with properly treating oxygen. The FPD results can be used to predict cohesive energies and metal atom exchange reactions. The addition of CO_2 to M_3O_6 and $M_3O_6^-$ was studied at the CCSD(T) using weighted core correlation consistent basis sets. The calculations showed that prior predictions on the Ti structures were not correct as the results require the use of weighted core functions. The calculations enabled comparisons of CO_2 binding energies to the neutral and anionic clusters as well the role that CO_2 binding has on the electron affinity of the cluster. Ethanol dehydration and dehydrogenation on $(TiO_2)_n$ nanoclusters, n = 2 to 4, which serve as models for the bulk TiO_2 surface were studied at the CCSD(T)/aD//B3LYP/DZVP2 level to provide insights into how metal oxides can be used to convert biofuel into fuels or feedstocks for the chemical industry. The Lewis/Brønsted acidity and basicity on the Ti and O sites were correlated with various energetics. The oxidation of small Mg clusters by F and Cl was studied to interpret the observed chemiluminescence. The

computational results provide the best available energetics for these species and are critical to interpreting the experiments which date back more than 40 years.

Key phrases: geochemistry, group IV transition metal oxides, CO_2 sequestration, catalysis, ethanol dehydration and dehydrogenation, Mg_2F

DEDICATION

This dissertation is dedicated to my family, my friends, my teachers and mentors who have inspired and motivated me to always go after my dreams in different stages of my life.

LIST OF ABBREVIATIONS AND SYMBOLS

AO	atomic orbital
ADF	Amsterdam Density Functional
ATcT	Active Thermochemical Tables
aug-cc-pVNZ	augmented, correlation consistent, polarized valence N zeta basis sets, where N = double (D), triple (T), quadruple (Q), or 5.
aug-cc-pVNZ-PP	aug-cc-pVNZ basis sets with pseudopotentials for heavy atoms, where N = double (D), triple (T), quadruple (Q),
aug-cc-pwCVNZ	augmented, correlation consistent, polarized weighted core-valence basis sets where N = double (D), triple (T), quadruple (Q),
aug-cc-pwCVNZ-DK	aug-cc-pwCVNZ basis sets with all electron DK basis sets where N = double (D), triple (T), quadruple (Q),
aug-cc-pwCVNZ-PP	aug-cc-pwCVNZ basis sets with pseudopotentials for heavy atoms where N = double (D), triple (T), quadruple (Q),
aN	aug-cc-pVNZ basis sets
aN-PP	aug-cc-pVNZ-PP basis sets
au	atomic units
awN	aug-cc-pwCVNZ basis sets
awN-DK	aug-cc-pwCVNZ-DK basis sets
awN-PP	aug-cc-pwCVNZ-PP basis sets
B3LYP	Becke 93 (exchange), Lee-Yang-Parr (correlation) DFT functional
BDE	bond dissociation energy
BP86	Beck (exchange), Perdew 86 (correlation) DFT functional
CBS	complete basis set
CDE	Coulombic dissociation energy

CC	coupled cluster
CCSD	coupled cluster singles and doubles
CCSD(T)	coupled cluster singles, doubles, and perturbative triples
CI	configuration interaction
CISD	configuration interaction singles and doubles
CV	core-valence
ΣD_0	total atomization energy
DFT	density functional theory
DK	Douglas-Kroll-Hess
DZVP2	DFT optimized double zeta valence basis set with polarization functions
ΔE_{CBS}	complete basis set energy change
ΔE_{CV}	core valence set energy change
ΔE_{SR}	scalar relativistic energy change
ΔE_{SO}	spin orbit energy change
ΔE_{ZPE}	zero point energy change
e^-	electron
η	hardness
EA	electron affinity
ECP	effective core potential
EDA	energy decomposition analysis
FA	fluoride affinity
FCI	full configuration interaction
FPD	Feller-Peterson-Dixon
ΔG_{gas}	gas phase Gibbs free energy
GGA	generalized gradient approximation

GTO	Gaussian-type orbital
$\Delta H_{f,0K}$	enthalpy of formation at 0 K
$\Delta H_{f,298K}$	enthalpy of formation at 298 K
ΔH_{rxn}	reaction change in enthalpy
$\hat{H}$	molecular Hamiltonian operator
h	Plancks's constant
H	enthalpy
HCTH407	Hamprecht-Cohen-Tozer-Handy exchange correlation DFT functional
HF	Hartree-Fock
HSE06	A recommended version of the full Heyd-Scuseria-Ernzerhof functional
IE	ionization energy
χ	electronegativity
K	equilibrium constant
k	rate constant
k_B	Boltzmann constant
KS	Kohn-Sham
LCAO	linear combination of atomic orbitals
LDA	local density approximation
M06	A hybrid DFT functional of Truhlar and Zhao
M06L	A hybrid DFT functional of Truhlar and Zhao
MBPT	many-body perturbation theory
MD	molecular dynamics
MVD	the mass-velocity and 1-electron Darwin terms in the Breit-Pauli Hamiltonian

MO	molecular orbital
MP*n*	n^{th} order Møller-Plesset perturbation theory
NIST	National Institute of Standards and Technology
NIST-JANAF	National Institute of Standards and Technology - Joint Army-Navy-Air Force
PA	Proton Affinity
PBE	Perdew-Burke-Ernzerhof (exchange), Perdew-Burke-Ernzerhof (correlation) DFT functional
PBE0	Perdew-Burke-Ernzerhof (exchange), Perdew-Burke-Ernzerhof (correlation) DFT functional
PP	pseudopotential
PW91	Perdew-Wang 91 (exchange), Perdew-Wang 91 (correlation) DFT functional
QCISD(T)	quadratic configuration interaction singles, doubles, and perturbative triples
R	gas constant
S	entropy
SCF	self-consistent field
SI	Supporting Information
SO	spin-orbit
SR	scalar relativistic
STO	Slater-type orbital
τ-HCTH	an improved HCTH407 DFT functional using the kinetic-energy Tau
τ-HCTHhyb	Hybrid functional using the τ-HCTH functional
T	temperature
TAE	total atomization energy

TC	temperature correction
TDE	total dissociation energy
TISE	time-independent Schrödinger equation
TMO	transition metal oxide
TPSSh	Tao-Perdew-Staroverov-Scuseria hybrid nonempirical metal-generalized gradient exchange-correlation DFT functional
TRDE	total reaction dissociation energy
TS	transition state
VEE	vertical excitation energy
W	partition function
ωB97X	Head-Gordon and coworkers' functional including long range corrections
ωB97X-D	Head-Gordon and coworkers' functional including long range and empirical dispersion corrections
ZPE	zero point energy
>	greater than
<	less than
=	equal to
~	approximately
Å	Angstrom
°	degrees
±	plus or minus

ACKNOWLEDGMENTS

I want to say thank you to my parents who raised me and encouraged me to follow my heart and to never be afraid of dreaming big. I also want to thank my grandma, Duodi Wang: you have used your whole life to show our family the significance of hard work and resilience. And you have always supported your children and grandchildren to pursue higher education for broader choices in life. These directions from my parents and my grandma have influenced me whenever I have faced a challenge, and this has helped me believe that I can reach my goals in the life stages in front of me.

I would like to thank my husband, Chris Floyd, for being my biggest supporter in what I have done and the choices I have made. Your deep trust in me and respect for me as a responsible, capable, and smart individual who is proactively in charge of my own life has encouraged my successes, and I support you in the same way. Together, we have been growing as individuals as well as a couple. The strength of our relationship is one of the main reasons that I am very excited and hopeful for our future.

I also want to express my thanks to my friends for companionship for the past five years. You have shared a variety of wisdom and new perspectives toward life. Because of you, I was able to see and understand the capacity of life and how different choices can influence one's life. Also, thank you for being there for me and comforting me when I felt down and was self-doubting. Because of your unending support, I found the belief that everything will turn out to be fine.

I would like to thank my group members. The past five years of this PhD program has been the most challenging period of my life, so thank you to each of you for accompanying me through the different phases of my life in research. You have taught me what a collaborative team is, what a reliable support group in research is, and how diligent hard work can make a difference in the long run. All of these have served me well. And I believe all of you can reach your life goals in the bright future ahead of you.

Finally, I want to thank my advisor Dr. David A. Dixon. When I joined the group, I did not have any background in computational chemistry, and I was intimidated by how complex this field of knowledge seemed to be. Thank you for showing me how to approach a problem like a scientist and how to break down complicated issues into several simple general chemistry questions. This mindset of thinking is one of the most valuable and useful things I have learned from you in the past five years, and I have drawn a great deal of courage and confidence from this. I feel I am capable of learning anything and tackling any scientific difficulties in the future.

CONTENTS

LIST OF TABLES

LIST OF FIGURES

CHAPTER 1

INTRODUCTION

Background

Global warming is leading to more extreme weather events like flooding, melting of glaciers and the polar ice caps, and high heat events. As greenhouse gases are released into the atmosphere, too much of the heat radiated from the Earth is trapped which contributes to a global temperature increase. CO_2 is one of the main greenhouse gases that is influencing global warming and climate change. Combustion of fossil fuels by man is a primary source for the release of CO_2 into the atmosphere. Since the beginning of the Industrial Revolution, the concentration of CO_2 has increased from 280 ppm to 419 ppm in 2022.[1] There are, in general, two ways of reducing the concentration of CO_2 in the atmosphere. One way is to prevent releasing CO_2 by not burning fossil fuels for their energy content and, instead, exploring alternative, environmental-friendly energy resources. The other way is to capture and sequester the existing gas phase CO_2 into liquid or solid phase.

Various methods have been developed to capture and sequester CO_2. Mineral carbonation is one way to fix CO_2 in the form of insoluble carbonates where CO_2 can be directly kept sequestered in the subsurface.[2,3,4] Ca and Mg are the most common elements forming minerals and these minerals exist in large quantity. Once CO_2 is fixed in the form of carbonates, regeneration of CO_2 is almost impossible since that requires input of energy equivalent to decomposition of calcite and magnesite, which are very thermodynamically stable[5,6,7] and have

existed on Earth for hundreds of millions of years. As the carbonation is exothermic, the kinetics of the reactions will need to be considered. Two ways of mineral carbonation have been studied, carbonation of minerals at high temperature or carbonation in aqueous solution.[8] One approach to predicting the heats of formation of carbonate minerals is to use *ab initio* thermodynamics based on density functional theory (DFT).[9,10,11,12,13] However, an issue with this approach is that errors that are not systematic can be found in the energetics. There is thus a need to develop a benchmark database of reliable gas phase heats of formation based on the Feller-Peterson-Dixon (FPD) approach.[14,15,16,17,18,19,20,21,22] This dissertation describes such calculations for metal carbonates, bicarbonates, and bicarbonate-hydroxides for a wide range of divalent metals. These results also provide data for the prediction of cohesive energies if the heats of formation of the mineral are known[5,6,7] which can be used to test convergence in terms of the size of a molecular cluster.[23,24,25,26,27,28]

Transition metal oxides (TMOs) are also promising materials for the capture and sequestration of CO_2, for example, TiO_2,[29,30,31,32,33] ZrO_2,[34,35,36,37] and WO_3,[38,39] which can act as a sorbent to physiosorb or chemisorb CO_2 or serve as a catalyst to sequester and convert CO_2 into organic molecules. The Dixon group had previously reported studies of the binding of CO_2 to Group 4 and Group 6 nanoclusters.[40] A subsequent experimental and computational study[41] suggested that there was a center carbonate binding site for CO_2 addition to the $Ti_3O_6^-$ anion. In the correction to this work,[42] the authors showed that the original calculations were flawed based on a preliminary communication from the Dixon group on the computational approach. Their structure for CO_2 binding to the anion was different from what had been reported for the neutral. This dissertation describes an extension of previous work[40] on the binding of CO_2 to the neutral trimer clusters to the trimer anions to better understand these binding sites. The current work

shows that the central binding site is only a low energy site on the $Ti_3O_6^-$ cluster and is not the lowest energy binding site for any of the anions.

TMOs can also serve as catalyst for the conversion of biofuel into fuels to provide a renewable energy source as a replacement for fossil fuels or feedstocks for the chemical industry. Ethanol is a model of biofuel which can undergo dehydration and dehydrogenation on group IV and VI transition metal oxide surfaces. It has been reported[43,44,45] that the active Lewis acid metal sites for $(WO_3)_3$ and $(MoO_3)_3$ nanoclusters can serve as catalyst sites for the conversion of alcohols. The reactivity was correlated with the Lewis acidity of the metal site and the reducibility of the cluster and it was found that at least two alcohols are needed to match experiment. This dissertation describes an extension of this work to the study of a single ethanol on TiO_2 nanoclusters to compare the Group 6 nanocluster catalysis and to catalysis on the surface of bulk rutile TiO_2 (110).[46,47,48,49,50]

Computational Chemistry

Computational chemistry is an important and time-efficient method to predict chemical properties and reaction energetics for different kinds of systems, especially for those that are difficult or expensive to perform experimentally, or to probe regions of the potential energy surface like transition states which cannot be readily accessed by experiment. Available experimental results can be interpreted by the use of computational chemistry as well as guided for reasonable future design. The last 50 years have witnessed a fast growth in the field of computational chemistry with contribution from improvements in computational methods and algorithms, chemical theories, and supercomputing resources.

The focus of this dissertation is on electronic structure theory, one of the two main areas in computational chemistry, the other being molecular dynamics (MD) simulations[51] with

molecular mechanics force fields. Electronic structure theory is based on solutions to the time-independent Schrödinger equation (TISE) to represent the motion of electrons in molecular system which is shown in equation (1.1):

$$\hat{H}\Psi = E\Psi \tag{1.1}$$

where $\hat{H}$ is the molecular Hamiltonian, which represents the total energy operator of all kinetic and electrostatic interactions in molecules, Ψ refers to the wavefunction, and E refers to the total energy of the molecular system. Electronic structure theory is the primary computational method used in this dissertation. There are three electronic structure methods that can be used to solve the TISE: semi-empirical molecular orbital theory (SEMO), DFT, and correlated molecular orbital (MO) theory. SEMO is the cheapest method to calculate computationally because it is totally dependent on experimental parameters or parameters from higher-level computational approaches. *Ab initio* methods, which include both MO theory and DFT, however, only use physical constants obtained from first principles to resolve the TISE.[52] We note that DFT may have exchange-correlation functionals that are parameterized with respect to experiment so are not fully *ab initio*. The Born-Oppenheimer[51,53] approximation is used to separate the electronic and nuclear motion because the nuclei are much heavier than the electrons. This enables the TISE for electrons to be solved without having to deal with the heavier nuclei. The corresponding electronic Hamiltonian ($\hat{H}_{elec}$) is given in equation (1.2)

$$\hat{H}_{elec} = -\sum_{i=1}^{N} \frac{1}{2}\nabla_i^2 - \sum_{i=1}^{N}\sum_{A=1}^{M} \frac{Z_A}{|R_A - r_i|} + \sum_{i=1}^{N}\sum_{j>i}^{N} \frac{1}{|r_j - r_i|} \tag{1.2}$$

where ∇ represents the gradient operator, N equals to the number of electrons of the molecular system, M is the number of nuclei, A represents the nuclei, Z is the atomic number, R and r represent coordinates of the nuclei and electrons respectively, and i and j are denoted as individual electrons. The three terms within $\hat{H}_{elec}$ in equation (1.2) are from left to right: the

repulsive kinetic energy of the electrons, the attractive nuclear-electron potential, and the repulsive electron-electron potential.

The first derivative of the energy and the nuclear coordinates $dE/\{dx_i\}$ allows the geometry to be optimized. When $dE/\{dx_i\} = 0$, the second derivative of the energy with the respect to the nuclear coordinates can be used to calculate vibrational frequencies. The second derivative can also be used to determine if the optimized molecular geometry, is an energy minimum, a transition state, or some other complex saddle points on the potential energy surface.

Molecular Orbital (MO) Theory

Hartree-Fock (HF) theory,[54,55,56,57,58,59,60,61] a self-consistent field method, was developed in the 1920's and 1930's, soon after the discovery of the TISE in 1926. The HF method is the earliest and simplest approach to describe the electronic structure of molecules mathematically as analytical solutions for many-electron systems do not exist, HF theory provides an approximate solution to the TISE by calculating the total energy using a basis set with hydrogen-like atomic orbitals in Slater determinants.[52] A mean-field theory is applied by approximating the interactions of each electron in a field of n-1 electrons by an average of all the electron-electron interactions with each electron. One problem arises though using this mean-field theory due to the lack of electron correlation of a pair of electrons in the same orbital. The Pauli exclusion principle[62] allows two electrons with the opposite spins to occupy in the same space. Coulomb repulsion, however, makes these two electrons avoid each other, even though the electron exchange energy is fully accounted for in the HF method. Another weakness of the original HF method comes to the neglection of relativistic effects which is an inherent assumption for the method as the non-relativistic TISE is being solved. Overall the energy from the HF wave

function is missing several percent of the total energy given a sufficiently large basis set, but the remaining the energy is needed to model chemical phenomena accurately.

To solve the TISE for any given system, a wavefunction composed of molecular orbitals is needed, and one way to do this is to use a linear combination of atomic orbitals (the LCAO approximation).[51] The LCAO approximation constructs molecular orbitals with individual mathematical functions that resemble atomic orbitals (AOs). These functions are called basis functions, and the collection of these functions is called a basis set. Once each atom is assigned a basis set, the best MO coefficients are achieved by variational minimization. There are two types of orbital function, Slater-type orbitals (STO) and Gaussian-type orbitals (GTO). GTOs with an exponent in r^2 are used in most electronic structure codes comparing to STOs since STOs are exponential functions in r which are difficult to integrate computationally. Therefore, STO-type basis functions are modeled as a linear combination of primitive GTOs because two-electron GTOs have simpler analytical solutions than STOs. Split valence basis sets, such as double zeta and triple zeta valence orbitals, provide multiple atomic functions for valence orbitals in each atom to provide better prediction of chemical interaction which mainly occur among valence orbitals. These multiple split valence basis sets provide different spatial properties which allows adjustment of the electron density according to the molecular environment through a linear combination. Increasing the number of basis functions leads to decreasing error for the LCAO approximation, and eventually achieves convergence of energy to the Hartree-Fock limit. The difference between the Hartree-Fock limit and the exact energy is defined as correlation energy.

Larger basis sets are usually required for more accurate energy, which means minimum basis sets are the least reliable because of over constraint of the MOs and less flexibility in the

orbital size adjustment needed for a good approximation of chemical bonding. To improve the approximation of electronic interactions besides using the split valence basis set[51] as mentioned above, polarization functions and augmented (aug) diffuse functions are also needed to provide more distortion capability on valence orbital and spatial extension of the basis set. , The latter is critical for anions who have large electron clouds, as well as in minimizing basis set superposition error (BSSE) referring to the situation where an atom overlaps and borrows basis sets from other atoms in a molecule. This dissertation mainly use correlation consistent (cc) polarized (p) valence (V) multiple split zeta (NZ) basis functions with augmented (aug) diffuse functions, denoted as aug-cc-pVNZ where N represents D, T, Q, 5, 6, etc. referring to double, triple, quadruple, quintuple, sextuple, etc, respectively.[63,64] The DFT calculation in the study of ethanol reactivity on $(TiO_2)_n$, n = 2 to 4, used the DFT optimized DZVP2 polarized valence double zeta basis set[65,66].

The lack of electron correlation in the self-consistent field solution of HF does not give reliable absolute energetics. By including electron correlation factor by adding more determinants to HF theory, a method known as post-HF, one can achieve an energy convergence to the exact solution of TISE.

Coupled-cluster (CC) methods[67] are a popular and reliable post-HF computational method for thermodynamic calculations on molecular system. The corresponding wavefunction is expressed exponentially as shown in equation (1.3).

$$\Psi_{CC} = e^{T} \Phi_0 \tag{1.3}$$

where Φ_0 is in the form of Slater determinant for HF molecular orbitals serving as a reference wavefunction. The exponential term e^T guarantees size extensity of wavefunction as well as

consistency which secures CC method to be one of the easiest-to-use post HF methods. The term e^T can be expanded as a Taylor series as shown in equation (1.4).

$$e^T = 1 + T + \frac{1}{2}T^2 + \frac{1}{6}T^3 + \cdots = \sum_{k=0}^{\infty} \frac{1}{k!}T^k \quad (1.4)$$

where T is the cluster operator which is determined by equation (1.5)

$$T = T_1 + T_2 + T_3 + \ldots + T_n \quad (1.5)$$

where n = 1 means single electron excitation, n = 2 means two electron excitation and so on. Including more electrons for excitation increases energy accuracy, like using CCSD (singles and doubles), CCSDT (singles, doubles and triples), etc. As n gets close to the number of electrons, the scale of excitations will reach full configuration interaction (CI), which is very expensive to calculate computationally. The CC method is a truncated version of full CI. CCSD(T)[68,69,70,71,72,73], however, uses a perturbative triples contribution from fourth-order Møller-Plesset (MP4) perturbation theory on top of the CCSD amplitudes. The CCSD method is iterative and scales approximately as N^6, where N refers to the number of basis functions, and CCSD(T) is non-iterative and scales as N^7.

The finite size of the basis sets introduces an error as well even though basis sets like aug-cc-pNVZ, (N = D, T, Q, etc.) for use in CCSD(T) calculations are quite large. An approximate complete basis set (CBS) limit can be obtained by using a variety of approaches[74] including a 3-point extrapolation formula in (1.6).

$$E_N = E_{CBS} + A \exp[-N(N-1)] + B \exp[-(N-1)^2] \quad (1.6)$$

where N = 2, 3, and 4 (D, T, and Q), E_N is the energy when the correlation consistent basis sets with the size N of apply, and E_{CBS} represents the CBS limit. There is also a 2-point extrapolation formula in (1.7)[75,76,77,78]

$$E_N = E_{CBS} + B/(l_{max})^3 \quad (1.7)$$

where N = 4 and 5 (Q and 5).

Density Functional Theory (DFT)

Density functional theory (DFT) is based on the theory by Hohenberg, Kohn and Sham[79,80] showing that ground state electronic energy can be determined by the electron density of a molecular system completely. DFT calculations are an alternative to *ab initio* MO methods for lower computational cost but with decent predictions of the resulting energy. The reason why DFT methods can cost less is that the energy calculations are performed in terms of a three-dimensional electron cloud, the density, which can be of lower cost in term of the growing size of the system. Compared to Hartree-Fock, a DFT calculation is more likely to provide more reliable results for a similar computational cost. The total energy *E* for DFT calculations is made of four components as shown in equation (1.8)

$$E[\rho] = T_s[\rho] + V_{ne}[\rho] + J[\rho] + E_{xc}[\rho] \quad (1.8)$$

where ρ represents the electron density, T_s represents the kinetic energy for the non-interacting system, V_{ne} represents the nuclear-electronic potential energy, J represents the classical electron-electron repulsive energy, and E_{xc} represents the exchange-correlation energy.[80] The exchange-correlation energy term is proposed by Kohn and Sham[80] to avoid the complexity of this term being distributed into the kinetic energy (small correction) and electronic repulsive energy in the exact functional. Kohn-Sham (KS) orbitals allow the use of machinery from the development of MO theory and are used in modern DFT calculations.

Different treatments of the exchange-correlation functional contribute to a variety of DFT methods. In general, there are three classes of DFT functional types: local density approximation (LDA) functionals[81,82] which only rely on electronic density, generalized gradient approximation

(GGA) functionals[83,84,85] which depend on both electronic density and it gradient, and hybrid functionals.[86] Hybrid functionals contain exchange-correlation energy partially from HF exact exchange with the remaining part of exchange and correlation from other sources.

A DFT hybrid functional B3LYP is the main DFT method used in this dissertation. The exchange-correlation energy term of B3LYP is comprised of the Becke 3-parameter exchange functional[87] and the Lee, Yang, Parr correlation functional[88] with an expression shown as below in equation (1.9)

$$E_{xc}^{B3LYP} = aE_x^{HF} + (1-a)E_x^{LDA} + b\Delta E_x^{B88} + cE_c^{LYP} + (1-c)E_c^{VWN} \quad (1.9)$$

where E_x^{HF}, E_x^{LDA} and ΔE_x^{B88} represent the exchange energy terms from HF, LDA, and GGA corrections, respectively; E_c^{LYP} and E_c^{VWN} represent the correlation energy terms from LYP and VWN corrections, respectively. The coefficients a, b and c come from experimental thermodynamic data and are equal to 0.20, 0.72, and 0.81, respectively. Although DFT methods provide better results than HF calculations, DFT calculations inherently lack of accurate through-space interaction energy,[89] and alternative approaches are usually needed to achieve more accurate thermodynamic values, for example, CCSD(T) methods as used in this dissertation work.

Composite Approaches

The most accurate composite method which can reach chemical accuracy of ±1 kcal/mol is the Feller-Peterson-Dixon method (FPD)[14,15,16,17,18,19,20,21,22] This method is developed by a collaboration between the Dixon group and the group of Peterson and Feller at Washington State University. The total atomization energy (TAE, $\Sigma D_{0,0K}$) is made up of five components; a large atomization energy term based on electronic energies extrapolated to the complete basis set (CBS) limit based on calculations at the single point CCSD(T) level using the aug-cc-pVNZ

basis sets where N = D, T and Q at least using the optimized geometries, and four additional smaller corrections (Equation 1.10). As an example, we assume the geometries are optimized at the B3LYP/aug-cc-pVTZ level, although they can be obtained at any accurate level.

$$TAE = \Delta E_{CBS} + \Delta E_{ZPE} + \Delta E_{CV} + \Delta E_{SR} + \Delta E_{SO} \quad (1.10)$$

The ΔE_{ZPE} correction is the zero-point energy correction from the B3LYP/aug-cc-pVTZ frequency calculation. The atomic spin orbit correction (ΔE_{SO}) is calculated by using the experimental values of each individual atom from Moore's tables.[90] The difference between the core and valence energies at the CCSD(T)/aug-cc-pwCVTZ level is denoted as the core-valence correction (ΔE_{CV}). A scalar-relativistic correction (ΔE_{SR}) is calculated with the second-order Douglas-Kroll-Hess (DK)[91,92,93] method using the all-electron aug-cc-pwCVTZ-DK basis set.[94] By following procedure from Curtiss and workers,[95] one can calculate gas phase heats of formation at both 0 K and 298 K as shown below using the TAE given in Equation 1.10 and the experimental heats of formation for the atoms with thermal corrections at 298 K (TC) of molecules from the B3LYP/aug-cc-pVTZ optimization level.

$$\Delta H_{f,0K,molecule} = \Sigma \Delta H_{f,0K,atoms} - TAE \quad (1.11)$$

$$\Delta H_{f,298K,molecule} = \Sigma \Delta H_{f,0K,molecule} + TC_{molecule} - \Sigma TC_{atoms} \quad (1.12)$$

Computational Thermodynamics

Energy changes in company with chemical and physical processes are associated with thermodynamics.[96] The change of internal energy (ΔU) of system equals the sum of heat (q) and work (w) as shown in equation (1.13) according to the 1st Law of Thermodynamics.

$$\Delta U = q + w \quad (1.13)$$

The internal energy of a molecule at 0 K is represented by the sum of molecular electronic energy and zero-point energy as shown in equation (1.14).

$$U_0 = E_{elec} + \sum_i \frac{1}{2} h\omega_i \quad (1.14)$$

The zero-point energy is a fundamental result of Heisenberg's Uncertainty Principle[97] and is approximated by using a quantum harmonic oscillator model. The internal energy of molecules of an ideal gas at any given temperature (T) requires addition of electronic, vibrational, translational, and rotational energy changes over the temperature range for U_0 as shown in equation (1.15) based on thermodynamic definition of an ideal gas.

$$U_T = U_0 + \Delta U_{0\rightarrow T}(elec) + \Delta U_{0\rightarrow T}(vib) + \Delta U_{0\rightarrow T}(rot) + \Delta U_{0\rightarrow T}(trans) \quad (1.15)$$

At constant pressure (P), the enthalpy (H) of the system is written in equation (1.16).

$$H = U + PV \quad (1.16)$$

For a given T, equation (1.16) can be rewritten as equation (1.17) using the ideal gas law for one mole of gas.

$$H_T = U_T + RT \quad (1.17)$$

According to the definition of the total entropy (S) of a system, S is related to the total number of all possible states in a system. S can be expressed as a function of a sum of contributions from electronic, translational, vibrational, and rotational motions of the molecule at any given T. The third law of thermodynamics is given in equation (1.18),

$$S = k_b \ln(W) \quad (1.18)$$

where k_b is Boltzmann's constant and W represents the number of states. The value of S can be obtained from the partition functions of translation, the harmonic oscillator, the rigid rotor, and any electronic contributions including symmetry aspects of a molecule.[98] Thus, the Gibb's free energy can be calculated from equation (1.19).

$$G = H - TS \quad (1.19)$$

The value of ΔG can be used to predict if a reaction is spontaneous at any given T and P. At the standard state, the change of ΔG is associated with the equilibrium constant (K) as shown in equation (1.20)

$$\Delta G^\circ = -RT\ln(K) \quad (1.20)$$

with T in degrees Kelvin and R the gas constant. Since the concept of chemical accuracy is defined by ± 1 kcal/mol, a factor of 10 at 298.15 K, corresponds to a difference in ΔG of 1.36 kcal/mol which is slightly larger than chemical accuracy.

Chapter Descriptions

It is critical to investigate possible solutions to reduce the CO_2 concentration and input into the atmosphere and feasible renewable energy sources to replace the use of fossil fuels. Understanding thermodynamics of mineral carbonates and transition metal oxides using computational methods provides us with useful insights on how CO_2 is captured and sequestered by different mechanisms, and how a simple model of biofuel, ethanol, could be converted into alternative chemicals.

Chapter 2 provides a set of accurate thermodynamic properties of divalent Ca, Mg, Fe, and Cd for carbonates, di-bicarbonates and bicarbonate-hydroxides as well as their corresponding hydrates, including gas phase heats of formation, cohesive energies, hydration energies and decomposition energies.[99] The gas phase heats of formation are calculated using the FPD approach where possible, which are used to benchmarked a set of various DFT functionals including those often used in bulk calculations and larger systems with a consideration of major issue for DFT functionals handling oxygen.

Chapter 3 is inspired from the work in chapter 2 and expands to a list of transition metals, Mn, Co, Ni, Cu, and Zn.[100] Besides studying the thermodynamics investigated in chapter 2,

chapter 3 also predicts metal exchange energies in the gas phase to show the reactivity of neutral and dication metals. The correlation between cohesive energy and ionic dissociation energy versus dication radii and hardness/softness was also examined. The work in chapter 2 and 3 allows further research on the growth and reactivity of carbonate nanoparticles, which has been studied by the Dixon group for the growth of MgO, $MgCO_3$, and $CaCO_3$ nanoparticles.[101,25,102] In addition, the work provides reliable thermodynamics to help better understand mineral formation mechanisms in nature as well as to interpret competitive incorporation into nanoparticles among mixed metal dications.

CO_2 can also be captured and sequestered by group IV and group VI metal oxides.[29, 31,32,33,3435,36,37,38,39] The Dixon group has studied the thermodynamics of neutral isomers of CO_2 binding to neutral group IV and VI metal oxides.[40] A novel neutral and anionic isomer of carbonate trimer titanium oxide was later reported[41,42] with a tridentate binding of CO_2 at the cluster center with 3 Ti-O bonded to 3 different Ti atoms. Chapter 4 investigated this new isomer together with previously available trimer isomers in neutral and ionic species for the group IV metals using couple cluster CCSD(T) theory with correlation-consistent weighted core basis sets on group IV metals based on density functional theory B3LYP geometries.[103] This work shows the same lowest energy structure as reported[40] by the Dixon group with the novel isomer considered. The lowest energy anionic structure has a terminal carbonate binding to the metal oxide cluster for all group IV metals with the center structure site having a slightly higher binding energy only for Ti. This study is important because it provides accurate thermodynamic CO_2 binding energies for neutral and anionic group IV transition metals with an exploration of a variety of isomers, which contributes insight on CO_2 capture and sequestration chemistry with transition metal oxides.

Ethanol is a very simple model of biofuel, which is a possible replacement as a renewable alternative energy source for fossil fuels. Group IV and VI transition metal oxide nanoclusters are effective catalysts for ethanol conversions. Ethanol reactivity on $(WO_3)_3$ and $(MoO_3)_3$ nanoclusters has been studied where the Lewis acidic metal site plays an important role in the physiosorption and chemisorption of ethanol; two ethanols are needed to match experiments. Chapter 5 studied ethanol dehydration and dehydrogenation on $(TiO_2)_n$ (n = 2 - 4) nanoclusters which serve as a model of active Lewis acidic sites of bulk TiO_2 surface at the CCSD(T)/aug-cc-pVDZ(-PP(Ti)) level. Only one ethanol is needed for the ethanol reaction on titanium oxide nanoclusters. Correlations between physisorption and chemisorption and ethylene removal energy versus Lewis/Brønsted acidity/basicity have been investigated to better understand the drive of the reactions.

Chapter 6 investigates possible ground state structures relevant to magnesium cluster oxidation reactions with halogens and the reaction thermodynamics with electronic structure calculations at the CCSD(T) level.[104] Vibrational frequencies for the ground states were also calculated as were UV-vis spectra transitions using time dependent DFT. The electronic structure results were used to interpret the results of chemiluminescent experiments which date back over 40 years. A near ultraviolet transition of Mg_2F in emission from the reaction between magnesium clusters and fluorine atoms was observed and assigned on the basis of the calculations. Heats of formation of possible structures of Mg_2F and Mg_3F were predicted using the FPD approach, as well as Mg_2Cl and Mg_3Cl. The formation of magnesium halides can be described as an ion pair of Mg_n^+ and F^-/Cl^-.

CHAPTER 2

THERMODYNAMICS OF METAL CARBONATES AND BICARBONATES AND THEIR HYDRATES FOR Mg, Ca, Fe, and Cd RELEVENT TO MINERAL ENERGETICS

Introduction

Metal carbonates play an important role in geological and industrial processes, including paleoindicators of conditions relevant to mineral deposition,[1,2,3,4,5,6] biomineralization[7,8,9,10] large scale sinks for CO_2,[11,12,13,14] environmental remediation,[15] precursors for the synthesis of complex nanostructures,[16,17,18] scale formation in pipelines and oilfields,[19] and properties of cement and concrete.[20] Although divalent Ca, Mg, Fe, and Cd all exhibit the same oxide structure (NaCl) and most stable anhydrous carbonate structure (calcite), their ability to form hydrated carbonate minerals is significantly different. Mg^{2+} forms the largest number of hydrated carbonate minerals of all the divalent cations (barringtonite $MgCO_3 \cdot 2H_2O$, nesquehonite $MgCO_3 \cdot 3H_2O$, lansfordite $MgCO_3 \cdot 5H_2O$, hydromagnesite $Mg_5(CO_3)_4(OH)_2 \cdot 4H_2O$, dypingite $Mg_5(CO_3)_4(OH)_2 \cdot 5H_2O$, pokrovskite $Mg_2(CO_3)(OH)_2$, and artinite $Mg_2(CO_3)(OH)_2 \cdot 3H_2O$), whereas Fe^{2+}, which has nearly an identical size,[21] does not exhibit any known hydrated carbonates. Two hydrated Ca carbonates are known in nature (monohydrocalcite $CaCO_3 \cdot H_2O$, and ikaite $CaCO_3 \cdot 6H_2O$), but no hydrated Cd carbonates are known. Although Ca forms the most abundant carbonates found in nature, Mg has been shown to play a key role in their formation, likely through the greater ability to bind and incorporate water.[22,23] Hence quantifying binding energies of coordinated species is important to understanding the basis of geochemical observations.

Understanding and controlling the formation and transformation of divalent carbonates and their hydrates in geological and industrial processes is aided by knowledge of the underlying thermodynamics. Whereas thermodynamic data exists for the most common minerals, it is not available for mixed carbonates such as Cd incorporation into Ca carbonates, which is important for remediation, or for intermediates such as clusters and amorphous species that may form along nucleation pathways. Hence, theoretical calculations based on methods such as density-functional theory (DFT) can be used to address this gap. Unfortunately, widely used DFT methods for total energy calculations of crystalline minerals or materials, such as the generalized gradient approximation (GGA), have been shown to exhibit nonsystematic errors for reaction enthalpies of formation from the metal oxides (MO), water, and CO_2,[24,25] even with the addition of empirical dispersion corrections.[26,27,28] (See Table 2.1) For use in thermodynamic calculations, the DFT-GGA calculated heats of formation require corrections for these errors. In order to assess the thermodynamic viability of species such as the Fe analogue of nesquehonite $FeCO_3•3H_2O$ or the Cd analogue of ikaite $CdCO_3•6H_2O$ to address the question of why they have not been observed in nature, reliable heats of formation are needed. Moreover, there is a need for benchmarking density-functional methods against accurate correlated molecular orbital theory based calculations on model complexes that address the range of coordination in hydrated and carbonated complexes of Mg, Ca, Fe, and Cd.

A variety of computational studies of carbonates and other simple ions such as hydroxide have been reported.[29,30,31,32,33] Most of these studies have been done on bulk systems using density functional theory. In a few cases,[34,35] the energetics of smaller clusters have been benchmarked against correlated molecular orbital theory. In general, however, it is not clear how accurate such methods are for the prediction of thermodynamic quantities of the simple species

that make up the monomers in mineral systems. We have previously reported reliable calculated gas phase thermodynamic properties for a number of simple alkali and alkaline earth compounds in the gas phase[35,36, 37,38] and then, we used these values to predict the cohesive energy of different solid materials using the Feller-Peterson-Dixon (FPD) approach.[39,40,41,42] This approach is based on extrapolating CCSD(T) energies to the complete basis set limit and including additional corrections to the total atomization energy with the goal of achieving chemical accuracy of ± 1 kcal/mol in the predictions.

Our goal in the current work is to provide a set of accurate thermodynamic properties of divalent Ca, Mg, Fe, and Cd for carbonates and using the FPD approach where possible. We have then benchmarked a set of density functional theory (DFT)[43,44,45] functionals that span a range of types including those often used in bulk calculations.

Computational Methods

All structures were optimized at the DFT level using the B3LYP[46,47] hybrid exchange-correlation functional. These calculations were done with the aug-cc-pVTZ basis set for H, C, and O,[48,49] as well as for Mg and Ca,[50,51] and with the aug-cc-pVTZ-PP basis sets with effective core pseudopotential (ECP)[52] for Fe[53] and Cd.[54] We denote these basis sets as aT. For the simple Mg and Ca carbonates and bicarbonates, the B3LYP optimized geometries were reoptimized at the MP2 level [55,56] using aT basis sets. All of the above calculations were performed using the Gaussian16 software package.[57] The geometries for the small molecules (MO, MCl_2 and $M(OH)_2$) for M = Fe and Cd were optimized at the CCSD(T) level following our previous reported approach for the corresponding molecules for M = Mg and Ca.[37]

Coupled cluster R/RCCSD(T) or R/UCCSD(T)[58,59,60,61,62,63,64] single point calculations were performed at the above optimized geometries to predict accurate thermodynamic properties

of these molecules. All CCSD(T) calculations were performed using the MOLPRO 2015.1 program package.[65,66] For Fe and Cd carbonates, bicarbonates and the hydrated structures, the CCSD(T) calculation were performed using aug-cc-pV*n*Z basis sets (*n* = D, T, Q) for H, C and O, and aug-cc-pV*n*Z-PP basis sets for Fe and Cd. The 10 electrons in the 1s2s2p orbitals for Fe and the 28 electrons in the 1s2s2p3s3p3d orbitals for Cd[67] are modeled by relativistic pseudopotentials (PPs). For Mg and Ca carbonates, bicarbonates and the hydrated structures the CCSD(T) calculation were performed using aug-cc-pV*n*Z basis sets for H, C and O, and cc-pwCV*n*Z basis sets for Mg and Ca;[50,51] the electrons in the 1s orbitals for the first row elements (C and O) and Mg and 1s2s2p orbitals for Ca were not correlated in the calculations. The CCSD(T) energies were extrapolated to the complete basis set (CBS) limit by fitting to a mixed Gaussian/exponential (Eq. 1):[68]

$$E(n) = E_{CBS} + A \exp[-(n-1)] + B \exp[-(n-1)^2] \quad (1)$$

where n = 2, 3, and 4 (D, T and Q).

The extrapolation to the complete basis set limit and additional small corrections were calculated following the Feller-Peterson-Dixon (FPD) approach.[39,40,41,42] Total atomization energies (TAEs or ΣD_0) at 0 K were calculated from the following expression (Eq. 2) with Δ referring to the difference between the molecule (reactant) and the atomic products for each energy component:

$$\Sigma D_0 = \Delta E_{CBS} + \Delta E_{SR} + \Delta E_{CV} + \Delta E_{ZPE} + \Delta E_{SO} \quad (2)$$

Additional corrections to the CCSD(T)/CBS energy (ΔE_{CBS}) are necessary to reach chemical accuracy. The zero point energies (ZPEs) were taken from MP2/aT or B3LYP/aT calculations for the new M = Mg and Ca, and from B3LYP/aT level calculations for M = Fe and Cd as these are the levels at which the geometries were optimized. The ZPEs for the Mg and Ca diatomics,

triatomics, and di-hydroxides are from our previous work[37] as is that for CdO[69] (see Table A2.43 for a summary). The additional core-valence corrections (ΔE_{CV}) were calculated at the CCSD(T) level with the aug-cc-pwCVTZ basis set[70,71] for C and O, cc-pwCVTZ for Mg and Ca atoms,[50,51] and cc-pwCVTZ-PP (denoted wCVTZ(-PP)) basis sets for M = Fe and Cd.[53,54] The electrons in the 1s orbitals for C, O and Mg, and the electrons in the 2s2p orbitals for Ca were correlated in the calculations. Scalar relativistic corrections (ΔE_{SR}) including the pseudopotential corrections (Eq. 3) were calculated at the second order Douglas-Kroll-Hess (DK)[72,73,74] level with the all-electron (aug-)cc-pwCVTZ-DK basis sets[51,75] (denoted as wCVTZ-DK):

$$\Delta E_{SR} = \Delta E_{wCVTZ\text{-}DK} - \Delta E_{wCVTZ(\text{-}PP)} \quad (3)$$

where $\Delta E_{wCVTZ\text{-}DK}$ and $\Delta E_{wCVTZ(\text{-}PP)}$ are the valence electronic energy differences calculated at the CCSD(T)-DK/awCVTZ-DK and CCSD(T)/awCVTZ(-PP) levels respectively for Cd. This correction may involve a minimal amount of double counting for the Cd scalar relativistic effect as discussed below; as noted above, this does include a pseudopotential correction. For Fe molecules, due to computational reasons, ΔE_{SR} was included at the CI-SD (configuration interaction singles and doubles) level of theory using the aug-cc-pVTZ basis set. ΔE_{SR} is taken as the sum of the mass-velocity and 1-electron Darwin (MVD) terms in the Breit-Pauli Hamiltonian.[76] A potential problem arises in computing the scalar relativistic correction for the molecules with a PP present. There is the possibility of "double counting" the relativistic effect on the Fe when applying a MVD correction to an energy that already includes most relativistic effects via the RECP. Because the MVD operators mainly sample the core region where the pseudo-orbitals are small, we assume any double counting to be small as has been found for halogen thermodynamics.[77] Test cases for Cd showed the MVD and DK approaches were in agreement within 0.2 kcal/mol. The atomic spin-orbit corrections (ΔE_{SO}) for the heats of

formation were taken from the experimental values (C = -0.08 kcal/mol, O = -0.22 kcal/mol and Fe = -1.20 kcal/mol).[78]

Heats of formation at 0 K were calculated from these TAEs and experimental heats of formation of the atoms at 0 K. The values for C, H, O, and Cl are from the Active Thermochemical Tables (ATcT)[79,80,81] and are: 51.63 ± 0.00 kcal/mol for H, 170.03 ± 0.01 kcal/mol for C, 59.00 ± 0.00 kcal/mol for O, and 28.59 ± 0.00 kcal/mol for Cl. The values for Mg, Ca, and Fe are from the JANAF Tables:[82] 34.87 ± 0.2 kcal/mol for Mg, 42.38 ± 0.2 kcal/mol for Ca, and 98.7 ± 0.3 kcal/mol for Fe. The value for Cd is 26.73 ± 0.1 kcal/mol from the Yungman and Wagman compilations.[83,84] Heats of formation at 298 K were then calculated by following the Curtiss et al. procedure[85] using thermal corrections for the atoms (H = 1.01 kcal/mol, C = 0.25 kcal/mol, O = 1.04 kcal/mol, Mg = 1.19 kcal/mol and Ca = 1.37 kcal/mol, Fe = 1.08 kcal/mol and Cd = 1.49 kcal/mol). The heats of formations of the larger molecules, (mostly for M = Fe) were calculated using the hydrolysis energies at CCSD(T)/aT or aD levels as described below.

The following functionals were used in the DFT benchmarking: PW91,[86,87] BP86,[88,89] M06,[90] PBE,[91,92] PBE0,[93] B3LYP,[46,47] HCTH407,[94,95,96] HSE06,[97] M06L,[98] τ-HCTH,[99] τ-HCTHhyb,[99] TPSSh,[100] ωB97X,[101] and ωB97X-D.[102,103] The DFT functionals were chosen to span a range of types as well as those often used in solid state calculations relevant to geochemical systems. The ZPEs for all of the DFT benchmarks were taken from the DFT (B3LYP/aT) calculations (see Table A2.43).

All calculations were performed on local parallel high-performance Xeon and Opteron based Penguin Computing clusters at The University of Alabama, the DMC computer at the Alabama Supercomputer Center, and the large computer in the Molecular Science Computing

Facility in the William R. Wiley Environmental Molecular Sciences Laboratory at Pacific Northwest National Laboratory.

Results and Discussion

Molecular Geometries The optimized geometry parameters are reported in the Supporting Information (SI) and the pictures are shown in Figure 2.1 (see Table A2.44 for a summary of the geometries used for each calculation). Some general trends are discussed below. The small molecules (MO, MCl_2 and $M(OH)_2$) do not show geometry variations with the metal. The geometries of MCO_3, $M(HCO_3)_2$, and $M(OH)(HCO_3)$ all have bidentate carbonate binding with bite angles (OMO) that vary from 58° to 76° (See table in the SI). The $M(HCO_3)_2$ have the two bicarbonate groups in approximately perpendicular planes with torsion angles of around 84° to 86°. The HOC bond angles are ~ 107° bent in $M(HCO_3)_2$ and in $M(OH)(HCO_3)$. The HOM bond angles are bent in $M(OH)(HCO_3)$, except for M = Ca, where ∠HOM is calculated to be linear, and for M = Mg where ∠HOM is close to being linear.

The addition of a single H_2O to $M(HCO_3)_2$ changes the structures, with the smallest change observed for the hardest and smallest metal (Mg^{2+}) and the largest geometry changes are observed for Cd^{2+}. The hardness was calculated using the formal density functional theory definition of $\eta = (IP - EA)/2$ where IP is the ionization potential and EA is the electron affinity. The experimental values[104] for the electron affinity and ionization potential were used (See SI) for the hardness and Shannon radii[105] were used for the ionic size. Note that IP = IP_3 and EA = IP_2 for a +2 ion. The largest metal ion is Ca^{2+}, and Cd^{2+} is just slightly smaller. The softest metal is Fe^{2+} followed by Cd^{2+}. The bicarbonates for M = Mg, Ca, and Fe remain bidentate but for M = Cd, one of the bicarbonate ligands becomes monodentate with a hydrogen bond between the H_2O and the free O on the bicarbonate. For M = Mg, Ca, and Fe, the O-H bond length in H_2O and the

asymmetric and symmetric stretch vibrational frequency and infrared intensities for the bound water molecule are similar to each other and to free H_2O. For M = Cd where the H_2O breaks the bidentate bonding of a bicarbonate ligand, a hydrogen bond forms between the water and the free oxygen. For $Cd(HCO_3)_2(H_2O)$, the water OH bond distance lengthens by 0.05 Å to 1.01 Å as compared to the corresponding OH bond in the water in the $Mg(HCO_3)_2(H_2O)$ complex. For $M(HCO_3)_2(H_2O)$, for M = Cd as compared to M = Mg, one O-H stretch of the water decreases by 51 cm^{-1} but the O-H stretch for the hydrogen bonded H decreases by 913 cm^{-1}. The shift is due to the partial proton transfer in the Cd structure from the H_2O to the HCO_3^- ligand with an increase in the O-H distance of 0.05 Å and a substantial decrease on the O-H…O hydrogen distance from 2.69 Å to 1.57 Å as compared to the Mg structure. There is a substantial increase in the IR intensity for the hydrogen bonded mode due to the partial proton transfer.

Addition of a second H_2O to $Mg(HCO_3)_2$ to form $Mg(HCO_3)_2(H_2O)_2$, leads to approximate octahedral coordination around the metal. Addition of the second H_2O to the $Ca(HCO_3)_2$ leads to a very distorted octahedral environment consistent with the fact that Ca^{2+} prefers a larger coordination number than 6.[106] For Fe, two different structures were optimized, one with octahedral coordination and one with two monodentate bicarbonate ligands, each of which is bonded to a different H_2O molecule. At the CCSD(T) level, the structure with octahedral coordination is lower in energy by 1.9 kcal/mol ($\Delta H_{f,0K}$). For $Cd(HCO_3)_2(H_2O)_2$, only one structure was optimized, where both bicarbonates are monodentate and form hydrogen bonds with the H_2O molecules.

The addition of two H_2O molecules to $M(OH)(HCO_3)$ leads to different type of structures depending on the M. For M = Mg, Ca, and Cd, the structures are similar with penta-coordination at the metal. For M = Fe, tetra-coordination at the metal is predicted with the bicarbonate ligand

becoming monodentate with a hydrogen bond between the H_2O and the free O on the bicarbonate.

Water binding to MCO_3 leads to different geometries (Figure 2.1). When one water binds to $MgCO_3$ the structure is planar with C_{2v} symmetry. For addition of one H_2O to $FeCO_3$ and $CdCO_3$, the hydrogen atoms from the water molecules slightly distort out of the plane to give a structure with C_s symmetry. For $CaCO_3$, the H_2O prefers to bind with an angle of about 130° to the metal-carbonate plane and one of the H_2O hydrogens is oriented toward a ligand oxygen to form a hydrogen bond (r = 1.74 Å). This structure is 6.0 kcal/mol (ΔH_{298}(B3LYP)) more stable than the corresponding planar C_{2v} structure. The addition of two waters leads to approximate axial binding with the $(H_2)O$-M-$O(H_2)$ angle varying from 120° to 180°. Addition of a third water leads to different orientation of the H_2O molecules depending on the metal. M = Fe in MCO_3 can take up to two waters in the first solvation shell, with the high spin Fe(II) being tetra-coordinate with this combination of ligands. The third H_2O goes into a second solvation shell. Addition of a fourth H_2O leads to approximate octahedral bonding at Mg and formation of Ca and Cd complexes with open sites.

Gas Phase Heats of Formation The CCSD(T) heats of formation for the gas phase species are given in Table 2.2. The error bars in the atomic heats of formation of the metals are all smaller than estimated errors in the electronic structure calculations. The values for Mg. Ca, and Fe are well-established as is the value for Cd. We have previously reported FPD values[37] for MgO, $Mg(OH)_2$, and $MgCl_2$ and the corresponding Ca compounds as well as CdO. Most of the experimental gas phase values for MgO are incorrect with only one value,[107] 36.0 ± 5.0, in agreement with all of the calculations as discussed previously. The experimental results for CaO are in better agreement with the calculations given the experimental error bars. For $MgCl_2$ and

$CaCl_2$ as well as $Mg(OH)_2$ and $Ca(OH)_2$, good agreement between experiment and the FPD results was found. The heat of formation for FeO is in good agreement with the value derived from the experimental dissociation energy from spectroscopy[108,109] and other calculations.[110] The heats of formation of $Fe(OH)_2$ and $FeCl_2$ are in good agreement with the JANAF values.[83] For CdO, our value for the dissociation energy is in good agreement with Peterson's value[111] obtained at the MRCI level but the heat of formation from the Russian compilation and another experimental report[112] is not consistent with our value. Although the agreement for $CdCl_2$ with the Russian compilation value[83] is outside of what we expect, it is still closer than the CdO value. Overall, the calculations show that we predict good values for the metal oxides, chlorides and hydroxides. We have previously shown that we can make reliable predictions of the heat of formation of HCO_3^- and H_2O.[113,114,115116]

For a number of hydrated compounds, the calculations become too large for full FPD. Thus, we used a different methodology to predict the heats of formation; first we calculated the hydration energy using reaction (4),

$$\text{metal complex} + n\ H_2O \rightarrow (\text{metal complex})(H_2O)_n \qquad (4)$$

and, second, we use the heat of formation of H_2O and of the metal complex to obtain the heat of formation of the hydrated complexes. The hydration energies as a function of basis set are given in the SI and do not exhibit a large basis set dependence. In all cases, the largest error from aD to CBS in the hydration energies is at most 3 kcal/mol, except for $CaCO_3(H_2O)_3$ with an error of 4 kcal/mol and for $Ca(CO_3)(H_2O)_4$ with an error of 6 kcal/mol. In all cases, the largest error between the aT basis set and the CBS limit in the hydration energies is at most 3 kcal/mol. Thus, our Fe heats of formation based on hydration energies at the aD level should be good to 3 kcal/mol assuming no error in the heats of formation of the dehydrated simpler clusters. Any

errors in the dehydrated clusters would increase the errors in the hydrated values for the Fe species. The aT values should be significantly closer to the CBS limit.

Cohesive Energies One can obtain information about cohesive energies of solid materials by combining the calculated heats of formation of the gaseous species with the experimental heats of formation of the solid.[35,117] The cohesive energy of a solid is the energy required to convert the solid into the gas. The cohesive energy is usually applied to monoatomic metals and is equivalent to the sublimation energy. All that is required to calculate the cohesive energy are the heat of formation of the solid and that of the gas phase species. Our focus is vaporization to the particular molecular monomer. The cohesive energies for the oxides follow the order Mg > Ca > Fe ~ Cd and are usually the largest. The cohesive energies for the carbonates follow the order Mg > Ca > Cd > Fe and are usually the second largest. For Fe, the cohesive energy for the oxide and carbonate are comparable. The chlorides tend to have lower cohesive energies than the other compounds followed by the hydroxides.

The compilation of Yungman[83] reports the heats of formation of the solid metal bicarbonates to be -304, -331.4, -224.6, and -207 kcal/mol, for Mg, Ca, Fe, and Cd, respectively. The corresponding cohesive energies are -57.1, -51.4, -50.7, and -75.5 kcal/mol for Mg, Ca, Fe, and Cd, respectively. The cohesive energies for the $M(HCO_3)_2$ are all negative so these species are not expected to be stable, consistent with the lack of observation of these species. This suggests that the heats of formation of the solid that have been reported are not for the pure bicarbonate composition.

Reaction Energies Gas phase decomposition reactions are reported in Table 2.3 for decomposition into the solid metal oxide, carbon dioxide, and water, as appropriate. The experimental values for the heats of formation at 298 K of H_2O of -57.8 kcal/mol, (the calculated

value is in good agreement) and of CO_2 of -94.1 kcal/mol were used.[83] The decomposition reaction for MCO_3 is the least endothermic and the order for the carbonates is Ca > Mg > Cd ~ Fe. The decomposition for the bicarbonates $Mg(HCO_3)_2$ requires the most energy and the order is Mg > Ca > Cd > Fe. The same order is found for the bicarbonate/hydroxide complexes. Fe^{2+} and Cd^{2+} are softer than Mg^{2+} and Ca^{2+}, which are relatively hard acids. The three bases CO_3^{2-}, OH^-. and HCO_3^- are all considered to be hard bases.[118]

The gas phase hydration reaction energies are in Table 2.4. As shown in the SI, there is not a strong dependence of the hydration energies on the augmented correlation-consistent basis sets in use here at the CCSD(T) level. Generally, for the same reactant, addition of a water molecule becomes easier as more water molecules are added because addition of more water molecules makes the ions less basic. For the bicarbonates, $M(HCO_3)_2$, the hydration energies are smaller than for the carbonates and are not that dependent on the metal. For the mixed bicarbonate/hydroxide, the hydration energies follow the order Ca ~ Mg > Fe > Cd. For MCO_3, the hydration energies are in the order Mg > Fe > Ca > Cd.

The fact that the strongest water binding energies are for $MgCO_3$ is consistent with the wide array of hydrated carbonates observed in nature. The water binding energies for $FeCO_3$ complexes are from 3.3 to 6.5 kcal/mol less than those for $MgCO_3$, which is noteworthy but not large. The Fe hydration energies are greater than for Ca, which does exhibit hydrates. Hence other reasons for the lack of hydrated $FeCO_3$ minerals observed in nature should be considered, namely kinetic aspects of the crystallization or dissolution process, larger thermodynamic differences that arise due to the crystal packing arrangements or solvation energies, or greater metastability relative to siderite than the hydrated Mg carbonates to magnesite.

$CdCO_3$ overall has the lowest hydration energies, with the exception of the monohydrate, which is a bit higher than the $CaCO_3$ complex. Hence monohydrootavite $CdCO_3 \cdot H_2O$ may form in nature, but the low concentration of Cd in the Earth's crust and the metastability of the monohydrate relative to otavite may make it extremely rare. The lower hydration energies compared to the $CaCO_3$ complex as the number of waters in the coordination sphere increases indicate that the crystal packing environment also contributes to greater metastability of monohydrootavite, as Cd is much softer than Ca. This softness is also reflected in the differences in the heats of formation between calcite and otavite. The relatively strong binding of the first water molecule to the $CdCO_3$ complex indicates that the presence of Cd will not significantly inhibit the crystallization pathways of calcium carbonates that utilize monohydrocalcite in environmental remedial applications.

Benchmark of DFT Functionals Because of the need to model larger systems, we benchmarked a number of DFT functionals. We first show examples for the simple models: H_2O, CO_2, HCO_3^- and the O_2 bond dissociation energy. The results are shown in Table 2.5 and Figure 2.2. An important result is that most of the functionals provide a reasonable treatment for H_2O but there are errors of up to 9 kcal/mol. The GGA functionals are known[91] to exhibit significant errors in the O_2 $\Delta H_{f,0K}$ and this is reflected in our results, namely that these functionals can have errors of up to 23 kcal/mol (almost 1 eV). These same functionals with errors in the O_2 $\Delta H_{f,0K}$ have large errors in predicting the heats of formation of CO_2 and HCO_3^-. These functionals include PW91, BP86 and PBE. The error distributions for the heats of formation of O_2, H_2O, CO_2 and HCO_3^- are shown in Figure 2.2. The breadth of the distributions follow the order of $HCO_3^- > CO_2 > O_2 > H_2O$. H_2O has the narrowest distribution.

For Mg (Figure 2.3), the errors for the ionic molecules MgO, $MgCl_2$ and $Mg(OH)_2$, are generally smaller than the errors for the Mg carbonates and bicarbonates and their hydrates. $MgCl_2$ has the narrowest error distribution among all the Mg molecules. The largest errors for $Mg(OH)_2$ and MgO are 16 kcal/mol and 15 kcal/mol, respectively. For the large molecules, PW91, BP86 and PBE share the similar error breadth from 23 kcal/mol to 55 kcal/mol. For B3LYP, the errors vary from 12 kcal/mol to 32 kcal/mol, and for TPSSh, the errors vary from 14 kcal/mol to 49 kcal/mol. For the remaining functionals, the errors vary from 1 kcal/mol to 36 kcal/mol. Addition of water molecules to $MgCO_3$, $Mg(HCO_3)_2$ and $Mg(HCO_3)(OH)$ generally increases the errors with all of the functionals, except for PW91, M06 and PBE, for which the trends in the errors vary as changing the number of water molecules can either increase or decrease the errors. The width of the error distributions are in the order $Mg(HCO_3)_2$ > $Mg(HCO_3)(OH)$ > $MgCO_3$. The width of the error distributions of $MgCO_3$, $Mg(HCO_3)_2$ and $Mg(HCO_3)(OH)$ increases after adding water molecules.

We also tested the dependence of the PBE and PW91 functionals often used in solid state calculations on the use of the numerical basis sets in DMol[3]. Two different real space cutoffs r_c were utilized for benchmarking of the DMol[3] basis sets, 4.3 Å and 5.1 Å. A r_c of 5.1 Å is the most accurate for the gas phase isolated complexes, but can result in excessive computational time for periodic systems as cpu time scales as r_c^6. Hence a r_c = 4.3 Å is a reasonable compromise of accuracy and cpu time for solid state calculations. The deviations in the heats of formation for the Mg and Ca (see below) compounds are very similar to the Gaussian orbital results and are not strongly dependent on the value of r_c, although the dependence cannot be completely ignored.

Similar trends are predicted for the other metals. For Ca (Figure 2.4), $CaCl_2$ has the narrowest distribution with most errors staying below 7 kcal/mol and the largest error being 19 kcal/mol. The errors are a bit larger for CaO and $Ca(OH)_2$, and the functionals with the largest errors are PW91, BP86, and PBE, 26 to 28 kcal/mol for CaO, and 12 to 17 kcal/mol for $Ca(OH)_2$. For CaO, THCTH also has a large error of 24 kcal/mol. For all the large molecules, PW91, BP86 and PBE have the largest errors from 32 to 70 kcal/mol. Addition of water molecules to $CaCO_3$, $Ca(HCO_3)_2$ and $Ca(HCO_3)(OH)$ generally increases the errors for the B3LYP, HSE06 and TPSSh functionals, and decreases the errors with the PBE functional. For the remaining functionals, the trends in the errors vary as changing the number of water molecules can either increase or decrease the errors. The width of the error distributions are in the order $Ca(HCO_3)(OH) \sim Ca(HCO_3)_2 > CaCO_3$. The width of the error distributions of $CaCO_3$, $Ca(HCO_3)_2$ and $Ca(HCO_3)(OH)$ increase after adding water molecules.

For Fe (Figure 2.5), $Fe(OH)_2$ has the narrowest distribution with the largest error being 15 kcal/mol. For FeO and $FeCl_2$, most errors are over 10 kcal/mol. The largest error for FeO is 29 kcal/mol and for $FeCl_2$ is 34 kcal/mol. Although $MgCl_2$ and $CaCl_2$ both have narrow distributions, that for $FeCl_2$ is much broader. For all the larger Fe molecules, B3LYP has the narrowest distribution and the errors for PW91, BP86, M06 and PBE are large varying from 27 kcal/mol to 74 kcal/mol. Addition of water molecules to $FeCO_3$, $Fe(HCO_3)_2$ and $Fe(HCO_3)(OH)$ decreases the errors with the PBE, PBE0, HSE06, τ-HCTHhyb, ωB97X and ωB97X-D functionals, and increases the errors with the functional TPSSh. For the remaining functionals, the trends in the errors vary as changing the number of water molecules can either increase or decrease the errors. As there are two structures for $^5Fe(HCO_3)_2(H_2O)_2$, we use the more stable one with two bidentate bicarbonates. The width of the error distributions are in the order $FeCO_3$

> $Fe(HCO_3)_2$ > $Fe(HCO_3)(OH)$. The width of the error distributions of $FeCO_3$, $Fe(HCO_3)_2$ and $Fe(HCO_3)(OH)$ increase after adding water molecules.

For Cd (Figure 2.6), the largest errors for $CdCl_2$, CdO, and $Cd(OH)_2$ are comparable at 10 to 13 kcal/mol. The largest errors for CaO and FeO are more than a factor of 2 larger than that for CdO. The largest errors for MgO are also larger than those for CdO by a smaller amount. For all of the larger molecules, PW91, BP86 and PBE have the largest errors from 25 to 55 kcal/mol. Adding water to $CdCO_3$, $Cd(HCO_3)_2$ and $Cd(HCO_3)(OH)$ results in an increase in the error with almost all the methods except for PW91 and HCTH407, where the errors do not increase or decrease consistently, and PBE, where the errors decrease. For $CdCO_3$, we were unable to get the wavefunction to converge properly for the HCTH407 and τ-HCTH functionals. The width of the error distributions are in the order $Cd(HCO_3)_2$ > $Cd(HCO_3)(OH)$ HCO_3> $CdCO_3$. The width of the error distributions of $CdCO_3$, $Cd(HCO_3)_2$ and $Cd(HCO_3)(OH)$ increase after adding water molecules.

Conclusions

There is significant interest in the properties of minerals containing Mg, Ca, Fe and Cd complexes with carbonate, bicarbonate and bicarbonate/hydroxide as well as various hydrates for a broad range of geochemical applications. The FPD approach based on CCSD(T) calculations extrapolated to the CBS limit was used to predict the heats of formation of a range of complexes of these metals in the +2 oxidation state. These values serve as benchmarks for more approximate DFT-based methods using different exchange-correlation functionals. For compounds whose heat of formation in the bulk is known, the cohesive energy was calculated. The cohesive energies of MO and MCO_3 are larger than MCl_2 and $M(OH)_2$, consistent with the Coulombic interaction of a + 2 and a -2 charge in the former and of two +2 and -1 interactions in

the latter. The cohesive energies of the Mg and Ca complexes are much larger than those of Fe and Cd, consistent with the fact that the former +2 ions are harder than the latter +2 ions. The calculations also show that there are likely errors with the reported heats of formation of the bicarbonates in the solid state as the cohesive energies are negative, consistent with the fact that these compounds are not observed. From the gas phase decomposition energies of MCO_3, $M(HCO_3)_2$ and $M(HCO_3)(OH)$ we can determine the order of reaction energies as $MCO_3 < M(HCO_3)(OH) < M(HCO_3)_2$ and by metal as: Mg ~ Ca > Cd ~ Fe. Mg^{2+} and Ca^{2+} are harder than Fe^{2+} and Cd^{2+} consistent with this order. The hydration energies of the complexes were also calculated. The average hydration energy per water decreases with additional water molecules. $MgCO_3$ has the largest hydration energy per water consistent with the fact that bulk $MgCO_3$ complexes with water are the ones most commonly observed in minerals. The gas phase hydration energies show the order as Mg > Fe > Ca ~ Cd. There are a number of bulk hydrated Mg complexes that exist as minerals consistent with these observations. However, there are also a number of hydrated Ca complexes that occur as minerals whereas there are few if any for Fe suggesting that a number of factors are important in determining the stability of the bulk mineral hydrates. Hydrated Cd compounds are rarely observed in nature consistent with a low hydration energy per water and the low concentration of Cd in the Earth's crust. The relative high hydration energy of adding the first water molecule to the $CdCO_3$ complex indicates that the presence of Cd will not significantly inhibit the crystallization pathways of calcium carbonates with one water complexed.

The reliable FPD heats of formation were used to benchmark various DFT exchange-correlation functionals. Not one DFT functional could provide chemical accuracy to ± 1 kcal/mol for all of the compounds calculated in this study. The approach used to calculate the DFT heats

of formation is based on atomization energies. In fact, the averages of the absolute values are all significant as shown in Table 2.6. Heats of formation involving oxygen have issues at the DFT level.

The issue with oxygen and the O_2 BDE is a well-known problem[91] for many DFT functionals and plays an important role here. The functionals producing the largest average unsigned errors of 34.2, 36.2, and 32.4 kcal/mol are BP86, PW91, and PBE, respectively. The latter two functionals are often used to model minerals in the solid state. The best functionals are ωB97X and ωB97X-D with average unsigned errors of 9.8 and 10.2 kcal/mol, respectively for the compounds containing metal atoms. The O_2 heat of formation errors are 4.1 and 3.7 kcal/mol for these functionals, respectively.

Tables

Table 2.1. Error compared to experiment for reaction enthalpies, ΔH (0K) for formation from the oxides (MO, CO_2, H_2O) normalized per metal cation in the stoichiometric formula (kcal/mol) PBE+G06 (with empirical dispersion).

Structure	**Stoichiometry**	Mg[24]	Ca[25]	Fe
Brucite (Mg)	$M(OH)_2$	0.9	2.8	11.8
Calcite (Ca)	MCO_3	6.2	6.9	5.5
Monohydrocalcite (Ca)	$MCO_3•H_2O$		2.5	
Nesquehonite (Mg)	$MCO_3•3H_2O$	-1.8		
Lansfordite (Mg)	$MCO_3•5H_2O$	-12.9[a]		
Ikaite (Ca)	$MCO_3•6H_2O$		-9.0	
Pokrovskite (Mg)	$M_2(OH)_2CO_3•3H_2O$	-0.7		
Hydromagnesite (Mg)	$M_5(CO_3)_4(OH)_2•4H_2O$	-19.1		

[a] Estimated using ab initio thermodynamics and experimental data

Table 2.2 Calculated gas phase heats of formation at 0K and 298 K, experimental heats of formation of the solid, and calculated cohesive energies all in kcal/mol.

Molecule	Calculation[a]	$\Delta H_{f,0K}$ gas	$\Delta H_{f,298K}$ gas	$\Delta H_{f,298K}$ solid	Cohesive E
MgO	FPD[37]	32.5	32.4	-143.7	176.1
$MgCl_2$	FPD[37]	-95.0	-95.1	-153.3	58.2
$Mg(OH)_2$	FPD[37]	-130.4	-132.7	-221.0 ± 0.2	88.3
$MgCO_3$	FPD[35]	-110.4	-111.7	-265.7	154.0
$Mg(HCO_3)_2$	FPD	-356.9	-360.9		
$Mg(HCO_3)(OH)$	FPD	-242.3	-245.0		
$Mg(HCO_3)_2(H_2O)$	FPD	-431.0	-435.6		
$Mg(HCO_3)_2(H_2O)_2$	Hydration	-501.9	-507.8		
$Mg(HCO_3)(OH)(H_2O)_2$	FPD	-391.9	-397.8		
$MgCO_3(H_2O)$	FPD	-200.6	-202.9		
$MgCO_3(H_2O)_2$	FPD	-285.9	-290.0		
$MgCO_3(H_2O)_3$	FPD	-363.5	-369.0	-472.5 ± 0.1	103.5
$MgCO_3(H_2O)_4$	FPD	-438.9	-446.1		
CaO	FPD[37]	5.0	4.7	-151.8	156.5
$CaCl_2$	FPD[37]	-113.9	-114.9	-190.2	75.3
$Ca(OH)_2$	FPD[37]	-144.0	-146.5	-235.7	89.2
$CaCO_3$	FPD	-148.1	-149.5	-288.5 ± 0.2	139.0
$Ca(HCO_3)_2$	FPD	-379.0	-382.6		
$Ca(HCO_3)(OH)$	FPD	-260.8	-263.4		
$Ca(HCO_3)_2(H_2O)$	FPD	-453.9	-458.4		
$Ca(HCO_3)_2(H_2O)_2$	FPD	-521.8	-527.4		
$Ca(HCO_3)(OH)(H_2O)_2$	FPD	-411.8	-417.3		
$CaCO_3(H_2O)$	FPD	-229.6	-232.3	-357.8 ± 0.2	125.5
$CaCO_3(H_2O)_2$	FPD	-310.9	-314.9		
$CaCO_3(H_2O)_3$	FPD	-385.2	-390.9		
$CaCO_3(H_2O)_4$	FPD	-465.2	-471.9		
^5FeO	FPD	61.8	61.8	-65.0	126.8
$^5FeCl_2$	FPD	-32.9	-32.7	-81.9	49.2
$^5Fe(OH)_2$	FPD	-80.7	-81.8	-137.2	55.4
$^5FeCO_3$	FPD	-50.8	-51.8	-179.4	127.6
$^5Fe(HCO_3)_2$	FPD	-271.7	-275.1		
$^5Fe(HCO_3)(OH)$	FPD	-172.5	-174.8		
$^5Fe(HCO_3)_2(H_2O)$	Hydration	-346.5	-350.7		
$^5Fe(HCO_3)_2(H_2O)_2$[b]	Hydration	-410.9	-417.4		
$^5Fe(HCO_3)_2(H_2O)_2$	Hydration	-412.8	-418.4		

$^5Fe(HCO_3)(OH)(H_2O)_2$	Hydration	-314.0	-319.3		
$^5FeCO_3(H_2O)$	Hydration	-137.8	-139.7		
$^5FeCO_3(H_2O)_2$	Hydration	-213.5	-217.0		
$^5FeCO_3(H_2O)_3$[c]	Hydration	-290.5	-295.8		
CdO	FPD[69]	64.9	64.6	-61.7	126.3
$CdCl_2$	FPD	-50.2	-50.4	-93.6	43.2
$Cd(OH)_2$	FPD	-68.8	-70.5	-134.1	63.6
$CdCO_3$	FPD	-47.3	-48.5	-179.4	130.9
$Cd(HCO_3)_2$	FPD	-278.2	-281.7		
$Cd(HCO_3)(OH)$	FPD	-171.8	-174.4		
$Cd(HCO_3)_2(H_2O)$	Hydration	-348.1	-353.2		
$Cd(HCO_3)_2(H_2O)_2$	Hydration	-418.3	-425.0		
$Cd(HCO_3)(OH)(H_2O)_2$	Hydration	-310.4	-313.1		
$CdCO_3(H_2O)$	Hydration	-129.5	-131.4		
$CdCO_3(H_2O)_2$	Hydration	-201.3	-205.2		
$CdCO_3(H_2O)_3$	Hydration	-276.7	-282.2		
$CdCO_3(H_2O)_4$	Hydration	-349.7	-356.5		

[a] All calculations at the CCSD(T) level. For the description of FPD, see the text. Heats of formation from hydration energies calculated from the reaction energy for Reaction (4) using the heat of formation of water and the calculated heat of formation of the metal complex. [b] Both bicarbonates are monodentate. [c] Only 2 H_2O in 1st solvation shell.

Table 2.3. Gas phase reaction energies from FPD values at 298 K in kcal/mol.

Reactant	Products	Reaction energies
$MgCO_3$	$MgO + CO_2$	50.0
$CaCO_3$	$CaO + CO_2$	60.1
$FeCO_3$	$FeO + CO_2$	19.5
$CdCO_3$	$CdO + CO_2$	19.0
$Mg(HCO_3)_2$	$MgO + 2\ CO_2 + H_2O$	147.3
$Ca(HCO_3)_2$	$CaO + 2\ CO_2 + H_2O$	141.3
$Fe(HCO_3)_2$	$FeO + 2\ CO_2 + H_2O$	90.9
$Cd(HCO_3)_2$	$CdO + 2\ CO_2 + H_2O$	100.3
$Mg(HCO_3)(OH)$	$MgO + CO_2 + H_2O$	125.5
$Ca(HCO_3)(OH)$	$CaO + CO_2 + H_2O$	116.2
$Fe(HCO_3)(OH)$	$FeO + CO_2 + H_2O$	84.7
$Cd(HCO_3)(OH)$	$CdO + CO_2 + H_2O$	87.1

Table 2.4. Gas phase hydration reaction energies from heats of formation, $\Delta H_{f,298K}$, in kcal/mol.

Product	ΔH	ΔH /H_2O
$MgCO_3(H_2O)$	-33.4	-33.4
$MgCO_3(H_2O)_2$	-62.7	-31.4
$MgCO_3(H_2O)_3$	-83.9	-28.0
$MgCO_3(H_2O)_4$	-103.2	-25.8
$Mg(HCO_3)_2(H_2O)$	-16.9	-16.9
$Mg(HCO_3)_2(H_2O)_2$	-31.3	-15.7
$Mg(HCO_3)(OH)(H_2O)_2$	-37.2	-18.6
$CaCO_3(H_2O)$	-25.0	-25.0
$CaCO_3(H_2O)_2$	-49.8	-24.9
$CaCO_3(H_2O)_3$	-68.0	-22.7
$CaCO_3(H_2O)_4$	-91.2	-22.8
$Ca(HCO_3)_2(H_2O)$	-18.0	-18.0
$Ca(HCO_3)_2(H_2O)_2$	-29.2	-14.6
$Ca(HCO_3)(OH)(H_2O)_2$	-38.3	-19.2
$^5FeCO_3(H_2O)$	-30.1	-30.1
$^5FeCO_3(H_2O)_2$	-49.6	-24.8
$^5FeCO_3(H_2O)_3$	-70.6	-23.5
$^5Fe(HCO_3)_2(H_2O)$	-17.8	-17.8
$^5Fe(HCO_3)_2(H_2O)_2$	-27.7	-13.9
$^5Fe(HCO_3)(OH)(H_2O)_2$	-28.9	-14.5
$CdCO_3(H_2O)$	-25.1	-25.1
$CdCO_3(H_2O)_2$	-41.1	-20.6
$CdCO_3(H_2O)_3$	-60.3	-20.1
$CdCO_3(H_2O)_4$	-76.8	-19.2
$Cd(HCO_3)_2(H_2O)$	-13.7	-13.7
$Cd(HCO_3)_2(H_2O)_2$	-27.7	-13.9
$Cd(HCO_3)(OH)(H_2O)_2$	-23.1	-11.6

Table 2.5. Errors in kcal/mol from FPD values for the $\Delta H_{f,0K}$ for O_2, H_2O, CO_2, and HCO_3^-.

Method	$^3O_2$	H_2O	CO_2	HCO_3^-
$\Delta H_{f,0K}$ gas	0.0	-57.1	-94.0	-171.8
PW91	-22.3	2.0	25.5	32.7
BP86	-21.1	6.8	22.0	30.8
M06	1.0	-2.9	8.2	3.3
PBE	-22.7	1.2	25.5	30.5
PBE0	-3.6	-6.0	1.2	-1.1
B3LYP	-2.8	-2.2	-2.7	-3.3
HCTH 407	-13.7	-2.4	9.1	7.8
HSE06	-2.4	-6.8	-0.3	-3.5
M06L	-3.1	-8.8	8.9	-4.4
τ-HCTH	-10.3	-4.3	3.8	1.8
τ-HCTH hyb	-7.7	-4.9	4.2	3.9
TPSSh	0.3	-6.3	-9.1	-15.6
ωB97X	-4.0	-4.3	-1.1	-1.5
ωB97X-D	-3.7	-3.1	-0.3	-2.2

Table 2.6. Average of absolute values of differences of heats of formation from FPD values for DFT functionals in kcal/mol.

Functional	Metal complexes	O_2, H_2O, CO_2, HCO_3^-
PW91	36.3	20.6
BP86	34.3	20.1
M06	12.6	3.8
PBE	32.6	19.9
PBE0	11.9	3.0
B3LYP	15.6	2.8
HCTH 407	12.9	8.1
HSE06	13.7	3.3
M06L	11.7	6.3
τ-HCTH	13.1	4.9
τ-HCTH hyb	12.6	5.1
TPSSh	24.0	7.9
ωB97X	9.7	2.8
ωB97X-D	10.0	2.4

Figures

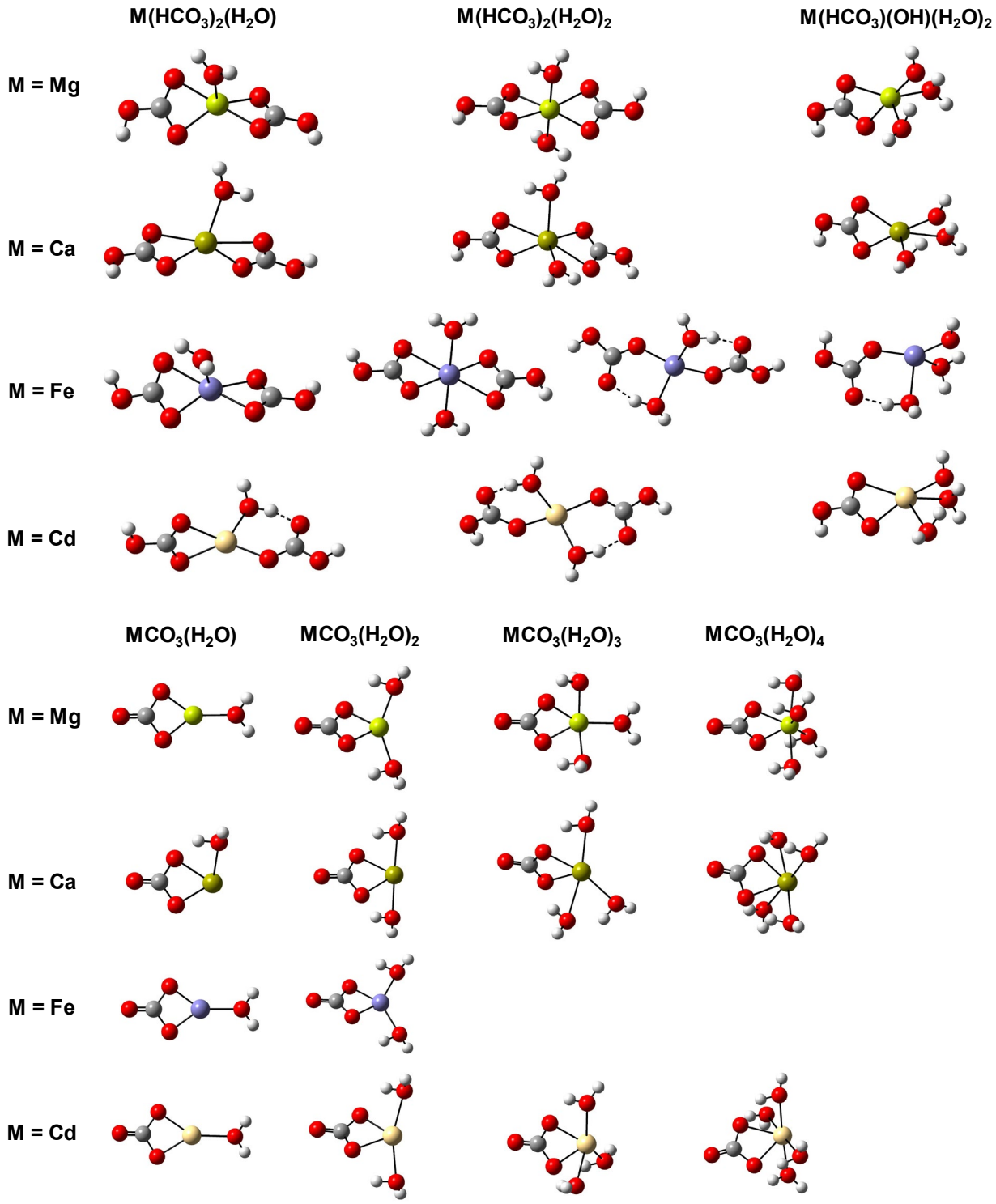

Figure 2.1. Optimized structures of the carbonate, di-bicarbonate and bicarbonate/OH^- complexes with additional water molecules (O = red, H = white, and C = gray).

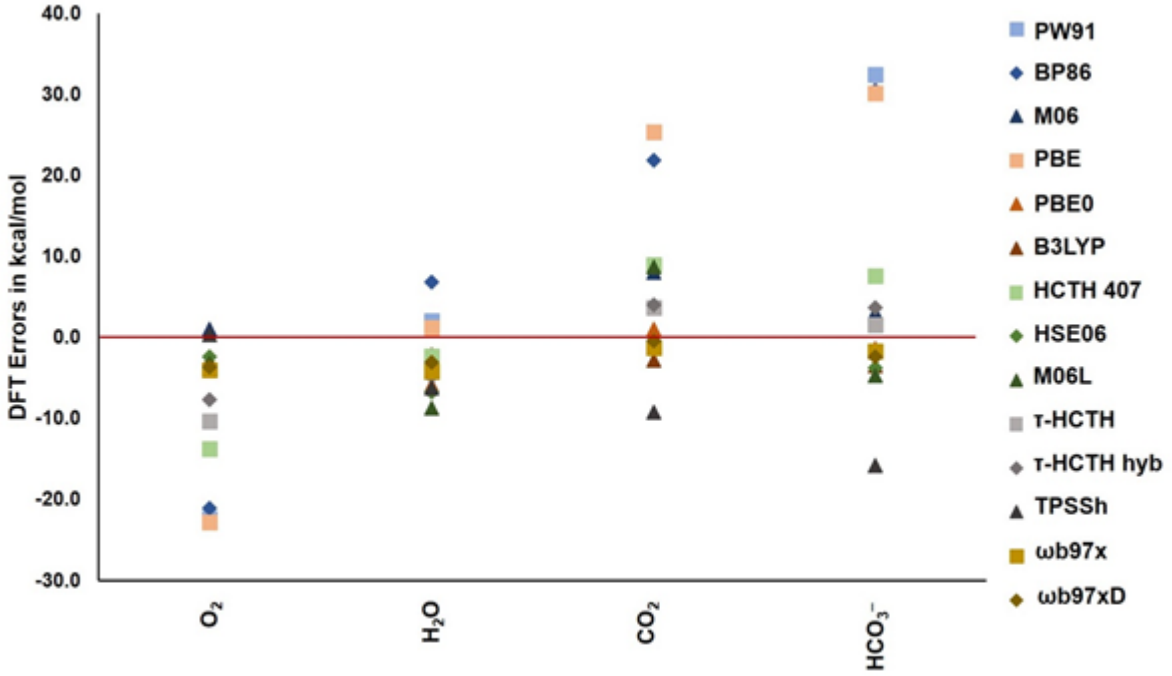

Figure 2.2. $\Delta H_{f,0K}$ (kcal/mol) distributions of DFT errors compared to the FPD results for O_2, H_2O, CO_2 and HCO_3^-.

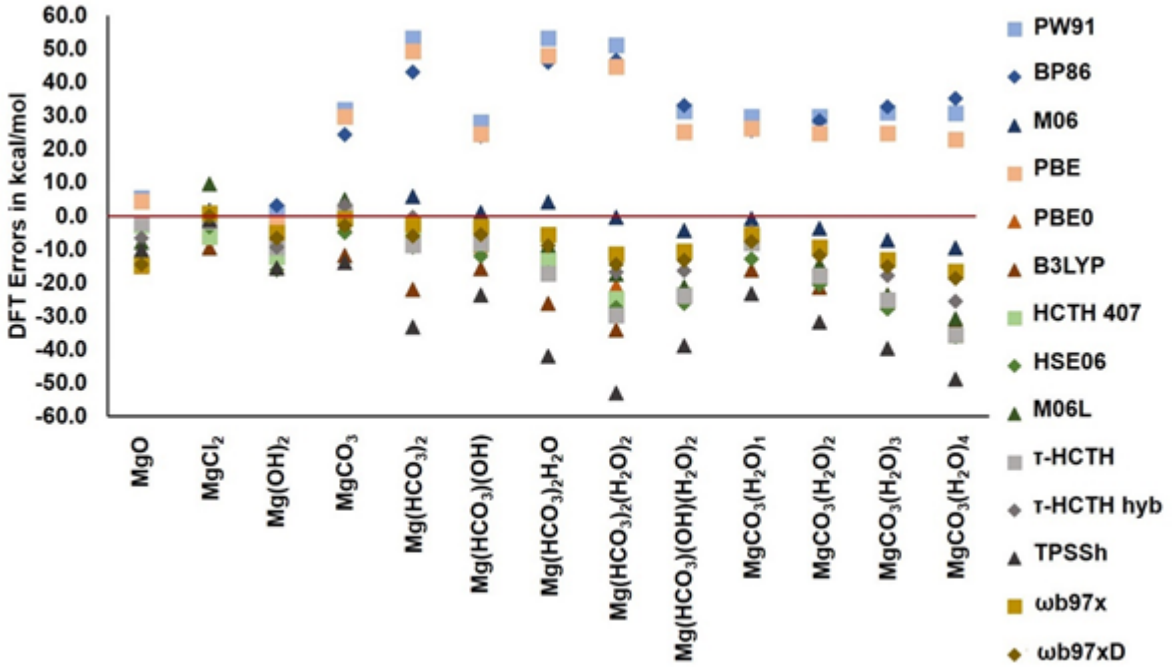

Figure 2.3. $\Delta H_{f,0K}$ (kcal/mol) distributions of DFT errors compared to the FPD results for Mg molecules.

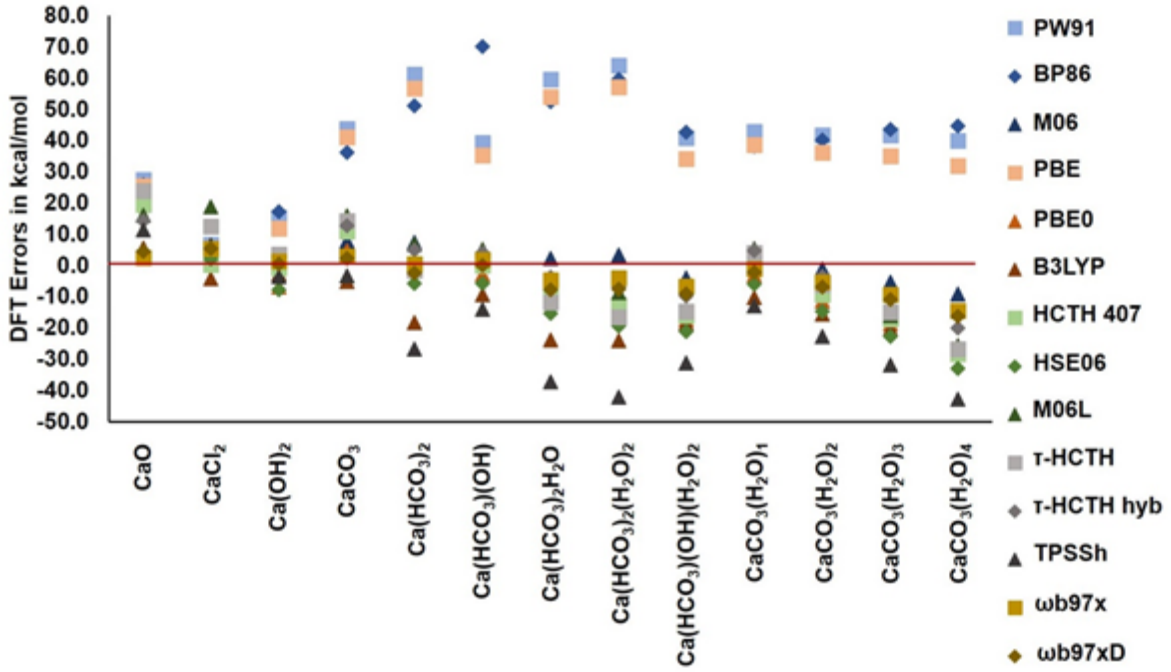

Figure 2.4. $\Delta H_{f,0K}$ (kcal/mol) distributions of DFT errors compared to the FPD results for Ca molecules.

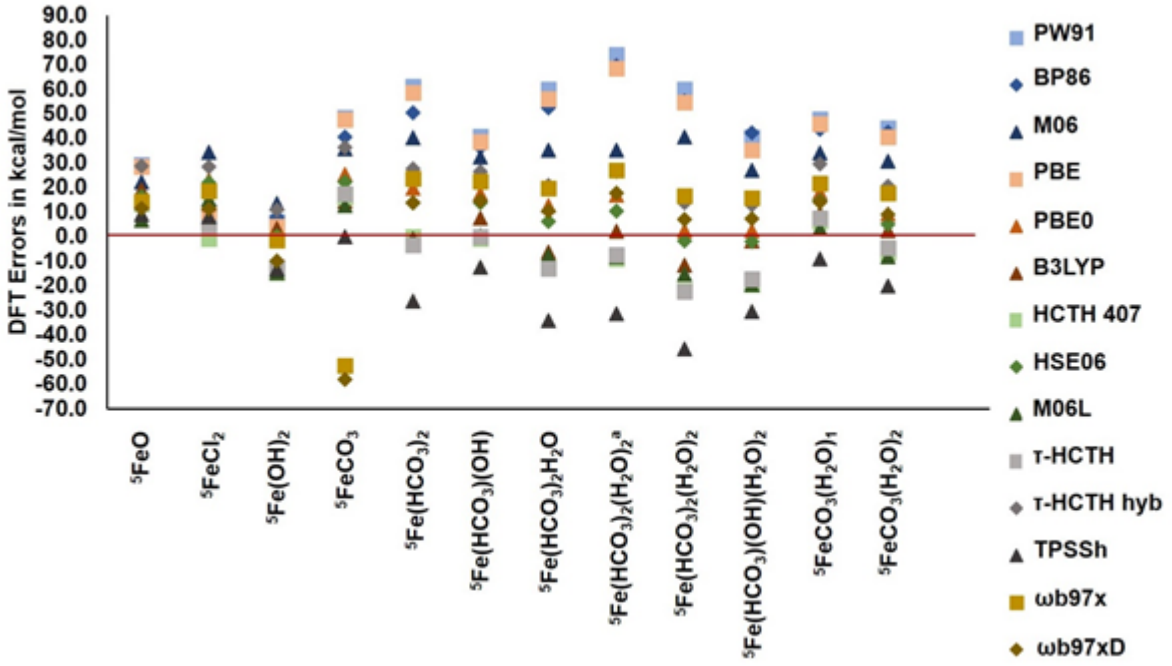

Figure 2.5. $\Delta H_{f,0K}$ (kcal/mol) distributions of DFT errors compared to the FPD results for Fe molecules.

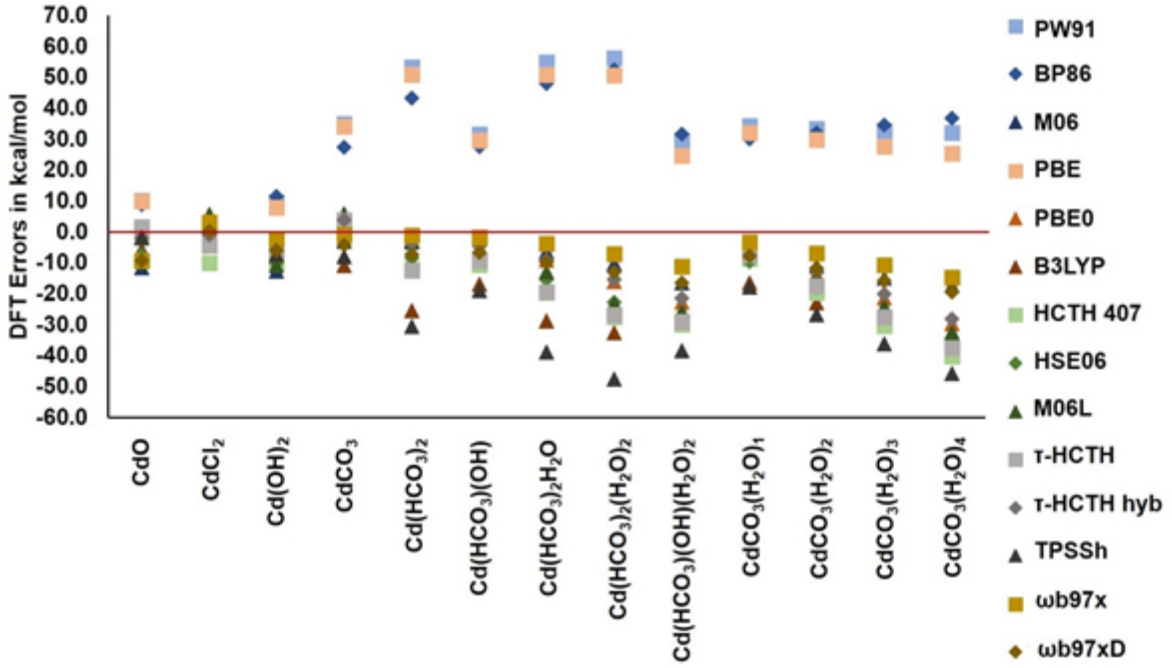

Figure 2.6. $\Delta H_{f,0K}$ (kcal/mol) distributions of DFT errors compared to the FPD results for Cd molecules.

References

[1] Nurnberg, D.; Bijma, J.; Hemleben, C. Assessing the Reliability of Magnesium in Foraminiferal Calcite as a Proxy for Water Mass Temperatures. *Geochim. Cosmochim. Acta* **1996**, *60*, 803−814.

[2] Riechelmann, S.; Buhl, D.; Schroder-Ritzrau, A.; Riechelmann, D. F. C.; Richter, D. K.; Vonhof, H. B.; Wassenburg, J. A.; Geske, A.; Spotl, C.; Immenhauser, A. The Magnesium Isotope Record of Cave Carbonate Archives. *Clim. Past* **2012**, *8*, 1849−1867.

[3] Russell, A. D.; Honisch, B.; Spero, H. J.; Lea, D. W. Effects of Seawater Carbonate Ion Concentration and Temperature on Shell U, Mg, and Sr in Cultured Planktonic Foraminifera. *Geochim. Cosmochim. Acta* **2004**, *68*, 4347−4361.

[4] Morse, J. W.; Mackenzie, F. T. *Geochemistry of Sedimentary Carbonates*. Elsevier: New York, 1990; Vol. 48, p 706.

[5] Swainson, I. P.; Hammond, R. P. Ikaite, $CaCO_3 \cdot 6H_2O$: Cold Comfort for Glendonites as Paleothermometers. *Am. Mineral.* **2001**, *86*, 1530−1533.

[6] De Lurio, J. L.; Frakes, L. A. Glendonites as a Paleoenvironmental Tool: Implications for Early Cretaceous High Latitude Climates in Australia. *Geochim. Cosmochim. Acta* **1999**, *63*, 1039−1048.

[7] Mann, S. General Principles of Biomineralization. In *Biomineralization: Principles and Concepts in Bioinorganic Materials Chemistry*. Oxford University Press: New York, NY, USA, 2002.

[8] Lowenstam, H. A.; Weiner, S. *On Biomineralization*; Oxford University Press: New York, NY, USA, 1989.

[9] Radha, A. V; Forbes, T. Z.; Killian, C. E.; Gilbert, P. U. P. A.; Navrotsky, A. Transformation and Crystallization Energetics of Synthetic and Biogenic Amorphous Calcium Carbonate. *Proc. Nat. Acad. Sci. USA* **2010**, *107*, 16438-16443.

[10] Beniash, E.; Metzler, R. A.; Lam, R. S. K.; Gilbert, P. U. P. A. Transient Amorphous Calcium Phosphate in Forming Enamel. *J. Struct. Biol.* **2009**, *166*, 133–143.

[11] Lackner, K. S.; Wendt, C. H.; Butt, D. P.; Joyce, E. L.; Sharp, D. H. Carbon Dioxide Disposal in Carbonate Minerals. *Energy* **1995***, 20,* 1153–1170.

[12] De Yoreo, J. J.; Waychunas, G. A.; Jun, Y.-S.; Fernandez-Martinez, A. In situ Investigations of Carbonate Nucleation on Mineral and Organic Surfaces. *Rev. Mineralogy Geochem.* **2013***, 77,* 229–257.

[13] Rysgaard, S.; Sogaard, D. H.; Cooper, M.; Pucko, M.; Lennert, K.; Papakyriakou, T. N.; Wang, F.; Geilfus, N. X.; Glud, R. N.; Ehn, J.; McGinnis, D. F.; Attard, K.; Sievers, J.; Deming, J. W.; Barber, D. Ikaite Crystal Distribution in Winter Sea Ice and Implications for CO_2 System Dynamics. *Cryosphere* **2013**, *7*, 707−718.

[14] Matter, J. M.; Kelemen, P. B. Permanent Storage of Carbon Dioxide in Geological Reservoirs by Mineral Carbonation. *Nat. Geosci.* **2009**, *2*, 837−841.

[15] Fukushi, K.; Munemoto, T.; Sakai, M.; Yagi, S. Monohydrocalcite: A Promising Remediation Material for Hazardous Anions. *Sci. Technol. Adv. Mater.* **2011**, *12*, 5318−5327.

[16] Wu, X. M.; Cao, H. Q.; Yin, G.; Yin, J. F.; Lu, Y. X.; Li, B. J. $MgCO_3 \cdot 3H_2O$ and MgO Complex Nanostructures: Controllable Biomimetic Fabrication and Physical Chemical Properties. *Phys. Chem. Chem. Phys.* **2011**, *13*, 5047-5052.

[17] Sutradhar, N.; Sinhamahapatra, A.; Roy, B.; Bajaj, H. C.; Mukhopadhyay, I.; Panda, A. B. Preparation of MgO Nano-Rods With Strong Catalytic Activity via Hydrated Basic Magnesium Carbonates. *Mater. Res. Bull.* **2011**, *46*, 2163-2167.

[18] Janet, C. M.; Viswanathan, B.; Viswanath, R. P.; Varadarajan, T. K. Characterization and Photoluminescence Properties of MgO Microtubes Synthesized From Hydromagnesite Flowers. *J. Phys. Chem. C* **2007**, *111*, 10267-10272.

[19] Chen, T.; Neville, A.; Yuan, M. D. Influence of Mg^{2+} on $CaCO_3$ Formation-Bulk Precipitation and Surface Deposition. *Chem. Eng. Sci.* **2006**, *61*, 5318−5327

[20] Laugesen, J. L. Density Functional Calculations of Elastic Properties of Portlandite, $Ca(OH)_2$. *Cem. Concr. Res.* **2005**, *35*, 199−202.

[21] Emsley, J. *The Elements, 2nd Ed.*, Oxford, Oxford, 1994.

[22] Blue, C. R.; Giuffre, A.; Mergelsberg, S.; Han, N.; De Yoreo, J. J.; Dove, P. M. Chemical and Physical Controls on the Transformation of Amorphous Calcium Carbonate into Crystalline $CaCO_3$ Polymorphs. *Geochim. Cosmochim. Acta* **2017**, *196*, 179−196.

[23] Rodriguez-Blanco, J. D.; Shaw, S.; Bots, P.; Roncal-Herrero, T.; Benning, L. G. The Role of Mg in the Crystallization of Monohydrocalcite. *Geochim. Cosmochim. Acta,* **2014**, *127*, 204−220.

[24] Chaka, A. M.; Felmy, A. R. Ab Initio Thermodynamic Model for Magnesium Carbonates and Hydrates. *J. Phys. Chem. A* **2014**, *118*, 7469−7488.

[25] Chaka, A. M. Ab Initio Thermodynamics of Hydrated Calcium Carbonates and Calcium Analogues of Magnesium Carbonates: Implications for Carbonate Crystallization Pathways. *ACS Earth Space Chem.* **2018**, *2*, 210−224.

[26] Grimme, S. Semiempirical GGA-Type Density Functional Constructed with a Long-Range Dispersion Correction. *J. Comput. Chem.* **2006**, *27*, 1787−1799.

[27] Grimme, S. Density Functional Theory With London Dispersion Corrections. *Comput. Mol. Sci.* **2011**, *1*, 211−228.

[28] Tkatchenko, A.; Scheffler, M. Accurate Molecular van der Waals Interactions from Ground-State Electron Density and Free Atom Reference Data. *Phys. Rev. Lett.* **2009**, *102*, 073005-1 - 073005-4.

[29] Chaka, A. M. Quantifying the Impact of Magnesium on the Stability and Water Binding Energy of Hydrated Calcium Carbonates by Ab Initio Thermodynamics. *J. Phys. Chem. A* **2019**, *123*, 2908−2923.

[30] Laugesen, J. L. Density Functional Calculations of Elastic Properties of Portlandite, $Ca(OH)_2$. *Cem. Concr. Res.* **2005**, *35*, 199−202.

[31] Chaka, A. M. Ab Initio Thermodynamics of Hydrated Calcium Carbonates and Calcium Analogues of Magnesium Carbonates: Implications for Carbonate Crystallization Pathways. *ACS Earth Space Chem.* **2018**, *2*, 210−224.

[32] Chaka, A. M.; Felmy, A. R. Ab Initio Thermodynamic Model for Magnesium Carbonates and Hydrates. *J. Phys. Chem. A* **2014**, *118*, 7469−7488.

[33] Chaka, A. M.; Felmy, A. R.; Qafoku, O. Ab initio Thermodynamics of Magnesium Carbonates and Hydrates in Water-Saturated Supercritical CO_2 and CO_2-rich Regions. *Chem. Geol.* **2016**, *434*, 1−11.

[34]Chen, C.; Dixon, D. A. Structure and Stability of Hydrolysis Reaction Products of MgO Nanoparticles Leading to the Formation of Brucite. *J. Phys. Chem. C* **2017**, *121*, 21750-21762.

[35] Chen, M.; Jackson, V. E.; Felmy, A. R.; Dixon, D. A. Structures and Energetics of $(MgCO_3)_n$ Clusters, $n \leq 16$. *J. Phys. Chem. A* **2015**, *119*, 3419–3428.

[36] Vasiliu, M.; Li, S.; Peterson, K. A.; Feller, D.; Gole, J. L.; Dixon D. A. Structures and Heats of Formation of Simple Alkali Metal Compounds: Hydrides, Chlorides, Fluorides, Hydroxides and Oxides for Li, Na and K. *J. Phys. Chem. A* **2010**, *114*, 4272-4281.

[37] Vasiliu, M.; Li, S.; Feller, D.; Gole, J. L.; Dixon, D. A. Structures and Heats of Formation of Simple Alkaline Earth Metal Compounds: Fluorides, Chlorides, Oxides, and Hydroxides for Be, Mg, and Ca. *J. Phys. Chem. A* **2010**, *114,* 9349–9358.

[38] Vasiliu, M.; Hill, J. G.; Peterson, K. A.; Dixon, D. A. Structures and Heats of Formation of Simple Alkaline Earth Metal Compounds II: Fluorides, Chlorides, Oxides, and Hydroxides for Ba, Sr, and Ra. *J. Phys. Chem. A* **2018**, *122,* 316-327.

[39] Dixon, D. A.; Feller, D.; Peterson, K. A. A Practical Guide to Reliable First Principles Computational Thermochemistry Predictions Across the Periodic Table. In *Annual Reports in Computational Chemistry*, Ralph, A. W., Ed.; Elsevier, Amsterdam: **2012**; Vol. 8, pp 1-28.

[40] Peterson, K. A.; Feller, D.; Dixon, D. A. Chemical Accuracy in Ab Initio Thermochemistry and Spectroscopy: Current Strategies and Future Challenges. *Theor. Chem. Acc.* **2012**, *131*, 1-20.

[41] Feller, D.; Peterson, K. A.; Dixon, D. A. Further Benchmarks of a Composite, Convergent, Statistically Calibrated Coupled Cluster Based Approach for Thermochemical and Spectroscopic Studies. *Mol. Phys.* **2012**, *110*, 2381-2399.

[42] Feller, D.; Peterson, K. A.; Dixon, D. A. The Impact of Larger Basis Sets and Explicitly Correlated Coupled Cluster Theory on the Feller-Peterson-Dixon Composite Method. In *Annual Reports in Computational Chemistry*, Vol. 12, Ed. D. A. Dixon, Elsevier, Amsterdam, **2016**, pp. 47-78.

[43] Hohenberg, P.; Kohn, W. Inhomogeneous Electron Gas. *Phys. Rev.* **1964**, *136,* B864-B871.

[44] Kohn, W.; Sham, L. J. Self-Consistent Equations Including Exchange and Correlation Effects. *Phys. Rev.* **1965**, *140*, A1133-A1138.

[45] Parr, R. G.; Yang, W. *Density-functional Theory of Atoms and Molecules.* Oxford University Press, Oxford, 1989.

[46] Becke, A. D. Density-Functional Thermochemistry. III. The Role of Exact Exchange. *J. Chem. Phys.* **1993**, *98*, 5648-5652.

[47] Lee, C.; Yang, W.; Parr, R. G. Accurate and Simple Analytic Representation of the Electron-Gas Correlation Energy. *Phys. Rev. B.* **1988**, *37*, 785-789.

[48] Dunning, T. H., Jr. Gaussian Basis Sets for Use in Correlated Molecular Calculations. I. The Atoms Boron Through Neon and Hydrogen. *J. Chem. Phys*. **1989**, *90*, 1007-1023.

[49] Kendall, R. A.; Dunning, T. H. Jr.; Harrison, R. J., Electron Affinities of the First Row Atoms Revisited. Systematic Basis Sets and Wave Functions. *J. Chem. Phys*. **1992**, *96*, 6796-6806.

[50] Prascher, B. P.; Peterson, K. A.; Woon, D. E.; Dunning, T. H., Jr.; Wilson, A. K . Gaussian Basis Sets for use in Correlated Molecular Calculations. VII. Valence, Core-Valence, and Scalar Relativistic Basis Sets for Li, Be, Na and Mg. *Theor. Chem. Acc.* ***2011***, *128*, 69-82.

[51] Hill, J. G.; Peterson, K. A. Gaussian Basis Sets for use in Correlated Molecular Calculations. XI. Pseudopotential-Based and all-Electron Relativistic Basis sets for Alkali Metal (K-Fr) and Alkaline Earth (Ca-Ra) Elements. *J. Chem. Phys.* **2017**, *147*, 244106-1 – 244106-12.

[52] Peterson, K.A. Gaussian Basis Sets for Quantum Mechanical (QM) Calculations. In *Computational Inorganic and Bioinorganic Chemistry*; Solomon, E.I.; Scott, R.A.; King, R. B. Eds.; John Wiley and Sons: Chicester, U.K., 2009; pp 187-200.

[53] Li, S.; Hennigan, J. M.; Dixon, D. A.; Peterson, K. A. Accurate Thermochemistry for Transition Metal Oxide Clusters. *J. Phys. Chem. A* **2009**, *113*, 7861-7877.

[54] Peterson, K. A.; Puzzarini, C. Systematically Convergent Basis Sets for Transitional metals. II. Pseudopotential-Based Correlation Consistent Basis Sets for Group 11 (Cu, Ag, Au) and 12 (Zn, Cd, Hg) elements. *Theor. Chem. Acc.* **2005**, *114*, 283-296.

[55] Møller, C.; Plesset, M. S. Note on an Approximation Treatment for Many-Electron Systems. *Phys. Rev.* **1934**, *46*, 0618-0622.

[56] Pople, J. A.; Binkley, J. S.; Seeger, R. Theoretical Models Incorporating Electron Correlation. *Int. J. Quantum. Chem.* **1976**, *10*, 1-19.

[57] Frisch, M. J.; Trucks, G. W.; Schlegel, H. B.; Scuseria, G. E.; Robb, M. A.; Cheeseman, J. R.; Scalmani, G.; Barone, V.; Petersson, G. A.; Nakatsuji, H.; Li, X.; Caricato, M.; Marenich, A. V.; Bloino, J.; Janesko, B. G.; Gomperts, R.; Mennucci, B.; Hratchian, H. P.; Ortiz, J. V.; Izmaylov, A. F.; Sonnenberg, J. L.; Williams-Young, D.; Ding, F.; Lipparini, F.; Egidi, F.; Goings, J.; Peng, B.; Petrone, A.; Henderson, T.; Ranasinghe, D.; Zakrzewski, V. G.; Gao, J.; Rega, N.; Zheng, G.; Liang, W.; Hada, M.; Ehara, M.; Toyota, K.; Fukuda, R.; Hasegawa, J.; Ishida, M.; Nakajima, T.; Honda, Y.; Kitao, O.; Nakai, H.; Vreven, T.; Throssell, K.; Montgomery, J. A., Jr.; Peralta, J. E.; Ogliaro, F.; Bearpark, M. J.; Heyd, J. J.; Brothers, E. N.; Kudin, K. N.; Staroverov, V. N.; Keith, T. A.; Kobayashi, R.; Normand, J.; Raghavachari, K.; Rendell, A. P.; Burant, J. C.; Iyengar, S. S.; Tomasi, J.; Cossi, M.; Millam, J. M.; Klene, M.; Adamo, C.; Cammi, R.; Ochterski, J. W.; Martin, R. L.; Morokuma, K.; Farkas, O.; Foresman, J. B.; Fox, D. J. Gaussian 16, Revision A.03, Gaussian, Inc., Wallingford CT, 2016.

[58] Purvis, G. D., III; Bartlett, R. J. A Full Coupled Cluster Singles and Doubles Model: The Inclusion of Disconnected Triples. *J. Chem. Phys.* **1982**, *76*, 1910-1918.

[59] Raghavachari, K.; Truck, G.W.; Pople, J.A.; Head-Gordon, M. A Fifth-Order Perturbation Comparison of Electron Correlation Theories. *Chem. Phys. Lett*. **1989**, *157*, 479-483.

[60] Watts, J. D.; Gauss, J.; Bartlett, R. J. Coupled-Cluster Methods with Noniterative Triple Excitations for Restricted Open Shell Hartree-Fock and Other General Single Determinant Reference Functions. Energies and Analytical Gradients. *J. Chem. Phys.* **1993**, *98*, 8718-8733.

[61] Bartlett, R. J.; Musial, M. Coupled Cluster Theory in Quantum Chemistry. *Rev. Mod. Phys.* **2007**, *79*, 291-352.

[62] Knowles, P. J.; Hampel, C.; Werner, H.-J. Coupled Cluster Theory for High Spin, Open Shell Reference Wave Functions. *J. Chem. Phys*. **1993**, *99*, 5219-5227.

[63] Knowles, P. J.; Hampel, C.; Werner, H.-J. Erratum: Coupled Cluster Theory for High Spin, Open Shell Reference Wave Functions. *J. Chem. Phys*. **2000**, *112*, 3106-3107.

[64] Deegan, M. J. O.; Knowles, P. J. Perturbative Corrections to Account for Triple Excitations in Closed and Open Shell Coupled Cluster Theories. *Chem. Phys. Lett*. **1994**, *227*, 321-327.

[65] Werner, H.-J.; Knowles, P. J.; Knizia, G.; Manby, F. R.; Schütz, M.; Celani, P.; Györffy, W.; Kats, T.; Korona, T.; Lindh, R.; Mitrushenkov, A.; Rauhut, G.; Shamasundar, K. R.; Adler, T. B.; Amos, R. D.; Bernhardsson, A.; Berning, A.; Cooper, D. L.; Deegan, M. J. O.; Dobbyn, A. J.; Eckert, F.; Goll, E.; Hampel, C.; Hesselmann, A.; Hetzer, G.; Hrenar, T.; Jansen, G.; Köppl, C.; Liu, Y.; Lloyd, A. W.; Mata, R. A.; May, A. J.; McNicholas, S. J.; Meyer, W.; Mura, M. E.; Nicklass, A.; O'Neill, D. P.;Palmieri, P.; Peng, D.; Pflüger, K.; Pitzer, R.; Reiher, M.; Shiozaki, T.; Stoll, H.; Stone, A. J.; Tarroni, R.; Thorsteinsson, T.; Wang, M. MOLPRO, version 2015.1, a package of *ab initio* programs, See http://www.molpro.net. Accessed March 1, 2016.

[66] Werner H.-J.; Knowles, P. J.; Knizia, G.; Manby, F. R.; Schütz, M. Molpro: A General-Purpose Quantum Chemistry Program Package. *WIREs Comput. Mol. Sci.* **2012**, *2*, 242-253.

[67] Figgen, D.; Rauhut, G.; Dolg, M.; Stoll, H. Energy-Consistent Pseudopotentials for Group 11 and 12 Atoms: Adjustment to Multi-Configuration Dirac–Hartree–Fock Data. *Chem. Phys.* **2005**, *311,* 227-244.

[68] Feller, D.; Peterson, K.A.; Hill, J. G. On the Effectiveness of CCSD(T) Complete Basis Set Extrapolations for Atomization Energies. *J. Chem. Phys.* **2011***, 135,* 044102-1 – 044102-18.

[69] Chen, M.; Vasiliu, M.; Hu, S.; Dixon, D. A. Stability and Electronic Properties of Rocksalt $(CdO)_n$, $(SrO)_n$, and $(BaO)_n$ Nanoparticles. *J. Phys. Chem. C*, **2018**, *122*, 25021–25034.

[70] Woon, D. E.; Dunning, T. H. Jr. Gaussian Basis Sets for Use in Correlated Molecular Calculations. V. Core-Valence Basis Sets for Boron Through Neon. *J. Chem. Phys.* **1995**, *103*, 4572-4585.

[71] Peterson, K. A.; Dunning, T. H., Jr. Accurate Correlation Consistent Basis sets for Molecular core–valence Correlation Effects: The Second Row Atoms Al–Ar, and the First Row Atoms B–Ne Revisited *J. Chem. Phys.* **2002**, *117*, 10548-10560.

[72] Douglas, M.; Kroll, N. M. Quantum Electrodynamical Corrections to the Fine Structure of Helium. *Ann. Phys.* **1974**, *82*, 89-155.

[73] Hess, B. A. Applicability of the No-Pair Equation with Free-Particle Projection Operators to Atomic and Molecular Structure Calculations. *Phys. Rev. A.* **1985**, *32*, 756-763.

[74] Hess, B. A. Relativistic Electronic-Structure Calculations Employing a Two-Component No-Pair Formalism with External-Field Projection Operators. *Phys. Rev. A.* **1986**, *33*, 3742-3748.

[75] De Jong, W. A.; Harrison, R. J.; Dixon, D. A. Parallel Douglas-Kroll Energy and Gradients in NWChem: Estimating Scalar Relativistic Effects Using Douglas-Kroll Contracted Basis Sets. *J. Chem. Phys*. **2001**, *114*, 48-53.

[76] Davidson, E. R.; Ishikawa, Y.; Malli, G. L. Validity of First-Order Perturbation Theory for Relativistic Energy Corrections. *Chem. Phys. Lett.* **1981**, *84*, 226-227.

[77] D. Feller, K. A. Peterson, W. A. de Jong, and D. A. Dixon, Performance of Coupled Cluster Theory in Thermochemical Calculations of Small Halogenated Compounds. *J. Chem. Phys.* **2003**, *118*, 3510-3522.

[78] Moore, C. E. *Atomic Energy Levels As Derived from the Analysis of Optical Spectra*; U.S. National Bureau of Standards Circular 467, COM-72-50282; U.S. Department of Commerce, National Technical Information Service: Washington, DC, 1949; Vol. *1*, H to V.

[79] https://atct.anl.gov/Thermochemical%20Data/version%201.122g/index.php accessed January 18, 2019.

[80] Ruscic, B.; Pinzon, R. E.; Morton, M. L.; von Laszewski, G.; Bittner, S.; Nijsure, S. G.; Amin, K. A.; Minkoff, M.; Wagner, A. F. Introduction to Active Thermochemical Tables: Several "Key" Enthalpies of Formation Revisited. *J. Phys. Chem. A* **2004**, *108*, 9979-9997.

[81] Changala, P. B.; Nguyen, T. L.; Baraban, J. H.; Ellison, G. B.; Stanton, J. F.; Bross, D. H.; Ruscic, B. Active Thermochemical Tables: The Adiabatic Ionization Energy of Hydrogen Peroxide. *J. Phys. Chem. A* **2017**, *121*, 8799-8806.

[82] Chase, M. W., Jr. *NIST-JANAF Thermochemical Tables*, 4th ed. *J. Phys. Chem. Ref. Data.*, *Mono. 9*; American Institute of Physics: Woodbury, NY, 1998; Suppl 1.

[83] Yungman, V. S.; Glushko, V. P.; Medvedev, V. A.; Gurvich, L. V., Eds., *Thermal Constants of Substances*, 8 Vols., Wiley: New York, 1999.

[84] Wagman, D. D.; Evans, W. H.; Parker, V. B.; Schumm, R. H.; Halow, I.; Bailey, S. M.; Churney, K. L.; Nuttall, R. L. *J. Phys. Chem. Ref. Data* **1982**, *11* (Suppl. 2).

[85] Curtiss, L. A.; Raghavachari, K.; Redfern, P. C.; Pople, J. A. Assessment of Gaussian-2 and Density Functional Theories for the Computation of Enthalpies of Formation. *J. Chem. Phys.* **1997**, *106*, 1063-1079.

[86] Perdew, J. P.; Wang, Y. Accurate and Simple Analytic Representation of the Electron Gas Correlation Energy. *Phys. Rev. B* **1992**, *45*. 13244-13249.

[87] Burke, K.; Perdew, J. P.; Wang, Y. Mixing Exact Exchange with GGA: When to Say When. In *Electronic Density Functional Theory: Recent Progress and New Directions*. Dobson, J. F.; Vignale, G.; Das. M. P. eds. (Plenum, New York, 1998) pp. 57-68.

[88] Becke, A. D. Density-Functional Exchange-Energy Approximation with Correct Asymptotic Behavior. *Phys. Rev. A* ***1988***, *38*, 3098-*3100*.

[89] Perdew, J. P. Density-Functional Approximation for the Correlation Energy of the Inhomogeneous Electron Gas. *Phys. Rev. B* **1986**, *33*, 8822-8824.

[90] Zhao, Y.; Truhlar, D. G. The M06 suite of Density Functionals for Main Group Thermochemistry, Thermochemical Kinetics, Noncovalent Interactions, Excited States, and Transition Elements: Two New Functionals and Systematic Testing of Four M06-class Functionals and 12 Other Functionals. *Theor. Chem. Acc.* **2008**, *120*, 215-41.

[91] Perdew, J. P.; Burke, K.; Ernzerhof, M. Generalized Gradient Approximation Made Simple. *Phys. Rev. Lett.* **1996**, *77*, 3865–3868.

[92] Perdew, J. P.; Burke, K.; Ernzerhof, M. Erratum 'Generalized Gradient Approximation Made Simple'. *Phys. Rev. Lett.* **1997***, 78*, 1396.

[93] Adamo, C.; Barone, V. Toward Reliable Density Functional Methods Without Adjustable Parameters: The PBE0 Model. *J. Chem. Phys.* **1999**, *110*, 6158-6169.

[94] Hamprecht, F. A.; Cohen, A.; Tozer, D. J.; Handy, N. C. Development and Assessment of New Exchange-Correlation Functionals. *J. Chem. Phys.* **1998**, *109*, 6264-6271.

[95] Boese, A. D.; Doltsinis, N. L.; Handy, N. C.; Sprik, M. New Generalized Gradient Approximation Functionals. *J. Chem. Phys.* **2000**, *112*, 1670-1678.

[96] Boese, A. D.; Handy, N. C. A New Parametrization of Exchange-Correlation Generalized Gradient Approximation Functionals. *J. Chem. Phys.* **2001**, *114*, 5497-5503.

[97] A. V. Krukau , O. A. Vydrov, A. F. Izmaylov, and G. E. Scuseria, Influence of the Exchange Screening Parameter on the Performance of Screened Hybrid Functionals. *J. Chem. Phys.* **2006**, *125*, 224106-1 – 224106-5.

[98] Zhao, Y.; Truhlar, D. G. A new Local Density Functional for Main-Group Thermochemistry, Transition Metal Bonding, Thermochemical Kinetics, and Noncovalent Interactions. *J. Chem. Phys.* **2006**, *125*, 194101-1 - 194101-18.

[99] Boese, A. D.; Handy, N. C. New Exchange-Correlation Density Functionals: The Role of the Kinetic-Energy Density. *J. Chem. Phys.* **2002**, *116*, 9559-9969.

[100] Staroverov, V. N.; Scuseria, G. E.; Tao, J.; Perdew, J. P. Comparative Assessment of a New Nonempirical Density Functional: Molecules and Hydrogen-Bonded Complexes. *J. Chem. Phys.* **2003**, *119*, 12129-12137.

[101] Chai, J.-D.; Head-Gordon, M. Systematic Optimization of Long-Range Corrected Hybrid Density Functionals. *J. Chem. Phys.* **2008**, *128*, 084106-1 - 084106-15.

[102] S. Grimme Semiempirical GGA-Type Density Functional Constructed with a Long-Range Dispersion Correction. *J. Comput. Chem.* **2006**, *27*, 1787-1799.

[103] Chai, J. D.; Head-Gordon, M. Long-Range Corrected Hybrid Density Functionals with Damped Atom-Atom Dispersion Corrections. *Phys. Chem. Chem. Phys.* **2008**, *10*, 6615-6620.

[104] Kramida, A., Ralchenko, Yu., Reader, J., and NIST ASD Team (2019). *NIST Atomic Spectra Database* (ver. 5.7.1), [Online]. Available: https://physics.nist.gov/asd [2019, November 10]. National Institute of Standards and Technology, Gaithersburg, MD. DOI: https://doi.org/10.18434/T4W30F.

[105] Shannon, R. D. Revised Effective Ionic Radii and Systematic Studies of Interatomic Distances in Halides and Chalcogenides. *Acta Cryst. A,* **1976**, *32*, 751-767.

[106] Jackson, V. E.; Felmy, A. R.; Dixon, D. A. The Prediction of the pK_a's of Aqueous Metal Ion +2 Complexes. *J. Phys. Chem. A* **2015**, *119*, 2926-2939.

[107] Operti, L.; Tews, E. C.; MacMahon, T. J.; Freiser, B. S. Thermochemical Properties of Gas-Phase MgOH and MgO Determined by Fourier Transform Mass Spectrometry. *J. Am. Chem. Soc.* **1989**, *111*, 9152-9156.

[108] Cheung, A. S.-C.; Lee, N.; Lyyra, A. M.; Merer, A. J.; Taylor, A. W. Spectroscopic Properties of the $^5\Delta_i$ Ground State of FeO. *J. Mol. Spectrosc.* **1982**, *95*, 213−225.

[109] Chestakov, D. A.; Parker, D. H.; Baklanov, A. V. Iron Monoxide Photodissociation. *J. Chem. Phys.* **2005**, *122*, 084302.

[110] Aoto, Y. A.; de Lima Batista, A. P.; Köhn, A.; de Oliveira-Filho, A. G. S. How to Arrive at Accurate Benchmark Values for Transition Metal Compounds: Computation or Experiment? *J. Chem. Theor. Comp.* **2017** *13*, 5291-5316.

[111] Peterson, K. A.; Shepler, B. C.; Singleton, J. M. The Group 12 Metal Chalcogenides: An Accurate Multireference Configuration Interaction and Coupled Cluster Study. *Mol. Phys*. **2007**, *105*, 1139-1155.

[112] Behrens, R. G.; Mason, C. F. V. A Mass Spectrometric Investigation of the Vaporization Thermodynamics and Vapor Composition of Cadmium Oxide. *J. Less-Common Metals,* **1981**, *77,* 169-184.

[113] Nguyen, M. T.; Matus, M. H.; Jackson, V. E.; Ngan, V. T.; Rustad, J. R.; Dixon, D. A. Mechanism of the Hydration of Carbon Dioxide: Direct Participation of H_2O Versus Microsolvation. *J. Phys. Chem. A*, **2008**, *112*, 10386-10398.

[114] Alexeev, Y.; Windus, T. L.; Dixon, D. A.; Zhan, C.-G. Accurate Heats of Formation and Acidities for H_3PO_4, H_2SO_4, and H_2CO_3 from Ab Initio Electronic Structure Calculations. *Int. J. Quantum Chem.* **2005**, *102*, 775-784.

[115] Alexeev, Y.; Windus, T. L.; Dixon, D. A.; Zhan, C.-G. Erratum: Accurate Heats of Formation and Acidities for H_3PO_4, H_2SO_4, and H_2CO_3 from Ab Initio Electronic Structure Calculations. *Int. J. Quantum Chem.* **2005**, *104*, 379-380.

[116] Ruscic, B.; Wagner, A. F.; Harding, L. B.; Asher, R. L.; Feller, D.; Dixon, D. A.; Peterson, K. A.; Song, Y.; Qian, X.; Ng, C.-Y.; Liu, J.; Chen, W.; Schwenke, D. W. On the Enthalpy of Formation of Hydroxyl Radical and Gas-Phase Bond Dissociation Energies of Water and Hydroxyl. *J. Phys. Chem. A* **2002**, *106*, 2727-2747.

[117] Chen, M.; Felmy, A. R.; Dixon, D. A. Structures and Stabilities of $(MgO)_n$ Nanoclusters. *J. Phys. Chem. A* **2014**, *118*, 3136–3146.

[118] Pearson, R. G. Hard and Soft Acids and Bases, HSAB, Part 1: Fundamental Principles. *J. Chem. Educ.* **1968**, *45*, 581-587.

Appendix: Thermodynamics of Metal Carbonates and Bicarbonates and Their Hydrates for Mg, Ca, Fe, and Cd Relevant to Mineral Energetics

Table A2.1. Angles for MCO_3, $M(HCO_3)_2$ and $M(HCO_3)(OH)$, M=Mg, Ca, Fe and Cd.

Metal	CO_3^{2-}		HCO_3^-				$[(HCO_3)(OH)]^{2-}$			
	<OMO	<OCO	<OMO	<OCO	<HOC	<Torsion	<OMO	<OCO	<HOC	<HOM
Mg^{2+}	76°	112°	67°	122°	106°	84°	67°	122°	106°	178°
Ca^{2+}	66°	111°	59°	124°	106°	86°	58°	124°	106°	180°
Fe^{2+}	73°	109°	65°	121°	108°	85°	65°	120°	108°	127°
Cd^{2+}	66°	113°	60°	123°	108°	85°	59°	123°	107°	111°

Mg and Ca are MP2/aT and Fe and Cd are B3LYP/aT-PP

Table A2.2. Bond lengths for MCO_3, $M(HCO_3)_2$ and $M(HCO_3)(OH)$, M=Mg, Ca, Fe and Cd.

Metal	CO_3^{2-}		HCO_3^-		$[(HCO_3)(OH)]^{2-}$	
	C – O	M – O	C – O	M – O	C – O	M – O
Mg^{2+}	1.38	1.86	1.28/1.26	2.00	1.28/1.26	2.01/2.00
Ca^{2+}	1.36	2.05	1.27/1.26	2.29/2.28	1.27	2.31
Fe^{2+}	1.37	1.86	1.27/1.26	2.05	1.27/1.26	2.08/2.04
Cd^{2+}	1.36	2.09	1.27/1.26	2.25/2.22	1.28/1.25	2.37/2.14

Table A2.3. Bond lengths, frequencies and IR intensities of $M(HCO_3)_2H_2O$, M=Mg, Ca, Fe and Cd.

$M(HCO_3)_2H_2O$	R(OH) in H_2O/Å	Asym OH $\upsilon(cm^{-1})$	Asym OH I(km/mol)	sym OH $\upsilon(cm^{-1})$	sym OH I(km/mol)
M=Mg	0.96/0.96	3898.5	139.8	3794.2	46.5
M=Ca	0.97/0.96	3888.8	148.1	3713.0	105.2
M=Fe	0.96/0.96	3879.7	130.0	3773.8	38.1
M=Cd	1.01/0.96	3847.6	92.5	2880.8	1336.9

Table A2.4. Bond lengths of MO and the differences of the bond lengths between MO and MCO3, $M(HCO_3)_2$ and $M(HCO_3)(OH)$, M=Mg, Ca, Fe and Cd.

MO	M=O	Δd with M – O in compounds		
		CO_3^{2-}	HCO_3^-	$[(HCO_3)(OH)]^{2-}$
Mg^{2+}	1.74	0.12	0.26	0.27/0.26
Ca^{2+}	1.83	0.22	0.46/0.45	0.48
Fe^{2+}	1.61	0.25	0.44	0.47/0.43
Cd^{2+}	1.90	0.19	0.35/0.32	0.47/0.24

Table A2.5. $(H_2)O$-M-$O(H_2)$ angles of $MCO3(H_2O)_2$, M=Mg, Ca, Fe and Cd.

$MCO_3(H_2O)_2$	< $(H_2)O$-M-$O(H_2)$
Mg	140°
Ca	178°
Fe	126°
Cd	160°

Table A2.6. Atomic Properties of Mg, Ca, Fe and Cd.

Metal	IP1(eV)	IP2(eV)	IP3(eV)	η =(IP-EA)/2	ionic radii Shannon (Å)	CN[a]
Mg	7.646236	15.035271	80.1436	32.55	0.72	6
Ca	6.1131554	11.871719	50.91316	19.52	1	6
Fe	7.9024681	16.1992	30.651	7.23	0.78	6 HS
Cd	8.993820	16.908313	37.468	10.28	0.95	6

[a] Coordination number for the Shannon radii.

Table A2.7. Electronic energies (au) for Mg and Ca complexes and hydrates with aug-cc-pwCVnZ basis sets for Mg and Ca the aug-cc-pVnZ basis sets for H, C and O.

Compound	awD	awT	awQ	CBS-DTQ	awT-DK	Core/awt	Valence/awT
$Mg(HCO_3)_2$	-727.644935	-728.228352	-728.422558	-728.533646	-728.8750218	-728.674850	-728.260279
$Mg(HCO_3)(OH)$	-539.421228	-539.848045	-539.993539	-540.077121	-540.3761809	-540.157355	-539.897262
$Mg(HCO_3)_2(H_2O)$	-1281.205055	-1281.800649	-1282.000359	-1282.114747	-1285.061135	-1282.409839	-1281.836991
$Mg(HCO_3)_2(H_2O)_2$	-880.251845	-880.969182	-881.204731	-881.339128	-881.7193739		
$Mg(HCO_3)(OH)(H_2O)_2$	-692.037640	-692.598990	-692.786073	-692.893111	-693.2307173	-693.023056	-692.656864
$MgCO_3(H_2O)$	-539.353749	-539.779673	-539.925138	-540.008731	-540.307942	-540.060432	-539.800159
$MgCO_3(H_2O)_2$	-615.677156	-616.171330	-616.337731	-616.433113	-616.751287	-616.509458	-616.195918
$MgCO_3(H_2O)_3$	-691.989943	-692.550763	-692.737667	-692.844600	-693.182486	-692.946212	-692.579485
$MgCO_3(H_2O)_4$	-768.300609	-768.928248	-769.135444	-769.253781	-769.611730	-769.380878	-768.960966
$CaCO_3$[a]	-940.455953	-940.935238	-941.164982	-941.303751			
$Ca(HCO_3)_2$	-1204.900929	-1205.42853	-1205.60719	-1205.709700	-1208.637232	-1205.9795	-1205.460641
$Ca(HCO_3)(OH)$	-1016.675413	-1017.04701	-1017.17637	-1017.250959	-1020.13713	-1017.432029	-1017.070104
$Ca(HCO_3)_2(H_2O)$	-1281.205055	-1281.800649	-1282.000359	-1282.114747	-1285.061135	-1282.409839	-1281.836991
$Ca(HCO_3)_2(H_2O)_2$	-1357.507738	-1358.171651	-1358.391199	-1358.516631	-1361.483964	-1358.834758	-1358.214609
$Ca(HCO_3)(OH)(H_2O)_2$	-1169.290146	-1169.796721	-1169.968107	-1170.066431	-1172.990559	-1170.297795	-1169.829648
$CaCO_3(H_2O)$	-1016.618866	-1016.992577	-1017.122559	-1017.197495	-1020.082627	-1017.377783	-1017.013099
$CaCO_3(H_2O)_2$	-1092.935652	-1093.376453	-1093.527332	-1093.614070	-1096.518317	-1093.819391	-1093.401155
$CaCO_3(H_2O)_3$	-1169.242117	-1169.750045	-1169.921503	-1170.019828	-1172.943727	-1170.250685	-1169.778889
$CaCO_3(H_2O)_4$	-1245.558032	-1246.133000	-1246.324385	-1246.433859	-1249.378521	-1246.692291	-1246.165773

[a] Aug-cc-pwCVnZ basis sets for all atoms with core electrons included.

Table A2.8. Electronic energies (au) for small Fe molecules with the aug-cc-pwCVnZ-DK basis sets.

Compound	awT-DK	awQ-DK	aw5-DK	CBS(Q,5)
^5FeO	-1347.206077	-1347.262977	-1347.285409	-1347.303624
$^5FeCl_2$	-2195.000174	-2195.176665	-2195.243963	-2195.314572
$^5Fe(OH)_2$	-1423.779779	-1423.863303	-1423.893534	-1423.925252

Table A2.9. Electronic energies (au) for small Cd molecules.

Compound	awD-PP	awT-PP	awQ-PP	CBS-DTQ	awT-DK
$CdCl_2$	-1087.227835	-1087.794685	-1088.002765	-1088.123821	-6514.025443
$Cd(OH)_2$	-318.910742	-319.265351	-319.381866	-319.448354	-5742.779186

Table A2.10. Electronic energies (au) for Fe and Cd complexes and hydrates.

Compound	aD	aT	aQ	CBS-DTQ	CISD	aT-DK	Core/awt	Valence/awT
$^5FeCO_3$	-386.002167	-386.261713	-386.344427	-386.391354	-0.199524		-386.944647	-386.288780
$^5Fe(HCO_3)_2$	-650.580461	-651.066502	-651.219890	-651.306748	-0.369129		-651.971277	-651.108919
$^5Fe(HCO_3)(OH)$	-462.381481	-462.710274	-462.814725	-462.873950	-0.251084		-463.450578	-462.741573
$^5Fe(HCO_3)_2(H_2O)$	-726.884811							
$^5Fe(HCO_3)_2(H_2O)_2$[a]	-803.174837							
$^5Fe(HCO_3)_2(H_2O)_2$	-803.177036							
$^5Fe(HCO_3)(OH)(H_2O)_2$	-614.979821	-615.445578						
$^5FeCO_3(H_2O)$	-462.326210	-462.654450						
$^5FeCO_3(H_2O)_2$	-538.633696	-539.030428						
$^5FeCO_3(H_2O)_3$[b]	-614.942441	-615.408032						
$CdCO_3$	-430.371974	-430.677638	-430.783381	-430.844285		-5854.287148	-431.279477	-430.715240
$Cd(HCO_3)_2$	-694.964923	-695.497526	-695.674414	-695.775554		-6119.276995	-696.321972	-695.550654
$Cd(HCO_3)(OH)$	-506.755460	-507.130930	-507.258576	-507.331870		-5930.792194	-507.790889	-507.172849
$Cd(HCO_3)_2(H_2O)$	-771.262709	-771.864117	-772.062014	-772.174972				
$Cd(HCO_3)_2(H_2O)_2$	-847.559984	-848.230313						
$Cd(HCO_3)(OH)(H_2O)_2$	-659.348126	-659.859344	-660.029211	-660.126344				
$CdCO_3(H_2O)$	-506.687260	-507.062248	-507.189790	-507.263030				
$CdCO_3(H_2O)_2$	-582.989735	-583.432760	-583.581397	-583.666542				
$CdCO_3(H_2O)_3$	-659.296961	-659.808161	-659.977773	-660.074734				
$CdCO_3(H_2O)_4$	-735.601653	-736.180331	-736.370677	-736.479318				

[a] Both HCO_3 are monodentate. [b] Only 2 H_2O in 1st solvation shell.

Table A2.11. Energy contribution to the total atomization energies in kcal/mol for Mg and Ca complexes and hydrates with the aug-cc-pwCVnZ basis sets for Mg and Ca the aug-cc-pVnZ basis sets for H, C and O. ΔE_{TC} = thermal corrections to convert from ΔH(0) to ΔH(298 K).

Compound	$\Delta E_{n=D}$	$\Delta E_{n=T}$	$\Delta E_{n=Q}$	$\Delta E_{CBS-DTQ}$	ΔE_{SR}	ΔE_{CV}	ΔE_{ZPE}	ΔE_{SO}	$\sum D_{0,0K}$	ΔE_{TC}
$Mg(HCO_3)_2$	1134.7	1195.4	1215.3	1226.7	-2.2	3.6	-37.2	-1.5	1189.4	4.0
$Mg(HCO_3)(OH)$	753.3	793.2	806.2	813.6	-1.7	2.0	-26.1	-1.0	786.8	2.6
$Mg(HCO_3)_2(H_2O)$	1374.6	1443.6	1466.3	1479.3	-2.3	4.1	-52.1	-1.7	1425.4	8.4
$Mg(HCO_3)(OH)(H_2O)_2$	1235.2	1291.5	1309.8	1320.2	-2.2	2.6	-58.3	-1.4	1260.9	5.9
$MgCO_3(H_2O)$	710.9	750.3	763.3	770.7	-1.4	2.1	-25.6	-1.0	744.8	5.4
$MgCO_3(H_2O)_2$	961.4	1009.6	1025.3	1034.3	-1.7	2.5	-41.6	-1.2	992.3	6.6
$MgCO_3(H_2O)_3$	1205.2	1261.2	1279.4	1289.8	-2.0	3.0	-57.1	-1.4	1232.2	8.2
$MgCO_3(H_2O)_4$	1447.7	1511.6	1532.1	1543.8	-2.3	3.4	-73.4	-1.6	1469.8	9.6
$CaCO_3$ [a]	498.1	531.2	543.2	550.2	-1.5[b]		10.2	-0.8	537.7	3.4
$Ca(HCO_3)_2$	1158.7	1219.9	1241.6	1254.2	-3.0	5.2	-36.1	-1.5	1218.8	3.6
$Ca(HCO_3)(OH)$	776.2	817.0	831.4	839.7	-2.5	2.0	-25.8	-1.0	812.5	2.6
$Ca(HCO_3)_2(H_2O)$	1397.1	1467.0	1491.5	1505.6	-3.0	6.1	-51.1	-1.7	1455.9	8.8
$Ca(HCO_3)_2(H_2O)_2$	1634.6	1713.3	1739.9	1755.1	-3.6	2.8	-62.2	-1.9	1690.2	5.6
$Ca(HCO_3)(OH)(H_2O)_2$	1257.1	1314.5	1334.5	1346.0	-3.0	2.7	-56.6	-1.4	1287.7	5.4
$CaCO_3(H_2O)$	740.7	782.8	797.6	806.2	-2.3	3.7	-25.4	-1.0	781.2	5.1
$CaCO_3(H_2O)_2$	987.1	1037.2	1054.7	1064.8	-2.6	4.4	-40.6	-1.2	1024.8	6.9
$CaCO_3(H_2O)_3$	1226.9	1285.2	1305.2	1316.7	-2.8	5.0	-55.9	-1.6	1261.4	8.6
$CaCO_3(H_2O)_4$	1472.7	1539.0	1561.1	1573.8	-3.0	6.4	-71.9	-1.6	1503.6	10.2

[a] Aug-cc-pwCVnZ basis sets for all atoms with core electrons included so there is no core-valence correction. [b] The value is from a MVD/CISD calculation.

Table A2.12. Energy contribution to the total atomization energies in kcal/mol for small Fe molecules.

Compound	$\Delta E_{n=T}$	$\Delta E_{n=Q}$	$\Delta E_{n=5}$	$\Delta E_{CBS(Q,5)}$	ΔE_{ZPE}	ΔE_{SO}	$\sum D_{0,0K}$	ΔE_{TC}
^5FeO	92.6	95.5	96.7	97.7	-1.2	-0.6	95.8	2.1
$^5FeCl_2$	184.9	189.8	191.4	193.0	-1.4	-2.9	188.7	3.4
$^5Fe(OH)_2$	394.0	400.6	402.6	404.7	-15.2	-1.6	387.9	4.0

Table A2.13. Energy contribution to the total atomization energies in kcal/mol for small Cd molecules.

Compound	$\Delta E_{n=D}$	$\Delta E_{n=T}$	$\Delta E_{n=Q}$	$\Delta E_{CBS-DTQ}$	ΔE_{SR}	ΔE_{ZPE}	ΔE_{SO}	$\sum D_{0,0K}$	ΔE_{TC}
$CdCl_2$	125.5	131.0	135.3	138.0	-0.9	-1.3	-1.7	134.1	3.5
$Cd(OH)_2$	308.8	324.1	330.1	333.6	-0.8	-15.6	-0.4	316.8	3.9

Table A2.14. Energy contribution to the total atomization energies in kcal/mol for Fe and Cd molecules

Compound	$\Delta E_{n=D}$	$\Delta E_{n=T}$	$\Delta E_{n=Q}$	$\Delta E_{CBS-DTQ}$	ΔE_{SR}	ΔE_{CV}	ΔE_{ZPE}	ΔE_{SO}	$\sum D_{0,0K}$	ΔE_{TC}
$^5FeCO_3$	464.2	492.3	502.4	508.3	-0.9	1.0	-9.9	-2.0	496.5	3.4
$^5Fe(HCO_3)_2$	1115.7	1174.4	1194.8	1206.6	-2.1	2.3	-36.4	-2.7	1167.7	6.4
$^5Fe(HCO_3)(OH)$	749.8	787.3	800.7	808.4	-1.3	1.4	-25.8	-2.2	780.5	5.2
$CdCO_3$	389.7	416.8	426.4	431.9	-1.2	0.0	-8.9	-0.8	421.1	3.7
$Cd(HCO_3)_2$	1050.3	1108.3	1128.6	1140.2	-2.3	1.7	-35.8	-1.5	1102.3	6.8
$Cd(HCO_3)(OH)$	677.9	714.8	727.7	735.2	-1.5	0.8	-25.7	-1.0	707.8	5.3

Table A2.15. Electronic energy contributions to the hydration energy in kcal/mol for Fe molecules with water complex.

Compound	$\Delta E_{n=D}$	$\Delta E_{n=T}$	$\Delta E_{n=Q}$	ΔE_{CBS}	ΔE_{ZPE}	ΔH_{0K}	ΔE_{TC}	ΔH_{298K}
$^5Fe(HCO_3)_2(H_2O)$	-19.1				1.4	-17.7	1.4	-17.8
$^5Fe(HCO_3)_2(H_2O)_2$[a]	-29.3				4.3	-25.0	2.6	-26.7
$^5Fe(HCO_3)_2(H_2O)_2$	-30.7				3.7	-26.9	3.0	-27.6
$^5Fe(HCO_3)(OH)(H_2O)_2$	-31.8	-31.8			4.5	-27.3	3.0	-28.9
$^5FeCO_3(H_2O)$	-31.5	-31.7			1.7	-29.9	1.6	-30.1
$^5FeCO_3(H_2O)_2$	-52.6	-52.8			4.3	-48.5	3.2	-49.6
$^5FeCO_3(H_2O)_3$[b]	-74.5	-75.0			6.5	-68.4	4.5	-70.5
$Cd(HCO_3)_2(H_2O)$	-15.0	-15.2	-15.1	-15.0	2.2	-12.8	1.3	-13.6
$Cd(HCO_3)_2(H_2O)_2$	-29.7	-30.3			4.4	-25.8	2.6	-27.6
$Cd(HCO_3)(OH)(H_2O)_2$	-28.2	-27.5	-27.3	-27.2	4.1	-23.1	2.9	-24.3
$CdCO_3(H_2O)$	-26.0	-26.5	-26.9	-27.1	2.0	-25.1	2.0	-25.1
$CdCO_3(H_2O)_2$	-44.0	-44.2	-44.5	-44.6	5.0	-39.6	3.5	-41.1
$CdCO_3(H_2O)_3$	-64.9	-65.0	-65.0	-65.1	7.1	-58.0	4.9	-60.2
$CdCO_3(H_2O)_4$	-84.3	-83.7	-83.4	-83.3	9.5	-73.8	6.6	-76.7

[a]Both HCO_3 are monodentate. [b] Only 2 H_2O in 1st solvation shell.

Table A2.16. Hydration reaction energies in kcal/mol.

Molecule	aD/wDZ	aT/wTZ	aQ/wQZ	CBS
$Mg(HCO_3)_2(H_2O)$	-20.5	-19.9	-19.7	-19.6
$Mg(HCO_3)_2(H_2O)_2$	-37.1	-35.3	-34.5	-34.1
$Mg(HCO_3)(OH)(H_2O)_2$	-43.1	-41.7	-41.0	-40.7
$MgCO_3(H_2O)$	-33.8	-34.8	-35.0	-35.1
$MgCO_3(H_2O)_2$	-64.9	-65.8	-65.8	-65.7
$MgCO_3(H_2O)_3$	-89.3	-89.1	-88.6	-88.2
$MgCO_3(H_2O)_4$	-112.4	-111.2	-110.1	-109.4
$Ca(HCO_3)_2(H_2O)$	-19.0	-18.7	-18.6	-18.5
$Ca(HCO_3)_2(H_2O)_2$	-37.1	-36.7	-36.3	-35.9
$Ca(HCO_3)(OH)(H_2O)_2$	-42.1	-40.9	-40.5	-40.4
$CaCO_3(H_2O)$	-27.7	-26.6	-26.3	-26.2
$CaCO_3(H_2O)_2$	-54.6	-52.7	-52.2	-52.0
$CaCO_3(H_2O)_3$	-75.1	-72.3	-71.4	-70.9
$CaCO_3(H_2O)_4$	-101.4	-97.8	-96.1	-95.0
$Cd(HCO_3)_2(H_2O)$	-15.0	-15.3	-15.1	-15.0
$Cd(HCO_3)_2(H_2O)_2$	-29.7	-30.3		
$Cd(HCO_3)(OH)(H_2O)_2$	-28.2	-27.5	-27.3	-27.2
$CdCO_3(H_2O)$	-26.0	-26.6	-26.9	-27.1
$CdCO_3(H_2O)_2$	-44.0	-44.3	-44.5	-44.6
$CdCO_3(H_2O)_3$	-64.9	-65.1	-65.1	-65.0
$CdCO_3(H_2O)_4$	-84.2	-83.8	-83.5	-83.3

Table A2.17. Electronic energies (au) with DFT functionals for O_2, H_2O, CO_2 and HCO_3^-.

Method	O_2	H_2O	CO_2	HCO_3^-
PW91	-150.350356	-76.438426	-188.612915	-264.501746
BP86	-150.393319	-76.466006	-188.669364	-264.581963
M06	-150.302632	-76.422525	-188.572453	-264.435269
PBE	-150.243527	-76.380205	-188.472120	-264.302025
PBE0	-150.229943	-76.379961	-188.459587	-264.287753
B3LYP	-150.384612	-76.466177	-188.663387	-264.573364
HCTH 407	-150.351963	-76.456891	-188.616921	-264.508746
HSE06	-150.243508	-76.386775	-188.477180	-264.311759
M06L	-150.358532	-76.444755	-188.642119	-264.519705
τ-HCTH	-150.341856	-76.449649	-188.599758	-264.487118
τ-HCTH hyb	-150.345388	-76.448477	-188.613643	-264.505672
TPSSh	-150.385645	-76.458128	-188.661665	-264.562942
ωB97X	-150.346568	-76.441451	-188.612560	-264.502210
ωB97X-D	-150.334159	-76.439881	-188.598407	-264.480919

Table A2.18. Electronic energies (au) with DFT functionals for MO, M=Mg, Ca, Fe and Cd.

Method	MgO	CaO	^{5}FeO	CdO
PW91	-275.222854	-752.822885	-198.629606	-242.930899
BP86	-275.278656	-752.912744	-198.670697	-242.984378
M06	-275.197246	-752.766347	-198.524669	-242.866158
PBE	-275.063053	-752.543552	-198.510875	-242.801996
PBE0	-275.058546	-752.565358	-198.438976	-242.769390
B3LYP	-275.274898	-752.846158	-198.584799	-242.921522
HCTH 407	-275.246667	-752.968038	-198.999168	-243.367160
HSE06	-275.080356	-752.592907	-198.444102	-242.775021
M06L	-275.226472	-752.805241	-198.585447	-242.970559
τ-HCTH	-275.241849	-752.999351	-199.017276	-243.393197
τ-HCTH hyb	-275.210768	-752.771850	-198.646577	-242.993338
TPSSh	-275.261871	-752.846719	-198.517265	-242.795762
ωB97X	-275.212612	-752.801142	-198.508331	-242.853082
ωB97X-D	-275.208615	-752.798833	-198.518726	-242.874611

Table A2.19. Electronic energies (au) with DFT functionals for $M(OH)_2$, M=Mg, Ca, Fe and Cd.

Method	$Mg(OH)_2$	$Ca(OH)_2$	$^5Fe(OH)_2$	$Cd(OH)_2$
PW91	-351.820949	-829.386653	-275.164859	-319.489326
BP86	-351.901526	-829.502101	-275.231364	-319.567890
M06	-351.803619	-829.332942	-275.074896	-319.415658
PBE	-351.600661	-829.047906	-274.987432	-319.301220
PBE0	-351.617049	-829.085210	-274.941085	-319.280900
B3LYP	-351.913028	-829.450492	-275.166105	-319.510238
HCTH 407	-351.861848	-829.544172	-275.552171	-319.936308
HSE06	-351.645248	-829.120015	-274.952681	-319.292642
M06L	-351.852320	-829.389157	-275.146957	-319.539049
τ-HCTH	-351.856396	-829.571345	-275.568896	-319.960886
τ-HCTH hyb	-351.832255	-829.354931	-275.211256	-319.567124
TPSSh	-351.890892	-829.438790	-275.086767	-319.379195
ωB97X	-351.845909	-829.395459	-275.067953	-319.436536
ωB97X-D	-351.835564	-829.385034	-275.066185	-319.448832

Table A2.20. Electronic energies (au) with DFT functionals for MCl_2, M=Mg, Ca, Fe and Cd.

Method	$MgCl_2$	$CaCl_2$	$^5FeCl_2$	$CdCl_2$
PW91	-1120.635826	-1598.198947	-1043.970325	-1088.319978
BP86	-1120.779658	-1598.377927	-1044.099346	-1088.460971
M06	-1120.634520	-1598.168423	-1043.907138	-1088.274616
PBE	-1120.177450	-1597.621765	-1043.554154	-1087.892795
PBE0	-1120.274553	-1597.744560	-1043.592330	-1087.959585
B3LYP	-1120.734151	-1598.273381	-1043.980651	-1088.352591
HCTH 407	-1120.818830	-1598.500352	-1044.501641	-1088.909362
HSE06	-1120.323557	-1597.800262	-1043.624992	-1087.992518
M06L	-1120.667395	-1598.208058	-1043.958937	-1088.375929
τ-HCTH	-1120.856079	-1598.579945	-1044.561915	-1088.977034
τ-HCTH hyb	-1120.587417	-1598.111415	-1043.960331	-1088.341980
TPSSh	-1120.725293	-1598.273392	-1043.912131	-1088.230694
ωB97X	-1120.674423	-1598.227931	-1043.898662	-1088.289732
ωB97X-D	-1120.674180	-1598.227741	-1043.907784	-1088.312280

Table A2.21. Electronic energies (au) with DFT functionals for Mg molecules without H_2O.

Method	MgO	$MgCl_2$	$Mg(OH)_2$	$MgCO_3$	$Mg(HCO_3)_2$	$Mg(HCO_3)(OH)$
PW91	-275.222854	-1120.635826	-351.820949	-463.917970	-729.121142	-540.470440
BP86	-275.278656	-1120.779658	-351.901526	-464.025916	-729.306994	-540.603643
M06	-275.197246	-1120.634520	-351.803619	-463.863617	-729.013539	-540.407616
PBE	-275.063053	-1120.177450	-351.600661	-463.615871	-728.618733	-540.109110
PBE0	-275.058546	-1120.274553	-351.617049	-463.616805	-728.623598	-540.119545
B3LYP	-275.274898	-1120.734151	-351.913028	-464.021341	-729.303971	-540.607774
HCTH 407	-275.246667	-1120.818830	-351.861848	-463.935303	-729.149558	-540.505104
HSE06	-275.080356	-1120.323557	-351.645248	-463.654472	-728.684427	-540.164063
M06L	-275.226472	-1120.667395	-351.852320	-463.955757	-729.195487	-540.522871
τ-HCTH	-275.241849	-1120.856079	-351.856396	-463.922150	-729.117901	-540.486488
τ-HCTH hyb	-275.210768	-1120.587417	-351.832255	-463.914277	-729.133737	-540.482256
TPSSh	-275.261871	-1120.725293	-351.890892	-464.012948	-729.288151	-540.588797
ωB97X	-275.212612	-1120.674423	-351.845909	-463.930329	-729.151705	-540.497935
ωB97X-D	-275.208615	-1120.674180	-351.835564	-463.907107	-729.107548	-540.470549

Table A2.22. Electronic energies (au) with DFT functionals for Mg molecules with H_2O.

Method	Mg $(HCO_3)_2$ H_2O	Mg $(HCO_3)_2$ $(H_2O)_2$	Mg(HCO_3) (OH) $(H_2O)_2$	$MgCO_3$ H_2O	$MgCO_3$ $(H_2O)_2$	$MgCO_3$ $(H_2O)_3$	$MgCO_3$ $(H_2O)_4$
PW91	-805.586601	-882.043559	-693.410230	-540.405734	-616.890192	-693.363447	-769.831915
BP86	-805.796934	-882.277891	-693.592894	-540.538954	-617.048105	-693.545896	-770.038736
M06	-805.467881	-881.912596	-693.317562	-540.337602	-616.809110	-693.266690	-769.723997
PBE	-805.025070	-881.422893	-692.930820	-540.044645	-616.469725	-692.883924	-769.293210
PBE0	-805.031792	-881.430506	-692.941986	-540.058463	-616.478045	-692.893042	-769.303687
B3LYP	-805.797134	-882.279103	-693.597967	-540.539944	-617.050216	-693.548652	-770.042605
HCTH 407	-805.628893	-882.096080	-693.466501	-540.438812	-616.931412	-693.416915	-769.894928
HSE06	-805.099821	-881.505680	-693.000882	-540.095369	-616.529851	-692.951851	-769.369878
M06L	-805.670997	-882.140808	-693.477700	-540.452240	-616.947069	-693.427339	-769.908583
τ-HCTH	-805.590696	-882.052304	-693.438768	-540.419529	-616.909482	-693.390162	-769.863955
τ-HCTH hyb	-805.609227	-882.074618	-693.439171	-540.414321	-616.908191	-693.390468	-769.868018
TPSSh	-805.772464	-882.248037	-693.564851	-540.522208	-617.025699	-693.517257	-770.004608
ωB97X	-805.625070	-882.089142	-693.446654	-540.426685	-616.918173	-693.396233	-769.872674
ωB97X-D	-805.577542	-882.038433	-693.412341	-540.400059	-616.887469	-693.362743	-769.836022

Table A2.23. Electronic energies (au) with DFT functionals for Ca molecules without H_2O.

Method	CaO	$CaCl_2$	Ca $(OH)_2$	$CaCO_3$	Ca $(HCO_3)_2$	Ca $(HCO_3)(OH)$
PW91	-752.822885	-1598.198947	-829.386653	-941.517966	-1206.688653	-1018.038104
BP86	-752.912744	-1598.377927	-829.502101	-941.660245	-1206.909339	-1018.262020
M06	-752.766347	-1598.168423	-829.332942	-941.427488	-1206.549235	-1017.941541
PBE	-752.543552	-1597.621765	-829.047906	-941.096841	-1206.067243	-1017.558046
PBE0	-752.565358	-1597.744560	-829.085210	-941.121132	-1206.095186	-1017.590681
B3LYP	-752.846158	-1598.273381	-829.450492	-941.593596	-1206.845639	-1018.148578
HCTH 407	-752.968038	-1598.500352	-829.544172	-941.653775	-1206.833187	-1018.189202
HSE06	-752.592907	-1597.800262	-829.120015	-941.165212	-1206.163064	-1017.642014
M06L	-752.805241	-1598.208058	-829.389157	-941.529768	-1206.737581	-1018.063697
τ-HCTH	-752.999351	-1598.579945	-829.571345	-941.674767	-1206.835502	-1018.203943
τ-HCTH hyb	-752.771850	-1598.111415	-829.354931	-941.473075	-1206.659962	-1018.007959
TPSSh	-752.846719	-1598.273392	-829.438790	-941.596167	-1206.838892	-1018.139284
ωB97X	-752.801142	-1598.227931	-829.395459	-941.513080	-1206.707367	-1018.051901
ωB97X-D	-752.798833	-1598.227741	-829.385034	-941.491071	-1206.662951	-1018.024393

Table A2.24. Electronic energies (au) with DFT functionals for Ca molecules with H_2O.

Method	Ca $(HCO_3)_2$ H_2O	Ca $(HCO_3)_2$ $(H_2O)_2$	Ca(HCO_3) (OH) $(H_2O)_2$	$CaCO_3$ H_2O	$CaCO_3$ $(H_2O)_2$	$CaCO_3$ $(H_2O)_3$	$CaCO_3$ $(H_2O)_4$
PW91	-1283.152555	-1359.615236	-1170.975933	-1017.993476	-1094.468433	-1170.934425	-1247.407432
BP86	-1283.397715	-1359.884826	-1171.193398	-1018.160728	-1094.660752	-1171.151655	-1247.649423
M06	-1282.999304	-1359.448367	-1170.846999	-1017.889920	-1094.351117	-1170.802027	-1247.263652
PBE	-1282.472152	-1358.875875	-1170.377662	-1017.513150	-1093.928986	-1170.335969	-1246.749980
PBE0	-1282.501520	-1358.905767	-1170.411338	-1017.540196	-1093.958010	-1170.366085	-1246.780476
B3LYP	-1283.337633	-1359.826832	-1171.137997	-1018.096867	-1094.599498	-1171.092293	-1247.591325
HCTH 407	-1283.311657	-1359.787480	-1171.149652	-1018.140202	-1094.626180	-1171.104810	-1247.588190
HSE06	-1282.576591	-1358.987966	-1170.477171	-1017.591589	-1094.016739	-1170.431905	-1246.853735
M06L	-1283.210023	-1359.681874	-1171.014360	-1018.013656	-1094.496554	-1170.969127	-1247.452926
τ-HCTH	-1283.306669	-1359.775710	-1171.155067	-1018.156994	-1094.638383	-1171.111673	-1247.589952
τ-HCTH hyb	-1283.133298	-1359.604616	-1170.962910	-1017.958715	-1094.443388	-1170.918552	-1247.400387
TPSSh	-1283.321191	-1359.801689	-1171.112952	-1018.090943	-1094.584800	-1171.068977	-1247.560135
ωB97X	-1283.178673	-1359.648054	-1170.999258	-1017.996985	-1094.479829	-1170.952190	-1247.432720
ωB97X-D	-1283.130440	-1359.595871	-1170.964340	-1017.970822	-1094.449393	-1170.918312	-1247.395443

Table A2.25. Electronic energies (au) with DFT functionals for Fe molecules without H_2O.

Method	^5FeO	$^5FeCl_2$	$^5Fe(OH)_2$	$^5FeCO_3$	$^5Fe(HCO_3)_2$	$^5Fe(HCO_3)(OH)$
PW91	-198.629606	-1043.970325	-275.164859	-387.264393	-652.412563	-463.793929
BP86	-198.670697	-1044.099346	-275.231364	-387.357479	-652.583299	-463.912608
M06	-198.524669	-1043.907138	-275.074896	-387.137638	-652.251924	-463.666125
PBE	-198.510875	-1043.554154	-274.987432	-387.005153	-651.953024	-463.475411
PBE0	-198.438976	-1043.592330	-274.941085	-386.942060	-651.900909	-463.425842
B3LYP	-198.584799	-1043.980651	-275.166105	-387.276937	-652.509596	-463.842537
HCTH 407	-198.999168	-1044.501641	-275.552171	-387.638202	-652.795874	-464.178366
HSE06	-198.444102	-1043.624992	-274.952681	-386.963091	-651.945316	-463.453788
M06L	-198.585447	-1043.958937	-275.146957	-387.254777	-652.440480	-463.800856
τ-HCTH	-199.017276	-1044.561915	-275.568896	-387.648950	-652.786401	-464.184276
τ-HCTH hyb	-198.646577	-1043.960331	-275.211256	-387.297515	-652.467410	-463.844655
TPSSh	-198.517265	-1043.912131	-275.086767	-387.211189	-652.434271	-463.766235
ωB97X	-198.508331	-1043.898662	-275.067953	-387.047915	-652.352367	-463.722628
ωB97X-D	-198.518726	-1043.907784	-275.066185	-387.038567	-652.317226	-463.705834

Table A2.26. Electronic energies (au) with DFT functionals for Fe molecules with H_2O.

Method	$^5Fe(HCO_3)_2 H_2O$	$^5Fe(HCO_3)_2 (H_2O)_2$[a]	$^5Fe(HCO_3)_2 (H_2O)_2$	$^5Fe(HCO_3)(OH) (H_2O)_2$	$^5FeCO_3 H_2O$	$^5FeCO_3 (H_2O)_2$
PW91	-728.876474	-805.350525	-805.330252	-616.715065	-463.749156	-540.212161
BP86	-729.072312	-805.571295	-805.550320	-616.883567	-463.868011	-540.355415
M06	-728.701553	-805.144780	-805.155550	-616.562812	-463.612484	-540.068172
PBE	-728.357420	-804.771768	-804.752120	-616.277921	-463.430836	-539.834672
PBE0	-728.309702	-804.722193	-804.701191	-616.231850	-463.370346	-539.779740
B3LYP	-729.002075	-805.501201	-805.481704	-616.817640	-463.789291	-540.281503
HCTH 407	-729.267521	-805.749582	-805.731863	-617.120864	-464.133287	-540.607463
HSE06	-728.361340	-804.781738	-804.764610	-616.274643	-463.398615	-539.815174
M06L	-728.918972	-805.392919	-805.383970	-616.737516	-463.749009	-540.223349
τ-HCTH	-729.258073	-805.739620	-805.717996	-617.120933	-464.139864	-540.611155
τ-HCTH hyb	-728.943442	-805.424895	-805.406559	-616.786847	-463.793313	-540.269309
TPSSh	-728.920380	-805.409223	-805.388252	-616.724752	-463.715358	-540.199827
ωB97X	-728.825119	-805.301278	-805.286768	-616.659260	-463.664927	-540.140694
ωB97X-D	-728.787448	-805.259985	-805.245448	-616.635065	-463.648755	-540.119641

Table A2.27. Electronic energies (au) with DFT functionals for Cd molecules without H_2O.

Method	CdO	$CdCl_2$	$Cd(OH)_2$	$CdCO_3$	$Cd(HCO_3)_2$	$Cd(HCO_3)(OH)$
PW91	-242.930899	-1088.319978	-319.489326	-431.572922	-696.746999	-508.115825
BP86	-242.984378	-1088.460971	-319.567890	-431.678402	-696.930492	-508.246876
M06	-242.866158	-1088.274616	-319.415658	-431.469389	-696.592982	-508.001824
PBE	-242.801996	-1087.892795	-319.301220	-431.302518	-696.276070	-507.786339
PBE0	-242.769390	-1087.959585	-319.280900	-431.271119	-696.248677	-507.762069
B3LYP	-242.921522	-1088.352591	-319.510238	-431.611363	-696.862613	-508.184135
HCTH 407	-243.367160	-1088.909362	-319.936308	-432.004545	-697.181684	-508.556998
HSE06	-242.775021	-1087.992518	-319.292642	-431.292509	-696.293551	-507.790411
M06L	-242.970559	-1088.375929	-319.539049	-431.641096	-696.851148	-508.192465
τ-HCTH	-243.393197	-1088.977034	-319.960886	-432.020698	-697.182105	-508.569244
τ-HCTH hyb	-242.993338	-1088.341980	-319.567124	-431.639797	-696.828676	-508.195379
TPSSh	-242.795762	-1088.230694	-319.379195	-431.492281	-696.737715	-508.055802
ωB97X	-242.853082	-1088.289732	-319.436536	-431.511321	-696.710506	-508.070773
ωB97X-D	-242.874611	-1088.312280	-319.448832	-431.512044	-696.687868	-508.065638

Table A2.28. Electronic energies (au) with DFT functionals for Cd molecules with H_2O.

Method	Cd $(HCO_3)_2$ H_2O	Cd $(HCO_3)_2$ $(H_2O)_2$	Cd(HCO_3) (OH) $(H_2O)_2$	$CdCO_3$ H_2O	$CdCO_3$ $(H_2O)_2$	$CdCO_3$ $(H_2O)_3$	$CdCO_3$ $(H_2O)_4$
PW91	-773.208734	-849.670498	-661.028553	-508.051000	-584.512383	-660.979219	-737.442464
BP86	-773.417322	-849.904165	-661.209542	-508.182077	-584.668065	-661.159818	-737.647608
M06	-773.039021	-849.484486	-660.887985	-507.933045	-584.382536	-660.836135	-737.288357
PBE	-772.678393	-849.080746	-660.580900	-507.721509	-584.123665	-660.531220	-736.935284
PBE0	-772.651750	-849.054397	-660.559061	-507.692442	-584.097037	-660.506715	-736.912195
B3LYP	-773.351008	-849.838932	-661.149071	-508.115960	-584.602954	-661.095785	-737.584815
HCTH 407	-773.654185	-850.126547	-661.492926	-508.491357	-584.961923	-661.438108	-737.912158
HSE06	-772.704127	-849.114277	-660.602008	-507.720981	-584.132848	-660.549869	-736.962721
M06L	-773.317919	-849.784468	-661.125622	-508.124995	-584.597278	-661.073690	-737.548541
τ-HCTH	-773.651498	-850.120822	-661.496345	-508.503244	-584.971334	-661.444640	-737.914257
τ-HCTH hyb	-773.299753	-849.770485	-661.126530	-508.127272	-584.598143	-661.074599	-737.547198
TPSSh	-773.216568	-849.695270	-661.006453	-507.988765	-584.469917	-660.955855	-737.437910
ωB97X	-773.178533	-849.645793	-660.997902	-507.999404	-584.469374	-660.944233	-737.415315
ωB97X-D	-773.152771	-849.617035	-660.985301	-507.995143	-584.460840	-660.932170	-737.400382

Table A2.29. Benchmarking errors in DFT functionals for MO in kcal/mol, M=Mg, Ca, Fe and Cd.

Method	MgO	CaO	^{5}FeO	CdO
$\Delta H_{f,0K}$ gas	32.5	5.0	61.8	64.9
PW91	5.5	27.6	29.4	10.2
BP86	4.2	25.9	27.7	8.8
M06	-11.5	4.7	22.3	-11.6
PBE	4.3	25.5	28.4	9.9
PBE0	-15.1	4.0	16.9	-6.9
B3LYP	-10.5	5.7	19.2	-5.8
HCTH 407	-2.9	19.6	13.3	-0.3
HSE06	-14.8	3.8	16.4	-7.4
M06L	-7.9	16.1	6.8	-1.8
τ-HCTH	-2.1	23.9	13.8	1.6
τ-HCTH hyb	-6.7	14.3	28.8	-1.9
TPSSh	-10.2	11.5	9.0	-1.7
ωB97X	-14.8	2.5	14.4	-9.3
ωB97X-D	-14.5	4.5	11.6	-9.3

Table A2.30. Benchmarking errors in DFT functionals for $M(OH)_2$ in kcal/mol, M=Mg, Ca, Fe and Cd.

Method	$Mg(OH)_2$	$Ca(OH)_2$	$^5Fe(OH)_2$	$Cd(OH)_2$
$\Delta H_{f,0K}$ gas	-130.4	-144.0	-80.7	-68.8
PW91	1.4	15.4	6.3	9.7
BP86	3.1	17.2	8.0	11.5
M06	-5.4	-0.6	13.7	-12.7
PBE	-2.1	11.8	4.2	7.9
PBE0	-15.4	-7.0	1.7	-8.2
B3LYP	-11.1	-2.6	3.4	-9.0
HCTH 407	-12.2	-0.8	-14.6	-10.1
HSE06	-16.2	-7.8	0.2	-10.0
M06L	-9.4	1.8	-14.6	-10.8
τ-HCTH	-9.3	3.6	-12.3	-6.5
τ-HCTH hyb	-9.3	1.1	11.0	-6.0
TPSSh	-15.6	-3.5	-13.3	-7.2
ωB97X	-5.0	1.4	-1.5	-2.3
ωB97X-D	-6.6	0.4	-9.9	-6.0

Table A2.31. Benchmarking errors in DFT functionals for MCl_2 in kcal/mol, M=Mg, Ca, Fe and Cd.

Method	$MgCl_2$	$CaCl_2$	$^5FeCl_2$	$CdCl_2$
$\Delta H_{f,0K}$ gas	-95.0	-113.9	-32.9	-50.2
PW91	-1.4	6.7	10.3	0.8
BP86	-4.6	3.8	6.6	-2.8
M06	1.8	5.1	34.3	-3.9
PBE	-2.9	4.8	9.7	0.3
PBE0	-2.8	2.4	23.1	1.7
B3LYP	-9.5	-4.2	13.5	-10.0
HCTH 407	-6.3	0.3	-0.7	-10.1
HSE06	-3.3	2.0	22.0	0.4
M06L	9.6	18.8	15.1	5.8
τ-HCTH	-1.7	12.5	3.8	-4.5
τ-HCTH hyb	-0.7	6.2	28.5	-1.0
TPSSh	-1.3	6.6	8.0	1.8
ωB97X	0.9	5.5	18.5	3.2
ωB97X-D	0.1	5.4	11.4	0.3

Table A2.32. Benchmarking errors in DFT functionals for Mg molecules without H_2O in kcal/mol.

Method	MgO	$MgCl_2$	$Mg(OH)_2$	$MgCO_3$	$Mg(HCO_3)_2$	$Mg(HCO_3)(OH)$
$\Delta H_{f,0K}$ gas	32.5	-95.0	-130.4	-110.4	-356.9	-242.3
PW91	5.5	-1.4	1.4	31.8	53.2	28.2
BP86	4.2	-4.6	3.1	24.3	43.1	24.0
M06	-11.5	1.8	-5.4	4.8	5.9	1.0
PBE	4.3	-2.9	-2.1	29.7	49.4	24.6
PBE0	-15.1	-2.8	-15.4	-2.8	-4.1	-8.9
B3LYP	-10.5	-9.5	-11.1	-11.8	-22.1	-15.7
HCTH 407	-2.9	-6.3	-12.2	0.4	-6.2	-8.3
HSE06	-14.8	-3.3	-16.2	-5.0	-9.4	-12.0
M06L	-7.9	9.6	-9.4	4.9	-0.5	-4.3
τ-HCTH	-2.1	-1.7	-9.3	1.4	-8.7	-8.1
τ-HCTH hyb	-6.7	-0.7	-9.3	3.1	-0.3	-4.0
TPSSh	-10.2	-1.3	-15.6	-14.0	-33.3	-23.6
ωB97X	-14.8	0.9	-5.0	-0.7	-2.5	-3.0
ωB97X-D	-14.5	0.1	-6.6	-2.8	-5.9	-5.6

Table A2.33. Benchmarking errors in DFT functionals for Mg molecules with H_2O in kcal/mol.

Method	Mg $(HCO_3)_2$ H_2O	Mg $(HCO_3)_2$ $(H_2O)_2$	Mg(HCO_3) (OH) $(H_2O)_2$	$MgCO_3$ H_2O	$MgCO_3$ $(H_2O)_2$	$MgCO_3$ $(H_2O)_3$	$MgCO_3$ $(H_2O)_4$
$\Delta H_{f,0K}$ gas	-431.0	-501.9	-391.9	-200.6	-285.9	-363.5	-438.9
PW91	53.4	51.3	31.4	29.7	29.8	31.1	30.8
BP86	46.1	46.5	33.1	25.5	28.6	32.7	35.1
M06	4.2	-0.4	-4.4	-0.9	-3.8	-7.2	-9.5
PBE	48.2	44.7	25.1	26.2	24.8	24.7	23.0
PBE0	-11.1	-21.0	-22.0	-5.1	-17.0	-23.6	-31.5
B3LYP	-26.1	-34.1	-24.1	-16.2	-21.4	-26.0	-31.9
HCTH 407	-13.2	-24.8	-23.4	-7.8	-18.5	-25.5	-35.8
HSE06	-17.0	-27.5	-26.1	-13.0	-20.5	-27.8	-36.2
M06L	-8.8	-17.5	-21.2	-6.5	-14.6	-23.7	-30.8
τ-HCTH	-17.3	-29.8	-23.8	-8.0	-17.8	-25.2	-35.6
τ-HCTH hyb	-7.0	-16.9	-16.4	-4.5	-11.6	-17.9	-25.7
TPSSh	-41.9	-53.0	-38.9	-23.3	-31.8	-39.7	-48.9
ωB97X	-5.6	-11.3	-10.6	-5.6	-9.3	-13.1	-16.6
ωB97X-D	-8.9	-14.6	-13.2	-7.7	-11.8	-15.3	-18.6

Table A2.34. Benchmarking errors in DFT functionals for Ca molecules without H_2O in kcal/mol.

Method	CaO	$CaCl_2$	Ca $(OH)_2$	$CaCO_3$	Ca $(HCO_3)_2$	Ca $(HCO_3)(OH)$
$\Delta H_{f,0K}$ gas	5.0	-113.9	-144.0	-148.1	-379.0	-260.8
PW91	27.6	6.7	15.4	43.9	61.1	39.3
BP86	25.9	3.8	17.2	36.1	51.1	70.2
M06	4.7	5.1	-0.6	7.8	7.4	4.5
PBE	25.5	4.8	11.8	41.2	56.8	35.3
PBE0	4.0	2.4	-7.0	4.8	-0.8	-2.8
B3LYP	5.7	-4.2	-2.6	-5.1	-18.3	-9.4
HCTH 407	19.6	0.3	-0.8	11.0	-1.2	0.1
HSE06	3.8	2.0	-7.8	2.4	-5.8	-5.7
M06L	16.1	18.8	1.8	15.9	6.7	5.2
τ-HCTH	23.9	12.5	3.6	14.4	-1.4	2.1
τ-HCTH hyb	14.3	6.2	1.1	12.7	5.1	4.2
TPSSh	11.5	6.6	-3.5	-3.3	-26.7	-14.1
ωB97X	2.5	5.5	1.4	3.0	0.4	1.9
ωB97X-D	4.5	5.4	0.4	2.3	-2.4	0.0

Table A2.35. Benchmarking errors in DFT functionals for Ca molecules with H_2O in kcal/mol.

Method	Ca $(HCO_3)_2$ H_2O	Ca $(HCO_3)_2$ $(H_2O)_2$	Ca(HCO_3) (OH) $(H_2O)_2$	$CaCO_3$ H_2O	$CaCO_3$ $(H_2O)_2$	$CaCO_3$ $(H_2O)_3$	$CaCO_3$ $(H_2O)_4$
$\Delta H_{f,0K}$ gas	-453.9	-521.8	-411.8	-229.6	-310.9	-385.2	-465.2
PW91	59.6	64.1	41.0	42.8	41.7	41.9	40.1
BP86	52.4	59.7	42.8	38.2	40.3	43.5	44.8
M06	2.3	3.4	-4.0	3.5	-1.1	-5.3	-9.1
PBE	54.0	57.2	34.2	38.7	36.2	35.1	32.0
PBE0	-9.7	-13.1	-17.3	-3.0	-11.3	-18.7	-28.6
B3LYP	-23.7	-24.1	-18.5	-10.3	-15.6	-20.2	-27.3
HCTH 407	-9.5	-12.6	-16.0	0.8	-9.3	-17.1	-28.3
HSE06	-15.3	-19.3	-21.2	-5.9	-14.6	-22.7	-32.9
M06L	-4.2	-8.6	-14.6	5.3	-5.6	-16.0	-25.7
τ-HCTH	-11.7	-16.6	-14.6	4.2	-6.3	-14.9	-26.7
τ-HCTH hyb	-3.7	-6.9	-9.8	4.8	-3.4	-10.6	-20.0
TPSSh	-37.3	-42.2	-31.2	-12.9	-22.8	-31.9	-42.9
ωB97X	-4.6	-4.0	-6.8	-1.0	-5.3	-9.3	-14.5
ωB97X-D	-7.7	-7.5	-9.1	-2.1	-7.0	-11.0	-16.2

Table A2.36. Benchmarking errors in DFT functionals for Fe molecules without H_2O in kcal/mol.

Method	^5FeO	$^5FeCl_2$	$^5Fe(OH)_2$	$^5FeCO_3$	$^5Fe(HCO_3)_2$	$^5Fe(HCO_3)(OH)$
$\Delta H_{f,0K}$ gas	61.8	-32.9	-80.7	-50.8	-271.7	-172.5
PW91	29.4	10.3	6.3	48.5	61.2	40.8
BP86	27.7	6.6	8.0	40.6	50.4	36.3
M06	22.3	34.3	13.7	35.8	40.3	32.5
PBE	28.4	9.7	4.2	47.7	58.7	38.5
PBE0	16.9	23.1	1.7	25.3	19.8	17.6
B3LYP	19.2	13.5	3.4	14.5	-1.4	7.7
HCTH 407	13.3	-0.7	-14.6	16.2	-0.2	-0.9
HSE06	16.4	22.0	0.2	22.3	13.9	13.8
M06L	6.8	15.1	-14.6	12.7	-0.9	0.5
τ-HCTH	13.8	3.8	-12.3	17.6	-3.3	0.1
τ-HCTH hyb	28.8	28.5	11.0	36.3	27.6	26.4
TPSSh	9.0	8.0	-13.3	0.1	-26.2	-12.4
ωB97X	14.4	18.5	-1.5	-52.5	23.6	22.6
ωB97X-D	11.6	11.4	-9.9	-58.1	13.7	14.5

Table A2.37. Benchmarking errors in DFT functionals for Fe molecules with H_2O in kcal/mol.

Method	$^5Fe(HCO_3)_2 H_2O$	$^5Fe(HCO_3)_2 (H_2O)_2$[a]	$^5Fe(HCO_3)_2 (H_2O)_2$	$^5Fe(HCO_3)(OH) (H_2O)_2$	$^5FeCO_3 H_2O$	$^5FeCO_3 (H_2O)_2$
$\Delta H_{f,0K}$ gas	-346.5	-410.9	-412.8	-314.0	-137.8	-213.5
PW91	60.0	74.2	60.1	40.6	48.0	44.2
BP86	52.5	69.8	55.2	42.3	43.6	42.6
M06	35.3	35.2	40.6	27.1	34.2	30.8
PBE	56.0	68.4	54.7	35.3	45.9	40.6
PBE0	12.8	17.0	2.4	2.5	18.1	9.3
B3LYP	-6.2	2.1	-11.5	-1.8	9.7	2.6
HCTH 407	-12.4	-9.2	-21.6	-19.6	6.2	-6.6
HSE06	6.3	10.4	-1.7	-2.0	14.5	5.2
M06L	-7.6	-8.3	-15.2	-19.4	3.3	-8.1
τ-HCTH	-12.9	-7.4	-22.4	-17.1	7.6	-4.4
τ-HCTH hyb	20.9	26.5	13.7	13.1	29.5	20.7
TPSSh	-34.0	-31.2	-45.8	-30.4	-8.9	-20.0
ωB97X	19.9	27.2	16.7	15.8	21.8	17.8
ωB97X-D	10.5	17.6	7.2	7.4	14.1	9.1

Table A2.38. Benchmarking errors in DFT functionals for Cd molecules without H_2O in kcal/mol.

Method	CdO	$CdCl_2$	$Cd(OH)_2$	$CdCO_3$	$Cd(HCO_3)_2$	$Cd(HCO_3)(OH)$
$\Delta H_{f,0K}$ gas	64.9	-50.2	-68.8	-47.3	-278.2	-171.8
PW91	10.2	0.8	9.7	35.0	53.4	31.7
BP86	8.8	-2.8	11.5	27.3	43.2	27.6
M06	-11.6	-3.9	-12.7	-3.1	-3.2	-7.8
PBE	9.9	0.3	7.9	34.2	50.9	29.6
PBE0	-6.9	1.7	-8.2	1.8	-2.5	-5.4
B3LYP	-5.8	-10.0	-9.0	-11.0	-25.6	-17.0
HCTH 407	-0.3	-10.1	-10.1	2.6	-12.0	-10.6
HSE06	-7.4	0.4	-10.0	-1.4	-8.5	-9.3
M06L	-1.8	5.8	-10.8	5.8	-2.9	-6.8
τ-HCTH	1.6	-4.5	-6.5	3.8	-12.5	-9.2
τ-HCTH hyb	-1.9	-1.0	-6.0	3.8	-3.4	-4.6
TPSSh	-1.7	1.8	-7.2	-8.0	-30.6	-18.9
ωB97X	-9.3	3.2	-2.3	-0.8	-1.1	-1.8
ωB97X-D	-9.3	0.3	-6.0	-4.2	-7.4	-6.7

Table A2.39. Benchmarking errors in DFT functionals for Cd molecules with H_2O in kcal/mol.

Method	$Cd(HCO_3)_2 H_2O$	$Cd(HCO_3)_2 (H_2O)_2$	$Cd(HCO_3)(OH)(H_2O)_2$	$CdCO_3 H_2O$	$CdCO_3 (H_2O)_2$	$CdCO_3 (H_2O)_3$	$CdCO_3 (H_2O)_4$
$\Delta H_{f,0K}$ gas	-348.1	-418.3	-310.4	-129.5	-201.3	-276.7	-349.7
PW91	55.0	56.4	29.7	34.3	33.4	32.8	32.0
BP86	48.0	52.6	31.7	30.1	32.2	34.6	36.7
M06	-6.4	-10.2	-16.4	-7.8	-11.0	-14.9	-17.5
PBE	50.9	50.6	24.8	32.1	29.8	27.7	25.5
PBE0	-9.0	-16.1	-22.7	-5.9	-13.6	-21.5	-29.8
B3LYP	-28.8	-32.7	-29.5	-16.6	-23.0	-28.9	-35.1
HCTH 407	-19.6	-27.5	-30.0	-8.6	-19.6	-30.4	-40.3
HSE06	-15.4	-22.8	-27.5	-9.6	-17.9	-26.2	-35.0
M06L	-12.9	-23.3	-25.6	-6.0	-14.7	-24.1	-32.4
τ-HCTH	-19.5	-26.7	-29.0	-7.4	-17.4	-27.4	-37.5
τ-HCTH hyb	-9.1	-15.3	-21.5	-4.2	-12.2	-20.0	-28.1
TPSSh	-38.9	-47.6	-38.5	-17.8	-26.9	-36.2	-45.8
ωB97X	-3.7	-7.1	-11.1	-3.4	-7.0	-10.7	-14.8
ωB97X-D	-9.8	-12.9	-16.5	-7.7	-11.9	-15.8	-19.5

Table A2.40. Total atomization energies with ZPE in kcal/mol using DMol[3] functionals and numerical basis sets. 4.3 and 5.1 represent different real space cutoffs in Å.

Molecule	PBE 4.3	PBE 5.1	PW91 4.3	PW91 5.1	B3LYP 4.3	B3LYP 5.1
$MgCO_3$	524.5	519.7	525.9	522.0	475.3	470.4
$MgCO_3(H_2O)_3$	1257.2	1251.3	1263.1	1257.9	1195.6	1190.3
$MgCO_3(H_2O)_4$	1493.3	1486.7	1500.7	1494.7	1427.7	1419.8
$Mg(HCO_3)_2$	1238.0	1232.1	1241.6	1236.2	1150.7	1144.8
$Mg(HCO_3)_2(H_2O)_2$	1701.4	1694.8	1707.8	1701.7	1607.6	1601.3
$Mg(HCO_3)(OH)$	811.6	806.6	815.3	811.0	764.0	759.1
$Mg(HCO_3)(OH)(H_2O)_2$	1286.1	1280.1	1292.0	1286.5	1227.6	1222.2
$CaCO_3$	588.0	574.7	590.0	576.6	534.1	520.5
$CaCO_3(H_2O)_3$	1302.2	1288.1	1308.3	1293.8	1236.7	1222.7
$CaCO_3(H_2O)_4$	1541.9	1527.2	1549.4	1534.3	1470.7	1456.4
$Ca(HCO_3)_2$	1283.4	1269.0	1287.2	1272.4	1194.7	1180.5
$Ca(HCO_3)_2(H_2O)_2$	1753.4	1738.7	1759.9	1745.3	1658.8	1644.4
$Ca(HCO_3)(OH)$	855.2	841.9	858.4	844.9	803.1	789.5
$Ca(HCO_3)(OH)(H_2O)_2$	1330.6	1316.4	1336.5	1321.9	1270.0	1256.3

Table A2.41. Errors from best values in $\Delta H_f(0K)$ in kcal/mol using DMol^3 functionals and numerical basis sets. 4.3 and 5.1 represent different real space cutoffs in Å.

Molecule	PBE 4.3	PBE 5.1	PW91 4.3	PW91 5.1	B3LYP 4.3	B3LYP 5.1
$MgCO_3$	32.2	27.4	33.6	29.7	-17.0	-21.9
$Mg(HCO_3)_2$	48.9	43.0	52.5	47.1	-38.4	-44.3
$Mg(HCO_3)(OH)$	25.1	20.1	28.8	24.5	-22.5	-27.4
$Mg(HCO_3)_2(H_2O)_2$	42.8	36.2	49.2	43.1	-51.0	-57.3
$Mg(HCO_3)(OH)(H_2O)_2$	25.5	19.5	31.4	25.9	-33.0	-38.4
$MgCO_3(H_2O)_3$	25.0	19.1	30.9	25.7	-36.6	-41.9
$MgCO_3(H_2O)_4$	23.5	16.9	30.9	24.9	-42.1	-50.0
$CaCO_3$	50.5	37.2	52.5	39.1	-3.4	-17.0
$Ca(HCO_3)_2$	64.7	50.3	68.5	53.7	-24.0	-38.2
$Ca(HCO_3)(OH)$	42.7	29.4	45.9	32.4	-9.4	-23.0
$Ca(HCO_3)_2(H_2O)_2$	67.4	52.7	73.9	59.3	-27.2	-41.6
$Ca(HCO_3)(OH)(H_2O)_2$	42.6	28.4	48.5	33.9	-18.0	-31.7
$CaCO_3(H_2O)_3$	40.8	26.7	46.9	32.4	-24.7	-38.7
$CaCO_3(H_2O)_4$	38.3	23.6	45.8	30.6	-33.0	-47.2

Table A2.42. Average of differences of heats of formation from **Table A2.41** in kcal/mol.

Average	Metal compounds
PBE 4.3	40.7
PBE 5.1	30.8
PW91 4.3	45.7
PW91 5.1	35.9
B3LYP 4.3	27.2
B3LYP 5.1	37.0

Table A2.43. Zero point energies in kcal/mol for all the molecules.

Molecule	MP2/aT	B3LYP/aT[a]	CCSD(T)
MgO		1.17	1.17[b,37]
$MgCl_2$		1.67	1.67[c,37]
$Mg(OH)_2$		15.14	15.14[c,37]
$MgCO_3$		10.23	10.45[d,]
$Mg(HCO_3)_2$	37.15	36.90	
$Mg(HCO_3)(OH)$	26.15	26.05	
$Mg(HCO_3)_2(H_2O)$		52.09	
$Mg(HCO_3)_2(H_2O)_2$		67.39	
$Mg(HCO_3)(OH)(H_2O)_2$	58.31	57.77	
$MgCO_3(H_2O)$		25.64	
$MgCO_3(H_2O)_2$		41.59	
$MgCO_3(H_2O)_3$		57.10	
$MgCO_3(H_2O)_4$		73.41	
CaO		1.12	1.04[b,37]
$CaCl_2$		1.00	1.00[c,37]
$Ca(OH)_2$		15.44	15.44[c,37]
$CaCO_3$		9.97	10.18[d]
$Ca(HCO_3)_2$	36.11	35.99	
$Ca(HCO_3)(OH)$	25.76	25.64	
$Ca(HCO_3)_2(H_2O)$		51.08	
$Ca(HCO_3)_2(H_2O)_2$		66.37	
$Ca(HCO_3)(OH)(H_2O)_2$		56.27	
$CaCO_3(H_2O)$		25.35	
$CaCO_3(H_2O)_2$		40.59	
$CaCO_3(H_2O)_3$		55.90	
$CaCO_3(H_2O)_4$		71.89	
^5FeO		1.29	
$^5FeCl_2$		1.43	
$^5Fe(OH)_2$		15.16	
$^5FeCO_3$		9.94	
$^5Fe(HCO_3)_2$		36.40	
$^5Fe(HCO_3)(OH)$		25.70	

$^5Fe(HCO_3)_2(H_2O)$		51.23	
$^5Fe(HCO_3)_2(H_2O)_2$[e]		67.56	
$^5Fe(HCO_3)_2(H_2O)_2$		67.01	
$^5Fe(HCO_3)(OH)(H_2O)_2$		57.20	
$^5FeCO_3(H_2O)$		25.05	
$^5FeCO_3(H_2O)_2$		41.12	
$^5FeCO_3(H_2O)_3$[f]		56.81	
CdO		0.88	0.86[d,105]
$CdCl_2$		1.30	
$Cd(OH)_2$		15.57	
$CdCO_3$		8.90	
$Cd(HCO_3)_2$		35.80	
$Cd(HCO_3)(OH)$		25.71	
$Cd(HCO_3)_2(H_2O)$		51.45	
$Cd(HCO_3)_2(H_2O)_2$		67.06	
$Cd(HCO_3)(OH)(H_2O)_2$		56.71	
$CdCO_3(H_2O)$		24.81	
$CdCO_3(H_2O)_2$		40.76	
$CdCO_3(H_2O)_3$		56.34	
$CdCO_3(H_2O)_4$		72.21	

[a] ZPE from B3LYP/ aT is used in benchmarking. ZPE contributing to the calculation of heat of formation is from geometry optimization used for CCSD(T) calculation. [b] awQ basis set diatomics. [c] awT basis set. [d]aD basis set. [e] Both bicarbonates are monodentate. [f] Only 2 H_2O in 1st solvation shell.

Table A2.44. Computational Level for Molecular Calculations.

Molecule	CCSD(T) geometry	DFT benchmark geometry
MgO	FPD	CCSD(T)
$MgCl_2$	FPD	CCSD(T)
$Mg(OH)_2$	FPD	CCSD(T)
$MgCO_3$	FPD	MP2
$Mg(HCO_3)_2$	MP2	MP2
$Mg(HCO_3)(OH)$	MP2	MP2
$Mg(HCO_3)_2(H_2O)$	B3LYP	B3LYP
$Mg(HCO_3)_2(H_2O)_2$	B3LYP	B3LYP
$Mg(HCO_3)(OH)(H_2O)_2$	MP2	MP2
$MgCO_3(H_2O)$	B3LYP	B3LYP
$MgCO_3(H_2O)_2$	B3LYP	B3LYP
$MgCO_3(H_2O)_3$	B3LYP	B3LYP
$MgCO_3(H_2O)_4$	B3LYP	B3LYP
CaO	FPD	CCSD(T)
$CaCl_2$	FPD	CCSD(T)
$Ca(OH)_2$	FPD	CCSD(T)
$CaCO_3$	FPD	Mp2
$Ca(HCO_3)_2$	MP2	MP2
$Ca(HCO_3)(OH)$	MP2	MP2
$Ca(HCO_3)_2(H_2O)$	B3LYP	B3LYP
$Ca(HCO_3)_2(H_2O)_2$	B3LYP	B3LYP
$Ca(HCO_3)(OH)(H_2O)_2$	B3LYP	B3LYP
$CaCO_3(H_2O)$	B3LYP	B3LYP
$CaCO_3(H_2O)_2$	B3LYP	B3LYP
$CaCO_3(H_2O)_3$	B3LYP	B3LYP
$CaCO_3(H_2O)_4$	B3LYP	B3LYP

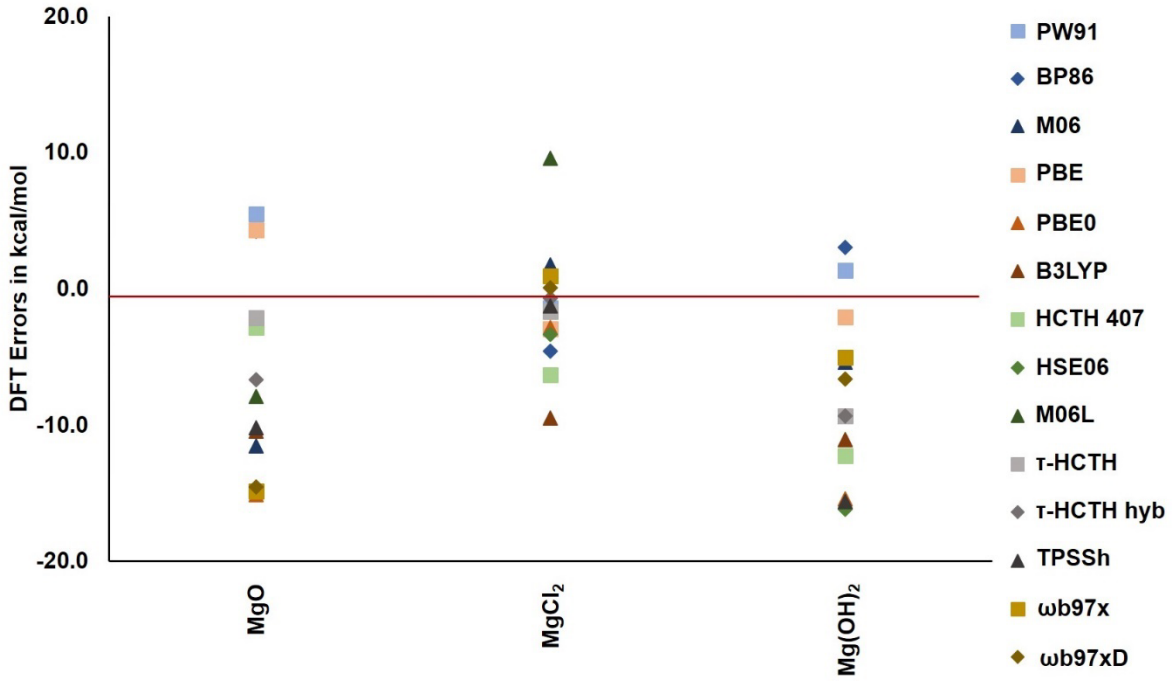

Figure A2.1. Distributions of DFT errors in terms of the $\Delta H_{f,0K}$'s for small molecules for Mg compared to the FPD results.

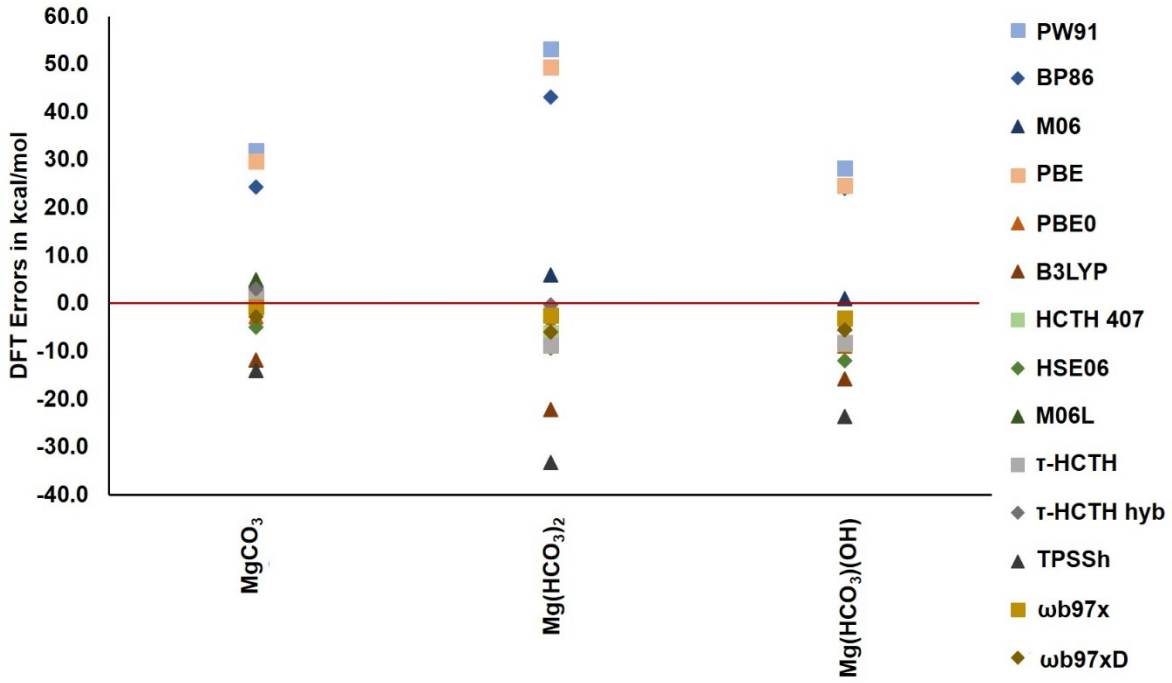

Figure A2.2. Distributions of DFT errors in terms of the $\Delta H_{f,0K}$'s for large molecules without H_2O for Mg compared to the FPD results.

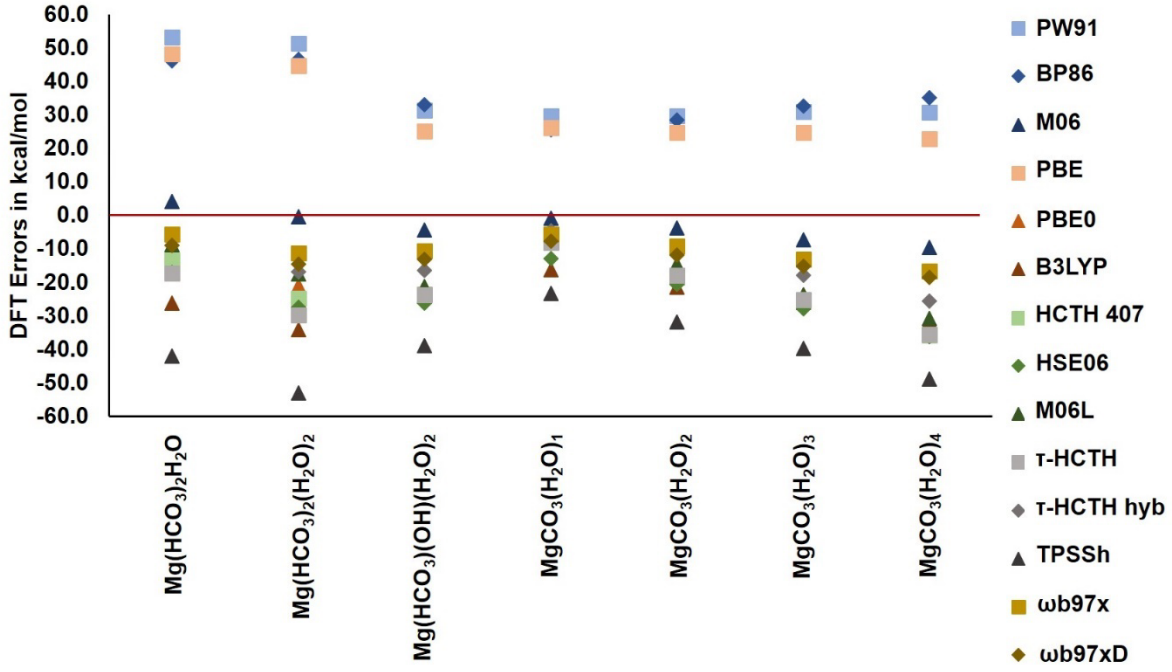

Figure A2.3. Distributions of DFT errors in terms of the $\Delta H_{f,0K}$'s for large molecules with H_2O for Mg compared to the FPD results.

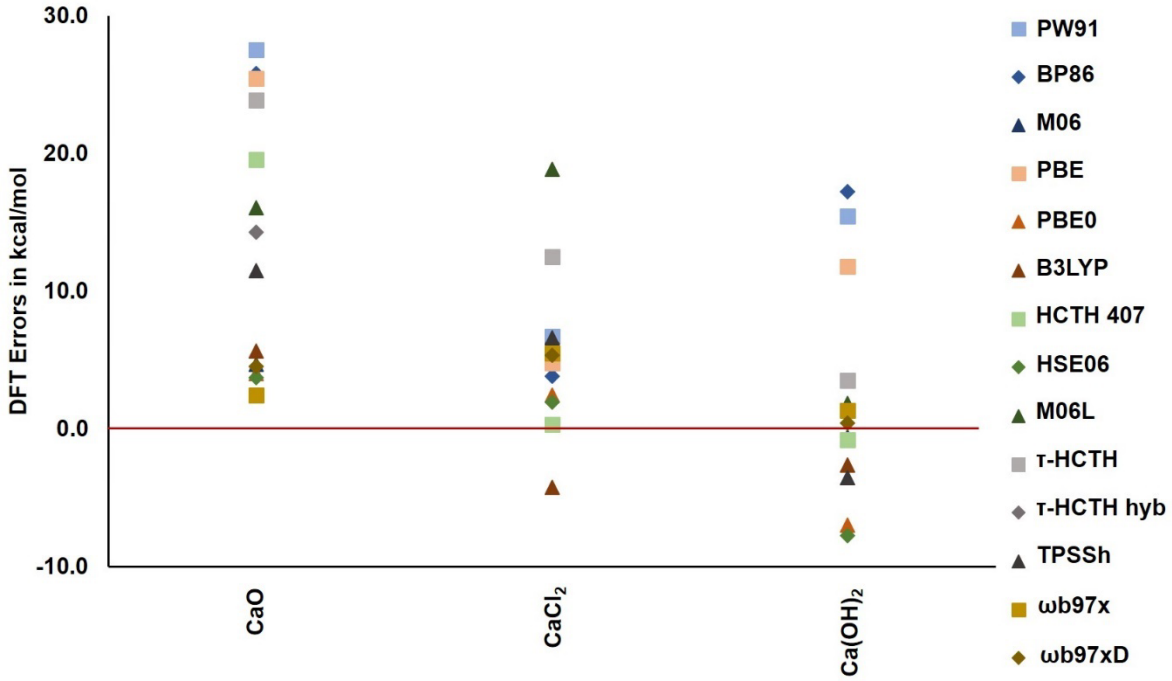

Figure A2.4. Distributions of DFT errors in terms of the $\Delta H_{f,0K}$'s for small molecules for Ca compared to the FPD results.

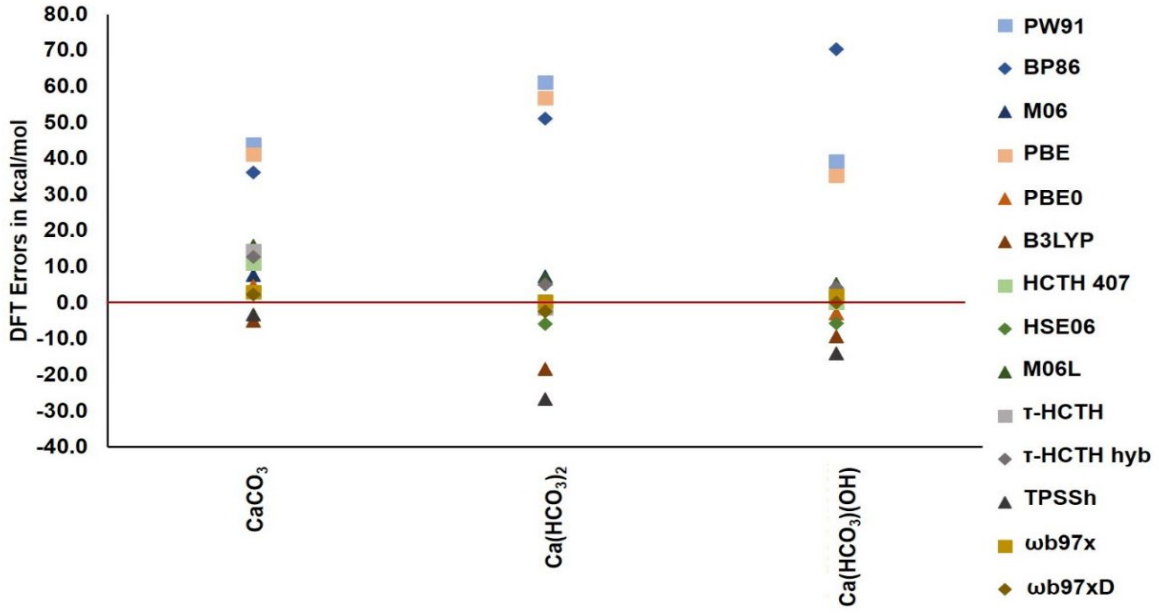

Figure A2.5. Distributions of DFT errors in terms of the $\Delta H_{f,0K}$'s for large molecules without H_2O for Ca compared to the FPD results.

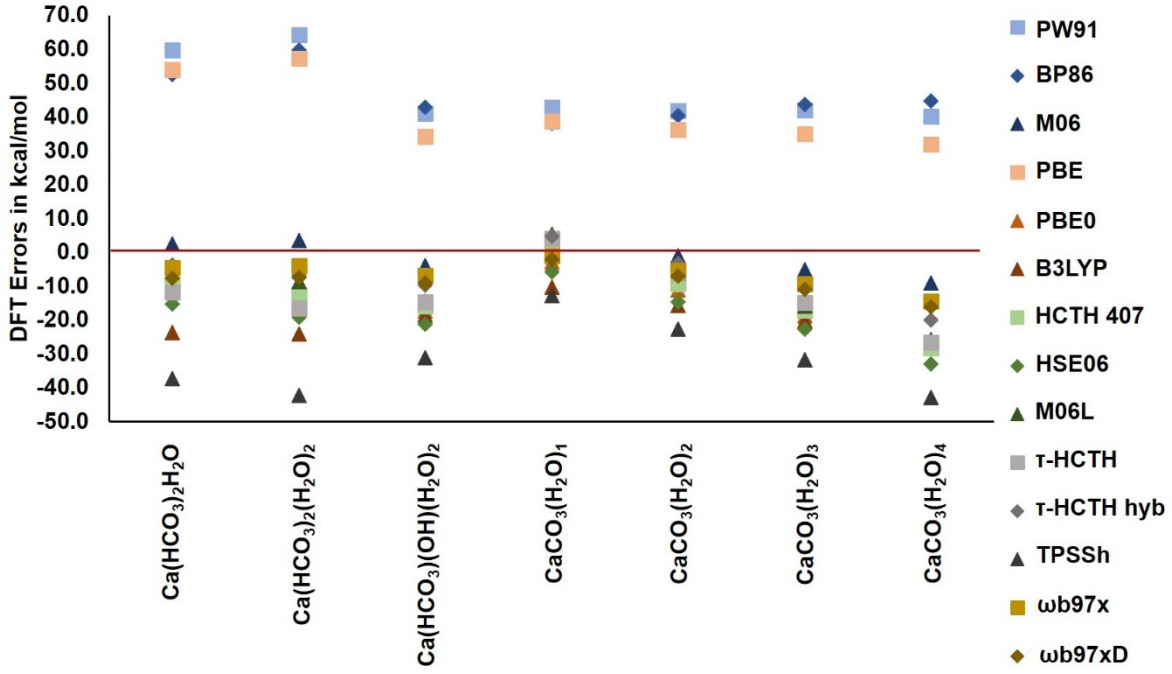

Figure A2.6. Distributions of DFT errors in terms of the $\Delta H_{f,0K}$'s for large molecules with H_2O for Ca compared to the FPD results.

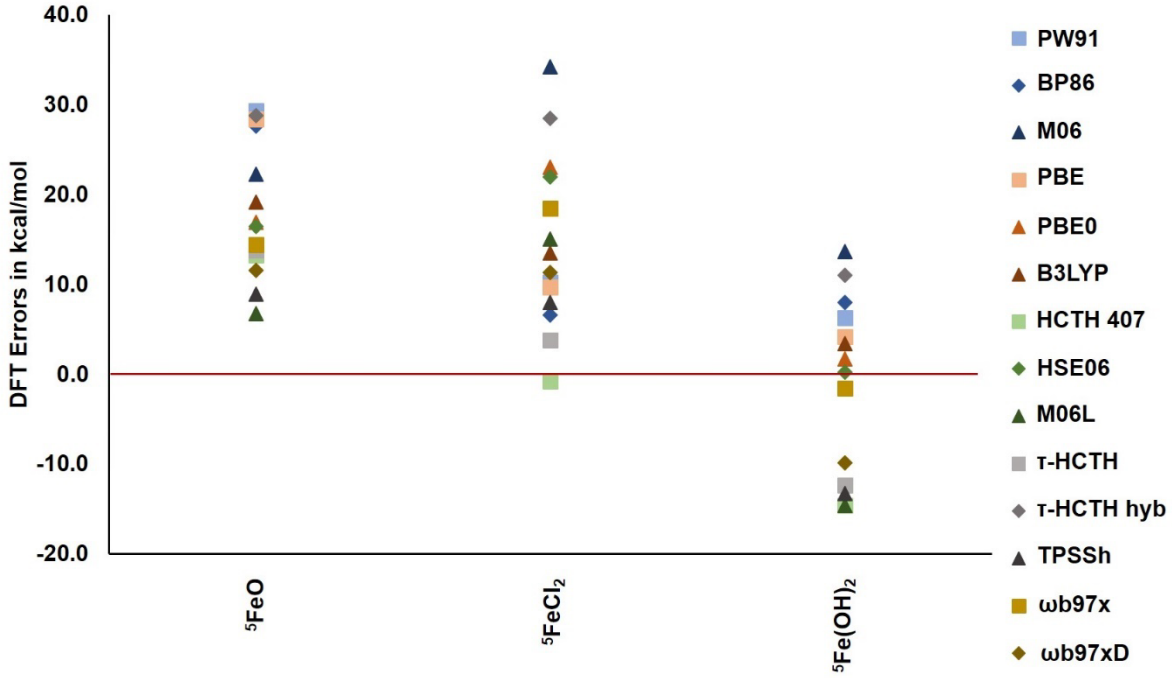

Figure A2.7. Distributions of DFT errors in terms of the $\Delta H_{f,0K}$'s for small molecules for Fe compared to the FPD results.

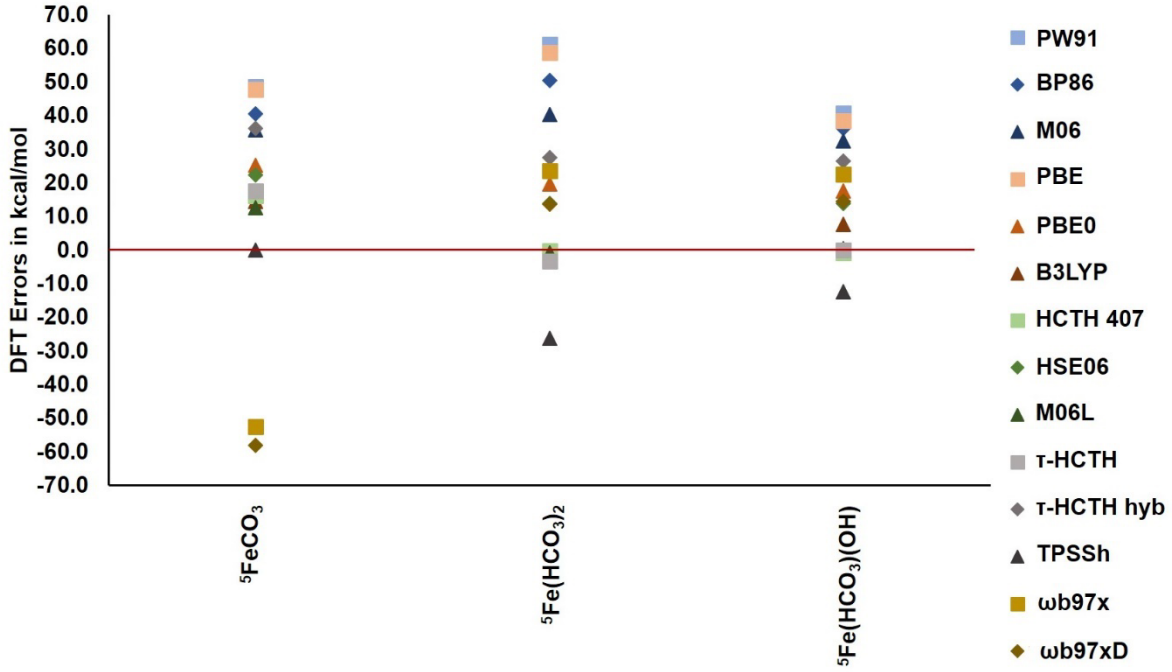

Figure A2.8. Distributions of DFT errors in terms of the $\Delta H_{f,0K}$'s for large molecules without H_2O for Fe compared to the FPD results.

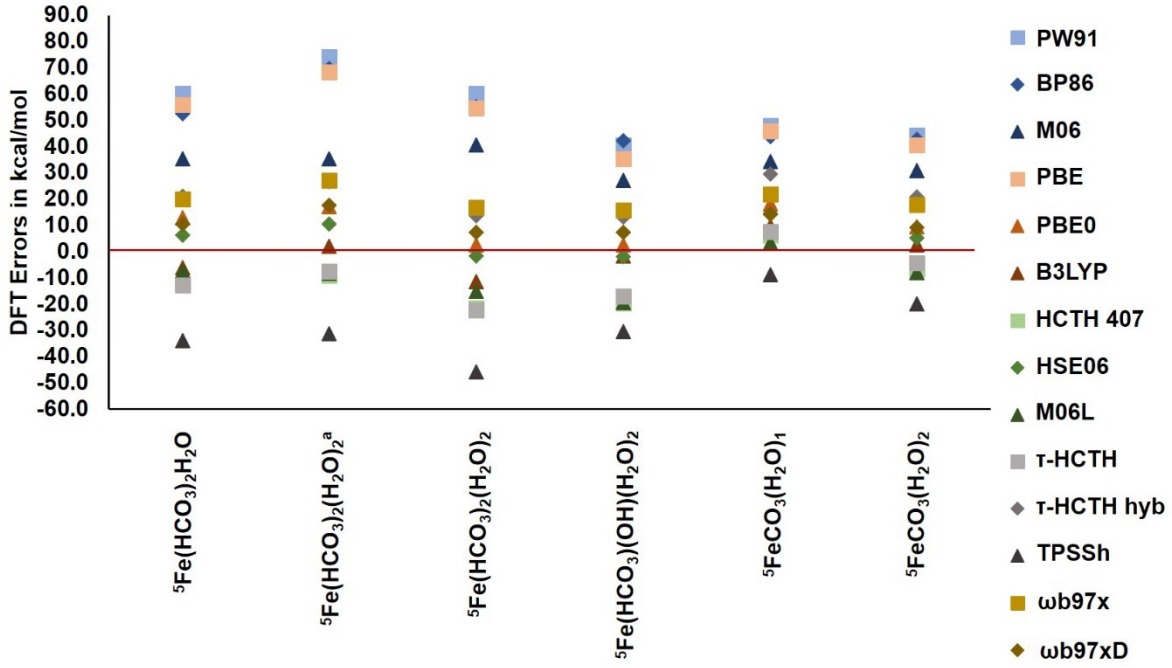

Figure A2.9. Distributions of DFT errors in terms of the $\Delta H_{f,0K}$'s for large molecules with H_2O for Fe compared to the FPD results.

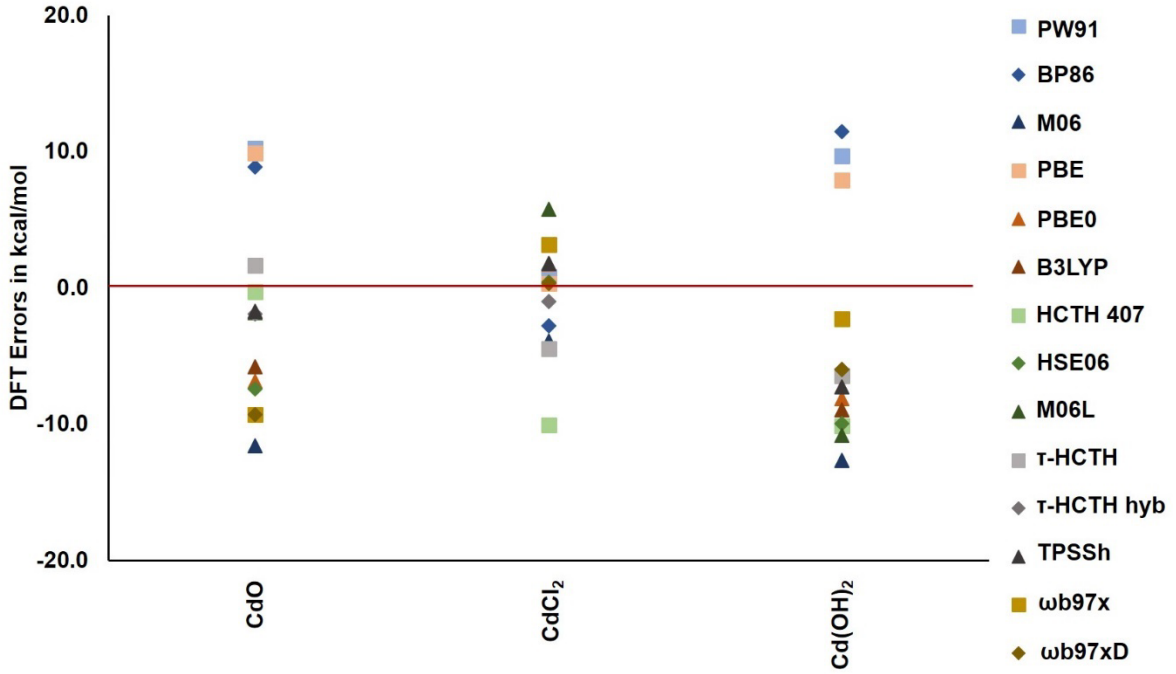

Figure A2.10. Distributions of DFT errors in terms of the $\Delta H_{f,0K}$'s for small molecules for Cd compared to the FPD results.

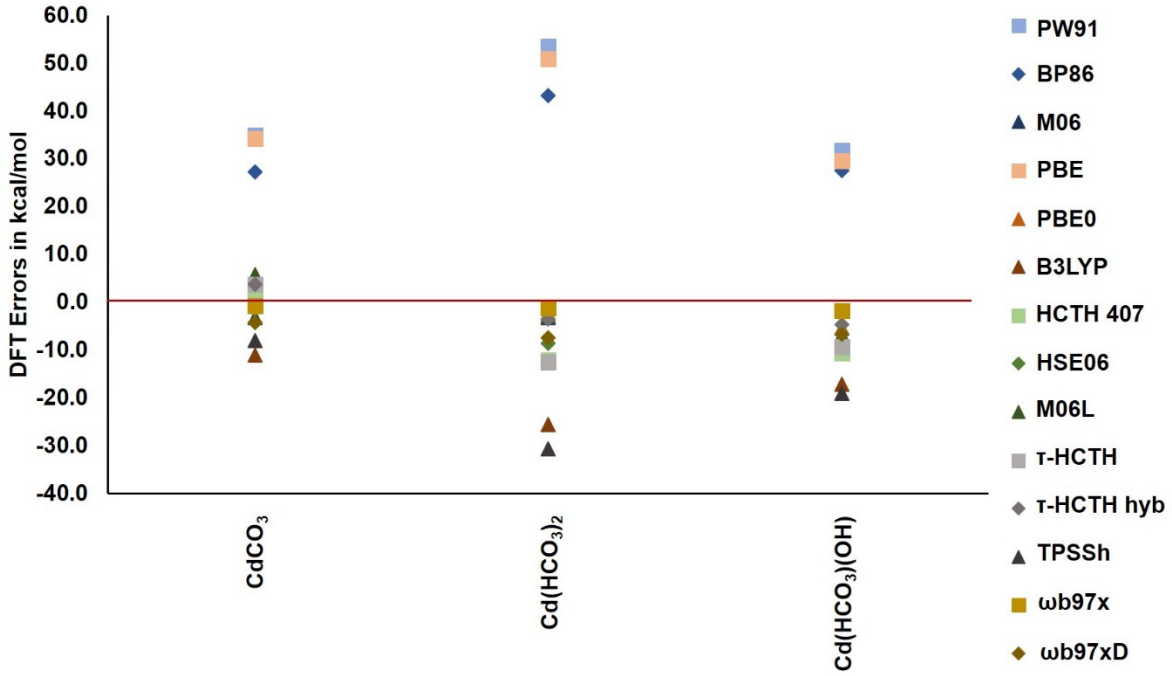

Figure A2.11. Distributions of DFT errors in terms of the $\Delta H_{f,0K}$'s for large molecules without H_2O for Cd compared to the FPD results.

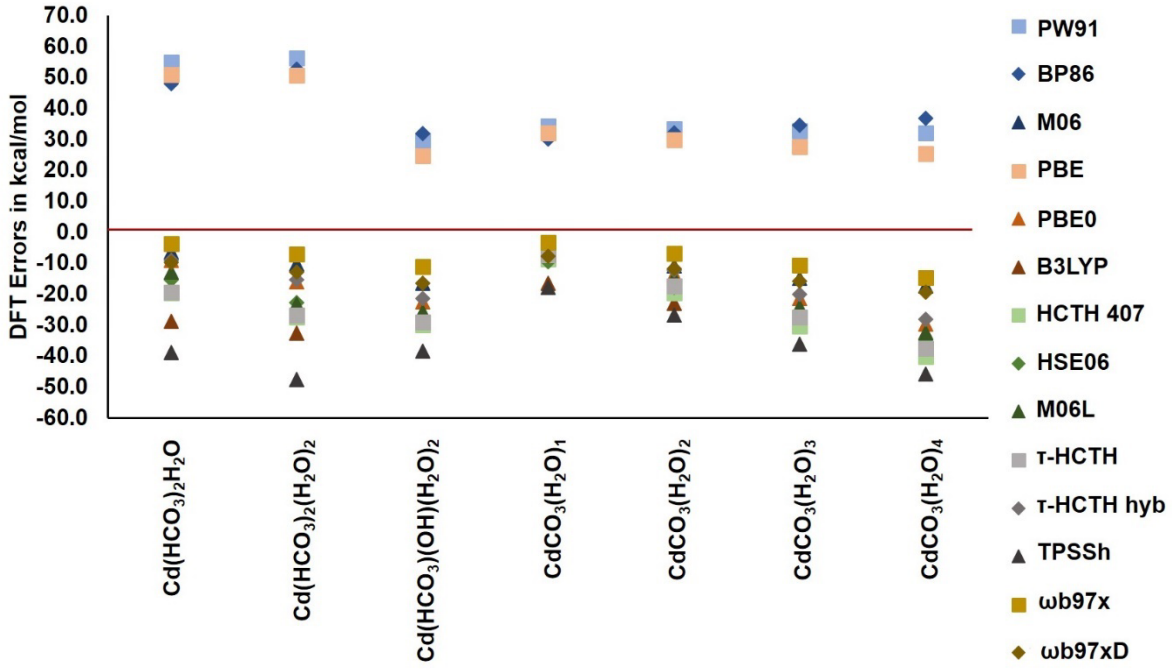

Figure A2.12. Distributions of DFT errors in terms of the $\Delta H_{f,0K}$'s for large molecules with H_2O for Cd compared to the FPD results.

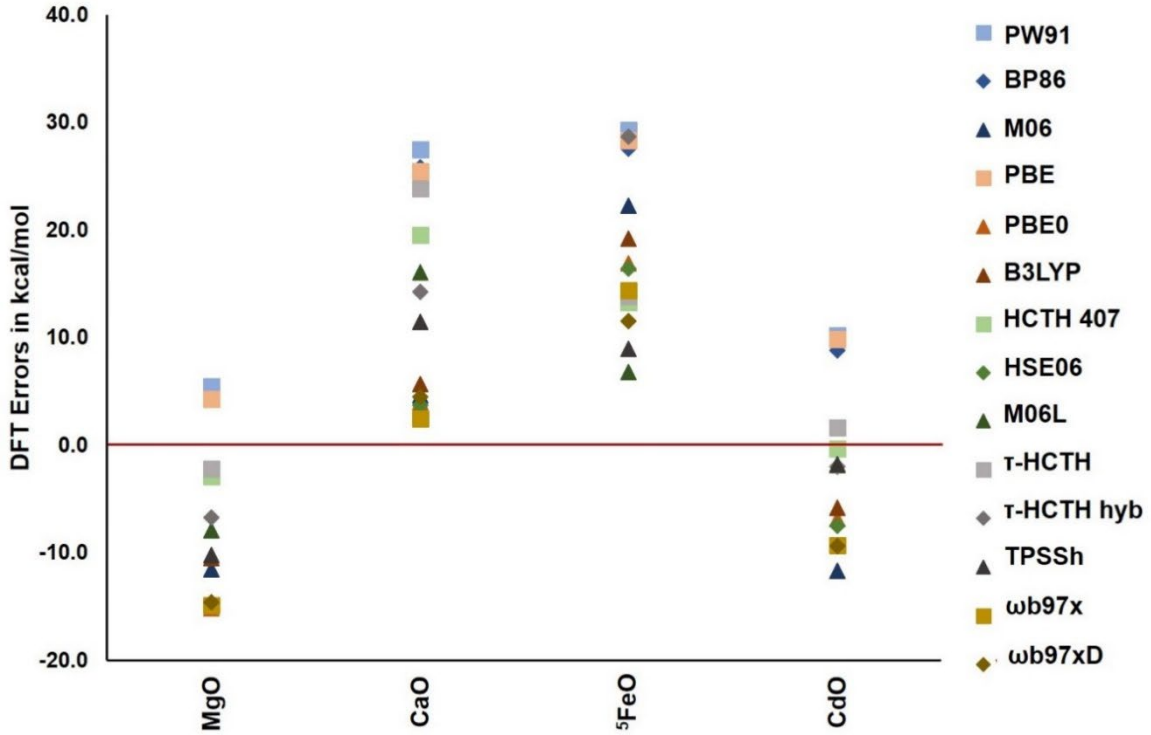

Figure A2.13. Distributions of DFT errors in terms of the $\Delta H_{f,0K}$'s for MO compared to the FPD results, M=Mg, Ca, Fe and Cd.

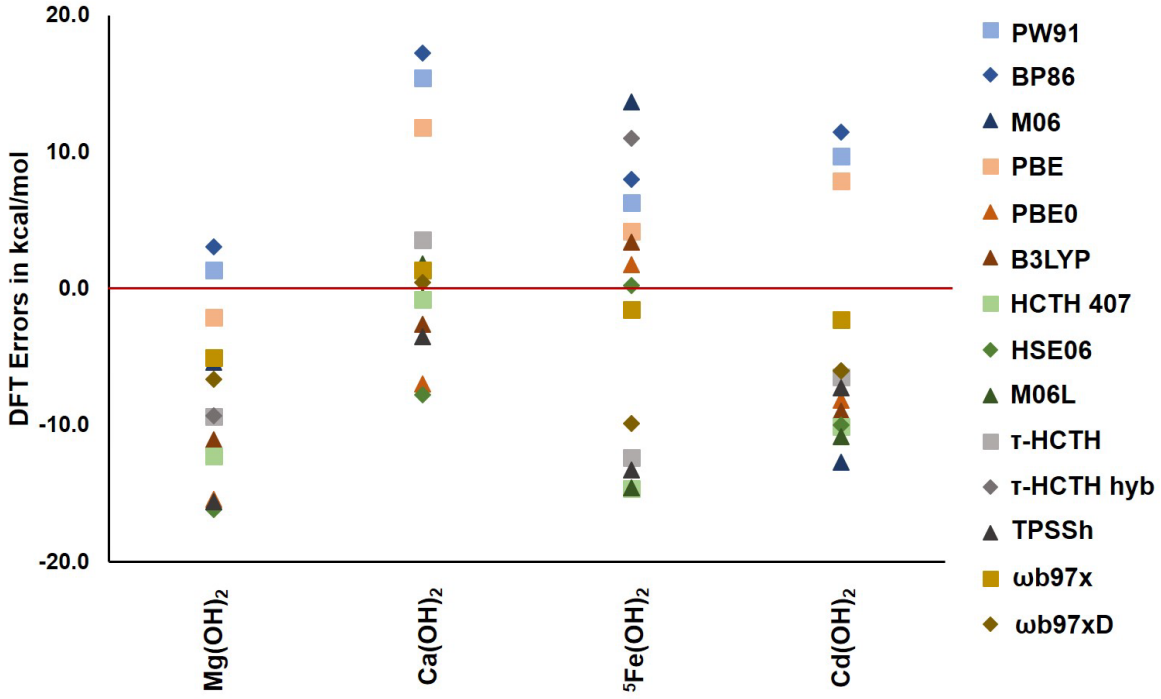

Figure A2.14. Distributions of DFT errors in terms of the $\Delta H_{f,0K}$'s for $M(OH)_2$ compared to the FPD results, M=Mg, Ca, Fe and Cd.

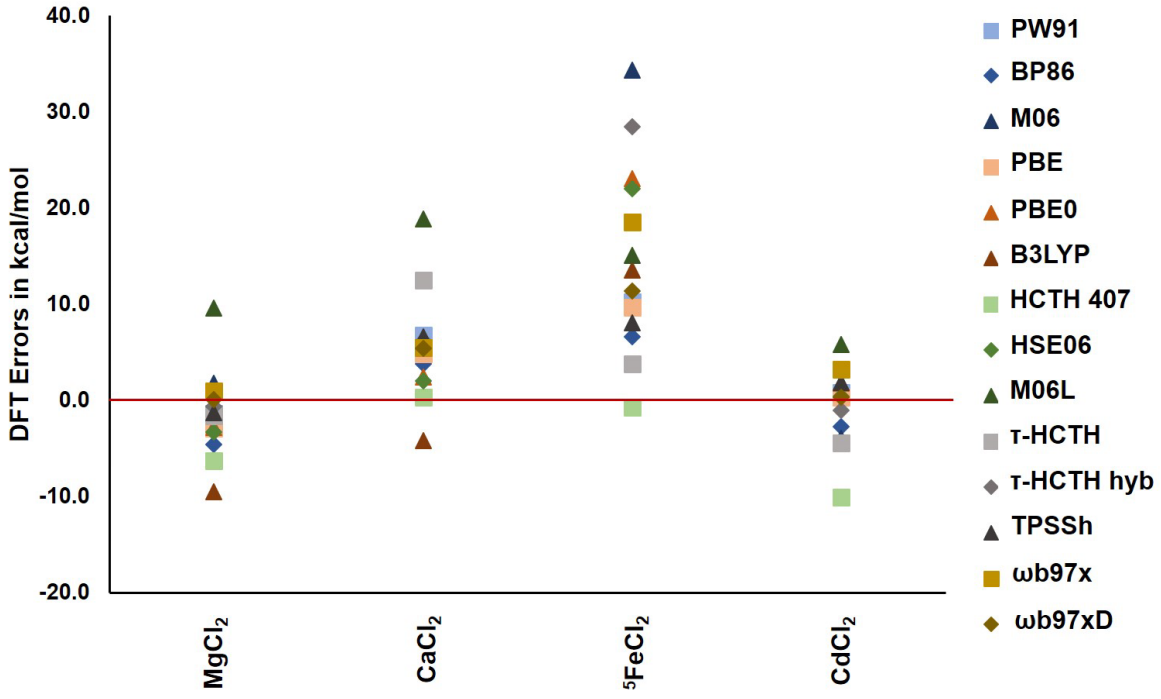

Figure A2.15. Distributions of DFT errors in terms of the $\Delta H_{f,0K}$'s for MCl_2 compared to the FPD results, M=Mg, Ca, Fe and Cd.

CHAPTER 3

THERMODYNAMICS OF THE METAL CARBONATES AND BICARBONATES OF Mn, Co, Ni, Cu, AND Zn RELEVANT TO MINERAL ENERGETICS

Introduction

The properties of metal carbonates underlie a range of geochemical processes such as subsurface sequestration of CO_2,[1,2,3,4] biomineralization,[5,6,7,8] environmental remediation,[9] and paleoindication of climate conditions.[10,11,12,13,14,15] The properties of the carbonates of divalent metals depend on the nature of the metal and its potential for hydration, but these trends are not fully understood. The smallest dication[16] usually found in carbonates is Mg^{2+} and it forms the largest number of hydrated carbonate minerals. In contrast, the much larger Ca^{2+} forms only two hydrated minerals, whereas Fe^{2+} forms none despite being similar in size to Mg^{2+}. How different carbonates form from small particles up to the bulk and the potential role of multiple metal ions are important for understanding and controlling these geochemical processes, but the geological record or complex industrial processes do not reveal the formation and transformation processes at the molecular level. They also do not reveal the competition between different cations to be incorporated, and whether a potentially toxic metal can be safely sequestered in an insoluble mineral or remains mobile to contaminate groundwater. Thermodynamics underlies this process, but unfortunately data exist primarily for the bulk mineral and not the monomeric and oligomeric species that constitute the precursors. Reliable simulations of the potential monomers and aggregated particles up to the bulk mineral require an accurate, efficient electronic structure

computational method to address the data gap. The method often used in the prediction of the properties of such species is density-functional theory (DFT). Unfortunately, no one functional has yet been identified that provides reliable thermodynamics for species such as metal oxides, carbonates, bicarbonates, and hydrates, particularly for transition metals, whether monomers or solids.

The need for a rigorous assessment of functionals has been demonstrated by our previous work with high level ab initio correlated molecular orbital theory using the Feller-Peterson-Dixon (FPD) approach[17,18,19,20] based on coupled cluster CCSD(T) theory to predict the thermodynamics of metal carbonates and di-bicarbonates for Mg, Ca, Fe, and Cd.[21] The resulting monomeric values were used to predict the cohesive energy of the bulk carbonates and di-bicarbonates; the latter compounds were predicted to be unstable in the bulk. A broad range of DFT functionals was benchmarked and none of the functionals provided reasonable agreement with the higher-level correlated molecular orbital theory calculations. The best agreement with the FPD results was found with the ωB97X and ωB97X-D functionals with average unsigned errors of 10 kcal/mol. The functionals showing the worst agreement were PW91, BP86, and PBE with average unsigned errors of > 30 kcal/mol. A major part of the issue with DFT was correlated with the well-established problem[22] of many DFT functionals handling oxygen and the bond dissociation energy of O_2.

In the current work, we have expanded our assessment of DFT functionals to calculate the structure and energies of carbonates, di-bicarbonates, and bicarbonate hydroxides to the metals Mn, Co, Ni, Cu and Zn. This assessment will enable investigation of the growth and reactivity of carbonate nanoparticles, as we have done in our prior work examining the growth of $MgCO_3$ and $CaCO_3$ nanoparticles as well as the growth of brucite from the hydrolysis of MgO

nanoparticles.[23,24,25] In addition, the assessment will provide reliable thermodynamics to assess competitive incorporation into nanoparticles between mixed metal dications.

Computational Methods

The geometries were optimized at the DFT level with the B3LYP[26,27,28] hybrid exchange-correlation functional. The aug-cc-pVTZ basis set was used for H, C and O,[29,30] and the aug-cc-pVTZ-PP basis set containing the effective core pseudopotentials (ECP)[31,32] was used for Mn, Co, Ni, Cu,[33], and Zn. Ten electrons are included in the 1s2s2p orbitals in the relativistic pseudopotentials (PPs) for the first-row transition metals. These basis sets are denoted as aT. For the open shell molecules, a variety of possible spin states was considered. The following functionals were used in the DFT benchmarking: PW91,[34,35] BP86,[36,37] M06,[38] PBE,[22,39] PBE0,[40] B3LYP, HSE06,[41] τ-HCTH,[42] ωB97X,[43] and ωB97X-D[44,45]. The open shell DFT calculations were done in the spin-unrestricted formalism. The DFT calculations were performed using the Gaussian16 software package.[46]

Coupled cluster R/RCCSD(T) (closed shell) or R/UCCSD(T) (open shell) [47,48,49,50,51,52,53] single-point calculations were conducted at the optimized DFT geometries to make reliable predictions of the thermodynamic properties. These calculations were performed using the MOLPRO program package.[54,55,56] The aug-cc-pVnZ basis sets (n = D, T, and Q) were used for H, C, and O and the corresponding aug-cc-pVnZ-PP basis sets were used for transition metal atoms. The CCSD(T) energies were extrapolated to the CBS limit by fitting to a mixed Gaussian/exponential (eq 1)

$$E(\mathrm{n}) = E_{\mathrm{CBS}} + A\ \exp[-(\mathrm{n}-1)] + B\ \exp[-(\mathrm{n}-1)^2] \quad (1)$$

where n = 2, 3, and 4 (D, T, and Q).[57]

Following the composite correlated molecular orbital theory FPD approach,[17,18,19,20] four smaller corrections were added to the CCSD(T) extrapolation to the CBS limit. Total atomization energies (TAEs) or ΣD_0 at 0 K were calculated using the expression below (eq 2).

$$\Sigma D_0 = \Delta E_{CBS} + \Delta E_{SR} + \Delta E_{CV} + \Delta E_{ZPE} + \Delta E_{SO} \quad (2)$$

Scalar relativistic corrections (ΔE_{SR}) including the PP corrections were calculated at the second-order Douglas-Kroll-Hess (DK)[58,59,60] level with the all-electron aug-cc-pVTZ-DK basis sets[61] (denoted as aVTZ-DK):

$$\Delta E_{SR} = \Delta E_{aVTZ\text{-}DK} + \Delta E_{aVTZ(\text{-}PP)} \quad (3)$$

where $\Delta E_{aVTZ\text{-}DK}$ and $\Delta E_{aVTZ(\text{-}PP)}$ are the valence electronic energy differences respectively calculated at the CCSD(T)/aVTZ-DK and CCSD(T)/aVTZ(-PP) levels. The core-valence corrections (ΔE_{CV}) were calculated at the CCSD(T) level with the aug-cc-pwCVTZ basis set[62,63] for C and O, and the aug-cc-pwCVTZ-PP[8] basis set for transition metal atoms (denoted as awCVTZ(-PP)).

$$\Delta E_{CV} = \Delta E_{awCVTZ(\text{-}PP),\ core} - \Delta E_{awCVTZ(\text{-}PP),\ valence} \quad (4)$$

The electrons in the 1s orbitals for C and O were correlated in the CV calculations. The zero-point energies (ZPEs) were taken from the B3LYP/aT calculations. The atomic spin-orbit corrections (ΔE_{SO}) were taken from experiment (C = -0.09 kcal/mol, O = -0.22 kcal/mol, Mn = 0, Co = -2.27 kcal/mol, Ni = -2.78 kcal/mol, Cu = 0, and Zn = 0).[64]

Heats of formation at 0 K were calculated using the TAEs and experimental[65,66,67,68,69,70,71] heats of formation of the atoms at 0 K given in Table 3.1. Heats of formation at 298 K were calculated following the procedure for the temperature correction of the atomization energy given by Curtiss et al.[72]. Experimental thermal corrections (TC) for the atoms are given in Table 3.1.

A Natural Population Analysis (NPA) based on the Natural Bond Orbitals (NBOs)[73,74] using NBO7[75,76] was performed. An Energy Decomposition Analysis (EDA) was performed in Amsterdam Density Functional (ADF) 2019.304.[77,78,79,80,81,82,83,84,85,86,87]The calculation was performed at the BLYP/TZ2P level using relativistic correction ZORA.

All calculations were performed on local parallel high-performance Xeon and Opteron-based Penguin Computing clusters at the University of Alabama, the DMC computer at the Alabama Supercomputer Center, and the large computer in the Molecular Science Computing Facility in the William R. Wiley Environmental Molecular Sciences Laboratory at the Pacific Northwest National Laboratory.

Results and Discussion

Molecular Geometries The lowest energy structures for MCO_3, $M(HCO_3)_2$ and $MHCO_3OH$ (M = Mn, Co, Ni, Cu and Zn) are shown in Figure 3.1. The lowest energy spin states for these structures for M = Mn, Co, Cu and Zn are the sextet, quartet, doublet, and singlet, respectively, with the relative energies of the spin states given in Table A3.1. T_1 values[88] are also shown in Table A3.1 and S2. Most of the T_1 values are acceptable but a few are greater than 0.05 suggesting the possible presence of some multi-reference character. The lowest energy spin states for $NiCO_3$ and $Ni(HCO_3)_2$ are the singlet and for $NiHCO_3OH$ the triplet.

The MCO_3 all have C_{2v} symmetry. Angles for MCO_3, $M(HCO_3)_2$ and $M(HCO_3)(OH)$ are given in Table A3.3. The O-M-O bite angles for the bidentate carbonate component for MCO_3, $M(HCO_3)_2$ and $MHCO_3OH$ vary from 63° to 75° with the largest values for the carbonates. Bond lengths are shown in Table A3.4.

The bicarbonate groups are approximately perpendicular to each other for $M(HCO_3)_2$ with M = Mn, Co, and Zn, as previously found for Fe and Cd,[21] with dihedral angles (in the order

of oxygen atoms 2, 5, 10, 7, Figure 3.1) of ~ 85° in C_2 symmetry, whereas the bicarbonate groups in $Ni(HCO_3)_2$ and $Cu(HCO_3)_2$ are co-planar in C_{2h} symmetry (Table A3.5-A3.7). The C_2 structures have approximately perpendicular bicarbonates with the deviation from being exactly perpendicular due to the orientation of the COH groups. The rotation about the C-O(H) bond can influence the actual energetics and this deviation is small, about 5°. The approximate perpendicular orientation will minimize the repulsion between the O atoms on one $HOCO_2^-$ ligand with those on the other $HOCO_2^-$ ligand. The C_2 and C_{2h} structures are very close in energy for most metals (see Table A3.5) so small changes in the electron configurations on the metal can affect the orientation. The C_2 structures have a half filled d^5 configuration for Mn(II) and a filled d^{10} configuration for Zn(II) and Cd(II) as well as noble gas configurations for Mg(II) and Ca(II).[21] Thus, if there is no preferred orientation of the occupied orbitals on the metal, the C_2 structure is preferred (see Table A3.8 for electron configurations). The C_{2h} structures for Mg, Ca, Mn, Zn and Cd are 2 to 5 kcal/mol higher in energy than the C_2 structures at the CCSD(T)/aT level and have one imaginary frequency consistent with being a transition state as shown in Table A3.5.

In contrast, the Fe and Cu complexes are planar. The Fe complex has one d electron in addition to what is in the d^5 Mn complex. In order to minimize the electron repulsion and allow for maximum electron donation from the ligands to the metal, it adopts a C_{2h} (^5A_g) conformer with a pair of elections in a doubly occupied out of plane orbital (see Table A3.8). The C_2 (^5B) conformer is also a minimum for Fe^{2+} and is ~1.9 kcal/mol higher than the C_{2h} (^5A_g) conformer at the CCSD(T)/aT(-PP) level (see Table A3.5). The Cu^{2+} complex has only one orbital with one electron which could be available to accept electron donation from the ligands and orients itself

so as to enable this to occur while minimizing the interactions of the other d orbitals by as much as possible. The C_2 conformer for Cu^{2+} optimized back to the C_{2h} geometry.

The situation for Ni^{2+} is more complicated. The triplet Ni di-carbonate complex has two minima of C_2 (^3B) and C_{2h} (^3B_g) symmetry which are very close in energy to the singlet complex (see Table A3.5). At the CCSD(T) level with the aD basis set, the C_2 (^3B) conformer is 1.5 kcal/mol lower than the C_{2h} (^1A_g) conformer but with the aT basis set, the C_2 (^3B) conformer is 0.7 kcal/mol higher in energy and with the aQ basis set it is 1.4 kcal/mol higher in energy. The ^3B_g state in C_{2h} symmetry is 2.6 kcal/mol higher with the aT basis set. With a d^8 configuration, the Ni complex has a choice between the C_{2h} and C_2 geometries as well as two spin states. In this case, the singlet C_{2h} geometry is the lowest energy structure with 1 orbital available for electron donation from the ligands to enable more electron density to be out of plane to minimize the electron repulsion (see Table A3.8).

For a transition metal complex without a half or fully filled set of d orbitals, only Co has a C_2 (^4B) symmetry ground state (see Table A3.5). The Co di-bicarbonate has one more electron than in the Fe complex and can optimize electron donation from the ligands to the metal and minimize electron repulsion best in the C_2 conformer. The C_{2h} (^4A_g) conformer for Co^{2+} has one imaginary frequency and is 2.6 kcal/mol less stable than the C_2 (^4B) conformer at the CCSD(T)/aT level. All of these results point to significant flexibility in the bicarbonate structures about the metal center in terms of a planar vs approximately perpendicular geometry with the actual structure depending on the number of available d electrons and their distribution in the five d orbitals (see Table A3.8).

An energy decomposition analysis (EDA) (Table A3.9) of the C_2 vs C_{2h} structures shows that the electrostatic interactions are larger for the lower energy structures, except for

$Fe(HCO_3)_2$. The lower energy structure of $Fe(HCO_3)_2$ (C_{2h}, ^5A_g) has a smaller electrostatic interaction than $Fe(HCO_3)_2$ (C_2, ^5B) by 0.33 eV, yet the latter has a stronger Pauli repulsion which leads to the total dissociation energy (TDE) being 0.09 eV less than the former structure.

The presence of low energy conformers or low energy transition states for the di-carbonates suggests that there may be some fluxional character to these molecules especially at higher temperatures. This would require an improved treatment of the vibrational contribution in terms of the zero-point energy and the molecular thermal corrections which is beyond the current study. This could affect the energies on the order of 1 kcal/mol which is below the accuracy of the electronic structure approach for transition metals that we are using.

The HOM angles for C_s $M(HCO_3)OH$ (M = Mn, Co, Ni, Zn) vary from 114° to 128°; for M = Cu, the out of plane dihedral angle is 91.3° (atom 5,4,7,2) (see Table A3.3). The corresponding OMO bite angles for M = Mg, Ca, Fe, and Cd range from 58° to 76°. The smallest bite angle of all of the carbonates and bicarbonates is for Ca^{2+}. In addition, the bicarbonate groups in $M(HCO_3)_2$ for M = Mg, Ca, Fe, and Cd are approximately perpendicular to each other as predicted for M = Mn, Co, and Zn.

Gas Phase Heats of Formation The FPD heats of formation at 298K derived from the total atomization energies are given in Table 3.2. The FPD heats of formation at 0K are given in Table A3.10. It is important to get the initial orbital occupancies correct for the correlated molecular orbital theory calculations. The Hartree-Fock (HF)/aT calculation was used to obtain the initial guess for the HF/aD calculations for sextet $MnCO_3$, sextet $Mn(HCO_3)_2$, sextet $Mn(HCO_3)(OH)$, quartet $MnCO_3$, quartet $Mn(HCO_3)(OH)$, doublet $MnCO_3$, sextet $Co(HCO_3)(OH)$ and quartet $CoCO_3$. The previously predicted thermodynamic data[21] for Ca, Mg, Fe and Cd are given for comparison. At the CCSD(T)/aT level, the C_{2h} structure for $Fe(HCO_3)_2$ is 4.5 kcal/mol more

stable than the C_2 (^5A) structure previously reported,[21] and 1.9 kcal/mol more stable than the C_2 (^5B) structure (see Table A3.5). The values in Table 3.2 for $Fe(HCO_3)_2$ are for the more stable C_{2h} structure, correcting our prior work.[21]

Cohesive Energies and Dissociation Energies Building on our previous work,[21] the cohesive energy of a solid is calculated as the difference in the heats of formation between the gas and solid phases with the latter obtained from experiment where available.[71] Only the heats of formation of the solid carbonates are known. The order of cohesive energy of carbonates is Mg > Ca > Mn ~ Zn ~ Co ~ Cd > Fe > Ni > Cu according to Table 3.2. We investigated the possibility that the cohesive energies would correlate with the ionic radii as the gas phase and solid state energies exhibit significant ionic character as discussed below. For this comparison, we use the well-established radii of Shannon based on an extensive analysis of crystal structures.[89] However, there is no obvious correlation between the cohesive energy and the Shannon ionic radius (Figure 3.2) if all metals are included. Removing Mg and Cu from the fit led to an almost flat line with a slight increase in cohesive energy increases as the Shannon radii increases. Thus, the cohesive energy does not really correlate with the metal ionic radii. As discussed below, there are other energies that do correlate with the ionic radii.

To provide more insights into the nature of the energies of these compounds, we consider them to be salts with the bonding potentially being all due to ionic interactions. We calculated the total reaction dissociation energies (TRDE) from the following reactions:

$$M(HCO_3)_2 \rightarrow M^{2+} + 2HCO_3^- \quad (5)$$

$$M(HCO_3)(OH) \rightarrow M^{2+} + HCO_3^- + OH^- \quad (6)$$

The heat of formation for OH^- at the FPD level is -33.0 kcal/mol at 0 K in excellent agreement with the value of -33.2 kcal/mol from the ATcT tables.[65] The heat of formation for HCO_3^- is

from FPD calculations.[21,90,91] The heat of formation of the M^{2+} was calculated from the ionization energy of the metal dications from the neutral at the FPD level and the heat of formation of the neutral. The calculated ionization energy to from the +2 metal ion is in excellent agreement with the sum of the first two experimental ionization energies[92] (see Table A3.11-A3.12) with the largest deviation of 1.0 kcal/mol for Cd^{2+}.The TRDE based on the experimental data for the heats of formation of OH^- and M^{2+} are essentially identical to the calculated values (see Table A3.13 for a comparison). We cannot perform such a dissociation energy calculation for the carbonate as the dianion is not stable to loss of an electron in the gas phase. The results are given in Table 3.3 and shown in Figure 3.3 where they are plotted against the ionic radii. We report Shannon radii in Table 3.1. There is a qualitative trend of increased TRDE with decreasing atomic radii.

Comparing the TRDEs in Table 3.3, the most positive value is for the di-bicarbonate and the bicarbonate hydroxide is for Cu. This most likely reflects the energy necessary to prepare the Cu^{2+} ion. The other metals all involve ionization of two valence s electrons. However, preparation of Cu^{2+} involves removal of a 4s and a 3d electron. This is the highest energy as the 3d electrons are closer to the core and require more energy to ionize. The generation of Zn^{2+} also requires more energy due to the orbital contraction and shielding changes as one proceeds from left to right across a row in the Periodic Table. In addition to the sum of the first two ionization energies, the heat for formation of the gaseous metal atom also plays a role. Although one might expect Mg^{2+} to have the largest TRDE, this is not the case due to the ease of generating the gaseous Mg atom.

In the above discussion, we considered the dissociation to be predominantly electrostatic. We can directly estimate the Coulombic dissociation energy (CDE) by assuming a positive

charge of +2 on the metal, a -2 on the carbonate centered on the C for CO_3^{2-}, a -1 on the HCO_3^- centered at the C and a -1 one the OH^- centered on the O using Coulomb's law. The distance was taken between M and C for the carbonate and bicarbonate, and between M and O for the hydroxide group. We assume no shielding of the positive charge on the metal from the interaction with the anions. Note that this assumes that the energy to prepare the dication is the same. The results are given in Table 3.3 and plotted in Figure 3.4 as a function of Shannon ionic radii. Here the Coulombic dissociation energy shows an excellent linear correlation with the Shannon ionic radii.

Comparison of the TRDE with the Coulombic values in Table 3.3, shows that the Coulombic dissociation energy for Mg is very similar to the TRDE for the di-bicarbonate suggesting that the dissociation in this species is predominantly ionic. The TRDE in Ca is less than the Coulombic value by a larger amount suggesting that the charge shielding of the +2 charge is higher in the Ca di-bicarbonate. The Coulombic energies are quite similar for the di-bicarbonate of the transition metals, increasing as one goes to larger atomic number up to Ni with decreases for Cu and Zn consistent with the changing ionic radii. Note that the values for Zn and Mg are similar as are the values for Ca and Cd. For the transition metals, the TRDE is larger than the Coulombic value. This can be explained by the fact that the preparation of the atomic metal ions is different and that this affects the TRDE as noted above, which is also the case for the open-shell transition metals. The total ionization energy for the 1^{st} and 2^{nd} electrons for transition metals increases periodically from Mn to Cu, and then decreases to Cd. Obviously removing electrons from 4s orbitals is easier than from 3d orbitals. A big difference in total IP of 2 eV from Ni to Cu is due to removing the 2^{nd} electron from the fully occupied 3d orbital on Cu.

This trend is found in the TRDE. The Coulombic dissociation energies do track the decreasing ionic radii up to Ni^{2+} as the 3d orbitals get closer to the nucleus due to the change in shielding.

For the bicarbonate hydroxides, the Coulombic dissociation energy is always larger than the TRDE. The TRDE for the bicarbonate hydroxides is larger than for the di-bicarbonates as the OH^- group has a higher charge localization on the O and the M-O bond is shorter. The difference in the Coulombic and TRDE decreases as one proceeds across the period. Thus, the screening effect of the other ligand decreases going across the period.

For the CO_3^{2-} ligand, the Coulombic dissociation energy is larger than for the di-bicarbonate consistent with the negative charge being closer to the metal. This difference decreases going across the period. The Coulombic dissociation energy for the carbonate is always less than the value for the bicarbonate hydroxide showing the importance of the closer interaction of the OH^- with the metal.

The TDE and the corresponding electrostatic interaction components were obtained from the EDA and are given in Table 3.3. Details of the specific components of the TDE are in Table A3.9. We treated each molecule as a complex of a metal dication with the appropriate carbonate, bicarbonate, or hydroxide. The EDA enabled the TDE for the carbonates to be calculated as there is no free CO_3^{2-} in the calcualtion. In general, the TRDE and CDE are very close to the TDE and electrostatic interaction from the EDA analysis, respectively. In general, the TDE and electrostatic interaction are higher than the TRDE and CDE, respectively; exceptions are predicted for Mg^{2+}, Mn^{2+} and Cd^{2+}. The TDE of $MgCO_3$ and $Mg(HCO_3)_2$ are larger than the electrostatic interaction as the favorable orbital interactions are larger than the Pauli repulsion term. For the transition metal dications, the TDE is less than the electrostatic interaction only for Mn^{2+} and Cd^{2+} due to the Pauli repulsions being larger in magnitude than the stabilizing orbital

interactions. Figure 3.3 shows a comparison of the TRDE and TDE versus Shannon radii, and Figure 3.4 shows a comparison of CDE and electrostatic interaction versus Shannon radii. The correlations of these energetics dominated by electrostatic interactions exhibit similar behavior.

The TRDE between open-shell transition metal cations and bicarbonate or hydroxide anions can be strengthened by electron donation from from adjacent oxygen lone pairs to the metal d-orbitals. This hypothesis is supported by an NBO/NPA analysis. Natural charges on the transition metals in Table A3.14 are slightly smaller than those on Mg and Ca, and the absolute values of natural charges on O atoms adjacent to transition metals are also smaller than those bound to Mg and Ca. Natural spin analysis on each atom shows that spin can be transferred to the oxygen atoms adjacent to the open shell transition metals (see Table A3.15). The excess d orbital electron population on the transition metals shows that the lone pair orbitals on the adjacent oxygen atoms donate electron density to the empty d orbitals. No such electron donation from the ligands to the metal is predicted for Zn and Cd, due to the almost zero excess d orbital population in Table A3.16 consistent with the d^{10} configuration of the dication. The excess 3d population on MCO_3 is larger than that on $M(HCO_3)_2$ and $M(HCO_3)(OH)$. There are significant populations in the valence s orbital on the metal cations showing that there is also electron donation from the ligands to the metal valence s orbitals as the metal s orbitals are the first to be removed on ionization. (see Table A3.16).

Decomposition reactions The salts can decompose to MO plus different products as given by the following reactions.

$$MCO_3 \rightarrow MO + CO_2 \quad (7)$$

$$M(HCO_3)_2 \rightarrow MO + 2CO_2 + H_2O \quad (8)$$

$$M(HCO_3)(OH) \rightarrow MO + CO_2 + H_2O \quad (9)$$

The data needed for these calculations are given in Table 3.4 and the decomposition energies are given in Table 3.5. The decomposition of MCO_3 (Reaction 3) shows that the most stable carbonates are Mg and Ca and that most of the transition metal carbonates have much lower decomposition energies. In the transition metals, $NiCO_3$ is surprisingly stable, and Co is the easiest to decompose. The di-bicarbonates are far more stable with respect to decomposition (Reaction 4) than are the carbonates. The di-bicarbonates follow similar patterns as for the carbonates although in this case, the Ni compound does not stand out as much. The decomposition of the bicarbonate-hydroxides (Reaction 5) are less endothermic that the di-bicarbonates but the pattern is essentially the same.

Metal exchange reactions The reactions to exchange metals for the neutral and for the dication are given in Table 3.6 and A3.17. The reactions for Ca atom displacing a metal are all exothermic so Ca will displace the other metals as a gas phase atom. A different trend is predicted for Ca^{2+} where Ca^{2+} never displaces a metal dication in the gas phase, consistent with its relative placement on the electrochemical series as Ca metal is a strong reducing agent and will always reduce transition metals. The ordering of the carbonate displacement reactions is Ca > Fe > Ni> Mg > Mn ~ Co > Cu > Zn > Cd. The ordering for the di-bicarbonate and bicarbonate hydroxide displacement reactions is Ca > Mg > Fe > Mn > Co > Ni > Cu > Zn > Cd. The reactivity for Mn and Co is very close for the di-bicarbonate. The reactivity for Co and Ni is very close for the bicarbonate hydroxide. The less reactive metals have endothermic reactions and these results are given in the Supporting Information. The reactivity ordering based on the electrochemical series is Ca > Mg > Mn > Zn > Fe > Cd > Co > Ni > Cu for the solid metal going to the aqueous dication.[93,94] For these reactions involving the gas phase metal atom being displaced, Ca is clearly the most reactive for all three types of ligand coordination consistent

with the ordering by the electrochemical series. For the carbonates, the remainder of the reactivity ordering does not really follow the electrochemical series. In all cases, the ordering of the least reactive in terms of displacement is Cu > Zn > Cd that never follows the electrochemical series. For the di-bicarbonate and carbonate hydroxide reactions, the next most reactive is Mg which follows the electrochemical series.

The most reactive dication is Cu^{2+} which is able to displace all the other metals from all three molecular species, which means it is the most reactive metal dication, and Ca^{2+} is the least reactive. The ordering of the carbonate displacement reactions is $Cu^{2+} > Ni^{2+} > Zn^{2+} > Co^{2+} > Fe^{2+} > Mn^{2+} > Cd^{2+} > Mg^{2+} > Ca^{2+}$. The ordering for di-bicarbonate is $Cu^{2+} > Ni^{2+} > Zn^{2+} > Co^{2+} > Fe^{2+} > Mg^{2+} > Mn^{2+} > Cd^{2+} > Ca^{2+}$, which is same to bi-carbonate hydroxide displacement except for the exchange of position of $Ni^{2+} > Zn^{2+}$. The main difference in the carbonate vs bicarbonate ordering is that Mg^{2+} is less reactive in the former. This clearly does not follow the redox reactivity ordering. However, Cu^{2+} being the most reactive dication matches the redox ordering where Cu is the least reactive. The TRDE for Cu^{2+} bi-carbonate and bi-carbonate hydroxide are the largest (see Table 3.3) and formation of Cu^{2+} is the most difficult (see Table 3.1), consistent with Cu^{2+} wanting to be stabilized by complex formation. The exact opposite applies to Ca^{2+}, which is the most stable free dication so it is the most readily displaced. The ordering of TRDE for bi-carbonate is the same as the displacement reaction ordering, $Cu^{2+} > Ni^{2+} > Zn^{2+} > Co^{2+} > Fe^{2+} > Mg^{2+} > Mn^{2+} > Cd^{2+} > Ca^{2+}$, and this is same to the ordering of bi-carbonate hydroxide displacement except for the exchange of position of $Ni^{2+} > Zn^{2+}$. The ordering of ΔH_{0K} of dications is similar as well, $Cu^{2+} > Ni^{2+} > Co^{2+} > Zn^{2+} > Fe^{2+} > Cd^{2+} > Mn^{2+} > Mg^{2+} > Ca^{2+}$. Yet, the highest TDE from EDA in ADF refers to Ni^{2+} in bi-carbonates and carbonates (see Table 3.3).

Qualitative Density Functional Theory Correlations The qualitative DFT descriptors of hardness (η) and electronegativity (χ)[95] can be calculated from the ionization energy (IE) and electron affinity (EA) from Equations (6) and (7) using the available experimental data.

$$\eta = (IE - EA)/2 \quad (6)$$

$$\chi = (IE + EA)/2 \quad (7)$$

In this case, one needs the second and third ionization potentials as the former corresponds to the electron affinity of the dication. The experimental values for the two ionization potentials (See Table 3.1) were used to calculate the hardness and electronegativity (See Table A3.18). As shown in Figures A3.14, there are no real correlations of the any of the dissociation energies (TRDE, CDE, TDE, and electrostatic, Table 3.3) with the hardness or electronegativity of the metal dication. There is a qualitative correlation of the cohesive energy with both the hardness and the electronegativity of the metal dications (Figure 3.5) after removing Cu. The harder cations, Mg^{2+} and Ca^{2+} have larger cohesive energies and are the hardest dications. Mg^{2+} is also the most electronegative dication and the cohesive energy is also largest for it. Note that on the electronegativity scale that Ca^{2+} is much closer to the transition metal dications. For both scales, Ni^{2+} is furthest from the linear correlation.

Benchmark of Selected DFT Functionals We have previously benchmarked a broad range of DFT functionals for these types of metal carbonates, di-bicarbonates, and bicarbonate-hydroxides for M = Mg, Ca, Fe, and Cd. We have benchmarked a smaller set of functionals which are relevant to bulk mineral calculations. Table 3.7 shows the average absolute $\Delta H_{f,0K}$ errors for metal carbonates, di-bicarbonates, and bicarbonate hydroxides. Figure 3.6 shows the distributions of DFT errors for $\Delta H_{f,0K}$ based on a comparison to the FPD results for MCO_3, $M(HCO_3)_2$ and $M(HCO_3)(OH)$ for M = Mn, Co, Ni, Cu and Zn. The corresponding data sets for

Figure 3.6 are in Table A3.19-A3.21. The τ-HCTH functional gives the lowest average absolute error, 8.3 kcal/mol for all of the metals from the current work and our prior work[21] for the carbonates, di-bicarbonates, and carbonate-hydroxides. For the limited set of metals, Mg, Ca, Fe, and Cd including the current anions, their hydrates and metal oxides, dichlorides, and dihydroxides from our prior work,[21] the best agreement with the FPD results was found with the ωB97X and ωB97X-D functionals with average absolute errors of 9.7 and 10.0 kcal/mol, respectively. For the compounds from our prior work,[21] the τ-HCTH functional had a somewhat larger average absolute error of 13.1 kcal/mol. When only the transition metals are included, the τ-HCTH functional performed just as well as with all of the metal atoms, but the ωB97X and ωB97X-D functionals showed larger average absolute errors of 18.0 and 15.3 kcal/mol. The next best functionals in the current work are PBE0 and HSE06 which have average absolute errors of 10.2 and 10.9 kcal/mol, respectively. The functionals PW91, BP86, and PBE had very large average absolute errors above 40.0 kcal/mol in the current work and above 30 kcal/mol in the prior work. [21] The common B3LYP functional had an average absolute error of 13.6 kcal/mol in the current work and 15.6 kcal/mol in the prior work.[21] The remaining functionals had average absolute errors falling between 11 and 15 kcal/mol in the current work. The average absolute errors for only the first-row transition metals, and the first-row transition metals including Ca were also presented in Table 3.7 and exhibit the same qualitative behavior with some small variations in the actual ordering of the average absolute errors. Even though the τ-HCTH functional had the lowest average absolute error in the current work, there were some outliers, notably the carbonates of Co, Ni, and Cu with errors of approximately 25, 12 and 15 kcal/mol, respectively. Thus, one must take additional care in testing functionals for the specific system of interest. Clearly, none of the functionals attains chemical accuracy of ±1 kcal/mol in terms of

agreement with the CCSD(T) results. We showed in prior work[21] that the major issue with the DFT functionals is the issue in how oxygen is treated which has a significant impact on the species under study in the current work.[22]

We now discuss the functionals that provide agreement within 10 kcal/mol of the CCSD(T) results in the current work. Most functionals behave poorly for the Mn complexes except for τ-HCTH which has errors below ±10 kcal/mol for all three species. For Co, none of the functionals are good to ±10 kcal/mol for all three species. M06, PBE0 and ωB97X give errors less than ± 10 kcal/mol for all Ni species. For Cu containing molecules, M06, PBE0, HSE06, ωB97X and ωB97X-D have errors less than ± 10 kcal/mol. Most of the functional exhibit improved behavior for the closed shell Zn^{2+} complexes with PBE0, HSE06, ωB97X and ωB97X-D having errors less than ±11 kcal/mol.

Conclusions

Thermodynamic properties have been determined for MCO_3, $M(HCO_3)_2$ and $M(HCO_3)(OH)$ (M = Mn, Co, Ni, Cu and Zn). These molecules were optimized at the B3LYP/aT level. Two symmetries of approximately perpendicular C_2 and C_{2h}, and multiple spin states are available for $M(HCO_3)_2$, where M = Mg, Ca, Mn, Fe, Co, Ni, Cu, Zn and Cd, depending on several factors including the electron repulsion of oxygen atoms, orientation of 3d orbitals on metals and the distribution of electrons in the 3d orbitals.

The FPD approach based on CCSD(T) calculations extrapolated to the CBS limit was used to predict the gas phase heats of formation. These values served as benchmarks for heats of formation calculated with various exchange-correlation DFT functionals, including those commonly used in solid-state mineral calculations. Cohesive energies for the carbonates were calculated based on the gas phase heats of formation at 298K from the FPD approach and the

experimental solid-state heats of formation.[71] The cohesive energy of Mg is the highest at 154 kcal/mol and Cu is the smallest at 71 kcal/mol. The remaining cohesive energies fall within a range of ~ 120 to 140 kcal/mol. The Coulombic dissociation energy (CDE) and total reaction dissociation energy (TRDE) of dications and anions were correlated with dication ionic radii and the dication hardness. There is a near linear correlation of CDE with the dication radii. Excluding Cu, there is an approximate linear correlation with the hardness of the metal dications, with Ni deviating most from the linear fit. The TRDEs of Mg and Ca are slightly smaller than their CDE likely due to a shielding effect, whereas the TRDEs of transition metals are higher than their CDE. In addition to differences in the energies needed to prepare the transition metal dications, electron donation to 3d orbitals of open-shell transition metal dications from lone pairs of adjacent O atoms will also play a role as shown by the NPA atomic charges and spins. No electron donation from the ligands to 3d orbitals for Zn^{2+} and Cd^{2+} was found, consistent with their d^{10} configurations.

Decomposition energies for generating MO, CO_2 and/or H_2O were calculated and the decomposition energies for the carbonates are much smaller than for the di-bicarbonates and bicarbonate hydroxides The Mg and Ca compounds have higher decomposition energies for reactions (7), (8), and (9) than do the transition metal compounds. For metal exchange reactions, Ca will always displace the other metals for the neutral atoms whereas Cu^{2+} will always displace the other dications. These results correlate qualitatively with the electrochemical series for the metal atom displacements for the former and with the ease of preparation of the dication for the latter.

The best agreement in the benchmarking of the DFT heats of formation vs. the FPD results is found for the τ-HCTH functional with an average absolute error of 8.3 kcal/mol. None

of the functionals can attain chemical accuracy of ±1 kcal/mol mainly due to DFT issues with the treatment of oxygen as discussed previously. Even for the τ-HCTH functional, there are outliers for the carbonates. The functionals with the largest average unsigned errors, 40 to 48 kcal/mol, are BP86, PW91, and PBE, the latter two of which are often used in periodic calculations for the solid state. The current results extend our prior work to more metals and provide further insights into the chemistry of the carbonate, di-bicarbonate, and bicarbonate-hydroxide complexes with metal dications. Such species may play an important role in the formation of nanoparticles,[24,25] which can serve as prenucleation sites in the formation of various bulk geochemical materials.

Tables

Table 3.1. Experimental Atomic Properties Including Ionization Energy (IE) and Heats of Formation in eV.

Metal	1st IE	2nd IE	3rd IE	ΔH_{0K} atom	ΔH_{0K} atom kcal/mol	1st IE + 2nd IE	TC[a] kcal/mol	ΔH_{0K} M^{2+}	η[b]	Ionic radii Shannon (Å)[89]	CN[c]
Mg	7.646236	15.035271	80.1436	1.51	34.9 ± 0.2[68]	22.681507	1.19[68]	24.19	32.55	0.72	6
Ca	6.1131554	11.871719	50.91316	1.84	42.4 ± 0.2[68]	17.984874	1.37[68]	19.82	19.52	1	6
Mn	7.434038	15.63999	33.668	2.90	66.8[69]	23.074028	1.19[69]	25.97	9.01	0.830	6 HS
Fe	7.9024681	16.1992	30.651	4.28	98.7 ± 0.3[68]	24.10217	1.08[68]	28.38	7.23	0.78	6 HS
Co	7.88101	17.0844	33.50[d]	4.41	101.6 ± 0.5[68]	24.9654	1.14[68]	29.37	8.21	0.745	6 HS
Ni	7.639878	18.168838	35.187	4.43	102.2[69]	25.808716	1.14[69]	30.24	8.51	0.690	6
Cu	7.72638	20.29239	36.841	3.49	80.4± 0.3[70,d]	28.01877	1.20[70]	31.51	8.27	0.73	6
Zn	9.394197	17.96439	39.72330	1.34	31.0± 0.1[70,d]	27.35859	1.35[70]	28.70	10.88	0.740	6
Cd	8.99382	16.908313	37.468	1.16	26.7 ± 0.1[69,71]	25.90213	1.49[69]	27.06	10.28	0.95	6

[a] TC = Thermal correction for atoms from 0 K to 298 K.
[b] Definition of hardness (η) is η = (IE-EA)/2 where IE = ionization energy and EA = electron affinity. For dication metals, η = (3rd IE - 2nd IE)/2. The 2nd IE is the EA for dication metals.
[c] CN = Coordination number for the Shannon radii. HS = high spin
[d] Value from ref. 70 at 298 K corrected to 0 K by results from reference 68.

Table 3.2. Symmetry, states, total atomization energy at 0K ($\Sigma D_{0,\,0K}$), gaseous heat of formation from the FPD calculation at 298K, solid state heat of formation from experiments at 298K, and cohesive energies at 298K of transition metal carbonates, di-bicarbonates and bicarbonate hydroxides in kcal/mol.

Molecule	Symm	State	$\Sigma D_{0,\,0K}$	$\Delta H_{f,298K}$(g)	$\Delta H_{f,298K}$ (s)[a]	Cohesive E
$MgCO_3$[21]	C_{2v}	$^1A_1$	492.3	-111.7	-265.7	154.0
$Mg(HCO_3)_2$[21]	C_2	^1A	1189.4	-360.9		
$Mg(HCO_3)(OH)$[21]	C_s	$^1A'$	786.8	-245.0		
$CaCO_3$[21]	C_{2v}	$^1A_1$	537.7	-149.5	-288.5 ± 0.2	139.0
$Ca(HCO_3)_2$[21]	C_2	^1A	1218.8	-382.6		
$Ca(HCO_3)(OH)$[21]	C_s	$^1A'$	812.5	-263.4		
$MnCO_3$	C_{2v}	$^6A_1$	491.0	-78.4	-210.721[b]	132.3
$Mn(HCO_3)_2$	C_2	^6A	1171.5	-310.7		
$Mn(HCO_3)(OH)$	C_s	$^6A'$	774.5	-200.8		
$FeCO_3$[21]	C_{2v}	$^5A_1$	496.5	-51.8	-179.4	127.6
$Fe(HCO_3)_2$[d,e]	C_{2h}	^5A_g	1173.0	-280.1	-224.6	
$Fe(HCO_3)(OH)$[21]	C_s	$^5A'$	780.5	-174.8		
$CoCO_3$	C_{2v}	$^4A_1$	494.7	-42.7	-174.6[c]	131.9
$Co(HCO_3)_2$	C_2	^4B	1170.3	-270.2		
$Co(HCO_3)(OH)$	C_s	$^4A'$	771.4	-158.5		
$NiCO_3$	C_{2v}	$^1A_1$	500.8	-47.2	-166	118.8
$Ni(HCO_3)_2$	C_{2h}	^1A_g	1166.7	-265.6		
$Ni(HCO_3)(OH)$	C_s	$^3A''$	770.4	-155.9		
$CuCO_3$	C_{2v}	$^2B_2$	465.9	-39.5	-110.43±0.21	70.9
$Cu(HCO_3)_2$	C_{2h}	^2A_g	1133.3	-259.3		
$Cu(HCO_3)(OH)$	C_1	^2A	735.6	-148.6		
$ZnCO_3$	C_{2v}	$^1A_1$	440.1	-63.4	-195.52±0.1	132.1
$Zn(HCO_3)_2$	C_2	^1A	1124.3	-299.5		
$Zn(HCO_3)(OH)$	C_s	$^1A'$	732.3	-194.7		
$CdCO_3$[21]	C_{2v}	$^1A_1$	421.1	-48.5	-179.4	130.9
$Cd(HCO_3)_2$[21]	C_2	^1A	1102.3	-281.7		
$Cd(HCO_3)(OH)$[21]	C_s	$^1A'$	707.8	-174.4		

[a] Experimental values from reference 71. [b] Rhodochrosite. [c] Sphaerocobaltite. [d] Following on our prior work in ref. 21, ΔE_{SR} for $Fe(HCO_3)_2$ is the sum of the mass-velocity and 1-electron Darwin (MVD) terms in the Breit-Pauli Hamiltonian calculated at the CI-SD (configuration interaction singles and doubles) level of theory using the aug-cc-pVTZ basis set. A comparison for Cd between the MVD and DK methods is small, 0.2 kcal/mol from ref. 21. [e] In ref. 21, the higher energy C_2 structure was used as the ground state for $Fe(HCO_3)_2$. Corrected hydration energies for the addition of one and two H_2O molecules for the C_{2h} structure of $Fe(HCO_3)_2$ are given in Table A3.23.

Table 3.3. Total reaction dissociation energy (TRDE), Coulombic dissociation energy (CDE), and total dissociation energy (TDE) and electrostatic interaction from energy decomposition analysis (EDA) in Amsterdam Density Functional (ADF) in eV at 0K.

Metal Cation	HCO_3^-				HCO_3^-/OH^-				CO_3^{2-}		
	TRDE	CDE	TDE	Electrostatic	TRDE	CDE	TDE	Electrostatic	CDE	TDE	Electrostatic
Mg^{2+}	24.72	24.98	25.13	24.76	25.80	28.57	26.30	26.77	25.83	27.55	27.04
Ca^{2+}	21.31	22.15	21.54	22.84	22.22	25.28	22.77	24.51	23.17	24.79	26.21
Mn^{2+}	24.35	23.83	25.30	26.01	25.67	27.57	26.95	29.26	24.72	28.92	29.34
Fe^{2+}	25.44	24.44	26.84	26.85	26.95	28.24	28.67	30.48	25.17	30.72	30.32
Co^{2+}	26.00	24.66	28.39	27.69	27.24	28.59	29.89	30.44	25.32	32.27	30.75
Ni^{2+}	26.65	25.86	30.66	30.39	28.00	28.91	30.87	31.79	25.66	34.66	32.18
Cu^{2+}	27.67	25.10	29.57	28.01	28.96	28.95	31.14	31.62	24.90	33.77	29.34
Zn^{2+}	26.62	24.75	27.51	27.21	28.16	28.52	29.27	30.82	25.48	30.67	29.69
Cd^{2+}	24.22	22.61	24.50	25.08	25.65	25.73	26.22	28.41	23.08	26.22	28.41

Table 3.4. Heats of formation for MO, H_2O and CO_2 at 0K in kcal/mol, and dissociation energies.

Molecule	D_0	$\Delta H_{f,0K}$ gas	$\Delta H_{f,298K}$ gas	ref
MgO	61.4	32.4	32.3	96
CaO	96.4	5.0	4.7	96
MnO	86.5±6	39.3		97
FeO	97.3±0.2	60.4		98
CoO	95.0± 2.1	65.6		99
NiO	87.5±7.2	73.7		100
CuO	68.7±2.8	70.7		101
ZnO		55.4	55.2	102
CdO	22.2	63.5		103
CO_2		-94.0±0.004	-94.0±0.004	65, 66, 67
H_2O		-57.1±0.006	-57.8±0.006	65, 66, 67

Table 3.5. Gas phase decomposition reactions at 0K in kcal/mol.

Reaction	ΔH_{0K}	Reaction	ΔH_{0K}	Reaction	ΔH_{0K}
$MgCO_3 \rightarrow MgO + CO_2$	48.8	$Mg(HCO_3)_2 \rightarrow MgO + 2CO_2 + H_2O$	144.2	$Mg(HCO_3)(OH) \rightarrow MgO + CO_2 + H_2O$	123.6
$CaCO_3 \rightarrow CaO + CO_2$	59.1	$Ca(HCO_3)_2 \rightarrow CaO + 2CO_2 + H_2O$	138.9	$Ca(HCO_3)(OH) \rightarrow CaO + CO_2 + H_2O$	114.7
$MnCO_3 \rightarrow MnO + CO_2$	22.5	$Mn(HCO_3)_2 \rightarrow MnO + 2CO_2 + H_2O$	101.5	$Mn(HCO_3)(OH) \rightarrow MnO + CO_2 + H_2O$	86.6
$FeCO_3 \rightarrow FeO + CO_2$	17.2	$Fe(HCO_3)_2 \rightarrow FeO + 2CO_2 + H_2O$	92.2	$Fe(HCO_3)(OH) \rightarrow FeO + CO_2 + H_2O$	81.8
$CoCO_3 \rightarrow CoO + CO_2$	13.2	$Co(HCO_3)_2 \rightarrow CoO + 2CO_2 + H_2O$	87.3	$Co(HCO_3)(OH) \rightarrow CoO + CO_2 + H_2O$	70.5
$NiCO_3 \rightarrow NiO + CO_2$	25.7	$Ni(HCO_3)_2 \rightarrow NiO + 2CO_2 + H_2O$	90.2	$Ni(HCO_3)(OH) \rightarrow NiO + CO_2 + H_2O$	76.0
$CuCO_3 \rightarrow CuO + CO_2$	15.1	$Cu(HCO_3)_2 \rightarrow CuO + 2CO_2 + H_2O$	81.2	$Cu(HCO_3)(OH) \rightarrow CuO + CO_2 + H_2O$	65.5
$ZnCO_3 \rightarrow ZnO + CO_2$	23.5	$Zn(HCO_3)_2 \rightarrow ZnO + 2CO_2 + H_2O$	106.2	$Zn(HCO_3)(OH) \rightarrow ZnO + CO_2 + H_2O$	96.3
$CdCO_3 \rightarrow CdO + CO_2$	16.8	$Cd(HCO_3)_2 \rightarrow CdO + 2CO_2 + H_2O$	96.6	$Cd(HCO_3)(OH) \rightarrow CdO + CO_2 + H_2O$	84.2

Table 3.6. Exothermic gas phase metal exchange energy at 0K in kcal/mol.

Displacement Reaction	ΔH_{0K} (g) neutral	ΔH_{0K} (g) dication
$Ca + MgCO_3 \rightarrow CaCO_3 + Mg$	-45.2	63.1
$Ca + MnCO_3 \rightarrow CaCO_3 + Mn$	-46.5	70.9
$Ca + FeCO_3 \rightarrow CaCO_3 + Fe$	-41.0	100.1
$Ca + CoCO_3 \rightarrow CaCO_3 + Co$	-47.3	113.7
$Ca + NiCO_3 \rightarrow CaCO_3 + Ni$	-42.3	138.1
$Ca + CuCO_3 \rightarrow CaCO_3 + Cu$	-71.6	159.7
$Ca + ZnCO_3 \rightarrow CaCO_3 + Zn$	-97.4	118.8
$Ca + CdCO_3 \rightarrow CaCO_3 + Cd$	-116.5	66.1
$Ca + Mg(HCO_3)_2 \rightarrow Ca(HCO_3)_2 + Mg$	-29.6	78.7
$Ca + Mn(HCO_3)_2 \rightarrow Ca(HCO_3)_2 + Mn$	-47.2	70.1
$Ca + Fe(HCO_3)_2 \rightarrow Ca(HCO_3)_2 + Fe$	-45.7	95.3
$Ca + Co(HCO_3)_2 \rightarrow Ca(HCO_3)_2 + Co$	-53.0	108.0
$Ca + Ni(HCO_3)_2 \rightarrow Ca(HCO_3)_2 + Ni$	-57.6	122.9
$Ca + Cu(HCO_3)_2 \rightarrow Ca(HCO_3)_2 + Cu$	-85.4	146.0
$Ca + Zn(HCO_3)_2 \rightarrow Ca(HCO_3)_2 + Zn$	-94.4	121.7
$Ca + Cd(HCO_3)_2 \rightarrow Ca(HCO_3)_2 + Cd$	-116.5	66.1
$Ca + Mg(HCO_3)(OH) \rightarrow Ca(HCO_3)(OH) + Mg$	-26.0	82.3
$Ca + Mn(HCO_3)(OH) \rightarrow Ca(HCO_3)(OH) + Mn$	-37.9	79.4
$Ca + Fe(HCO_3)(OH) \rightarrow Ca(HCO_3)(OH) + Fe$	-32.0	109.1
$Ca + Co(HCO_3)(OH) \rightarrow Ca(HCO_3)(OH) + Co$	-45.6	115.4
$Ca + Ni(HCO_3)(OH) \rightarrow Ca(HCO_3)(OH) + Ni$	-47.6	132.8
$Ca + Cu(HCO_3)(OH) \rightarrow Ca(HCO_3)(OH) + Cu$	-76.9	154.5
$Ca + Zn(HCO_3)(OH) \rightarrow Ca(HCO_3)(OH) + Zn$	-80.2	136.0
$Ca + Cd(HCO_3)(OH) \rightarrow Ca(HCO_3)(OH) + Cd$	-104.7	77.9
$Mg + MnCO_3 \rightarrow MgCO_3 + Mn$	-1.3	7.8
$Mg + CoCO_3 \rightarrow MgCO_3 + Co$	-2.1	50.6
$Mg + CuCO_3 \rightarrow MgCO_3 + Cu$	-26.4	96.6
$Mg + ZnCO_3 \rightarrow MgCO_3 + Zn$	-52.2	55.7
$Mg + CdCO_3 \rightarrow MgCO_3 + Cd$	-71.2	3.0
$Mg + Mn(HCO_3)_2 \rightarrow Mg(HCO_3)_2 + Mn$	-17.6	-8.6
$Mg + Fe(HCO_3)_2 \rightarrow Mg(HCO_3)_2 + Fe$	-16.1	16.6
$Mg + Co(HCO_3)_2 \rightarrow Mg(HCO_3)_2 + Co$	-23.4	29.3
$Mg + Ni(HCO_3)_2 \rightarrow Mg(HCO_3)_2 + Ni$	-28.0	44.2
$Mg + Cu(HCO_3)_2 \rightarrow Mg(HCO_3)_2 + Cu$	-55.7	67.3
$Mg + Zn(HCO_3)_2 \rightarrow Mg(HCO_3)_2 + Zn$	-64.8	43.0
$Mg + Cd(HCO_3)_2 \rightarrow Mg(HCO_3)_2 + Cd$	-86.8	-12.6
$Mg + Mn(HCO_3)(OH) \rightarrow Mg(HCO_3)(OH) + Mn$	-11.9	-2.9
$Mg + Fe(HCO_3)(OH) \rightarrow Mg(HCO_3)(OH) + Fe$	-6.0	26.8
$Mg + Co(HCO_3)(OH) \rightarrow Mg(HCO_3)(OH) + Co$	-19.6	33.1
$Mg + Ni(HCO_3)(OH) \rightarrow Mg(HCO_3)(OH) + Ni$	-21.6	50.5
$Mg + Cu(HCO_3)(OH) \rightarrow Mg(HCO_3)(OH) + Cu$	-50.9	72.2

$Mg + Zn(HCO_3)(OH) \rightarrow Mg(HCO_3)(OH) + Zn$	-54.2	53.7
$Mg + Cd(HCO_3)(OH) \rightarrow Mg(HCO_3)(OH) + Cd$	-78.6	-4.4
$Mn + CoCO_3 \rightarrow MnCO_3 + Co$	-0.8	42.8
$Mn + CuCO_3 \rightarrow MnCO_3 + Cu$	-25.2	88.9
$Mn + ZnCO_3 \rightarrow MnCO_3 + Zn$	-50.9	47.9
$Mn + CdCO_3 \rightarrow MnCO_3 + Cd$	-70.0	-4.7
$Mn + Co(HCO_3)_2 \rightarrow Mn(HCO_3)_2 + Co$	-5.8	37.9
$Mn + Ni(HCO_3)_2 \rightarrow Mn(HCO_3)_2 + Ni$	-10.3	52.7
$Mn + Cu(HCO_3)_2 \rightarrow Mn(HCO_3)_2 + Cu$	-38.1	75.9
$Mn + Zn(HCO_3)_2 \rightarrow Mn(HCO_3)_2 + Zn$	-47.2	51.6
$Mn + Cd(HCO_3)_2 \rightarrow Mn(HCO_3)_2 + Cd$	-69.2	-4.0
$Mn + Co(HCO_3)(OH) \rightarrow Mn(HCO_3)(OH) + Co$	-7.6	36.0
$Mn + Ni(HCO_3)(OH) \rightarrow Mn(HCO_3)(OH) + Ni$	-9.7	53.4
$Mn + Cu(HCO_3)(OH) \rightarrow Mn(HCO_3)(OH) + Cu$	-39.0	75.1
$Mn + Zn(HCO_3)(OH) \rightarrow Mna(HCO_3)(OH) + Zn$	-42.2	56.6
$Mn + Cd(HCO_3)(OH) \rightarrow Mn(HCO_3)(OH) + Cd$	-66.7	-1.5
$Fe + MgCO_3 \rightarrow FeCO_3 + Mg$	-4.2	-37.0
$Fe + MnCO_3 \rightarrow FeCO_3 + Mn$	-5.5	-29.2
$Fe + CoCO_3 \rightarrow FeCO_3 + Co$	-6.3	13.6
$Fe + NiCO_3 \rightarrow FeCO_3 + Ni$	-1.3	38.1
$Fe + CuCO_3 \rightarrow FeCO_3 + Cu$	-30.7	59.7
$Fe + ZnCO_3 \rightarrow FeCO_3 + Zn$	-56.4	18.7
$Fe + CdCO_3 \rightarrow FeCO_3 + Cd$	-75.5	-34.0
$Fe + Mn(HCO_3)_2 \rightarrow Fe(HCO_3)_2 + Mn$	-1.5	-25.2
$Fe + Co(HCO_3)_2 \rightarrow Fe(HCO_3)_2 + Co$	-7.3	12.7
$Fe + Ni(HCO_3)_2 \rightarrow Fe(HCO_3)_2 + Ni$	-11.8	27.5
$Fe + {}^{2}Cu(HCO_3)_2 \rightarrow Fe(HCO_3)_2 + Cu$	-39.6	50.7
$Fe + Zn(HCO_3)_2 \rightarrow Fe(HCO_3)_2 + Zn$	-48.7	26.4
$Fe + Cd(HCO_3)_2 \rightarrow {}^{5}Fe(HCO_3)_2 + Cd$	-70.4	-28.8
$Fe + Mn(HCO_3)(OH) \rightarrow Fe(HCO_3)(OH) + Mn$	-6.0	-29.7
$Fe + Co(HCO_3)(OH) \rightarrow Fe(HCO_3)(OH) + Co$	-13.6	6.3
$Fe + Ni(HCO_3)(OH) \rightarrow Fe(HCO_3)(OH) + Ni$	-15.6	23.7
$Fe + Cu(HCO_3)(OH) \rightarrow Fe(HCO_3)(OH) + Cu$	-44.9	45.4
$Fe + Zn(HCO_3)(OH) \rightarrow Fe(HCO_3)(OH) + Zn$	-48.2	26.9
$Fe + Cd(HCO_3)(OH) \rightarrow Fe(HCO_3)(OH) + Cd$	-72.7	-31.2
$Co + CuCO_3 \rightarrow CoCO_3 + Cu$	-24.3	46.1
$Co + ZnCO_3 \rightarrow CoCO_3 + Zn$	-49.9	5.3
$Co + CdCO_3 \rightarrow CoCO_3 + Cd$	-69.1	-47.5
$Co + Ni(HCO_3)_2 \rightarrow Co(HCO_3)_2 + Ni$	-4.6	14.9
$Co + Cu(HCO_3)_2 \rightarrow Co(HCO_3)_2 + Cu$	-32.4	38.0
$Co + Zn(HCO_3)_2 \rightarrow Co(HCO_3)_2 + Zn$	-41.5	13.7
$Co + Cd(HCO_3)_2 \rightarrow Co(HCO_3)_2 + Cd$	-63.5	-41.9
$Co + Ni(HCO_3)(OH) \rightarrow Co(HCO_3)(OH) + Ni$	-2.0	17.4
$Co + Cu(HCO_3)(OH) \rightarrow Co(HCO_3)(OH) + Cu$	-31.3	39.1
$Co + Zn(HCO_3)(OH) \rightarrow Co(HCO_3)(OH) + Zn$	-34.6	20.6

$Co + Cd(HCO_3)(OH) \rightarrow Co(HCO_3)(OH) + Cd$	-59.1	-37.5
$Ni + MgCO_3 \rightarrow NiCO_3 + Mg$	-2.9	-75.0
$Ni + MnCO_3 \rightarrow NiCO_3 + Mn$	-4.2	-67.3
$Ni + CoCO_3 \rightarrow NiCO_3 + Co$	-5.0	-24.5
$Ni + CuCO_3 \rightarrow NiCO_3 + Cu$	-29.4	21.6
$Ni + ZnCO_3 \rightarrow NiCO_3 + Zn$	-55.1	-19.3
$Ni + CdCO_3 \rightarrow NiCO_3 + Cd$	-74.2	-72.0
$Ni + Cu(HCO_3)_2 \rightarrow Ni(HCO_3)_2 + Cu$	-27.8	23.2
$Ni + Zn(HCO_3)_2 \rightarrow Ni(HCO_3)_2 + Zn$	-36.9	-1.1
$Ni + Cd(HCO_3)_2 \rightarrow Ni(HCO_3)_2 + Cd$	-58.9	-56.7
$Ni + Cu(HCO_3)(OH) \rightarrow Ni(HCO_3)(OH) + Cu$	-29.3	21.7
$Ni + Zn(HCO_3)(OH) \rightarrow Ni(HCO_3)(OH) + Zn$	-32.5	3.2
$Ni + Cd(HCO_3)(OH) \rightarrow Ni(HCO_3)(OH) + Cd$	-57.0	-54.9
$Cu + ZnCO_3 \rightarrow CuCO_3 + Zn$	-25.7	-40.9
$Cu + CdCO_3 \rightarrow CuCO_3 + Cd$	-44.8	-93.6
$Cu + Zn(HCO_3)_2 \rightarrow Cu(HCO_3)_2 + Zn$	-9.1	-24.3
$Cu + Cd(HCO_3)_2 \rightarrow Cu(HCO_3)_2 + Cd$	-31.1	-79.9
$Cu + Zn(HCO_3)(OH) \rightarrow Cu(HCO_3)(OH) + Zn$	-3.3	-18.5
$Cu + Cd(HCO_3)(OH) \rightarrow Cu(HCO_3)(OH) + Cd$	-27.7	-76.6
$Zn + CdCO_3 \rightarrow ZnCO_3 + Cd$	-19.1	-52.7
$Zn + Cd(HCO_3)_2 \rightarrow Zn(HCO_3)_2 + Cd$	-22.0	-55.6
$Zn + Cd(HCO_3)(OH) \rightarrow Zn(HCO_3)(OH) + Cd$	-24.5	-58.1

Table 3.7. Average absolute $\Delta H_{f,0K}$ errors of DFT functionals compared to FPD results in kcal/mol for MCO_3, $M(HCO_3)_2$, $M(HCO_3)(OH)$ (M = Mg, Ca, Mn, Fe, Co, Ni, Cu, Zn and Cd).

Functional	All M atoms	1st row transition M	1st row transition M + Ca
PW91	47.5	50.3	50.0
BP86	40.3	41.2	42.8
M06	14.9	19.8	17.9
PBE	44.0	46.5	46.2
PBE0	10.2	13.4	11.9
B3LYP	13.6	12.8	12.5
HSE06	10.9	13.1	11.9
τ-HCTH	8.3	8.8	8.4
ωB97X	12.6	18.0	15.7
ωB97X-D	11.6	15.3	13.4

Figures

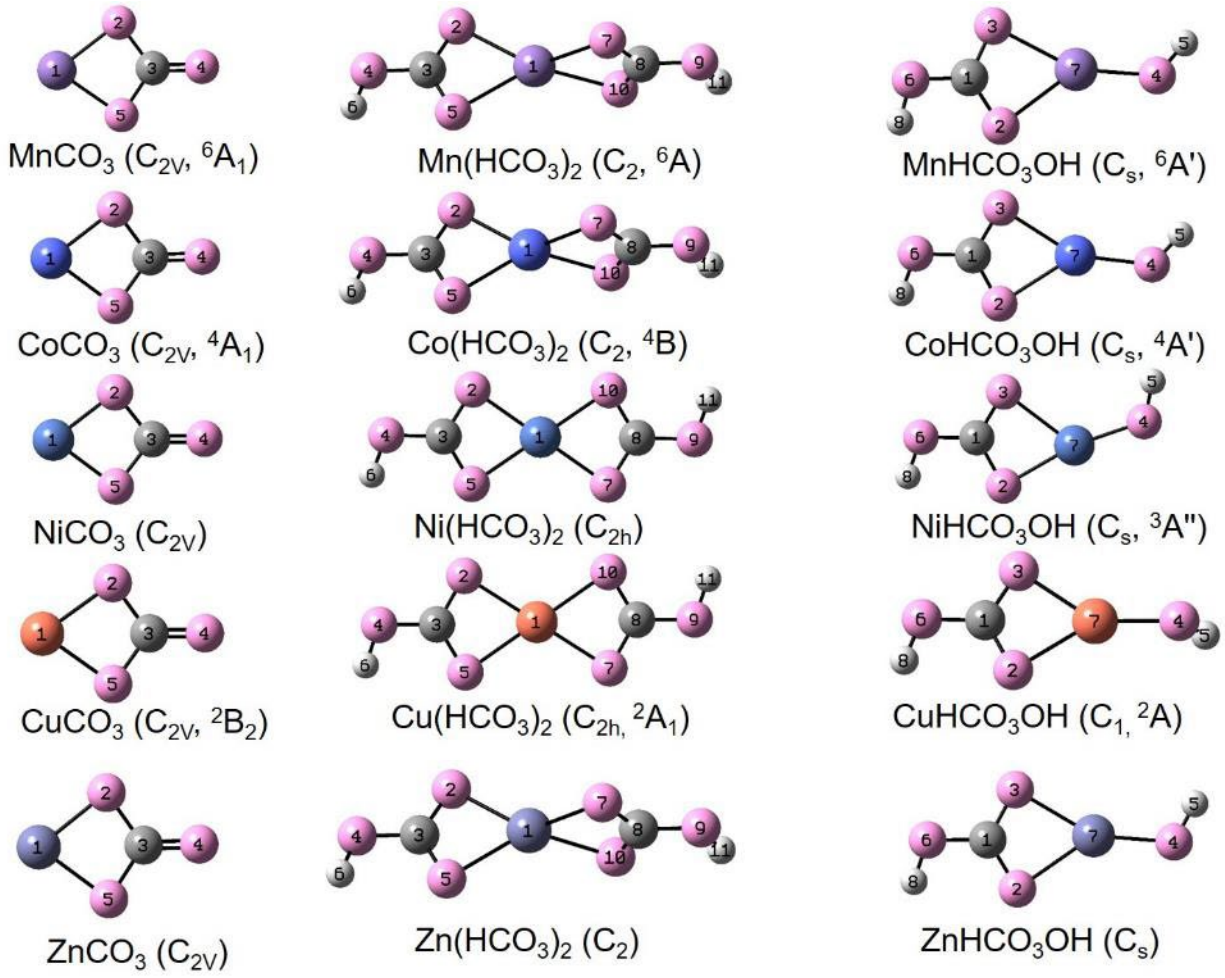

Figure 3.1. Geometries, symmetry and spin states for MCO_3, $M(HCO_3)_2$ and $MHCO_3OH$ (M = Mn, Co, Ni, Cu and Zn) (O = pink, H = white, C = gray, Mn = purple, Co = blue, Ni = light blue, Cu = orange, Zn = light purple).

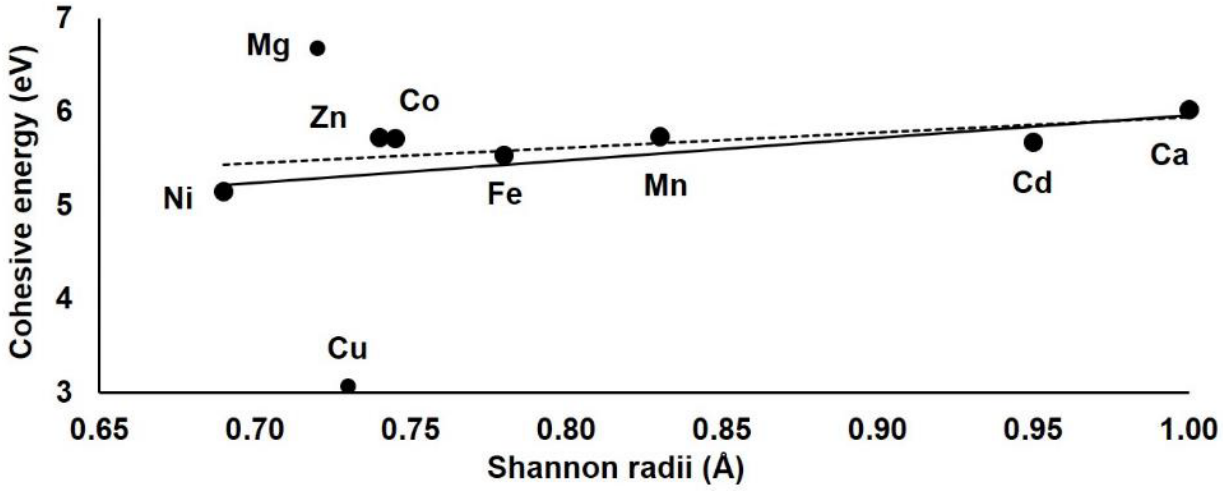

Figure 3.2. Cohesive energy of MCO_3 at 0K vs. Shannon radii of the metal cations. The linear fit equation for all the metals (solid line) is $y = 2.41x + 3.56$ ($R^2 = 0.07$). The linear fit equation for metals not including Mg and Cu (square dot line) is $y = 1.63x + 4.32$ ($R^2 = 0.50$).

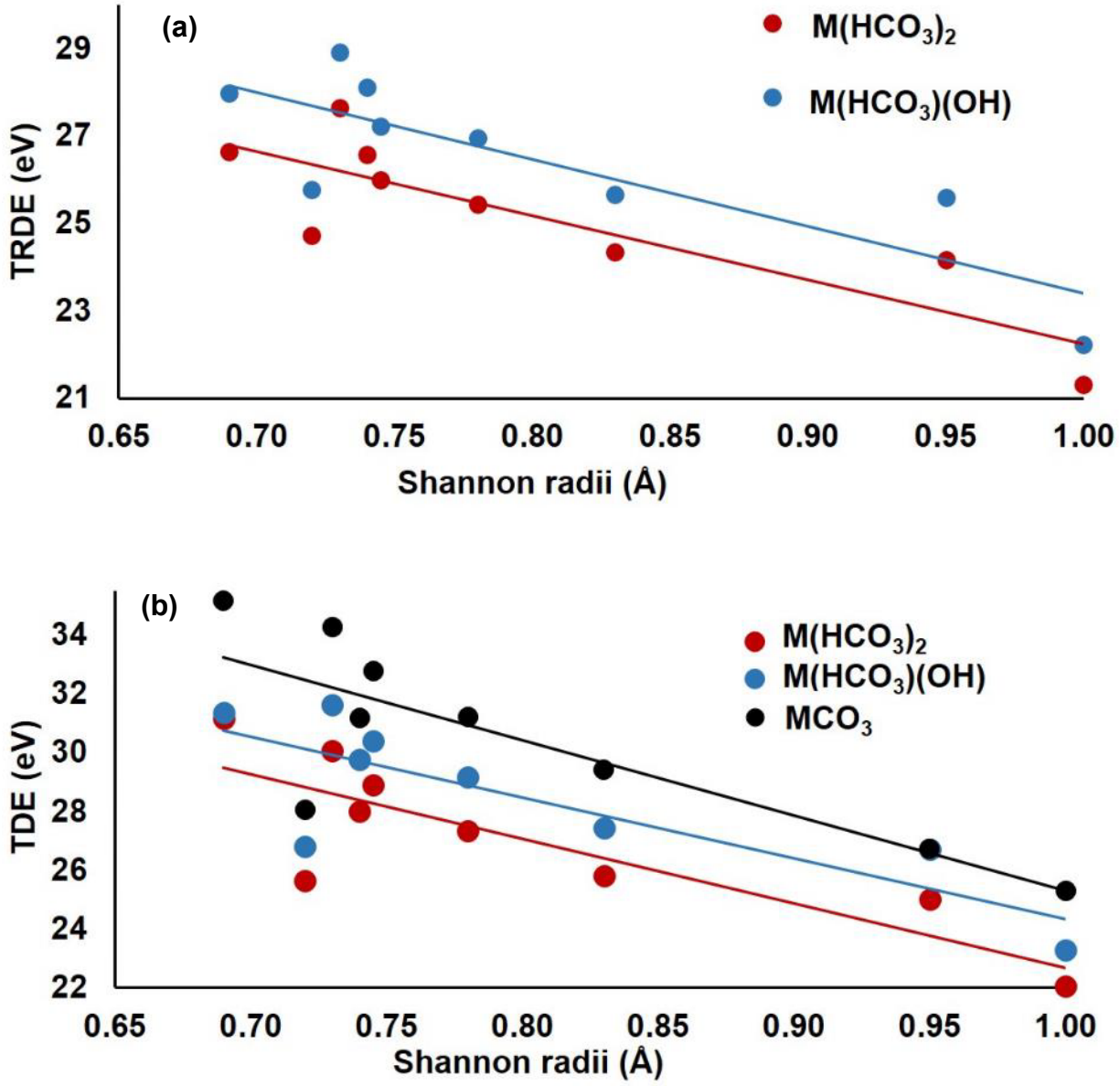

Figure 3.3.(a) TRDE of $M(HCO_3)_2$ and $M(HCO_3)(OH)$ at 0K vs. Shannon radii of metal cations. The linear fit equations for $M(HCO_3)_2$ and $M(HCO_3)(OH)$ are $y = -14.71x + 36.95$ ($R^2 = 0.73$) and $y = -15.32x + 38.72$ ($R^2 = 0.72$), respectively. **(b)** TDE of MCO_3, $M(HCO_3)_2$ and $M(HCO_3)(OH)$ at 0K vs. Shannon radii of metal cations. The linear fit equations for MCO_3, $M(HCO_3)_2$ and $M(HCO_3)(OH)$ are $y = -25.61x + 50.40$ ($R^2 = 0.68$), $y = -21.97x + 44.14$ ($R^2 = 0.72$), and $y = -20.66x + 44.50$ ($R^2 = 0.69$), respectively.

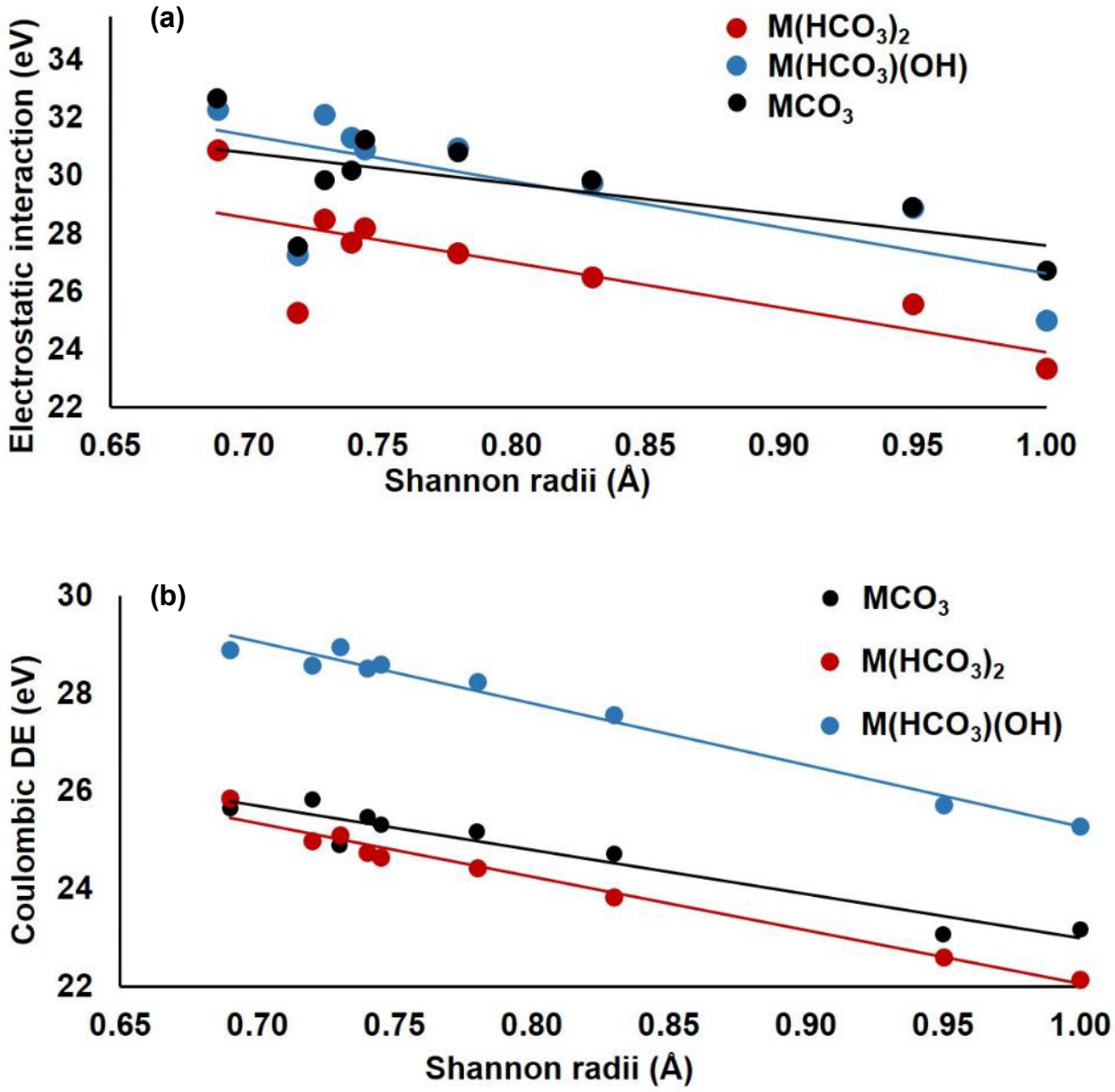

Figure 3.4. (a) Coulombic dissociation energy of MCO_3, $M(HCO_3)_2$ and $M(HCO_3)(OH)$ at 0K vs. Shannon radii of metal cations. The linear fit equations for MCO_3, $M(HCO_3)_2$ and $M(HCO_3)(OH)$ are $y = -9.03x + 32.02$ ($R^2 = 0.92$), $y = -10.98x + 33.03$ ($R^2 = 0.98$), and $y = -12.60x + 37.88$ ($R^2 = 0.98$), respectively. **(b)** Electrostatic interaction of MCO_3, $M(HCO_3)_2$ and $M(HCO_3)(OH)$ at 0K vs. Shannon radii of metal cations. The linear fit equations for MCO_3, $M(HCO_3)_2$ and $M(HCO_3)(OH)$ are $y = -10.80x + 37.88$ ($R^2 = 0.41$), $y = -15.66x + 39.04$ ($R^2 = 0.60$), and $y = -16.03x + 42.14$ ($R^2 = 0.52$), respectively.

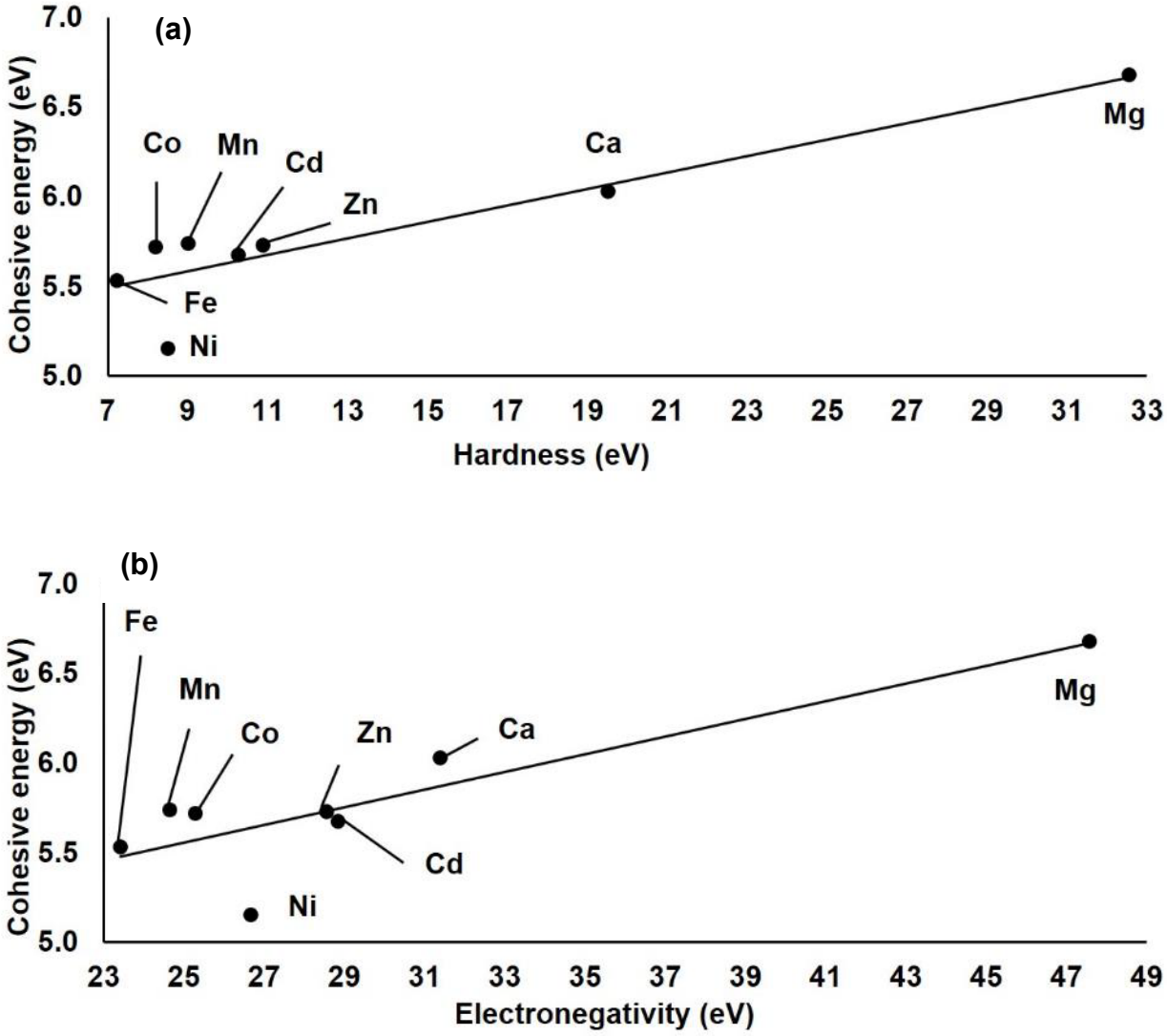

Figure 3.5. Cohesive energy of MCO_3 at 0K vs. hardness and electronegativity of metal cations, not including Cu. (a) The linear fit equation for hardness is $y = 0.05x + 5.17$ ($R^2 = 0.83$). (b) The linear fit equation for electronegativity is $y = 0.05x + 4.33$ ($R^2 = 0.75$).

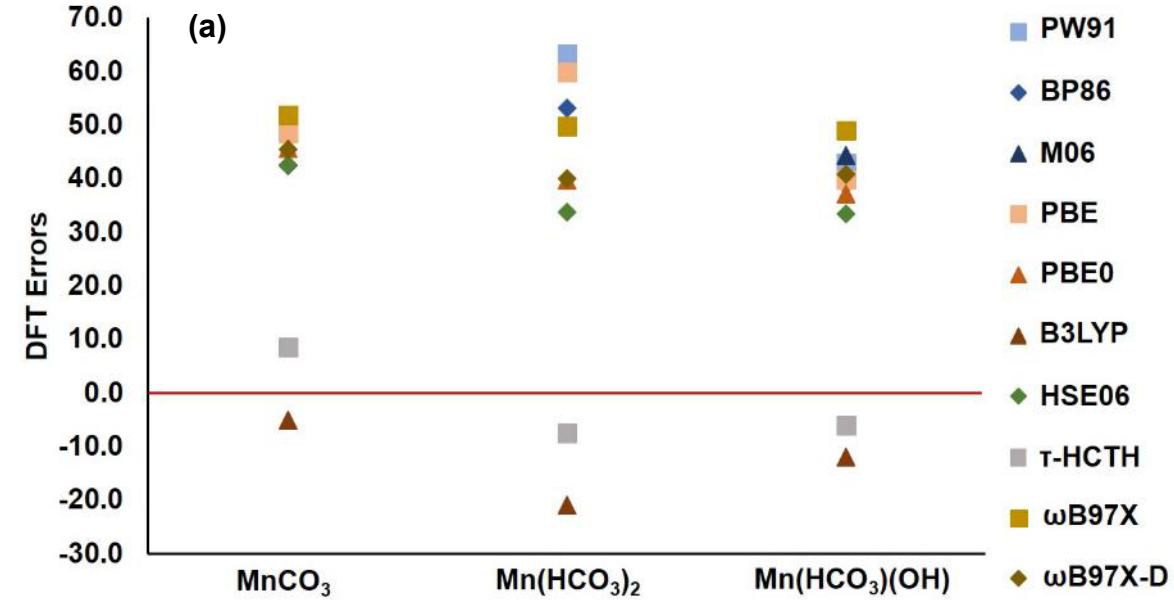
(a)
DFT Errors
70.0
60.0
50.0
40.0
30.0
20.0
10.0
0.0
-10.0
-20.0
-30.0
MnCO3
Mn(HCO3)2
Mn(HCO3)(OH)
PW91
BP86
M06
PBE
PBE0
B3LYP
HSE06
τ-HCTH
ωB97X
ωB97X-D

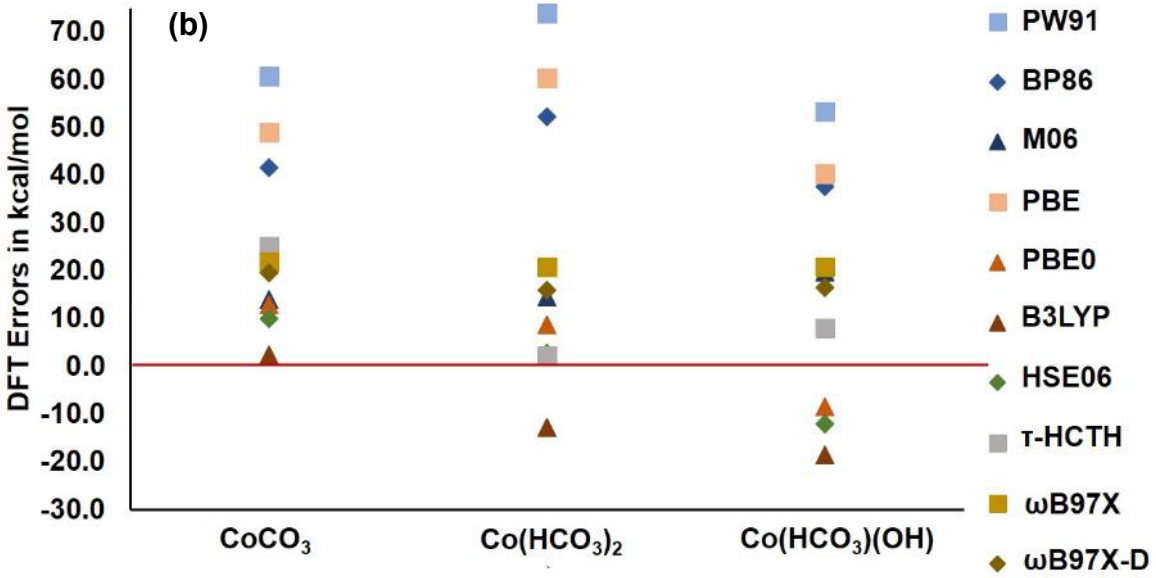
(b)
DFT Errors in kcal/mol
70.0
60.0
50.0
40.0
30.0
20.0
10.0
0.0
-10.0
-20.0
-30.0
CoCO3
Co(HCO3)2
Co(HCO3)(OH)
PW91
BP86
M06
PBE
PBE0
B3LYP
HSE06
τ-HCTH
ωB97X
ωB97X-D

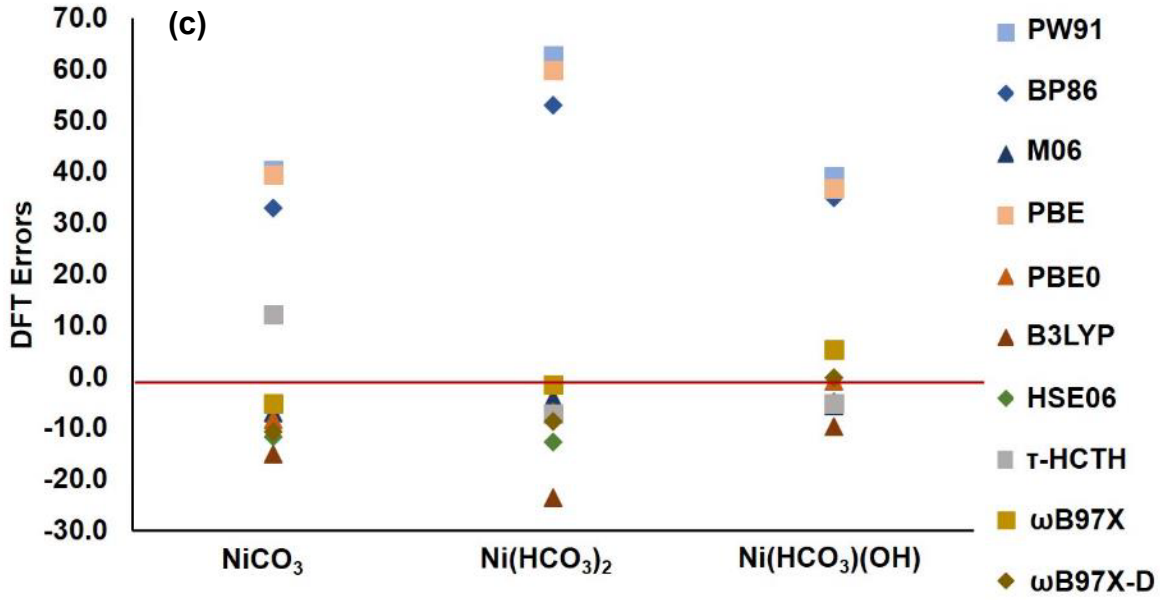
(c)
70.0
60.0
50.0
40.0
30.0
20.0
10.0
0.0
-10.0
-20.0
-30.0
DFT Errors
NiCO3
Ni(HCO3)2
Ni(HCO3)(OH)
PW91
BP86
M06
PBE
PBE0
B3LYP
HSE06
τ-HCTH
ωB97X
ωB97X-D

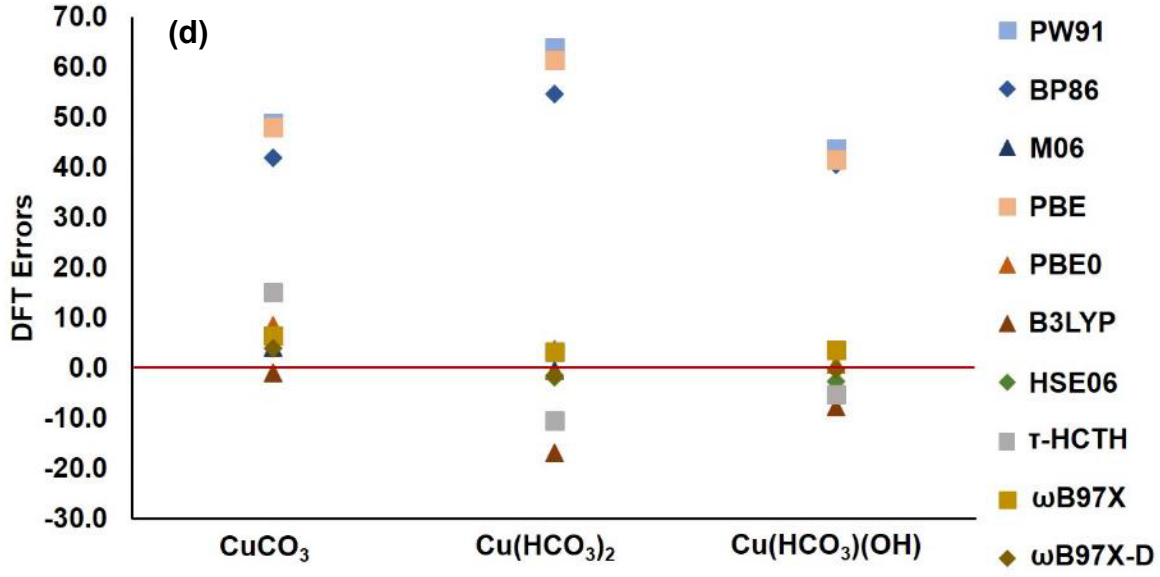
(d)
70.0
60.0
50.0
40.0
30.0
20.0
10.0
0.0
-10.0
-20.0
-30.0
DFT Errors
CuCO3
Cu(HCO3)2
Cu(HCO3)(OH)
PW91
BP86
M06
PBE
PBE0
B3LYP
HSE06
τ-HCTH
ωB97X
ωB97X-D

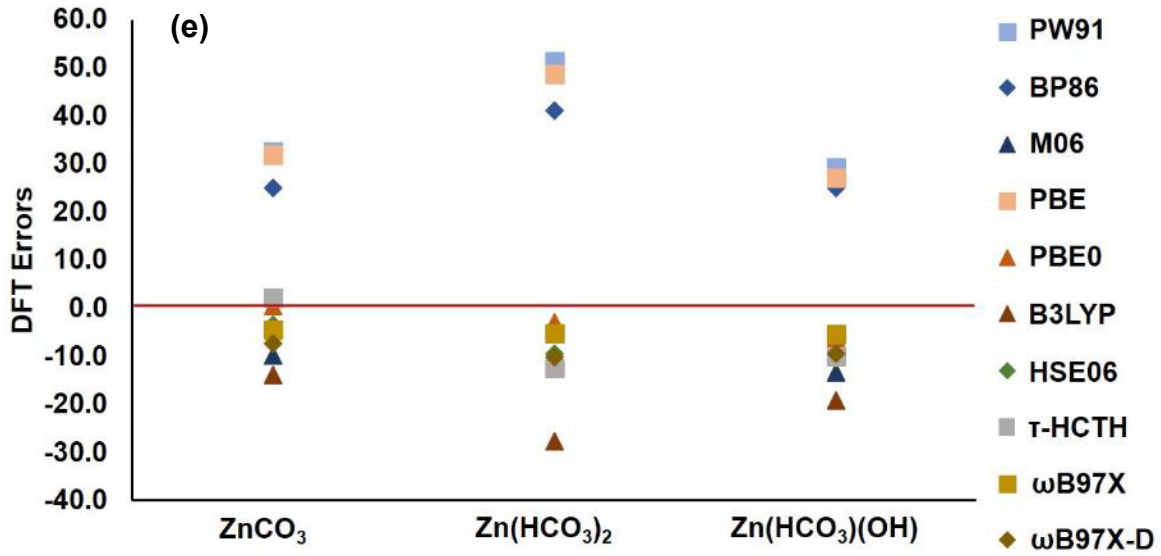

Figure 3.6. $\Delta H_{f,0K}$ in kcal/mol distributions of DFT errors compared to the FPD results for (a) Mn, (b) Co, (c) Ni, (d) Cu, and (e) Zn.

References

[1] Lackner, K. S.; Wendt, C. H.; Butt, D. P.; Joyce, E. L.; Sharp, D. H. Carbon Dioxide Disposal in Carbonate Minerals. *Energy* **1995***, 20,* 1153–1170.

[2] De Yoreo, J. J.; Waychunas, G. A.; Jun, Y.-S.; Fernandez-Martinez, A. *In situ* Investigations of Carbonate Nucleation on Mineral and Organic Surfaces. *Rev. Mineralogy Geochem.* **2013***, 77,* 229–257.

[3] Rysgaard, S.; Sogaard, D. H.; Cooper, M.; Pucko, M.; Lennert, K.; Papakyriakou, T. N.; Wang, F.; Geilfus, N. X.; Glud, R. N.; Ehn, J.; McGinnis, D. F.; Attard, K.; Sievers, J.; Deming, J. W.; Barber, D. Ikaite Crystal Distribution in Winter Sea Ice and Implications for CO_2 System Dynamics. *Cryosphere* **2013**, *7*, 707−718

[4] Matter, J. M.; Kelemen, P. B. Permanent Storage of Carbon Dioxide in Geological Reservoirs by Mineral Carbonation. *Nat. Geosci.* **2009**, *2*, 837−841.

[5] Mann, S. *Biomineralization: Principles and Concepts in Bioinorganic Materials Chemistry*. Oxford University Press: New York, NY, USA, 2002.

[6] Lowenstam, H. A.; Weiner, S. *On Biomineralization*; Oxford University Press: New York, NY, USA, 1989.

[7] Radha, A. V; Forbes, T. Z.; Killian, C. E.; Gilbert, P. U. P. A.; Navrotsky, A. Transformation and Crystallization Energetics of Synthetic and Biogenic Amorphous Calcium Carbonate. *Proc. Nat. Acad. Sci. USA* **2010**, *107*, 16438-16443.

[8] Beniash, E.; Metzler, R. A.; Lam, R. S. K.; Gilbert, P. U. P. A. Transient Amorphous Calcium Phosphate in Forming Enamel. *J. Struct. Biol.* **2009**, *166*, 133–143.

[9] Fukushi, K.; Munemoto, T.; Sakai, M.; Yagi, S. Monohydrocalcite: A Promising Remediation Material for Hazardous Anions. *Sci. Technol. Adv. Mater.* **2011**, *12*, 5318−5327.

[10] Nurnberg, D.; Bijma, J.; Hemleben, C. Assessing the Reliability of Magnesium in Foraminiferal Calcite as a Proxy for Water Mass Temperatures. *Geochim. Cosmochim. Acta*, **1996**, *60*, 803−814.

[11] Riechelmann, S.; Buhl, D.; Schroder-Ritzrau, A.; Riechelmann, D. F. C.; Richter, D. K.; Vonhof, H. B.; Wassenburg, J. A.; Geske, A.; Spotl, C.; Immenhauser, A. The Magnesium Isotope Record of Cave Carbonate Archives. *Clim. Past*, **2012**, *8*, 1849−1867.

[12] Russell, A. D.; Honisch, B.; Spero, H. J.; Lea, D. W. Effects of Seawater Carbonate Ion Concentration and Temperature on Shell U, Mg, and Sr in Cultured Planktonic Foraminifera. *Geochim. Cosmochim. Acta* **2004**, *68*, 4347−4361.

[13] Morse, J. W.; Mackenzie, F. T. *Geochemistry of Sedimentary Carbonates*. Elsevier: New York, 1990; Vol. 48, p 706.

[14] Swainson, I. P.; Hammond, R. P. Ikaite, $CaCO_3 \cdot 6H_2O$: Cold Comfort for Glendonites as Paleothermometers. *Am. Mineral.* **2001**, *86*, 1530−1533.

[15] De Lurio, J. L.; Frakes, L. A. Glendonites as a Paleoenvironmental Tool: Implications for Early Cretaceous High Latitude Climates in Australia. *Geochim. Cosmochim. Acta* **1999**, *63*, 1039−1048.

[16] Emsley, J. *The Elements, 2nd Ed.*, Oxford, Oxford, 1994.

[17] Dixon, D. A.; Feller, D.; Peterson, K. A. A Practical Guide to Reliable First Principles Computational Thermochemistry Predictions Across the Periodic Table. In *Annual Reports in Computational Chemistry*, Wheeler, R. A., Ed.; Elsevier, Amsterdam: **2012**; Vol. 8, pp 1-28.

[18] Peterson, K. A.; Feller, D.; Dixon, D. A. Chemical Accuracy in Ab Initio Thermochemistry and Spectroscopy: Current Strategies and Future Challenges. *Theor. Chem. Acc.* **2012**, *131*, 1-20.

[19] Feller, D.; Peterson, K. A.; Dixon, D. A. Further Benchmarks of a Composite, Convergent, Statistically Calibrated Coupled Cluster Based Approach for Thermochemical and Spectroscopic Studies. *Mol. Phys.* **2012**, *110*, 2381-2399.

[20] Feller, D.; Peterson, K. A.; Dixon, D. A. The Impact of Larger Basis Sets and Explicitly Correlated Coupled Cluster Theory on the Feller-Peterson-Dixon Composite Method. In *Annual Reports in Computational Chemistry*, Vol. 12, Dixon, D. A., Ed., Elsevier, Amsterdam, **2016**, pp. 47-78.

[21] Hu, Y.; Vasiliu, M.; Thanthiriwatte, K. S.; Jackson, V. E.; Chaka, A. M.; Dixon, D. A. Thermodynamics of Metal Carbonates and Bicarbonates and Their Hydrates for Mg, Ca, Fe, and Cd Relevant to Mineral Energetics. *J. Phys. Chem. A* **2020**, *124*, 1829−1840.

[22] Perdew, J. P.; Burke, K.; Ernzerhof, M. Generalized Gradient Approximation Made Simple. *Phys. Rev. Lett.* **1996**, *77*, 3865–3868.

[23]Chen, C.; Dixon, D. A. Structure and Stability of Hydrolysis Reaction Products of MgO Nanoparticles Leading to the Formation of Brucite. *J. Phys. Chem. C* **2017**, *121*, 21750-21762.

[24] Chen, M.; Jackson, V. E.; Felmy, A. R.; Dixon, D. A. Structures and Energetics of $(MgCO_3)_n$ Clusters, $n \leq 16$. *J. Phys. Chem. A* **2015**, *119*, 3419–3428.

[25] Chen, M.; McNeill, A. S.; Hu, Y.; Dixon, D. A. Elucidation of Bottom-Up Growth of $CaCO_3$ Involving Prenucleation Clusters from Structure Predictions and Decomposition of Globally Optimized $(CaCO_3)_n$ Nanoclusters. *ACS Nano*, **2020**, *14*, 4, 4153-4165.

[26] Becke, A. D. Density-Functional Thermochemistry. III. The Role of Exact Exchange. *J. Chem. Phys.* **1993**, *98*, 5648−5652.

[27] Lee, C.; Yang, W.; Parr, R. G. Accurate and Simple Analytic Representation of the Electron-Gas Correlation Energy. *Phys. Rev. B: Condens. Matter Mater. Phys.* **1988**, *37*, 785−789.

[28] Stephens, P. J.; Devlin, F. J.; Frisch, M. J.; Chabalowski, C. F. Ab initio Calculation of Vibrational Absorption and Circular Dichroism Spectra Using Density Functional Force Fields *J. Phys. Chem.*, **1994,** *98*, 11623-11627.

[29] Dunning, T. H., Jr. Gaussian Basis Sets for Use in Correlated Molecular Calculations. I. The Atoms Boron Through Neon and Hydrogen. *J. Chem. Phys.* **1989**, *90*, 1007−1023.

[30] Kendall, R. A.; Dunning, T. H., Jr.; Harrison, R. J. Electron Affinities of the First Row Atoms Revisited. Systematic Basis Sets and Wave Functions. *J. Chem. Phys.* **1992**, *96*, 6796−6806.

[31] Peterson, K. A. Gaussian Basis Sets for Quantum Mechanical (QM) Calculations. In Computational Inorganic and Bioinorganic Chemistry; Solomon, E. I., Scott, R. A., King, R. B., Eds.; John Wiley and Sons: Chicester, UK, 2009; pp 187−200.

[32] Dolg, M. Improved Relativistic Energy-consistent Pseudopotentials for 3d-trantision metals. *Theor. Chem. Acc.* **2005**, *114*, 297–304.

[33] Peterson, K. A.; Puzzarini, C. Systematically Convergent Basis Sets for Transitional metals. II. Pseudopotential-Based Correlation Consistent Basis Sets for Group 11 (Cu, Ag, Au) and 12 (Zn, Cd, Hg) elements. *Theor. Chem. Acc.* **2005**, *114*, 283−296.

[34] Perdew, J. P.; Wang, Y. Accurate and Simple Analytic Representation of the Electron Gas Correlation Energy. *Phys. Rev. B*, **1992**, *45*. 13244-13249.

[35] Burke, K.; Perdew, J. P.; Wang, Y. In Electronic Density Functional Theory: Recent Progress and New Directions. Dobson, J. F.; Vignale, G.; Das. M. P. eds. (Plenum, **1998**).

[36] Becke, A. D. Density-Functional Exchange-Energy Approximation with Correct Asymptotic Behavior. *Phys. Rev. A* **1988***, 38,* 3098-*3100*.

[37] Perdew, J. P. *Density-Functional Approximation for the Correlation Energy of the Inhomogeneous Electron Gas. Phys. Rev. B*, **1986**, *33*, 8822-8824.

[38] Zhao, Y.; Truhlar, D. G. The M06 suite of Density Functionals for Main Group Thermochemistry, Thermochemical Kinetics, Noncovalent Interactions, Excited States, and Transition Elements: Two New Functionals and Systematic Testing of Four M06-class Functionals and 12 Other Functionals. *Theor. Chem. Acc.* **2008**, *120*, 215-41.

[39] Perdew, J. P.; Burke, K.; Ernzerhof, M. Erratum 'Generalized Gradient Approximation Made Simple'. *Phys. Rev. Lett.* **1997**, *78*, 1396.

[40] Adamo, C.; Barone, V. Toward Reliable Density Functional Methods Without Adjustable Parameters: The PBE0 Model. *J. Chem. Phys.* **1999**, *110*, 6158-6169.

[41] A. V. Krukau , O. A. Vydrov, A. F. Izmaylov, and G. E. Scuseria, Influence of the Exchange Screening Parameter on the Performance of Screened Hybrid Functionals. *J. Chem. Phys.* **2006**, *125*, 224106.

[42] Boese, A. D.; Handy, N. C. New Exchange-Correlation Density Functionals: The Role of the Kinetic-Energy Density. *J. Chem. Phys.* **2002,** *116*, 9559-9969.

[43] Chai, J.-D.; Head-Gordon, M. Systematic Optimization of Long-Range Corrected Hybrid Density Functionals. *J. Chem. Phys.* **2008**, *128*, 084106.

[44] Grimme S. Semiempirical GGA-Type Density Functional Constructed with a Long-Range Dispersion Correction. *J. Comput. Chem.* **2006**, *27*, 1787-1799.

[45] Chai, J. D.; Head-Gordon, M. Long-Range Corrected Hybrid Density Functionals with Damped Atom-Atom Dispersion Corrections. *Phys. Chem. Chem. Phys.* **2008**, *10*, 6615-6620.

[46] Frisch, M. J.; Trucks, G. W.; Schlegel, H. B.; Scuseria, G. E.; Robb, M. A.; Cheeseman, J. R.; Scalmani, G.; Barone, V.; Petersson, G. A.; Nakatsuji, H.; Li, X.; Caricato, M.; Marenich, A. V.; Bloino, J.; Janesko, B. G.; Gomperts, R.; Mennucci, B.; Hratchian, H. P.; Ortiz, J. V.; Izmaylov, A. F.; Sonnenberg, J. L.; Williams-Young, D.; Ding, F.; Lipparini, F.; Egidi, F.; Goings, J.; Peng, B.; Petrone, A.; Henderson, T.; Ranasinghe, D.; Zakrzewski, V. G.; Gao, J.; Rega, N.; Zheng, G.; Liang, W.; Hada, M.; Ehara, M.; Toyota, K.; Fukuda, R.; Hasegawa, J.; Ishida, M.; Nakajima, T.; Honda, Y.; Kitao, O.; Nakai, H.; Vreven, T.; Throssell, K.; Montgomery, J. A., Jr.; Peralta, J. E.; Ogliaro, F.; Bearpark, M. J.; Heyd, J. J.; Brothers, E. N.; Kudin, K. N.; Staroverov, V. N.; Keith, T. A.; Kobayashi, R.; Normand, J.; Raghavachari, K.; Rendell, A. P.; Burant, J. C.; Iyengar, S. S.; Tomasi, J.; Cossi, M.; Millam, J. M.; Klene, M.; Adamo, C.; Cammi, R.; Ochterski, J. W.; Martin, R. L.; Morokuma, K.; Farkas, O.; Foresman, J. B.; Fox, D. J. Gaussian 16, Revision A.03, Gaussian, Inc., Wallingford CT, 2016.

[47] Purvis, G. D., III; Bartlett, R. J. A Full Coupled Cluster Singles and Doubles Model: The Inclusion of Disconnected Triples. *J. Chem. Phys.* **1982**, *76*, 1910−1918.

[48] Raghavachari, K.; Trucks, G. W.; Pople, J. A.; Head-Gordon, M. A Fifth-Order Perturbation Comparison of Electron Correlation Theories. *Chem. Phys. Lett.* **1989**, *157*, 479−483.

[49] Watts, J. D.; Gauss, J.; Bartlett, R. J. Coupled-Cluster Methods with Noniterative Triple Excitations for Restricted Open Shell Hartree-Fock and Other General Single Determinant Reference Functions. Energies and Analytical Gradients. *J. Chem. Phys.* **1993**, *98*, 8718−8733.

[50] Bartlett, R. J.; Musiał, M. Coupled Cluster Theory in Quantum Chemistry. *Rev. Mod. Phys.* **2007**, *79*, 291−352.

[51] Knowles, P. J.; Hampel, C.; Werner, H. J. Coupled Cluster Theory for High Spin, Open Shell Reference Wave Functions. *J. Chem. Phys.* **1993**, *99*, 5219−5227.

[52] Knowles, P. J.; Hampel, C.; Werner, H.-J. Erratum: Coupled Cluster Theory for High Spin, Open Shell Reference Wave Functions. *J. Chem. Phys.* **2000**, *112*, 3106−3107.

[53] Deegan, M. J. O.; Knowles, P. J. Perturbative Corrections to Account for Triple Excitations in Closed and Open Shell Coupled Cluster Theories. *Chem. Phys. Lett.* **1994**, *227*, 321−326.

[54] Werner, H-J.; Knowles, P. J.; Manby, F. R.; Black, J. A.; Doll, K.; Heßelmann, A.; Kats, D.; Köhn, A.; Korona, T.; Kreplin, D. A.; Ma, Q.; Miller III, T. F.; Mitrushchenkov, A.; Peterson, K. A.; Polyak, I.; Rauhut, G.; Sibaev, M. The Molpro Quantum Chemistry Package *J. Chem. Phys.* **2020**, *152*, 144107.

[55] Werner, H.-J.; Knowles, P. J.; Knizia, G.; Manby, F. R.; Schütz, M.; Celani, P.; Györffy, W.; Kats, D.; Korona, T.; Lindh, R.; Mitrushenkov, A.; Rauhut, G.; Shamasundar, K. R.; Adler, T. B.; Amos, R. D.; Bennie, S. J.; Bernhardsson, A.; Berning, A.; Cooper, D. L.; Deegan, M. J. O.; Dobbyn, A. J.; Eckert, F.; Goll, E.; Hampel, C.; Hesselmann, A.; Hetzer, G.; Hrenar, T.; Jansen, G.; Köppl, C.; Lee, S. J. R.; Liu, Y.; Lloyd, A. W.; Ma, Q.; Mata, R. A.; May, A. J.; McNicholas, S. J.; Meyer, W.; Miller III, T. F.; Mura, M. E.; Nicklass, A.; O'Neill, D. P.; Palmieri, P.; Peng, D.; Petrenko, T.; Pflüger, K.; Pitzer, R.; Reiher, M.; Shiozaki, T.; Stoll, H.; Stone, A. J.; Tarroni, R.; Thorsteinsson, T.; Wang, M.; Welborn, M. MOLPRO, version 2018.2, a package of *ab initio* programs, See http://www.molpro.net. Accessed August 1, 2021.

[56] Werner, H.-J.; Knowles, P. J.; Knizia, G.; Manby, F. R.; Schütz, M. Molpro: A General-Purpose Quantum Chemistry Program Package. *Wiley Interdiscip. Rev.: Comput. Mol. Sci.* **2012**, *2*, 242−253.

[57] Feller, D.; Peterson, K. A.; Hill, J. G. On the effectiveness of CCSD(T) complete basis set extrapolations for atomization energies. *J. Chem. Phys.* **2011**, *135*, 044102.

[58] Douglas, M.; Kroll, N. M. Quantum Electrodynamical Corrections to the Fine Structure of Helium. *Ann. Phys.* **1974**, *82*, 89−155.

[59] Hess, B. A. Applicability of the No-Pair Equation with Free- Particle Projection Operators to Atomic and Molecular Structure Calculations. *Phys. Rev. A*, **1985**, *32*, 756−763.

[60] Hess, B. A. Relativistic Electronic-Structure Calculations Employing a Two-Component No-Pair Formalism with External- Field Projection Operators. *Phys. Rev. A*, **1986**, *33*, 3742−3748.

[61] De Jong, W. A.; Harrison, R. J.; Dixon, D. A. Parallel Douglas- Kroll Energy and Gradients in NWChem: Estimating Scalar Relativistic Effects Using Douglas-Kroll Contracted Basis Sets. *J. Chem. Phys.* **2001**, *114*, 48−53.

[62] Woon, D. E.; Dunning, T. H., Jr. Gaussian Basis Sets for Use in Correlated Molecular Calculations. V. Core-Valence Basis Sets for Boron Through Neon. *J. Chem. Phys.* **1995**, *103*, 4572−4585.

[63] Peterson, K. A.; Dunning, T. H., Jr. Accurate Correlation Consistent Basis sets for Molecular core−valence Correlation Effects: The Second Row Atoms Al−Ar, and the First Row Atoms B−Ne Revisited. *J. Chem. Phys.* **2002**, *117*, 10548−10560.

[64] Moore, C. E. *Atomic Energy Levels As Derived from the Analysis of Optical Spectra. Vol. 1, H to V*. U.S. National Bureau of Standards Circular 467, COM-72-50282; U.S. Department of Commerce, National Technical Information Service: Washington, DC, 1949.

[65] Ruscic, B.; Active Thermochemical Tables, Argonne National Laboratory, Argonne, IL. https://atct.anl.gov/Thermochemical%20Data/version%201.122g/index.php (accessed January 18, 2019).

[66] Ruscic, B.; Pinzon, R. E.; Morton, M. L.; von Laszevski, G.; Bittner, S. J.; Nijsure, S. G.; Amin, K. A.; Minkoff, M.; Wagner, A. F. Introduction to Active Thermochemical Tables: Several "Key" Enthalpies of Formation Revisited. *J. Phys. Chem. A* **2004**, *108*, 9979−9997.

[67] Changala, P. B.; Nguyen, T. L.; Baraban, J. H.; Ellison, G. B.; Stanton, J. F.; Bross, D. H.; Ruscic, B. Active Thermochemical Tables: The Adiabatic Ionization Energy of Hydrogen Peroxide. *J. Phys. Chem. A* **2017**, *121*, 8799−8806.

[68] Chase, M. W., Jr. *NIST-JANAF Thermochemical Tables*, 4th ed. *J. Phys. Chem. Ref. Data.*, *Mono. 9*; American Institute of Physics: Woodbury, NY, 1998, Suppl. 1.

[69] Wagman, D. D.; Evans, W. H.; Parker, V. B.; Schumm, R. H.; Halow, I.; Bailey, S. M.; Churney, K. L.; Nuttall, R. L. The NBS Tables of Chemical Thermodynamic Properties. Selected Values for Inorganic and C1 and C2 Organic Substances in SI Units. *J. Phys. Chem. Ref. Data*, **1982**, *11*, Suppl. 2.

[70] Cox, J. D., Wagman, D. D., and Medvedev, V. A., *CODATA Key Values for Thermodynamics*, Hemisphere Publishing Corp., New York, 1989.

[71] Yungman, V. S.; Glushko, V. P.; Medvedev, V. A.; Gurvich, L. V., Eds., *Thermal Constants of Substances*, 8 Vols., Wiley: New York, 1999.

[72] Curtiss, L. A.; Raghavachari, K.; Redfern, P. C.; Pople, J. A. Assessment of Gaussian-2 and Density Functional Theories for the Computation of Enthalpies of Formation. *J. Chem. Phys.* **1997**, *106*, 1063−1079.

[73] Reed, A. E.; Curtiss, L. A.; Weinhold, F. Intermolecular Interactions from a Natural Bond Orbital, Donor-Acceptor Viewpoint. *Chem. Rev.* **1988**, *88*, 899-926.

[74] Weinhold, F.; Landis, C. R. *Valency and Bonding: A Natural Bond Orbital Donor-Acceptor Perspective*, University Press: Cambridge, U.K., 2005

[75] Glendening, E. D.; Badenhoop, J. K.; Reed, A. E.; Carpenter, J. E.; Bohmann, J. A; Morales, C. M.; Karafiloglou; P.; Landis, C. R.; Weinhold, F. Natural Bond Order 7.0, Theoretical Chemistry Institute, University of Wisconsin, Madison, WI, 2018.

[76] Glendening, E. D.; Landis, C. R.; Weinhold, F. NBO 7.0: New Vistas in Localized and Delocalized Chemical Bonding Theory. *J. Comput. Chem.* **2019**, *40*, 2234-2241.

[77] te Velde, G.; Bickelhaupt, F. M.; Baerends, E. J.; Fonseca Guerra, C.; van Gisbergen, S. J. A.; Snijders, J. G.; Ziegler, T. Chemistry with ADF. *J. Comput. Chem.* **2001**, *22*, 931-967.

[78] Fonseca Guerra, C.; Snijders, J.; te Velde, G.; Baerends, E. J. Towards an order-N DFT method. *Theor Chem Acc* **1998**, *99*, 391–403.

[79] Baerends, E. J.; Ziegler, T.; Atkins, A. J.; Autschbach, J.; Baseggio, O.; Bashford, D.; Bérces, A.; Bickelhaupt, F. M.; Bo, C.; Boerrigter, P. M.; Cavallo, L.; Daul, C.; Chong, D. P.; Chulhai, D. V.; Deng, L.; Dickson, R. M.; Dieterich, J. M.; Ellis, D. E.; van Faassen, M.; Fan, L.; Fischer, T. H.; Fonseca Guerra, C.; Franchini, M.; Ghysels, A.; Giammona, A.; van Gisbergen, S. J. A.; Goez, A.; Götz, A. W.; Groeneveld, J. A.; Gritsenko, O. V.; Grüning, M.; Gusarov, S.; Harris, F. E.; van den Hoek, P.; Hu, Z.; Jacob, C. R.; Jacobsen, H.; Jensen, L.; Joubert, L.; Kaminski, J. W.; van Kessel, G.; König, C.; Kootstra, F.; Kovalenko, A.; Krykunov, M. V.; van Lenthe, E.; McCormack, D. A.; Michalak, A.; Mitoraj, M.; Morton, S. M.; Neugebauer, J.; Nicu, V. P.; Noodleman, L.; Osinga, V. P.; Patchkovskii, S.; Pavanello, M.; Peeples, C. A.; Philipsen, P. H. T.; Post, D.; Pye, C. C.; Ramanantoanina, H.; Ramos, P.; Ravenek, W.; Rodríguez, J. I.; Ros, P.; Rüger, R.; Schipper, P. R. T.; Schlüns, D.; van Schoot, H.; Schreckenbach, G.; Seldenthuis, J. S.; Seth, M.; Snijders, J. G.; Solà, M.; Stener, M.; Swart, M.; Swerhone, D.; Tognetti, V.; te Velde, G.; Vernooijs, P.; Versluis, L.; Visscher, L.; Visser, O.; Wang, F.; Wesolowski, T. A.; van Wezenbeek, E. M.; Wiesenekker, G.; Wolff, S. K.; Woo, T. K.; Yakovlev, A. L. ADF2019, SCM, Theoretical Chemistry, Vrije Universiteit, Amsterdam, The Netherlands, http://www.scm.com. Accessed September 12th, 2022.

[80] Autschbach, J. Magnitude of Finite-Nucleus-Size Effects in Relativistic Density Functional Computations of Indirect NMR Nuclear Spin–Spin Coupling Constants. *ChemPhysChem*, **2009**, *10*, 2274-2283.

[81] Van Lenthe, E.; Baerends, E.J. Optimized Slater-Type Basis Sets for the Elements 1–118. *J. Comput. Chem.* **2003**, *24*, 1142-1156.

[82] van Lenthe, E.; Ehlers, A.; Baerends, E. J. Geometry Optimizations in the Zero Order Regular Approximation for Relativistic Effects. *J. Chem. Phys.* **1999**, *110*, 8943-8953.

[83] van Lenthe, E.; Baerends, E. J.; Snijders, J. G. Relativistic Total Energy using Regular Approximations. *J. Chem. Phys.* **1994**, *101*, 9783-9792.

[84] van Lenthe, E.; Baerends, E. J.; Snijders, J. G. Relativistic Regular Two-Component Hamiltonians. *J. Chem. Phys.* **1993**, *99*, 4597-4610.

[85] Ziegler, T.; Rauk, A. CO, CS, N_2, PF_3, and $CNCH_3$ as σ Donors and π Acceptors. A Theoretical Study by the Hartree-Fock-Slater Transition-State Method. *Inorg. Chem.* **1979**, 18, 1755–1759.

[86] Ziegler, T.; Rauk, A. A Theoretical Study of the Ethylene-Metal Bond in Complexes between Cu^+, Ag^+, Au^+, Pt^0, or Pt^{2+} and Ethylene, Based on the Hartree-Fock-Slater Transition-State Method. *Inorg. Chem.* **1979**, *18*, 1558–1565.

[87] Bickelhaupt, F.M.; Baerends, E. J. In *Reviews in Computational Chemistry;* Lipkowitz, K.B., Boyd, D.B., Eds.; Wiley-VCH: New York, 2000; Vol. 15, pp 1-86.

[88] Lee, T.J.; Taylor, P.R. A Diagnostic for Determining the Quality of Single-Reference Electron Correlation Methods. *Int. J. Quantum Chem.* **1989**, *36*, 199-207.

[89] Shannon, R. D. Revised Effective Ionic Radii and Systematic Studies of Interatomic Distances in Halides and Chalcogenides. *Acta Cryst. A,* **1976**, *32*, 751-767.

[90] Alexeev, Y.; Windus, T. L.; Dixon, D. A.; Zhan, C.-G. Accurate Heats of Formation and Acidities for H_3PO_4, H_2SO_4, and H_2CO_3 from ab initio Electronic Structure Calculations. *Int. J. Quantum Chem.* **2005**, *102*, 775-784;.

[91] Alexeev, Y.; Windus, T. L.; Dixon, D. A.; Zhan, C.-G. Accurate Heats of Formation and Acidities for H_3PO_4, H_2SO_4, and H_2CO_3 from ab initio Electronic Structure Calculations. *Int. J. Quantum Chem.* erratum, **2005**, *104*, 379-380

[92] Kramida, A., Ralchenko, Yu., Reader, J., and NIST ASD Team (2019). *NIST Atomic Spectra Database* (ver. 5.7.1), [Online]. Available: https://physics.nist.gov/asd [2019, November 10]. National Institute of Standards and Technology, Gaithersburg, MD. DOI: https://doi.org/10.18434/T4W30F.

[93] Bard, A. J.; Parsons, B.; Jordon, J., Eds. *Standard Potentials in Aqueous Solutions*, Dekker: New York, 1985.

[94] Greenwood, N. N.; Earnshaw, A. *Chemistry of the Elements*. Oxford: Pergamon Press. 1984, pp. 82–87.

[95] Parr, R. G.; Pearson, R. G. Absolute Harness: Companion Parameter to Absolute Electronegativity. *J. Am. Chem. Soc*. **1983**, *105*, 7512-7516.

[96] Vasiliu, M.; Feller, D.; Gole, J. L.; Dixon, D. A. Structures and Heats of Formation of Simple Alkaline Earth Metal Compounds: Fluorides, Chlorides, Oxides, and Hydroxides for Be, Mg, and Ca. *J. Phys. Chem. A* **2010**, *114,* 9349–9358.

[97] Smoes, S.; Drowart, J. Determination of the Dissociation Energies of Gaseous Iron Monoxide and Manganese Monoxide by the Mass Spectrometric Knudsen Cell Method. *High Temp. Sci.* **1984**, *17*, 31-52.

[98] Chestakov, D. A.; Parke, D. H.; Baklanov, A. V. Iron monoxide photodissociation. *J. Chem. Phys.* **2005**, *122*, 084302.

[99] Liu, F.; Li, F-X.; Armentrout, P. B. Guided ion-beam studies of the reactions of Co_n^+ (n=2–20) with O_2: Cobalt cluster-oxide and -dioxide bond energies. *J. Chem. Phys.* **2005**, *123*, 064304.

[100] Watson, L. R.; Thiem, T. L.; Dressier, R. A.; Salter, R. H.; Murad, E. High Temperature Mass Spectrometric Studies of the Bond Energies of Gas-Phase ZnO, NiO, and CuO. *J. Phys. Chem.* **1993**, *97*, 5577-5580.

[101] Rodgers, M. T.; Walker, B.; Armentrout, P. B. Reactions of Cu^+ (^{1}S and ^{3}D) with O_2, CO, CO_2, N_2, NO, N_2O, and NO_2 studied by guided ion beam mass spectrometry. *Int. J. Mass Spectrom.* **1999**, *182/183*, 99 –120.

[102] Chen, M.; Straatsma, T. P.; Fang, Z.; Dixon, D. A. Structural and Electronic Property Study of $(ZnO)_n$, $n \leq 168$: Transition from Zinc Oxide Molecular Clusters to Ultrasmall Nanoparticles. *J. Phys. Chem. C* **2016**, *120*, 20400−20418.

[103] Chen, M.; Vasiliu, M.; Hu, S.; Dixon, D. A. Stability and Electronic Properties of Rocksalt $(CdO)_n$, $(SrO)_n$, and $(BaO)_n$ Nanoparticles. *J. Phys. Chem. C* **2018**, *122*, 25021−25034.

Appendix: Thermodynamics of the Metal Carbonates and Bicarbonates of Mn, Co, Ni, Cu, and Zn Relevant to Mineral Energetics

Update for $Fe(HCO_3)_2$ and $FeCO_3$ from Reference 21.

We found the lowest energy structure for in C_{2h} with the ^5A_g state, instead of the previous reported C_2 (^5B) structure in reference 21. Thus, we updated results related to the $Fe(HCO_3)_2$ C_{2h} (^5A_g) structure as a correction in the SI, including the gas phase heat of formation at 0 K (see Table A3.10), DFT errors benchmarking the FPD heat of formation at 0 K (see Table A3.22), hydration energies (see Table A3.23), the contributions to total atomization energy at the CCSD(T) level and the related electronic energies (see Table A3.26-A3.28), and geometries (see Table A3.36). The electronic energies calculated with the ωB97X and ωB97X-D functionals and their errors against the FPD heat of formation were corrected for $FeCO_3$ (C_{2v}, $^5A_1$) in Table A3.24.

Table A3.1. Relative electronic energies, ΔE, in kcal/mol for different spin states at the B3LYP/aT level (S^2) and the CCSD(T)/aD level, T_1 values at the CCSD(T)/aD level.

Molecules	Symmetry	State	B3LYP S^2	ΔE B3LYP/aT	ΔE CCSD(T)/aD	T_1/aD
$MnCO_3$	C_{2v}	$^6A_1$	8.75	0.0	0.0	0.030
$MnCO_3$	C_{2v}	$^4B_2$	3.77	22.2	37.1	0.019
$MnCO_3$	C_{2v}	$^2A_2$	0.75	58.5	73.9	0.022
$Mn(HCO_3)_2$	C_2	^6A	8.75	0.0	0.0	0.064
$Mn(HCO_3)_2$	C_{2h}	^4A_g	3.75	26.2	44.8	0.048
$Mn(HCO_3)_2$ 1	C_{2v}	$^2A_2$	0.75	62.6	87.1	0.035
$Mn(HCO_3)_2$ 2	C_{2h}	^2B_g	0.75	61.1	84.2	0.046
$Mn(HCO_3)(OH)$	C_s	$^6A'$	8.75	0.0	0.0	0.022
$Mn(HCO_3)(OH)$	C_1	^4A	3.75	35.9	50.8	0.028
$Mn(HCO_3)(OH)$	C_1	^2A	0.75	63.0	73.9	0.041
$CoCO_3$	C_{2v}	$^4A_1$	3.75	0.0	0.0	0.041
$CoCO_3$	C_{2v}	$^2A_2$	0.75	12.0	10.8	0.055
$CoCO_3$	C_{2v}	$^6B_2$	8.75	42.6	56.4	0.169
$Co(HCO_3)_2$	C_2	^4B	3.75	0.0	0.0	0.023
$Co(HCO_3)_2$	C_{2h}	^2B_g	0.75	14.3	18.1	0.032
$Co(HCO_3)_2$	C_2	^6A	8.76	97.0	97.8	0.041
$Co(HCO_3)(OH)$	C_s	$^4A'$	3.75	0.0	0.0	0.028
$Co(HCO_3)(OH)$	C_s	^2B	0.76	14.0	26.7	0.041
$Co(HCO_3)(OH)$	C_1	^6A	8.75	76.1	75.2	0.048
$NiCO_3$	C_{2v}	$^1A_1$	0.00	0.0	0.0	0.064
$NiCO_3$	C_{2v}	$^3B_1$	2.00	1.5	6.0[a]	0.052
$Ni(HCO_3)_2$	C_{2h}	^1A_g	0.00	0.0	0.0[b]	0.032
$Ni(HCO_3)_2$	C_2	^3B	2.00	0.3	1.4[b]	0.024
$Ni(HCO_3)(OH)$	C_s	$^3A''$	2.00	0.0	0.0	0.034
$Ni(HCO_3)(OH)$	C_1	^1A	0.00	17.6	16.0	0.047

[a] ΔE(aT) = 7.8, ΔE(aQ) = 8.4 kcal/mol.

[b] Value at the CCSD(T)/aQ level. The state ordering switches between the aD and aT basis sets at the CCSD(T) level. ΔE (aD) = 1.5 kcal/mol favoring the triplet. ΔE (aT) = 0.7 kcal/mol favoring the singlet.

Table A3.2. T_1 values at the CCSD(T) level.

Molecules	Symm	State	aD	aT	aQ	aT-DK	awT (core)	awT (valence)
$MnCO_3$	C_{2v}	$^6A_1$	0.030	0.028	0.028	0.028	0.025	0.028
$Mn(HCO_3)_2$	C_2	^6A	0.019	0.018	0.018	0.018	0.016	0.016
$Mn(HCO_3)(OH)$	C_s	$^6A'$	0.022	0.020	0.020	0.020	0.018	0.020
$Fe(HCO_3)_2$	C_{2h}	^5A_g	0.025	0.023	0.022		0.020	0.023
$CoCO_3$	C_{2v}	$^4A_1$	0.041	0.040	0.039	0.040	0.034	0.040
$Co(HCO_3)_2$	C_2	^4B	0.023	0.022	0.021	0.022	0.019	0.019
$Co(HCO_3)(OH)$	C_s	$^4A'$	0.028	0.027	0.026	0.027	0.023	0.023
$NiCO_3$	C_{2v}	$^3B_1$	0.052	0.050	0.050	0.050	0.042	0.050
$Ni(HCO_3)_2$	C_2	^3B	0.024	0.023	0.023	0.023	0.020	0.020
$Ni(HCO_3)(OH)$	C_s	$^3A''$	0.034	0.033	0.032	0.033	0.028	0.033
$NiCO_3$	C_{2v}	$^1A_1$	0.064	0.061	0.060	0.062	0.050	0.061
$Ni(HCO_3)_2$	C_{2h}	^1A_g	0.032	0.031	0.030	0.031	0.026	0.030
$CuCO_3$	C_{2v}	$^2B_2$	0.079	0.075	0.075	0.075	0.062	0.075
$Cu(HCO_3)_2$	C_{2h}	^2A_g	0.028	0.026	0.026	0.026	0.022	0.026
$Cu(HCO_3)(OH)$	C_1	^2A	0.035	0.034	0.033	0.034	0.028	0.033
$ZnCO_3$	C_{2v}	$^1A_1$	0.026	0.024	0.023	0.024	0.020	0.024
$Zn(HCO_3)_2$	C_2	^1A	0.018	0.017	0.017	0.017	0.015	0.017
$Zn(HCO_3)(OH)$	C_s	$^1A'$	0.019	0.018	0.017	0.018	0.015	0.018
Mn	$D_{\infty h}$	$^6\Sigma^+_g$	0.020	0.022	0.023	0.023	0.020	0.023
Co	$D_{\infty h}$	$^4\Sigma^+_g$	0.021	0.023	0.023	0.023	0.019	0.023
Ni	$D_{\infty h}$	$^3\Sigma^+_g$	0.020	0.023	0.023	0.023	0.022	0.023
Cu	$D_{\infty h}$	$^2\Sigma^+_g$	0.024	0.025	0.025	0.026	0.021	0.025
Zn	$D_{\infty h}$	$^1\Sigma^+_g$	0.018	0.021	0.021	0.021	0.018	0.021
C	$D_{\infty h}$	$^3\Sigma^-_g$	0.008	0.007	0.007	0.007	0.006	0.007
O	$D_{\infty h}$	$^3\Sigma^-_g$	0.009	0.007	0.006	0.007	0.005	0.006
H	$D_{\infty h}$	$^2\Sigma^+_g$	0.000	0.000	0.000	0.000	0.000	0.000

Table A3.3. Angles for MCO_3, $M(HCO_3)_2$ and $M(HCO_3)(OH)$ for M a first row transition metal.

Metal	CO_3^{2-}		HCO_3^-				$[(HCO_3)(OH)]^{2-}$			
	<OMO	<OCO	<OMO	<OCO	<HOC	<Torsion (2,5,10,7)	<OMO	<OCO	<HOC	<HOM
Mn^{2+}	71.9°	109.5°	63.2°	121.2°	107.9°	85.2°	63.0°	121.2°	107.8°	127.5°
Fe^{2+} [a]	73.4°	108.6°	64.5°	120.4°	108.0°	0	64.6°	120.5°	107.9°	127.3°
Co^{2+}	74.0°	107.8°	65.7°	112.0°	108.1°	84.8°	64.6°	120.5°	107.9°	127.3°
Ni^{2+}	74.1°	104.0°	69.3°	117.5°	108.4°	0	66.2°	119.8°	108.3°	121.3°
Cu^{2+}	70.8°	108.2°	66.9°	119.4°	108.2°	0	67.0°	119.0°	108.4°	91.3° [b]
Zn^{2+}	74.8°	111.4°	65.9°	120.7°	108.1°	84.8°	65.7°	120.5°	108.1°	114.0°

[a] Angles for $FeCO_3$ and $Fe(HCO_3)(OH)$ are from our previous work, reference 21 in the text. [b] Dihedral angle of atom 5, 4, 7, 2.

Table A3.4. Bond lengths (Å) for MCO_3, $M(HCO_3)_2$ and $M(HCO_3)(OH)$, for M a first row transition metal.

Metal	CO_3^{2-}		HCO_3^-		$[(HCO_3)(OH)]^{2-}$	
	C − O	M − O	C − O	M − O	C − O	M − O
Mn^{2+}	1.368/1.198	1.903	1.333/1.273/1.262	2.112/2.101	1.333/1.269/1.264	2.138/2.090/1.835
Fe^{2+} [a]	1.367/1.195	1.858	1.329/1.273/1.263	2.067/2.056	1.330/1.270/1.264	2.076/2.044/1.790
Co^{2+}	1.369/1.194	1.839	1.328/1.273/1.263	2.029/2.021	1.330/1.271/1.265	2.076/2.044/1.790
Ni^{2+}	1.353/1.191	1.770	1.323/1.273/1.263	1.907/1.907	1.327/1.289/1.249	2.081/1.931/1.748
Cu^{2+}	1.341/1.202	1.874	1.327/1.272/1.263	1.988/1.979	1.326/1.272/1.262	1.981/1.975/1.758
Zn^{2+}	1.375/1.799	1.871	1.329/1.273/1.265	2.037/2.015	1.329/1.270/1.267	2.048/2.009/1.780

[a] Bond lengths for $FeCO_3$ and $Fe(HCO_3)(OH)$ are from our our previous work, reference 21 in the text.

Table A3.5. Relative electronic energy in kcal/mol as compared to the lowest energy structure for C_2 and C_{2h} $M(HCO_3)_2$ optimized at the level.

Metal	ground state	Higher energy state	B3LYP/aT	Imaginary ν (cm^{-1})	CCSD(T)/aD [a]	CCSD(T)/aT [a]
Mg	C_2, ^1A	C_{2h}, ^1A_g	3.7	67.2i	3.8	3.7
Ca	C_2, ^1A	C_{2h}, ^1A_g	2.9	57.4i	2.2	2.4
Mn	C_2, ^6A	C_{2h}, ^6A_g	4.1	71.9i	3.4	3.6
Fe	C_{2h}, ^5A_g	C_2, ^5B	1.1	a	2.5	1.9
Co	C_2, ^4B	C_{2h}, ^4A_g	3.0	56.3i	2.3	2.6
Ni	C_{2h}, ^1A_g	C_2, ^1A	44.5	b		
		C_2, ^3B	0.3	a	-1.5	0.7
		C_{2h}, ^3B_g	2.1	a	0.0	2.6
Cu	C_{2h}, ^2A_g	C_2, ^2A	16.9	b		
Zn	C_2, ^1A	C_{2h}, ^1A_g	4.5	73.1i	4.7	4.9
Cd	C_2, ^1A	C_{2h}, ^1A_g	2.6	53.5i	2.7	2.8

[a] The structures are minima. [b] The single point energy of C_2 structures were calculated by simply replacing Co atom with Ni atom in the model of C_2 $Co(HCO_3)_2$ without optimizing the geometry. Under optimization, the symmetry reverts back to C_{2h} for Ni.
[a] The cc-pwcvnz basis set were used for Ca and Mg, n = D and T.

Table A3.6. Electronic energies for higher energy states of $M(HCO_3)_2$ in Table A3.5 at the CCSD(T)/aD and aT levels.

	Higher energy state	aD	aT
Mg[a]	C_{2h}, ^1A_g	-727.638875	-728.222427
Ca[a]	C_{2h}, ^1A_g	-1204.897477	-1205.424690
Mn	C_{2h}, ^6A_g	-631.141167	-631.613151
Fe	C_2, ^5B	-650.584221	-651.070793
Co	C_{2h}, ^4A_g	-672.414878	-672.912781
Ni	C_2, ^3B	-696.756242	-697.269169
Ni	C_{2h}, ^3B_g	-696.753889	-697.266158
Zn	C_{2h}, ^1A_g	-754.179299	-754.705667
Cd	C_{2h}, ^1A_g	-694.960668	-695.493082

[a] The cc-pwcvnz basis set were used for Ca and Mg, n = D and T.

Table A3.7. T_1 values at the CCSD(T)/aD and aT levels for Table A3.6.

	Higher energy state	aD	aT
Mg[a]	C_{2h}, ^1A_g	0.016	0.015
Ca[a]	C_{2h}, ^1A_g	0.016	0.015
Mn	C_{2h}, ^6A_g	0.019	0.018
Fe	C_2, ^5B	0.021	0.020
Co	C_{2h}, ^4A_g	0.022	0.021
Ni	C_2, ^3B	0.024	0.023
Ni	C_{2h}, ^3B_g	0.024	0.023
Zn	C_{2h}, ^1A_g	0.018	0.017
Cd	C_{2h}, ^1A_g	0.019	0.018

[a] The cc-pwcvnz basis set were used for Ca and Mg, n = D and T.

Table A3.8. 3d orbital occupancy from NBO analysis.

3d orbital	Mn	Fe	Co	Ni	Cu	Zn	Cd
MCO_3							
d_{xy}	1.05	1.06	1.09	2.00	2.00	2.00	2.00
d_{xz}	1.05	1.06	1.08	1.99	2.00	2.00	2.00
d_{yz}	1.17	1.28	1.27	0.82	1.65	1.99	1.99
$d_{x^2y^2}$	1.00	1.64	1.97	1.95	1.98	1.99	1.99
d_{z^2}	1.03	1.29	1.98	1.97	1.98	2.00	1.99
$M(HCO_3)_2$							
d_{xy}	1.07	1.05	1.12	1.83	1.90	2.00	2.00
d_{xz}	1.01	1.02	2.00	2.00	2.00	2.00	2.00
d_{yz}	1.07	1.03	1.12	1.99	2.00	2.00	2.00
$d_{x^2y^2}$	1.01	1.14	1.72	0.82	1.44	1.99	1.98
d_{z^2}	1.01	1.92	1.26	1.93	1.97	2.00	1.99
$M(HCO_3)(OH)$							
d_{xy}	1.07	1.11	1.15	1.21	1.37	2.00	1.99
d_{xz}	1.01	1.01	1.02	1.66	2.00	2.00	2.00
d_{yz}	1.07	1.08	1.12	1.50	2.00	2.00	2.00
$d_{x^2y^2}$	1.02	1.16	1.91	1.97	1.96	1.97	1.97
d_{z^2}	1.00	1.87	1.95	1.94	1.96	1.98	1.98

Table A3.9 EDA in eV.

	Symm	State	Total BE	Electrostatic Interaction[a,b]	Pauli Repulsion[a]	Orbital Interactions[a]	Kinetic Energy[b]	Coulomb (Steric+OrbInt) Energy[b]	XC Energy[b]
$MgCO_3$	C_{2v}	$^1A_1$	-27.55	-27.04	4.26	-4.76	35.62	-32.13	-4.00
$Mg(HCO_3)_2$	C_2	^1A	-25.13	-24.76	4.16	-4.52	33.66	-27.92	-6.11
$Mg(HCO_3)_2$	C_{2h}	^1A	-25.04	-24.48	3.89	-4.45	32.35	-27.05	-5.87
$Mg(HCO_3)(OH)$	C_s	$^1A'$	-26.30	-26.77	4.55	-4.08	32.76	-26.52	-5.77
$CaCO_3$	C_{2v}	$^1A_1$	-24.79	-26.21	7.05	-5.63	47.36	-39.20	-6.74
$Ca(HCO_3)_2$	C_2	^1A	-21.54	-22.84	5.37	-4.07	37.16	-29.28	-6.57
$Ca(HCO_3)_2$	C_{2h}	^1A	-21.44	-22.56	5.01	-3.88	35.41	-27.99	-6.30
$Ca(HCO_3)(OH)$	C_s	$^1A'$	-22.77	-24.51	5.73	-3.99	37.55	-29.45	-6.36
$MnCO_3$	C_{2v}	$^6A_1$	-28.92	-29.34	8.09	-7.67	24.70	-22.57	-1.71
$Mn(HCO_3)_2$	C_2	^6A	-25.30	-26.01	6.71	-5.99	21.48	-17.48	-3.29
$Mn(HCO_3)_2$	C_{2h}	^6A_g	-25.09	-25.63	6.33	-5.79	21.56	-17.74	-3.29
$Mn(HCO_3)(OH)$	C_s	$^6A'$	-26.95	-29.26	8.55	-6.24	18.66	-13.95	-2.41
$FeCO_3$	C_{2v}	$^5A_1$	-30.72	-30.32	11.09	-11.48	26.42	-24.01	-2.81
$Fe(HCO_3)_2$	C_{2h}	^5A_g	-26.84	-26.85	10.01	-10.00	21.96	-17.75	-4.20
$Fe(HCO_3)_2$	C_2	^5B	-26.75	-27.18	10.43	-10.00	25.75	-20.18	-5.14
$Fe(HCO_3)(OH)$	C_s	$^5A'$	-28.67	-30.48	9.56	-7.75	21.36	-15.58	-3.97
$CoCO_3$	C_{2v}	$^4A_1$	-32.27	-30.75	10.26	-11.78	31.23	-28.31	-4.44
$Co(HCO_3)_2$	C_2	^4B	-28.39	-27.69	9.57	-10.27	26.24	-21.41	-5.53
$Co(HCO_3)_2$	C_{2h}	^4A_g	-28.13	-27.43	9.36	-10.06	27.68	-22.21	-6.17
$Co(HCO_3)(OH)$	C_s	$^4A'$	-29.89	-30.44	8.88	-8.32	20.76	-16.28	-3.92
$NiCO_3$	C_{2v}	$^1A_1$	-34.66	-32.18	10.75	-13.23	36.09	-31.80	-6.77
$Ni(HCO_3)_2$	C_{2h}	^1A_g	-30.66	-30.39	12.04	-12.31	29.78	-22.32	-7.72
$Ni(HCO_3)(OH)$	C_s	$^3A''$	-30.87	-31.79	10.18	-9.26	27.02	-20.48	-5.62
$CuCO_3$	C_{2v}	$^2B_2$	-33.77	-29.34	6.78	-11.21	33.63	-33.19	-4.87
$Cu(HCO_3)_2$	C_{2h}	^2A_g	-29.57	-28.01	8.15	-9.71	29.87	-25.36	-6.07
$Cu(HCO_3)(OH)$	C_1	^2A	-31.14	-31.62	9.44	-8.96	28.43	-22.66	-5.30
$ZnCO_3$	C_{2v}	$^1A_1$	-30.67	-29.69	6.41	-7.39	22.25	-21.61	-1.61

$Zn(HCO_3)_2$	C_2	^1A	-27.51	-27.21	6.17	-6.47	20.40	-17.00	-3.69
$Zn(HCO_3)_2$	C_{2h}	^1A	-27.37	-26.81	5.85	-6.41	20.20	-17.21	-3.55
$Zn(HCO_3)(OH)$	C_s	$^1A'$	-29.27	-30.82	7.88	-6.33	18.10	-13.59	-2.97
$CdCO_3$	C_{2v}	$^1A_1$	-27.87	-27.36	6.00	-6.50	23.70	-23.06	-1.14
$Cd(HCO_3)_2$	C_2	^1A	-24.50	-25.08	5.80	-5.22	20.87	-17.32	-2.97
$Cd(HCO_3)_2$	C_{2h}	^1A	-24.43	-24.81	5.58	-5.19	21.15	-17.85	-2.91
$Cd(HCO_3)(OH)$	C_s	$^1A'$	-26.22	-28.41	7.64	-5.45	19.34	-14.83	-2.31

[a] The sum of terms footnoted by a is Total BE. [b] The sum of terms footnoted by b is Total BE. [c] For $M(HCO_3)_2$ with C_{2h} and C_2 symmetries possible, the one put first of two in the order is the lowest energy and is used in heat of formation calculation with the FPD method.

Table A3.10. Gas phase heat of formation in kcal/mol.

Molecules	Symm	State	$\Delta H_{f,0K}$ gas	$\Delta H_{f,298K}$ gas
$MgCO_3$	C_{2v}	$^1A_1$	-110.4	-111.7
$Mg(HCO_3)_2$	C_2	^1A	-356.9	-360.9
$Mg(HCO_3)(OH)$	C_s	$^1A'$	-242.3	-245
$CaCO_3$	C_{2v}	$^1A_1$	-148.1	-149.5
$Ca(HCO_3)_2$	C_2	^1A	-379.0	-382.6
$Ca(HCO_3)(OH)$	C_s	$^1A'$	-260.8	-263.4
$MnCO_3$	C_{2v}	$^6A_1$	-77.2	-78.4
$Mn(HCO_3)_2$	C_2	^6A	-307.4	-310.7
$Mn(HCO_3)(OH)$	C_s	$^6A'$	-198.5	-200.8
$FeCO_3$	C_{2v}	$^5A_1$	-50.8	-51.8
$Fe(HCO_3)_2$	C_{2h}	^5A_g	-276.9	-280.1
$Fe(HCO_3)(OH)$	C_s	$^5A'$	-172.5	-174.8
$CoCO_3$	C_{2v}	$^4A_1$	-41.6	-42.7
$Co(HCO_3)_2$	C_2	^4B	-266.8	-270.2
$Co(HCO_3)(OH)$	C_s	$^4A'$	-156.0	-158.5
$Co(HCO_3)(OH)$	C_s	^2B	-133.4	-136.0
$NiCO_3$	C_{2v}	$^3B_1$	-36.6	-37.7
$Ni(HCO_3)_2$	C_2	^3B	-259.0	-262.6
$Ni(HCO_3)(OH)$	C_s	$^3A''$	-153.4	-155.9
$NiCO_3$	C_{2v}	$^1A_1$	-46.0	-47.2
$Ni(HCO_3)_2$	C_{2h}	^1A_g	-261.6	-265.6
$CuCO_3$	C_{2v}	$^2B_2$	-38.4	-39.5
$Cu(HCO_3)_2$	C_{2h}	^2A_g	-255.6	-259.3
$Cu(HCO_3)(OH)$	C_1	^2A	-145.9	-148.6
$ZnCO_3$	C_{2v}	$^1A_1$	-62.1	-63.4
$Zn(HCO_3)_2$	C_2	^1A	-295.9	-299.5
$Zn(HCO_3)(OH)$	C_s	$^1A'$	-192.0	-194.7
$CdCO_3$	C_{2v}	$^1A_1$	-47.3	-48.5
$Cd(HCO_3)_2$	C_2	^1A	-278.2	-281.7
$Cd(HCO_3)(OH)$	C_s	$^1A'$	-171.8	-174.4
H	$D_{\infty h}$	$^2\Sigma^+_g$	51.63	52.64
C	$D_{\infty h}$	$^3\Sigma^-_g$	170.03	170.28
O	$D_{\infty h}$	$^3\Sigma^-_g$	59.00	60.04
Mg	$D_{\infty h}$	$^1\Sigma^+_g$	34.87	36.06
Ca	$D_{\infty h}$	$^1\Sigma^+_g$	42.38	43.75
Mn	$D_{\infty h}$	$^6\Sigma^+_g$	66.77	67.96
Fe	$D_{\infty h}$	$^5\Sigma^+_g$	98.7	99.78
Co	$D_{\infty h}$	$^4\Sigma^+_g$	101.6	102.74
Ni	$D_{\infty h}$	$^3\Sigma^+_g$	102.2	103.34
Cu	$D_{\infty h}$	$^2\Sigma^+_g$	80.4	81.60
Zn	$D_{\infty h}$	$^1\Sigma^+_g$	31.0	32.35
Cd	$D_{\infty h}$	$^1\Sigma^+_g$	26.73	28.22

Table A3.11. Comparison of calculated and experimental values of the sum of 1st and 2nd IE for metals in eV.

	awt-dk	awq-dk	aw5-dk	cbs(tq5)	ΔE_{SO}	Calc	Exp. Sum
Mg	22.625	22.665	22.677	22.684	0.000	22.684	22.682
Ca[a]	17.751	17.917	17.958	17.981	0.000	17.981	17.985
Mn	23.045	23.062	23.071	23.076	0.000	23.076	23.074
Fe	24.058	24.081	24.090	24.096	-0.001	24.095	24.102
Co	24.931	24.961	24.972	24.978	-0.003	24.975	24.965
Ni[b]	21.393	21.398	21.466	21.506	-0.003	25.822	25.809
Cu	27.948	28.072	28.117	28.154	-0.104	28.050	28.019
Zn	27.292	27.356	27.379	27.393	0.000	27.393	27.359
Cd[c]	25.511	25.739	25.830	25.883	0.000	25.947	25.902

[a] n = D, T, Q. [b] The cc-pVNZ-DK basis sets were used, where N = T, Q and 5. The core-valence correction is 4.32 eV, calculated with the cc-pVQZ-DK and cc-pwcVQZ-DK basis sets. [c] The cc-pwcVNZ-PP basis sets were used, where N = T, Q and 5. The scalar relativistic correction is 0.06 eV, calculated with the cc-pwcVTZ-PP and cc-pwcVTZ-DK basis sets.

Table A3.12. Electronic energies contributed to the sum of 1st and 2nd IE for metals in Hartrees.

	awt-dk	awq-dk	aw5-dk	cbs(tq5)
Mg^{2+}	-199.362901	-199.415866	-199.437677	-199.450396
$Ca^{2+,a}$	-679.192062	-679.252113	-679.291720	-679.316431
Mn^{2+}	-1157.090657	-1157.117511	-1157.129040	-1157.135768
Fe^{2+}	-1271.090764	-1271.122902	-1271.137156	-1271.145479
Co^{2+}	-1391.661352	-1391.699005	-1391.716134	-1391.726139
$Ni^{2+,b}$	-1518.471917	-1518.497145	-1518.507239	-1518.513122
Cu^{2+}	-1653.030973	-1653.079034	-1653.101328	-1653.114352
Zn^{2+}	-1794.186807	-1794.240500	-1794.265240	-1794.279692
Cd^{2+}	-166.718156	-166.789965	-166.821576	-166.8400287
Mg	-200.194329	-200.248771	-200.271029	-200.284006
Ca[a]	-679.844390	-679.910525	-679.951665	-679.977200
Mn	-1157.937543	-1157.964990	-1157.976845	-1157.983764
Fe	-1271.974862	-1272.007837	-1272.022442	-1272.030969
Co	-1392.577533	-1392.616274	-1392.633805	-1392.644043
Ni[b]	-1519.258067	-1519.283499	-1519.296089	-1519.303452
Cu	-1654.058035	-1654.110644	-1654.134587	-1654.148957
Zn	-1795.189739	-1795.245773	-1795.271390	-1795.286353
Cd[c]	-167.655653	-167.735821	-167.770781	-167.7911862

[a] n = D, T, Q. [b] The cc-pVNZ-DK basis sets were used, where N = T, Q and 5. The electronic energies with the cc-pwcVQZ-DK basis set are -1518.963368 and -1519.908396 in Hartrees for Ni cation and neutral, respectively. The core-valence corrections for Ni cation and neutral are -0.466222 and -0.624897 in Hartrees, respectively. [c] The cc-pwcVNZ-PP basis sets were used, where N = T, Q and 5. The electronic energies calculated with the cc-pwcVTZ-DK basis sets are -5590.131743 and -5591.071591 for Cd cation and neutral, respectively. The electronic scalar relativistic corrections for Cd cation and neutral are -5423.413587 and -5423.415937, respectively.

Table A3.13. Comparison of calculated and experimental TRDE in eV at 0K using calculated sum of 1st and 2nd IP and heat of formation of OH^- versus those from experiments.

Metal Cation	HCO_3^-		HCO_3^-/OH^-	
	Calculated	Exprimental	Calculated	Exprimental
Mg^{2+}	-24.725	-24.723	-25.798	-25.785
Ca^{2+}	-21.306	-21.310	-22.223	-22.217
Mn^{2+}	-24.353	-24.351	-25.672	-25.660
Fe^{2+}	-25.437	-25.443	-26.950	-26.947
Co^{2+}	-26.002	-25.993	-27.240	-27.220
Ni^{2+}	-26.651	-26.638	-27.998	-27.975
Cu^{2+}	-27.674	-27.643	-28.956	-28.915
Zn^{2+}	-26.623	-26.588	-28.159	-28.114
Cd^{2+}	-24.222	-24.178	-25.650	-25.596

Table A3.14. Natural population analysis for atomic charges.[a]

Atom	Mg	Ca	Mn	Fe	Co	Ni	Cu	Zn	Cd
MCO_3									
M	1.74	1.71	1.44	1.33	1.31	1.00	1.12	1.49	1.44
C	0.90	0.92	0.92	0.92	0.92	0.92	0.91	0.91	0.90
O x2	-1.01	-0.99	-0.88	-0.83	-0.82	-0.68	-0.73	-0.91	-0.87
O	-0.62	-0.65	-0.60	-0.58	-0.58	-0.57	-0.57	-0.59	-0.61
$M(HCO_3)_2$									
M	1.80	1.84	1.58	1.50	1.47	1.10	1.36	1.61	1.60
C x2	0.94	0.95	0.96	0.95	0.96	0.95	0.95	0.96	0.95
$O_{2,7}$ x2	-0.83	-0.83	-0.78	-0.76	-0.75	-0.66	-0.73	-0.79	-0.78
$O_{4,9}$ x2	-0.65	-0.67	-0.65	-0.65	-0.65	-0.64	-0.65	-0.65	-0.66
$O_{5,10}$ x2	-0.86	-0.87	-0.81	-0.79	-0.79	-0.70	-0.76	-0.82	-0.81
H x2	0.49	0.49	0.50	0.50	0.50	0.50	0.50	0.50	0.50
$M(HCO_3)(OH)$									
M	1.85	1.86	1.53	1.46	1.42	1.36	1.32	1.58	1.54
C	0.94	0.95	0.95	0.96	0.96	0.96	0.95	0.95	0.95
O_2	-0.87	-0.87	-0.81	-0.80	-0.78	-0.81	-0.76	-0.82	-0.80
O_3	-0.83	-0.83	-0.79	-0.77	-0.75	-0.71	-0.72	-0.79	-0.78
$O_{OH(4)}$	-1.43	-1.39	-1.20	-1.17	-1.17	-1.12	-1.11	-1.24	-1.20
$O_{COH(6)}$	-0.65	-0.67	-0.66	-0.65	-0.65	-0.65	-0.65	-0.65	-0.66
H_{OH}	0.49	0.47	0.47	0.48	0.48	0.47	0.47	0.47	0.46
H_{COH}	0.50	0.49	0.50	0.50	0.50	0.50	0.50	0.50	0.50

[a] See Figure 3.1 and A3.1 for labels

Table A3.15. Natural population analysis for atomic spins in open shell molecules.

Atom	Mn	Fe	Co	Ni	Cu
MCO_3					
M	4.70	3.55	2.53	a	0.30
C	0.01	0.00	-0.02		-0.03
O x2	0.15	0.22	0.23		0.32
O	0.01	0.02	0.02		0.09
$M(HCO_3)_2$					
M	4.79	3.74	2.71	a	0.64
C x2	0.01	0.01	0.00		-0.01
$O_{2,7}$ x2	0.05	0.06	0.07		0.10
$O_{4,9}$ x2	0.00	0.00	0.00		0.00
$O_{5,10}$ x2	0.05	0.06	0.07		0.09
H x2	0.00	0.00	0.00		0.00
$M(HCO_3)(OH)$					
M	4.80	3.71	2.71	1.64	0.61
C	0.01	0.01	0.00	0.00	-0.01
O_2	0.04	0.06	0.07	0.05	0.09
O_3	0.03	0.05	0.06	0.10	0.10
O_4	0.10	0.16	0.15	0.21	0.21
O_6	0.00	0.00	0.00	0.00	0.00
H_5	0.01	0.01	0.00	0.00	-0.01
H_8	0.00	0.00	0.00	0.00	0.00

[a] Singlet states.

Table A3.16. Natural population analysis for excess valence s and d orbital population on metal dications.

Atom	MCO_3		$M(HCO_3)_2$		$M(HCO_3)(OH)$	
	3d	valence s	3d	valence s	3d	valence s
Mg		0.23		0.18		0.12
Ca		0.05		0.06		0.03
Mn	0.30	0.21	0.17	0.22	0.17	0.28
Fe	0.33	0.31	0.16	0.32	0.23	0.28
Co	0.39	0.27	0.22	0.30	0.15	0.41
Ni	0.73	0.25	0.57	0.32	0.28	0.35
Cu	0.61	0.24	0.31	0.32	0.29	0.37
Zn	-0.02	0.46	-0.01	0.38	-0.05	0.43
Cd	-0.03	0.51	-0.03	0.39	-0.06	0.49

Table A3.17. Gas phase metal exchange energy at 0K in kcal/mol.

Metal Exchange Reactions	ΔH_{0K} (g) neutral	ΔH_{0K} (g) dication
$Ca + MgCO_3 \rightarrow CaCO_3 + Mg$	-45.2	63.1
$Ca + MnCO_3 \rightarrow CaCO_3 + Mn$	-46.5	70.9
$Ca + FeCO_3 \rightarrow CaCO_3 + Fe$	-41.0	100.1
$Ca + CoCO_3 \rightarrow CaCO_3 + Co$	-47.3	113.7
$Ca + NiCO_3 \rightarrow CaCO_3 + Ni$	-42.3	138.1
$Ca + CuCO_3 \rightarrow CaCO_3 + Cu$	-71.6	159.7
$Ca + ZnCO_3 \rightarrow CaCO_3 + Zn$	-97.4	118.8
$Ca + CdCO_3 \rightarrow CaCO_3 + Cd$	-116.5	66.1
$Ca + Mg(HCO_3)_2 \rightarrow Ca(HCO_3)_2 + Mg$	-29.6	78.7
$Ca + Mn(HCO_3)_2 \rightarrow Ca(HCO_3)_2 + Mn$	-47.2	70.1
$Ca + Fe(HCO_3)_2 \rightarrow Ca(HCO_3)_2 + Fe$	-45.7	95.3
$Ca + Co(HCO_3)_2 \rightarrow Ca(HCO_3)_2 + Co$	-53.0	108.0
$Ca + Ni(HCO_3)_2 \rightarrow Ca(HCO_3)_2 + Ni$	-57.6	122.9
$Ca + Cu(HCO_3)_2 \rightarrow Ca(HCO_3)_2 + Cu$	-85.4	146.0
$Ca + Zn(HCO_3)_2 \rightarrow Ca(HCO_3)_2 + Zn$	-94.4	121.7
$Ca + Cd(HCO_3)_2 \rightarrow Ca(HCO_3)_2 + Cd$	-116.5	66.1
$Ca + Mg(HCO_3)(OH) \rightarrow Ca(HCO_3)(OH) + Mg$	-26.0	82.3
$Ca + Mn(HCO_3)(OH) \rightarrow Ca(HCO_3)(OH) + Mn$	-37.9	79.4
$Ca + Fe(HCO_3)(OH) \rightarrow Ca(HCO_3)(OH) + Fe$	-32.0	109.1
$Ca + Co(HCO_3)(OH) \rightarrow Ca(HCO_3)(OH) + Co$	-45.6	115.4
$Ca + Ni(HCO_3)(OH) \rightarrow Ca(HCO_3)(OH) + Ni$	-47.6	132.8
$Ca + Cu(HCO_3)(OH) \rightarrow Ca(HCO_3)(OH) + Cu$	-76.9	154.5
$Ca + Zn(HCO_3)(OH) \rightarrow Ca(HCO_3)(OH) + Zn$	-80.2	136.0
$Ca + Cd(HCO_3)(OH) \rightarrow Ca(HCO_3)(OH) + Cd$	-104.7	77.9
$Mg + CaCO_3 \rightarrow MgCO_3 + Ca$	45.2	-63.1
$Mg + MnCO_3 \rightarrow MgCO_3 + Mn$	-1.3	7.8
$Mg + FeCO_3 \rightarrow MgCO_3 + Fe$	4.2	37.0
$Mg + CoCO_3 \rightarrow MgCO_3 + Co$	-2.1	50.6
$Mg + NiCO_3 \rightarrow MgCO_3 + Ni$	2.9	75.0
$Mg + CuCO_3 \rightarrow MgCO_3 + Cu$	-26.4	96.6
$Mg + ZnCO_3 \rightarrow MgCO_3 + Zn$	-52.2	55.7
$Mg + CdCO_3 \rightarrow MgCO_3 + Cd$	-71.2	3.0
$Mg + Ca(HCO_3)_2 \rightarrow Mg(HCO_3)_2 + Ca$	29.6	-78.7
$Mg + Mn(HCO_3)_2 \rightarrow Mg(HCO_3)_2 + Mn$	-17.6	-8.6
$Mg + Fe(HCO_3)_2 \rightarrow Mg(HCO_3)_2 + Fe$	-16.1	16.6
$Mg + Co(HCO_3)_2 \rightarrow Mg(HCO_3)_2 + Co$	-23.4	29.3
$Mg + Ni(HCO_3)_2 \rightarrow Mg(HCO_3)_2 + Ni$	-28.0	44.2
$Mg + Cu(HCO_3)_2 \rightarrow Mg(HCO_3)_2 + Cu$	-55.7	67.3
$Mg + Zn(HCO_3)_2 \rightarrow Mg(HCO_3)_2 + Zn$	-64.8	43.0
$Mg + Cd(HCO_3)_2 \rightarrow Mg(HCO_3)_2 + Cd$	-86.8	-12.6
$Mg + Ca(HCO_3)(OH) \rightarrow Mg(HCO_3)(OH) + Ca$	26.0	-82.3

$Mg + Mn(HCO_3)(OH) \rightarrow Mg(HCO_3)(OH) + Mn$	-11.9	-2.9
$Mg + Fe(HCO_3)(OH) \rightarrow Mg(HCO_3)(OH) + Fe$	-6.0	26.8
$Mg + Co(HCO_3)(OH) \rightarrow Mg(HCO_3)(OH) + Co$	-19.6	33.1
$Mg + Ni(HCO_3)(OH) \rightarrow Mg(HCO_3)(OH) + Ni$	-21.6	50.5
$Mg + Cu(HCO_3)(OH) \rightarrow Mg(HCO_3)(OH) + Cu$	-50.9	72.2
$Mg + Zn(HCO_3)(OH) \rightarrow Mg(HCO_3)(OH) + Zn$	-54.2	53.7
$Mg + Cd(HCO_3)(OH) \rightarrow Mg(HCO_3)(OH) + Cd$	-78.6	-4.4
$Mn + MgCO_3 \rightarrow MnCO_3 + Mg$	1.3	-7.8
$Mn + CaCO_3 \rightarrow MnCO_3 + Ca$	46.5	-70.9
$Mn + FeCO_3 \rightarrow MnCO_3 + Fe$	5.5	29.2
$Mn + CoCO_3 \rightarrow MnCO_3 + Co$	-0.8	42.8
$Mn + NiCO_3 \rightarrow MnCO_3 + Ni$	4.2	67.3
$Mn + CuCO_3 \rightarrow MnCO_3 + Cu$	-25.2	88.9
$Mn + ZnCO_3 \rightarrow MnCO_3 + Zn$	-50.9	47.9
$Mn + CdCO_3 \rightarrow MnCO_3 + Cd$	-70.0	-4.7
$Mn + Mg(HCO_3)_2 \rightarrow Mn(HCO_3)_2 + Mg$	17.6	8.6
$Mn + Ca(HCO_3)_2 \rightarrow Mn(HCO_3)_2 + Ca$	47.2	-70.1
$Mn + Fe(HCO_3)_2 \rightarrow Mn(HCO_3)_2 + Fe$	1.5	25.2
$Mn + Co(HCO_3)_2 \rightarrow Mn(HCO_3)_2 + Co$	-5.8	37.9
$Mn + Ni(HCO_3)_2 \rightarrow Mn(HCO_3)_2 + Ni$	-10.3	52.7
$Mn + Cu(HCO_3)_2 \rightarrow Mn(HCO_3)_2 + Cu$	-38.1	75.9
$Mn + Zn(HCO_3)_2 \rightarrow Mn(HCO_3)_2 + Zn$	-47.2	51.6
$Mn + Cd(HCO_3)_2 \rightarrow Mn(HCO_3)_2 + Cd$	-69.2	-4.0
$Mn + Mg(HCO_3)(OH) \rightarrow Mn(HCO_3)(OH) + Mg$	11.9	2.9
$Mn + Ca(HCO_3)(OH) \rightarrow Mn(HCO_3)(OH) + Ca$	37.9	-79.4
$Mn + Fe(HCO_3)(OH) \rightarrow Mn(HCO_3)(OH) + Fe$	6.0	29.7
$Mn + Co(HCO_3)(OH) \rightarrow Mn(HCO_3)(OH) + Co$	-7.6	36.0
$Mn + Ni(HCO_3)(OH) \rightarrow Mn(HCO_3)(OH) + Ni$	-9.7	53.4
$Mn + Cu(HCO_3)(OH) \rightarrow Mn(HCO_3)(OH) + Cu$	-39.0	75.1
$Mn + Zn(HCO_3)(OH) \rightarrow Mna(HCO_3)(OH) + Zn$	-42.2	56.6
$Mn + Cd(HCO_3)(OH) \rightarrow Mn(HCO_3)(OH) + Cd$	-66.7	-1.5
$Fe + MgCO_3 \rightarrow FeCO_3 + Mg$	-4.2	-37.0
$Fe + CaCO_3 \rightarrow FeCO_3 + Ca$	41.0	-100.1
$Fe + MnCO_3 \rightarrow FeCO_3 + Mn$	-5.5	-29.2
$Fe + CoCO_3 \rightarrow FeCO_3 + Co$	-6.3	13.6
$Fe + NiCO_3 \rightarrow FeCO_3 + Ni$	-1.3	38.1
$Fe + CuCO_3 \rightarrow FeCO_3 + Cu$	-30.7	59.7
$Fe + ZnCO_3 \rightarrow FeCO_3 + Zn$	-56.4	18.7
$Fe + CdCO_3 \rightarrow FeCO_3 + Cd$	-75.5	-34.0
$Fe + Mg(HCO_3)_2 \rightarrow Fe(HCO_3)_2 + Mg$	16.1	-16.6
$Fe + Ca(HCO_3)_2 \rightarrow Fe(HCO_3)_2 + Ca$	45.7	-95.3
$Fe + Mn(HCO_3)_2 \rightarrow Fe(HCO_3)_2 + Mn$	-1.5	-25.2
$Fe + Co(HCO_3)_2 \rightarrow Fe(HCO_3)_2 + Co$	-7.3	12.7
$Fe + Ni(HCO_3)_2 \rightarrow Fe(HCO_3)_2 + Ni$	-11.8	27.5
$Fe + Cu(HCO_3)_2 \rightarrow Fe(HCO_3)_2 + Cu$	-39.6	50.7

$Fe + Zn(HCO_3)_2 \rightarrow Fe(HCO_3)_2 + Zn$	-48.7	26.4
$Fe + Cd(HCO_3)_2 \rightarrow Fe(HCO_3)_2 + Cd$	-70.4	-28.8
$Fe + Mg(HCO_3)(OH) \rightarrow Fe(HCO_3)(OH) + Mg$	6.0	-26.8
$Fe + Ca(HCO_3)(OH) \rightarrow Fe(HCO_3)(OH) + Ca$	32.0	-109.1
$Fe + Mn(HCO_3)(OH) \rightarrow Fe(HCO_3)(OH) + Mn$	-6.0	-29.7
$Fe + Co(HCO_3)(OH) \rightarrow Fe(HCO_3)(OH) + Co$	-13.6	6.3
$Fe + Ni(HCO_3)(OH) \rightarrow Fe(HCO_3)(OH) + Ni$	-15.6	23.7
$Fe + Cu(HCO_3)(OH) \rightarrow Fe(HCO_3)(OH) + Cu$	-44.9	45.4
$Fe + Zn(HCO_3)(OH) \rightarrow Fe(HCO_3)(OH) + Zn$	-48.2	26.9
$Fe + Cd(HCO_3)(OH) \rightarrow Fe(HCO_3)(OH) + Cd$	-72.7	-31.2
$Co + MgCO_3 \rightarrow CoCO_3 + Mg$	2.1	-50.6
$Co + CaCO_3 \rightarrow CoCO_3 + Ca$	47.3	-113.7
$Co + MnCO_3 \rightarrow CoCO_3 + Mn$	0.8	-42.8
$Co + FeCO_3 \rightarrow CoCO_3 + Fe$	6.3	-13.6
$Co + NiCO_3 \rightarrow CoCO_3 + Ni$	5.0	24.5
$Co + CuCO_3 \rightarrow CoCO_3 + Cu$	-24.3	46.1
$Co + ZnCO_3 \rightarrow CoCO_3 + Zn$	-49.9	5.3
$Co + CdCO_3 \rightarrow CoCO_3 + Cd$	-69.1	-47.5
$Co + Mg(HCO_3)_2 \rightarrow Co(HCO_3)_2 + Mg$	23.4	-29.3
$Co + Ca(HCO_3)_2 \rightarrow Co(HCO_3)_2 + Ca$	53.0	-108.0
$Co + Mn(HCO_3)_2 \rightarrow Co(HCO_3)_2 + Mn$	5.8	-37.9
$Co + Fe(HCO_3)_2 \rightarrow Co(HCO_3)_2 + Fe$	7.3	-12.7
$Co + Ni(HCO_3)_2 \rightarrow Co(HCO_3)_2 + Ni$	-4.6	14.9
$Co + Cu(HCO_3)_2 \rightarrow Co(HCO_3)_2 + Cu$	-32.4	38.0
$Co + Zn(HCO_3)_2 \rightarrow Co(HCO_3)_2 + Zn$	-41.5	13.7
$Co + Cd(HCO_3)_2 \rightarrow Co(HCO_3)_2 + Cd$	-63.5	-41.9
$Co + Mg(HCO_3)(OH) \rightarrow Co(HCO_3)(OH) + Mg$	19.6	-33.1
$Co + Ca(HCO_3)(OH) \rightarrow Co(HCO_3)(OH) + Ca$	45.6	-115.4
$Co + Mn(HCO_3)(OH) \rightarrow Co(HCO_3)(OH) + Mn$	7.6	-36.0
$Co + Fe(HCO_3)(OH) \rightarrow Co(HCO_3)(OH) + Fe$	13.6	-6.3
$Co + Ni(HCO_3)(OH) \rightarrow Co(HCO_3)(OH) + Ni$	-2.0	17.4
$Co + Cu(HCO_3)(OH) \rightarrow Co(HCO_3)(OH) + Cu$	-31.3	39.1
$Co + Zn(HCO_3)(OH) \rightarrow Co(HCO_3)(OH) + Zn$	-34.6	20.6
$Co + Cd(HCO_3)(OH) \rightarrow Co(HCO_3)(OH) + Cd$	-59.1	-37.5
$Ni + MgCO_3 \rightarrow NiCO_3 + Mg$	-2.9	-75.0
$Ni + CaCO_3 \rightarrow NiCO_3 + Ca$	42.3	-138.1
$Ni + MnCO_3 \rightarrow NiCO_3 + Mn$	-4.2	-67.3
$Ni + FeCO_3 \rightarrow NiCO_3 + Fe$	1.3	-38.1
$Ni + CoCO_3 \rightarrow NiCO_3 + Co$	-5.0	-24.5
$Ni + CuCO_3 \rightarrow NiCO_3 + Cu$	-29.4	21.6
$Ni + ZnCO_3 \rightarrow NiCO_3 + Zn$	-55.1	-19.3
$Ni + CdCO_3 \rightarrow NiCO_3 + Cd$	-74.2	-72.0
$Ni + Mg(HCO_3)_2 \rightarrow Ni(HCO_3)_2 + Mg$	28.0	-44.2
$Ni + Ca(HCO_3)_2 \rightarrow Ni(HCO_3)_2 + Ca$	57.6	-122.9
$Ni + Mn(HCO_3)_2 \rightarrow Ni(HCO_3)_2 + Mn$	10.3	-52.7

$Ni + Fe(HCO_3)_2 \rightarrow Ni(HCO_3)_2 + Fe$	11.8	-27.5
$Ni + Co(HCO_3)_2 \rightarrow Ni(HCO_3)_2 + Co$	4.6	-14.9
$Ni + Cu(HCO_3)_2 \rightarrow Ni(HCO_3)_2 + Cu$	-27.8	23.2
$Ni + Zn(HCO_3)_2 \rightarrow Ni(HCO_3)_2 + Zn$	-36.9	-1.1
$Ni + Cd(HCO_3)_2 \rightarrow Ni(HCO_3)_2 + Cd$	-58.9	-56.7
$Ni + Mg(HCO_3)(OH) \rightarrow Ni(HCO_3)(OH) + Mg$	21.6	-50.5
$Ni + Ca(HCO_3)(OH) \rightarrow Ni(HCO_3)(OH) + Ca$	47.6	-132.8
$Ni + Mn(HCO_3)(OH) \rightarrow Ni(HCO_3)(OH) + Mn$	9.7	-53.4
$Ni + Fe(HCO_3)(OH) \rightarrow Ni(HCO_3)(OH) + Fe$	15.6	-23.7
$Ni + Co(HCO_3)(OH) \rightarrow Ni(HCO_3)(OH) + Co$	2.0	-17.4
$Ni + Cu(HCO_3)(OH) \rightarrow Ni(HCO_3)(OH) + Cu$	-29.3	21.7
$Ni + Zn(HCO_3)(OH) \rightarrow Ni(HCO_3)(OH) + Zn$	-32.5	3.2
$Ni + Cd(HCO_3)(OH) \rightarrow Ni(HCO_3)(OH) + Cd$	-57.0	-54.9
$Cu + MgCO_3 \rightarrow CuCO_3 + Mg$	26.4	-96.6
$Cu + CaCO_3 \rightarrow CuCO_3 + Ca$	71.6	-159.7
$Cu + MnCO_3 \rightarrow CuCO_3 + Mn$	25.2	-88.9
$Cu + FeCO_3 \rightarrow CuCO_3 + Fe$	30.7	-59.7
$Cu + CoCO_3 \rightarrow CuCO_3 + Co$	24.3	-46.1
$Cu + NiCO_3 \rightarrow CuCO_3 + Ni$	29.4	-21.6
$Cu + ZnCO_3 \rightarrow CuCO_3 + Zn$	-25.7	-40.9
$Cu + CdCO_3 \rightarrow CuCO_3 + Cd$	-44.8	-93.6
$Cu + Mg(HCO_3)_2 \rightarrow Cu(HCO_3)_2 + Mg$	55.7	-67.3
$Cu + Ca(HCO_3)_2 \rightarrow Cu(HCO_3)_2 + Ca$	85.4	-146.0
$Cu + Mn(HCO_3)_2 \rightarrow Cu(HCO_3)_2 + Mn$	38.1	-75.9
$Cu + Fe(HCO_3)_2 \rightarrow Cu(HCO_3)_2 + Fe$	39.6	-50.7
$Cu + Co(HCO_3)_2 \rightarrow Cu(HCO_3)_2 + Co$	32.4	-38.0
$Cu + Ni(HCO_3)_2 \rightarrow Cu(HCO_3)_2 + Ni$	27.8	-23.2
$Cu + Zn(HCO_3)_2 \rightarrow Cu(HCO_3)_2 + Zn$	-9.1	-24.3
$Cu + Cd(HCO_3)_2 \rightarrow Cu(HCO_3)_2 + Cd$	-31.1	-79.9
$Cu + Mg(HCO_3)(OH) \rightarrow Cu(HCO_3)(OH) + Mg$	50.9	-72.2
$Cu + Ca(HCO_3)(OH) \rightarrow Cu(HCO_3)(OH) + Ca$	76.9	-154.5
$Cu + Mn(HCO_3)(OH) \rightarrow Cu(HCO_3)(OH) + Mn$	39.0	-75.1
$Cu + Fe(HCO_3)(OH) \rightarrow Cu(HCO_3)(OH) + Fe$	44.9	-45.4
$Cu + Co(HCO_3)(OH) \rightarrow Cu(HCO_3)(OH) + Co$	31.3	-39.1
$Cu + Ni(HCO_3)(OH) \rightarrow Cu(HCO_3)(OH) + Ni$	29.3	-21.7
$Cu + Zn(HCO_3)(OH) \rightarrow Cu(HCO_3)(OH) + Zn$	-3.3	-18.5
$Cu + Cd(HCO_3)(OH) \rightarrow Cu(HCO_3)(OH) + Cd$	-27.7	-76.6
$Zn + MgCO_3 \rightarrow ZnCO_3 + Mg$	52.2	-55.7
$Zn + CaCO_3 \rightarrow ZnCO_3 + Ca$	97.4	-118.8
$Zn + MnCO_3 \rightarrow ZnCO_3 + Mn$	50.9	-47.9
$Zn + FeCO_3 \rightarrow ZnCO_3 + Fe$	56.4	-18.7
$Zn + CoCO_3 \rightarrow ZnCO_3 + Co$	49.9	-5.3
$Zn + NiCO_3 \rightarrow ZnCO_3 + Ni$	55.1	19.3
$Zn + CuCO_3 \rightarrow ZnCO_3 + Cu$	25.7	40.9
$Zn + CdCO_3 \rightarrow ZnCO_3 + Cd$	-19.1	-52.7

$Zn + Mg(HCO_3)_2 \rightarrow Zn(HCO_3)_2 + Mg$	64.8	-43.0
$Zn + Ca(HCO_3)_2 \rightarrow Zn(HCO_3)_2 + Ca$	94.4	-121.7
$Zn + Mn(HCO_3)_2 \rightarrow Zn(HCO_3)_2 + Mn$	47.2	-51.6
$Zn + Fe(HCO_3)_2 \rightarrow Zn(HCO_3)_2 + Fe$	48.7	-26.4
$Zn + Co(HCO_3)_2 \rightarrow Zn(HCO_3)_2 + Co$	41.5	-13.7
$Zn + Ni(HCO_3)_2 \rightarrow Zn(HCO_3)_2 + Ni$	36.9	1.1
$Zn + Cu(HCO_3)_2 \rightarrow Zn(HCO_3)_2 + Cu$	9.1	24.3
$Zn + Cd(HCO_3)_2 \rightarrow Zn(HCO_3)_2 + Cd$	-22.0	-55.6
$Zn + Mg(HCO_3)(OH) \rightarrow Zn(HCO_3)(OH) + Mg$	54.2	-53.7
$Zn + Ca(HCO_3)(OH) \rightarrow Zn(HCO_3)(OH) + Ca$	80.2	-136.0
$Zn + Mn(HCO_3)(OH) \rightarrow Zn(HCO_3)(OH) + Mn$	42.2	-56.6
$Zn + Fe(HCO_3)(OH) \rightarrow Zn(HCO_3)(OH) + Fe$	48.2	-26.9
$Zn + Co(HCO_3)(OH) \rightarrow Zn(HCO_3)(OH) + Co$	34.6	-20.6
$Zn + Ni(HCO_3)(OH) \rightarrow Zn(HCO_3)(OH) + Ni$	32.5	-3.2
$Zn + Cu(HCO_3)(OH) \rightarrow Zn(HCO_3)(OH) + Cu$	3.3	18.5
$Zn + Cd(HCO_3)(OH) \rightarrow Zn(HCO_3)(OH) + Cd$	-24.5	-58.1
$Cd + MgCO_3 \rightarrow CdCO_3 + Mg$	71.2	-3.0
$Cd + CaCO_3 \rightarrow CdCO_3 + Ca$	116.5	-66.1
$Cd + MnCO_3 \rightarrow CdCO_3 + Mn$	70.0	4.7
$Cd + FeCO_3 \rightarrow CdCO_3 + Fe$	75.5	34.0
$Cd + CoCO_3 \rightarrow CdCO_3 + Co$	69.1	47.5
$Cd + NiCO_3 \rightarrow CdCO_3 + Ni$	74.2	72.0
$Cd + CuCO_3 \rightarrow CdCO_3 + Cu$	44.8	93.6
$Cd + ZnCO_3 \rightarrow CdCO_3 + Zn$	19.1	52.7
$Cd + Mg(HCO_3)_2 \rightarrow Cd(HCO_3)_2 + Mg$	86.8	12.6
$Cd + Ca(HCO_3)_2 \rightarrow Cd(HCO_3)_2 + Ca$	116.5	-66.1
$Cd + Mn(HCO_3)_2 \rightarrow Cd(HCO_3)_2 + Mn$	69.2	4.0
$Cd + Fe(HCO_3)_2 \rightarrow Cd(HCO_3)_2 + Fe$	70.4	28.8
$Cd + Co(HCO_3)_2 \rightarrow Cd(HCO_3)_2 + Co$	63.5	41.9
$Cd + Ni(HCO_3)_2 \rightarrow Cd(HCO_3)_2 + Ni$	58.9	56.7
$Cd + Cu(HCO_3)_2 \rightarrow Cd(HCO_3)_2 + Cu$	31.1	79.9
$Cd + Zn(HCO_3)_2 \rightarrow Cd(HCO_3)_2 + Zn$	22.0	55.6
$Cd + Mg(HCO_3)(OH) \rightarrow Cd(HCO_3)(OH) + Mg$	78.6	4.4
$Cd + Ca(HCO_3)(OH) \rightarrow Cd(HCO_3)(OH) + Ca$	104.7	-77.9
$Cd + Mn(HCO_3)(OH) \rightarrow Cd(HCO_3)(OH) + Mn$	66.7	1.5
$Cd + Fe(HCO_3)(OH) \rightarrow Cd(HCO_3)(OH) + Fe$	72.7	31.2
$Cd + Co(HCO_3)(OH) \rightarrow Cd(HCO_3)(OH) + Co$	59.1	37.5
$Cd + Ni(HCO_3)(OH) \rightarrow Cd(HCO_3)(OH) + Ni$	57.0	54.9
$Cd + Cu(HCO_3)(OH) \rightarrow Cd(HCO_3)(OH) + Cu$	27.7	76.6
$Cd + Zn(HCO_3)(OH) \rightarrow Cd(HCO_3)(OH) + Zn$	24.5	58.1

Table A3.18. Electronegativity (χ) for metal dications in eV.

Metal	χ^a
Mg	47.59
Ca	31.39
Mn	24.65
Fe	23.43
Co	25.29
Ni	26.68
Cu	28.57
Zn	28.84
Cd	27.19

[a] χ = (IE+EA)/2.

Table A3.19. DFT errors of $\Delta H_{f,0K}$ in kcal/mol compared to FPD values for $MnCO_3$, $Mn(HCO_3)_2$, $Mn(HCO_3)(OH)$, $CoCO_3$, $Co(HCO_3)_2$ and $Co(HCO_3)(OH)$.

Functionals	$MnCO_3$	$Mn(HCO_3)_2$	$Mn(HCO_3)(OH)$	$CoCO_3$	$Co(HCO_3)_2$	$Co(HCO_3)(OH)$
PW91	50.1	63.2	42.9	60.7	73.9	53.3
BP86	42.4	53.1	38.8	41.6	52.3	37.7
M06	50.7	49.8	44.3	13.9	14.5	19.8
PBE	48.5	59.9	39.9	49.0	60.4	40.3
PBE0	45.6	39.6	37.1	12.9	8.6	-8.5
B3LYP	-5.2	-21.0	-12.1	2.3	-12.8	-18.7
HSE06	42.5	33.7	33.4	9.9	2.7	-12.0
τ-HCTH	8.5	-7.6	-6.1	25.1	2.2	7.9
ωB97X	51.9	49.8	48.9	21.9	20.8	20.9
ωB97X-D	45.4	40.0	40.8	19.5	15.9	16.6

Table A3.20. DFT errors of $\Delta H_{f,0K}$ in kcal/mol compared to FPD values for $NiCO_3$, $Ni(HCO_3)_2$, $Ni(HCO_3)(OH)$. $CuCO_3$, $Cu(HCO_3)_2$ and $Cu(HCO_3)(OH)$.

Functionals	$NiCO_3$	$Ni(HCO_3)_2$	$Ni(HCO_3)(OH)$	$CuCO_3$	$Cu(HCO_3)_2$	$Cu(HCO_3)(OH)$
PW91	40.3	62.8	39.1	48.9	64.1	43.9
BP86	33.0	53.0	34.9	41.9	54.7	40.6
M06	-7.0	-4.2	-5.7	4.2	-0.4	-3.2
PBE	39.5	59.8	36.8	48.1	61.4	41.7
PBE0	-8.3	-6.9	-0.8	8.5	3.8	0.8
B3LYP	-15.0	-23.6	-9.7	-0.9	-16.9	-7.7
HSE06	-11.6	-12.8	-4.8	5.7	-1.8	-2.6
τ-HCTH	12.2	-7.2	-5.1	15.1	-10.4	-5.2
ωB97X	-5.1	-1.6	5.4	6.6	3.2	3.6
ωB97X-D	-10.7	-8.7	-0.2	3.9	-1.4	-0.3

Table A3.21. DFT errors of $\Delta H_{f,0K}$ in kcal/mol compared to FPD values for $ZnCO_3$, $Zn(HCO_3)_2$, and $Zn(HCO_3)(OH)$.

Functionals	$ZnCO_3$	$Zn(HCO_3)_2$	$Zn(HCO_3)(OH)$
PW91	32.6	51.3	29.2
BP86	25.0	41.0	25.0
M06	-9.8	-9.7	-13.4
PBE	32.0	48.7	27.1
PBE0	0.4	-2.8	-6.1
B3LYP	-13.9	-27.6	-19.2
HSE06	-3.4	-9.5	-10.5
τ-HCTH	2.2	-12.5	-10.0
ωB97X	-4.6	-5.3	-5.4
ωB97X-D	-7.4	-10.2	-9.5

Table A3.22. Electronic energies (au) with DFT functionals with the aug-cc-pVTZ(-PP) basis set and DFT errors of $\Delta H_{f,0K}$ in kcal/mol compared to FPD values for $^5Fe(HCO_3)_2$ (C_{2h}, ^5A_g).

Functionals	Total E	DFT error
PW91	-652.418927	60.3
BP86	-652.589833	49.7
M06	-652.253832	36.7
PBE	-651.959349	57.9
PBE0	-651.889509	7.8
B3LYP	-652.516993	-1.6
HCTH 407	-652.798879	-3.1
HSE06	-651.945316	9.0
M06L	-652.450261	0.4
τ-HCTH	-652.786401	-8.1
τ-HCTH hyb	-652.452169	13.2
TPSSh	-652.443390	-25.3
ωB97X	-652.352367	18.8
ωB97X-D	-652.317226	8.8

Table A3.23. Gas phase hydration reaction energies from heats of formation, $\Delta H_{f,298K}$, in kcal/mol. Corrected values for reference 21 with new more stable structure for $Fe(HCO_3)_2$.

Product	$\Delta H_{f,298K}$	$\Delta H_{f,298K}$ /H_2O
$Fe(HCO_3)_2(H_2O)$	-12.8	-12.8
$Fe(HCO_3)_2(H_2O)_2$	-22.7	-11.4

Table A3.24. Electronic energies (au) with the DFT functional ωB97X with the aug-cc-pVTZ(-PP) basis set and DFT errors of $\Delta H_{f,0K}$ in kcal/mol compared to FPD values for $FeCO_3$ (C_{2v}, $^5A_1$).

Functionals	Total E	DFT error
ωB97X	-387.170676	21.9
ωB97X-D	-387.159718	19.5

Table A3.25. Electronic atomization energy plus ZPE at the CCSD(T) level and B3LYP/aT levels in kcal/mol.

Molecules	Symm	State	CCSD(T)	B3LYP/aT	ΔE[a]
$MnCO_3$	C_{2v}	$^6A_1$	491.8	485.9	-5.9
$Mn(HCO_3)_2$	C_2	^6A	1173.0	1150.4	-22.6
$Mn(HCO_3)(OH)$	C_s	$^6A'$	775.5	762.4	-13.1
$FeCO_3$	C_{2v}	$^5A_1$	498.5	511.0	+12.5
$Fe(HCO_3)_2$	C_{2h}	^5A_g	1175.7	1171.4	-4.3
$Fe(HCO_3)(OH)$	C_s	$^5A'$	782.7	788.2	+5.5
$CoCO_3$	C_{2v}	$^4A_1$	493.2	492.5	-0.7
$Co(HCO_3)_2$	C_2	^4B	1169.5	1153.0	-16.5
$Co(HCO_3)(OH)$	C_s	$^4A'$	770.1	762.8	-7.3
$NiCO_3$	C_{2v}	$^3B_1$	480.5	478.9	-1.6
$Ni(HCO_3)_2$	C_2	^3B	1162.8	1139.0	-23.9
$Ni(HCO_3)(OH)$	C_s	$^3A''$	768.6	756.2	-12.4
$NiCO_3$	C_{2v}	$^1A_1$	498.7	481.3	-17.5
$Ni(HCO_3)_2$	C_{2h}	^1A_g	1165.4	1138.5	-26.9
$CuCO_3$	C_{2v}	$^2B_2$	466.6	464.9	-1.7
$Cu(HCO_3)_2$	C_{2h}	^2A_g	1134.8	1116.4	-18.4
$Cu(HCO_3)(OH)$	C_1	^2A	736.5	727.9	-8.6
$ZnCO_3$	C_{2v}	$^1A_1$	440.9	426.3	-14.6
$Zn(HCO_3)_2$	C_2	^1A	1125.8	1096.7	-29.1
$Zn(HCO_3)(OH)$	C_s	$^1A'$	733.3	713.1	-20.1
$CdCO_3$	C_{2v}	$^1A_1$	421.9	410.1	-11.8
$Cd(HCO_3)_2$	C_2	^1A	1103.8	1076.7	-27.1
$Cd(HCO_3)(OH)$	C_s	$^1A'$	708.8	690.8	-18.0

[a] B3LYP – CCSD(T)

Table A3.26. Contributions to total atomization energy at the CCSD(T) level.

Molecules	Sym	State	$\Delta E_{n=aD}$	$\Delta E_{n=aT}$	$\Delta E_{n=aQ}$	$\Delta E_{CBS-DTQ}$	ΔE_{SR}	ΔE_{CV}	ΔE_{ZPE}	ΔE_{SO}	$\Sigma D_{0,\,0K}$
$MnCO_3$	C_{2v}	$^6A_1$	457.6	485.9	496.2	502.2	-1.3	0.8	-9.9	-0.8	491.0
$Mn(HCO_3)_2$	C_2	^6A	1118.1	1176.5	1197.1	1209.0	-2.0	2.1	-36.1	-1.5	1171.5
$Mn(HCO_3)(OH)$	C_s	$^6A'$	743.3	780.5	793.9	801.6	-1.6	1.1	-25.7	-1.0	774.5
$Fe(HCO_3)_2$	C_{2h}	^5A_g	1120.5	1178.9	1199.5	1211.3	-2.1	2.5	-36.0	-2.7	1173.0
$CoCO_3$	C_{2v}	$^4A_1$	459.5	487.4	497.6	503.5	-1.4	1.1	-10.0	-3.0	490.2
$Co(HCO_3)_2$	C_2	^4B	1114.2	1173.0	1193.5	1205.3	-2.1	2.5	-36.3	-3.8	1165.7
$Co(HCO_3)(OH)$	C_s	$^4A'$	738.4	775.7	788.9	796.5	-1.6	1.3	-26.1	-3.2	766.9
$NiCO_3$	C_{2v}	$^3B_1$	456.2	483.7	493.8	499.6	-1.4	1.1	-10.0	-3.5	485.8
$Ni(HCO_3)_2$	C_2	^3B	1107.8	1166.7	1187.3	1199.1	-2.3	2.5	-36.5	-4.3	1158.5
$Ni(HCO_3)(OH)$	C_s	$^3A''$	736.4	774.2	787.5	795.2	-2.0	1.6	-26.2	-3.8	764.8
$NiCO_3$	C_{2v}	$^1A_1$	462.2	491.5	502.1	508.3	-1.8	2.6	-10.3	-3.5	495.2
$Ni(HCO_3)_2$	C_{2h}	^1A_g	1106.3	1167.5	1188.7	1200.9	-3.1	4.8	-37.2	-4.3	1161.1
$CuCO_3$	C_{2v}	$^2B_2$	436.8	462.1	470.9	475.9	-1.0	1.3	-9.6	-0.8	465.9
$Cu(HCO_3)_2$	C_{2h}	^2A_g	1083.9	1140.6	1159.7	1170.7	-2.3	3.0	-36.5	-1.5	1133.3
$Cu(HCO_3)(OH)$	C_1	^2A	708.9	744.5	756.3	763.1	-1.7	1.5	-26.4	-1.0	735.6
$ZnCO_3$	C_{2v}	$^1A_1$	409.1	435.9	445.6	451.3	-1.3	0.6	-9.7	-0.8	440.1
$Zn(HCO_3)_2$	C_2	^1A	1072.5	1129.8	1150.2	1161.9	-2.4	2.5	-36.3	-1.5	1124.3
$Zn(HCO_3)(OH)$	C_s	$^1A'$	702.9	739.5	752.5	760.0	-1.7	1.1	-26.1	-1.0	732.3

Table A3.27. Electronic energies at the CCSD(T) level with aD, aT and aQ basis sets and that extropolated to the complete basis set limit.

Molecule	Symm	State	aD	aT	aQ	CBS
$MnCO_3$	C_{2v}	$^6A_1$	-366.553827	-366.800634	-366.878413	-366.922445
$Mn(HCO_3)_2$	C_2	^6A	-631.146539	-631.618888	-631.767380	-631.851403
$Mn(HCO_3)(OH)$	C_s	$^6A'$	-442.933346	-443.248579	-443.347831	-443.404009
$Fe(HCO_3)_2$	C_{2h}	^5A_g	-650.588256	-651.073749	-651.227267	-651.314233
$CoCO_3$	C_{2v}	$^4A_1$	-407.835080	-408.106616	-408.194943	-408.245250
$Co(HCO_3)_2$	C_2	^4B	-672.418613	-672.916975	-673.076009	-673.166259
$Co(HCO_3)(OH)$	C_s	$^4A'$	-484.203805	-484.544565	-484.654198	-484.716511
$NiCO_3$	C_{2v}	$^3B_1$	-432.177649	-432.462821	-432.557006	-432.610804
$Ni(HCO_3)_2$	C_2	^3B	-696.756242	-697.269169	-697.434257	-697.528096
$Ni(HCO_3)(OH)$	C_s	$^3A''$	-508.548368	-508.904187	-509.020108	-509.086152
$NiCO_3$	C_{2v}	$^1A_1$	-432.187170	-432.475329	-432.570354	-432.624616
$Ni(HCO_3)_2$	C_{2h}	^1A_g	-696.753831	-697.270357	-697.436509	-697.530944
$CuCO_3$	C_{2v}	$^2B_2$	-459.821819	-460.114654	-460.213380	-460.269983
$Cu(HCO_3)_2$	C_{2h}	^2A_g	-724.393339	-724.913750	-725.083254	-725.179822
$Cu(HCO_3)(OH)$	C_1	^2A	-536.179745	-536.543139	-536.663342	-536.732020
$ZnCO_3$	C_{2v}	$^1A_1$	-489.589309	-489.889771	-489.992942	-490.052286
$Zn(HCO_3)_2$	C_2	^1A	-754.186720	-754.713444	-754.887751	-754.987349
$Zn(HCO_3)(OH)$	C_s	$^1A'$	-565.981680	-566.352002	-566.477023	-566.548720
Mn	$D_{\infty h}$	$^6\Sigma^+_g$	-103.283018	-103.308038	-103.315474	-103.319634
Co	$D_{\infty h}$	$^4\Sigma^+_g$	-144.561371	-144.611695	-144.629819	-144.640330
Ni	$D_{\infty h}$	$^3\Sigma^+_g$	-168.909158	-168.973804	-168.997966	-169.012064
Cu	$D_{\infty h}$	$^2\Sigma^+_g$	-196.584267	-196.659997	-196.690844	-196.709080
Zn	$D_{\infty h}$	$^1\Sigma^+_g$	-226.395844	-226.476879	-226.510619	-226.530627
C	$D_{\infty h}$	$^3\Sigma^-_g$	-37.764803	-37.781729	-37.786775	-37.789599
O	$D_{\infty h}$	$^3\Sigma^-_g$	-74.925570	-74.978823	-74.995132	-75.004312
H	$D_{\infty h}$	$^2\Sigma^+_g$	-0.499334	-0.499821	-0.499948	-0.500017

[a] The scalar-relativistic correction was calculated at the CI-SD/aT(-PP) level, the same as those in the previous paper for Fe complex.

Table A3.28. Electronic energies for scalar relativistic effects and core-valence corrections at the CCSD(T) level, and the ZPE corrections at the B3LYP/aT level.

Molecule	Sym	State	aT-DK	awT, core	awT, valence	ZPE
$MnCO_3$	C_{2v}	$^6A_1$	-1421.180375	-367.468408	-366.823668	0.015757
$Mn(HCO_3)_2$	C_2	^6A	-1686.169266	-632.508524	-631.657355	0.057536
$Mn(HCO_3)(OH)$	C_s	$^6A'$	-1497.680191	-443.973524	-443.275736	0.040966
$Fe(HCO_3)_2$	C_{2h}	^5A_g	[a]	-651.971313[b]	-651.110762[b]	0.057423
$CoCO_3$	C_{2v}	$^4A_1$	-1655.796456	-408.798697	-408.138162	0.015892
$Co(HCO_3)_2$	C_2	^4B	-1920.777374	-673.831150	-672.963883	0.057790
$Co(HCO_3)(OH)$	C_s	$^4A'$	-1732.286371	-485.293509	-484.580054	0.041611
$NiCO_3$	C_{2v}	$^3B_1$	-1783.075669	-433.160377	-432.498942	0.015905
$Ni(HCO_3)_2$	C_2	^3B	-2048.052358	-698.188825	-697.320779	0.058189
$Ni(HCO_3)(OH)$	C_s	$^3A''$	-1859.568472	-509.659207	-508.944465	0.041819
$NiCO_3$	C_{2v}	$^1A_1$	-1783.087524	-433.175711	-432.511874	0.016455
$Ni(HCO_3)_2$	C_{2h}	^1A_g	-2048.052277	-698.194308	-697.322530	0.059346
$CuCO_3$	C_{2v}	$^2B_2$	-1917.227027	-460.803643	-460.153551	0.015235
$Cu(HCO_3)_2$	C_{2h}	^2A_g	-2182.195771	-725.825481	-724.968321	0.058189
$Cu(HCO_3)(OH)$	C_1	^2A	-1457.163598	-537.289209	-536.586308	0.042017
$ZnCO_3$	C_{2v}	$^1A_1$	-2058.321828	-490.571445	-489.931654	0.015416
$Zn(HCO_3)_2$	C_2	^1A	-2323.315453	-755.618147	-754.770909	0.057783
$Zn(HCO_3)(OH)$	C_s	$^1A'$	-2134.835618	-567.091231	-566.398103	0.041670
Mn	$D_{\infty h}$	$^6\Sigma^+_g$	-1157.518172	-103.753688	-103.314631	
Co	$D_{\infty h}$	$^4\Sigma^+_g$	-1392.132042	-145.081757	-144.627338	
Ni	$D_{\infty h}$	$^3\Sigma^+_g$	-1519.417238	-169.449513	-168.994275	
Cu	$D_{\infty h}$	$^2\Sigma^+_g$	-1653.602334	-197.127382	-196.683830	
Zn	$D_{\infty h}$	$^1\Sigma^+_g$	-1794.739298	-226.937312	-226.502907	
C	$D_{\infty h}$	$^3\Sigma^-_g$	-37.796689	-37.830303	-37.783498	
O	$D_{\infty h}$	$^3\Sigma^-_g$	-75.031069	-75.036051	-74.983514	
H	$D_{\infty h}$	$^2\Sigma^+_g$	-0.499828	-0.499821	-0.499821	

[a] The scalar-relativistic correction was calculated at the CI-SD/aT(-PP) level, the same as those in the previous paper for Fe complex. [b] The cc-pwCVTZ(-PP) basis set was used.

Table A3.29. Electronic energies for higher energy structures at the CCSD(T)/aD level.

Molecules	Symm	State	aD
$MnCO_3$	C_{2v}	$^4B_2$	-366.494758
$Mn(HCO_3)_2$	C_{2h}	^4A_g	-631.075086
$Mn(HCO_3)(OH)$	C_1	^4A	-442.848987
$MnCO_3$	C_{2v}	$^2A_2$	-366.436122
$Mn(HCO_3)_2$ 1	C_{2v}	$^2A_2$	-631.007677
$Mn(HCO_3)_2$ 2	C_{2h}	^2B_g	-631.012298
$Mn(HCO_3)(OH)$	C_1	^2A	-442.795069
$CoCO_3$	C_{2v}	$^6B_2$	-407.745139
$Co(HCO_3)_2$	C_2	^6A	-408.036238
$Co(HCO_3)(OH)$	C_1	^6A	-672.262810
$CoCO_3$	C_{2v}	$^2A_2$	-407.817946
$Co(HCO_3)_2$	C_{2h}	^2B_g	-672.389812
$Co(HCO_3)(OH)$	C_s	^2B	-484.161208
$Ni(HCO_3)(OH)$	C_1	^1A	-508.522803

Table A3.30. Electronic energies (au) with DFT functionals for $MnCO_3$, $Mn(HCO_3)_2$, $Mn(HCO_3)(OH)$, $CoCO_3$, $Co(HCO_3)_2$ and $Co(HCO_3)(OH)$.

Functionals	$MnCO_3$	$Mn(HCO_3)_2$	$Mn(HCO_3)(OH)$	$CoCO_3$	$Co(HCO_3)_2$	$Co(HCO_3)(OH)$
PW91	-367.745642	-632.908883	-444.275446	-409.158354	-674.314064	-485.677512
BP86	-367.835774	-633.077162	-444.391315	-409.253483	-674.487154	-485.798150
M06	-367.622016	-632.741946	-444.144987	-409.010655	-674.125270	-485.542777
PBE	-367.493994	-632.456815	-443.964636	-408.890613	-673.845750	-485.350862
PBE0	-367.447480	-632.419944	-443.929354	-408.814299	-673.781816	-485.265398
B3LYP	-367.769123	-633.016034	-444.333772	-409.159528	-674.400006	-485.691411
HSE06	-367.468931	-632.464805	-443.957899	-408.834637	-673.825525	-485.292899
τ-HCTH	-368.070953	-633.230311	-444.610187	-409.601286	-674.742138	-486.126129
ωB97X	-367.660340	-632.854430	-444.209841	-409.055394	-674.243492	-485.597738
ωB97X-D	-367.653043	-632.822970	-444.196545	-409.043479	-674.208753	-485.579394

Table A3.31. Electronic energies (au) with DFT functionals for $NiCO_3$, $Ni(HCO_3)_2$, $Ni(HCO_3)(OH)$. $CuCO_3$, $Cu(HCO_3)_2$ and $Cu(HCO_3)(OH)$.

Functionals	$NiCO_3$	$Ni(HCO_3)_2$	$Ni(HCO_3)(OH)$	$CuCO_3$	$Cu(HCO_3)_2$	$Cu(HCO_3)(OH)$
PW91	-433.564866	-698.721089	-510.082308	-461.244191	-726.391361	-537.757256
BP86	-433.661662	-698.895858	-510.204045	-461.341337	-726.566669	-537.880195
M06	-433.414269	-698.518257	-509.927713	-461.105794	-726.200479	-537.606860
PBE	-433.289245	-698.244331	-509.747434	-460.960156	-725.906552	-537.413955
PBE0	-433.184091	-698.146380	-509.669582	-460.861774	-725.816960	-537.324753
B3LYP	-433.542077	-698.778448	-510.104218	-461.222726	-726.450020	-537.767273
HSE06	-433.203961	-698.190231	-509.696541	-460.881057	-725.859713	-537.351253
τ-HCTH	-434.092579	-699.224722	-510.605604	-461.861403	-726.986454	-538.371249
ωB97X	-433.440035	-698.621209	-509.989172	-461.127696	-726.300371	-537.656926
ωB97X-D	-433.424019	-698.583779	-509.969584	-461.110864	-726.261624	-537.634683

Table A3.32. Electronic energies (au) with DFT functionals for $ZnCO_3$, $Zn(HCO_3)_2$, $Zn(HCO_3)(OH)$.

Functionals	$ZnCO_3$	$Zn(HCO_3)_2$	$Zn(HCO_3)(OH)$
PW91	-491.002338	-756.180802	-567.553018
BP86	-491.100592	-756.357016	-567.676699
M06	-490.886618	-756.014617	-567.428955
PBE	-490.710472	-755.688292	-567.201908
PBE0	-490.632362	-755.615736	-567.132515
B3LYP	-490.991976	-756.248782	-567.574056
HSE06	-490.650515	-755.657225	-567.157698
τ-HCTH	-491.705276	-756.873354	-568.263222
ωB97X	-490.908600	-756.111377	-567.476456
ωB97X-D	-490.890961	-756.071522	-567.453421

Table A3.33. Electronic energies (au) with DFT functionals for transition metal atoms.

Functionals	Mn	Co	Ni	Cu	Zn
PW91	-103.854049	-145.251141	-169.679951	-197.395256	-227.219948
BP86	-103.871981	-145.292154	-169.703888	-197.419007	-227.245938
M06	-103.747605	-145.196012	-169.622909	-197.346226	-227.189993
PBE	-103.799548	-145.196557	-169.600157	-197.306944	-227.123715
PBE0	-103.722856	-145.142970	-169.536377	-197.237025	-227.061261
B3LYP	-103.837493	-145.217156	-169.617079	-197.324970	-227.155621
HSE06	-103.721573	-145.140431	-169.533965	-197.233138	-227.057726
τ-HCTH	-104.218804	-145.723894	-170.225618	-198.039473	-227.944568
ωB97X	-103.711097	-145.155184	-169.572703	-197.291306	-227.130699
ωB97X-D	-103.735469	-145.168489	-169.586876	-197.300159	-227.138984

Table A3.34. Atomic ionic radii from Emsley, J. *The Elements, 2nd Ed.,* Clarendon Press, Oxford, 1994.

Metal	standard ionic radii
Mg	0.78
Ca	1.06
Mn	0.91
Fe	0.82
Co	0.82
Ni	0.78
Cu	0.72
Zn	0.83
Cd	1.03

Table A3.35. Average absolute $\Delta H_{f,0K}$ errors of DFT functionals compared to FPD results in kcal/mol for MCO_3, $M(HCO_3)_2$, $M(HCO_3)(OH)$ (M = Mg, Ca, Mn, Fe, Co, Ni, Cu, Zn and Cd).

Functional	Mg, Ca, Fe, Cd
PW91	43.9
BP86	39.5
M06	12.5
PBE	41.3
PBE0	7.0
B3LYP	13.3
HSE06	8.1
τ-HCTH	7.2
ωB97X	7.1
ωB97X-D	6.9

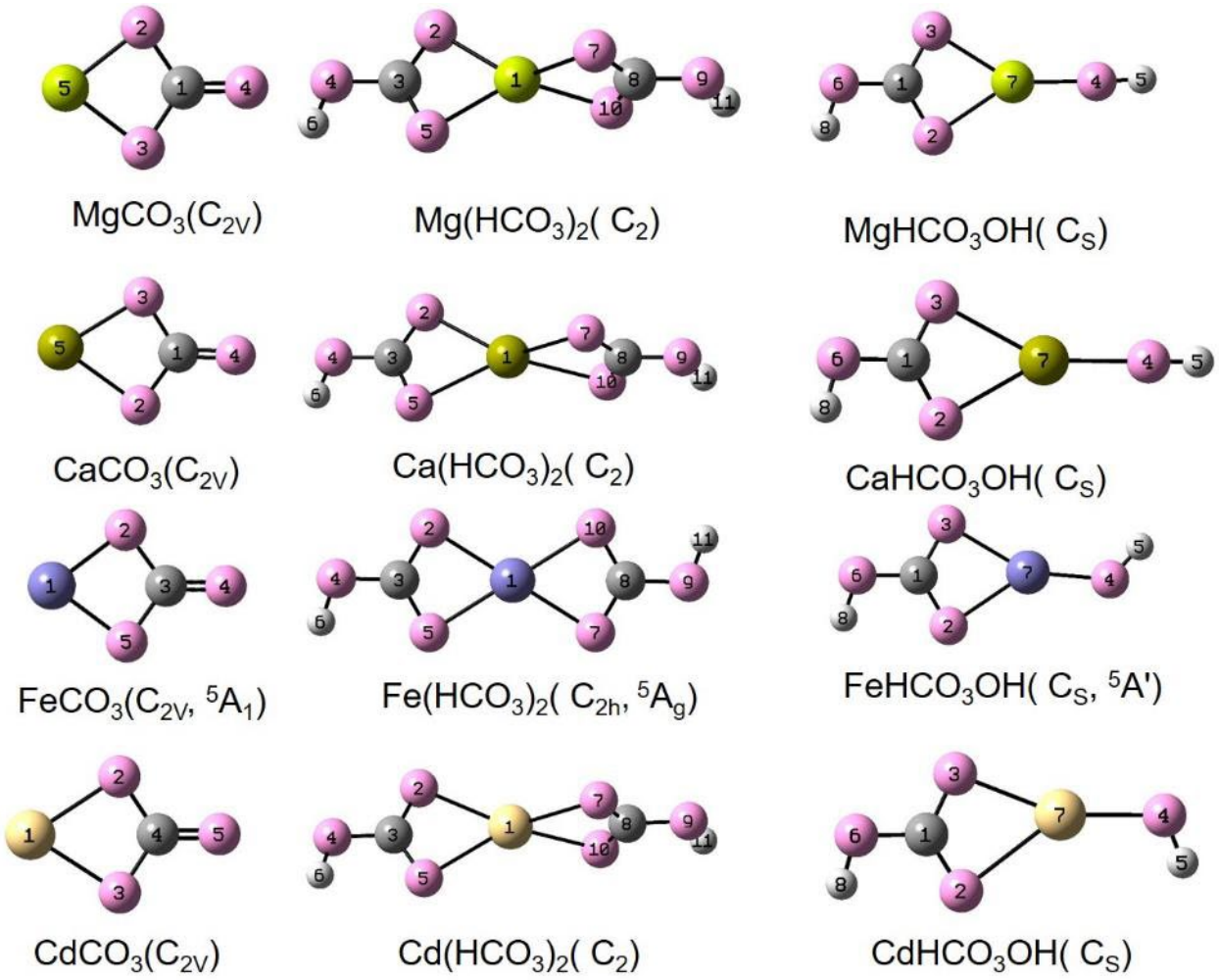

Figure A3.1. Numbering schemes for MCO_3, $M(HCO_3)_2$ and $MHCO_3OH$ (M = Mg, Ca, Fe and Cd) (O = pink, H = white, C = gray, Mg = green, Ca = dark green, Fe = blue purple, Cd = egg white).

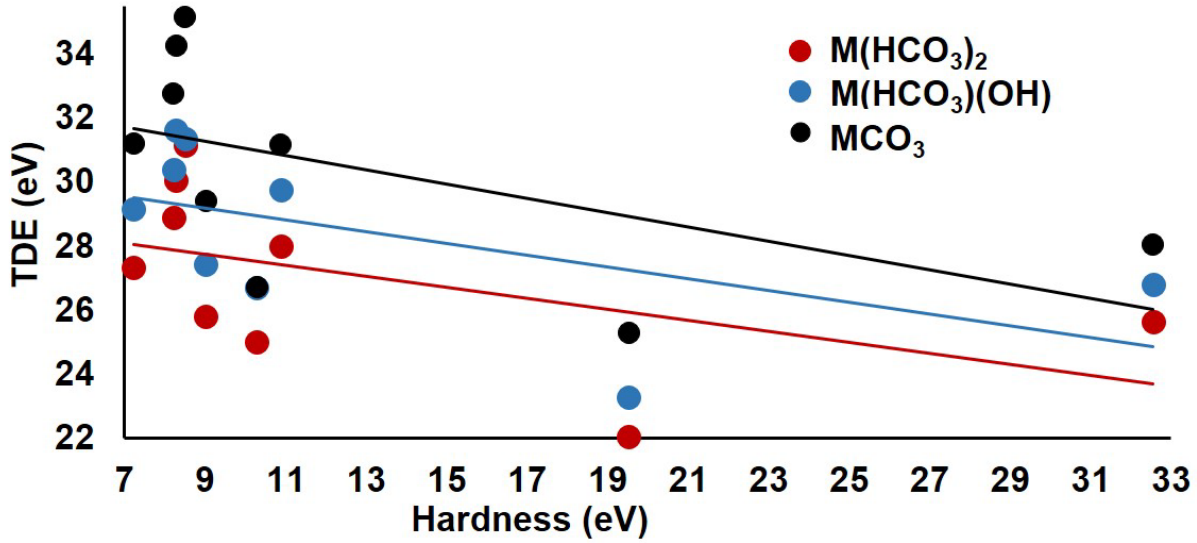

Figure A3.2. TDE of MCO_3, $M(HCO_3)_2$ and $M(HCO_3)(OH)$ at 0K vs. hardness of metal cations. The linear fit equations for MCO_3, $M(HCO_3)_2$ and $M(HCO_3)(OH)$ are $y = -0.22x + 32.78$ ($R^2 = 0.30$), $y = -0.13x + 28.80$ ($R^2 = 0.26$), and $y = -0.18x + 30.36$ ($R^2 = 0.32$), respectively.

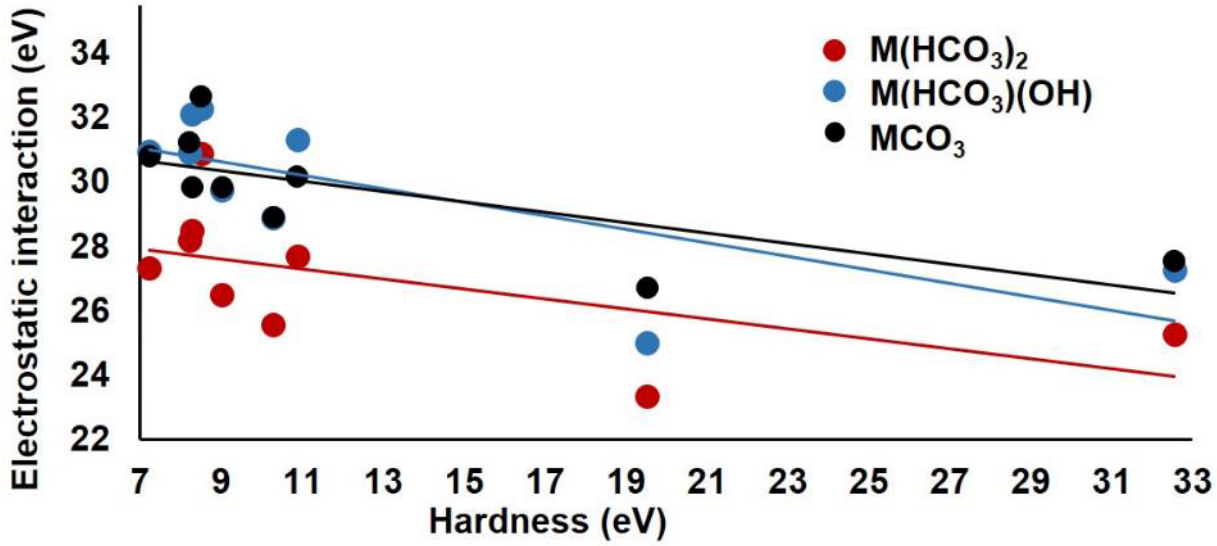

Figure A3.3. Electrostatic interaction of MCO_3, $M(HCO_3)_2$ and $M(HCO_3)(OH)$ at 0K vs. hardness of metal cations. The linear fit equations for MCO_3, $M(HCO_3)_2$ and $M(HCO_3)(OH)$ are $y = -0.16x + 31.31$ ($R^2 = 0.53$), $y = -0.16x + 28.52$ ($R^2 = 0.35$), and $y = -0.21x + 32.02$ ($R^2 = 0.52$), respectively.

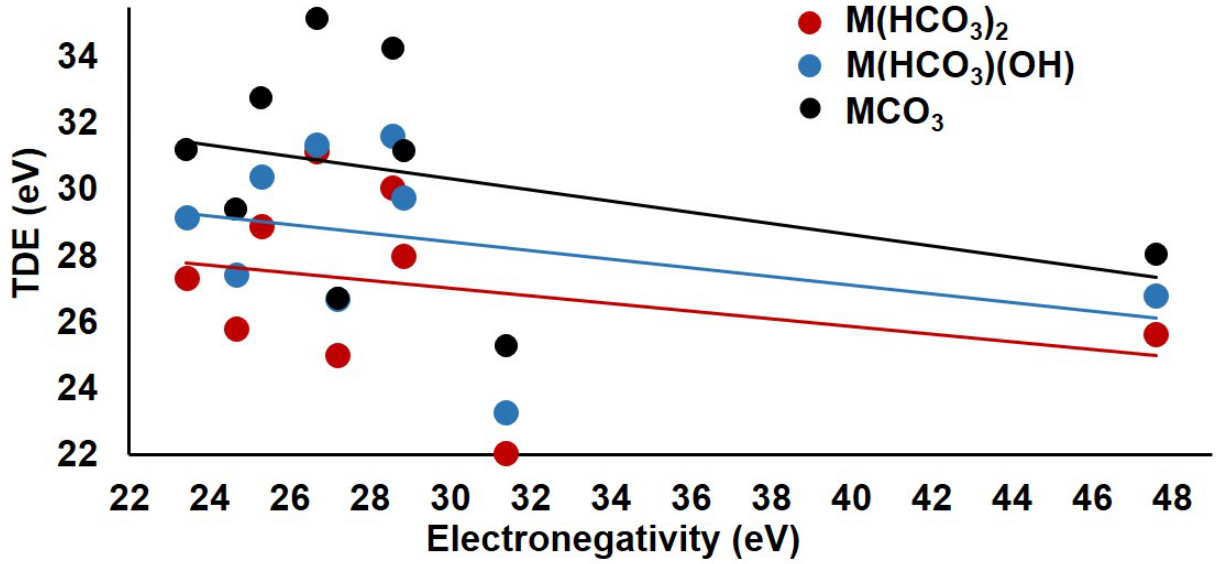

Figure A3.4. TDE of MCO_3, $M(HCO_3)_2$ and $M(HCO_3)(OH)$ at 0K vs. electronegativity of metal cations. The linear fit equations for MCO_3, $M(HCO_3)_2$ and $M(HCO_3)(OH)$ are $y = -0.17x + 34.89$ ($R^2 = 0.13$), $y = -0.12x + 29.98$ ($R^2 = 0.09$), and $y = -0.13x + 31.84$ ($R^2 = 0.12$), respectively.

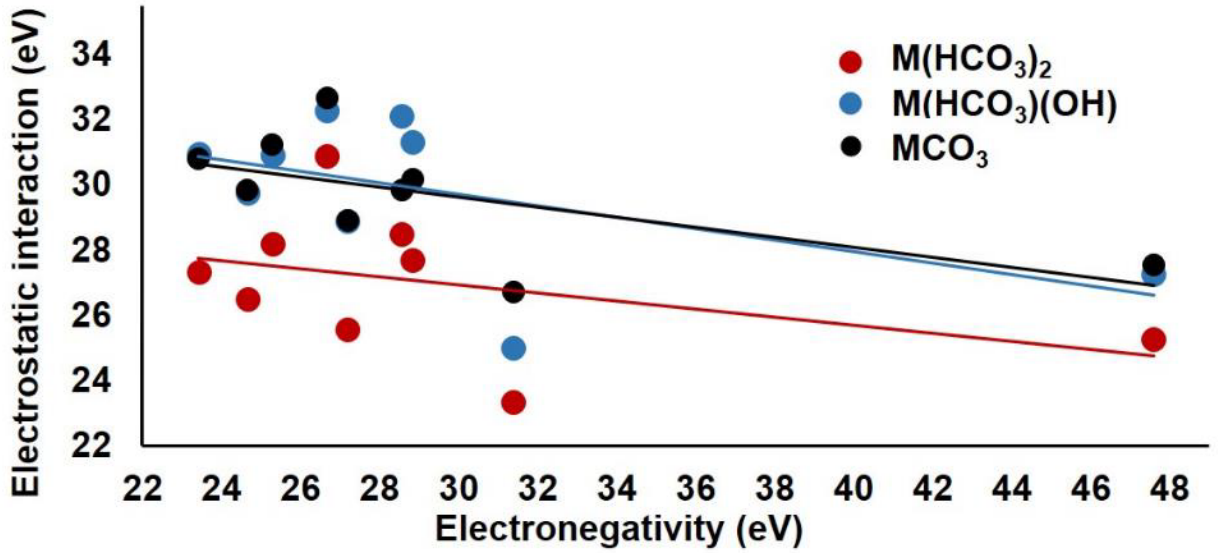

Figure A3.5. Electrostatic interaction of MCO_3, $M(HCO_3)_2$ and $M(HCO_3)(OH)$ at 0K vs. electronegativity of metal cations. The linear fit equations for MCO_3, $M(HCO_3)_2$ and $M(HCO_3)(OH)$ are $y = -0.16x + 33.80$ ($R^2 = 0.38$), $y = -0.12x + 30.18$ ($R^2 = 0.17$), and $y = -0.18x + 34.51$ ($R^2 = 0.28$), respectively.

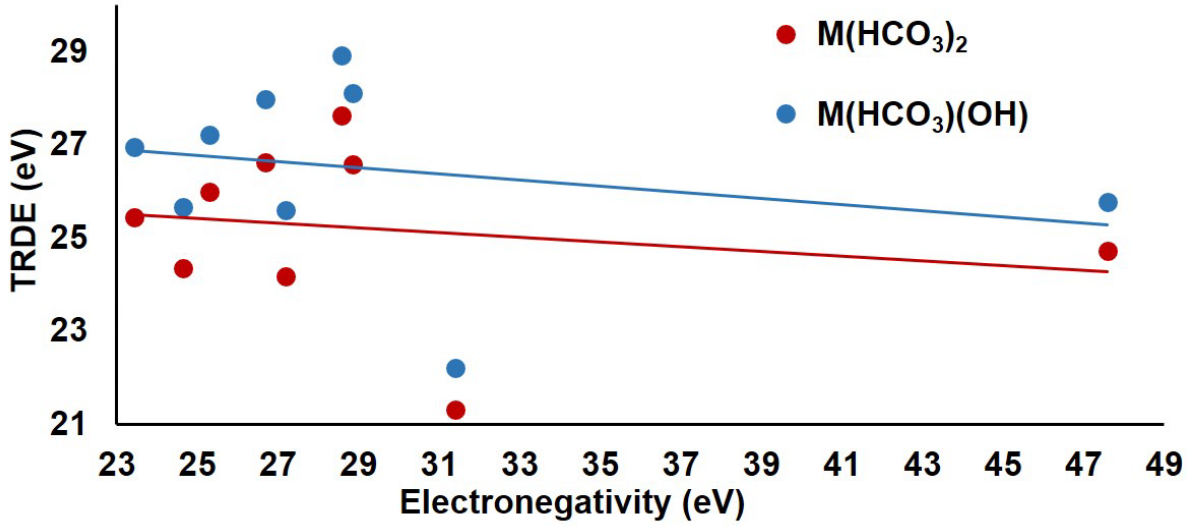

Figure A3.6. TRDE of MCO_3, $M(HCO_3)_2$ and $M(HCO_3)(OH)$ at 0K vs. electronegativity of metal cations. The linear fit equations for $M(HCO_3)_2$ and $M(HCO_3)(OH)$ are $y = -0.05x + 26.70$ ($R^2 = 0.04$), $y = -0.07x + 28.44$ ($R^2 = 0.06$), respectively.

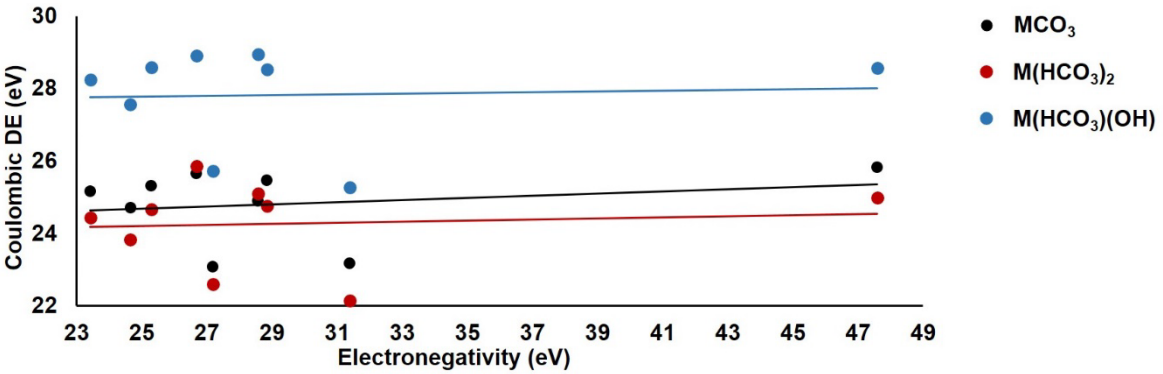

Figure A3.7. Coulombic DE of MCO_3, $M(HCO_3)_2$ and $M(HCO_3)(OH)$ at 0K vs. electronegativity of metal cations. The linear fit equations for MCO_3, $M(HCO_3)_2$ and $M(HCO_3)(OH)$ are $y = 0.03x + 23.95$ ($R^2 = 0.05$), $y = 0.02x + 23.81$ ($R^2 = 0.01$), and $y = 0.01x + 27.51$ ($R^2 = 0.00$), respectively.

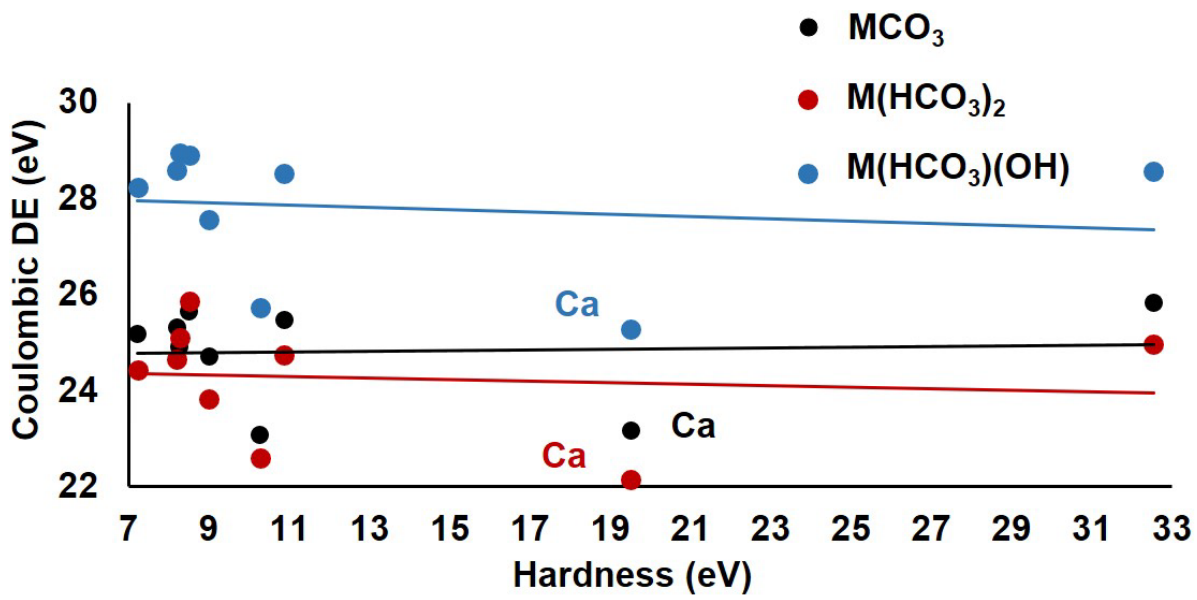

Figure A3.8. Coulombic DE of MCO_3, $M(HCO_3)_2$ and $M(HCO_3)(OH)$ at 0K vs. hardness of metal cations. The linear fit equations for MCO_3, $M(HCO_3)_2$ and $M(HCO_3)(OH)$ are $y = -0.01x + 24.72$ ($R^2 = 0.00$), $y = -0.02x + 24.46$ ($R^2 = 0.01$), and $y = -0.02x + 28.12$ ($R^2 = 0.02$), respectively.

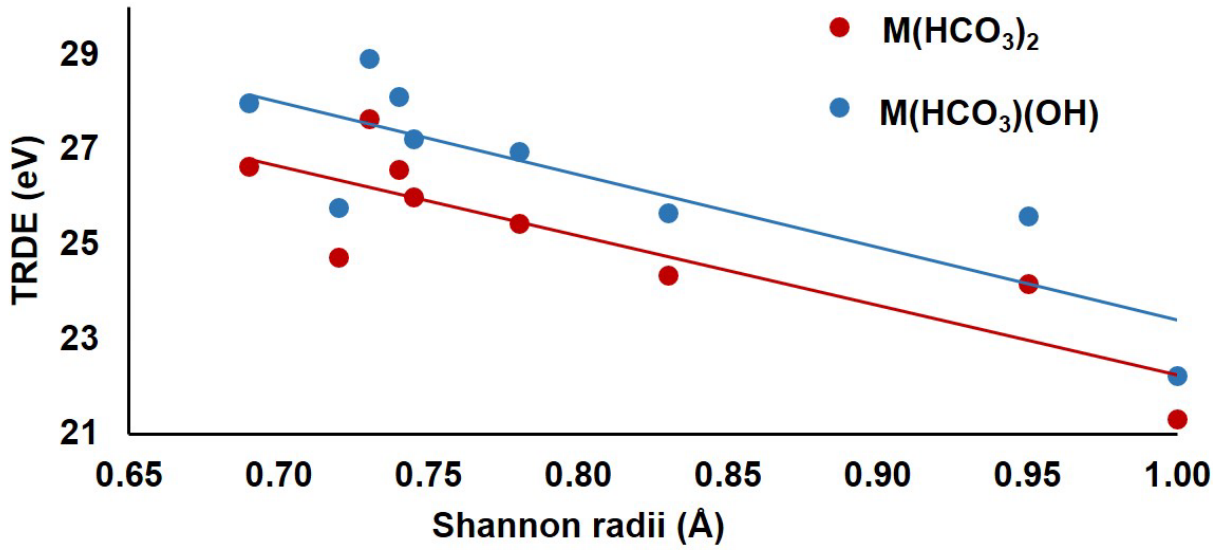

Figure A3.9. TRDE of $M(HCO_3)_2$ and $M(HCO_3)(OH)$ at 0K vs. hardness of metal cations . The linear fit equations for $M(HCO_3)_2$ and $M(HCO_3)(OH)$ are $y = -0.10x + 26.47$ ($R^2 = 0.20$), and $y = -0.12x + 27.96$ ($R^2 = 0.23$), respectively.

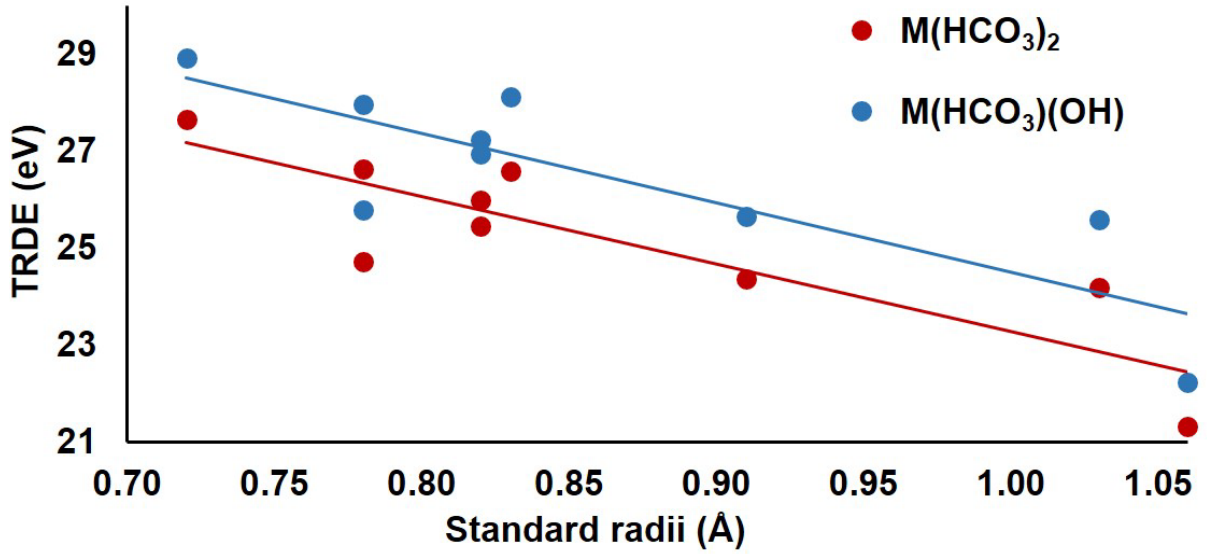

Figure A3.10. TRDE of $M(HCO_3)_2$ and $M(HCO_3)(OH)$ at 0K vs. Standard radii of metal cations. The linear fit equations for $M(HCO_3)_2$ and $M(HCO_3)(OH)$ are $y = -13.87x + 37.15$ ($R^2 = 0.75$) and $y = -14.33x + 38.84$ and ($R^2 = 0.70$), respectively.

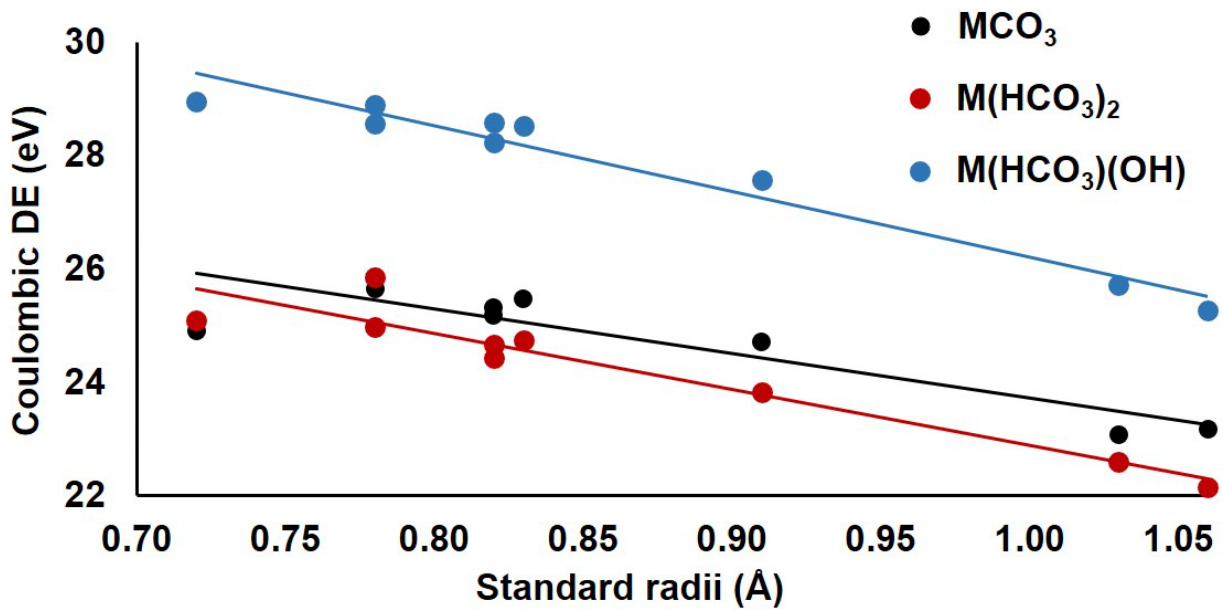

Figure A3.11. Coulombic dissociation energy of MCO_3, $M(HCO_3)_2$ and $M(HCO_3)(OH)$ at 0K vs. Standard radii of metal cations. The linear fit equations for MCO_3, $M(HCO_3)_2$ and $M(HCO_3)(OH)$ are $y = -7.83x + 31.55$ ($R^2 = 0.80$), $y = -9.87x + 32.76$ ($R^2 = 0.91$), and $y = -11.59x + 37.80$ ($R^2 = 0.95$), respectively.

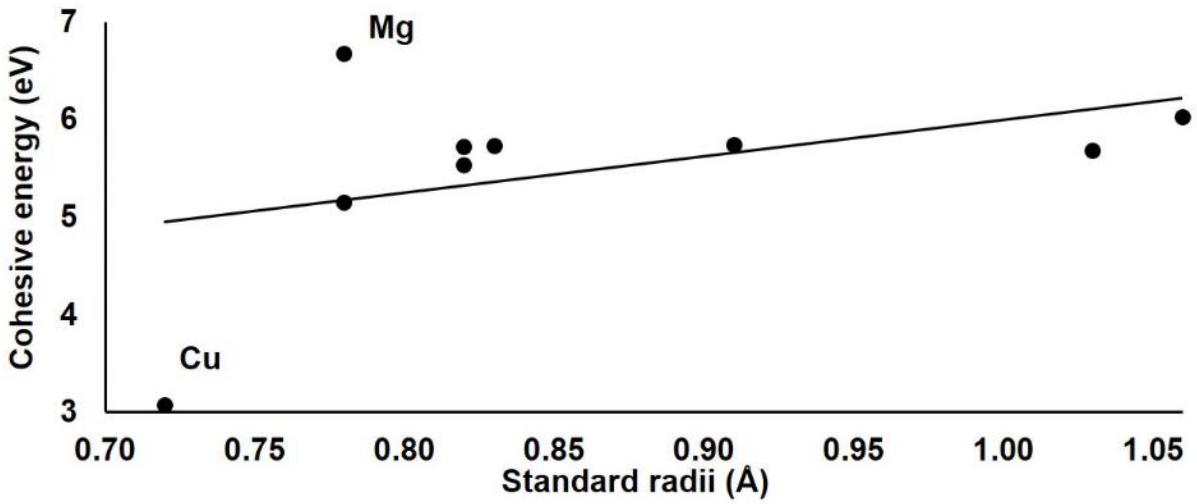

Figure A3.12. Plot of cohesive energy of MCO_3 at 0K vs. Standard radii of metal cations. The linear fit equation is y = 3.74x + 2.26 (R^2 =0.19).

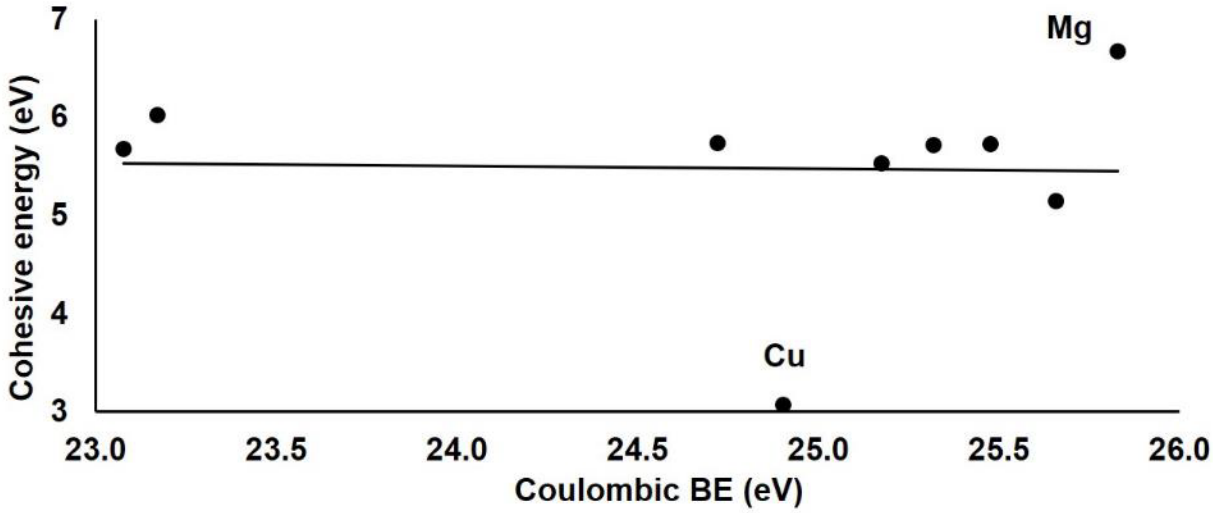

Figure A3.13. Plot of cohesive energy of MCO_3 at 0K vs. Cloulombic BE. The linear fit equation is y = -0.03x + 6.18 (R^2 =0.00).

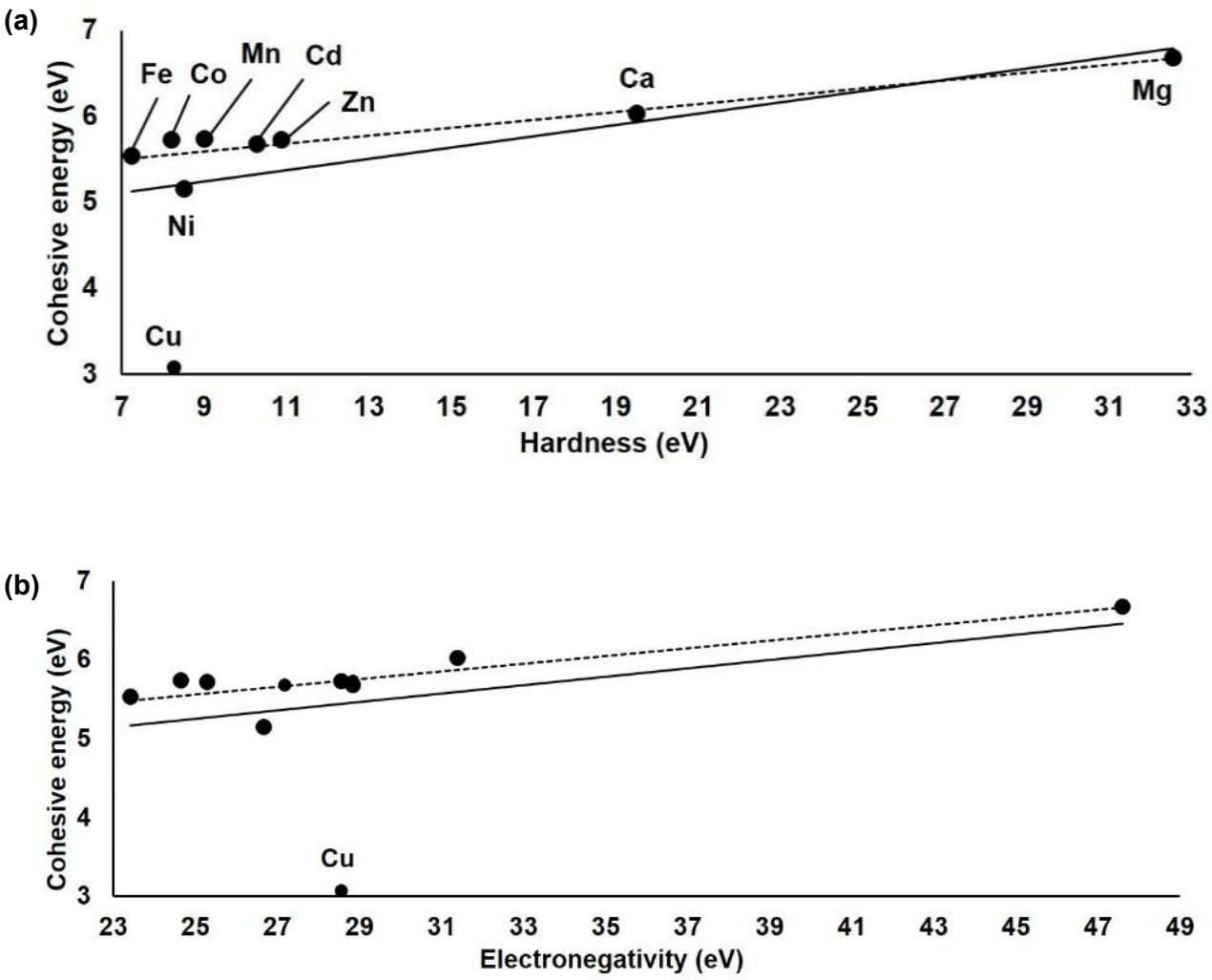

Figure A3.14. Cohesive energy of MCO_3 at 0K vs. (a) hardness and (b) electronegativity of metal cations (a) The linear fit equation for all the metals (solid line) is $y = 0.07x + 4.64$($R^2 = 0.30$). The linear fit equation for all the metals except for Cu (squared dot line) is $y = 0.05x + 5.17$ ($R^2 = 0.83$). (b) The linear fit equation for all the metals (solid line) is $y = 0.05x + 3.91$ ($R^2 = 0.15$). The linear fit equation for all the metals except for Cu (squared dot line) is $y = 0.05x + 4.33$ ($R^2 = 0.75$).

CHAPTER 4

ROLE OF CARBONATE BINDING IN THE ADDITION OF CO_2 TO $M_3O_6^-$ for M = Ti, Zr, Hf: THE IMPORTANCE OF CORE-VALENCE CORRELATION IN PREDICTING ISOMER ENERGETICS

Introduction

There is significant interest in the capture and conversion of CO_2 using a variety of species ranging from metal-organic frameworks (MOFs),[1,2,3] to zeolites,[4,5] to metal oxides as well as amines. It is also possible to fix CO_2 by mineral carbonation[6,7,8] leading to the formation of an insoluble carbonate salt. The reverse of such process in the subsurface is also being studied to demonstrate that CO_2 will remain sequestered. Transition metal oxides (MO_x) have also been explored as sorbents and catalysts for the sequestration and conversion of CO_2. Examples include the use of TiO_2 and ZrO_2 as photocatalysts for the conversion of CO_2, often with other reagents such as H_2.[9,10,11,12,13,14,15,16,17]

It has recently been reported[18] that CO_2 addition to the $Ti_3O_6^-$ anion forms a novel carbonate structure with tridentate binding in the center of the cluster (**Center**) with 3 Ti-O bonds (Figure 4.1) to 3 different Ti atoms. In the correction to their manuscript,[19] it was reported that at the CCSD(T)/def2-TZVP level, the **Center** anionic structure is predicted to be the most stable structure, with **3-4Ta** higher in energy by 1.2 kcal/mol, **3-4Bc** higher in energy by 3.9 kcal/mol, and **3-4Ba** higher in energy by 4.8 kcal/mol (all $\Delta H(0K)$). The best fit of the spectrum derived from a low fluence IRPD D_2-tagged anion was assigned to **3-4Bc**. With higher fluence, features consistent with transitions of the **Center** structure were observed. In their correction,

the authors noted that for neutral $Ti_3O_6CO_2$, the **Center** structure is 7.6 kcal/mol above **3-4Ba**, the lowest energy structure.

We had previously reported[20] that the lowest energy neutral structure for binding CO_2 to M_3O_6 (M = Ti and Zr) is the tridentate bridging carbonate (**3-4Ba**) where the CO_2 carbon binds to a bridging oxygen, the CO_2 oxygens are bound to the 2 metal centers with M=O terminal bonds (Figure 4.1). For the M = Hf trimer, the lowest energy structure with a terminal bidentate carbonate (**3-4Ta**) (Figure 4.1) is 6 kcal/mol lower in energy than the bridge tridentate structure (**Center**). Our original calculations were performed at the CCSD(T)/aug-cc-pVTZ(C, O)/aug-cc-pwCVTZ-PP(M) level using B3LYP/aug-cc-pVDZ(-PP) optimized geometries. Zero point energies and thermal corrections were taken from the B3LYP calculations.

In the current work, we expand our prior reported calculations on the neutral metal and carbonate clusters to include the anionic metal and carbonate clusters for M_3O_6 with M = Ti, Zr and Hf. We include the **Center** structure for the neutral to compare to our previous work.

Computational Methods

The geometries were optimized and vibrational frequencies were calculated at the density functional theory (DFT)[21] level with the B3LYP exchange-correlation functional [22,23] and aug-cc-pVDZ basis sets for C and O[24,25] and aug-cc-pVDZ-PP basis sets for the metals.[26,27,28] For Ti, there are 10 electrons in the PP, for Zr, there are 28 electrons in the PP and for Hf, there are 60 electrons in the PP. The density functional theory calculations were performed using the Gaussian16 software package.[29] The optimized geometries were then used in single point R/RCCSD(T) (neutral) or R/UCCSD(T) (anion) calculations[30,31,32,33,34,35,36] with the aug-cc-pVDZ basis sets for C and O and weighted core, aug-cc-pwCVDZ-PP[26,27,28] basis sets for the metals. In addition, for the neutrals, close shell species, calculations were performed at the

CCSD(T) level using aug-cc-pVTZ(C and O)/aug-cc-pwCVTZ-PP(Ti, Zr, and Hf) basis sets. These basis sets are labeled at aD and aT. For these CCSD(T) calculations, the 1s electrons for the C and O are not correlated. The CCSD(T) calculations were performed using the MOLPRO 2015.1 program package.[37,38]

Results and Discussion

Isomeric Energies The relative energies of both neutral and anionic carbonate M_3O_6 clusters are reported in Table 4.1. For the neutral Ti cluster, we predict that the bridge tridentate binding motif structure, **3-4Ba** is lower in energy by 9.6 kcal/mol at the aD level and by 7.9 kcal/mol at the aT level; the latter value is completely consistent with the prior corrected results.[19] There is no change in the energy difference between our lowest bridge tridentate **3-4Ba** and the new added **Center** tridentate binding motifs when the single point CCSD(T) calculations were done by changing the starting orbital[39] for the CCSD(T) calculations to those generated using the PW91 generalized gradient exchange-correlation functional.[40,41,42] We note that there are five chemisorbed isomers for the neutral Ti cluster that are 6.2 to 9.3 kcal/mol higher in energy than **3-4Ba**.

For the anion, $Ti_3O_6CO_2^-$, we predict that the terminal bidentate carbonate structure (**3-4Ta**) is 0.2 kcal/mol more stable the **Center** tridentate structure at the R/UCCSD(T)/aD level using B3LYP/aug-cc-pVDZ(-PP) optimized geometry and by 0.4 kcal/mol using the ωb97xD[43]/aug-cc-pVTZ(-PP) optimized geometry. This differs from the previously reported corrected results[19] for the anion where the **Center** structure is the lowest energy isomer with the terminal bidentate structure **3-4Ta** higher in energy by 1.2 kcal/mol. We predict that structure **3-4Bc** is 2.9 kcal/mol higher in energy than **3-4Ta**. The prior corrected results[19] predicted an energy difference of 3.9 kcal/mol for **3-4Bc** relative to the **Center** structure. We also predict that

3-4Ba is 3.2 kcal/mol higher in energy than **3-4Ta** and the prior corrected results[19] predicted an energy difference of 4.8 kcal/mol. Our results suggest that multiple structures for the anion could be observed in the experiment. In contrast, only one structure would be observed for the neutral at equilibrium at 298 K. We note that the def2-TZVP basis set used for the single point CCSD(T) previously reported corrected results[19] is smaller than the aug-cc-pVDZ(C,O)/aug-cc-pwCVDZ-PP(Ti) basis sets used in the current work and def2-TZVP does not have diffuse functions to account for anionic behavior.

As previously reported,[20] weighted core basis sets are necessary for the Group 4 metals, especially for M = Ti, as correlation of the outer core, ms^2 and mp^6 electrons (where m = 3, 4, and 5 for Ti, Zr, and Hf, respectively) is necessary to obtain correct binding energies, or in this case, relative energies, due to the low-lying O 2s orbital energies potentially mixing with the electrons in these outer core orbitals of the metal (see Table 4.2). For the anion carbonates, the use of cc-pVDZ-PP or cc-pVTZ-PP basis sets for M = Ti with no core-valence correction predicts the **Center** structure to be lower in energy by ~2 kcal/mol than the **3-4Ta** for both B3LYP and ωb97xD starting optimized geometries for the CCSD(T) single point calculations. Thus, core-valence corrections are indeed important for even getting the correct relative energies of the isomeric structures for these titanium oxide clusters.

Our calculated infrared spectra are given in the Supporting Information for the $Ti_3O_6CO_2^-$ isomers. It is clear that the calculated spectra for **3-4Ba** and **Center** are not consistent with the experimental low fluence spectrum even though there is the possibility of the **Center** structure energetically. As noted previously, the spectrum for **3-4Bc** is in reasonable agreement with experiment. We also note that the calculated IR spectrum for lowest energy structure **3-4Ta** is in good agreement with most of the experimental spectral peak positions, although the intensities

are not in as good agreement. However, the experimental spectrum does not exclude the presence of this isomer.

As part of the current work, we included the **Center** tridentate binding structure for the neutral structures for M = Zr and Hf as well. For Zr, the bridge tridentate structure **3-4Ba** is more stable by 15.8 kcal/mol at the CCSD(T)/aD level and by 13.6 kcal/mol at the CCSD(T)/aT level than the **Center** tridentate structure. For Hf, the lowest energy structure is the terminal bidentate (**3-4Ta**) with the **Center** tridentate structure higher in energy by 20.1 and 18.5 kcal/mol at the CCSD(T) aD and aT levels, respectively.

We performed similar calculations for CO_2 addition to $M_3O_6^-$ for M = Zr and Hf. The anion structures of M = Zr and Hf are similar to those of M = Ti shown in Figure 4.1. The terminal bidentate structure (**3-4Ta**) is the most stable structure for all three metals at the CCSD(T)/aD level of theory. For Zr, the next lowest energy structure is **3-4Ba**, 4.2 kcal/mol higher in energy. The **Center** structure is 11.9 kcal/mol higher in energy than **3-4Ta** for Zr. For Hf, the **3-4Ba** structure is 11.2 kcal/mol higher in energy than **3-4Ta** and the **Center** tridentate structure is 18.0 kcal/mol higher in energy. The results clearly show that the **Center** structure is not important for the heavier metals and only can play some role in the Ti trimer anion.

Spin Densities The spin densities for the lowest energy **3-4Ta** structures and **Center** structures for $M_3O_6CO_2^-$ and for $M_3O_6^-$ are shown in Figure 4.2. In all cases, the spin is localized on the initial unique metal so there is very little change in the spin density on chemisorption to the trimer anion.

Chemisorption binding energies Using our prior results for $M_3O_6^-$,[20] we can predict the chemisorption binding energy of CO_2 to the anions (Table 4.3). The CCSD(T)/aD binding energies at 298K for the most stable structures are 26, 41, and 47 kcal/mol for M = Ti, Zr, and

Hf, respectively. In contrast, the chemisorption binding energy to the neutral for the trimers are 23, 35, and 41 kcal/mol for M = Ti, Zr, and Hf, respectively at the at the same level of theory. The chemisorption binding energy of CO_2 to neutral M_3O_6 is also shown in Table 4.3.[20] The effect of using the larger aT basis sets is at most 2 kcal/mol for the binding energies for the neutral.

Adiabatic electron affinities The CCSD(T)/aD adiabatic electron affinities are calculated for the lowest energy neutral and anion $M_3O_6CO_2$ structures at 0K for M = Ti, Zr and Hf (Table 4.4). The lowest energy structure for $M_3O_6CO_2$ anions is the terminal bidentate structure (**3-4Ta**) and the lowest energy for the neutral is the bridge tridentate **3-4Ba** for M = Ti and Zr and the terminal bidentate structure **3-4Ta** for M = Hf. Thus, the adiabatic value for M = Hf will most closely resemble a vertical attachment/detachment process. For M = Ti and Zr, the vertical detachment and attachment processes are different from each other. The electron affinity of $M_3O_6CO_2$ are 0.15 to 0.21 eV larger than the electron affinity of M_3O_6 calculated at a comparable level.[44,45] The difference in electron affinities between the structures with and without CO_2 added increases from Ti to Zr by 0.01eV, and increases from Zr to Hf by 0.06 eV. The lowest electron affinity for the metal oxide and for the CO_2 added structure is predicted for M = Zr and the highest is for M = Hf so there is no real trend for the column. As shown above for the spin density, the addition of the CO_2 to the metal oxide cluster anion does not change the location of the additional spin even though the selected oxygen atoms are perturbed by the formation of the carbonate.

The vertical detachment energies using optimized **3-4Ta** structures of the anion and neutral for M = Ti and Zr are 3.33 and 3.08 eV, respectively. The vertical attachment energy for optimized **3-4Ba** structures of the anion and neutral for M = Ti and Zr are 2.90 and 2.76 eV,

respectively. The vertical electron affinities for the remaining structures are reported in the Supporting Information.

Conclusions

Coupled cluster (CCSD(T)) theory in conjunction with geometries optimized at the density functional theory level has been used to study the chemisorption of CO_2 to Group 4 neutral and anionic metal oxide M_3O_6 nanoclusters. The lowest energy structure for neutral $M_3O_6CO_2$ is **3-4Ba** for Ti and Zr, and **3-4Ta** for Hf, whereas for the anion $M_3O_6CO_2^-$, the lowest energy structure is **3-4Ta** for all three metals. For $M_3O_6CO_2^-$, the **Center** structure for M = Ti is essentially the same energy (within 0.5 kcal/mol) as that of **3-4Ta,** but the **Center** structure is significantly higher than **3-4Ta** by 12 and 18 kcal/mol for M = Zr and Hf, respectively. Weighted core basis sets are needed to make accurate predictions for the relative energies of these Group 4 metal oxide nanoclusters isomers because the lower-lying 2s orbital in O atom can mix with the outer core orbitals of the metal. The **Center** structure will not play any significant role in the neutral M_3O_6 clusters. Thus, the potential for finding a central bridging carbonate structure is possible only for $Ti_3O_6^-$, and consistent with the available experimental observations,[18,19] it is likely not to be the lowest energy structure. We note that the use of the B3LYP functional favors **3-4Ta** as the ground state for $Ti_3O_6CO_2^-$ over the **Center** structure and that the ωB97xD functional favors the **Center** structure over **3-4Ta**, both by ~ 2 kcal/mol. Thus, if density functional theory is to be used for calculating the relative isomeric energies, the choice of the functional is important. The electron affinities of the metal oxide cluster increase by only ~ 0.2 eV when CO_2 is chemisorbed to the cluster. The small change is consistent with the lack of change of spin density for the cluster with or without CO_2. The chemisorption energies for CO_2 addition show a slight increase from the neutral cluster to the anion.

Tables

Table 4.1. Calculated CCSD(T) relative energies, ΔH_{298K}, in kcal/mol.[a]

Molecule	**3-4Ba**		**3-4Ta**		**3-4Tb**		**3-4Bc**		**3-4Bb**		**Center**	
	aD	aT	aD	aT	aD	aT	aD	aT	aD	aT	aD	aT
$Ti_3O_6CO_2$	0.0	0.0	6.8	6.2	8.9	7.5	8.0	8.4	9.6	9.3	9.6	7.9
$Zr_3O_6CO_2$	0.0	0.0	3.1	2.9	9.3	8.2	17.0	16.8	15.2	14.5	15.8	13.6
$Hf_3O_6CO_2$	4.5	5.5	0.0	0.0	6.2	4.6	21.9	22.5	19.5	20.0	20.1	18.5
$Ti_3O_6CO_2^-$	3.2		0.0		6.3		2.9		5.9		0.2	
$Zr_3O_6CO_2^-$	4.2		0.0		11.6		17.3		14.2		11.9	
$Hf_3O_6CO_2^-$	11.2		0.0		12.5		26.3		20.8		18.0	

[a] aD = aug-cc-pVDZ(C and O)/aug-cc-pwCVDZ-PP(Ti, Zr, and Hf) basis sets and aT = aug-cc-pVTZ(C and O)/aug-cc-pwCVTZ-PP(Ti, Zr, and Hf) basis sets

Table 4.2. Calculated relative energies at different level of theory, ΔH_{298K}, in kcal/mol for the **3-4Ta** and **Center** isomers of $Ti_3O_6CO_2^-$.

CCSD(T)	Geometry	**3-4Ta**	**Center**
aug-cc-pVDZ(C,O)/aug-cc-pwCVDZ-PP(Ti)	B3LYP	0.0	0.2
aug-cc-pVDZ(C,O)/cc-pVDZ-PP(Ti)	B3LYP	2.2	0.0
aug-cc-pVDZ(-PP)	B3LYP	2.1	0.0
aug-cc-pVTZ(C,O)/cc-pVTZ-PP(Ti)	B3LYP	2.8	0.0
aug-cc-pVDZ(C,O)/cc-pVDZ-PP(Ti)	ωB97xD	2.2	0.0
aug-cc-pVDZ(C,O)/aug-cc-pwCVDZ-PP(Ti)	ωB97xD	0.0	0.4

Table 4.3. Calculated CCSD(T) enthalpies at 298K (ΔH_{298K}) in kcal/mol for the CO_2 binding to Group 4 M_3O_6 neutral and anion nanoclusters.[a]

Cluster	**3-4Ta**		**3-4Tb**		**3-4Ba**		**3-4Bb**		**3-4Bc**		**Center**	
	aD	aT	aD	aT	aD	aT	aD	aT	aD	aT	aD	aT
Ti_3O_6	-15.4	-16.4	-13.3	-15.2	-22.2	-22.6	-12.7	-13.3	-14.2	-14.3	-12.6	-14.8
Zr_3O_6	-32.1	-32.2	-26.0	-26.9	-35.2	-35.1	-20.0	-20.6	-18.2	-18.3	-19.4	-21.5
Hf_3O_6	-40.1	-41.5	-33.9	-36.9	-35.6	-36.0	-20.5	-21.5	-18.2	-19.0	-20.0	-23.0
$Ti_3O_6^-$	-26.4		-20.1		-23.2		-20.5		-23.5		-26.1	
$Zr_3O_6^-$	-40.8		-29.2		-36.6		-26.6		-23.5		-28.9	
$Hf_3O_6^-$	-47.1		-34.6		-35.9		-26.3		-20.8		-29.1	

[a] aD = aug-cc-pVDZ(C and O)/aug-cc-pwCVDZ-PP(Ti, Zr, and Hf) basis sets and aT = aug-cc-pVTZ(C and O)/aug-cc-pwCVTZ-PP(Ti, Zr, and Hf) basis sets

Table 4.4 Calculated CCSD(T) adiabatic electron affinities for $M_3O_6CO_2$ and M_3O_6 in eV at 0K.

M	M_3O_6[a]	$Mi_3O_6CO_2$	ΔEA
Ti	2.89 (2.88)[44]	3.04	0.15
Zr	2.79 (2.72)[45]	2.95	0.16
Hf	3.18 (3.12)[45]	3.39	0.21

[a] Values at the aD level. Values in parentheses at the aT level.

Figures

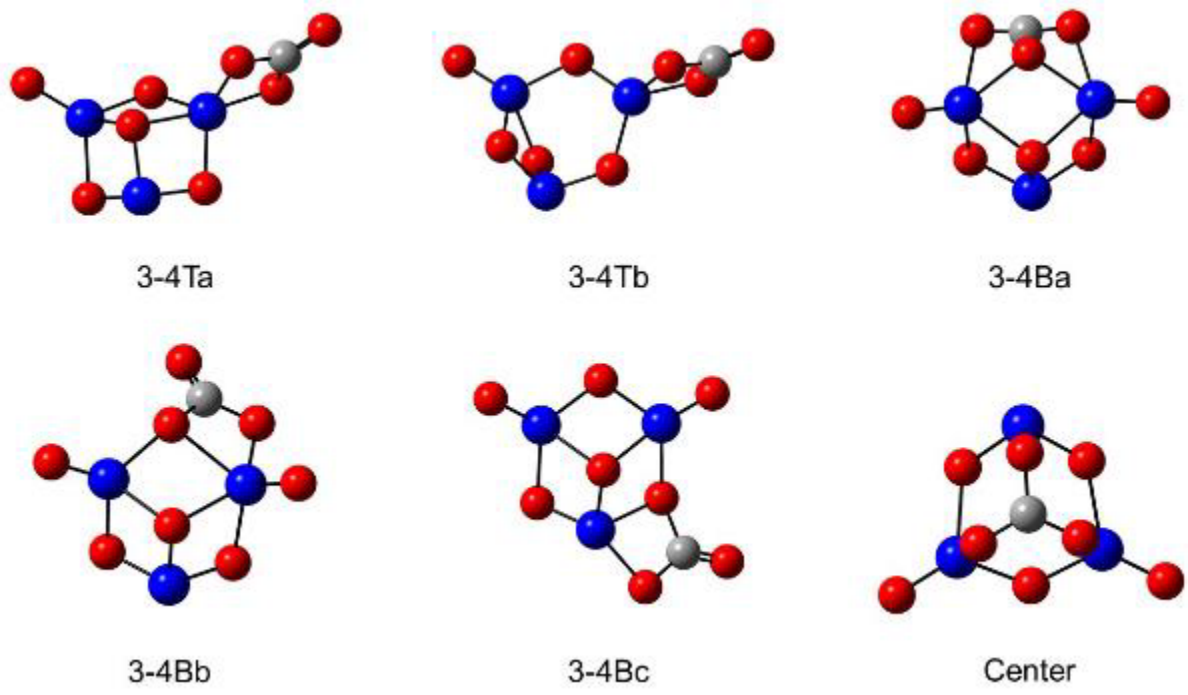

Figure 4.1. Group 4 $Ti_3O_6CO_2$ neutral and anion chemisorbed nanoclusters. For a given geometry, the neutral and anion have similar structures. Terminal chemisorbed bidentate carbonate clusters (**3-4Ta** and **3-4Tb**), bridge chemisorbed tridentate carbonate clusters (**3-4Ba**), bridge chemisorbed bidentate carbonate clusters (**3-4Bb** and **3-4Bc**) and center chemisorbed tridentate carbonate cluster (**Center**). Metals are blue, oxygen is red and carbon is gray.

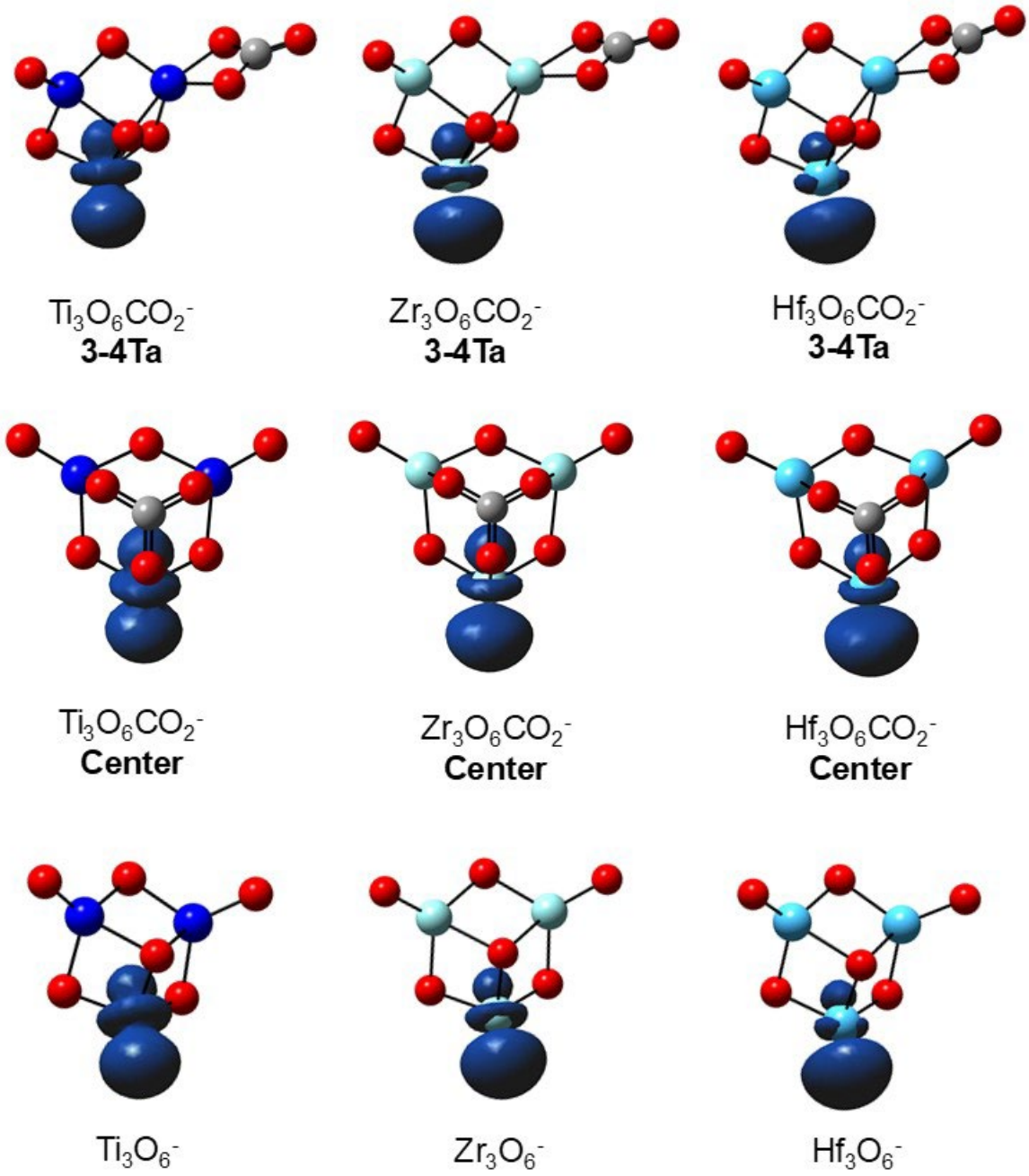

Figure 4.2. Spin densities for the lowest energy structure **3-4Ta** (top row), **Center** (middle row) for Group 4 $M_3O_6CO_2^-$ and $M_3O_6^-$ (bottom row) nanoclusters for M = Ti, Zr and Hf (Contour = 0.005).

References

[1] Caskey, S. R.; Wong-Foy, A. G.; Matzger, A. J. Dramatic Tuning of Carbon Dioxide Uptake Via Metal Substitution in a Coordination Polymer with Cylindrical Pores. *J. Am. Chem. Soc*. **2008**, *130*, 10870-10871.

[2] Bao, Z.; Yu, L.; Ren, Q.; Lu, X.; Deng, S. Adsorption of CO_2 and CH_4 on a Magnesium-Based Metal Organic Framework. *J. Colloid Interface Sci.* **2011**, *353*, 549-556.

[3] Yan, X.; Komarneni, S.; Zhang, Z.; Yan, Z. Extremely Enhanced CO_2 Uptake by HKUST-1 Metal-Organic Framework Via a Simple Chemical Treatment. *Microporous Mesoporous Mater.* **2014**, *183*, 69-73.

[4] Choi, S.; Drese, J. H.; Jones, C. W., Adsorbent Materials for Carbon Dioxide Capture from Large Anthropogenic Point Sources. *ChemSusChem* **2009**, *2*, 796-854.

[5] D'Alessandro, D. M.; Smit, B.; Long, J. R., Carbon Dioxide Capture: Prospects for New Materials. *Angew. Chem. Int. Ed.* **2010**, *49*, 6058-6082.

[6] Gupta, H.; Fan, L.-S., Carbonation-Calcination Cycle Using High Reactivity Calcium Oxide for Carbon Dioxide Separation from Flue Gas. *Ind. Eng. Chem. Res.* **2002**, *41*, 4035-4042.

[7] Yu, F.-C.; Phalak, N.; Sun, Z.; Fan, L.-S., Activation Strategies for Calcium-Based Sorbents for CO_2 Capture: A Perspective. *Ind. Eng. Chem. Res.* **2012**, *51*, 2133-2142.

[8] Chen, H.; Zhao, C.; Yu, W., Calcium-Based Sorbent Doped with Attapulgite for CO_2 Capture. *Appl. Energy* **2013**, *112*, 67-74.

[9] Inoue, T.; Fujishima, A.; Konishi, S.; Honda, K., Photoelectrocatalytic Reduction of Carbon Dioxide in Aqueous Suspensions of Semiconductor Powders. *Nature* **1979**, *277*, 637-638.

[10] Ong, W.-J.; Tan, L.-L.; Chai, S.-P.; Yong, S.-T., Facet-Dependent Photocatalytic Properties of TiO_2-Based Composites for Energy Conversion and Environmental Remediation. *ChemSusChem* **2014**, *7*, 690-719.

[11] Ong, W.-J.; Tan, L.-L.; Chai, S.-P.; Yong, S.-T.; Mohamed, A. R., Self-Assembly of Nitrogen-Doped TiO_2 with Exposed {001} Facets on a Graphene Scaffold as Photo-Active Hybrid Nanostructures for Reduction of Carbon Dioxide to Methane. *Nano Res.* **2014**, *7*, 1528-1547.

[12] Tan, L.-L.; Ong, W.-J.; Chai, S.-P.; Mohamed, A. R., Band Gap Engineered, Oxygen-Rich TiO_2 for Visible Light Induced Photocatalytic Reduction of CO_2. *Chem. Commun.* **2014**, *50*, 6923-6926.

[13] Yuan, L.; Han, C.; Pagliaro, M.; Xu, Y.-J., Origin of Enhancing the Photocatalytic Performance of TiO_2 for Artificial Photoreduction of CO_2 Through a SiO_2 Coating Strategy. *J. Phys. Chem. C* **2016**, *120*, 265-273.

[14] Kohno, Y.; Tanaka, T.; Funabiki, T.; Yoshida, S., Photoreduction of Carbon Dioxide with Hydrogen Over ZrO_2. *Chem. Commun.* **1997**, 841-842.

[15] Kohno, Y.; Tanaka, T.; Funabiki, T.; Yoshida, S., Identification and Reactivity of a Surface Intermediate in the Photoreduction of CO_2 with H_2 Over ZrO_2. *J. Chem. Soc., Faraday Trans.* **1998**, *94*, 1875-1880.

[16] Kohno, Y.; Tanaka, T.; Funabiki, T.; Yoshida, S., Photoreduction of CO_2 with H_2 over ZrO_2. A Study of Interaction of Hydrogen with Photoexcited CO_2. *Phys. Chem. Chem. Phys.* **2000**, *2*, 2635-2639.

[17] Kohno, Y.; Tanaka, T.; Funabiki, T.; Yoshida, S., Reaction Mechanism in the Photoreduction of CO_2 with CH_4 Over ZrO_2. *Phys. Chem. Chem. Phys*. **2000**, *2*, 5302-5307.

[18] Debnath, S.; Song, X.; Fagiani, M. R.; Weichman, M. L.; Gao, M.; Maeda, S.; Taketsugu, T.; Schöllkopf, W.; Lyalin, A.; Neumark, D. M.; et al. CO_2 Adsorption on $Ti_3O_6^-$: A Novel Carbonate Binding Motif. *J. Phys. Chem. C* **2019**, *123*, 8439−8446.

[19] Debnath, S.;Song, X.; Fagiani, M. R.; Weichman, M. L.; Gao, M.; Maeda, S.; Taketsugu, T.; Schöllkopf, W.; Lyalin, A.; Neumark, D. M.; et al. Correction to "CO_2 Adsorption on $Ti_3O_6^-$: A Novel Carbonate Binding Motif". *J. Phys. Chem. C* **2020**, *124*, 6952-6953.

[20] Flores, L. A.; Murphy, J. G.; Copeland, W. B.; Dixon, D. A. Reaction of CO_2 with Groups 4 and 6 Transition Metal Oxide Clusters. *J. Phys. Chem. A* **2017**, *121*, 8719-8727.

[21] Parr, R. G.; Yang, W. *Density-Functional Theory of Atoms and Molecules*. Oxford University Press: New York, 1989.

[22] Becke, A. D. Density-Functional Thermochemistry. III. The Role of Exact Exchange. *J. Chem. Phys.* **1993**, *98*, 5648-5652.

[23] Lee, C.; Yang, W.; Parr, R. G., Development of the Colle-Salvetti Correlation-Energy Formula into a Functional of the Electron Density. *Phys. Rev. B* **1988**, *37*, 785-789.

[24] Dunning, T.H., Jr. Gaussian Basis Sets for Use in Correlated Molecular Calculations. I. The Atoms Boron Through Neon and Hydrogen. *J. Chem. Phys*. **1989**, *90*, 1007-1023.

[25] Kendall, R. A.; Dunning, T. H.; Harrison, R. J. Electron Affinities of the First-Row Atoms Revisited. Systematic Basis Sets and Wave Functions. *J. Chem. Phys.* **1992**, *96*, 6796-6806.

[26] Li, S.; Hennigan, J. M.; Dixon, D. A.; Peterson, K. A. Accurate Thermochemistry for Transition Metal Oxide Clusters. *J. Phys. Chem. A* **2009**, *113*, 7861-7877.

[27] Figgen, D.; Peterson, K. A.; Dolg, M.; Stoll, H. Energy-consistent Pseudopotentials and Correlation Consistent Basis Sets for the 5d Elements Hf–Pt. *J. Chem. Phys.* **2009**, *130*, 164108-1-164108-12.

[28] Peterson, K. A.; Figgen, D.; Dolg, M.; Stoll, H. Energy-Consistent Relativistic Pseudopotentials and Correlation Consistent Basis Sets for the 4d Elements Y–Pd. *J. Chem. Phys.* **2007**, *126*, 124101/1-124101/12.

[29] Frisch, M. J.; Trucks, G. W.; Schlegel, H. B.; Scuseria, G. E.; Robb, M. A.; Cheeseman, J. R.; Scalmani, G.; Barone, V.; Petersson, G. A.; Nakatsuji, H.; et al. Gaussian 16, Revision A.03, Gaussian, Inc., Wallingford CT, 2016.

[30] Purvis, G. D., III; Bartlett, R. J. A Full Coupled Cluster Singles and Doubles Model: The Inclusion of Disconnected Triples. *J. Chem. Phys.* **1982**, *76*, 1910-1918.

[31] Raghavachari, K.; Truck, G.W.; Pople, J.A.; Head-Gordon, M. A Fifth-Order Perturbation Comparison of Electron Correlation Theories. *Chem. Phys. Lett*. **1989**, *157*, 479-483.

[32] Watts, J. D.; Gauss, J.; Bartlett, R. J. Coupled-Cluster Methods with Noniterative Triple Excitations for Restricted Open Shell Hartree-Fock and Other General Single Determinant Reference Functions. Energies and Analytical Gradients. *J. Chem. Phys.* **1993**, *98*, 8718-8733.

[33] Bartlett, R. J.; Musial, M. Coupled Cluster Theory in Quantum Chemistry. *Rev. Mod. Phys.* **2007**, *79*, 291-352.

[34] Knowles, P. J.; Hampel, C.; Werner, H.-J. Coupled Cluster Theory for High Spin, Open Shell Reference Wave Functions. *J. Chem. Phys*. **1993**, *99*, 5219-5227.

[35] Knowles, P. J.; Hampel, C.; Werner, H.-J. Erratum: Coupled Cluster Theory for High Spin, Open Shell Reference Wave Functions. *J. Chem. Phys*. **2000**, *112*, 3106-3107.

[36] Deegan, M. J. O.; Knowles, P. J. Perturbative Corrections to Account for Triple Excitations in Closed and Open Shell Coupled Cluster Theories. *Chem. Phys. Lett*. **1994**, *227*, 321-327.

[37] Werner H.-J.; Knowles, P. J.; Knizia, G.; Manby, F. R.; Schütz, M.; Celani, P.; Györffy, W.; Kats, T.; Korona, T.; Lindh, R.; et al. MOLPRO, version 2015.1, a package of *ab initio* programs, See http://www.molpro.net. Accessed March 1, 2016.

[38] Werner H.-J.; Knowles, P. J.; Knizia, G.; Manby, F. R.; Schütz, M. Molpro: A General-Purpose Quantum Chemistry Program Package. *WIREs Comput. Mol. Sci.* **2012**, *2*, 242-253.

[39] Fang, Z.; Lee, Z.; Peterson, K. A.; Dixon, D. A. Use of Improved Orbitals for CCSD(T) Calculations for Predicting Heats of Formation of Group IV and Group VI Metal Oxide Monomers and Dimers and UCl_6. *J. Chem. Theory Comput.* **2016**, *12*, 3583−3592

[40] Perdew, J. P.; Wang, Y. Accurate and Simple Analytic Representation of the Electron Gas Correlation Energy. *Phys. Rev. B* **1992**, *45*. 13244-13249.

[41] Burke, K.; Perdew, J. P.; Wang, Y. Mixing Exact Exchange with GGA: When to Say When. In *Electronic Density Functional Theory: Recent Progress and New Directions*. Dobson, J. F.; Vignale, G.; Das. M. P. Eds.; Plenum: New York, 1998; pp. 57-68.

[42] Burke, K.; Perdew, J. P.; Wang, Y. Derivation of a Generalized Gradient Approximation: The PW91 Density Functional in *Electronic Density Functional Theory: Recent Progress and New Directions*, Eds. Dobson, J.F.; Vignale, G.; Das M.P. Plenum, New York, 1997, pp. 81-122.

[43] Chai, J.-D.; Head-Gordon, M. Long-Range Corrected Hybrid Density Functionals with Damped Atom-Atom Dispersion Corrections. *Phys. Chem. Chem. Phys.,* **2008**, *10*, 6615-6620.

[44] Li, S.; Dixon, D. A. Molecular Structures and Energetics of the $(TiO_2)_n$ (n = 1-4) Clusters and Their Anions. *J. Phys. Chem. A* **2008**, *112*, 6646–6666.

[45] Li, S.; Dixon, D. A. Molecular Structures and Energetics of the $(ZrO_2)_n$ and $(HfO_2)_n$ (n = 1-4) Clusters and Their Anions. *J. Phys. Chem. A* **2010**, *114*, 2665–2683.

Table A4.1. Total energies (Hartrees) at the B3LYP/aug-cc-pVDZ(-PP) and CCSD(T)/aug-cc-pVDZ/aug-cc-pwCVDZ-PP and CCSD(T)/aug-cc-pVTZ/aug-cc-wc-pwCVTZ-PP levels.

Molecules	Enthalpies at 298K	Free Energies Correction at 298K	Electronic Energies		
	B3LYP/aD	B3LYP/aD	B3LYP/aD	CCSD(T)/aD	CCSD(T)/aT
CO_2	-188.599082	-0.009140	-188.614214	-188.185662	-188.340595
Ti_3O_6	-625.899442	-0.013213	-625.932877	-624.733531	-625.287042
$Ti_3O_6^-$	-626.013920	-0.014091	-626.046622	-624.837657	
Zr_3O_6	-592.693159	-0.018983	-592.724615	-591.386749	-591.946273
$Zr_3O_6^-$	-592.792667	-0.019770	-592.823598	-591.485594	
Hf_3O_6	-597.796988	-0.021266	-597.828237	-596.245325	-596.816532
$Hf_3O_6^-$	-597.909138	-0.022195	-597.939875	-596.358379	
$Ti_3O_6CO_2$ – 3-4Ba	-814.519375	-0.000992	-814.569819	-812.956469	-813.665607
$Ti_3O_6CO_2$ – 3-4Bb	-814.510857	-0.003427	-814.560875	-812.940825	-813.650266
$Ti_3O_6CO_2$ – 3-4Bc	-814.513853	-0.003648	-814.563684	-812.943031	-813.651626
$Ti_3O_6CO_2$ – 3-4Ta	-814.522010	-0.003379	-814.571884	-812.945087	-813.655098
$Ti_3O_6CO_2$ – 3-4Tb	-814.523628	-0.004861	-814.573333	-812.941500	-813.652923
$Ti_3O_6CO_2$ – Center	-814.512135	-0.001382	-814.562263	-812.940842	-813.652754
$Ti_3O_6CO_2^-$ – 3-4Ba	-814.635870	-0.002513	-814.685536	-813.062084	
$Ti_3O_6CO_2^-$ – 3-4Bb	-814.639729	-0.004432	-814.689167	-813.057615	
$Ti_3O_6CO_2^-$ – 3-4Bc	-814.646211	-0.004914	-814.695503	-813.062232	
$Ti_3O_6CO_2^-$ – 3-4Ta	-814.653222	-0.003988	-814.702556	-813.066866	
$Ti_3O_6CO_2^-$ – 3-4Tb	-814.649443	-0.005883	-814.698658	-813.056738	
$Ti_3O_6CO_2^-$ – Center	-814.649922	-0.002569	-814.699302	-813.066535	
$Zr_3O_6CO_2$ – 3-4Ba	-781.335423	-0.006433	-781.383969	-779.630529	-780.344747
$Zr_3O_6CO_2$ – 3-4Bb	-781.317833	-0.009157	-781.365981	-779.605917	-780.321259
$Zr_3O_6CO_2$ – 3-4Bc	-781.315010	-0.009469	-781.363017	-779.602901	-780.317425
$Zr_3O_6CO_2$ – 3-4Ta	-781.339061	-0.008549	-781.387113	-779.625066	-780.339631
$Zr_3O_6CO_2$ – 3-4Tb	-781.334969	-0.010926	-781.382778	-779.614994	-780.331033
$Zr_3O_6CO_2$ - Center	-781.319267	-0.007489	-781.367506	-779.605024	-780.322736

$Zr_3O_6CO_2^-$ – 3-4Ba	-781.438561	-0.007621	-781.486589	-779.731489	
$Zr_3O_6CO_2^-$ – 3-4Bb	-781.429417	-0.009878	-781.477144	-779.715311	
$Zr_3O_6CO_2^-$ – 3-4Bc	-781.427218	-0.010177	-781.474832	-779.710186	
$Zr_3O_6CO_2^-$ – 3-4Ta	-781.452680	-0.009470	-781.500318	-779.737796	
$Zr_3O_6CO_2^-$ – 3-4Tb	-781.441591	-0.011732	-781.489061	-779.719211	
$Zr_3O_6CO_2^-$ – Center	-781.437314	-0.008629	-781.484971	-779.718912	
$Hf_3O_6CO_2$ – 3-4Ba	-786.441142	-0.008633	-786.489494	-784.489729	-785.216534
$Hf_3O_6CO_2$ – 3-4Bb	-786.423224	-0.011305	-786.471150	-784.465275	-785.192978
$Hf_3O_6CO_2$ – 3-4Bc	-786.419057	-0.011677	-786.466801	-784.461397	-785.188827
$Hf_3O_6CO_2$ – 3-4Ta	-786.455431	-0.010937	-786.503265	-784.496336	-785.224783
$Hf_3O_6CO_2$ – 3-4Tb	-786.451828	-0.013254	-786.499433	-784.486284	-785.217184
$Hf_3O_6CO_2$ - Center	-786.425240	-0.009608	-786.473322	-784.464626	-785.195528
$Hf_3O_6CO_2^-$ – 3-4Ba	-786.554693	-0.009827	-786.602551	-784.603267	
$Hf_3O_6CO_2^-$ – 3-4Bb	-786.545991	-0.012122	-786.593536	-784.587671	
$Hf_3O_6CO_2^-$ – 3-4Bc	-786.539156	-0.012614	-786.586570	-784.578719	
$Hf_3O_6CO_2^-$ – 3-4Ta	-786.579128	-0.011691	-786.626605	-784.620726	
$Hf_3O_6CO_2^-$ – 3-4Tb	-786.566047	-0.014303	-786.613343	-784.600551	
$Hf_3O_6CO_2^-$ – Center	-786.552994	-0.010760	-786.600580	-784.592142	

Table A4.2. Total energies (Hartrees) at the ωb97xD/aug-cc-pVTZ(-PP) level and CCSD(T)/aug-cc-pVDZ/aug-cc-pwCVDZ-PP.

	Enthalpies at 298K	Free Energies Correction at 298K	Electronic Energies	
	ωb97xD /aT	ωb97xD /aT	ωb97xD /aT	CCSD(T)/aD
$Ti_3O_6CO_2$ – 3-4Ba	-814.391054	0.000439	-814.442384	-812.952815
$Ti_3O_6CO_2$ – Center	-814.384019	-0.000217	-814.435022	-812.937235
$Ti_3O_6CO_2^-$ – 3-4Ba	-814.500604	-0.000912	-814.551190	-813.059439
$Ti_3O_6CO_2^-$ – 3-4Bc	-814.508625	-0.003706	-814.558672	-813.059470
$Ti_3O_6CO_2^-$ – 3-4Ta	-814.512366	-0.002894	-814.562446	-813.064604
$Ti_3O_6CO_2^-$ – Center	-814.515797	-0.001593	-814.565853	-813.063884

Table A4.3. Relative energies with thermal correction at 298 K in kcal/mol. at the CCSD(T)/aug-cc-pVDZ/aug-cc-pwCVDZ-PP level usingf ωb97xD/aug-cc-pVTZ(-PP) optimized geometries.

Molecule	**3-4Ba**	**3-4Bc**	**3-4Ta**	**Center**
$Ti_3O_6CO_2^-$	3.6	3.2	0.0	0.4

Table A4.4. Calculated relative energies at different level of theory, ΔH_{298K}, in kcal/mol for $Ti_3O_6CO_2^-$ isomers.

Level of theory	**geom**	**3-4Ba**	**3-4Ta**	**3-4Tb**	**3-4Bc**	**3-4Bb**	**Center**
CCSD(T)/aug-cc-pVDZ(C and O)/ aug-cc-pwCVDZ-PP(Ti)	B3LYP	3.2	0.0	6.3	2.9	5.9	0.2
CCSD(T)/aug-cc-pVDZ(C and O)/ cc-pVDZ-PP(Ti)	B3LYP	4.9	2.2	7.2	2.9	6.6	0.0
CCSD(T)/aug-cc-pVDZ(-PP)	B3LYP		2.1				0.0
CCSD(T)/aug-cc-pVTZ(C and O)/ cc-pVTZ-PP(Ti)	B3LYP	5.5	2.8	7.4	3.3	7.4	0.0
B3LYP/aD	B3LYP	10.9	0.0	2.4	4.4	8.5	2.1
wB97xD/aT	ωB97xD	9.5	2.2		4.5		0.0
CCSD(T)/aug-cc-pVDZ(C and O)/ cc-pVDZ-PP(Ti)	ωB97xD		2.2				0.0
CCSD(T)/aug-cc-pVDZ(C and O)/ aug-cc-pwCVDZ-PP(Ti)	ωB97xD	3.6	0.0		3.2		0.4

Table A4.5. Vertical electron detachment energies (VDE, eV) for $M_3O_6CO_2^-$ and $M_3O_6^-$ (M = Ti, Zr and Hf) at 0K at the CCSD(T)/ aug-cc-pVDZ/aug-cc-pwCVDZ-PP level.

Isomer	Ti	Zr	Hf
3-4Ba	2.90	2.76	3.11
3-4Bb	3.19	2.99	3.34
3-4Bc	3.26	2.93	3.20
3-4Ta	3.33	3.08	3.39
3-4Tb	3.15	2.85	3.12
Center	3.44	3.12	3.49
M_3O_6	2.85	2.70	3.09

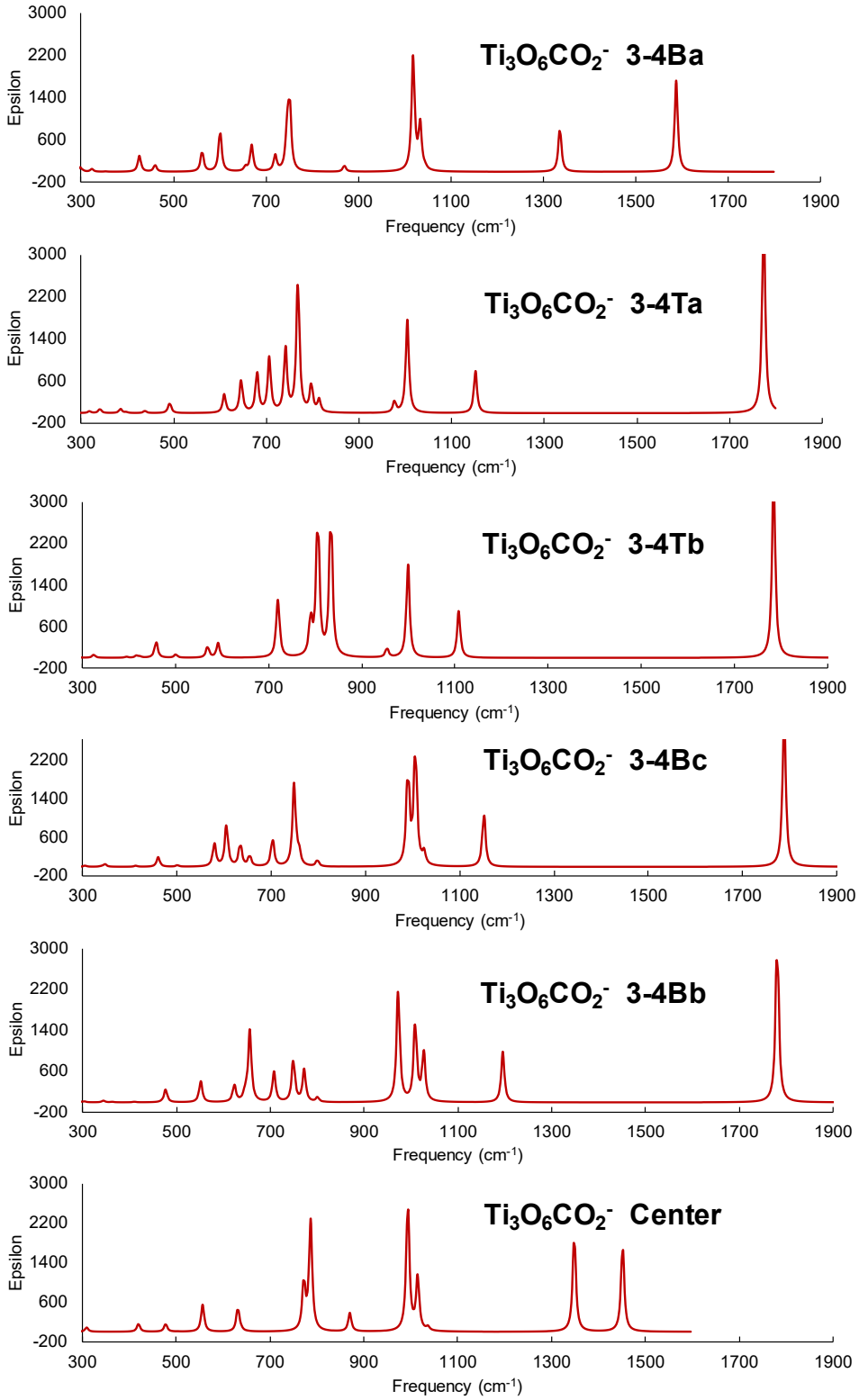

Figure A4.1. Calculated IR spectra for the $Ti_3O_6CO_2^-$ isomers at B3LYP/aug-cc-pVDZ(-PP) level.

CHAPTER 5

COMPUTATIONAL STUDY OF DEHYDRATION AND DEHYDROGENATION OF ETHANOL ON $(TiO_2)_n$ (n = 2 - 4) NANOCLUSTERS

Introduction

Studies of the dehydration and dehydrogenation of ethanol are relevant to renewable energy sources, for example, formation of ethylene. Many oxides catalyze the dehydration and dehydrogenation of ethanol, including γ-Al_2O_3[1], MO_x (M = W, Mo)[2,3,4], SiO_2, ZnO and CdO[5]. The properties of rutile TiO_2 (110), a well-known catalytic material, have been studied from the perspective of excess surface electrons[6] and charge transfer[7,8], the role of oxygen vacancies,[9] the presence of Ti^{3+} sites,[10] and the influence of subsurface defects and impurities.[11] A key reactivity site are defect sites where an oxygen ion is missing; this defect is called a bridge-bonded oxygen vacancy (BBO_V)[12,13,14]. Whether an alcohol undergoes dehydration or dehydrogenation on rutile TiO_2 (110) surface has been studied experimentally. Zhang et al.[15] found that, if methanol coverage was lower than the BBO_V coverage, methanol dissociates via O-H bond cleavage on a BBO_V. If the situation is reversed, the oxygen of methanol can bind to a five-coordinated Ti_{5c} site. If an ethoxy group is bound to a Ti_{5c} site after addition of ethanol, there is a deprotonation/protonation dynamic equilibrium.[16] Li et al.[17] studied absolute coverages for small aliphatic alcohols (C_1 - C_4) using a combination of temperature-programmed desorption and liquid nitrogen cooled quartz crystal microbalance measurements. They found that the saturation coverages of primary alcohols on Ti^{4+} were ~ 0.77 ML with almost no influence from the length of the alkyl chain. Kim et al.[18] explored product yields and selectivity of ten C_2-C_8

aliphatic alcohols on the rutile TiO_2 (110) surface with a 3.5% concentration of surface oxygen vacancies by using ultrahigh vacuum temperature-programmed desorption. They found that dehydration is preferred over dehydrogenation; dehydration at high temperatures (480 to 650 K) occurs for all alcohols, and dehydration at low temperatures (300 to 425 K) occurred for all except t-butanol and 3- and 4-octanol. For those that can dehydrate at both temperatures, they produce greater amounts of products at high temperature than at low temperature. They showed that the low temperature pathway for dehydration is at the Ti^{4+} sites. Below room temperature, it has been shown that alcohols can add to the surface Ti_{5c}^{4+} sites molecularly or may dissociate by proton transfer to a bridge O site, whereas only dissociation occurs at BBO_V sites.[15,19] Kim et al.[20] correlated the activation energy for alkene formation on BBO_V in the high temperature region with the Taft inductive parameter and showed that ethanol had the highest activation energy as compared to more highly substituted alcohols.

Wang et al.[21] studied the hydrolysis reactions of the ground and first excited triplet states of TiO_2 nanoclusters. It is important to involve both the singlet and the triplet in the study of H_2 and O_2 production from water splitting.[22] After an initial Lewis acid-base complex is formed a hydrogen atom transfers to generate an OH group. Hydrogen atom transfer from the OH group leads to formation of an M-H bond via proton coupled electron transfer (PCET) reaction, with one electron transferred for the triplet state and two transferred for the singlet state of the complex.

Experimental and computational studies[2,3,4,23,24,25,26] of dehydration, dehydrogenation and condensation of C_1 to C_4 alcohols have been performed on cyclic $(MO_3)_3$ clusters for M = Mo and W. The first alcohol[2,4] is physiosorbed to the metal $O=M^{VI}=O$ in a Lewis acid-base reaction. This is followed by proton transfer processes until the appropriate products are formed.

Building on the prior studies on the reactions of alcohols on cyclic $(WO_3)_3$ and $(MoO_3)_3$ clusters, the current work describes a computational study of the reactivity of $(TiO_2)_n$ nanoclusters, n = 2 – 4 with a focus on the reactions initiated at the Ti^{4+} sites. Dehydration (1) and dehydrogenation (2) of ethanol was selected as a model to probe both the Lewis/Brønsted acid/base and redox properties of Ti. Although the complete reactions (1) and (2) are endothermic in terms of the enthalpy (ΔH_{0K}) and Gibbs free energy (ΔG_{298K}) as shown below,[27,28,29,30] we can gain useful insights into the reaction and the key intermediates.

$CH_3CH_2OH \rightarrow H_2O + CH_2{=}CH_2$ ΔH_{0K}=9.4 kcal/mol ΔG_{298K}=1.8 kcal/mol (1)

$CH_3CH_2OH \rightarrow H_2 + CH_3CHO$ ΔH_{0K}=14.9 kcal/mol ΔG_{298K}=8.7 kcal/mol (2)

Computational Methods

Geometry optimizations were performed at the density functional theory (DFT)[31] level with the B3LYP[32,33] hybrid exchange correlation functional and the DZVP2 based set[34] for dehydration and dehydrogenation of ethanol on the transition metal oxide clusters $(TiO_2)_n$, n = 2 - 4.[22,35,36] The cc-pVDZ-PP basis set with a relativistic effective core potential was used for W and Mo.[37,38] The synchronous transit-guided quasi-Newton (STQN) method was used to find transition states.[39] Zero-point energies (ZPE) are obtained at the DFT level. The DFT calculations were carried out with the Gaussian 16 program package.[40]

The DFT optimized geometries were used in single point CCSD(T)[41,42,43,44] calculations with the correlation-consistent basis sets aug-cc-pVDZ[45,46] for C, H and O, and the aug-cc-pVDZ-PP[47] basis set which incorporates a pseudopotential for Ti. The 10 electrons in the 1s2s2p orbitals are modeled by the relativistic pseudopotentials (-PP). These basis sets is denoted as aD. All CCSD(T) calculations were performed with the MOLPRO 2018.2 program.[48,49,50]

The calculations were performed on the local Xeon and Opteron based Penguin Computing clusters at the University of Alabama and the Xeon and Opteron based Dense Memory Cluster (DMC) at the Alabama Supercomputer Center.

Results and Discussion

The clusters used for the reaction coordinates for ethanol catalysis are shown in Figure 5.1. The lowest energy structure for Ti_2O_4 has C_{2h} symmetry, for Ti_3O_6 has C_s symmetry, and for Ti_4O_8 has C_{2v} symmetry with a tetradentate bridging O atom. The ethanol dehydration (1) and dehydrogenation (2) reaction energies are endothermic by 9.4 and 15.0 kcal/mol (CCSD(T)/aD level at 0 K plus ZPE corrections), respectively, in agreement with the values derived from the Active Thermochemical Tables (ATcT).[28,29]

Dimer Dehydration The overall reaction pathways and two lowest energy pathways of ethanol dehydration for the dimers at the CCSD(T)/aD//B3LYP/DZVP2 level are shown in Figure 5.2 (a) and (b), respectively. The remaining related structures are in the Supporting Information (SI). Structures with the dimers, trimers and tetramers are prelabeled with d, t and q, respectively.

The dehydration reaction on the dimer $(TiO_2)_2$ starts with formation of a physiosorbed complex **d1** at the Ti_1 site by an ethanol molecule via a Lewis acid-base interaction. The physisorption energy is *ca.* -40 kcal/mol, followed by a proton transfer from the O-H bond on the C_2H_5OH to a terminal O_{ter1} with a barrier of ~ 17 kcal/mol, with the transition state dTS 1 below the reactant asymptote. Formation of the chemisorbed complex, Ti-hydroxide **d2**, is *ca.* -24 kcal/mol more stable than the physisorption complex.

The β hydrogen transfers to an O atom of the Ti_2O_4H structure of **d2** in three ways: (i) transfers to the terminal O_{ter1} via **dTS 2c** to form a $Ti_2O_4(C_{2v})$-C_2H_4-H_2O complex **d3c**, (ii) transfers to the second terminal O_{ter2} via **dTS 2b** to form a $Ti_2O_5H_2$-C_2H_4 complex **d3a** with two

terminal OH groups and a C_2H_4 physiosorbed to the H of the terminal $O_{ter2}H$ group, and (iii) transfers to a bridged O_{br1} via **dTS 2a** to form **d3b** with one terminal $O_{ter1}H$ and one bridged $O_{br1}H$ groups and a C_2H_4 physiosorbed to the terminal O that is originally from the ethanol. The energy barriers via **dTS 2c** and **dTS 2b** are similar, ~ 55 and ~ 53 kcal/mol, respectively. The energy barrier via **dTS 2a** is a bit lower, ~ 46 kcal/mol. The enthalpies of these transition states are all below the reactant asymptote. The β hydrogen transfer reactions are all endothermic. The least endothermic reaction, 16 kcal/mol, occurs at the pathway (2). The β hydrogen transfer reaction energy of the pathway (1) is ~ 28 kcal/mol. The pathway (3) has the highest reaction energy of ~ 39 kcal/mol. Among these three pathways from **d2** to **d3**, **dTS 2a** is the lowest energy barrier and is ~ 7 kcal/mol lower than the second lowest transition state **dTS 2b**. Reaction **d3a** has the lowest endothermicity, and is ~ 12 kcal/mol lower than the second lowest product **d3b**. Thus, the steps **d2 → dTS 2a → d3b** and **d2 → dTS 2b → d3a**, are two possible lowest energy pathways and both likely to occur thermodynamically.

Removal of C_2H_4 is an additional endothermic process, but the energy is still below the reactant asymptote. Approximately, 2 kcal/mol is required for **d3b** to form **d4b** and ~ 4 kcal/mol for **d3a** to form **d4a**, so ethylene desorption is a low energy process. Thus, the steps **d3b → d4b** and **d3a → d4a** are still both likely to occur.

The final step is removal of a water molecule. The bridge $Ti_2O_5H_2$ **d4b** has one bridge $O_{bri1}H$ group and one terminal $O_{ter1}H$ group. The bridge proton transfers either to the terminal $O_{ter1}H$ group, endothermically forming the Ti_2O_4 and H_2O complex **d4c**, or transfers to the terminal oxygen at Ti_1 to form **d5** which has two terminal OH groups at Ti_1. The latter pathway is preferred with a lower energy barrier of ~ 24 kcal/mol and an exothermicity of *ca.* -14 kcal/mol. The terminal $Ti_2O_5H_2$ **d4a** has two terminal OH groups, the $O_{ter1}H$ group and the

$O_{ter2}H$ group. The terminal H of the $O_{ter2}H$ group transfers to the O_{ter1} of the $O_{ter1}H$ group to form a $Ti_2O_4(C_{2h})$-H_2O complex **d6** in three ways: (2.1) transfers to the bridge O_{bri1} via **dTS 4e** to form **d4b**, (2.2) transfers to the O_{ter1} via **dTS 4b** to form **d6** directly, (2.3) transfers to the only available terminal O at Ti_1 via **dTS 4a** to form **d5**. Pathway (2.1) is unlikely to occur as the transition state **dTS 4e** is above the reactant asymptote by ~ 1 kcal/mol. The transition states of (2.2) and (2.3) are both below the reaction asymptote. The transition energy barrier of (2.3) is ~ 21 kcal/mol, and that of (2.2) is only ~ 3 kcal/mol higher. The reaction energy of (2.3) has an exothermicity of *ca.* -4 kcal/mol and yet the reaction of (2.2) is endothermic with the product **d6** only 0.7 kcal/mol below the transition state **dTS 4b**. Thus, the pathway (2.3) is more favorable thermodynamically. Therefore, the lowest energy pathways from **d4b** and **d4a** are **d4b → dTS 4c → d5** and **d4a → dTS 4a → d5**, respectively. The overall processes D1 and D2 can both occur.

d2 → dTS 2a → d3b → d4b → dTS 4c → d5 (D1)

d2 → dTS 2b → d3a → d4a → dTS 4a → d5 (D2)

Formation of **d6** from **d5** is endothermic with a reaction energy of ~ 27 kcal/mol accompanied by a high energy barrier of ~ 40 kcal/mol. This suggests that **d5** might become a new Brönsted acid catalytic center with two OH group at the same Ti site. The hydration energy of 9.4 kcal/mol at **dcat** is above the reactant asymptote, which means the overall reaction might terminate at **d6** in the form of the $Ti_2O_4(C_{2h})$-H_2O complex.

The removal of C_2H_4 from the $Ti_2O_4(C_{2v})$-C_2H_4-H_2O complex **d3c** to form **d4c** requires 9 kcal/mol**,** and an additional ~ 31 kcal/mol is required to remove a H_2O to form **dcat 1**. The total reaction energy of this pathway is 14.7 kcal/mol at **dcat 1**, which includes the hydration energy of ethanol, 9.4 kcal/mol, and the energy needed for the structure transformation from C_{2h} to C_{2v}.

Since **dcat 1** is above the reactant asymptote, this pathway is likely to terminate in the form of the $Ti_2O_4(C_{2v})$-H_2O complex at **d4c**.

Dimer Dehydrogenation Dehydrogenation of ethanol on dimers starts from the chemisorbed complex **d2** (Figure 5.3). PCET occurs when the α hydrogen of the ethoxy transfers to Ti_1 via **dTS 7a** to form a $Ti_2O_4(C_{2h})$-C_2H_4O complex **d8a**, changing the charge of the hydrogen from +1 to -1. This reaction is exothermic by *ca.* -6 kcal/mol with an energy barrier of ~ 48 kcal/mol. It is the thermodynamically more preferable pathway as compared to the other pathway of transferring the α hydrogen to the bridge O_{bri1} via **dTS 7b** forming another $Ti_2O_4(C_{2h})$-C_2H_4O complex **d8b**. The latter has a higher energy barrier by ~ 8 kcal/mol and is an endothermic reaction. We note that the energy of **d8b** is higher than its transition state at the CCSD(T)/aD(-PP) level but lower than its transition state at the B3LYP/DZVP2 level so the B3LYP/DZVP2 structure may not be the optimized structure that would be found at the CCSD(T)/aD(-PP) level. Removing a C_2H_4O from **d8a** to form **d9a** requires ~ 14 kcal/mol and **d9a** is below the reactant asymptote. Next step is to remove a H_2 from **d9a**, which has a terminal $O_{ter1}H$ group and a hydride at Ti_1, to form a $Ti_2O_4(C_{2h})$-H_2 complex **d10b**. Formation of H_2 probably occurs by recombination of a protonic site, the terminal H of the terminal $O_{ter1}H$ group, and a hydridic site, the hydride at Ti_1, which is an endothermic reaction of ~ 16 kcal/mol with an energy barrier of ~ 27 kcal/mol. Removal of H_2 from **d10b** requires ~ 7 kcal/mol. The dehydrogenation energy of ethanol is 15.0 kcal/mol. However, since **dTS 9a**, **d10b** and **cat** are all above the reactant asymptote, the pathway may stop at **d9a** which can be viewed as a potential new catalyst.

Removal of C_2H_4O from **d8b** to form **d9b** which has a terminal $O_{ter1}H$ group and a bridge $O_{bri1}H$ group is endothermic by ~ 20 kcal/mol. To generate a H_2, the bridge H has to transfer to the Ti_1 site first, which is exothermic by *ca.* ~ 25 kcal/mol with an energy barrier of ~ 23

kcal/mol, a PCET process. The combination of two H with opposite formal charges on **d10a** is endothermic by ~ 23 kcal/mol with an energy barrier of ~ 31 kcal/mol. Approximately 7 kcal/mol is required to remove a H_2 from the $Ti_2O_4(C_{2v})$-H_2 complex **d11** to form **dcat 1** $Ti_2O_4(C_{2v})$. The dehydrogenation energy of ethanol of this pathway is 20.3 kcal/mol, which includes the dehydrogenation energy ofethanol of 15.0 kcal/mol, and the energy needed to transform Ti_2O_4 from C_{2h} to C_{2v}. Since **d9b** is above the reactant asymptote, this pathway may terminate at **d8b**.

Trimer Dehydration The reaction coordinates for dehydration for the trimers at the CCSD(T)/aD level are shown in Figure 5.4 (a). As expected, the process is initiated by formation of a physiosorbed Ti_3O_6-CH_3CH_2OH complex **t1** at Ti_1, a *ca.* -44 kcal/mol exothermic step. The proton on the OH group of ethanol transfers to the closest bidentate O_{dibr12} of Ti_3O_6 via **tTS 1** with an energy barrier of ~ 18 kcal/mol. The product **t2** is *ca.* -17 kcal/mol more exothermic than **t1**. The β hydrogen of the ethoxy at **t2** can transfer to five oxygen sites on Ti_3O_6, including two dibridged O_{dibr13} and O_{dibr23}, one tribridge O_{tribr}, two terminal O_{ter2} and O_{ter3}, plus one oxygen site originated from ethanol, thus, in total 6 pathways.

Considering the complexity of these pathways, the two possible lowest energy pathways T1 and T2 as shown in Figure 5.4 (b) are now discussed.

tcat → t1 → tTS 1 → t2 → tTS 2a → t3e → t4c → tTS 4d → t5b → tTS 5a → t6 → tcat (T1)

tcat → t1 → tTS 1 → t2 → tTS 2d → t3a→ t4a → tTS 4a→ t5a → tTS 5d → t6 → tcat (T2)

The remaining 4 pathways are described in the SI. In pathway T1, the β hydrogen of the ethoxy transfers to the closest bidentate O_{dibr13} via transition state **tTS 2a** with an energy barrier of ~ 43 kcal/mol to form a physiosorbed $Ti_3O_7H_2$-C_2H_4 complex **t3e** which has two bidentate OH groups, the $O_{dibr12}H$ group and the $O_{dibr13}H$ group with an ethylene molecule physiosorbed to the

H of the $O_{dibr13}H$ group. **t3e** is ~ 15 kcal/mol higher than **t2**. Approximately 7 kcal/mol is needed to remove

the ethylene to form **t4c**. The next step is to generate and remove a water molecule from **t4c**. The proton of the $O_{dibr12}H$ group transfers to the terminal oxygen originally from ethanol, via transition state **tTS 4d** with a barrier of ~ 39 kcal/mol to form $Ti_3O_7H_2$ **t5b** with a terminal OH group at Ti_1 and an $O_{dibr13}H$ group; the transition state is only 0.7 kcal/mol below the reactant asymptote. Thereaction is exothermic by *ca.* -6 kcal/mol. Transferring the proton at the $O_{dibr13}H$ group toward the oxygen of the terminal OH at Ti_1 has an energy barrier of ~ 35 kcal/mol via transition state **tTS 5a** forming a Ti_3O_6-H_2O complex **t6** with an endothermic reaction energy of ~ 21 kcal/mol. Approximately 35 kcal/mol is required to remove the water molecule. The dehydration energy of ethanol is 9.4 kcal/mol at 0K regardless of the cluster of the catalyst, yet the reaction may terminate at **t6** as **tcat** is above the reactant asymptote.

In pathway T2, the β hydrogen of the ethoxy transfers to the closest terminal O_{ter3} from **t2** via transition state **tTS 2d** to form a physiosorbed $Ti_3O_7H_2$-C_2H_4 complex **t3a** which has one bidentate $O_{dibr12}H$ group and one terminal $O_{ter3}H$ group with an ethylene molecule physiosorbed to the H of the $O_{ter3}H$ group, with an energy barrier of ~ 55 kcal/mol and a small endothermicity of 1 kcal/mol. The transition state **tTS 2d** is ~ 7 kcal/mol below the reactant asymptote and ~ 12 kcal/mol higher than **tTS 2a** in pathway T1, yet this β hydrogen transfer reaction energy is *ca.* -14 kcal/mol more exothermic than that in pathway T1. Removal of the ethylene molecule at **t3a** requires ~ 4 kcal/mol to form **t4a**, which has a bidentate $O_{dibr12}H$ group and a terminal $O_{ter3}H$ group. The next step is to generate and remove a water molecule from **t4a**. The proton of the bidentate $O_{dibr12}H$ group transfers to the terminal oxygen originally from the ethanol molecule, via transition state **tTS 4a** to form **t5a** which has two terminal OH groups, the terminal OH

group at Ti_1 and the terminal $O_{ter3}H$ group, with a barrier energy of ~ 37 kcal/mol and an exothermicity of *ca.* -11 kcal/mol. Then the proton of the terminal OH group at Ti_1 transfers to the O_{ter3} of the terminal $O_{ter3}H$ group via transition state **tTS 5d** to form the Ti_3O_6-H_2O complex **t6** with a large energy barrier of ~ 63 kcal/mol; **tTS 5d** is still below the reactant asymptote by ~ 4 kcal/mol. **t6** is ~ 42 kcal/mol higher than **t5a**. Thus, **t5a** might become a new Brönsted acid catalytic center.

Physisorption of ethanol at the bridge Ti_1 instead of the terminal Ti=O is the lowest energy pathway thermodynamically as shown in Figure 5.5. Overall, the process is like that at the bridge Ti_1, except that it is less exothermic. The overall chemisorption reaction is still more negative than the reactant asymptote. Physisorption of ethanol at terminal Ti_3=O_{ter3} is predicted to be less exothermic by 14 to 15 kcal/mol than that at Ti_1. There are two physiosorbed complexes **tt1a** and **tt1b** that are essentially iso-energetic differing only in the orientation of the OH group on the ethanol. The proton of the hydroxy at **tt1a** transfers to the terminal O_{ter3} via transition state **ttTS 1a** to form **tt2a** accompanied. The transition state energy of **ttTS 1a** is ~ 13 kcal/mol higher in energy than that of **tTS 1**, and the product **tt2a** is ~ 11 kcal/mol higher in energy than **t2**. The actual proton transfer barrier via **ttTS 1a** is ~ 17 kcal/mol, which is comparable to the barrier of ~ 18 kcal/mol via **tTS 1**. Transferring the proton of the hydroxy of **tt1b** to the bidentate O_{dibr13} has a transition state **ttTS 1b** that is essentially isoenergetic with **ttTS 1a** and product **tt2b** is ~ 42 kcal/mol higher in energy than **t2** and is ~ 32 kcal/mol higher in energy than **tt2a**. Thus physisorption and chemisorption of ethanol prefer to occur at the bridge Ti_1 instead of the terminal Ti=O on the trimer $(TiO_2)_3$ nanocluster.

Trimer Dehydrogenation One pathway is predicted for ethanol dehydrogenation (Figure 5.6) and begins with formation of the chemisorbed complex **t2** at Ti_1. The α hydrogen of the ethoxy

transfers to Ti_1 where PCET occurs to form **t8**, with an energy barrier of ~ 40 kcal/mol and an endothermicity of ~ 35 kcal/mol. **t8** is a physiosorbed $Ti_3O_6H_2$-CH_3CHO complex with a bidentate $O_{dibr12}H$ group and a hydride at Ti_1; an acetaldehyde is physiosorbed to Ti_1. Approximately 26 kcal/mol is required to remove an acetaldehyde from **t8** to form **t9** which is at the same energy as the reactant asymptote. The reaction may stop at this point and **t9** can be a new catalyst with two hydrogens containing opposite charges. If this pathway continues, the proton on the bidentate $O_{dibr12}H$ group will transfer to the hydride at Ti_1 to form a physiosorbed Ti_3O_6-H_2 complex **t10** with a reaction energy of ~ 8 kcal/mol and an energy barrier of ~ 27 kcal/mol. Removal of the hydrogen molecule requires ~ 8 kcal/mol to recover the trimer molecule **tcat**.

Tetramer Dehydration The reaction coordinates for dehydration for the tetramers at the CCSD(T)/aD level are shown in Figure 5.7 (a). Physisorption of ethanol on Ti_4O_8 at Ti_1 is exothermic by *ca.* -36 kcal/mol. The proton of the OH group of the ethoxy group transfers to the closest bidentate O_{dibr12} of Ti_4O_8 from **q1** via **qTS 1** to **q2** with an energy barrier of ~ 8 kcal/mol and an exothermic energy of *ca.* -16 kcal/mol. The pathways start to diverge at **q2**, and the lowest energy pathway is Q1 as shown in Figure 5.7 (b).

qcat → q1 → qTS 1 → q2 → qTS 2a → q3a → q4a → qTS 4a → q5b → qTS 5b → q6a → qcat. (Q1)

In this pathway, the β hydrogen on the ethoxy transfers to the closest bidentate O_{dibr13} via **qTS 2a** to form a physiosorbed $Ti_4O_9H_2$-C_2H_4 complex **q3a** with two dibridged OH groups, the $O_{dibr12}H$ group and the $O_{dibr13}H$ group, and an ethylene molecule physiosorbed to the H of the $O_{dibr13}H$ group, with an energy barrier of ~ 39 kcal/mol and an endothermic reaction energy of ~ 10 kcal/mol. Approximately 6 kcal/mol is needed to remove the ethylene molecule to form $Ti_4O_9H_2$

q4a. The next step is to generate and remove the water molecule from **q4a**. The proton of the $O_{dibr12}H$ group transfers to the terminal oxygen from ethanol, via the transition state **qTS 4a** to form **q5b** with an energy barrier of ~ 30 kcal/mol. The reaction is essentially thermoneutral with an exothermicity of *ca.* -1 kcal/mol. Transfer of the proton from the $O_{dibr13}H$ group to the terminal OH group has an energy barrier of ~ 23 kcal/mol; the reaction is endothermic by ~ 17 kcal/mol. The physiosorbed Ti_4O_8-H_2O complex **q6a** will be the final state along the pathway since **qcat** exceeds the reactant asymptote. An energy of ~ 29 kcal/mol is needed to remove H_2O from **q6a** to recover the tetramer **qcat**.

Physisorption of ethanol at the terminal Ti_2=O_{ter2} is ~ 7 kcal/mol higher in energy than at the bridge Ti_1 as shown in Figure 5.8, but the overall process at the terminal Ti_2=O_{ter2} is still below the reactant asymptote including chemisorption. The proton of the hydroxy at **qt1** transfers to the terminal O_{ter2} via transition state **qtTS 1** to form **qt2**; the transition state energy of **qtTS 1** is ~ 18 kcal/mol higher than that of **qTS 1**, and the product **qt2** is ~ 10 kcal/mol higher than **q2**. The energy barrier for proton transfer via **qtTS 1** of ~ 18 kcal/mol is comparable to that for the terminal Ti=O in the trimer and substantially larger than at the bridge Ti in the tetramer.

Tetramer Dehydrogenation The reaction coordinates for dehydrogenation for the tetramers at the CCSD(T)/aD level are shown in Figure 5.9 (a). Figure 5.9 (b) shows the lowest energy pathway Q2.

qcat → q1 → qTS 1 → q2 → qTS 7b → q8c → q9b → qTS 9b → q12a → qcat (Q2)

The α hydrogen on the ethoxy transfers through **qTS 7b** to Ti_1 via a PCET process forming **q8c** with an energy barrier of ~ 48 kcal/mol and an endothermic reaction of ~ 43 kcal/mol. **q8c** is a physiosorbed $Ti_4O_8H_2$-C_2H_4O complex with an bridge $O_{dibr12}H$ group, and a hydride and an physiosorbed acetaldehyde molecule at Ti_1 which requires ~ 16 kcal/mol to remove the

acetaldehyde to form **q9b**. By recombining the proton of the bridge $O_{dibr12}H$ group and the hydride at Ti_1, a physiosorbed Ti_4O_8-H_2 complex **q12a** is generated with a transition energy of ~ 21 kcal/mol and a reaction energy of ~ 3 kcal/mol. Approximately 5 kcal/mol is needed to remove the hydrogen molecule to recover the tetramer catalytic molecule **qcat**. However, **q9b** is higher in energy than the reactant asymptote so the process may stop at **q8c**.

Reaction summary Table 5.1 compares reaction energies (ΔH_{0K}) and energy barriers ($\Delta H^{\ddagger}_{0K}$) of dehydration and dehydrogenation of one ethanol molecule at the Ti_1 site of the $(TiO_2)_n$, n = 2 to 4, for the lowest energy pathways. Table 5.2 shows the physisorption energies of C_2H_4, C_2H_4O, H_2O and H_2 on the $(TiO_2)_n$ and the related structures, n = 2 to 4. The physisorption energies of one ethanol molecule at the bridge Ti_1 site of the trimer $(TiO_2)_3$ and the tetramer $(TiO_2)_4$ nanocluster are the most exothermic, -44 to -36 kcal/mol, respectively. Physisorption of one ethanol molecule at the terminal Ti=O sites of $(TiO_2)_n$ nanocluster, n = 2 to 4, are less exothermic, varying between -29 to -40 kcal/mol. Binding to the terminal Ti=O site of the trimer $(TiO_2)_3$ and the tetramer $(TiO_2)_4$, essentially have the same energy of -30 and -29 kcal/mol, respectively. The physisorption energies of ethanol at the dioxo W site of $(WO_3)_3$ and the dioxo Mo site of $(MoO_3)_3$ are *ca.* -25 and -20 kcal/mol,[2,4] respectively, at the CCSD(T)/aD//B3YP/aD level. The physisorption energies for the dioxo W and Mo sites are less negative than the terminal Ti=O site of the $(TiO_2)_4$ nanocluster.

The reaction energies from the physiosorbed complex to the chemisorbed complex at the bridge Ti_1 of $(TiO_2)_3$ and $(TiO_2)_4$ are essentially isoenergetic; however, the transition barriers are quite different at 18 and 8 kcal/mol, respectively. The reaction energies from the physiosorbed complex to the chemisorbed complex at the terminal Ti=O of $(TiO_2)_n$ nanocluster, become less exothermic from -24 to -13 kcal/mol as the size of the cluster increases from n = 2 to 4; yet the

transition barrier energies are all isoenergetic. In comparison, the comparable binding energies to dioxo W and Mo sites of $(WO_3)_3$ and $(MoO_3)_3$ are endothermic by ~ 2 and ~ 11 kcal/mol,[4] respectively, with energy barriers of 26 and 28 kcal/mol.[4] The transition state energy for $(WO_3)_3$ is almost the same as the reactant asymptote and that for $(MoO_3)_3$ is greater than the reactant asymptote by ~ 9 kcal/mol.[4] Thus, physisorption and chemisorption of one ethanol molecule at the terminal Ti=O of $(TiO_2)_n$ nanocluster, n = 2 to 4, are thermodynamically possible and more preferred than at the dioxo W/Mo=O sites of $(WO_3)_3$ and $(MoO_3)_3$. The order of metal sites for the chemisorption of one ethanol molecule is: the Ti_1 site of the dimer $(TiO_2)_2$ > the bridge Ti_1 site of the trimer $(TiO_2)_3$ > the bridge Ti_1 site of the tetramer $(TiO_2)_4$ ~ the terminal Ti=O site of the trimer $(TiO_2)_3$ > the terminal Ti=O site of the tetramer $(TiO_2)_4$ > the dioxo W site of the $(WO_3)_3$ > the dioxo Mo site of the $(MoO_3)_3$, with chemisorption energies with respect to the reactant asymptote of *ca.* -64, -61, -52, -51, -42, -24[4] and -9[4] kcal/mol, respectively.

The β H transfer reactions for the $(TiO_2)_{2,4}$ and $(WO_3)_3$[4] are endothermic, whereas the lowest energy β H transfer reactions for $(TiO_2)_3$ and $(MoO_3)_3$[4] are approximately thermoneutral. The dimer $(TiO_2)_2$ has the highest β H transfer reaction energy, ~ 28 kcal/mol. The β H transfer barriers on $(WO_3)_3$ and $(MoO_3)_3$ are between 32 to 35 kcal/mol, [4] lower than those for $(TiO_2)_n$, n = 2 to 4, which are between 39 to 54 kcal/mol. The β H transfer transition states of the $(TiO_2)_n$, n = 2 to 4, are all below the reactant asymptote, whereas those for $(WO_3)_3$ and $(MoO_3)_3$ are above the reactant asymptote by ~ 11 and ~ 23 kcal/mol,[4] respectively. The removal of C_2H_4 from $(WO_3)_3$ and $(MoO_3)_3$ requires ~ 8 and ~ 11 kcal/mol, [4] respectively, which are higher than the values for the $(TiO_2)_n$ nanoclusters, n = 2 to 4, that range from 2 to 7 kcal/mol. The energy required to remove H_2O from the $(WO_3)_3$ and $(MoO_3)_3$ is ~ 16 and ~ 8 kcal/mol,[4] respectively, which are lower than that for the $(TiO_2)_n$ nanoclusters ranging from 29 to 35 kcal/mol, n = 2 to 4.

The α H transfer for $(WO_3)_3$ and $(MoO_3)_3$ is at least 11 kcal/mol[4] less endothermic than for $(TiO_2)_n$, n = 2 to 4. $(MoO_3)_3$[4] has the overall lowest energy barrier of 26 kcal/mol and that on the $(WO_3)_3$[4] is 32 to 33 kcal/mol, lower than that on the trimer $(TiO_2)_3$, 39 kcal/mol, which is the lowest among the $(TiO_2)_n$, n = 2 to 4; the α H transfer on the $(WO_3)_3$ prefers to transfer to the W site where PCET occurs, [4] and the same is predicted for the $(TiO_2)_n$, n = 2 to 4,. In contrast, the α H on $(MoO_3)_3$ prefers to transfer to an O site.[4] The transition states and the products of α H transfer for $(TiO_2)_n$, n = 2 to 4, are both below the reactant asymptote. The transition state for α H transfer for $(WO_3)_3$ is above the reactant asymptote, although the product is below the reactant asymptote[4]; whereas both are above the reactant asymptote for $(MoO_3)_3$.[4] The energy range required to remove C_2H_4O is comparable for $(TiO_2)_n$, n = 2 to 4, $(WO_3)_3$[4] and $(MoO_3)_3$.[4]

Dehydration of one ethanol molecule is preferred over dehydrogenation on $(TiO_2)_n$, n = 2 to 4, $(WO_3)_3$ and $(MoO_3)_3$. Dehydration and dehydrogenation of one ethanol occur below reactant asymptote for $(TiO_2)_n$, n = 2 to 4, whereas this is unlikely for $(WO_3)_3$ and $(MoO_3)_3$. However, addition of a second ethanol molecule makes the physiosorbed complexes very stable thermodynamically and allows dehydration and dehydrogenation to occur below the reactant asymptote for $(WO_3)_3$ and $(MoO_3)_3$.[2,4] The physisorption enthalpy energy of the second ethanol molecule at the dioxo W site of $(WO_3)_3$ is *ca.* -21 kcal/mol, and that at the dioxo Mo site of $(MoO_3)_3$ is the same as the physisorption of the first ethanol at the dioxo Mo site.[2,4] The total physisorption of two ethanols on $(WO_3)_3$ and $(MoO_3)_3$ is *ca.* -47 and -39 kcal/mol,[2,4] respectively, with the former being close to the physisorption of one ethanol at the bridge Ti_1 on $(TiO_2)_3$, and the latter close to the physisorption of one ethanol at the bridge Ti_1 on $(TiO_2)_4$. The reaction energy of the proton transfer of one OH group from one of the two physiosorbed ethanol to a terminal O atom on $(WO_3)_3$ is *ca.* -9 kcal/mol with an energy barrier of ~ 18 kcal/mol, and

on $(MoO_3)_3$ is *ca.* -3 kcal/mol with an energy barrier of ~ 25 kcal/mol.[2] Thus, the chemisorption of $(WO_3)_3$ with two ethanols is -56 kcal/mol,[2] between the chemisorption at the bridge Ti_1 on $(TiO_2)_3$ and $(TiO_2)_4$ with one ethanol; the chemisorption barrier on the $(WO_3)_3$ and $(TiO_2)_3$ are comparable, 18 to 19 kcal/mol. The reaction from the physiosorbed complex to the chemisorbed complex is endothermic for $(MoO_3)_3$, ~ 3 kcal/mol. Thus, the chemisorption of $(MoO_3)_3$ with two ethanol has the highest energy of all, *ca.* -36 kcal/mol.[2]

A combined computational and experimental study of one methanol (CD_3OH) on rutile TiO_2 (110) showed that the average physisorption electronic energy at the 5-fold coordinated titanium (Ti_{5c}^{4+}) site is predicted to be -0.75 eV (-17 kcal/mol)[51] using the Perdew-Burke-Ernzerhof (PBE) functional;[52] in comparison, this is much weaker binding than the physisorption energy of one ethanol on $(TiO_2)_n$, n = 2 to 4. The thermodynamics for the chemisorption transfer of the proton of the OH group of CH_3OH physiosorbed to the Ti_{5c}^{4+} to the bridging O is approximately thermoneutral with an energy barrier of 0.25 eV (6 kcal/mol).[51] The α-H transfer step is endothermic by 1.03 eV (24 kcal/mol) with an energy barrier of 1.57 eV (36 kcal/mol).[51] The CD_2O and the barrier to reach it are both above the reactant energy asymptote in contrast to what is predicted for ethanol on the TiO_2 nanoclusters in the current study where these types of processes are below the reactant asymptote.

Our computational results on the Ti sites that do not have a terminal O on the n = 3 and n = 4 nanoclusters can be compared to the experimental results[18,20] for addition of ethanol to the Ti_{5c}^{4+} site. In this case, we find, as is found experimentally, that physisorption and dissociative chemisorption of the ethanol to form an alkoxy bonded to the Ti should occur at low temperatures as the calculated energies for the complexes and associated transition states are below the reactant asymptote. The energy required to lose C_2H_4 is also below the asymptote

consistent with the experimental observations. We predict that this can happen with a single ethanol whereas in some of the experimental work,[18] it is suggested that an additional ethanol may be interacting with the alkoxy as is found for $(WO_3)_3$.[2,4] The loss of H_2O with regeneration of the catalyst is endothermic as required by the enthalpy of reaction (1) and requires higher temperatures as found experimentally. The dehydrogenation reaction is more endothermic than dehydration and formation of the aldehyde will only occur at higher temperatures as found experimentally.[18] In fact it is likely that H_2 is not lost from the catalyst but remains on the surface when an aldehyde or ketone is generated as the PCET process has substantial energy barriers that are above the reactant asymptote.

Energetic reactivity correlations The fluoride affinity (FA) serves as an estimate of the Lewis acidity of the metal sites.[23,53] The FA values were calculated relative to that of FA($(WO_3)_3$) = 116.2 kcal/mol.[23] Figure 5.10 shows the correlation between the FAs (See Table A5.7) at terminal and bridge Ti sites of $(TiO_2)_n$, n = 2 to 4, as well as the metal dioxo sites of $(WO_3)_3$ and $(MoO_3)_3$ versus physisorption of one ethanol at the corresponding sites. As would be expected, there is a qualitative correlation between higher FA (larger Lewis acidity) and stronger physisorption. The order of the FA of the bridge Ti_1 site of $(TiO_2)_3$ > the bridge Ti_1 site of $(TiO_2)_4$ > the Ti_1 site of $(TiO_2)_2$ correlates with the order of electron affinity (EA) of these clusters, 38, 66, and 58 kcal/mol, respectively, with the spin of the anions located at the corresponding Ti sites.[35] There is also a qualitative correlation of physisorption of one H_2O with the FA (See Figure A5.22 and Table A5.10) for the final loss of H_2O step.

There is a qualitative quadratic correlation between the chemisorption barrier of one ethanol on $(TiO_2)_n$, n = 2 to 4, and $(WO_3)_3$ and $(MoO_3)_3$ and the proton affinity (PA = $-\Delta H_{298K}$ for the reaction $B + H^+ \rightarrow BH^+$) at the oxygen to which the proton is transferred in the

chemisorption process (Figure 5.11 from PA values in Table A5.8). Figure 5.11 shows that the chemisorption barrier reaches a minimum when the PA is near 205 kcal/mol. The PA of CH_3CH_2OH is 186 kcal/mol.[54] Thus it is not surprising that the sites with a lower PA have a higher barrier. Apparently if the PA is too large then, the barrier also increases. The optimal barrier is for sites with a PA comparable to that of NH_3 (PA is ~ 204 kcal/mol). This suggests that other interactions are also important.

In addition, there are linear correlations of the energy to remove C_2H_4 with the PA and acidity at the OH site from which the C_2H_4 is lost (Figure 5.12). A weaker acid requires less energy to remove an ethylene. The interaction between the proton of the OH group and the π bond of the ethylene is weaker as the proton is held more strongly by the O of the OH site by the weaker acid. There will be more proton transfer for the stronger acid increasing the binding energy. In a similar way, the lower proton affinity has a higher C_2H_4 binding energy as the proton is more transferred towards the C_2H_4. The more the proton is held by the oxygen base, the less interaction with the C_2H_4 and the lower binding energy.

Conclusions

Correlated molecular orbital theory CCSD(T)/aD calculations were used to explore dehydration and dehydrogenation of an ethanol molecule on $(TiO_2)_n$ nanoclusters, n = 2 to 4, based on the geometries optimized at the B3LYP/DZVP2 level. Multiple pathways for ethanol dehydration and dehydrogenation on $(TiO_2)_n$ nanoclusters, n = 2 to 4, were predicted. Dehydration of ethanol is thermodynamically preferred over dehydrogenation on $(TiO_2)_n$, n = 2 to 4. There are two low energy pathways where the β hydrogen on ethoxy transfer either to the adjacent terminal oxygen, or to the adjacent bidentate oxygen for dehydration of ethanol on the dimer $(TiO_2)_2$ and trimer $(TiO_2)_3$. Dehydration of ethanol on the tetramer $(TiO_2)_4$ has the latter β

hydrogen transfer for the lowest energy pathway. Removal of the ethylene from the $(TiO_2)_nOH_2$-C_2H_4 complex at 0K, n = 2 to 4 requires 2 to 7 kcal/mol. The dihydroxide $(TiO_2)_nOH_2$ can rearrange to the $(TiO_2)_n \cdot H_2O$ complex. Removal of the water molecule requires 29 to 35 kcal/mol. The $(TiO_2)_n(OH)_2$ are stable thermodynamically and can serve as new proton acid catalysts. For dehydrogenation, the pathway transferring the α hydrogen to the adjacent Ti atom is the lowest energy. Removal of the acetaldehyde molecule from the $(TiO_2)_nH_2$-C_2H_4O complex requires 14 to 26 kcal/mol; an additional 5 to 8 kcal/mol is needed to remove the hydrogen molecule via a PCET process. Dehydration and dehydrogenation of an ethanol occur below the reactant asymptote for $(TiO_2)_n$, n = 2 to 4. In contrast, two ethanols are required for $(WO_3)_3$ and $(MoO_3)_3$ for dehydration and dehydrogenation to occur below the reactant asymptote. Physisorption and chemisorption of one ethanol on $(TiO_2)_n$ nanoclusters, n = 2 to 4, are predicted to be more negative than the corresponding values of one methanol on the surface of rutile TiO_2(110).

The Lewis acidity (fluoride affinity) has an approximate linear correlation with physisorption of one ethanol molecule or one water molecule. There is a quadratic correlation between the chemisorption barrier of one ethanol and proton affinity. There is a regime where there is a low proton barrier to a site that is ~ 20 kcal/mol more basic than ethanol. If the site is less basic than ethanol or is too basic, there is an increase in the proton transfer barrier for chemisorption. There are linear correlations between the C_2H_4 removal energies and the basicity or acidity of the corresponding oxygen sites. The less basic the oxygen site or the more acidic the site, the higher the binding energy to the C_2H_4 due to the amount that the proton on the OH group can interact with the departing C_2H_4.

The current study of ethanol dehydration and dehydrogenation on $(TiO_2)_n$ (n = 2 to 4) nanoclusters provides further insights into how these simple processes occur on transition metal oxide nanoclusters.

Tables

Table 5.1. Reaction energies (ΔH_{0K}) and transition energy barriers ($\Delta H^{\ddagger}_{0K}$) and in kcal/mol of physisorption, physiosorbed to chemisorbed complex reaction, and β hydrogen transfer in the lowest pathways of dehydration and α hydrogen transfer in the lowest pathways of ethanol dehydrogenation on $(TiO_2)_n$ nanoclusters, n = 2 - 4.

Reaction	ΔH_{0K}	structure	$\Delta H^{\ddagger}_{0K}$	structure	ΔH_{0K}	structure	$\Delta H^{\ddagger}_{0K}$	structure	ΔH_{0K}	structure	$\Delta H^{\ddagger}_{0K}$	structure
n	2	2	2	2	3	3	3	3	4	4	4	4
EtOH physi (at bridge Ti_1)					-44	**t1**			-36	**q1**		
EtOH physi (at terminal Ti=O)	-40	**d1**			-30	**tt1a**			-29	**qt1**		
Physi → Chemi (at bridge Ti_1)					-17	**t2**	18	**tTS 1**	-16	**q2**	8	**qTS 1**
Physi → Chemi (at terminal Ti=O)	-24	**d2**	17	**dTS 1**	-21	**tt2a**	17	**ttTS 1a**	-13	**qt2**	18	**qtTS 1**
β H Transfer (to O_{bri})	28	**d3b**	46	**dTS 2a**	15	**t3e**	43	**tTS 2a**	10	**q3a**	39	**qTS 2a**
β H Transfer (to O_{ter})	16	**d3a**	53	**dTS 2b**	1	**t3a**	54	**tTS 2d**	Cannot transfer to O_{ter}			
α H Transfer	43	**d8a**	48	**dTS 7a**	35	**t8**	39	**tTS 7**	43	**q8c**	48	**qTS 7b**

Table 5.2. Physisorption energies (ΔH_{0K}) in kcal/mol of C_2H_4 and H_2O in dehydration, and C_2H_4O and H_2 in dehydrogenation on $(TiO_2)_n$ nanoclusters, n = 2- 4.

n	C_2H_4 (β H Transfer to O_{bri})	C_2H_4 (β H Transfer to O_{ter})	C_2H_4O	H_2O	H_2
2	-2 **(d3b)**	-4 **(d3e)**	-14 **(d8a)**	-31 **(d6)**	-7 **(d10b)**
3	-7 **(t3e)**	-4 **(d3a)**	-26 **(t8)**	-35 **(t6)**	-8 **(t10)**
4	-6 **(q3a)**		-17 **(q8c)**	-29 **(q6a)**	-5 **(q12a)**

Figures

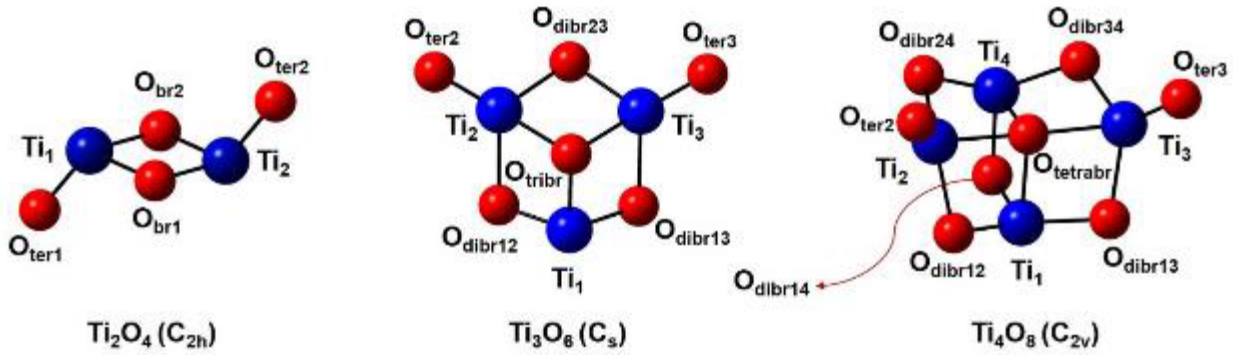

Figure 5.1. The lowest energy structures for $(TiO_2)_n$ (n = 2-4) optimized at the B3LYP/DZVP2 level with atomic labels.

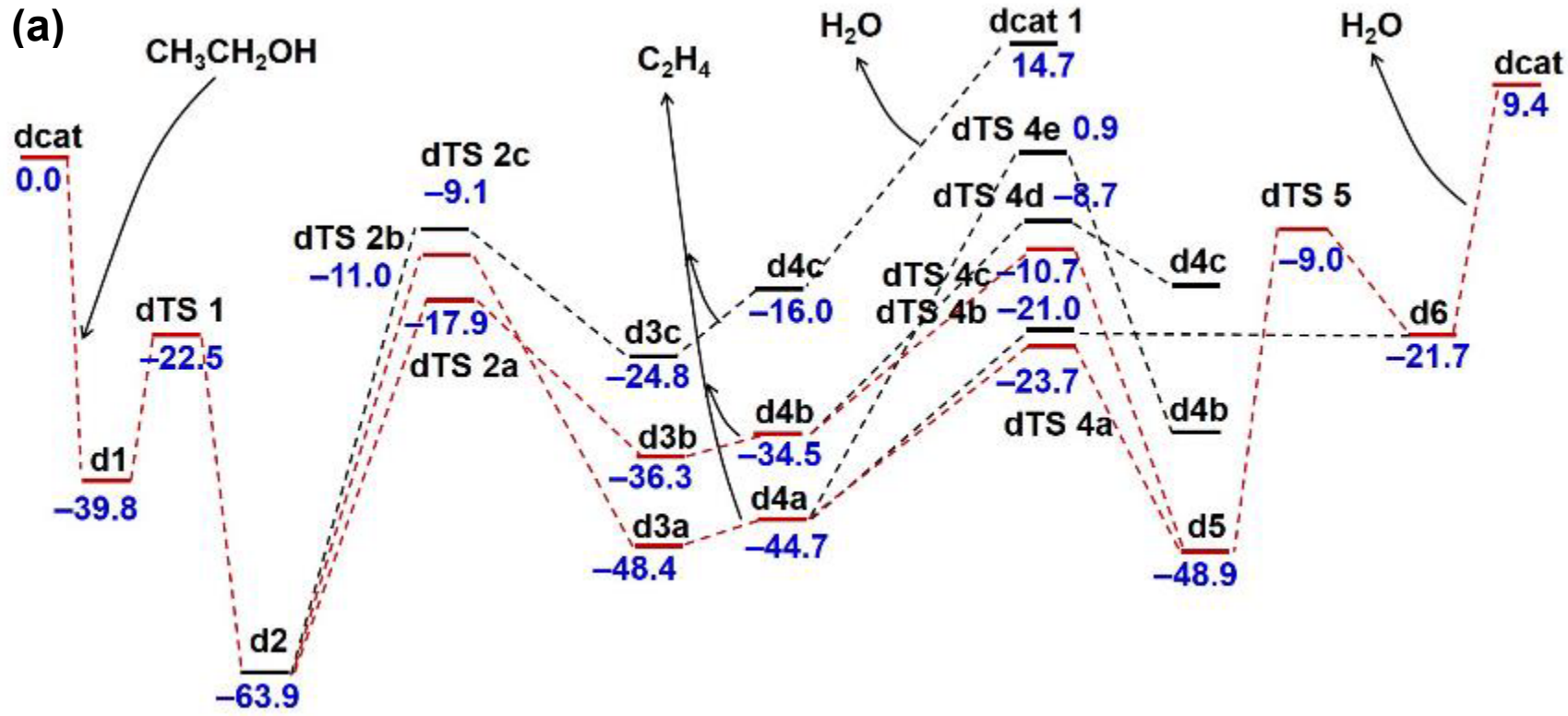
(a)
CH3CH2OH
dcat
0.0
dTS 1
−22.5
d1
−39.8
d2
−63.9
dTS 2c
−9.1
dTS 2b
−11.0
−17.9
dTS 2a
C2H4
d3c
−24.8
d3b
−36.3
d3a
−48.4
H2O
d4c
−16.0
d4b
−34.5
d4a
−44.7
dcat 1
14.7
dTS 4e 0.9
dTS 4d −8.7
dTS 4c −10.7
dTS 4b −21.0
−23.7
dTS 4a
d4c
d4b
d5
−48.9
dTS 5
−9.0
H2O
d6
−21.7
dcat
9.4

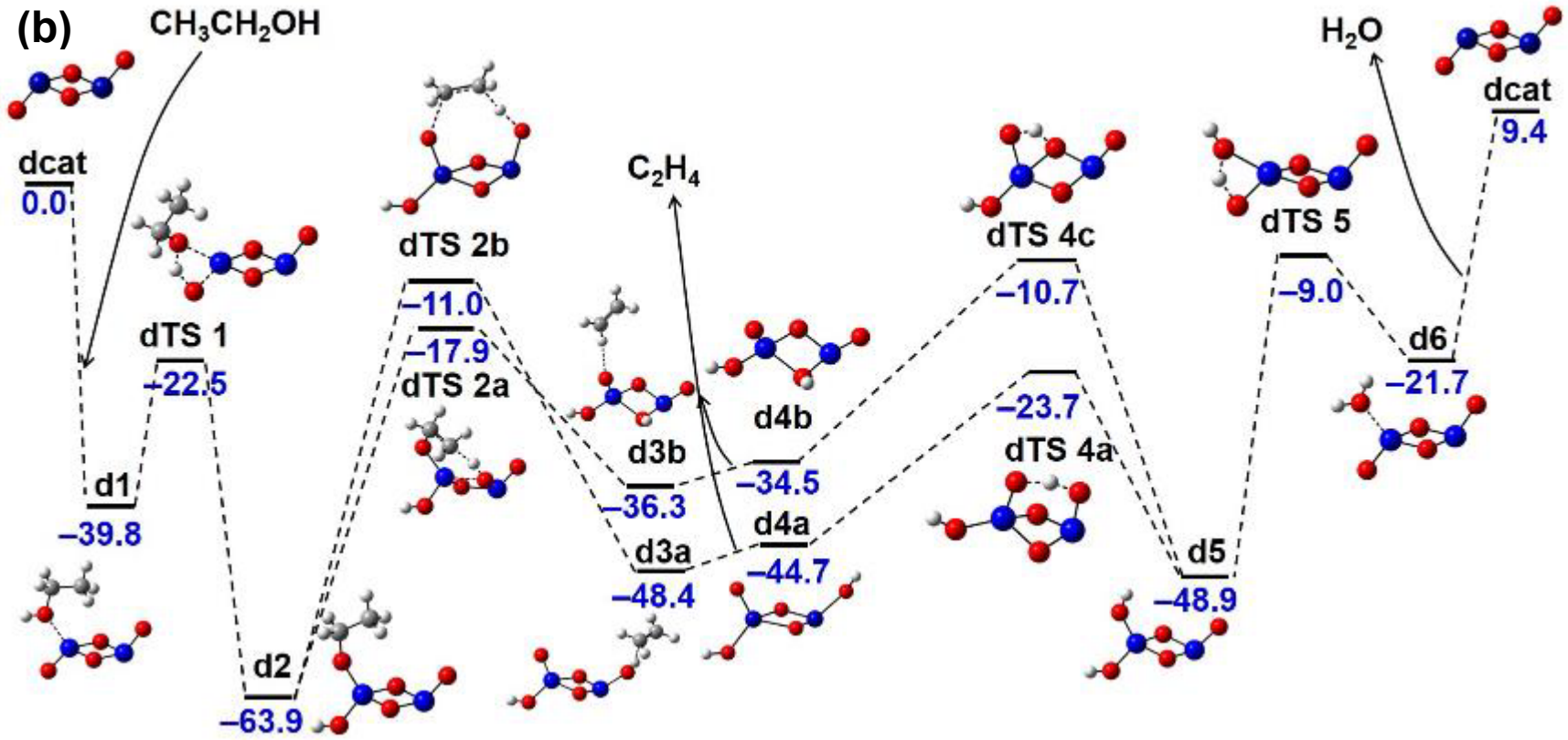

Figure 5.2. (a) Reaction coordinates (ΔH_{0K}, kcal/mol) for $CH_3CH_2OH \rightarrow C_2H_4 + H_2O$ on Ti_2O_4 nanoclusters at the CCSD(T)/aD//B3LYP/DZVP2 level. The two pathways in red indicate the lowest energy pathways D1 and D2 and these are shown with structures in (b).

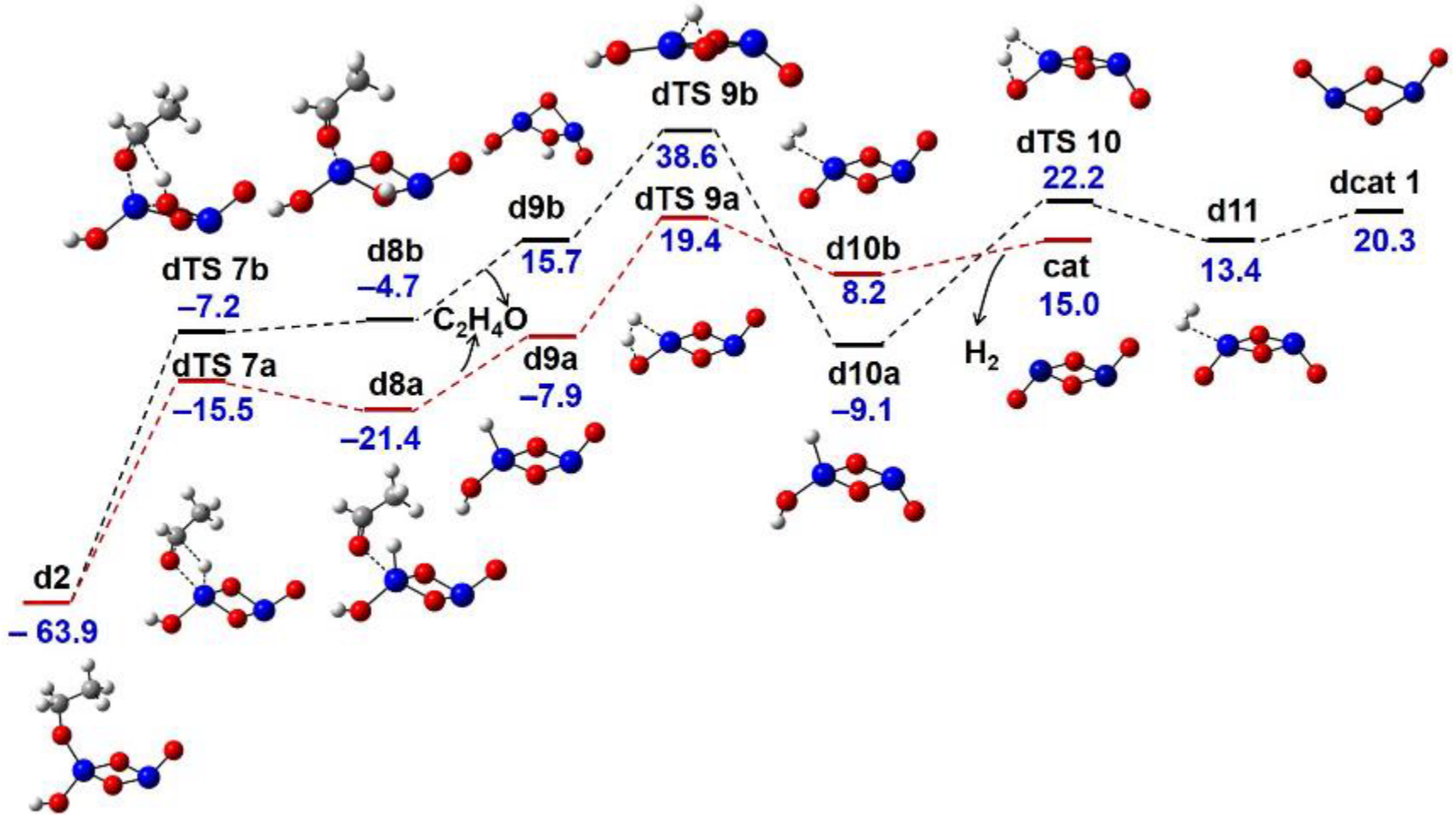

Figure 5.3. Reaction coordinates (ΔH_{0K}, kcal/mol) for $CH_3CH_2OH \rightarrow C_2H_4O + H_2$ on Ti_2O_4 nanoclusters at the CCSD(T)/aD//B3LYP/DZVP2 level. The pathway in red indicates the lowest energy pathway.

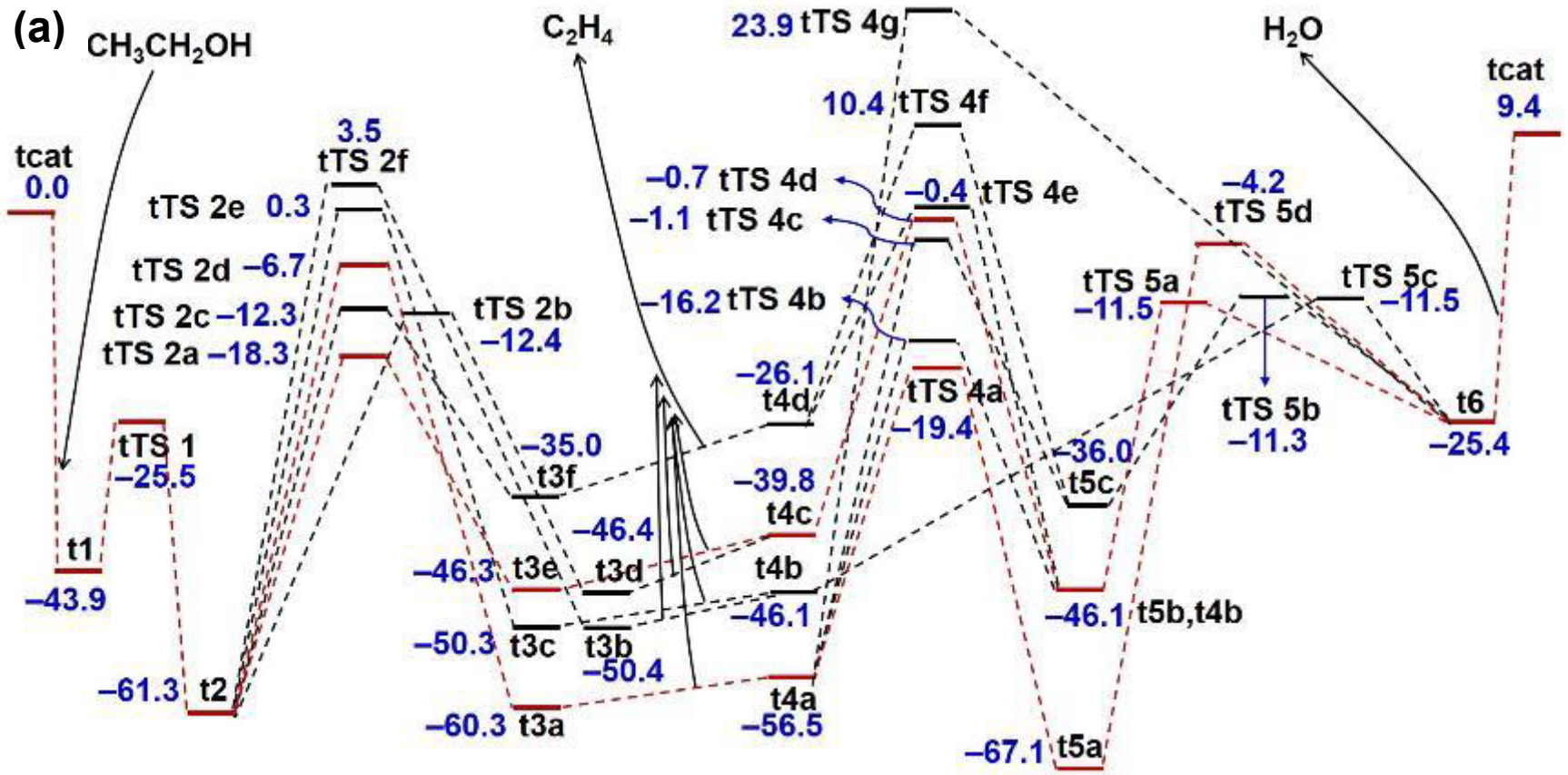
(a)
CH3CH2OH
C2H4
H2O
tcat
0.0
tTS 1
−25.5
t1
−43.9
tTS 2e 0.3
tTS 2d −6.7
tTS 2c −12.3
tTS 2a −18.3
3.5
tTS 2f
tTS 2b
−12.4
−61.3 t2
−35.0
t3f
−46.4
−46.3 t3e
t3d
−50.3 t3c
t3b
−50.4
−60.3 t3a
23.9 tTS 4g
10.4 tTS 4f
−0.7 tTS 4d
−1.1 tTS 4c
−16.2 tTS 4b
−0.4 tTS 4e
tTS 4a
−19.4
−26.1
t4d
−39.8
t4c
t4b
−46.1
t4a
−56.5
−4.2
tTS 5d
tTS 5a
−11.5
tTS 5c
−11.5
tTS 5b
−11.3
−36.0
t5c
−46.1 t5b,t4b
−67.1 t5a
tcat
9.4
t6
−25.4

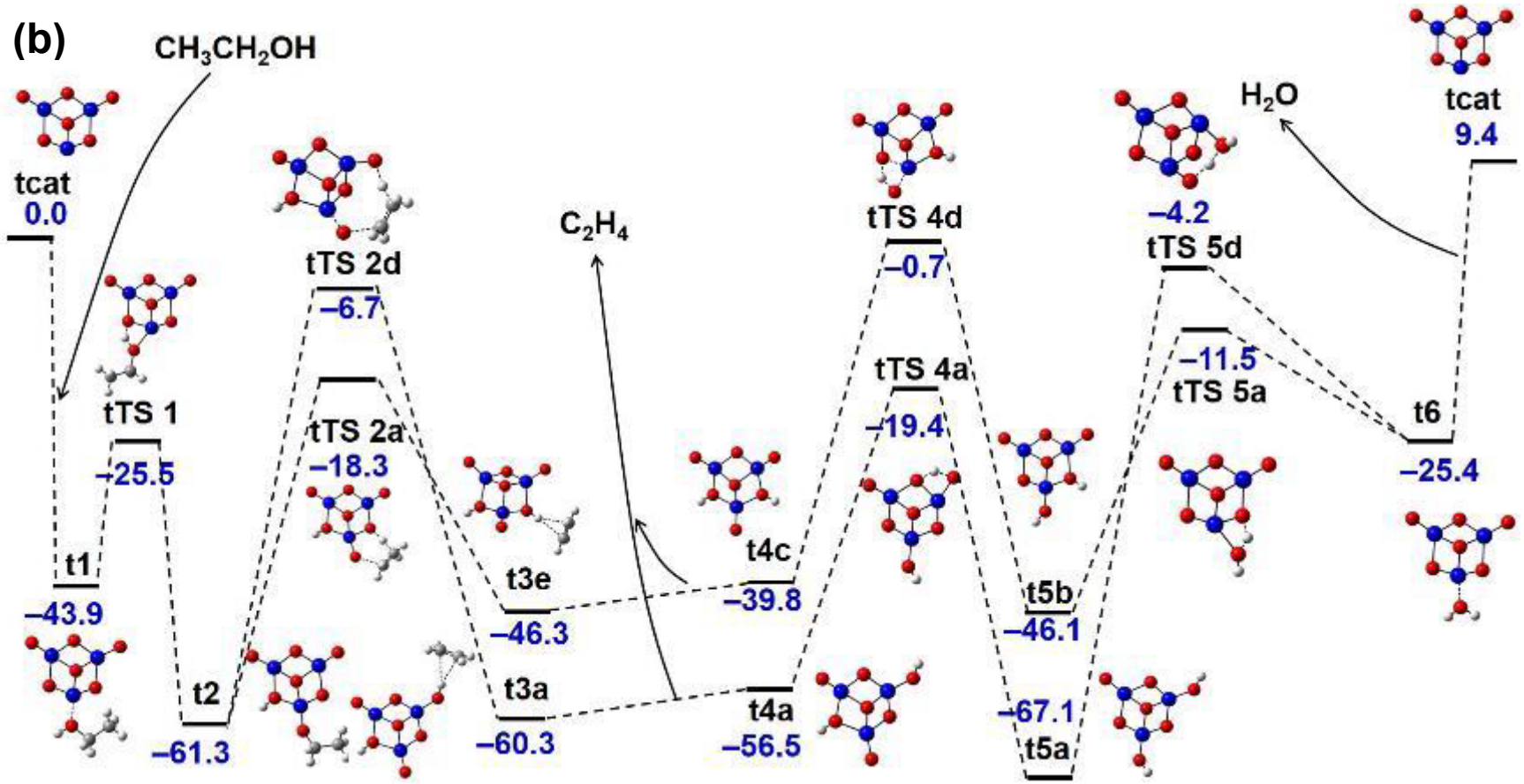

Figure 5.4. (a) Reaction coordinates (ΔH_{0K}, kcal/mol) for $CH_3CH_2OH \rightarrow C_2H_4 + H_2O$ at the CCSD(T)/aD//B3LYP/DZVP2 level on a Ti_3O_6 nanocluster. The two pathways in red indicate the lowest energy pathways T1 and T2 and these are shown with structures in (b).

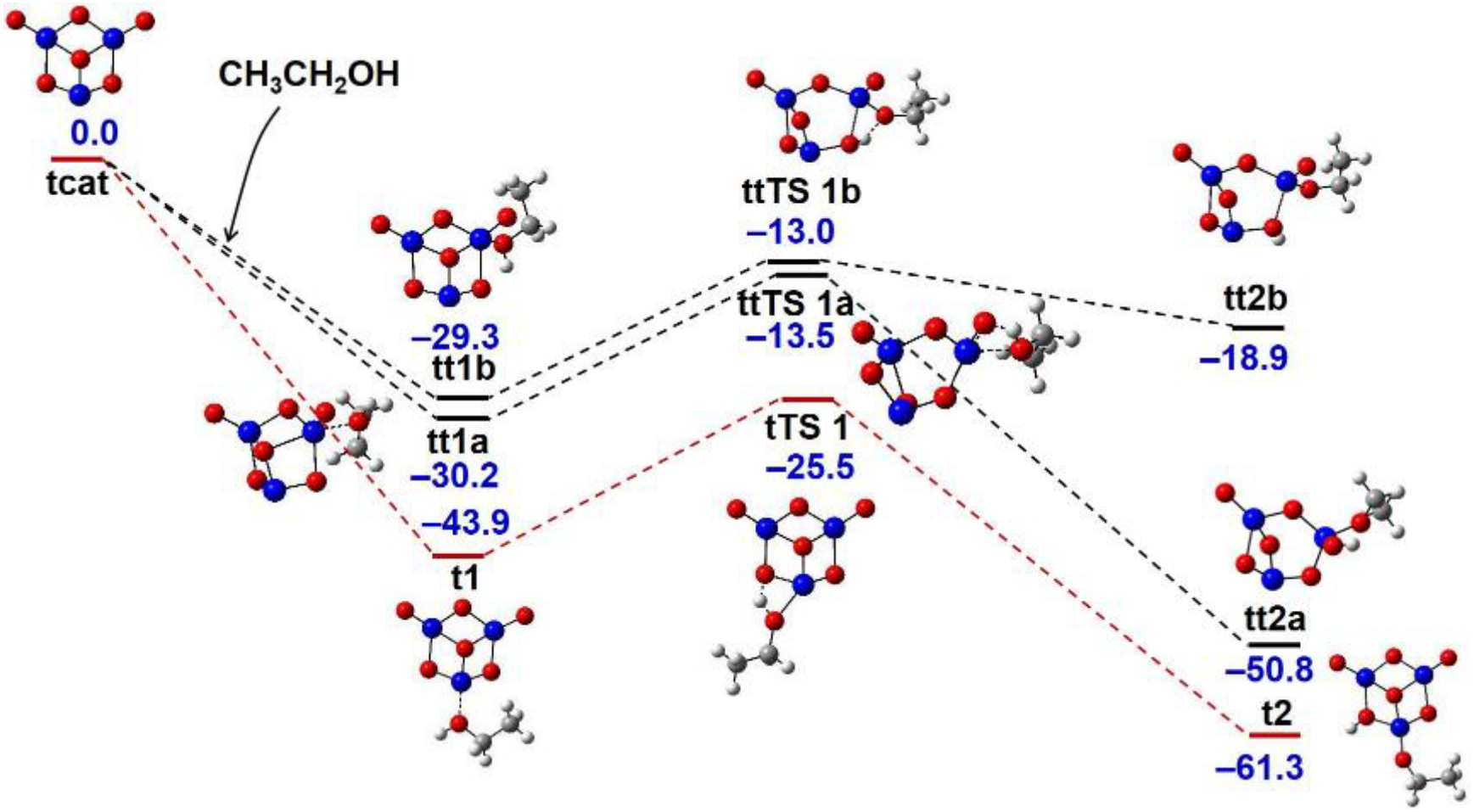

Figure 5.5. Reaction coordinates (ΔH_{0K}, kcal/mol) for physisorption and chemisorption of ethanol at the terminal Ti=O or the bridge Ti at the CCSD(T)/aD//B3LYP/DZVP2 level on a Ti_3O_6 nanocluster.

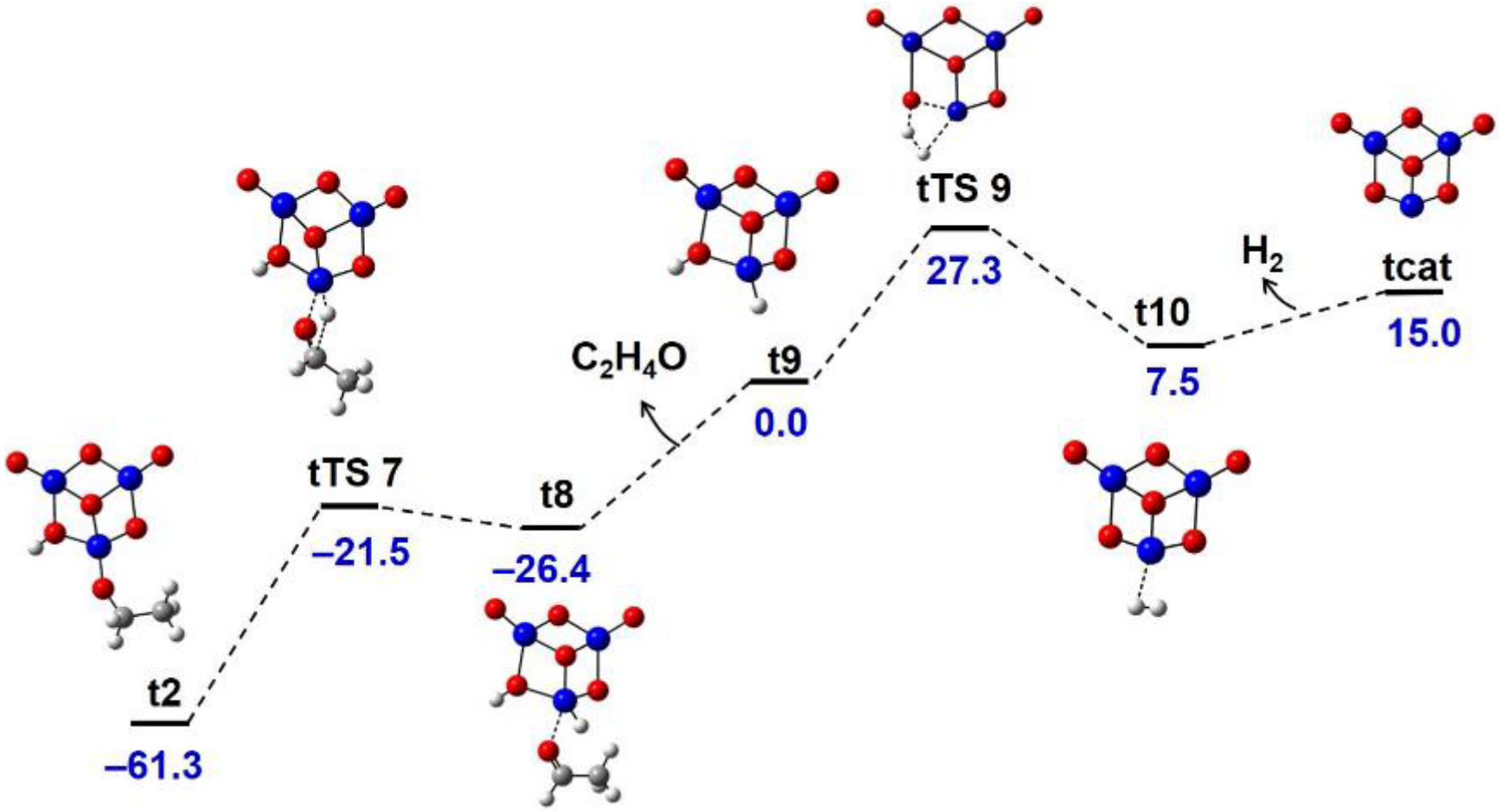

Figure 5.6. Reaction coordinate (ΔH_{0K}, kcal/mol) for $CH_3CH_2OH \rightarrow C_2H_4O + H_2$ at the CCSD(T)/aD//B3LYP/DZVP2 level on Ti_3O_6 nanoclusters.

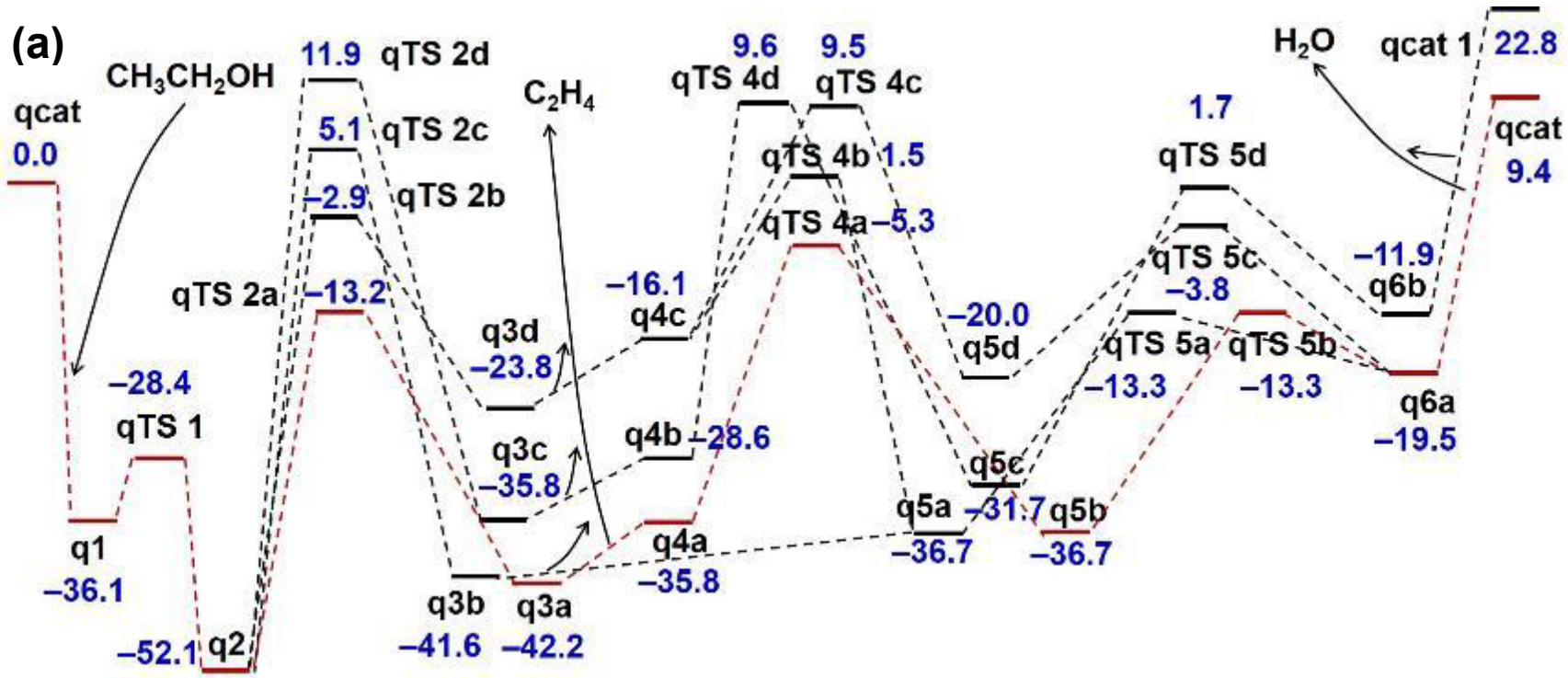
(a)
qcat
0.0
CH3CH2OH
11.9
qTS 2d
5.1
qTS 2c
−2.9
qTS 2b
qTS 2a
−13.2
C2H4
9.6
qTS 4d
9.5
qTS 4c
qTS 4b
1.5
qTS 4a
−5.3
H2O
qcat 1
22.8
qcat
9.4
1.7
qTS 5d
qTS 5c
−3.8
qTS 5a
−13.3
qTS 5b
−13.3
−11.9
q6b
q6a
−19.5
−20.0
q5d
q5c
−31.7
q5a
−36.7
q5b
−36.7
−16.1
q4c
q4b
−28.6
q4a
−35.8
q3d
−23.8
q3c
−35.8
q3b
−41.6
q3a
−42.2
−28.4
qTS 1
q1
−36.1
−52.1
q2

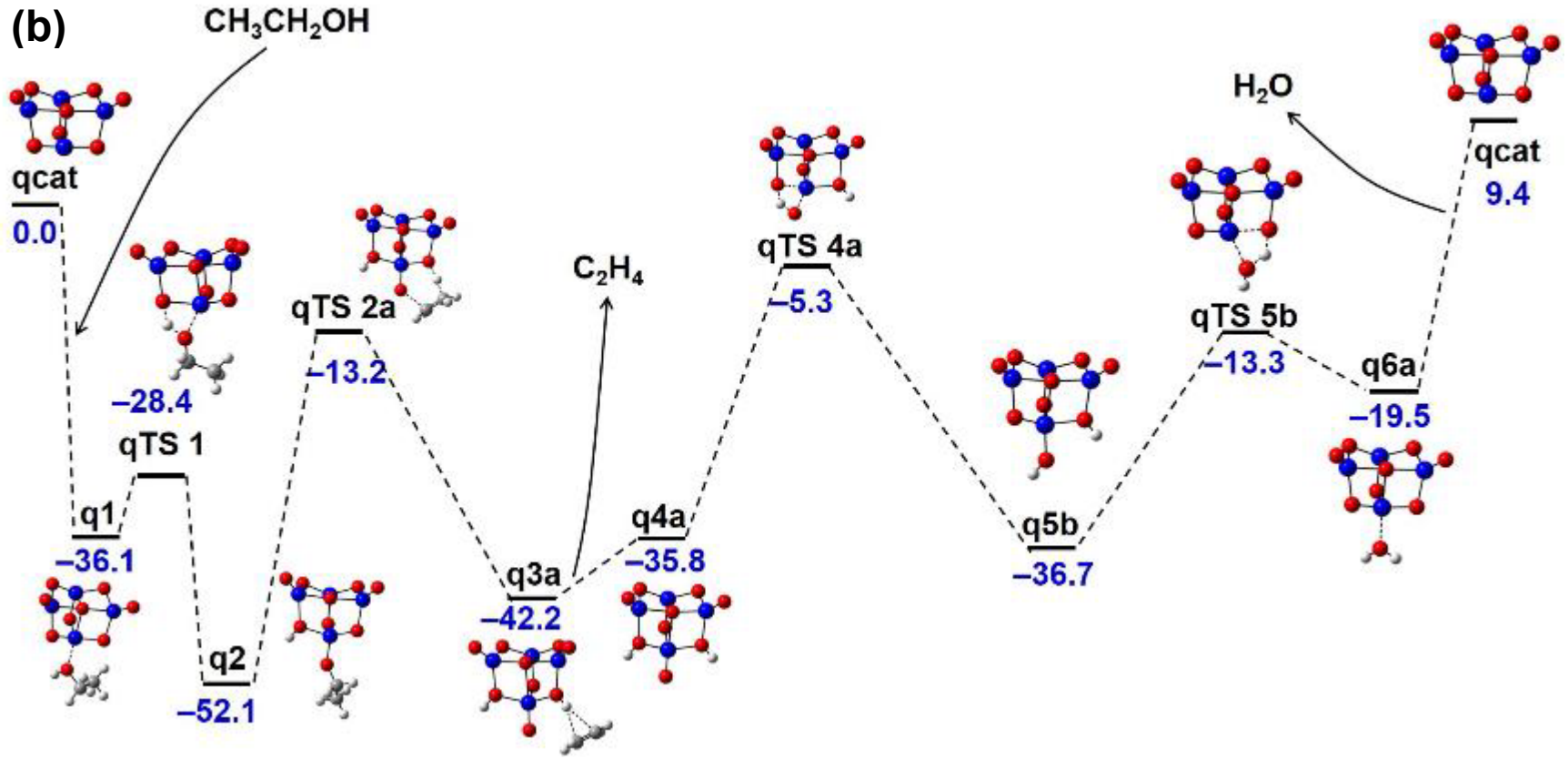

Figure 5.7. (a) Reaction coordinates (ΔH_{0K}, kcal/mol) for $CH_3CH_2OH \rightarrow C_2H_4 + H_2O$ at the CCSD(T)/aD//B3LYP/DZVP2 level on Ti_4O_8 nanoclusters. The pathway in red indicates the lowest energy pathway Q1 and this is shown with structures in (b).

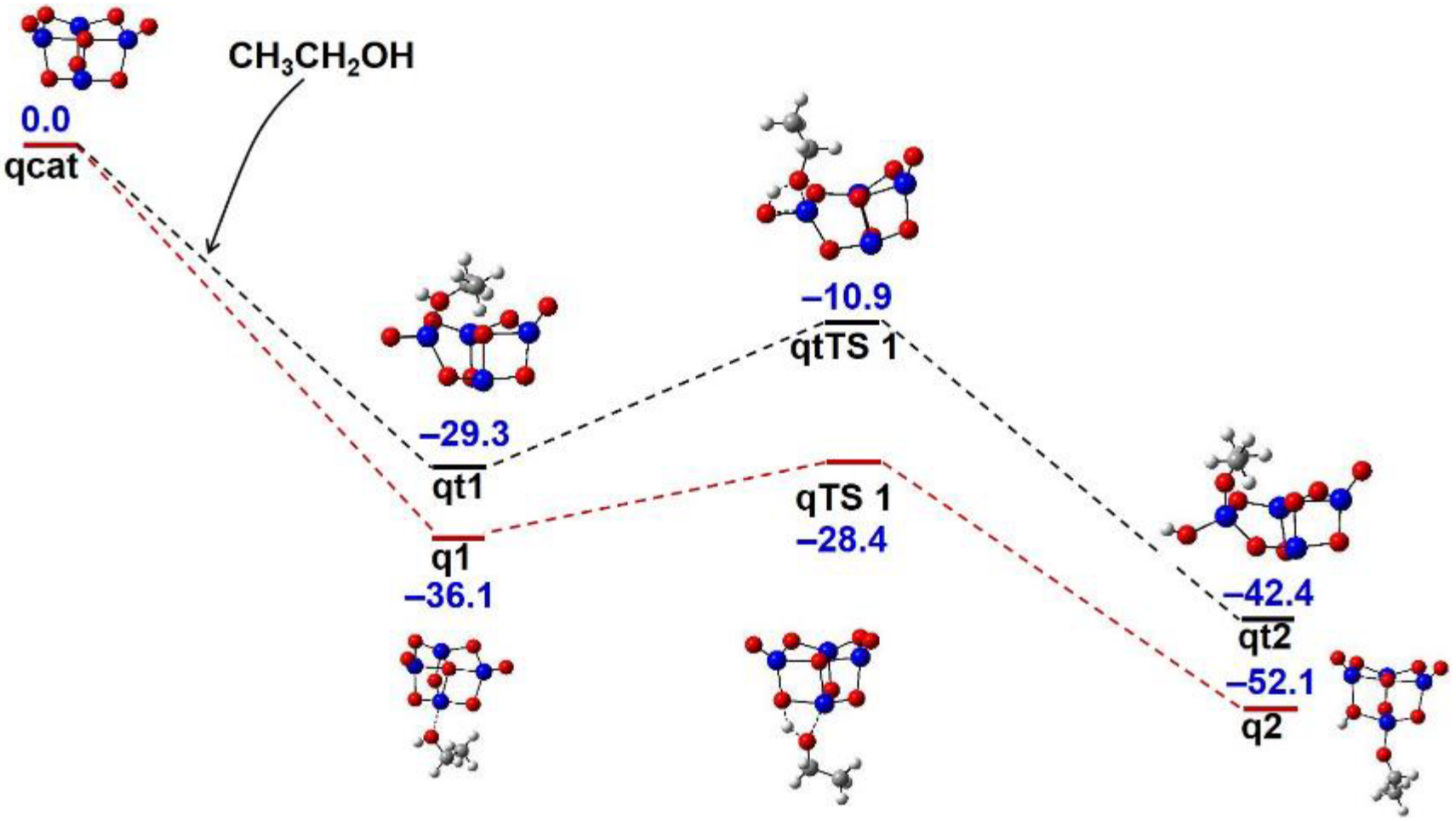

Figure 5.8. Reaction coordinates (ΔH_{0K}, kcal/mol) for physisorption and chemisorption of ethanol at the terminal Ti=O or the bridge Ti at the CCSD(T)/aD//B3LYP/DZVP2 level on a Ti_4O_8 nanocluster.

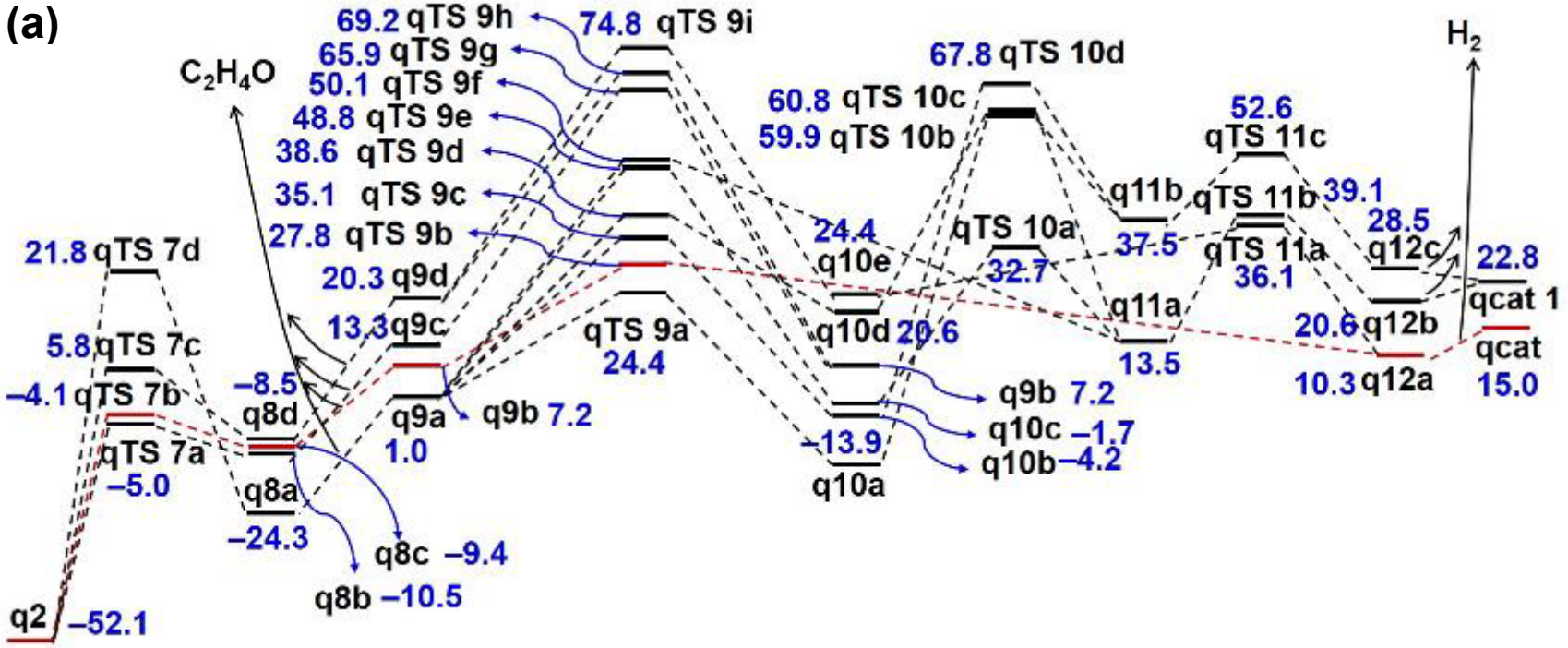
(a)
C_2H_4O
H_2
69.2 qTS 9h
74.8 qTS 9i
65.9 qTS 9g
50.1 qTS 9f
48.8 qTS 9e
38.6 qTS 9d
35.1 qTS 9c
27.8 qTS 9b
20.3 q9d
13.3 q9c
qTS 9a
24.4
21.8 qTS 7d
5.8 qTS 7c
−4.1 qTS 7b
qTS 7a
−5.0
q2
−52.1
−8.5
q8d
q8a
−24.3
q8c −9.4
q8b −10.5
q9a
q9b 7.2
1.0
67.8 qTS 10d
60.8 qTS 10c
59.9 qTS 10b
24.4
q10e
qTS 10a
32.7
q10d 20.6
q10a
−13.9
q9b 7.2
q10c −1.7
q10b −4.2
q11b
37.5
q11a
13.5
52.6
qTS 11c
qTS 11b
39.1
qTS 11a
36.1
28.5
q12c
20.6 q12b
10.3 q12a
22.8
qcat 1
qcat
15.0

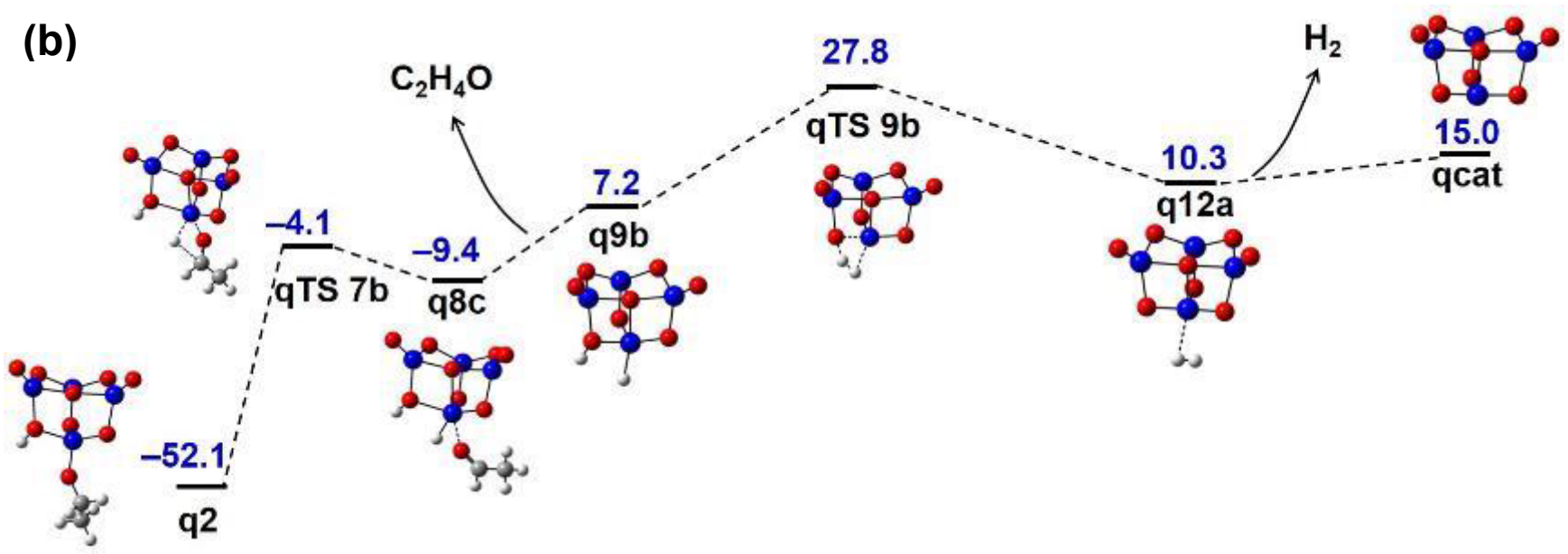

Figure 5.9. (a) Reaction coordinates (ΔH_{0K}, kcal/mol) for $CH_3CH_2OH \rightarrow C_2H_4O + H_2$ at the CCSD(T)/aD//B3LYP/DZVP2 level on Ti_4O_8 nanoclusters. The pathway in red indicates the lowest energy pathway Q2, and this is shown with structures in (b).

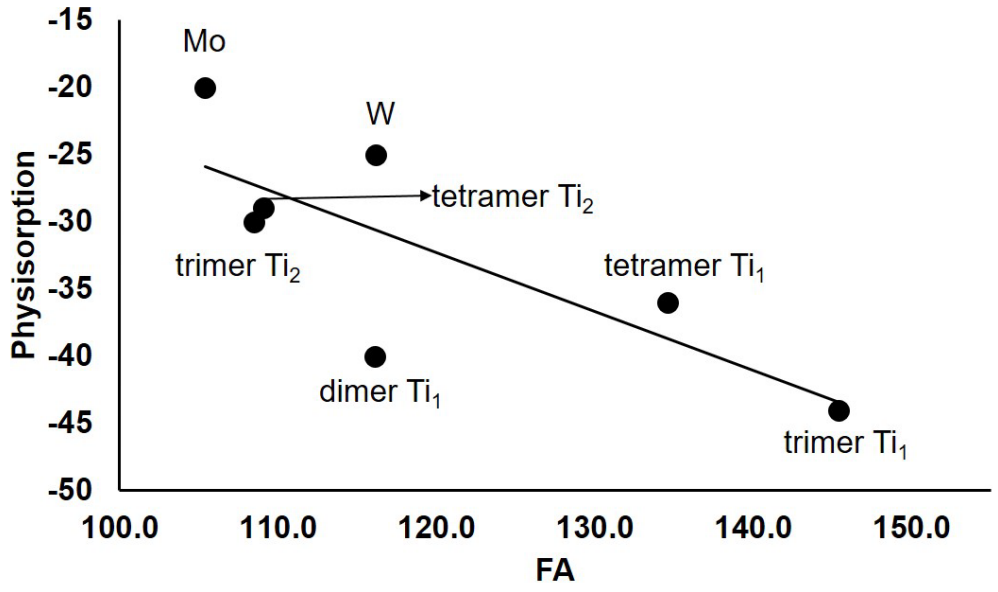

Figure 5.10. Correlation between physisorption of one ethanol to metal sites and FA in kcal/mol. The linear fit equation is $y = -0.44x + 20.14$ ($R^2 = 0.60$).

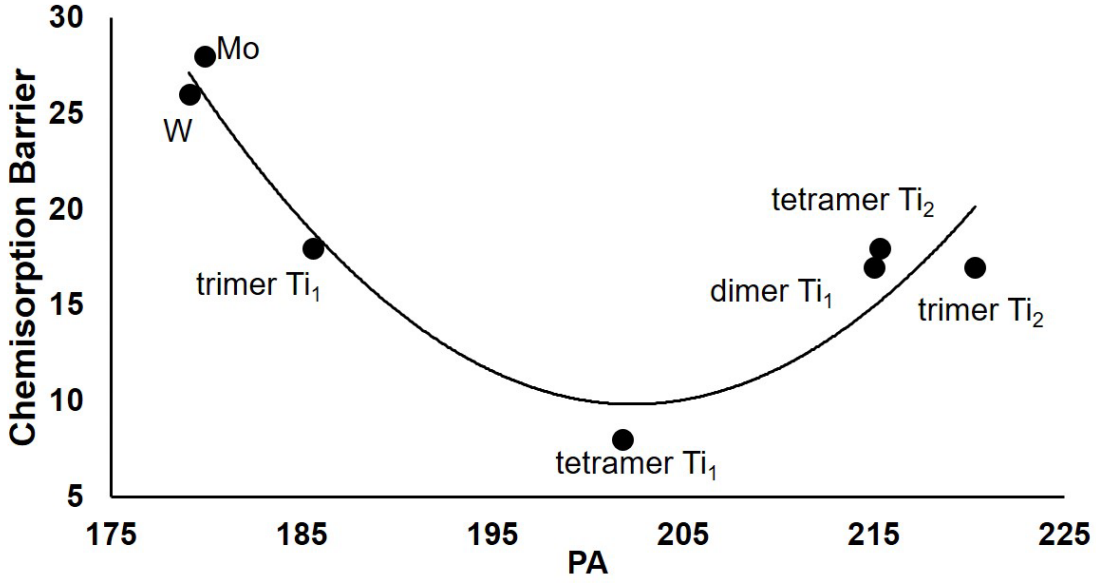

Figure 5.11. Correlation between chemisorption barriers of one ethanol to metal sites and PA in kcal/mol. The quadratic fit equation is $y = 0.03x^2 - 12.92x + 1316.90$ ($R^2 = 0.88$).

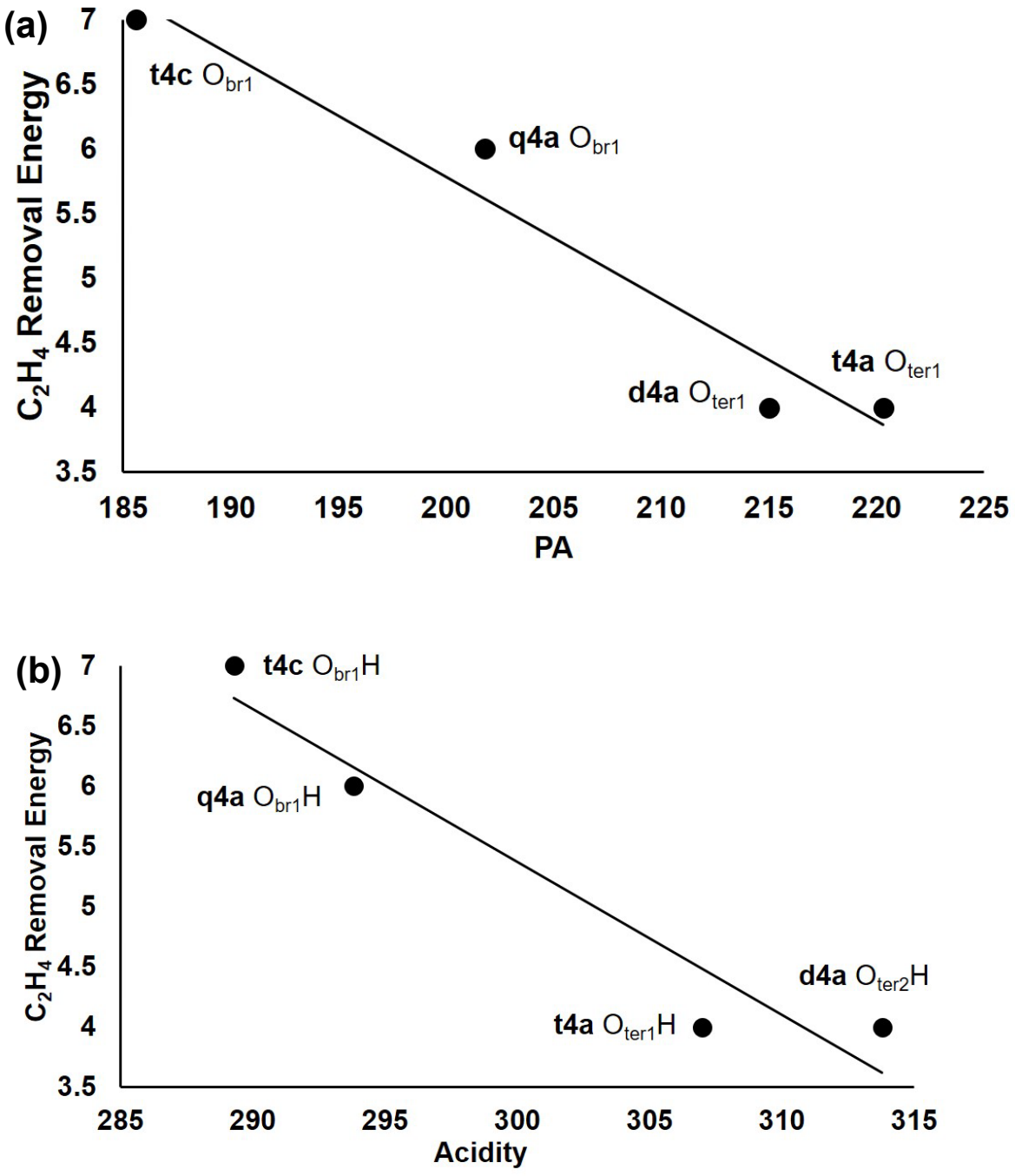

Figure 5.12. Correlation between C_2H_4 removal energy versus (a) PA and (b) acidity in kcal/mol. The linear fit equation for (a) is y = -0.09x + 24.70 (R^2 = 0.95). The linear fit equation for (b) is y = -0.13x + 43.50 (R^2 = 0.93).

References

[1] Fang, Z.; Wang, Y.; Dixon, D. A. Computational Study of Ethanol Conversion on Al_8O_{12} as a Model for γ-Al_2O_3. *J. Phys. Chem. C* **2015**, *119*, 23413−23421.

[2] Li, Z.; Fang, Z.; Kelly, M. S.; Kay, B. D.; Rousseau, R.; Dohnalek, Z.; Dixon, D. A. Ethanol Conversion on Cyclic $(MO_3)_3$ (M = Mo, W) Clusters. *J. Phys. Chem. C* **2014**, *118*, 4869−4877.

[3] Rousseau, R.; Dixon, D. A.; Kay, B. D.; Dohnálek, Z. Dehydration, Dehydrogenation and Condensation of Alcohols on Supported Oxide Catalysts based on Cyclic $(WO_3)_3$ and $(MoO_3)_3$ Clusters. *Chem. Soc. Rev.*, **2014**, *43*, 7664.

[4] Fang, Z.; Li, Z.; Kelley, M. S.; Kay, B. D.; Li, S.; Hennigan, J. M.; Rousseau, R.; Dohnálek, Z.; Dixon, D. A. Oxidation, Reduction, and Condensation of Alcohols over $(MO_3)_3$ (M = Mo, W) Nanoclusters. *J. Phys. Chem. C* **2014**, *118*, 22620−22634.

[5] Shinohara, Y.; Nakajima, T.; Suzuki, S. A Theoretical Study of the Dehydration and the Dehydrogenation Processes of Alcohols on Metal Oxides using MOPAC. *J. Mol. Struct.* **1999**, *460*, 231-244.

[6] Deskins, N. A.; Rousseau, R.; Dupuis, M. Defining the Role of Excess Electrons in the Surface Chemistry of TiO_2. *J. Phys. Chem. C* **2010**, *114*, 5891–5897.

[7] Yoon, Y.; Wang, Y.-G.; Rousseau, R.; Glezakou, V.-A. Impact of Nonadiabatic Charge Transfer on the Rate of Redox Chemistry of Carbon Oxides on Rutile TiO_2(110) Surface. *ACS Catal.* **2015**, *5*, 1764−1771.

[8] Li, Y.-F.; Selloni, A. Theoretical Study of Interfacial Electron Transfer from Reduced Anatase TiO_2(101) to Adsorbed O_2. *J. Am. Chem. Soc.* **2013**, *135*, 9195−9199.

[9] Zhang, Z.; Rousseau, R.; Gong, J.; Li, S.-C.; Kay, B. D.; Ge, Q.; Dohnálek, Z. Vacancy-Assisted Diffusion of Ethoxy Species on Rutile TiO_2(110). *PRL* **2008**, *101*, 156103.

[10] Deskins, N. A.; Rousseau, R.; Dupuis, M. Distribution of Ti^{3+} Surface Sites in Reduced TiO_2. *J. Phys. Chem. C* **2011**, *115*, 7562–7572.

[11] Yoon, Y.; Du, Y.; Garcia, J. C.; Zhu, Z.; Wang, Z.-T.; Petrik, N. G.; Kimmel, G. A.; Dohnálek, Z.; Henderson, M. A.; Rousseau, R.; Deskins, N. A.; Lyubinetsky, I. Anticorrelation between Surface and Subsurface Point Defects and the Impact on the Redox Chemistry of TiO_2 (110). *ChemPhysChem* **2015**,*16*, 313 – 321.

[12] Henderson, M. A.; Otero-Tapia, S.; Castro, M. E. The Chemistry of Methanol on the TiO_2(110) Surface: The Influence of Vacancies and Coadsorbed Species. *Faraday Discuss.* **1999**, *114*, 313-329.

[13] Henderson, M. A. A Surface Science Perspective on TiO_2 Photocatalysis. *Surf. Sci. Rep.* **2011**, *66*, 185-297.

[14] Pang, C. L.; Lindsay, R.; Thornton, G. Structure of Clean and Adsorbate-Covered Single-Crystal Rutile TiO_2 Surfaces. *Chem. Rev.* **2013**, *113*, 3887−3948.

[15] Zhang, Z.; Bondarchuk, O.; White, J. M.; Kay, B. D.; Dohnálek, Z. Imaging Adsorbate O-H Bond Cleavage: Methanol on TiO_2(110). *J. Am. Chem. Soc.* **2006**, *128*, 4198-4199.

[16]Zhang, Z.; Yoon, Y.; Lin, X.; Acharya, D.; Kay, B. D.; Rousseau, R.; Dohnalek, Z. OH Group Dynamics of 1,3-Propanediol on TiO_2(110). *J. Phys. Chem. Lett.* **2012**, *3*, 3257−3263.

[17] Li, Z.; Smith, R. S.; Kay, B. D.; Dohnálek, Z. Determination of Absolute Coverages for Small Aliphatic Alcohols on TiO_2(110). *J. Phys. Chem. C* **2011,** *115,* 22534–22539

[18] Kim, Y. K.; Kay, B. D.; White, J. M.; Dohnálek, Z. Alcohol Chemistry on Rutile TiO_2(110): The Influence of Alkyl Substituents on Reactivity and Selectivity. *J. Phys. Chem. C* **2007**, *111*, 18236-18242.

[19] Zhang, Z.; Bondarchuk, O.; White, J. M.; Kay, B. D.; Dohnálek, Z. Direct Visualization of 2-Butanol Adsorption and Dissociation on TiO2(110). *J. Phys. Chem. C*, **2007**, *111*, 3021-3027.

[20] Kim, Y. K.; Kay, B. D.; White, J. M.; Dohnálek, Z. Inductive Effect of Alkyl Chains on Alcohol Dehydration at Bridge-bonded Oxygen vacancies on TiO_2(110). *Catal. Lett.* **2007**, *119*, 1-4.

[21] Wang, T.; Fang, Z.; Gist, N. W.; Li, S.; Dixon, D. A.; Gole, J. L. Computational Study of the Hydrolysis Reactions of the Ground and First Excited Triplet States of Small TiO_2 Nanoclusters. *J. Phys. Chem. C* **2011**, *115*, 9344−9360.

[22] Fang, Z.; Dixon, D. A. Computational Study of H_2 and O_2 Production from Water Splitting by Small $(MO_2)_n$ Clusters (M = Ti, Zr, Hf). *J. Phys. Chem. A* **2013**, *117*, 3539−3555.

[23] Li, S.; Dixon, D. A. Molecular and Electronic Structures, Brönsted Basicities, and Lewis Acidities of Group VIB Transition Metal Oxide Clusters. *J. Phys. Chem. A* **2006**, *110*, 6231-6244.

[24] Li, S.; Guenther, C. L.; Kelley, M. S.; Dixon, D. A. Molecular Structures, Acid-Base Properties, and Formations of Group 6 Transition Metal Hydroxides. *J. Phys. Chem. C* **2011**, *115*, 8072−8103.

[25] Fang, Z.; Zetterholm, P.; Dixon, D. A. 1,2-Ethanediol and 1,3-Propanediol Conversions over $(MO_3)_3$ (M = Mo, W) Nanoclusters: A Computational Study. *J. Phys. Chem. A* **2016**, *120*, 1897−1907.

[26] Li, S.; Dixon, D. A. Structural and Electronic Near Degeneracy of M_3O_9 (M = Cr, Mo, W). *J. Phys. Chem. C* **2011**, *115*, 19190–19196.

[27] https://atct.anl.gov/Thermochemical%20Data/version%201.122g/index.php (accessed January 18, 2019).

[28] Ruscic, B.; Pinzon, R. E.; Morton, M. L.; von Laszevski, G.; Bittner, S. J.; Nijsure, S. G.; Amin, K. A.; Minkoff, M.; Wagner, A. F. Introduction to Active Thermochemical Tables: Several "Key" Enthalpies of Formation Revisited. *J. Phys. Chem. A* **2004**, *108*, 9979−9997.

[29] Changala, P. B.; Nguyen, T. L.; Baraban, J. H.; Ellison, G. B.; Stanton, J. F.; Bross, D. H.; Ruscic, B. Active Thermochemical Tables: The Adiabatic Ionization Energy of Hydrogen Peroxide. *J. Phys. Chem. A* **2017**, *121*, 8799−8806.

[30] Frenkel, M.; Kabo, G. J.; Marsh. K. N.; Roganov, G. N.; Wilhoit, R. C. *Thermodynamics of Organic Compounds in the Gas State, Vol. I.* TRC Data Series, Thermodynamics Research Center, College Station TX, 1994.

[31] Parr, R. G.; Yang, W. *Density-Functional Theory of Atoms and Molecules*. Oxford University Press: New York, 1989.

[32] Beck, A. D. Density-Functional Thermochemistry. III. The Role of Exact Exchange. *J. Chem. Phys.* **1993**, *98*, 5648-5652.

[33] Lee, C.; Yang, W.; Parr, R. G. Accurate and Simple Analytic Representation of the Electron-Gas Correlation Energy. *Phys. Rev. B.* **1988**, *37*, 785-789.

[34] Godbout, N.; Salahub, D. R.; Andzelm, J.; Wimmer, E. Optimization of Gaussian-Type Basis Sets for Local Spin Density Functional Calculations. Part I. Boron Through Neon, Optimization Technique and Validation. *Can. J. Chem.* **1992**, *70*, 560−571.

[35] Li, S.; Dixon, D. A. Molecular Structures and Energetics of the $(TiO_2)_n$ (n = 1−4) Clusters and Their Anions. *J. Phys. Chem. A* **2008**, *112*, 6646−6666.

[36] Fang, Z.; Vasiliu, M.; Peterson, K. A.; Dixon. D. A. Computational Study of Molecular Hydrogen Adsorption over Small $(MO_2)_n$ Nanoclusters (M = Ti, Zr, Hf, n = 1 to 4). *J. Phys. Chem. A* **2018**, *122*, 4338–4349.

[37] Figgen, D.; Peterson, K. A.; Dolg, M.; Stoll, H. Energy-Consistent Pseudopotentials and Correlation Consistent Basis Sets for the 5d Elements Hf-Pt. *J. Chem. Phys.* **2009**, *130*, 164108.

[38] Peterson, K.A.; Figgen, D.; Dolg, M.; Stoll, H. Energy-Consistent Relativistic Pseudopotentials and Correlation Consistent Basis Sets for the 4d Elements Y-Pd. *J. Chem. Phys.* **2007**, *126*, 124101.

[39] Peng, C.; Schlegel, H. B. Combining Synchronous Transit and Quasi-Newton Methods to Find Transition States. Isr. J. Chem. 1993, 33, 449−454.

[40] Frisch, M. J.; Trucks, G. W.; Schlegel, H. B.; Scuseria, G. E.; Robb, M. A.; Cheeseman, J. R.; Scalmani, G.; Barone, V.; Petersson, G. A.; Nakatsuji, H.; Li, X.; Caricato, M.; Marenich, A. V.; Bloino, J.; Janesko, B. G.; Gomperts, R.; Mennucci, B.; Hratchian, H. P.; Ortiz, J. V.; Izmaylov, A. F.; Sonnenberg, J. L.; Williams-Young, D.; Ding, F.; Lipparini, F.; Egidi, F.; Goings, J.; Peng, B.; Petrone, A.; Henderson, T.; Ranasinghe, D.; Zakrzewski, V. G.; Gao, J.; Rega, N.; Zheng, G.; Liang, W.; Hada, M.; Ehara, M.; Toyota, K.; Fukuda, R.; Hasegawa, J.; Ishida, M.; Nakajima, T.; Honda, Y.; Kitao, O.; Nakai, H.; Vreven, T.; Throssell, K.; Montgomery, J. A., Jr.; Peralta, J. E.; Ogliaro, F.; Bearpark, M. J.; Heyd, J. J.; Brothers, E. N.; Kudin, K. N.; Staroverov, V. N.; Keith, T. A.; Kobayashi, R.; Normand, J.; Raghavachari, K.; Rendell, A. P.; Burant, J. C.; Iyengar, S. S.; Tomasi, J.; Cossi, M.; Millam, J. M.; Klene, M.; Adamo, C.; Cammi, R.; Ochterski, J. W.; Martin, R. L.; Morokuma, K.; Farkas, O.; Foresman, J. B.; Fox, D. J. Gaussian 16, Revision A.03, Gaussian, Inc., Wallingford CT, 2016.

[41] Purvis, G. D., III; Bartlett, R. J. A Full Coupled Cluster Singles and Doubles Model: The Inclusion of Disconnected Triples. *J. Chem. Phys.* **1982**, *76*, 1910-1918.

[42] Raghavachari, K.; Truck, G.W.; Pople, J.A.; Head-Gordon, M. A Fifth-Order Perturbation Comparison of Electron Correlation Theories. *Chem. Phys. Lett*. **1989**, *157*, 479-483.

[43] Bartlett, R. J.; Musial, M. Coupled Cluster Theory in Quantum Chemistry. *Rev. Mod. Phys.* **2007**, *79*, 291-352.

[44] Deegan, M. J. O.; Knowles, P. J. Perturbative Corrections to Account for Triple Excitations in Closed and Open Shell Coupled Cluster Theories. *Chem. Phys. Lett*. **1994**, *227*, 321-327.

[45] Kendall, R. A.; Dunning, T. H.; Harrison, R. J. Electron-Affinities of the 1st-Row Atoms Revisited - Systematic Basis-Sets and Wave-Functions. *J. Chem. Phys.* **1992**, *96*, 6796−6806.

[46] Dunning, T.H., Jr. Gaussian Basis Sets for Use in Correlated Molecular Calculations. I. The Atoms Boron Through Neon and Hydrogen. *J. Chem. Phys*. **1989**, *90*, 1007-1023.

[47] Li, S.; Hennigan, J. M.; Dixon, D. A.; Peterson, K. A. Accurate Thermochemistry for Transition Metal Oxide Clusters. *J. Phys. Chem. A* **2009**, *113*, 7861-7877.

[48] Werner, H.-J.; Knowles, P. J.; Knizia, G.; Manby, F. R.; Schütz, M.; Celani, P.; Györffy, W.; Kats, D.; Korona, T.; Lindh, R.; Mitrushenkov, A.; Rauhut, G.; Shamasundar, K. R.; Adler, T. B.; Amos, R. D.; Bennie, S. J.; Bernhardsson, A.; Berning, A.; Cooper, D. L.; Deegan, M. J. O.; Dobbyn, A. J.; Eckert, F.; Goll, E.; Hampel, C.; Hesselmann, A.; Hetzer, G.; Hrenar, T.; Jansen, G.; Köppl, C.; Lee, S. J. R.; Liu, Y.; Lloyd, A. W.; Ma, Q.; Mata, R. A.; May, A. J.; McNicholas, S. J.; Meyer, W.; Miller III, T. F.; Mura, M. E.; Nicklass, A.; O'Neill, D. P.; Palmieri, P.; Peng, D.; Petrenko, T.; Pflüger, K.; Pitzer, R.; Reiher, M.; Shiozaki, T.; Stoll, H.; Stone, A. J.; Tarroni, R.; Thorsteinsson, T.; Wang, M.; Welborn, M. MOLPRO, version 2018.2, a package of ab initio programs, See http://www.molpro.net. Accessed June 23rd, 2022.

[49] Werner H.-J.; Knowles, P. J.; Knizia, G.; Manby, F. R.; Schütz, M. Molpro: A General-Purpose Quantum Chemistry Program Package. *WIREs Comput. Mol. Sci.* **2012**, *2*, 242-253.

[50] Werner, H-J.; Knowles, P. J.; Manby, F. R.; Black, J. A.; Doll, K.; Heßelmann, A.; Kats, D.; Köhn, A.; Korona, T.; Kreplin, D. A.; Ma, Q.; Miller III, T. F.; Mitrushchenkov, A.; Peterson, K. A.; Polyak, I.; Rauhut, G.; Sibaev, M. The Molpro Quantum Chemistry Package *J. Chem. Phys.* **2020**, *152*, 144107.

[51] Guo, Q.; Xu, C.; Ren, Z.; Yang, W.; Ma, Z.; Dai, D.; Fan, H.; Minton, T. K.; Yang, X. Stepwise Photocatalytic Dissociation of Methanol and Water on TiO_2(110). *J. Am. Chem. Soc.* **2012**, *134*, 13366–13373.

[52] Perdew, J. P.; Burke, K.; Ernzerhof, M. Generalized Gradient Approximation Made Simple. *Phys. Rev. Lett.* **1996**, *77*, 3865−3868.

[53] Christe, K. O.; Dixon, D. A.; McLemore, D. K.; Wilson, W. W.; Sheehy, J.; Boatz, J. A. On a Quantitative Scale for Lewis Acidity and Recent Progress in Polynitrogen Chemistry. *J. Fluor. Chem.*, **2000**, *101*, 151-153

[54] Hunter, E.P.; Lias, S.G. Evaluated Gas Phase Basicities and Proton Affinities of Molecules: An Update. *J. Phys. Chem. Ref. Data* **1998**, *27*, 413-656.

Additional Higher Energy Pathways for Trimer Dehydration The remaining four pathways for transfer of the β hydrogen of the ethoxy to O sites of the Ti_3O_7H fragment of **t2** are discussed here. Transferring the β hydrogen to the tridentate O_{tribr} can occur at both sides of the plane of three Ti atoms, which results in two transition states, **tTS 2b** to form **t3d**, and **tTS 2c** to form **t3f**, with transition barriers of ~ 49 kcal/mol, which between the transition barriers of **tTS 2a** and **tTS 2d**. The reaction energy from **t2** to **t3d** is the same as that to **t3e**, ~15 kcal/mol. The reaction energy from **t2** to **t3f** is the most endothermic of all, ~26 kcal/mol. Transferring the β H to the oxygen from ethanol through **tTS 2e** to form **t3c**, and to the terminal O_{ter2} through **tTS 2f** to form **t3b**, are bot endothermic by ~ 11 kcal/mol, with both of their transition barriers slightly above the reactant asymptote. Removal of an ethylene from these **t3** products requires 4 to 9 kcal/mol. Structure **t4d** has a bidentate $O_{dibr12}H$ group and a tridentate $O_{tribr}H$ group. The reactions for transferring the proton of the bidentate $O_{dibr12}H$ group to the terminal O from ethanol through **tTS 4e** to form **t5b** or transferring the proton of the tridentate $O_{tribr}H$ group through **tTS 4f** to form **t5c**, are exothermic by *ca.* -20 and -10 kcal/mol, respectively. Transition state **tTS 4e** is essentially isoenergetic with the reactant asymptote, and **tTS 4f** is above the reactant asymptote by ~10 kcal/mol. Transferring the proton of the tridentate $O_{tribr}H$ group from **t5c** to the terminal OH is endothermic by ~11 kcal/mol with a transition barrier of ~25 kcal/mol.

There are an additional three possible pathways from the reactant **t4a**. The proton on the bidentate $O_{dibr12}H$ group of **t4a** can transfer to a bidentate O_{dirb23} via **tTS 4b**, forming the product **t4b**. Structure **t4b** is essentially same as **t5b**. The energy barrier is ~40 kcal/mol, with **tTS 4b** being ~3 kcal/mol higher than **tTS 4a**; the reaction is endothermic by ~10 kcal/mol. The proton on the bidentate $O_{dibr12}H$ group of **t4a** can also transfer to the tridentate O_{tribr} via **tTS4c** forming **t5c** with an energy barrier of ~55 kcal/mol and an endothermic

reaction energy of ~ 21 kcal/mol; **tTS4c** is ~1 kcal/mol below the reactant asymptote. Directly transferring the proton of the bidentate $O_{dibr12}H$ group of **t4a** to the oxygen of the terminal OH group via **tTS 4g** forms the Ti_3O_6-H_2O complex **t6**, though with the highest energy barrier of ~80 kcal/mol.

Additional Higher Energy Pathways for Tetramer Dehydration Three additional pathways from **q2** for the β H on the tetramers are discussed below. Transferring the β H to the bidentate O_{dibr14} via **qTS 2b** is the most endothermic, ~ 28 kcal/mol, reaction with the second lowest transition barrier of ~ 49 kcal/mol. Transition states **qTS 2c** for transfer of the β H to the O from ethanol to form **q3b** and **qTS 2d** for transfer of the β H to the tetradentate $O_{tetrabr}$ to form **q3c** are both above the reactant asymptote. The reaction energy from **q2** to **q3b** is close to that for forming **q3a**. An energy of 5 to 7 kcal/mol is needed to remove an ethylene. Structure **q4c** has a bidentate $O_{dibr12}H$ group and a bidentate $O_{dibr14}H$ group. Transfer of the proton of the bidentate $O_{dibr14}H$ group to the terminal oxygen from ethanol through **qTS 4b** to form **q5a** is exothermic by *ca.* -21 kcal/mol with a transition barrier of ~ 18 kcal/mol with the transition state being ~ 2 kcal/mol above the reactant asymptote. Transfer of the proton of the bidentate $O_{dibr12}H$ group to the terminal OH group from **q5a** through **qTS 5a** to form the Ti_4O_8-H_2O complex **q6a** is endothermic by ~ 17 kcal/mol with a transition barrier of ~ 23 kcal/mol. The proton of the bidentate $O_{dibr12}H$ group can also transfer to the terminal oxygen from ethanol at **q4c** via **qTS 4c** to form **q5d**, which is exothermic by *ca.* -4 kcal/mol, ~ 12 kcal/mol less exothermic than the reaction from **q4c** to **q5a**. The transition barrier between **qTS 4c** and **q4c** is ~ 8 kcal/mol higher as compared to **qTS 4b**. Transfer of the proton of the bidentate $O_{dibr14}H$ group to the terminal OH group at **q5d** is thermoneutral with a transition barrier of ~ 16 kcal/mol. Structure **q4b** has a bidentate $O_{dibr12}H$ group and a tridentate $O_{tetrabr}H$ group. Transfer of the proton of the tridentate $O_{tetrabr}H$ group to the terminal O_{ter2} through **qTS 4d** to form **q5c** is exothermic by *ca*. -3 kcal/mol with

a large transition barrier of ~ 38 kcal/mol; **qTS 4d** has the same energy as **qTS 4c**. Then, transfer of the proton of the bidentate $O_{dibr12}H$ group to the terminal OH group via **qTS 5d** to form **q6b** is endothermic by ~ 20 kcal/mol with a transition barrier ~ 30 kcal/mol with **qTS 5d** being above the reactant asymptote by ~ 2 kcal/mol. Removal of a water from **q6b** is endothermic by ~ 56 kcal/mol. The reaction energy for **qcat 1**, 22.8 kcal/mol, includes the dehydration energy of one ethanol and the transformation energy of Ti_4O_8 from **qcat** to **qcat 1**.

Additional Higher Energy Pathways for Tetramer Dehydrogenation The other 3 pathways from **q2** are transfer of the α hydrogen: (1) to the bidentate O_{dibr13} via **qTS 7a** to form **q8b**, (2) to the bidentate O_{dibr14} via **qTS 7c** to form **q8d**, and (3) to the tetradentate $O_{tetrabr}$ through **qTS 7d**. Transition states **qTS 7c** and **qTS 7d** are above the reactant asymptote. Pathway (3) has the lowest endothermicity of ~ 28 kcal/mol, yet the highest transition barrier of ~ 74 kcal/mol. Pathway (1) has the lowest transition barrier of ~ 47 kcal/mol with an endothermicity of ~ 42 kcal/mol, so most of the barrier is due to the reaction endothermicity. Pathway (2) is endothermic by ~ 44 kcal/mol with a transition barrier of ~ 58 kcal/mol. Removal of an acetaldehyde requires 17 to 29 kcal/mol.

Structure **q9a** has a transformed Ti_4O_8 compared to **qcat** with a bidentate $O_{dibr12}H$ group and a bidentate $O_{tetrabr}H$ group. The proton of the bidentate $O_{dibr12}H$ group transfers to the terminal O_{ter2} via **qTS 9a** to form **q10a** with an exothermicity of *ca.* -15 kcal/mol and a transition barrier of ~ 23 kcal/mol. The proton of the bidentate $O_{tetrabr}H$ group transfers to the terminal O_{ter2} via **qTS 9c** to form **q10b** with an exothermicity of *ca.* -5 kcal/mol and a transition barrier of ~ 34 kcal/mol. Transferring the proton of the bidentate $O_{tetrabr}H$ group to the Ti_1 via **qTS 9e** to form **q10c** is exothermic by *ca.* -3 kcal/mol with a transition barrier of ~ 48 kcal/mol. Transfers of the proton from the bidentate $O_{tetrabr}H$ group to the bidentate O_{dibr13} via **qTS 9d** to form **q10d**, or to the Ti_1 directly via **qTS 9f** to form **q11a**, result in

transition barriers of ~ 38 and ~ 48 kcal/mol with endothermic reaction energies of ~ 13 and ~ 20 kcal/mol, respectively. Structure **q9c** has a bidentate $O_{dibr12}H$ group and a bidentate $O_{dibr13}H$ group. Transfer of the proton of the bidentate $O_{dibr13}H$ group to the Ti_1 site where PCET occurs via **qTS 9g** to form **q9b** is endothermic by ~6 kcal/mol with a transition barrier of ~ 53 kcal/mol. Structure **q9d** has a bidentate $O_{dibr12}H$ group and a bidentate $O_{dibr14}H$ group. Transfer of the proton of the bidentate $O_{dibr14}H$ group to the Ti_1 site via **qTS 9h** to form **q9b** is exothermic by *ca.* -13 kcal/mol with a transition barrier of ~ 49 kcal/mol. Transfer of the proton of the bidentate $O_{dibr12}H$ group to the Ti_1 site via **qTS 9i** to form **q10e** is endothermic by ~ 4 kcal/mol with a transition barrier of ~ 55 kcal/mol. All the **q9** reactants, **qTS 9** transition states, and products **q9b**, **q10d** and **q10e** are above the reactant asymptote, and the reactants **q10a**, **q10b** and **q10c** are below the reactant asymptote.

Structure **q10a** has a transformed Ti_4O_8 with a terminal $O_{ter2}H$ group and a bidentate $O_{tetrabr}H$ group. Transfer of the proton of the bidentate $O_{tetrabr}H$ group to the Ti_2 site via **qTS 10b** to form **q11b** is very endothermic ~ 51 kcal/mol, with a high transition barrier of ~ 74 kcal/mol. Structure **q10b** has a transformed Ti_4O_8 with a terminal $O_{ter2}H$ group and a bidentate $O_{dibr12}H$ group. Transfer of the proton of the bidentate $O_{dibr12}H$ group to the Ti_2 site via **qTS 10d** to form **q11b** is also endothermic by ~ 51 kcal/mol with a high transition barrier of ~ 72 kcal/mol. Structure **q10c** has a transformed Ti_4O_8 with a hydride at the Ti_1 site and a bidentate $O_{tetrabr}H$ group. Transfer of the proton to the bidentate O_{dibr12} via **qTS 10a** to form **q11a** is endothermic by ~ 15 kcal/mol with a transition barrier of ~ 34 kcal/mol. Structure **q10d** also has a transformed Ti_4O_8 with a bidentate $O_{dibr12}H$ group and a bidentate $O_{dibr13}H$ group. Transfer of the proton to the bidentate O_{dibr13} to form **q11a** via **qTS 10c** is exothermic by *ca.* -7 kcal/mol with a transition barrier of ~ 40 kcal/mol. Transfer of the proton of the $O_{dibr14}H$ group to generate the hydride at the Ti_1 site from **q10e** via **qTS 11a** to form **q12a** is

exothermic by *ca.* -14 kcal/mol with a transition barrier of ~ 12 kcal/mol. All the **qTS 10** transition states and the **q11** products are above the reactant asymptote.

Structure **q11a** has a transformed Ti_4O_8 with a hydride at the Ti_1 site and a bidentate $O_{dibr12}H$ group. Transfer of the proton to the hydride via **qTS 11b** to form **q12b** is endothermic by ~ 7 kcal/mol with a transition barrier of ~ 26 kcal/mol. Structure **q11b** has a transformed Ti_4O_8 with a hydride at the Ti_2 site and a terminal $O_{ter2}H$ group. Transfer of the proton to the hydride via **qTS 11c** to form **q12c** is endothermic by *ca.* -9 kcal/mol with a transition barrier of ~ 15 kcal/mol. Removal of a H_2 from **q12b** requires ~ 2 kcal/mol. Structure **q12c** will release ~ 6 kcal/mol for removal of a H_2 and forms **qcat 1**. The reaction energy shown at **qcat 1**, 22.8 kcal/mol, includes the dehydrogenation energy of one ethanol and the transformation energy of Ti_4O_8 from **qcat**.

Table A5.1. Electronic energies, zero-point energies, thermal, Gibbs free energy corrections at 298K and enthalpies at 0K for structures in dehydration and dehydrogenation on $(TiO_2)_2$ nanocluster at the B3LYP/DZVP2 level, single-point electronic energies and enthalpies at 0K at the CCSD(T)/aug-cc-pVDZ(-PP) level, and overall reaction energies at both levels in kcal/mol at 0K.

Structure	B3LYP/DZVP2						CCSD(T)/aug-cc-pVDZ(-PP)		
	ZPE	Thermal Corrections at 298K	Gibbs Free Energy Correction at 298 K	Electronic Energies	Electronic Energies +ZPE	Overall Reaction Energy	Electronic Energies	Electronic Energies +ZPE	Overall Reaction Energy
Ethanol	0.080067	0.085326	0.054633	-155.091918	-155.011700		-154.665592	-154.585525	
$C_2H_4O_1$	0.055524	0.060373	0.030555	-153.874321	-153.818797		-153.462419	-153.406895	
H_2O	0.021447	0.025227	0.003793	-76.456993	-76.435546		-76.273837	-76.252390	
C_2H_4	0.050953	0.054945	0.030067	-78.608727	-78.557774	11.5[a]	-78.369156	-78.318203	9.4[a]
H_2	0.010164	0.013468	-0.001324	-1.179286	-1.169122	14.9[b]	-1.164899	-1.154735	15.0[b]
dcat	0.014187	0.021590	-0.016943	-1999.963318	-1999.949131		-415.715130	-415.700943	
dcat 1	0.013963	0.021465	-0.017300	-1999.953336	-1999.939373	17.7	-415.706491	-415.692528	14.7
Dehydration									
d1	0.096613	0.109539	0.056607	-2155.113052	-2155.016439	-34.9	-570.446537	-570.349924	-39.8
dTS 1	0.091456	0.103802	0.051385	-2155.083899	-2154.992443	-19.8	-570.413804	-570.322348	-22.5
d2	0.094358	0.107654	0.053216	-2155.152444	-2155.058086	-61.0	-570.482688	-570.388330	-63.9
dTS 2a	0.088958	0.101066	0.051417	-2155.072772	-2154.983814	-14.4	-570.403989	-570.315031	-17.9
dTS 2b	0.087327	0.099775	0.049285	-2155.065153	-2154.977826	-10.7	-570.391342	-570.304015	-11.0
dTS 2c	0.087792	0.100472	0.049029	-2155.060147	-2154.972355	-7.2	-570.388802	-570.301010	-9.1
d3a	0.089764	0.104852	0.044243	-2155.117277	-2155.027513	-41.8	-570.453334	-570.363570	-48.4
d3b	0.089940	0.104381	0.044668	-2155.097746	-2155.007806	-29.5	-570.434245	-570.344305	-36.3
d3c	0.091500	0.106250	0.048131	-2155.081845	-2154.990345	-18.5	-570.417520	-570.326020	-24.8
d4a	0.037150	0.047670	0.001644	-2076.502814	-2076.465664	-39.3	-492.076626	-492.039476	-44.7
d4b	0.038199	0.048339	0.003140	-2076.486983	-2076.448784	-28.7	-492.061432	-492.023233	-34.5
d4c	0.038534	0.049296	0.001879	-2076.459757	-2076.421223	-11.4	-492.032221	-491.993687	-16.0
dTS 4a	0.034297	0.042945	0.001619	-2076.473037	-2076.438740	-22.4	-492.040336	-492.006039	-23.7
dTS 4b	0.035021	0.043868	0.001989	-2076.468235	-2076.433214	-18.9	-492.036818	-492.001797	-21.0

dTS 4c	0.033826	0.043210	-0.000318	-2076.447405	-2076.413579	-6.6	-492.019207	-491.985381	-10.7
dTS 4d	0.034601	0.043916	0.000394	-2076.441676	-2076.407075	-2.5	-492.016783	-491.982182	-8.7
dTS 4e	0.034126	0.043512	-0.000028	-2076.427169	-2076.393044	6.3	-492.000923	-491.966797	0.9
d5	0.036577	0.047162	0.001440	-2076.513074	-2076.476497	-46.1	-492.082703	-492.046126	-48.9
d6	0.034582	0.043845	0.000374	-2076.447080	-2076.412498	-5.9	-492.017259	-491.982677	-9.0
d7	0.038736	0.049395	0.002440	-2076.470414	-2076.431678	-18.0	-492.041660	-492.002924	-21.7
Dehydrogenation									
dTS 7a	0.087779	0.100766	0.048692	-2155.066293	-2154.978514	-11.1	-570.398943	-570.311164	-15.5
dTS 7b	0.090376	0.103028	0.052063	-2155.051288	-2154.960912	-0.1	-570.388317	-570.297941	-7.2
d8a	0.087998	0.101905	0.047459	-2155.076909	-2154.988911	-17.6	-570.408638	-570.320640	-21.4
d8b	0.089888	0.104637	0.045599	-2155.055235	-2154.965347	-2.8	-570.383835	-570.293947	-4.7
d9a	0.029962	0.039118	-0.003594	-2001.183196	-2001.153234	-7.0	-416.922098	-416.892136	-7.9
d9b	0.033593	0.043001	-0.000175	-2001.150177	-2001.116584	16.0	-416.888173	-416.854580	15.7
dTS 9a	0.027536	0.035577	-0.004846	-2001.134593	-2001.107057	21.9	-416.876117	-416.848581	19.4
dTS 9b	0.027493	0.036683	-0.006584	-2001.106005	-2001.078511	39.9	-416.845474	-416.817981	38.6
d10a	0.030023	0.039090	-0.003426	-2001.184788	-2001.154766	-8.0	-416.924078	-416.894055	-9.1
d10b	0.028703	0.038004	-0.004956	-2001.154089	-2001.125386	10.4	-416.895215	-416.866512	8.2
dTS 10	0.027530	0.035672	-0.005046	-2001.129360	-2001.101830	25.2	-416.871690	-416.844160	22.2
d11	0.028774	0.038030	-0.004815	-2001.144735	-2001.115961	16.4	-416.886920	-416.858146	13.4

[a] Dehydration energy. [b] Dehydrogenation energy.

Table A5.2. Electronic energies, zero-point energies, thermal, Gibbs free energy corrections at 298K and enthalpies at 0K for structures in dehydration and dehydrogenation on $(TiO_2)_3$ nanocluster at the B3LYP/DZVP2 level, single-point electronic energies and enthalpies at 0K at the CCSD(T)/aug-cc-pVDZ(-PP) level, and overall reaction energies at both levels in kcal/mol at 0K.

Structure	B3LYP/DZVP2						CCSD(T)/aug-cc-pVDZ(-PP)		
	ZPE	Thermal Corrections at 298K	Gibbs Free Energy Correction at 298 K	Electronic Energies	Electronic Energies +ZPE	Overall Reaction Energy	Electronic Energies	Electronic Energies +ZPE	Overall Reaction Energy
tcat	0.022520	0.033310	-0.013651	-3000.037298	-3000.014778		-623.679877	-623.657357	
Dehydration									
t1	0.104765	0.121199	0.060010	-3155.193670	-3155.088905	-39.2	-778.417661	-778.312896	-43.9
tTS 1	0.099728	0.115543	0.055753	-3155.159741	-3155.060013	-21.0	-778.383264	-778.283536	-25.5
t2	0.103500	0.120008	0.058868	-3155.220679	-3155.117179	-56.9	-778.444094	-778.340594	-61.3
tTS 2a	0.096785	0.112499	0.054962	-3155.146186	-3155.049401	-14.4	-778.368807	-778.272022	-18.3
tTS 2b	0.096197	0.112158	0.054014	-3155.136440	-3155.040242	-8.6	-778.358768	-778.262571	-12.4
tTS 2c	0.096263	0.112208	0.054106	-3155.136498	-3155.040235	-8.6	-778.358763	-778.262500	-12.3
tTS 2d	0.096518	0.112416	0.053946	-3155.130221	-3155.033704	-4.5	-778.350005	-778.253487	-6.7
tTS 2e	0.095253	0.111191	0.051402	-3155.119952	-3155.024699	1.1	-778.337732	-778.242479	0.3
tTS 2f	0.097572	0.112563	0.056885	-3155.106933	-3155.009360	10.7	-778.334952	-778.237380	3.5
t3a	0.098740	0.116889	0.048605	-3155.210047	-3155.111307	-53.2	-778.437740	-778.339000	-60.3
t3b	0.098487	0.116782	0.048615	-3155.195051	-3155.096564	-44.0	-778.421715	-778.323228	-50.4
t3c	0.098654	0.116864	0.050010	-3155.195126	-3155.096472	-43.9	-778.421703	-778.323049	-50.3
t3d	0.099508	0.117514	0.051413	-3155.185766	-3155.086258	-37.5	-778.416395	-778.316887	-46.4
t3e	0.099579	0.117575	0.051496	-3155.185734	-3155.086155	-37.4	-778.416261	-778.316682	-46.3
t3f	0.099436	0.117512	0.051848	-3155.169335	-3155.069899	-27.2	-778.398108	-778.298672	-35.0
t4a	0.046280	0.059726	0.007579	-3076.595658	-3076.549378	-50.6	-700.061000	-700.014720	-56.5
t4b	0.045973	0.059630	0.006884	-3076.579639	-3076.533666	-40.8	-700.044046	-699.998073	-46.1
t4c	0.047159	0.060484	0.008377	-3076.568120	-3076.520961	-32.8	-700.035235	-699.988076	-39.8
t4d	0.046921	0.060551	0.007110	-3076.549323	-3076.502402	-21.1	-700.013116	-699.966195	-26.1
tTS 4a	0.041558	0.054597	0.002912	-3076.533687	-3076.492129	-14.7	-699.997232	-699.955674	-19.4

tTS 4b	0.042090	0.055001	0.003551	-3076.523128	-3076.481037	-7.7	-699.992518	-699.950428	-16.2
tTS 4c	0.041341	0.054818	0.001705	-3076.501126	-3076.459785	5.6	-699.967842	-699.926501	-1.1
tTS 4d	0.042707	0.055488	0.004343	-3076.504119	-3076.461412	4.6	-699.968438	-699.925731	-0.7
tTS 4e	0.042260	0.055084	0.003991	-3076.504038	-3076.461778	4.3	-699.967644	-699.925384	-0.4
tTS 4f	0.042317	0.055334	0.003169	-3076.489099	-3076.446782	13.8	-699.950390	-699.908073	10.4
tTS 4g	0.043308	0.055648	0.005240	-3076.463189	-3076.419881	30.6	-699.929885	-699.886577	23.9
t5a	0.045287	0.058972	0.006404	-3076.613374	-3076.568087	-62.4	-700.076842	-700.031555	-67.1
t5b	0.045973	0.059622	0.006909	-3076.579755	-3076.533782	-40.8	-700.044061	-699.998088	-46.1
t5c	0.046054	0.059798	0.006180	-3076.565544	-3076.519490	-31.9	-700.028069	-699.982015	-36.0
tTS 5a	0.042901	0.055589	0.004579	-3076.521539	-3076.478638	-6.2	-699.985904	-699.943003	-11.5
tTS 5b	0.042909	0.055556	0.004828	-3076.521178	-3076.478270	-6.0	-699.985540	-699.942631	-11.3
tTS 5c	0.042882	0.055582	0.004527	-3076.521451	-3076.478569	-6.2	-699.985873	-699.942991	-11.5
tTS 5d	0.043430	0.055377	0.006659	-3076.511416	-3076.467986	0.5	-699.974840	-699.931410	-4.2
t6	0.047145	0.061118	0.006836	-3076.549558	-3076.502413	-21.2	-700.012294	-699.965149	-25.4
Dehydrogenation									
tTS 7	0.096932	0.113201	0.053560	-3155.148312	-3155.051380	-15.6	-778.374064	-778.277132	-21.5
t8	0.097331	0.114380	0.052818	-3155.156899	-3155.059568	-20.8	-778.382341	-778.285010	-26.4
t9	0.039128	0.051267	0.001904	-3001.242176	-3001.203048	2.9	-624.875119	-624.835991	0.0
tTS 9	0.035655	0.047128	-0.001086	-3001.193446	-3001.157791	31.3	-624.828165	-624.792510	27.3
t10	0.035984	0.049232	-0.003165	-3001.227047	-3001.191063	10.4	-624.860061	-624.824077	7.5

Table A5.3. Electronic energies, zero-point energies, thermal, Gibbs free energy corrections at 298K and enthalpies at 0K for structures in dehydration and dehydrogenation on $(TiO_2)_4$ nanocluster at the B3LYP/DZVP2 level, single-point electronic energies and enthalpies at 0K at the CCSD(T)/aug-cc-pVDZ(-PP) level, and overall reaction energies at both levels in kcal/mol at 0K.

Structure	B3LYP/DZVP2						CCSD(T)/aug-cc-pVDZ(-PP)		
	ZPE	Thermal Corrections at 298K	Gibbs Free Energy Correction at 298 K	Electronic Energies	Electronic Energies +ZPE	Overall Reaction Energy	Electronic Energies	Electronic Energies +ZPE	Overall Reaction Energy
qcat	0.030814	0.044819	-0.008300	-4000.116802	-4000.085988		-831.653691	-831.622877	
qcat 1	0.030519	0.044942	-0.008919	-4000.104822	-4000.074303	18.9	-831.632060	-831.601541	22.8
Dehydration									
q1	0.113103	0.132722	0.065100	-4155.262748	-4155.149645	-32.6	-986.379097	-986.265994	-36.1
qTS 1	0.108322	0.127281	0.061274	-4155.246841	-4155.138519	-25.6	-986.361921	-986.253599	-28.4
q2	0.111782	0.131663	0.063421	-4155.291705	-4155.179923	-51.6	-986.403156	-986.291374	-52.1
qTS 2a	0.105128	0.124256	0.059585	-4155.223323	-4155.118195	-12.9	-986.334613	-986.229485	-13.2
qTS 2b	0.104260	0.123650	0.058259	-4155.205286	-4155.101026	-2.1	-986.317237	-986.212977	-2.9
qTS 2c	0.104420	0.124308	0.057089	-4155.195617	-4155.091197	4.1	-986.304740	-986.200320	5.1
qTS 2d	0.104361	0.123799	0.058308	-4155.181653	-4155.077293	12.8	-986.293869	-986.189508	11.9
q3a	0.108085	0.129402	0.057205	-4155.264489	-4155.156404	-36.8	-986.383731	-986.275646	-42.2
q3b	0.107013	0.128511	0.055401	-4155.265834	-4155.158821	-38.4	-986.381676	-986.274663	-41.6
q3c	0.107740	0.129344	0.056603	-4155.260779	-4155.153039	-34.7	-986.373221	-986.265481	-35.8
q3d	0.107303	0.128825	0.055802	-4155.234239	-4155.126936	-18.4	-986.353628	-986.246325	-23.8
q4a	0.055593	0.072288	0.013174	-4076.647478	-4076.591885	-32.6	-908.002766	-907.947173	-35.8
q4b	0.055263	0.072288	0.012387	-4076.643069	-4076.587806	-30.1	-907.991098	-907.935835	-28.6
q4c	0.054523	0.071777	0.011223	-4076.615588	-4076.561065	-13.3	-907.970456	-907.915933	-16.1
qTS 4a	0.050900	0.066915	0.009142	-4076.596667	-4076.545767	-3.7	-907.949491	-907.898591	-5.3
qTS 4b	0.050665	0.066738	0.008843	-4076.584609	-4076.533944	3.7	-907.938464	-907.887799	1.5
qTS 4c	0.050709	0.066902	0.008458	-4076.572163	-4076.521454	11.6	-907.925720	-907.875011	9.5
qTS 5a	0.051538	0.067358	0.009896	-4076.607664	-4076.556126	-10.2	-907.962902	-907.911365	-13.3
qTS 5b	0.051537	0.067356	0.009897	-4076.607664	-4076.556127	-10.2	-907.962902	-907.911365	-13.3

qTS 5c	0.051062	0.066925	0.009471	-4076.591953	-4076.540891	-0.6	-907.947353	-907.896291	-3.8
qTS 4d	0.050722	0.067188	0.008283	-4076.579214	-4076.528492	7.2	-907.925602	-907.874880	9.6
q5a	0.054451	0.071335	0.011847	4076.650660	-4076.596209	-35.3	-908.003213	-907.948763	-36.7
q5b	0.054450	0.071335	0.011844	-4076.650660	-4076.596210	-35.3	-908.003213	-907.948763	-36.7
q5c	0.054283	0.071478	0.011424	-4076.649330	-4076.595047	-34.6	-907.995050	-907.940767	-31.7
q5d	0.054392	0.071373	0.011478	-4076.624890	-4076.570498	-19.2	-907.976418	-907.922026	-20.0
qTS 5d	0.050990	0.067276	0.008874	-4076.591123	-4076.540132	-0.1	-907.938540	-907.887550	1.7
q6a	0.055724	0.072682	0.012510	-4076.621322	-4076.565598	-16.1	-907.976946	-907.921222	-19.5
q6b	0.055434	0.072883	0.011644	-4076.617723	-4076.562290	-14.0	-907.964552	-907.909118	-11.9
Dehydrogenation									
qTS 7a	0.107255	0.126260	0.061614	-4155.208782	-4155.101526	-2.4	-986.323599	-986.216344	-5.0
qTS 7b	0.105282	0.124948	0.057955	-4155.203662	-4155.098380	-0.4	-986.320160	-986.214878	-4.1
qTS 7c	0.106273	0.125392	0.060514	-4155.198312	-4155.092039	3.5	-986.305448	-986.199175	5.8
qTS 7d	0.105386	0.124572	0.059916	-4155.170330	-4155.064944	20.5	-986.279090	-986.173704	21.8
q8a	0.109114	0.129962	0.060752	-4155.248545	-4155.139431	-26.2	-986.356243	-986.247129	-24.3
q8b	0.108434	0.129167	0.059297	-4155.216870	-4155.108435	-6.7	-986.333641	-986.225207	-10.5
q8c	0.106383	0.126487	0.058801	-4155.216145	-4155.109762	-7.6	-986.329743	-986.223360	-9.4
q8d	0.108717	0.129460	0.060893	-4155.220298	-4155.111581	-8.7	-986.330738	-986.222021	-8.5
q9a	0.051590	0.067318	0.010564	-4001.334550	-4001.282960	-2.6	-832.851450	-832.799860	1.0
q9b	0.047799	0.063123	0.006942	-4001.315351	-4001.267552	7.1	-832.837823	-832.790024	7.2
q9c	0.051005	0.066783	0.010017	-4001.309009	-4001.258004	13.1	-832.831298	-832.780293	13.3
q9d	0.051094	0.066856	0.009953	-4001.300054	-4001.248961	18.8	-832.820277	-832.769183	20.3
qTS 9a	0.047424	0.062325	0.007166	-4001.296072	-4001.248648	19.0	-832.810119	-832.762695	24.4
qTS 9b	0.044226	0.058970	0.003848	-4001.275629	-4001.231403	29.8	-832.801391	-832.757165	27.8
qTS 9c	0.047252	0.062267	0.006894	-4001.278936	-4001.231684	29.6	-832.792810	-832.745558	35.1
qTS 9d	0.046983	0.062251	0.006140	-4001.265443	-4001.218460	37.9	-832.786961	-832.739978	38.6
qTS 9e	0.045395	0.060748	0.004552	-4001.257289	-4001.211894	42.0	-832.769135	-832.723740	48.8
qTS 9f	0.047002	0.062154	0.006623	-4001.249917	-4001.202915	47.7	-832.768683	-832.721681	50.1
qTS 9g	0.044799	0.060421	0.003378	-4001.225296	-4001.180497	61.7	-832.741232	-832.696433	65.9
qTS 9h	0.044725	0.060221	0.003671	-4001.222391	-4001.177666	63.5	-832.735919	-832.691194	69.2
qTS 9i	0.045177	0.060627	0.004052	-4001.213727	-4001.168550	69.2	-832.727560	-832.682383	74.8

q10a	0.050730	0.066600	0.009686	-4001.361650	-4001.310919	-20.1	-832.874410	-832.823680	-13.9
q10b	0.050489	0.066439	0.009306	-4001.344629	-4001.294140	-9.6	-832.858753	-832.808264	-4.2
q10c	0.047972	0.063358	0.007237	-4001.337159	-4001.289187	-6.5	-832.852127	-832.804155	-1.7
q10d	0.050079	0.066516	0.008097	-4001.303864	-4001.253786	15.8	-832.818781	-832.768702	20.6
q10e	0.047573	0.063043	0.006439	-4001.289504	-4001.241931	23.2	-832.810219	-832.762646	24.4
qTS 10a	0.043759	0.058523	0.003418	-4001.273138	-4001.229379	31.1	-832.793204	-832.749445	32.7
qTS 10b	0.043178	0.059008	0.001600	-4001.232571	-4001.189393	56.2	-832.749301	-832.706123	59.9
qTS 10c	0.044895	0.060649	0.003494	-4001.237357	-4001.192463	54.2	-832.749438	-832.704543	60.8
qTS 10d	0.043151	0.059355	0.001135	-4001.227822	-4001.184671	59.1	-832.736598	-832.693447	67.8
q11a	0.047150	0.062958	0.005900	-4001.312464	-4001.265314	8.5	-832.827194	-832.780044	13.5
q11b	0.046693	0.062598	0.005229	-4001.278667	-4001.231974	29.4	-832.788404	-832.741711	37.5
qTS 11a	0.043897	0.058692	0.003480	-4001.263303	-4001.219407	37.3	-832.787861	-832.743964	36.1
qTS 11b	0.043755	0.058854	0.003073	-4001.265659	-4001.221904	35.8	-832.782985	-832.739230	39.1
qTS 11c	0.043994	0.058991	0.003180	-4001.246779	-4001.202785	47.8	-832.761604	-832.717610	52.6
q12a	0.044516	0.060767	0.002571	-4001.303280	-4001.258764	12.6	-832.829575	-832.785059	10.3
q12b	0.044278	0.061070	0.000962	-4001.295727	-4001.251449	17.2	-832.812919	-832.768641	20.6
q12c	0.042470	0.060148	-0.004191	-4001.285102	-4001.242632	22.8	-832.798581	-832.756111	28.5

Table A5.4. Electronic energies, zero-point energies, thermal, Gibbs free energy corrections at 298K and enthalpies at 0K for H^+, and structures with removal of H^+ from OH groups at the B3LYP/DZVP2 level for acidity calculation.

Structure	ZPE	Thermal Corrections at 298K	Gibbs Free Energy Correction at 298 K	Electronic Energies
d2 $O_{ter1}H$	0.083189	0.095741	0.043402	-2154.617080
d4a $O_{ter1}H$	0.025454	0.035369	-0.008902	-2075.979091
d4a $O_{ter2}H$	0.026546	0.036174	-0.007911	-2075.983221
d4b $O_{ter1}H$	0.027177	0.036370	-0.006100	-2075.978599
d4b $O_{br1}H$	0.026546	0.036174	-0.007911	-2075.983221
d9a $O_{ter1}H$	0.019128	0.027360	-0.013490	-2000.654924
t2 $O_{br1}H$	0.092159	0.107856	0.047710	-3154.743418
t4a $O_{ter1}H$	0.035738	0.048389	-0.002139	-3076.086651
t4a $O_{br1}H$	0.035125	0.047839	-0.002756	-3076.107967
t4c $O_{br1}H$	0.035738	0.048389	-0.002139	-3076.086651
t9 $O_{br1}H$	0.028405	0.039448	-0.007475	-3000.778763
q2 $O_{br1}H$	0.100130	0.119301	0.052333	-4154.807121
q4a $O_{br1}H$	0.043924	0.060092	0.002103	-4076.158160
H^+	0.000000	0.002360	-0.010000	0.000000

Table A5.5. Electronic energies, zero-point energies, thermal, Gibbs free energy corrections at 298K and enthalpies at 0K for structures with additon of H^+ at the terminal or bridging oxygen sites at the B3LYP/DZVP2 level for proton affinity calculation.

Structure	ZPE	Thermal Corrections at 298K	Gibbs Free Energy Correction at 298 K	Electronic Energies
dcat O_{ter1}	0.024631	0.033021	-0.008250	-2000.290891
dcat O_{bri1}	0.024212	0.032606	-0.008494	-2000.314599
tcat O_{ter1}	0.033074	0.044490	-0.003697	-3000.397208
tcat O_{dibr12}	0.033097	0.044970	-0.004973	-3000.342407
tcat O_{dibr23}	0.033976	0.045251	-0.002639	-3000.382951
tcat O_{tribr}	0.033100	0.044941	-0.005100	-3000.349727
qcat O_{ter1}	0.040767	0.055731	0.000056	-4000.468514
qcat O_{dibr12}	0.041674	0.056550	0.000856	-4000.447780
qcat O_{dibr14}	0.040823	0.056235	-0.000850	-4000.415590
qcat $O_{tetrabr}$	0.041929	0.056872	0.001875	-4000.471455
$(WO_3)_3$[a]	0.041310	0.057500	-0.005751	-880.598260
$(MoO_3)_3$[a]	0.041501	0.057485	-0.003808	-882.034529

[a] The cc-pVDZ-PP basis set was used for W and Mo.

Table A5.6. Electronic energies, zero-point energies, thermal, Gibbs free energy corrections at 298K and enthalpies at 0K for structures at the B3LYP/DZVP2 level for fluoride affinity calculation.

Structure	ZPE	Thermal Corrections at 298K	Gibbs Free Energy Correction at 298 K	Electronic Energies
$Ti_2O_4F^-$	0.015670	0.024676	-0.018358	-2100.039351
$Ti_3O_6F^-$ Ti_1	0.024513	0.036550	-0.013022	-3100.160504
$Ti_3O_6F^-$ Ti_2	0.024029	0.036511	-0.014733	-3100.101290
$Ti_4O_8F^-$ Ti_1	0.032420	0.047943	-0.008841	-4100.222398
$Ti_4O_8F^-$ Ti_2	0.032466	0.048087	-0.009532	-4100.181904
$(WO_3)_3$[a]	0.030890	0.046364	-0.014215	-880.304031
$(WO_3)_3F^-$[a]	0.032517	0.049441	-0.016248	-980.380386
$(MoO_3)_3$[a]	0.031185	0.046413	-0.012248	-881.739204
$(MoO_3)_3F^-$[a]	0.032704	0.049450	-0.014800	-981.798261

[a] The cc-pVDZ-PP basis set was used for W and Mo.

Table A5.7. Fluoride affinity (FA) ΔH_{0K} at the B3LYP/DZVP2 level.

Structure	FA
dcat terminal Ti_1=O	116.1
tcat bridge Ti_1	145.4
qcat bridge Ti_1	134.6
tcat terminal Ti_2=O	108.5
qcat terminal Ti_2=O	109.1
$(WO_3)_3$[a]	116.2[b] (reference molecule)
$(MoO_3)_3$[a]	105.4

[a] The cc-pVDZ-PP basis set was used for W and Mo. [b] Text Reference 21.

Table A5.8. Proton affinity (PA) ΔH_{298K} of clusters at the B3LYP/DZVP2 level in kcal/mol.

Structure	PA
tcat O_{ter1}	220.3
qcat $O_{tetrabr}$	216.5
qcat O_{ter1}	215.3
dcat O_{ter1}	215.0
tcat O_{dibr23}	210.9
qcat O_{dibr12}	201.8
dcat O_{br1}	199.9
tcat O_{tribr}	190.2
tcat O_{dibr12}	185.6
qcat O_{dibr14}	181.8
$(MoO_3)_3$[a]	179.9
$(WO_3)_3$[a]	179.1

[a] The cc-pVDZ-PP basis set was used for W and Mo.

Table A5.9. Acidity of acidic clusters at the B3LYP/DZVP2 level at 298 K in kcal/mol.

Structure	Acidity ΔH_{298K}	Acidity ΔG_{298K}
Chemisorbed Complex		
d2 $O_{ter1}H$	330.0	323.5
q2 $O_{br1}H$	297.8	290.8
t2 $O_{br1}H$	293.3	286.2
Structure with OH Groups in Dehydration		
d4a $O_{ter1}H$	322.4	315.7
d4a $O_{ter2}H$	320.3	313.8
t4a $O_{ter1}H$	313.8	307.0
d4b $O_{ter1}H$	313.0	306.9
d4b $O_{br1}H$	310.0	302.9
q4a $O_{br1}H$	300.9	293.8
t4a $O_{br1}H$	300.1	293.3
t4c $O_{br1}H$	296.0	289.3
Structure with OH Groups in Dehydrogenation		
d9a $O_{ter1}H$	325.6	319.0
t9 $O_{br1}H$	284.9	278.6

Table A5.10. Energy (ΔH_{0K}) in kcal/mol needed to remove one H_2O from physiosorbed $(MO_3)_3$-H_2O complexes, M = W and Mo.

Structure	ΔH_{0K}
$(WO_3)_3$[a]	11
$(MoO_3)_3$[a]	16

[a] Text Reference 2 and 4.

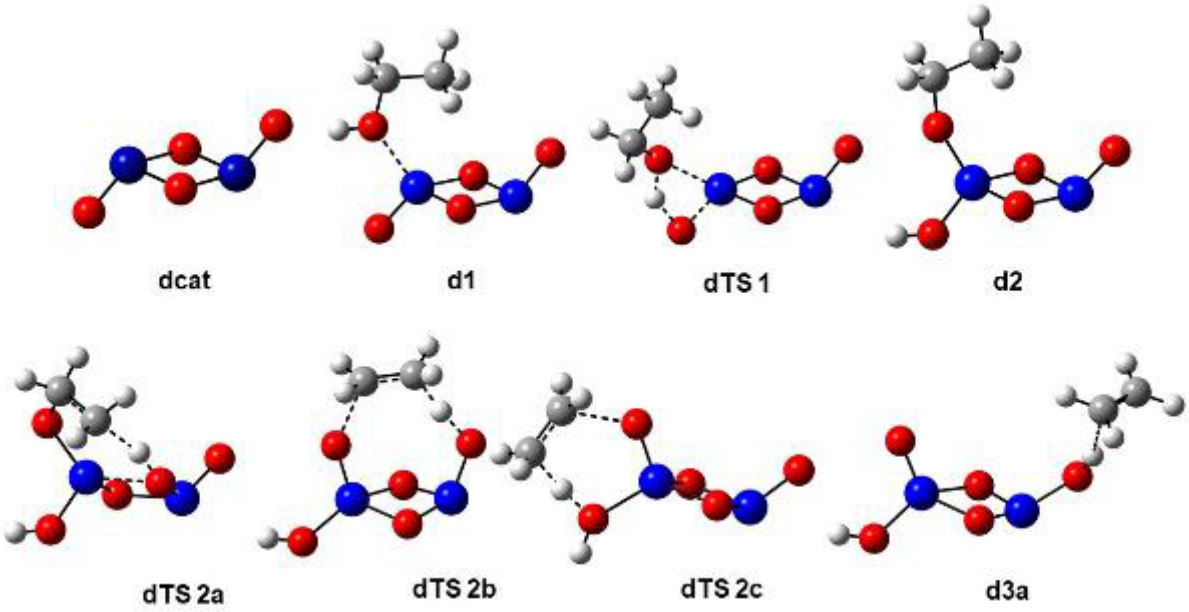

Figure A5.1. Structures in the pathways of ethanol dehydration on Ti_2O_4 (C_{2h}) nanoclusters optimized at B3LYP/DZVP2 level (continue).

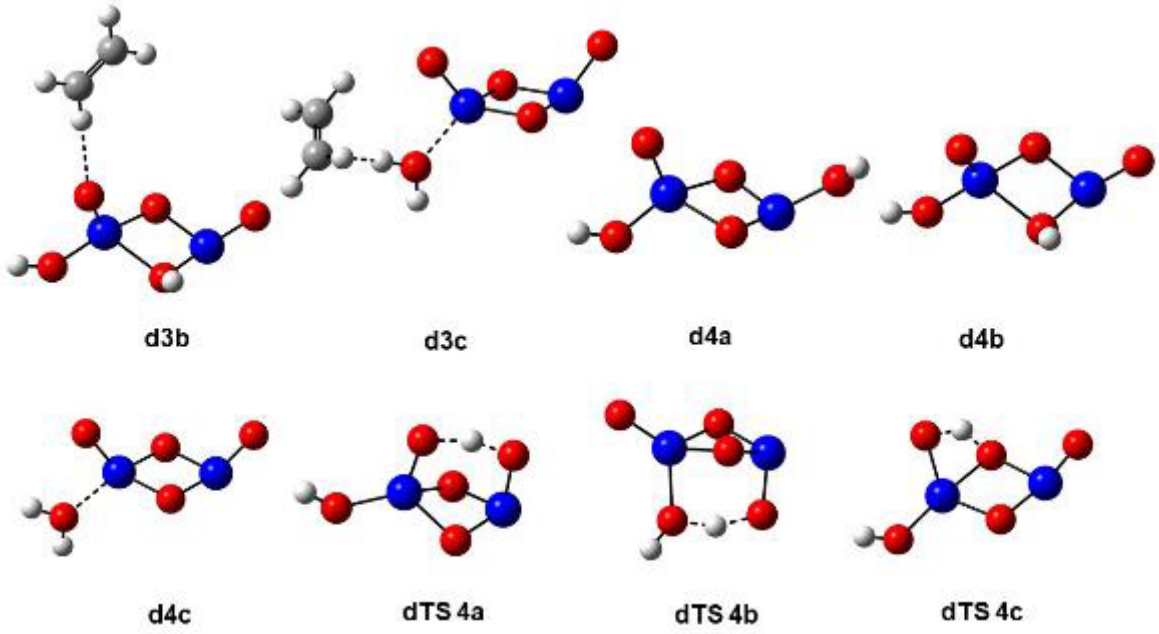

Figure A5.2. Structures in the pathways of ethanol dehydration on Ti_2O_4 (C_{2h}) nanoclusters optimized at B3LYP/DZVP2 level (continue).

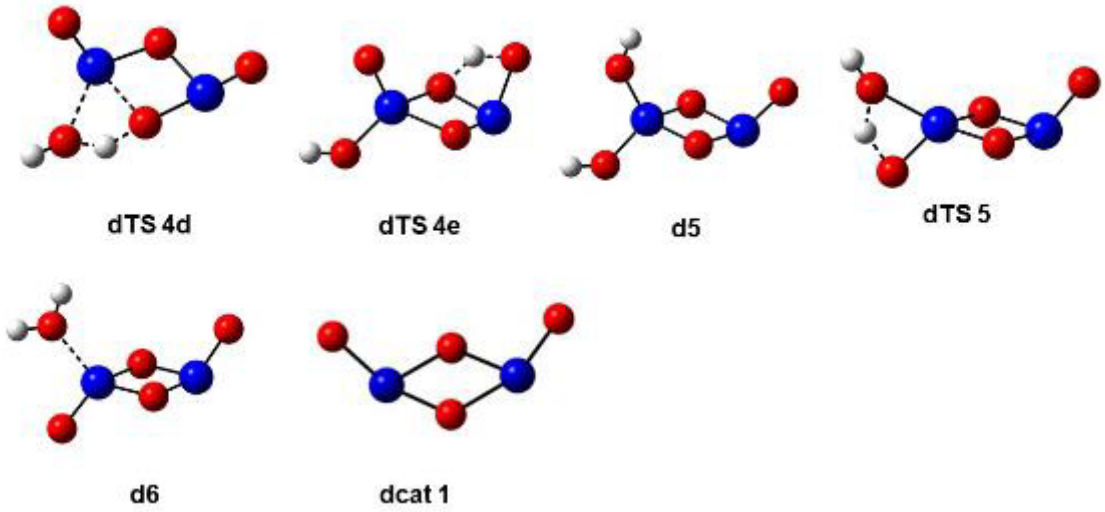

Figure A5.3. Structures in the pathways of ethanol dehydration on Ti_2O_4 (C_{2h}) nanoclusters optimized at B3LYP/DZVP2 level.

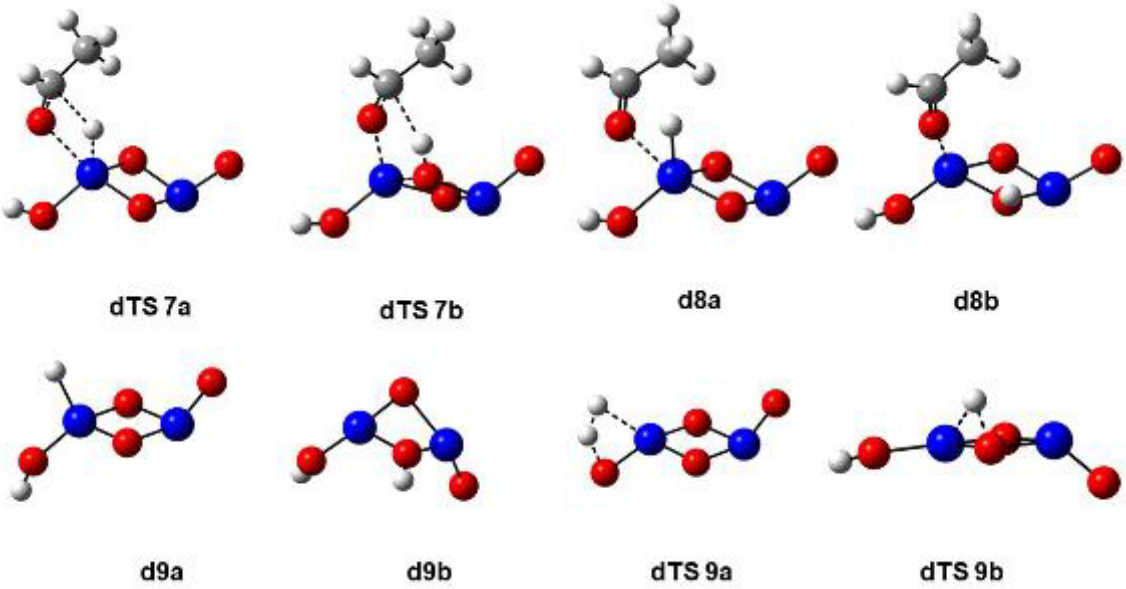

Figure A5.4. Structures in the pathways of ethanol dehydrogenation on Ti_2O_4 (C_{2h}) nanoclusters optimized at B3LYP/DZVP2 level (continue).

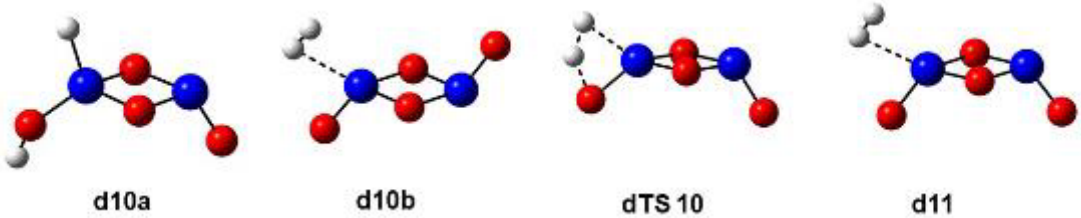

Figure A5.5. Structures in the pathways of ethanol dehydrogenation on Ti_2O_4 (C_{2h}) nanoclusters optimized at B3LYP/DZVP2 level.

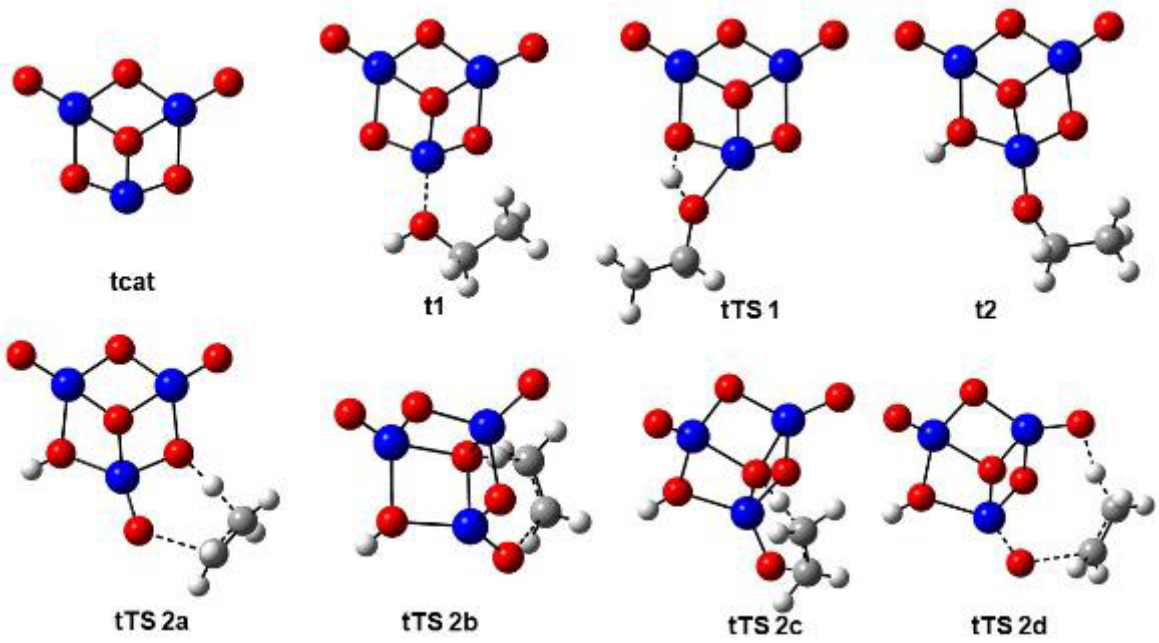

Figure A5.6. Structures in the pathways of ethanol dehydration on Ti_3O_6 (C_s) nanoclusters optimized at B3LYP/DZVP2 level (continue).

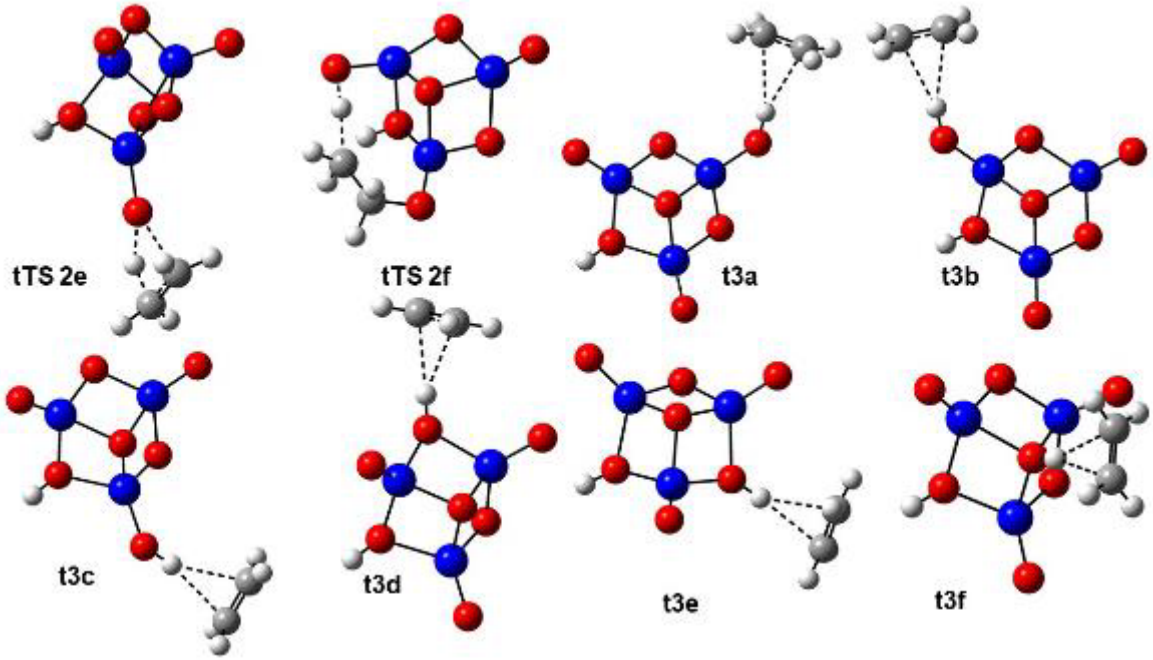

Figure A5.7. Structures in the pathways of ethanol dehydration on Ti_3O_6 (C_s) nanoclusters optimized at B3LYP/DZVP2 level (continue).

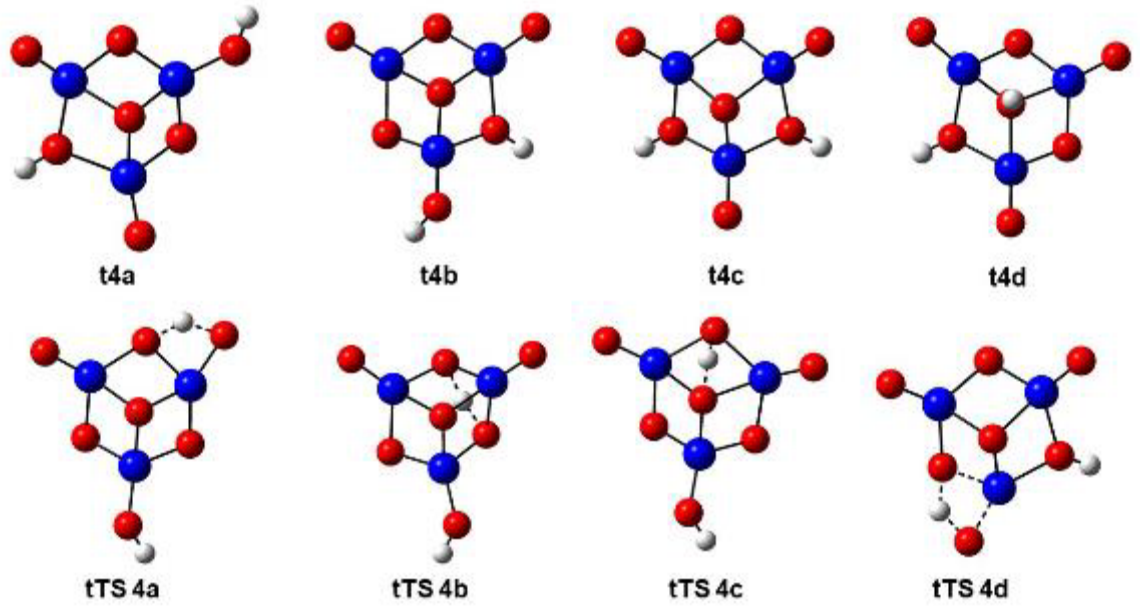

Figure A5.8. Structures in the pathways of ethanol dehydration on Ti_3O_6 (C_s) nanoclusters optimized at B3LYP/DZVP2 level (continue).

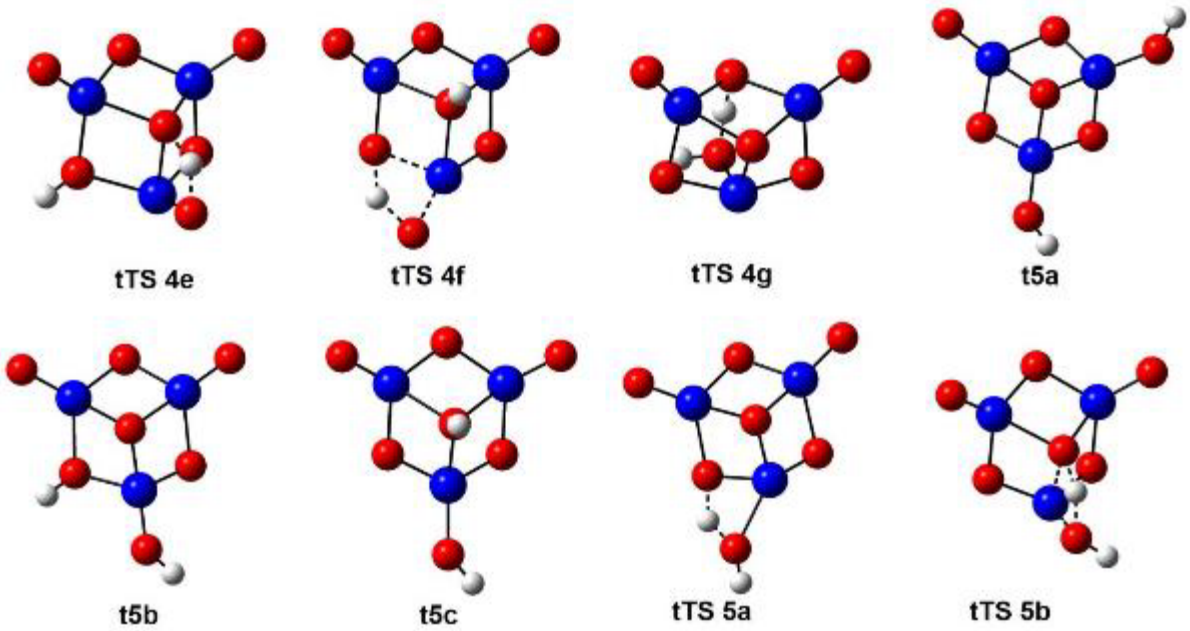

Figure A5.9. Structures in the pathways of ethanol dehydration on Ti_3O_6 (C_s) nanoclusters optimized at B3LYP/DZVP2 level (continue).

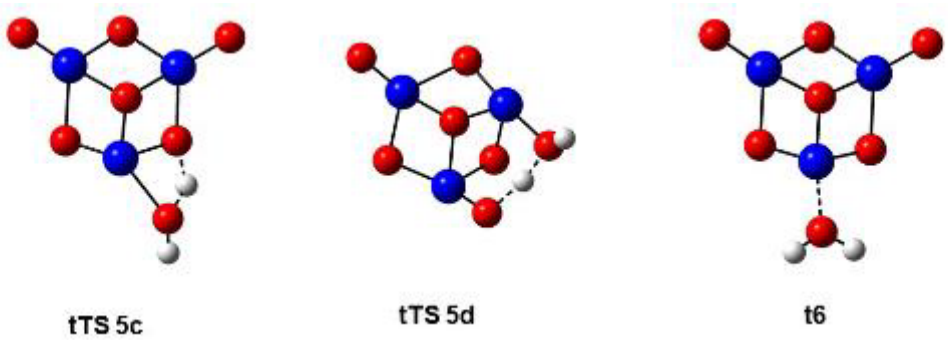

Figure A5.10. Structures in the pathways of ethanol dehydration on Ti_3O_6 (C_s) nanoclusters optimized at B3LYP/DZVP2 level.

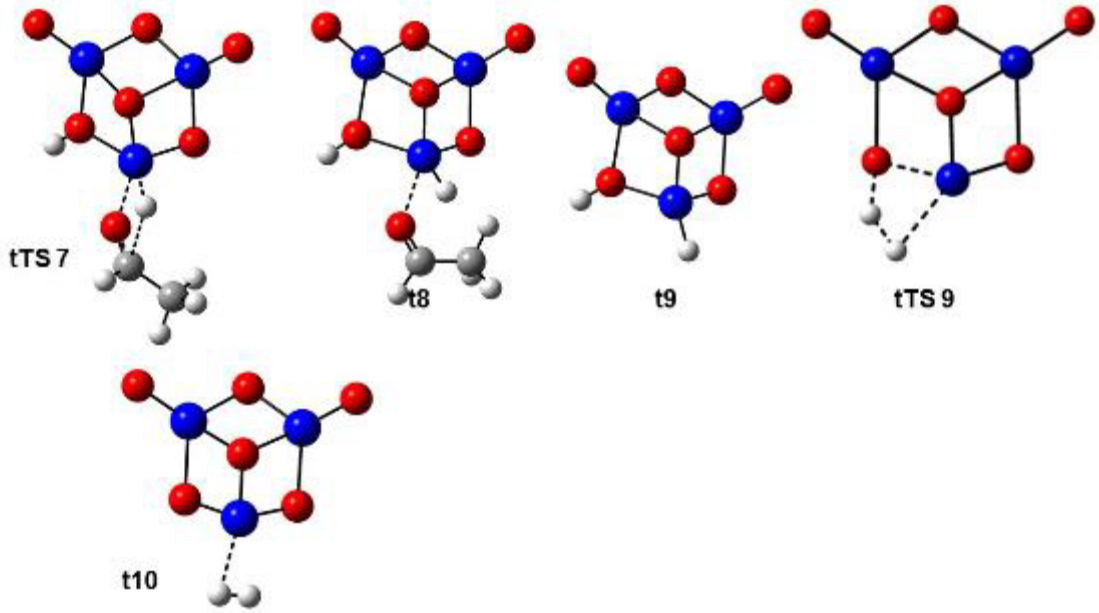

Figure A5.11. Structures in the pathways of ethanol dehydrogenation on Ti_3O_6 (C_s) nanoclusters optimized at B3LYP/DZVP2 level.

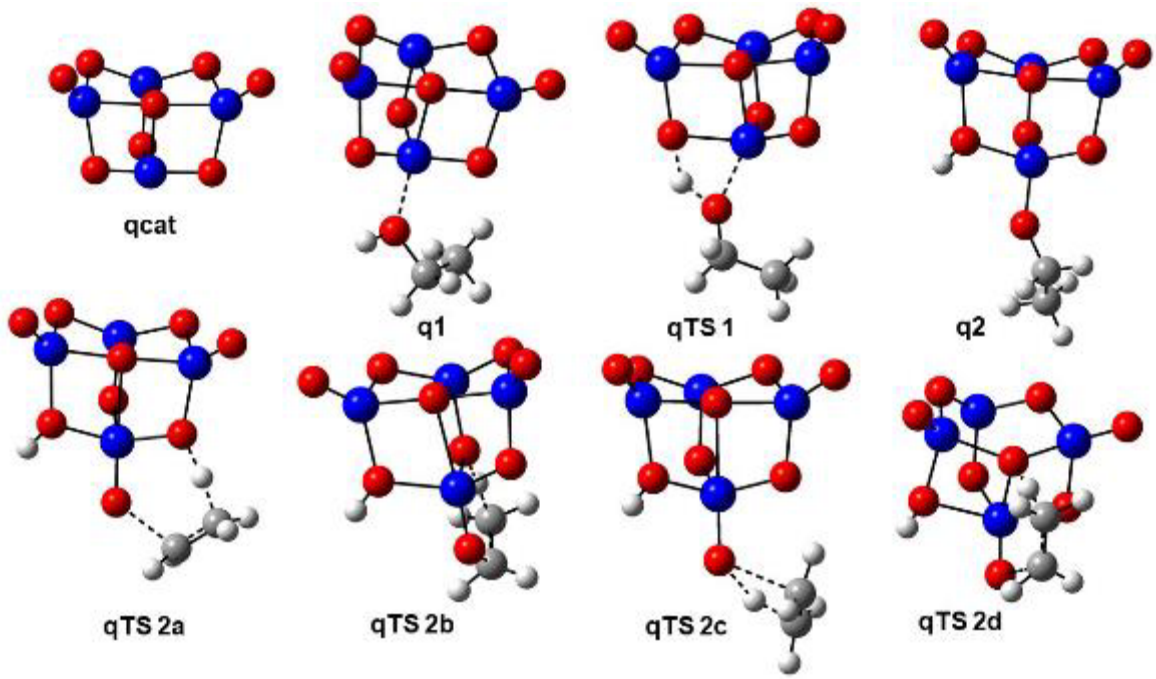

Figure A5.12. Structures in the pathways of ethanol dehydration on Ti_4O_8 (C_{2v}) nanoclusters optimized at B3LYP/DZVP2 level (continue).

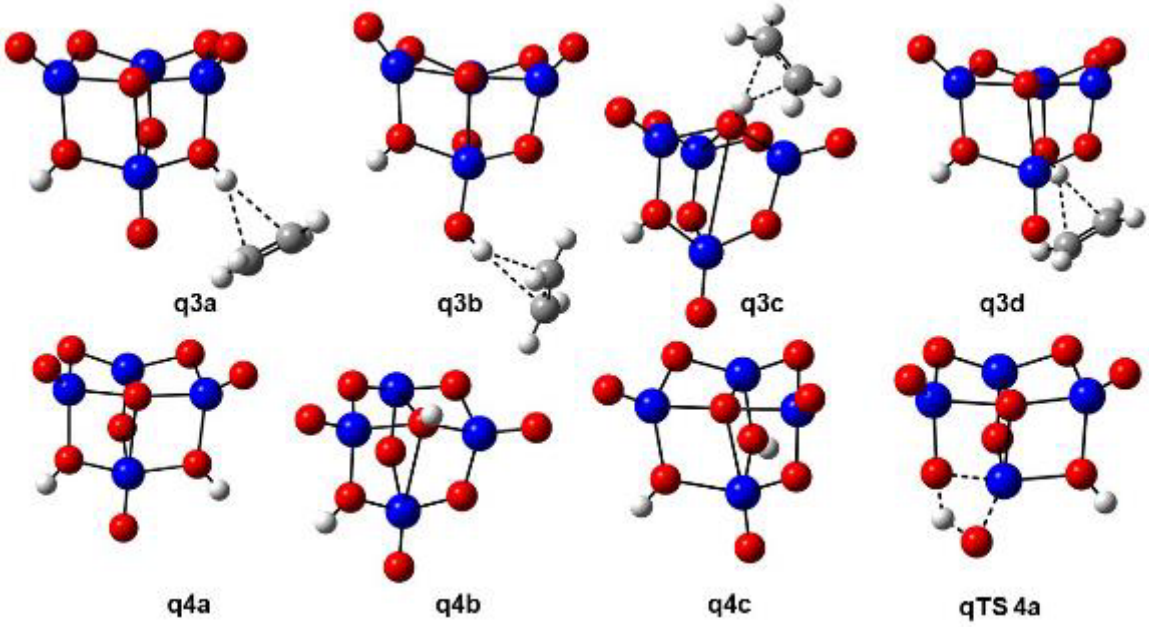

Figure A5.13. Structures in the pathways of ethanol dehydration on Ti_4O_8 (C_{2v}) nanoclusters optimized at B3LYP/DZVP2 level (continue).

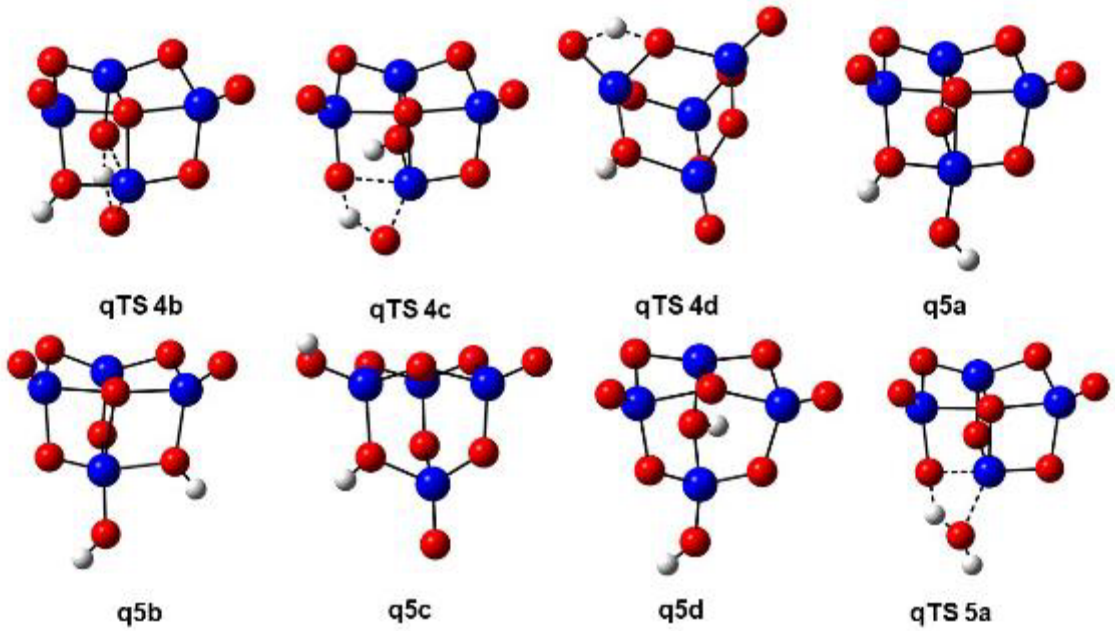

Figure A5.14. Structures in the pathways of ethanol dehydration on Ti_4O_8 (C_{2v}) nanoclusters optimized at B3LYP/DZVP2 level (continue).

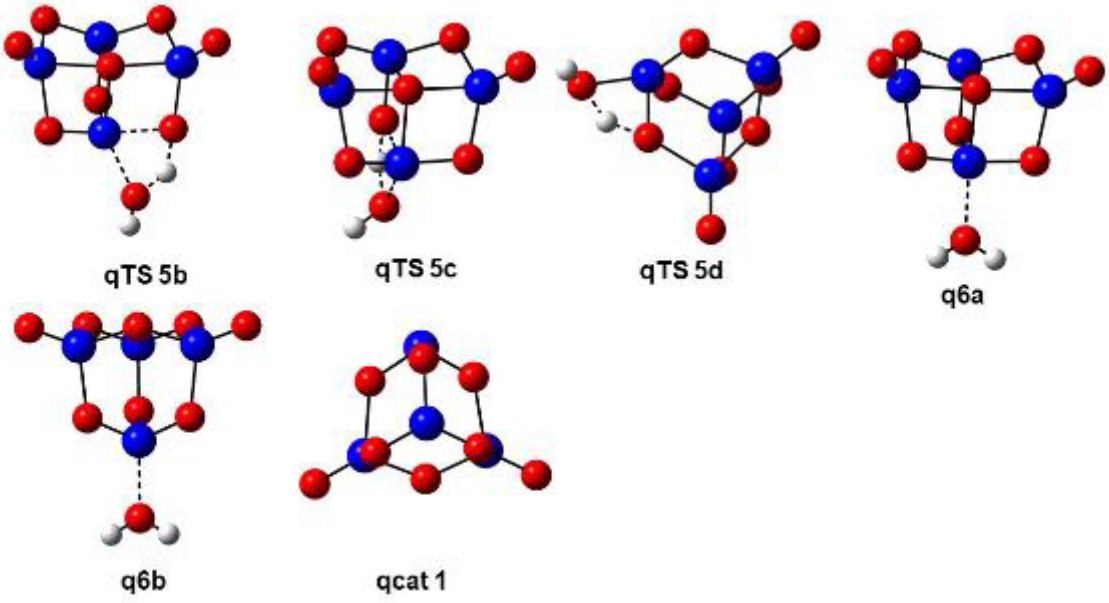

Figure A5.15. Structures in the pathways of ethanol dehydration on Ti_4O_8 (C_{2v}) nanoclusters optimized at B3LYP/DZVP2 level.

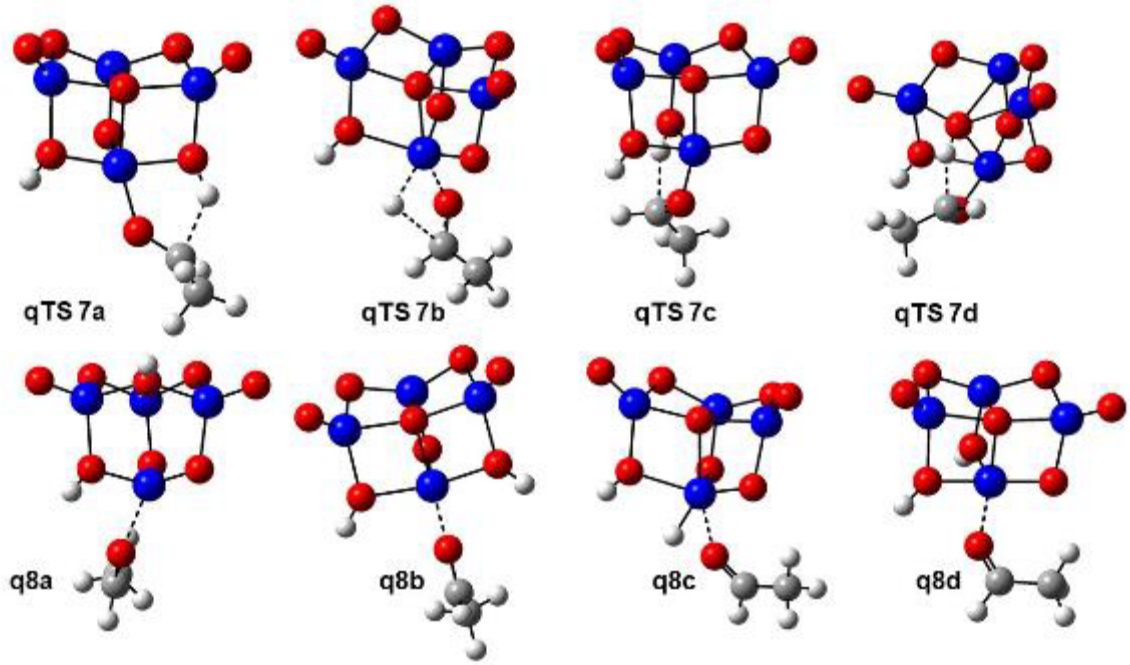

Figure A5.16. Structures in the pathways of ethanol dehydrogenation on Ti_4O_8 (C_{2v}) nanoclusters optimized at B3LYP/DZVP2 level (continue).

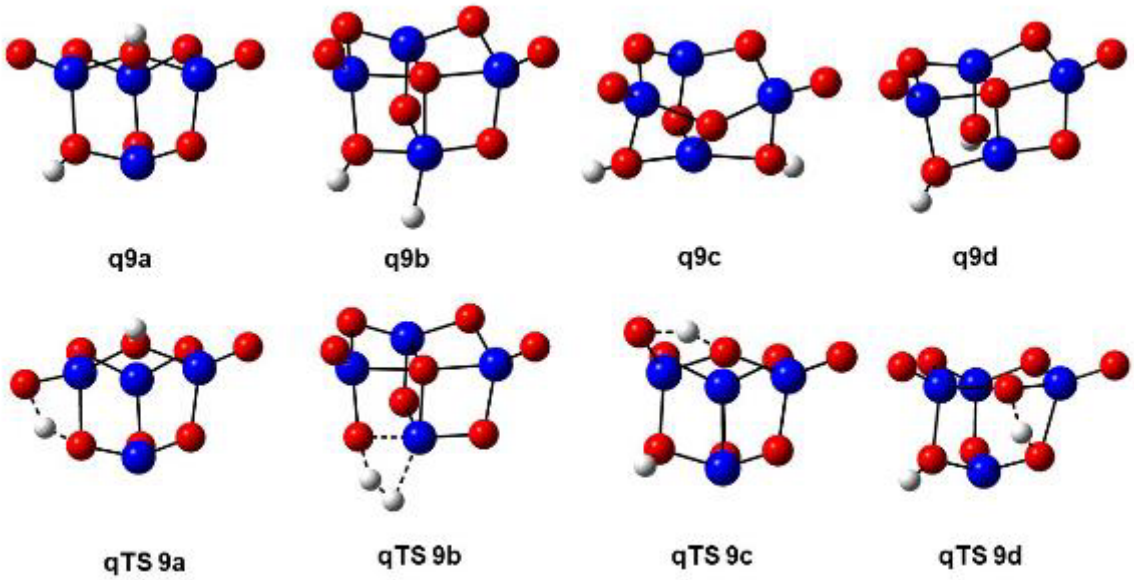

Figure A5.17. Structures in the pathways of ethanol dehydrogenation on Ti_4O_8 (C_{2v}) nanoclusters optimized at B3LYP/DZVP2 level (continue).

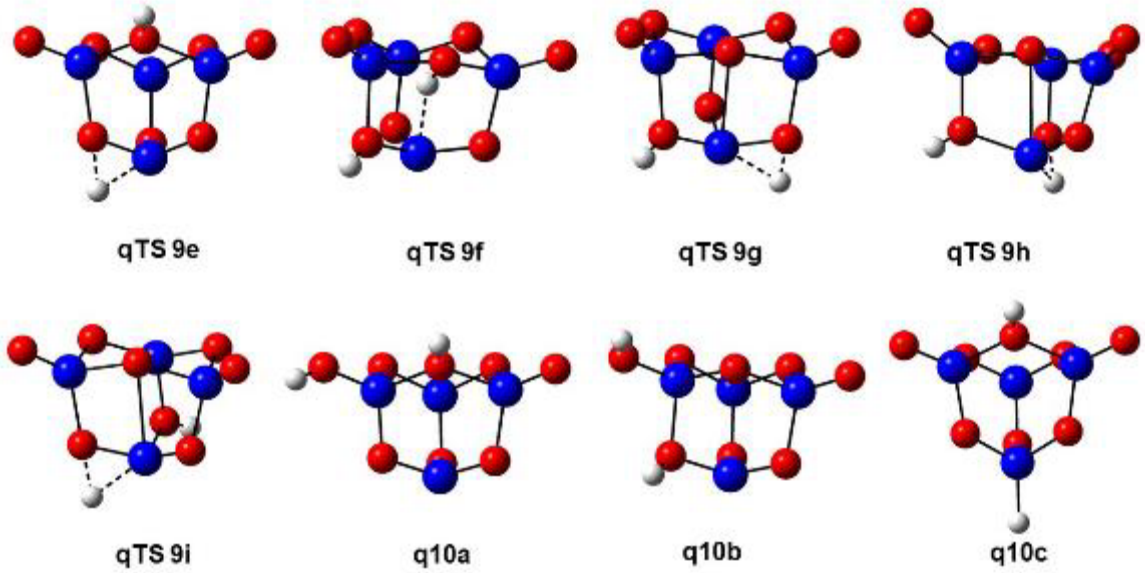

Figure A5.18. Structures in the pathways of ethanol dehydrogenation on Ti_4O_8 (C_{2v}) nanoclusters optimized at B3LYP/DZVP2 level (continue).

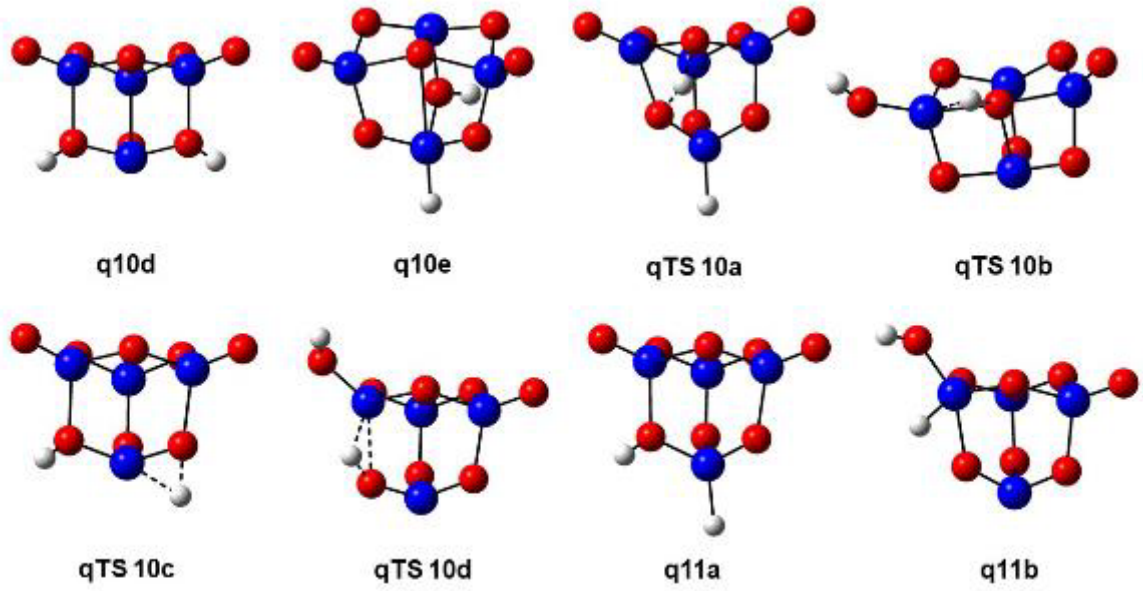

Figure A5.19. Structures in the pathways of ethanol dehydrogenation on Ti_4O_8 (C_{2v}) nanoclusters optimized at B3LYP/DZVP2 level (continue).

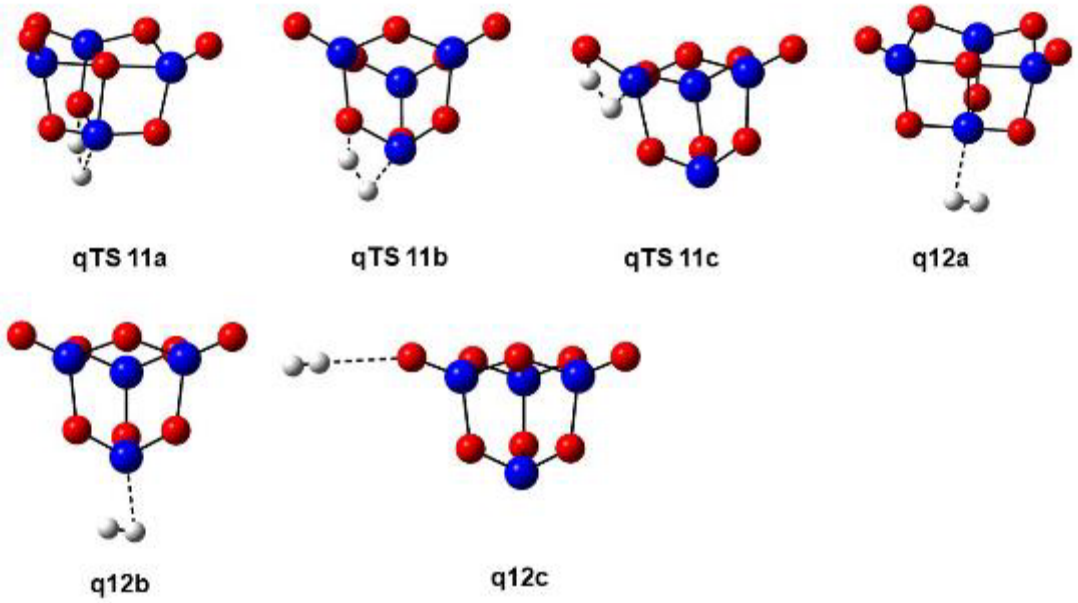

Figure A5.20. Structures in the pathways of ethanol dehydrogenation on Ti_4O_8 (C_{2v}) nanoclusters optimized at B3LYP/DZVP2 level.

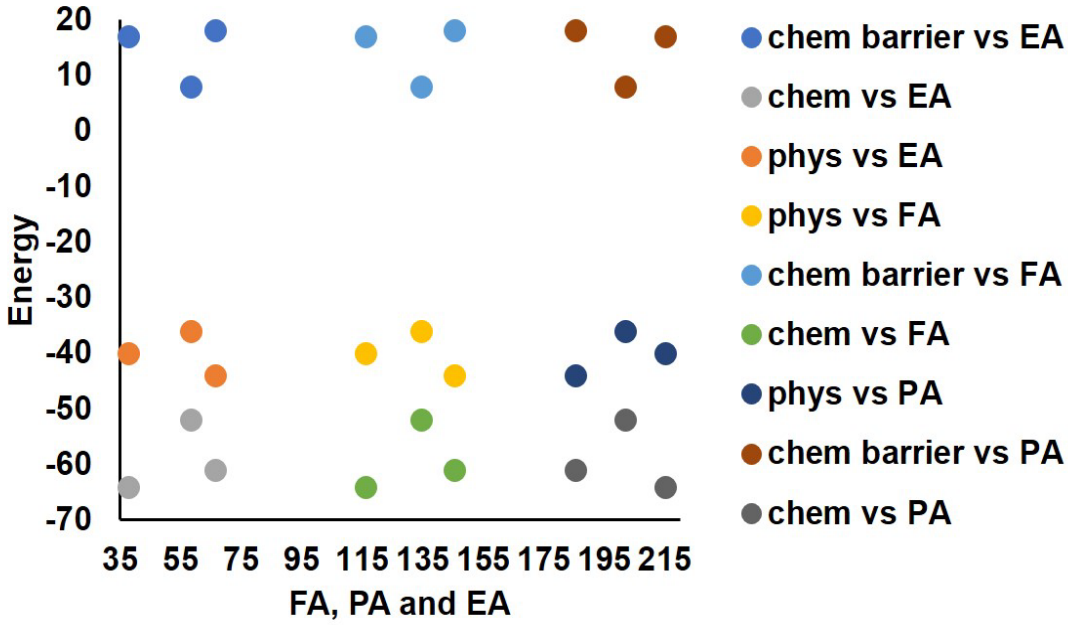

Figure A5.21. Correlation between physisorption, chemisorption and chemisorption barrier versus FA, PA and EA in kcal/mol.

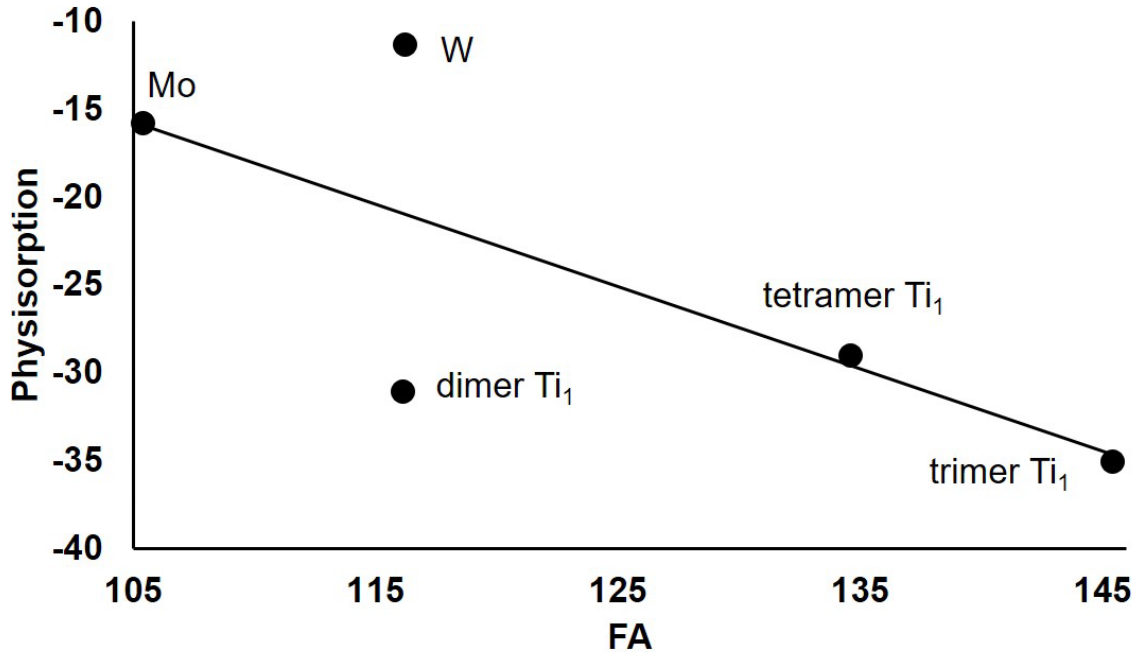

Figure A5.22. Correlation between physisorption of one H_2O and FA in kcal/mol. The linear fit equation is $y = -0.47x + 33.35$ ($R^2 = 0.54$).

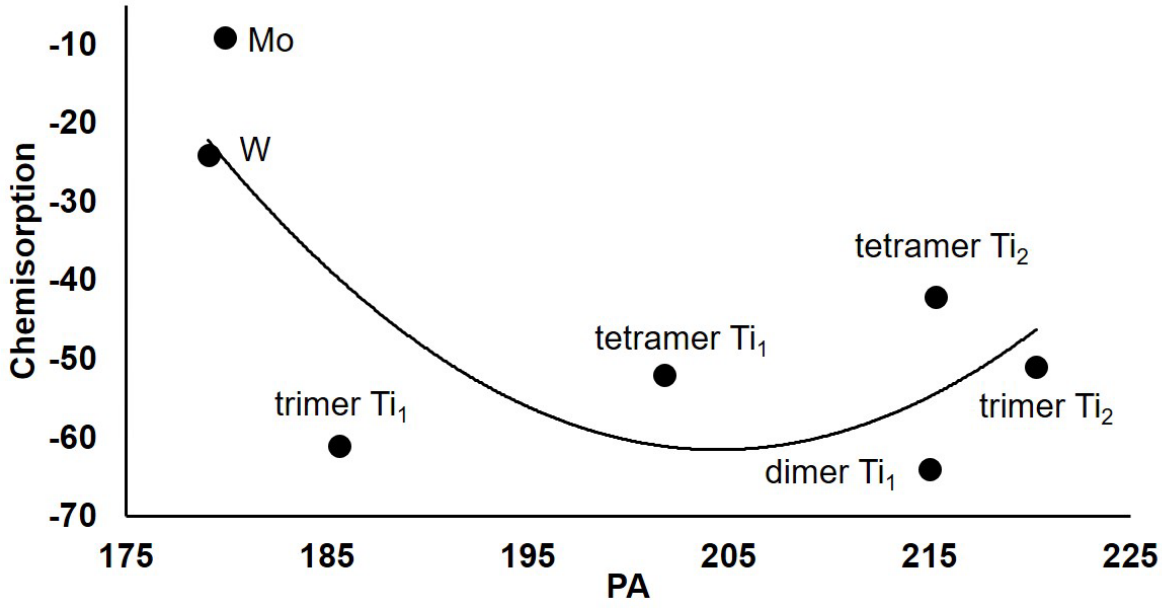

Figure A5.23. Correlation between chemisorption of one ethanol to metal sites and PA in kcal/mol. The quadratic fit equation is $y = 0.06x^2 - 24.96x + 2490.20$ ($R^2 = 0.57$).

CHAPTER 6

ELECTRONICALLY EXCITED COMPLEX FORMATION IN MAGNESIUM CLUSTER – HALOGEN ATOM REACTIONS

Introduction

Metal cluster oxidation reactions demonstrate an unusual and unexpected reactive branching that is not readily explained by the direct extension of the concepts associated with metal atom A + BC oxidative processes. However, cluster reactions, through a multicentered reaction capability, do extrapolate the A + BC reactive process by providing the means for pooling considerably more energy into a product molecule[1,2] thereby accessing higher energy internal electronic states in the products of these reactions. Kinetics, rather than thermodynamics, often determines the initial products of cluster reactions, which are not the thermodynamically most stable product in many instances. Cluster oxidation reactions often produce metal rich compounds containing metal-metal bonds. As such, the study of these reactions addresses bonding regions that bridge the gap between atomic and surface oxidation from the study of asymmetrical metal clustered oxides or halides. For example, the unique characteristics of metal cluster oxidation reactions permitted the analysis of previously undetected energy levels of BiF,[3] CrO,[4] CrF,[5] and NiF[6]. Vibrationally resolved optical signatures for the metal cluster oxides of boron (metalloid),[7,8]copper,[6] silver,[6,9] and manganese[6,10] and the metal cluster halides of chromium,[5] silver, and copper were also obtained using this method.

The metal cluster oxidation reactions of the alkali trimers and halogen atoms are particularly intriguing. The sodium trimer + halogen atom reactive encounters signal a surprising chemistry.[11,12,13,14] The extremely high cross section Na_n (n = 2,3) + X (X = Cl, Br, I) reactions create a continuous electronic population inversion by chemically pumping the sodium dimer Na_2 formed during the reaction. Optical gain through stimulated emission has been associated with the population of select vibrational and rotational levels of the Na_2 B $^1\Pi_u$ – X $^1\Sigma_g^+$ band system. The Na_2 amplifiers characterized in the visible region operate on bound-weakly bound transitions. It is easy to envision possible extrapolations on the Na_3 + X reaction concept to the alkaline earth metal trimers. These molecules might also react to form excited state dimers that can undergo subsequent bound-free excimer transitions.

The magnesium trimer + halogen atom reactions represent the closest analogs to the sodium trimer reactions. As expected for two closed shell atoms with $(3s)^2$ outer electron configurations, the Mg dimer is a very weakly bonded van der Waals molecule.[15,16] Couple cluster CCSD(T) calculations[17] with a basis set including up to f functions predicted a Mg_2-Mg bond strength of 0.24 eV in Mg_3, lower than that of Na_3. This indicates that the Mg_3 + F atom reactions should be sufficiently exothermic to populate the Mg_2 A state[18] and could represent the driving force for an Mg_2 excimer based laser. We have explored the reactions of magnesium clusters, including Mg_2 and Mg_3, formed in high metal flux agglomeration flows, with fluorine or chlorine atoms. The results reported herein show the formation of excited state Mg_xF and Mg_xCl charge transfer complexes where x is most likely 2. In addition, we report high level electronic structure calculations using the Feller-Peterson-Dixon (FPD) approach[19,20,21,22] for key species to predict the thermodynamics of possible reactions involving these clusters.

Experimental Methods

The dry ice cooled oven-based metal cluster source used in this investigation has been discussed in detail elsewhere.[6,23] Magnesium was evaporated from a specially machined graphite (Micro-mechanisms, Billerica, MA) crucible that was resistively heated using a tungsten basket heater (R. D. Mathis, Long Beach, CA). This assembly was wrapped in Zirconia Cloth (Zircar, Florida, NY) to provide thermal insulation. The magnesium was heated to temperatures ranging between 900 and 1250 K to give a maximum metal vapor pressure of ~250 Pa. The metal flux was entrained in an argon (Holox 99.999%) or helium (99.999%) flow cooled to 196 K by passage through a dry ice/methanol slush bath.[7] The high metal flux forms the seed for agglomeration and further cooling enhances clustering while the metal flux travels to the reaction zone. This cooling is needed to form small alkaline earth metal clusters which are weakly bound.

Fluorine atoms were formed by passing a flow of either SF_6 or CF_4 through an electric discharge. The process with SF_6 was used previously to study the Bi_2 + F reaction.[3] The rupture of an S-F bond with a bond dissociation energy of 105 kcal/mol[24] to form F atoms is considerably more efficient than the discharge in CF_4 that requires the rupture of a 131 kcal/mole C-F bond.[25] The discharge was created by applying a voltage between 800 and 1400V to 2 copper electrodes separated by 1/4" within a ¼" i.d. insulated glass tube. The SF_6 discharge technique is a well-established means of forming F atoms as shown by the fluorine atomic emission lines in the spectrum of the discharge. Chlorine atoms were produced from a similar discharge through CCl_4 with a lower C-Cl bond energy.[25] The effluents from the discharge intersected the magnesium metal flow in the chemical reaction zone producing a visible flame.

The discharge voltage and the SF_6, CF_4 or CCl_4 flows were adjusted to produce a stable flame and maximize the production of the desired product.

The experiments were conducted under multiple collision conditions using total pressures (primarily argon or helium) ranging from 60 to 333 Pa as measured by a thermocouple gauge (Veeco) attached to the side of the reaction chamber. The system was evacuated by a Welch 1397B pump. A liquid nitrogen cooled glass trap was placed between the chamber and the vacuum pump to collect the condensable gases and prevent fouling of the pump oil.

The chemiluminescent emission was focused onto the entrance slit of a one meter scanning monochromator (Spex 1704) operated in first order with a Bausch and Lomb 1200 groove/mm grating blazed at 500nm. A cooled RCA 1P28 photomultiplier tube was used to detect the dispersed fluorescence at 1 nm resolution for the chemiluminescence spectra. The signal from the phototube was sent to a Keithley 485 auto-ranging fast picoammeter. The analog signal from the picoammeter was digitized using a computer, displayed in real time, and stored for further analysis.

The observed chemiluminescence served as a guide for subsequent laser induced fluorescence studies. The experimental configuration for studying both chemiluminescence and dispersed laser induced fluorescence (DLIF) is depicted schematically in Figure 6.1. For the DLIF experiments, the current from the photomultiplier monitoring the LIF was amplified by a 20-dB video amplifier (Comlinear CLC100) prior to being sent to a gated boxcar integrator (Stanford Research SR-250 with a gate width of ~ 100 ns). An A/D converter was used to transfer the data to a computer for storage and further analysis.

Computational Methods

All structures were initially optimized at the DFT level using the B3LYP[26,27] hybrid exchange-correlation functional with the aug-cc-pVTZ basis set for F,[28,29] Cl, and Mg[30] using the Gaussian16 software package.[31] These calculations are denoted as aT.

The coupled cluster R/RCCSD(T) or R/UCCSD(T)[32,33,34,35,36,37,38] geometry optimizations were initiated from the DFT optimized geometries. The CCSD(T) calculation were performed using aug-cc-pwCV*n*Z basis sets for F,[39] Cl, [40] and Mg.[30] It is necessary to include the 2s and 2p electrons on the Mg in the effective valence space since they have energies comparable to the 2s orbital on the fluorine. The 1s electrons on the fluorine were not correlated. For consistency, the 2s and 2p electrons on the Cl were also correlated in these calculations. We denote these bases sets as awn (n = D, T, Q). For the diatomics, the geometries were optimized at the CCSD(T) level using aug-cc-pwCVnZ-DK basis sets with n = D, T, Q. These basis sets are denoted as awn-DK. Frequencies were calculated at the same levels of theory. For the polyatomics, the geometries were optimized with at least the aT basis set, and the frequencies were calculated at the optimized geometries. Pure polyatomic Mg clusters were optimized up to the awQ-DK basis set and the frequencies were calculated with at least the awT-DK basis set. All CCSD(T) calculations were performed using the MOLPRO 2018.1 program package.[41,42,43] The CCSD(T) energies were extrapolated to the complete basis set (CBS) limit by fitting them to a mixed Gaussian/exponential (Equation 1):[44]

$$E(n) = E_{CBS} + A \exp[-(n-1)] + B \exp[-(n-1)^2] \quad (1)$$

where n = 2, 3, and 4 (D, T and Q). The CCSD(T) energies for diatomics were extrapolated to the complete basis set (CBS) limit by fitting to Equation (2):[45]

$$E(n) = E_{CBS} + A \exp[-B*n] \quad (2)$$

where n = 4 and 5 (Q and 5).

The extrapolation to the complete basis set limit and additional small corrections were calculated following the FPD approach.[19,20,21,22] Total atomization energies (TAEs or ΣD_0) at 0 K were calculated from Equation (3) with ΔE referring to the difference between the molecule (reactant) and the atomic products for each energy component:

$$\Sigma D_0 = \Delta E_{CBS} + \Delta E_{SR} + \Delta E_{ZPE} + \Delta E_{SO} \quad (3)$$

Additional corrections to the CCSD(T)/CBS energy (ΔE_{CBS}) are necessary to reach chemical accuracy. Scalar relativistic corrections (ΔE_{SR}) (Equation (4)) were calculated at the second order Douglas-Kroll-Hess (DK)[46,47,48] level with the all-electron aug-cc-pwCVTZ-DK basis sets[49] (denoted as wCVTZ-DK):

$$\Delta E_{SR} = \Delta E_{wCVTZ\text{-}DK} + \Delta E_{wCVTZ} \quad (4)$$

The atomic spin-orbit corrections (ΔE_{SO}) for the heats of formation were taken from the experimental values with Mg = 0, F = -0.39 kcal/mol, and Cl = -0.84 kcal/mol.[50]

Heats of formation at 0 K were calculated from these TAEs and experimental heats of formation of the atoms at 0 K. The values for F and Cl used from the Active Thermochemical Tables (ATcT)[51,52,53] are 18.47 ± 0.01 kcal/mol for F and 28.59 ± 0.00 kcal/mol for Cl. The value for Mg is 34.87 ± 0.2 kcal/mol and is taken from the JANAF Tables[54]. Heats of formation at 298 K were then calculated by following the Curtiss et al. procedure[55] using thermal corrections for the atoms of F = 1.05 kcal/mol, Mg = 1.19 kcal/mol, Cl = 1.10 kcal/mol.

Results and Discussion

Nature of the Observed Chemiluminescent Spectra The reaction between a moderate flux of dry-ice cooled magnesium vapor and the fluorine atoms produced in an SF_6 discharge consistently

produced the spectrum depicted in Figure 6.2. Features corresponding to the $3d^3D - 3p^3P$, and $4s^3S - 3p^3P - 3s^2\,^1S$ magnesium atom transitions[50] and the $A\,^2\Pi - X\,^2\Sigma^+$ system[56] of MgF are readily identified. In addition, the spectrum contains a progression of features between 390 and 490 nm. Several of these features show additional structure that may indicate a further short progression suggesting this emitter is a polyatomic molecule. As the magnesium flux is increased, the intensity of this system increases significantly relative to the intensity of the other features in the spectrum suggesting that this molecular emitter may contain more than one magnesium atom. The increasing intensity relative to the other emission features suggests this emitter results from fluorine atom oxidation of a small magnesium cluster since the number of clusters is expected to increase as the Mg vapor pressure increases.

The spectrum obtained from the reaction between dry ice cooled magnesium vapor and discharged CF_4 is depicted in Figure 6.3. Although less intense than the spectrum obtained by using a similar metal flux and discharged SF_6 as the source of fluorine atoms, the bands of the 390 to 490 nm system are easily identified. These results indicate that the observed band system is formed when fluorine atoms are present independent of the source of F atoms indicating this emitter contains only magnesium and fluorine

Using CCl_4 to produce a significant chlorine atom concentration gave the spectrum depicted in Figure 6.4 with a large magnesium flux. The chlorine-based spectrum also extends from ~390 to 490 nm but the maximum intensity is considerably shifted to the red of the fluorine-based system and the emission features are not clearly resolved.

The spectrum of the 390 to 490 nm Mg_xF system at moderate resolution (5Å) obtained at the highest controlled magnesium fluxes employed in these experiments is shown in Figure 6.5.

The strongest features in the spectrum are shown in a Deslandres Table (Table 6.1) and fit to within their measured uncertainty by Equation (3).

$$\upsilon = 25766(10) - 516(10)\ \upsilon_1'' - 104(10)\ \upsilon_2'' \quad (3)$$

The intensity pattern for the 390 to 490 nm system indicates that both frequency separations correspond to ground state vibrational frequencies. The 516 cm^{-1} frequency is reasonably assigned to an Mg-F stretching mode since the symmetric stretching frequency of MgF_2 is 552 cm^{-1}.[57,58,59,6061] Whereas the 104 cm^{-1} separations might be assigned to a bending frequency, this separation is also consistent with the ground state stretching frequencies calculated for Mg_3 (see below). Hence, the 104 cm^{-1} frequency could suggest that the emitting molecule contains at least two interacting Mg atoms.

Since there are at least two ground state frequencies associated with the 390 to 490 nm feature, the emitter producing the blue system is a polyatomic molecule. Whereas several possible magnesium-fluorine based species can be considered, the most likely emitter, consistent with the magnesium flux dependence, the fluorine atom dependence, and the calculated reaction exothermicities is Mg_2F. Since the observed emission features result from the reaction of small magnesium clusters and correspond to a polyatomic emitter and the 104 cm^{-1} separation is consistent with a molecule containing a Mg-Mg interaction, this further supports the assignment of the emitter to a magnesium cluster fluoride, Mg_xF. The simplicity of the observed spectrum suggests that x = 2 or 3, and dynamical arguments favor the assignment of the molecule to x =2, Mg_2F.

Engelke[62] has reported that the reaction between magnesium atoms and F_2 produces a continuum chemiluminescent spectrum from 390 to 690 nm corresponding to MgF_2. The spectrum of the "MgF_2" continuum depicted in Figure 6.6 was obtained in the present study

under similar multiple collision conditions in the absence of a discharge and with no effort to cluster the magnesium. Although the MgF_2 molecule bending mode is reported[60] as 154 cm^{-1} and chemiluminscence from MgF_2 might encompass some of the frequency separations shown in Figures 6.2 and 6.5, there are enough differences in the spectra shown in Figures 6.5 and 6.6, taken at similar total pressures, to indicate that they do not correspond to the same emitter. Since the lowest electronic transitions for MgF_2 are calculated[63,64,65] to be from a highly bent excited state to a linear or nearly linear ground state, long progressions in the bending mode are expected. The continuum in Figure 6.6 is consistent with a long unresolved progression in the MgF_2 bending mode obtained under moderate multiple collision conditions. The features in Figure 6.6 are thus inconsistent with the spectrum shown in Figure 6.5 as they display only short progressions in a 104 cm^{-1} vibration. The 154 cm^{-1} bending frequency predicted for MgF_2 is also larger than the 104 cm^{-1} frequency observed for the blue system. Further, the symmetric stretch frequency reported[66] for MgF_2 (550 cm^{-1}) is significantly larger than the 516 cm^{-1} frequency associated with the blue system assigned as Mg_2F.

Dispersed Laser Induced Fluorescence (DLIF) Using the observed 390 to 490 nm chemiluminescence as a guide, we performed several DLIF studies to further investigate the excited state of Mg_2F. The results of this study are summarized in Table 6.2 and outlined in Figure 6.7 and in the SI (Figure A6.1). The spectra are dominated by symmetric stretching modes of the ground and pumped excited electronic state and show some low frequency coupling with bending or Mg-Mg interaction modes in both states. These mode couplings (~ 100 cm^{-1} ground state and ~ 70 cm^{-1} excited state) appear intermittent.

Computational Results: Geometries and Relative Energies for Mg_nF_m Correlated molecular orbital calculations were performed to assess the structures of various Mg_nF_m species and to predict their vibrational spectra and reaction energetics.

We first describe the energetics and structures of the reactant Mg clusters. The results from the highest level calculations are reported in Table 6.3 with results for the smaller basis sets given in the Supporting Information. The behavior of these small clusters has been discussed in detail before,[67,68] and we focus in the current work on the structures and energetics. The results for Mg_{2-4} are consistent with rare gas matrix Raman spectroscopic measurements given the effect of the matrix.[69] The diatomic curve for Mg_2 was calculated with a basis set superposition (BSSE) correction as were the energetics of the Mg_{2-4} clusters. The total atomization energies were obtained at the FPD level. The T_1 diagnostics[70] for the Mg clusters are all near 0.01 suggesting that there is not significant multireference character; the T_1 values are not strongly dependent on the cluster size (see Supporting Information).

The dimer has a calculated bond length of 3.99 Å, consistent with a van der Waals dimer arising from the closed shell $(\sigma_{3s})^2(\sigma_{3s}^*)^2$ configuration. The calculated value is slightly longer than the bond distance of 3.893 Å calculated from very high level CCSD(T) calculations with a full configuration interaction correction.[71] The latter value is in excellent agreement with the experimental value of 3.89309 Å.[72,73,74] The calculated vibrational frequency agrees with the experimental vibrational frequency, 47.8 cm^{-1}, for the v = 0 to v = 1 transition to within 3 cm^{-1}. Two dissociation energies from the minimum have been reported as 431.4 cm^{-1} (1.23 kcal/mol)[71] and 430.472 cm^{-1} (1.23 kcal/mol).[72,73,74] Mg_2 has a heat of formation approximately equal to that of two Mg atoms with a weak van der Waals binding energy of ~ 1 kcal/mol. This value is consistent with the reported heat of formation of 68.7 kcal/mol at 0 K.[54]

The predicted structure of Mg_3 is D_{3h} with a Mg-Mg bond distance of 3.35 Å. For the trimer, the linear structure is predicted to be 3.8 kcal/mol above the minimum D_{3h} structure. At 0 K, Mg_3 is bound by 5.4 kcal/mol with respect to 3 Mg atoms showing that the addition of Mg to Mg_2 moderately increases the stabilization of the trimer. The normalized clustering energy is 1.9 kcal/mol/Mg. Previous calculations at the CCSD/7631 level give a bond distance of 3.67 Å and a binding energy of 2.1 kcal/mol, while those done at the MRCI level with the same basis set produced a bond distance of 3.37 Å and a binding energy of 6.3 kcal/mol.[75] A CCSD(T)/7631 level calculation[17] predicted a value of 5.3 kcal/mol for the atomization energy. Only the 3s orbitals were correlated in those prior calculations.

The Mg_4 tetramer has T_d symmetry with a Mg-Mg bond distance of 3.07 Å. The addition of Mg to Mg_3 is exothermic by -17.4 kcal/mol. This increases the stability of Mg_4 with respect to Mg_3 but the normalized clustering energy for Mg_4 is still only 5.9 kcal/mol/Mg. Previous calculations of Mg_4 at the CCSD/652 level give a bond distance of 3.23 Å.[17] The binding energies found were 13.6 kcal/mol at the CCSD/7631 level and 16.2 kcal/mol at the MRCI/531 level. The CCSD(T)/7631 level gave the atomization energy as 22.5 kcal/mol.[17] The calculated values for the harmonic frequencies at the CCSD(T)/7631 level[17] are in good agreement with the current values obtained for both Mg_3 and Mg_4. The TAE for Mg_4 is consistent with a CCSD(T) value of 24.6 ± 1.6 kcal/mol calculated using a similar approach.[76] It has been noted that the bonding in Mg_4 is due to correlation effects.[67]

The three structures investigated for Mg_2F are shown in Figure 6.8 and their relative energies are summarized in Table 6.4. At the FPD level, the most stable structure for Mg_2F is the C_2v structure with a linear Mg-Mg-F ($C_{\infty v}$) structure 6.8 kcal/mol higher in energy. Since neither has imaginary frequencies, both are minima. The linear Mg-F-Mg ($D_{\infty h}$) structure is 6.4 kcal/mol

higher in energy (Table 6.4) but it has an imaginary bending frequency indicating it is a transition state for inversion converting the C_{2v} structure.

The Mg-F bond distance in the ground state C_{2v} Mg_2F structure is predicted to be 1.906 Å (Figure 6.8) at the awCVTZ level. For comparison, the Mg-F bond distance in MgF_2 ($^1\Sigma_g^+$, $D_{\infty h}$) is 1.742 Å and for MgF ($^2\Sigma^+$) is 1.755 Å at this level. Thus, the Mg-F bond length in Mg_2F increases by ~0.15 Å. The ∠Mg-F-Mg is 98.6° giving an Mg-Mg distance 0.13 Å shorter than the Mg_2^+ bond length determined at this computational level. The positive charge and spin are located evenly on the Mg atoms and the best description for the ground state is an ionic species, $Mg_2^+F^-$. (Table 6.5). The calculated bond lengths for the $C_{\infty v}$ structure of Mg_2F are similar to the bond lengths in MgF and Mg_2^+ with the latter being 0.07 Å longer in the diatomic ion. The charges show that the Mg adjacent to the F has a large positive charge with more spin (0.55) than the terminal Mg (0.40). There is a small spin polarization on the F. Since the F^- can circumnavigate the Mg_2^+ core with an energy less than 10 kcal/mol, the cluster has potential fluxional character. The transition state for inversion has a Mg-F bond distance slightly shorter than that in the C_{2v} structure. The electronic properties of the linear structure do not really change with the positive charge and the spin split between the two terminal Mg atoms. The T_1 diagnostics for the Mg_xF are given in the Supporting Information and are again modest, on the order of 0.01 to 0.02 for x = 2 and < 0.025 for x = 3. These values are consistent with little if any multireference character in these clusters.

Reaction between F atoms and Mg_x ($x \geq 4$) could produce Mg_3F. Possible Mg_3F structures are shown in Figure 6.9. The most stable structure has the F atom added to the edge of the triangle giving structure Mg_3F **a** with C_{2v} symmetry in a $^2A_1$ state (see Figure 6.9). The Mg-F bond distance is essentially the same as that in C_{2v} Mg_2F. The unique Mg-Mg distance is 0.12 Å

longer than that in C_{2v} Mg_2F. The two long Mg-Mg distances deviate little from that in the bare trimer. Structure **b** is higher in energy by 6.2 kcal/mol and has no imaginary frequencies. The remaining structures of Mg_3F have imaginary frequencies indicating they are transition structures. The lowest energy state of Mg_3F can again be described as an F^- interacting with Mg_3^+ with the spin on the Mg_3^+ approximately equally shared by the Mg atoms.

Another possibility for the emitter is the MgF dimer, Mg_2F_2, in D_{2h} symmetry. However, the fact that F_2 is not present under the experimental conditions for producing the chemiluminescent spectra in Figures 6.2 through 6.5 and that dimerization of 2 MgF molecules does not produce sufficient energy to excite the observed emission (see next section), means that this species is not the emitter. The results for Mg_2F_2 are presented in the SI.

Computational Results: Energetics for Mg_nF_m. The heats of formation for the relevant magnesium-fluorine based systems are given in Table 6.6. On the basis of prior work on small Mg compounds[61] and the results given above, we estimate that the error bars on the heats of formation are ± 1 kcal/mol. The heats of formation were used to predict the energies for reacting F atoms with the clusters as given in Table 6.7. The error bars on the reaction energies due to errors in the heats of formation are also on the order of ± 1 kcal/mol.

The reaction between F atoms and Mg_3 to form Mg_2F is sufficiently exothermic to produce the observed chemiluminescence as is the reaction to produce MgF with the release of 2 Mg atoms. The reactions of F atoms with Mg_4 to produce either Mg_3F, Mg_2F or MgF are also substantially exothermic. It is useful to compare the bond dissociation energies (BDEs) for the loss of an F atom from Mg clusters. The BDE for loss of an F atom at 0 K increases from 105.8 kcal/mol for MgF[61] to 121.1 kcal/mol for Mg_2F. There is only a small increase in the BDE for removing an F atom from Mg_3F. One can also predict the loss of Mg from Mg_xF. For Mg_2F, the

loss of Mg requires 16.4 kcal/mol at 0 K whereas for Mg_3F, the loss of a Mg atom requires only 6.5 kcal/mol.

Computational Results: Vibrations for Mg_nF_m The calculated vibrations (Table 6.8) for Mg_2F do not agree as well with the experimental values observed in the chemiluminescence experiments as expected from the good agreement found for Mg_x and MgF. The calculated symmetric stretch of 470 cm^{-1} is 46 cm^{-1} lower than the value of 516 cm^{-1} observed experimentally and the calculated bend at 172 cm^{-1} is significantly larger than the experimental value of 104 cm^{-1}. However, the symmetric stretch and the bend are of the same symmetry type, so they will be coupled, especially in a ring like system. In addition, we have not included the effects of fluxional behavior. We note that the bend frequency decreases to 72 cm^{-1} in linear Mg-Mg-F and the Mg-F stretch increases to 708 cm^{-1} showing significant changes as the fluorine atom moves. An increase in the stretch corresponds to a decrease in the bend. This suggests the likelihood of some fluxional character when Mg_2F is formed during a highly exothermic reaction. The stretching frequency of $[Mg_2]^+$ is significantly higher than the lowest frequency mode in C_{2v} Mg_2F which suggests that this mode in Mg_2F is predominantly associated with the Mg-F-Mg bend. The stretching frequencies for ground state Mg_3F are clearly not consistent with the observed transition although there are lower frequency modes at 117 and 96 cm^{-1} that are similar to the observed features at 104 cm^{-1}. Thus, it is most reasonable to assign the emitter as Mg_2F (C_{2v}) which possesses some fluxional character.

Computational Results: TD-DFT for Mg_nF_m Time-dependent DFT (TD-DFT) calculations[77,78,79] were performed with the TPSS,[80] CAM-B3LYP,[81] and B3LYP functionals with the results for the TPSS functional given in Table 6.9 and with the other functionals in the Supporting Information. We discuss the results with the TPSS functional and note that the other functionals

give essentially the same results although the ordering of some of the LUMOs may change. The predicted transitions for $Mg_2^+F^-$ with reasonable intensities in the spectral region of interest are from the singly occupied Mg_2^+ 3s σ* antibonding orbital and the doubly occupied Mg_2^+ 3s σ bonding orbital of the Mg_2^+ fragment to unoccupied orbitals on the Mg_2^+.We seek to identify transitions predicted to occur in the region of the observed chemiluminescence that also satisfy the observations made in dispersed laser induced fluorescence. Specifically, we observe a decrease in the ground state symmetric stretching mode from ~516 to ~370 cm^{-1}. This suggests that a viable assignment must be associated with a decrease in bonding character corresponding to a change from bonding to antibonding or nonbonding character in transition. We thus seek transitions falling in the correct wavelength range, consistent with the observed decrease in frequency (bond strength).

The SOMO → LUMO transition for Mg_2F is predicted to lie too far to the red to account for the observed chemiluminescence. The LUMO is derived from the in-plane 3p σ bonding orbital on the Mg_2^+ which is the LUMO of the bare diatomic cation. The LUMO+1 is the bonding out-of-plane 3p π orbital on the Mg_2^+, and the LUMO + 2 is the antibonding out-of-plane 3p π orbital on the Mg_2^+. The LUMO+3 is an anti-bonding Mg-F orbital derived from the remaining 3p π orbital on the Mg_2^+ mixing with the 3p σ orbital. Thus, low lying transitions in Mg_2F are predominantly due to transitions on the Mg_2^+ with some distortion of the orbitals caused by F^-. The best assignment for the observed chemiluminescence (Figure 6.5) and dispersed laser induced fluorescence (Figures 6.7 and A6.1) based on the TD-DFT calculations is the SOMO → LUMO + 3 transition at 3.53 eV (352 nm) which is of symmetry $^2B_2 \rightarrow {}^2B_2$. We note that there is a predicted high intensity transition in Mg_2^+ at 3.64 eV (341.1 nm, f = 0.88) that is composed of the Mg_2^+ DOMO1 (3s σ bonding) to the SOMO (3s σ* antibonding orbital) and

SOMO to LUMO (3p σ bonding orbital). This predicted transition is very close to the predicted transition for $Mg_2^+F^-$ at 352 nm. In addition, it is useful to note that there are many predicted absorptions that are essentially forbidden with zero or very low intensities in $Mg_2^+F^-$ and Mg_2^+.

Computational Results: Mg_nCl_m We also calculated the properties of the corresponding Mg_2Cl molecule. The results for Mg_2Cl are given in Figure 6.8 and Tables 6.5 to 6.8 and 6.10. The linear MgMgCl structure is calculated to be 3.6 kcal/ mol lower in energy than the C_{2v} MgClMg structure indicating it is the ground state. The $D_{\infty h}$ MgClMg structure is much higher in energy. The Mg-Mg bond distance in the ground state linear structure is comparable to that in the corresponding Mg_2F structure. The C_{2v} structure has a smaller bond angle and a shorter Mg-Mg bond distance than in C_{2v} Mg_2F. The frequencies for Mg_2Cl are lower than the corresponding ones in Mg_2F consistent with the larger masses for the chloride and the weaker bond energies. In addition, there will be even more fluxional character affecting the vibrations in Mg_2Cl as well as a change in geometry. The small difference in energy between the two isomers may account, at least in part, for the more densely packed Mg_xCl emission feature (Figure 6.4). The molecular charges are similar to those in Mg_2F although with less ionic character in Mg_2Cl.

The first intense transition predicted by TD-DFT for Mg_2Cl is at 3.40 eV (364 nm) and is the SOMO → LUMO+2 transition ($^2\Sigma^+ \rightarrow {}^2\Sigma^+$). The SOMO is the Mg-Mg 3s+3s σ* bond and the LUMO+2 is another σ* bond composed of 3p orbitals. Note that the experimental chemiluminescence spectrum associated with Mg_xCl is shifted to the red of that associated with Mg_xF (Figure 6.5). This is consistent with the shift from the transition at 3.53 eV in Mg_2F to 3.40 eV in Mg_2Cl.

Mechanistic Considerations Several sources could account for the magnesium atom emission features observed in Figures 6.2 to 6.6. Energy transfer collisions by magnesium atoms with

highly vibrationally excited MgF could result in direct energy transfer pumping of Mg* ^{3}P atoms as well as subsequent energy transfer pooling reactions where the relatively long-lived ^{3}P state energy is transfer pumped to the Mg* ^{3}S and ^{3}D states in a second collision with MgF. We have also observed significant magnesium atom excitation producing the ^{3}S and ^{3}P states in the absence of a fluorine atom donor in experiments that used argon as a discharge constituent. The ^{3}S – ^{3}P and ^{3}D – ^{3}P emissions were pumped by energy transfer from metastable argon to magnesium vapor. Introducing SF_6 into the discharge quenched this process by decreasing the amount of metastable Ar produced. Nevertheless, the results reported in Figures 6.2 to 6.5 were obtained by using a helium discharge exclusively, leading to minimal Mg* formation due to metastable energy transfer from the discharge.

Kowalski and Menzinger[82] reported that the reaction between metastable Mg (^{3}P) and SF_6 will excite weak chemiluminescence from the A state of MgF. Since Mg (^{3}P) atoms are available, the MgF emission observed with the SF_6 based discharge configuration could result, at least in part, from this reaction. We observe that the magnesium ^{3}P – ^{1}S emission feature diminishes as the MgF A-X feature grows into the spectrum. Both the MgF and magnesium atom emission features are also quenched relative to the blue (Mg_xF) system at higher magnesium fluxes (Figure 6.5) indicating they are produced from different chemical reactions.

There is evidence that highly exothermic magnesium dimer reaction (5)

$$Mg_2 + F \rightarrow MgF^* + Mg \qquad (5)$$

will produce the emission from the MgF A state. The monitored behavior of the MgF emission (Figures 6.2 and 6.3) when both CF_4 and SF_6 are used to provide the F atoms and the growth of the MgF emission with increasing magnesium concentration in the reaction zone is consistent with some contribution to this emission from the dimer reaction.

The chemiluminescence from the Mg_2F emitter increases more rapidly as a function of metal atom concentration than does the MgF emission. The MgF signal is expected to increase at a rate which is roughly second order in the magnesium atom concentration (Reactions (6) and (7)) if the Mg dimer is involved.

$$Mg + Mg + M \rightarrow Mg_2 + M \quad (6)$$

$$Mg_2 + F \rightarrow MgF^* + Mg \quad (7)$$

where M is an atom or molecule that is present in the system. Other second order sources for MgF emission involving an excited state of Mg. are given by reactions (8) and (9).

$$MgF + Mg(^1S) \rightarrow Mg\ (^3P) + MgF \quad (8)$$

$$Mg(^3P) + SF_6 \rightarrow MgF + SF_5 \quad (9)$$

This result suggests that the Mg_2F formation rate is at least second order (and possibly higher) in the magnesium atom concentration. This observed behavior suggests the manifestation of a metal cluster oxidation process since reaction with Mg_3 could be a third order process in the magnesium atom concentration, reaction (10).

$$Mg_2 + Mg + M \rightarrow Mg_3 + M \quad (10)$$

The calculated magnesium atom ionization energy (IE) of 7.639 eV at the CCSD(T)/CBS limit and 7.648 eV at the CCSD(T)/CBS-DK limit agree well with the experimental value of 7.646236 ± 0.000004 eV.[83] The FPD calculated IE for Mg_2 is 6.39 eV. The CCSD(T)/CBS adiabatic IE for Mg_3 is 5.87 eV (the vertical IE is 6.47 eV) and is accompanied by a large change in geometry as Mg_3 is a D_{3h} triangle and Mg_3^+ is linear with r(Mg-Mg) = 3.047 Å at the CCSD(T)/awQ-DK level. Based upon an anticipated electron jump reaction, we might envision either a metal dimer or metal trimer – fluorine atom reaction to produce the observed 390-490 nm emission system. The increase in stability associated with the clustered alkaline earth metals,

M_x ($x \geq 3$) versus the corresponding van der Waal's dimers suggests, in conjunction with the observed metal flux dependence, that a readily ionized magnesium trimer interacts with a fluorine atom to form the ionic Mg_2F complex. The dimer + halogen reaction might produce the complex through a collisionally stabilized (helium) three body radiative association. However, this process should lead to a much more significant internal excitation than we observe in the present study.[84] If we assume a trimer-fluorine atom reaction, reaction (11),

$$Mg_3 + F \rightarrow Mg_2F^* + Mg \qquad (11)$$

the exiting magnesium atom obviates the need for collisional stabilization of a complex. Reaction (11) is facilitated by a weak interaction of one of the magnesium atoms in the Mg_3-F atom collision complex that removes excess energy as it leaves the reaction zone, facilitating collisional deactivation of upper state vibrational levels. These factors also lead us to believe that the trimer reaction forms the Mg_2F complex. The ready formation and subsequent reaction of small magnesium clusters in the present experiments, employing a dry ice cooled agglomeration flow, is consistent with observations in other laboratories. In fact, Martin et al.[85] have used the inert gas condensation technique to produce large magnesium clusters, Mg_n, $n \geq 10$.

The metal dependence, the low IE for Mg_3, and the electron affinity of the fluorine atom suggests that the trimer reaction occurs by an electron jump-harpoon mechanism.[86] The actual electron jump is predicted to occur at 6.0 Å using the above IE for Mg_3 and the electron affinity of 3.40 eV for F.[51] The resulting electron transfer produces the excited, strongly bound, $Mg_3^+F^-$ complex that then relaxes through the loss of a magnesium atom (Reaction 12). Note that the

$$Mg_3 + F \rightarrow Mg_3^+ \bullet\bullet F^- \rightarrow Mg_3^+F^- \rightarrow Mg + Mg_2F^* \qquad (12)$$

electron jump will lead to a dramatic change in the Mg_3 fragment from highly bent to linear, enhancing the loss of the Mg atom. The increased stability of the Mg_3^+ as well as Mg_2^+ ions relative to their neutral counterpart certainly can also contribute to the maintenance of a metal-metal bond during this reactive collision.

Conclusions

A near ultraviolet transition of Mg_2F has been observed in emission following the reaction of magnesium clusters (most likely Mg_3) with fluorine atoms. As observed in previous studies,[7,8,9] the upper state internal excitation appears to quenched to the lowest excited state vibrational levels based on the observed chemiluminescence. The results obtained from dispersed laser induced fluorescence experiments indicated excitation of four vibrational levels with an excited state symmetric frequency on the order of 370 ± 30 cm^{-1}. The strongest bands in the spectrum emanate from the lowest of these upper state levels to various vibrationally excited state levels in the ground state. Two (of possibly three) vibrational frequencies, $\upsilon_1 = 516 \pm 10$ cm^{-1}, and $\upsilon_2 = 104 \pm 10$ cm^{-1} have been established experimentally. The third frequency, υ_3, is estimated to be ~ 394 cm^{-1}. Mg_2F is highly fluxional so there is substantial coupling between the symmetric stretch and the bend. Like the MgF A-X transition, the observed transition in Mg_2F is largely localized on orbitals on the magnesium dimer ion.

High level electronic structure calculations at the CCSD(T) level predict that ground state Mg_2F is of C_{2v} symmetry but is fluxional and can reasonably be modeled as an $Mg_2^+F^-$ ion pair. Mg_2F is likely formed by the reaction of Mg_3 + F. The BDEs for loss of F from the small Mg clusters are large, from 100 to 125 kcal/mol. TD-DFT calculations predict that there are many possible transitions, most of which are silent. These transitions are primarily localized on the Mg_2^+ moiety and involve transitions from the bonding 3s σ orbital and the half-filled antibonding

3s σ* orbital to the empty 3p orbitals on the Mg_2^+ fragment. The observed transition is assigned to the eighth excitation, a $^2B_2 \rightarrow {}^2B_2$ transition in Mg_2F based on TD-DFT calculations which predict an intense transition at 352 nm. The observed transition near 350 nm in $Mg_2^+F^-$ is very similar to the first predicted large intensity transition in Mg_2^+.

Tables

Table 6.1. Observed Bands (cm^{-1}) and Assignments for Mg_2F Presented in a Deslandres Format.[a]

Assignment	$1°_x$	$1°_x2°_1$	$1°_x2°_2$	$1°_x2°_3$
$x\downarrow$				
0	25766 (528)			
1	25238 (508)			
2	24730 (121) (538)	24609 (514)		
3	24192 (97) (516)	24095 (524)		
4	23676 (105)	23571 (103) (523)	23468 (525)	
5		23048 (105) (506)	22943 (508)	
6		22542 (107)	22435 (107) (523)	22328
7			21912 (100) (505)	21812
8			21407 (91)	21316

[a] The 1 corresponds to ν_1 denoting a stretching mode and the 2 corresponds to ν_2 denoting a bending mode or Mg-Mg interaction.

Table 6.2. $Mg_{x=2}F$ Transition Combinations and Appropriate Wavelengths in nm.[a]

	$n' = 0$	$n' = 1$	$n' = 2$	$n' = 3$	$n' = 4$
$n" - 3$	366.0	(361.2-361.4)	(356.8)	(352.6)	(348.8)
$n" - 2$	373.0	368.3	363.8	(358.6)	354.5
$n" - 1$	380.4	376.0	370.7	365.5	361.4
$n"$	388.0[b]	383.0	378.0	373.2	368.3
$n" + 1$	396.2[b,c]	391.0	385.0	380.5	375.9
$n" + 2$	404.2[b,c]	(399.0)	394.0	388.2-388.5	383.3
$n" + 3$	413.2[b,c]	(407.4)	(402.2)	396.1	391.0
$n" + 4$	422.2[b,c]				
$n" + 5$	433.7[b,c]				
$n" + 6$	443.5[b,c]				
$n" + 7$	456.2[b,d]				
$n" + 8$	467.0[b,d]				

[a] Table 6.2 is an extension of Table 6.1 and correlates with Figures 6.6 and 6.7 and with the spectra in the SI. The Table now includes assignments of excited state values obtained from DLIF experiments (Figures 6.7 and A6.1) which are fit to $v = 25766 + 370(30)v'_1$ ($w_e x_e = 5\ cm^{-1}$) $- 516\ v"_1 - 104\ v"_2$ (cm^{-1}).

[b] Chemiluminescent emission.

[c] Plus one quantum in ground state bend /Mg-Mg stretch.

[d] Plus two quanta in ground state bend/Mg-Mg stretch.

Table 6.3. Calculated r(Mg-Mg), Frequencies, and Total Atomization Energies[a] for Mg_{2-4} at the CCSD(T) level.

Molecule	symmetry	Basis set	r (Å)	ω_e (cm^{-1})	$TAE_{electronic}$ (kcal/mol)	TAE(0 K) kcal/mol
Mg_2	$D_{\infty h}$	aw5-DK	3.985	45.4[b]	1.1	1.0
Mg_2^+	$D_{\infty h}$	aw5-DK	3.014	214.5[c]	30.4[d]	30.0 [d]
Mg_3	D_{3h}	awQ-DK	3.350	111.9 E´ 105.8 A_1´	6.2	5.7
Mg_3	$D_{\infty h}$	awQ-DK	3.840	69.9 Σ_u^+ 35.7 Σ_g^+ 6.8*i* Π_u	2.4	2.2
Mg_4	T_d	awT-DK	3.064	194.8 A_1 148.7 E 173.8 T_2	25.1	23.6

[a] CCSD(T)/CBS values. TAE(0K) includes ZPE corrections. [b] $\omega_e\chi_e = 1.7cm^{-1}$. [c] $\omega_e\chi_e = 1.1cm^{-1}$. [d] $Mg^{2+} \rightarrow Mg + Mg^+$.

Table 6.4. Conformer Relative Energies (kcal/mol) for Mg_2F and Mg_3F at the CCSD(T)/CBS level.

Molecule	symmetry	state	ΔE	imaginary ω (cm^{-1})
Mg_2F	C_{2v}	$^2B_2$	0.0	0
Mg_2F	$D_{\infty h}$	$^2\Sigma_u^+$	6.4	54.6i π
Mg_2F	$C_{\infty v}$	$^2\Sigma^+$	6.8	0
Mg_3F **a**	C_{2v}	$^2A_1$	0.0	0
Mg_3F **a** [a]	C_{2v}	$^2B_2$	5.5	51.2i, 21.0i
Mg_3F **b**	C_{2v}	$^2A_1$	6.2	0
Mg_3F **c** [a]	C_{2v}	$^2B_2$	6.5	48.8i
Mg_3F **d** [a]	C_{2v}	$^2A_1$	9.4	42.3i

[a] Single point calculation at the CCSD(T)/awQ level. Frequencies obtained at the CCSD(T)/awD level.

Table 6.5. NPA Charges and Spins for Mg_2F and Mg_3F at the B3LYP/aT Level.

Molecule	Atom	Charge	Spin
Mg_2F C_{2v} $^2B_2$	Mg	0.51	0.48
	F	-1.02	0.04
	Mg	0.51	0.48
Mg_2F $C_{\infty v}$ $^2\Sigma^+$	Mg	0.16	0.40
	Mg	0.83	0.55
	F	-0.99	0.05
Mg_2F $D_{\infty h}$ $^2\Sigma_u^+$	Mg	0.50	0.48
	F	-1.00	0.04
	Mg	0.50	0.48
Mg_3F **a** C_{2v} $^2A_1$	F	-1.00	0.04
	Mg	0.24	0.30
	Mg	0.38	0.33
	Mg	0.38	0.33
Mg_2Cl C_{2v} $^2B_2$	Mg	0.47	0.48
	Cl	-0.94	0.04
	Mg	0.47	0.48
Mg_2Cl $C_{\infty v}$ $^2\Sigma^+$	Mg	0.18	0.40
	Mg	0.71	0.54
	Cl	-0.89	0.06
Mg_2Cl $D_{\infty h}$ $^2\Sigma_u^+$	Mg	0.46	0.45
	Cl	-0.92	0.10
	Mg	0.46	0.45

Table 6.6. FPD Heats of Formation (kcal/mol) at 0K and 298K.

Molecule	Symmetry	State	$\Delta H_{f,0K}$	$\Delta H_{f,298K}$
Mg_2	$D_{\infty h}$	$^1\Sigma_g^+$	68.7	69.0
Mg_2^+	$D_{\infty h}$	$^2\Sigma_u^+$	216.1	216.1
Mg_3	D_{3h}	$^1A_1'$	98.9	99.1
Mg_3	$D_{\infty h}$	$^1\Sigma_g^+$	102.4	101.9
Mg_3^+	$D_{\infty h}$	$^2\Sigma_g^+$	234.3	234.6
Mg_4	T_d	$^1A_1$	115.9	115.9
MgF[a]	$C_{\infty v}$	$^2\Sigma^+$	-52.4	-52.5
MgF_2[a]	$D_{\infty h}$	$^1\Sigma_g^+$	-174.1	-174.4
Mg_2F	C_{2v}	$^2B_2$	-33.9	-34.1
Mg_2F	$D_{\infty h}$	$^2\Sigma_u^+$	-28.0	-27.9
Mg_2F	$C_{\infty v}$	$^2\Sigma^+$	-27.0	-26.9
Mg_2F_2	D_{2h}	^1A_g	-157.9	-158.6
Mg_3F **a**	C_{2v}	$^2A_1$	-5.5	-5.6
Mg_3F **b**	C_{2v}	$^2A_1$	0.1	0.3
MgCl[a]	$C_{\infty v}$	$^2\Sigma^+$	-12.8	-12.8
Mg_2Cl	$C_{\infty v}$	$^2\Sigma^+$	12.4	12.3
Mg_2Cl	C_{2v}	$^2B_2$	15.7	15.7
Mg_2Cl	$D_{\infty h}$	$^2\Sigma_u^+$	25.2	25.4
Mg		^1S	34.9	36.1
F[b]		^2P	18.5	19.5
Cl[b]		^2P	28.6	29.7

[a] Ref. 61. [b] Experimental. Refs. 51, 52, 53.

Table 6.7. Reaction Energies (kcal/mol) at 0K and 298K from Heats of Formation in Table 6.6.

Reaction	$\Delta H_{r,0K}$	$\Delta H_{r,298K}$
F Cluster Formation		
$F + Mg_2 \rightarrow MgF + Mg$	-104.7	-104.9
$F + Mg_3\ D_{3h} \rightarrow Mg_2F\ C_{2v}\ ^2B_2 + Mg$	-116.4	-116.6
$F_2 + Mg_3\ D_{3h} \rightarrow Mg_2F_2\ C_{2v}\ ^1Ag + Mg$	-221.9	-221.6
$F + Mg_3\ D_{3h} \rightarrow MgF + 2Mg$	-100.0	-98.9
$F + Mg_4 \rightarrow Mg_3F$ **a** $^2A_1 + Mg$	-105.0	-104.9
$F + Mg_4 \rightarrow Mg_3F$ **b** $C_{2v}\ ^2A_1 + Mg$	-99.4	-99.0
$F + Mg_4 \rightarrow Mg_2F\ C_{2v}\ ^2B_2 + 2Mg$	-98.5	-97.3
$F + Mg_4 \rightarrow MgF + 3Mg$	-82.1	-79.6
$2MgF \rightarrow Mg_2F_2$	-53.1	-53.6
F Cluster Decomposition		
$MgF \rightarrow F + Mg$	105.8	108.1
$Mg_2F \rightarrow F + Mg_2$	121.1	122.6
$Mg_3F \rightarrow F + Mg_3$	122.9	124.2
Cl Cluster Formation		
$Cl + Mg_2 \rightarrow MgCl + Mg$	-75.2	-75.4
$Cl + Mg_3\ D_{3h} \rightarrow Mg_2Cl\ ^2\Sigma^+ + Mg$	-80.2	-80.4
$Cl + Mg_3\ D_{3h} \rightarrow MgCl\ ^2\Sigma^+ + 2Mg$	-70.5	-69.4

Table 6.8. Harmonic Frequencies (cm^{-1}) at the CCSD(T)/aug-cc-wc-pVTZ Level.

Molecule	symmetry	ω
Mg_2F C_{2v} $^2B_2$	A_1	469.5
	A_1	172.4
	B_2	393.5
Mg_2F $C_{\infty v}$ $^2\Sigma^+$	Σ^+	707.5
	Σ^+	194.3
	Π	72.3
Mg_2F $D_{\infty h}$ $^2\Sigma_u^+$	Σ_g^+	349.8
	Σ_u^+	330.3
	Π_u	54.6i
Mg_3F **a** C_{2v} $^2A_1$	A_1	401.3
	A_1	222.1
	A_1	116.9
	B_1	95.5
	B_2	416.8
	B_2	159.2
Mg_3F **b** C_{2v} $^2A_1$	A_1	308.6
	A_1	139.0
	A_1	109.4
	B_1	65.5
	B_2	266.8
	B_2	142.6
Mg_2Cl $C_{\infty v}$ $^2\Sigma^+$	Σ^+	472.7
	Σ^+	181.0
	Π	57.6
Mg_2Cl C_{2v} $^2B_2$	A_1	318.5
	A_1	135.8
	B_2	189.3
Mg_2Cl $D_{\infty h}$ $^2\Sigma_u^+$	Σ_u^+	341.5i
	Σ_g^+	237.5
	Π_u	22.0

Table 6.9. Lowest Lying Intense Transitions in Mg_2X for X = F and Cl at the TPSS/aug-cc-pVTZ Level.

No.[a]	eV	nm	f	Assignment
Mg_2F				
4	2.37	522.6	0.294	SOMO → LUMO
8	3.53	351.7	0.442	SOMO → LUMO + 3
10	3.91	317.1	0.715	DOMO1 → LUMO+1, SOMO → LUMO+2
11	3.94	314.4	0.348	highly mixed
19	4.57	271.2	0.166	DOMO1 → LUMO+3
Mg_2Cl				
8	3.40	364.1	0.514	SOMO → LUMO+2
12	4.24	292.3	0.364	SOMO → LUMO+5

[a] Number of the excitation. Missing numbers have either 0 or very low f values.

Table 6.10. Relative energies for Mg_2Cl in kcal/mol calculated at the CCSD(T)/awn level and the CBS limit, and the number of imaginary frequencies.

Molecule	Pt grp	state	ΔE CBS	imaginary ω (cm^{-1})
Mg_2Cl	$C_{\infty v}$	$^2\Sigma^+$	0.0	N/A
Mg_2Cl	C_{2v}	$^2B_2$	3.6	N/A
Mg_2Cl	$D_{\infty h}$	$^2\Sigma_u^+$	14.6	341.5i

Figures

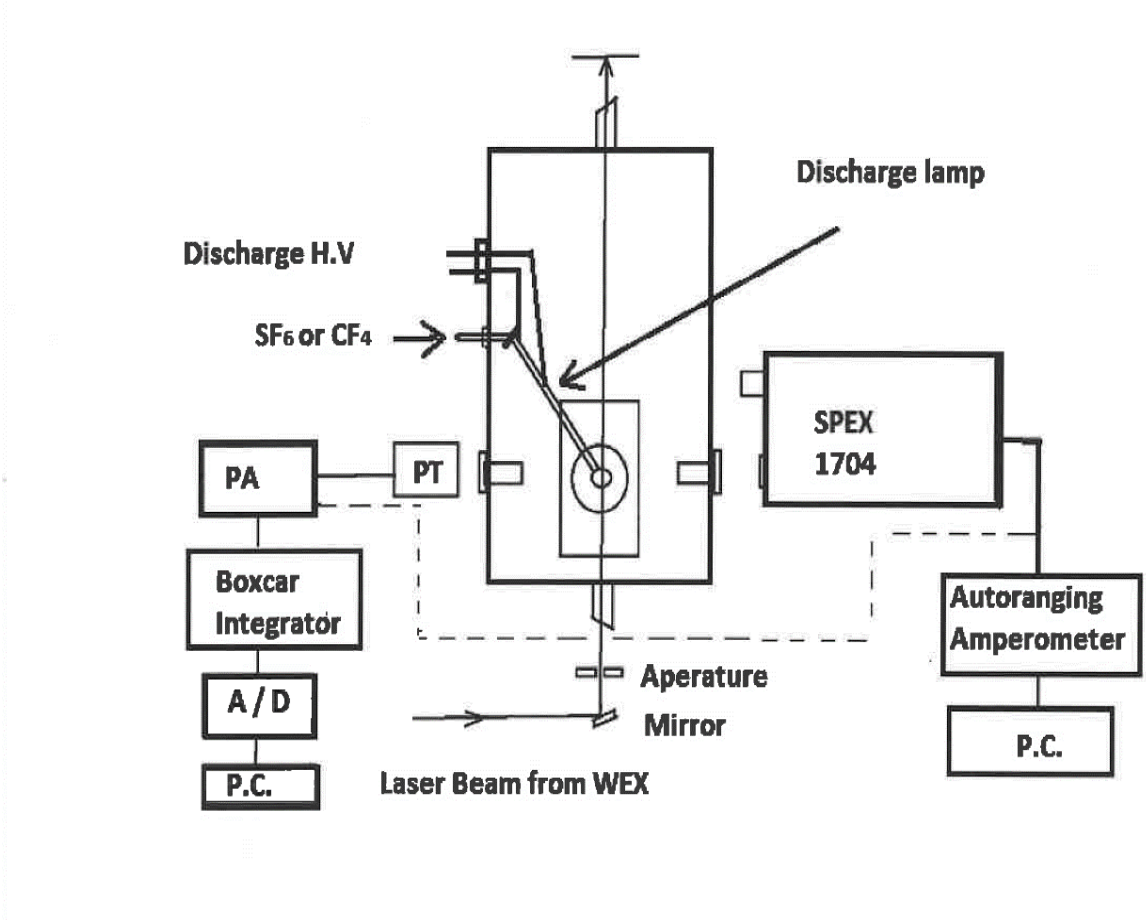

Figure 6.1. Schematic view of experimental configuration for recording both chemiluminescence (CL) and dispersed laser induced fluorescence (DLIF) from Mg_x + F reactions. PT=phototube, PA= preamplifier, PC=personal computer. Other devices are identified in the figure.

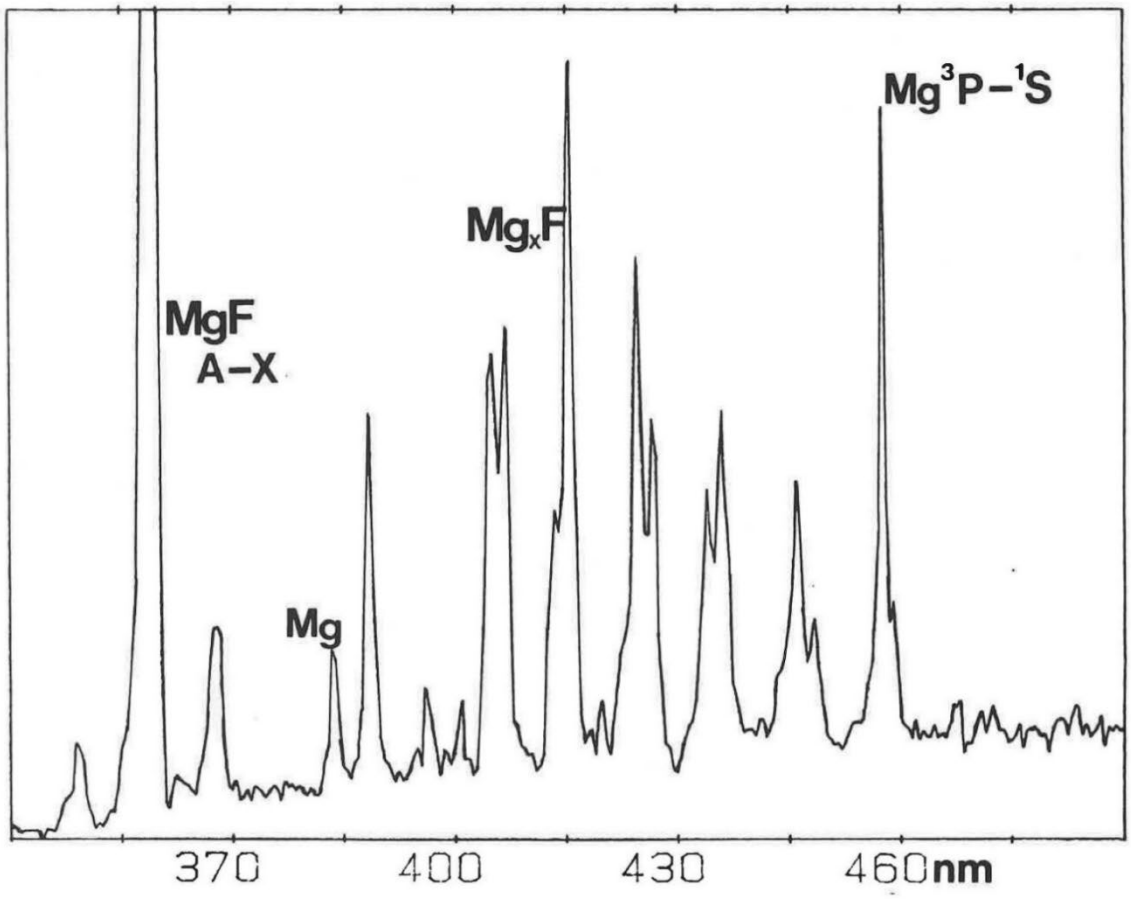

Figure 6.2. Chemiluminescent spectrum resulting from the reaction of a moderate flux of dry ice cooled, helium entrained, magnesium vapor with helium entrained fluorine atoms obtained in a discharge through SF_6 molecules. The observed spectrum consists of MgF $A^2\Pi$ - $X^2\Sigma^+$, Mg atomic, and Mg_xF emission features where x is most likely 2.

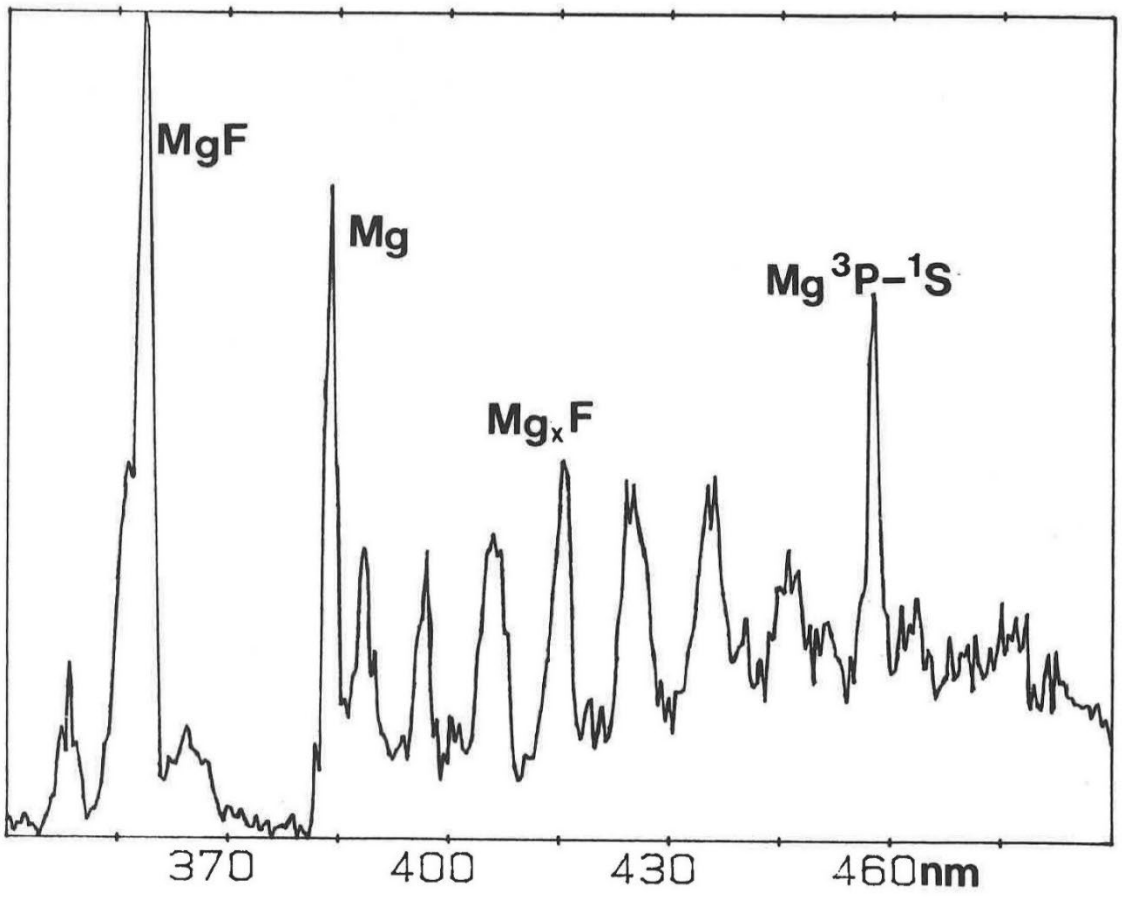

Figure 6.3. Chemiluminescent spectrum resulting from the reaction of a moderate flux of dry ice cooled, helium entrained, magnesium atoms and clusters (Mg_2, Mg_3) with helium entrained fluorine atoms obtained in a discharge through CF_4 molecules. The observed spectrum consists of MgF $A^2\Pi$ - $X^2\Sigma^+$, Mg ^3P – ^1S, and ^3D – ^3P atomic emission, and Mg_xF emission features where x is most likely 2.

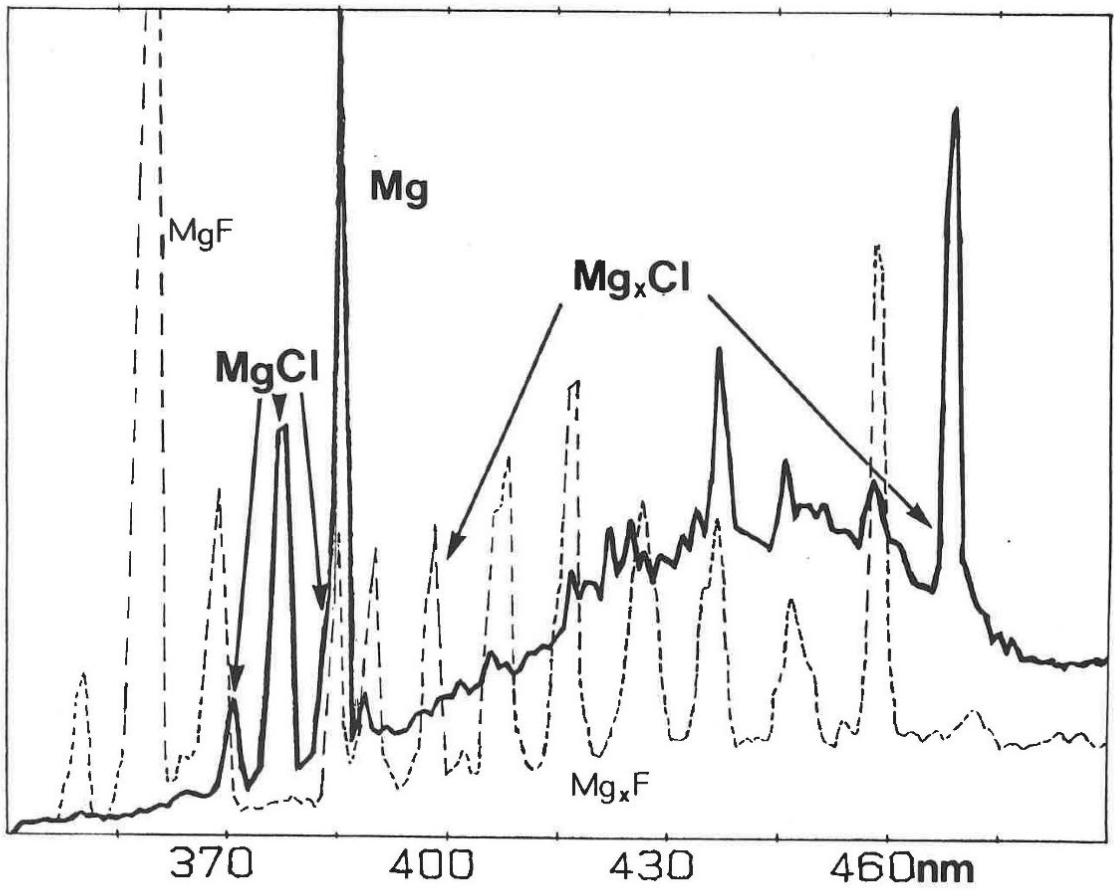

Figure 6.4. Chemiluminescent spectrum (solid line) resulting from the reaction of a moderate flux of dry ice cooled, helium entrained, magnesium atoms and clusters (Mg_2, Mg_3) with helium entrained (CCl_4 discharge) chlorine atoms. The observed spectrum consists of MgCl $A^2\Pi$ - $X^2\Sigma^+$, Mg atomic emission, and Mg_xCl emission features where x is most likely 2. The background spectrum (dashed line) corresponds to that resulting from a fluorine atom (SF_6 discharge) based system.

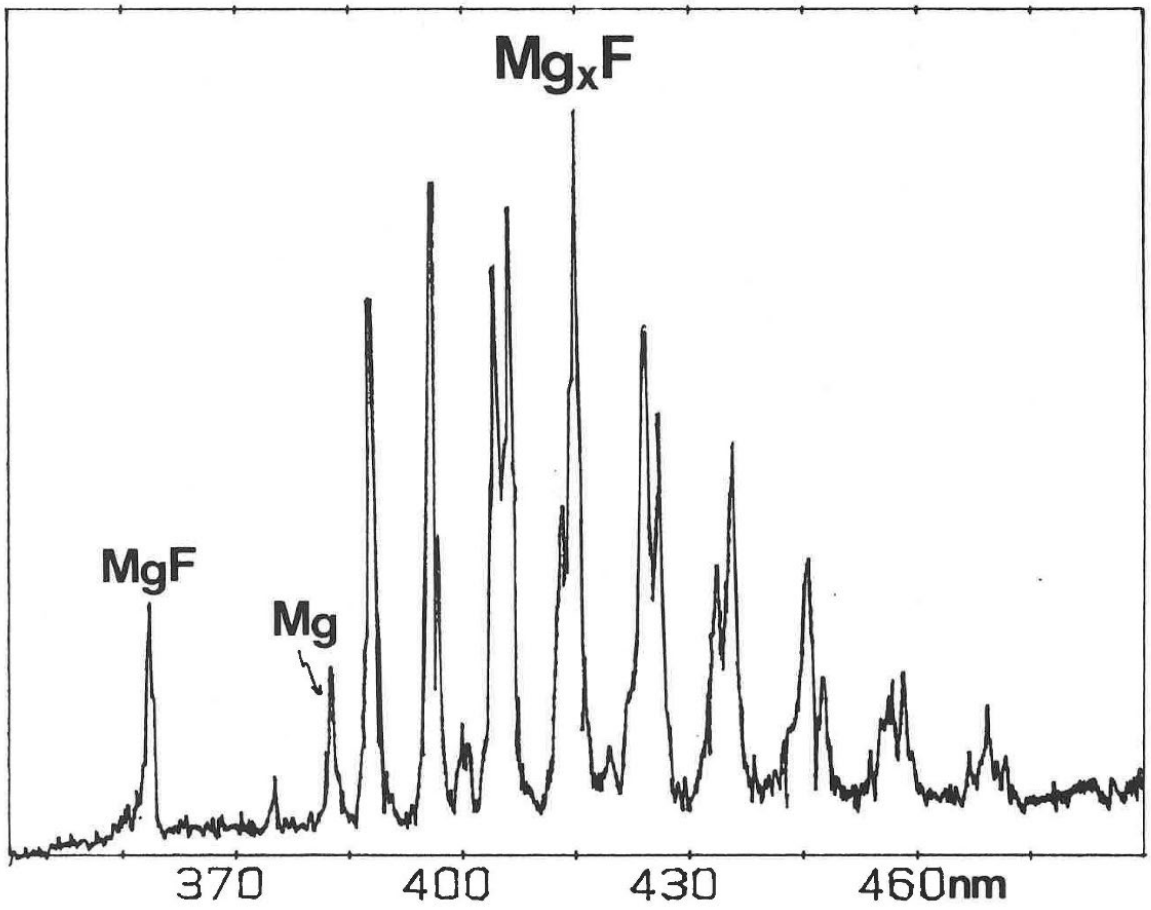

Figure 6.5. Chemiluminescent spectrum resulting from the reaction of a high flux of dry ice cooled, helium entrained, magnesium atoms and clusters (Mg_2, Mg_3) with helium entrained fluorine atoms and SF_x molecules. The observed spectrum consists of MgF $A^2\Pi$ - $X^2\Sigma^+$, $\Delta v = 0$, diagonal sequence structure much weaker than that in Figures 6.2 and 6.3. The Mg ^3D – ^3P atomic feature is also considerably weaker and the Mg ^3P – ^1S and ^3S – ^3P emission features are virtually absent.

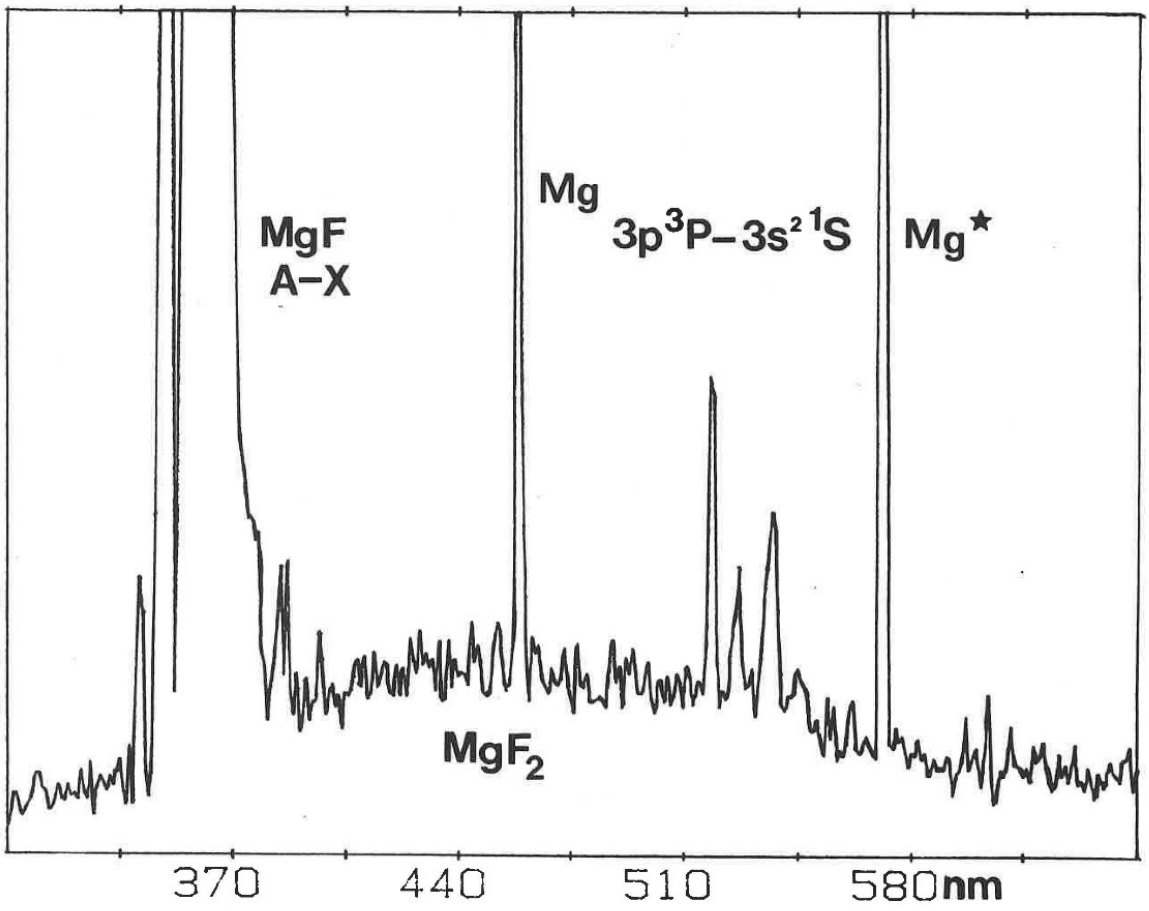

Figure 6.6. Chemiluminescent spectrum resulting from the reaction of a moderate flux of helium entrained magnesium atoms with molecular fluorine. The observed spectrum consists of MgF $A^2\Pi$ - $X^2\Sigma^+$, Mg ^3P – ^1S, ^3S – ^3P, and ^3D – ^3P atomic, and MgF_2 emission features. The unresolved MgF_2 emission feature extending from ~370-580 nm likely corresponds to a long progression in excited and ground state bending modes.

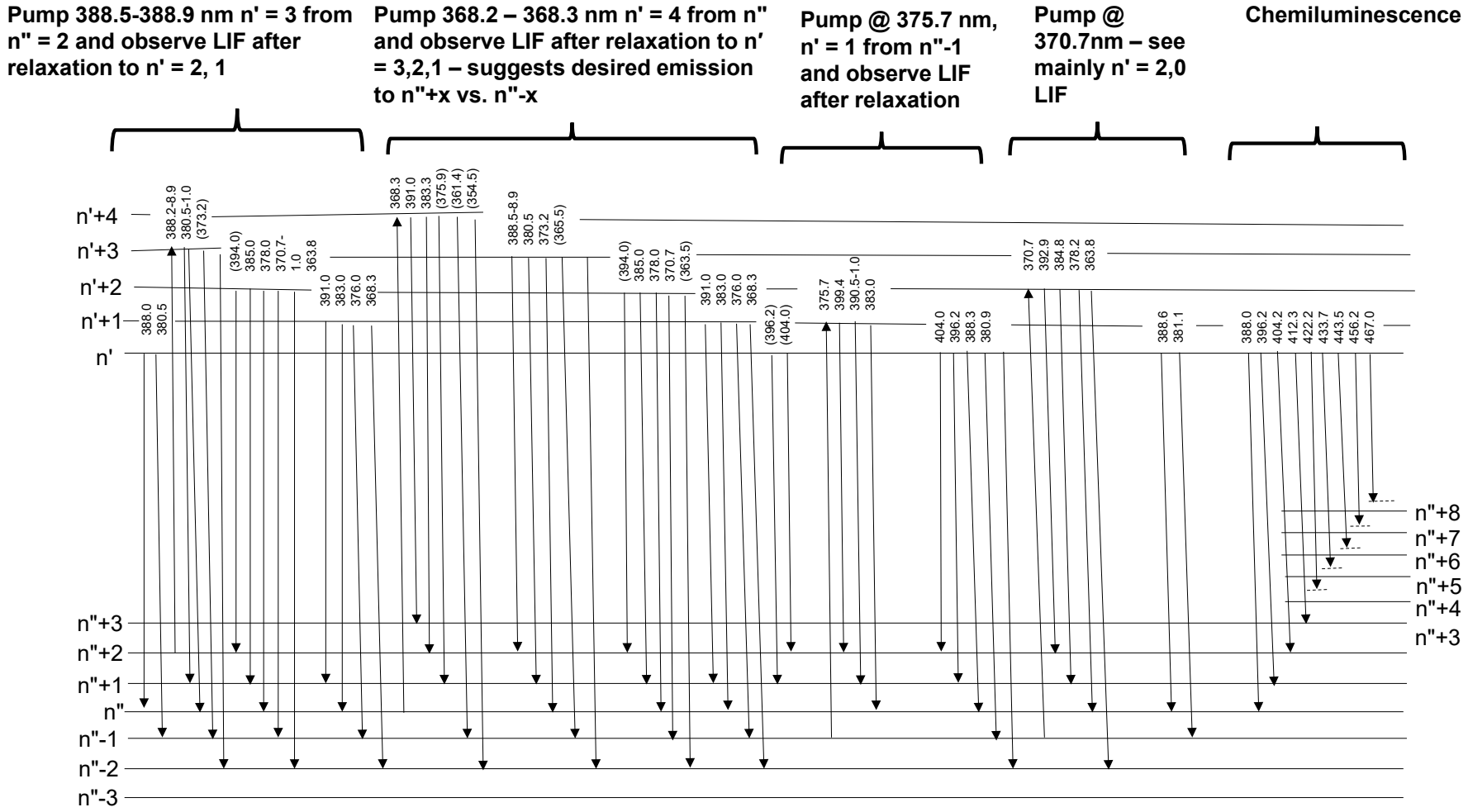

Figure 6.7. Outlined assignments for dispersed laser induced fluorescence experiments and chemiluminescence emission features. Tentative assignments relative to n′′ (ground state) and n′ (excited state) levels where n′, based on the chemiluminescence results is most likely zero. Additional assignments, n′+ 4→n′′- 1 (365.8 nm), n′ + 4→n′′- 2 (359.2 nm), n′+ 3→n′′- 2 (358.4 nm), n′→ n′′- 2 (373.5 nm). The spectra are dominated by symmetric stretching modes. There is evidence for additional frequency separations most likely associated with additional coupling of the ground and excited state bending modes and the Mg_2^+ stretching mode.

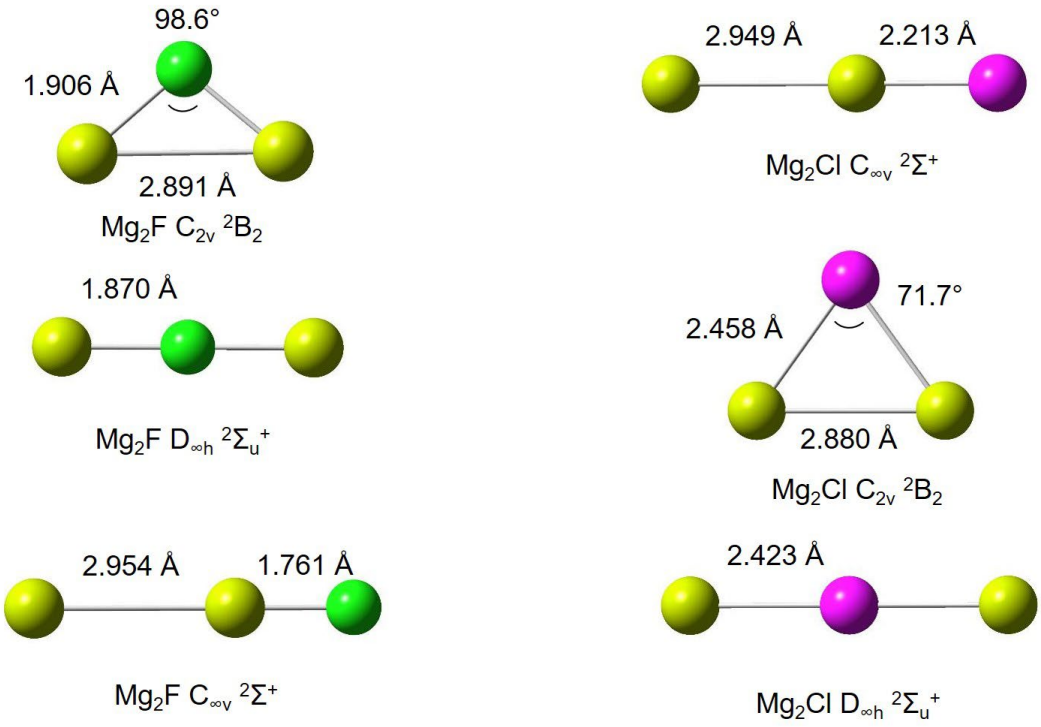

Figure 6.8. Molecular geometries for Mg_2F and Mg_2Cl.

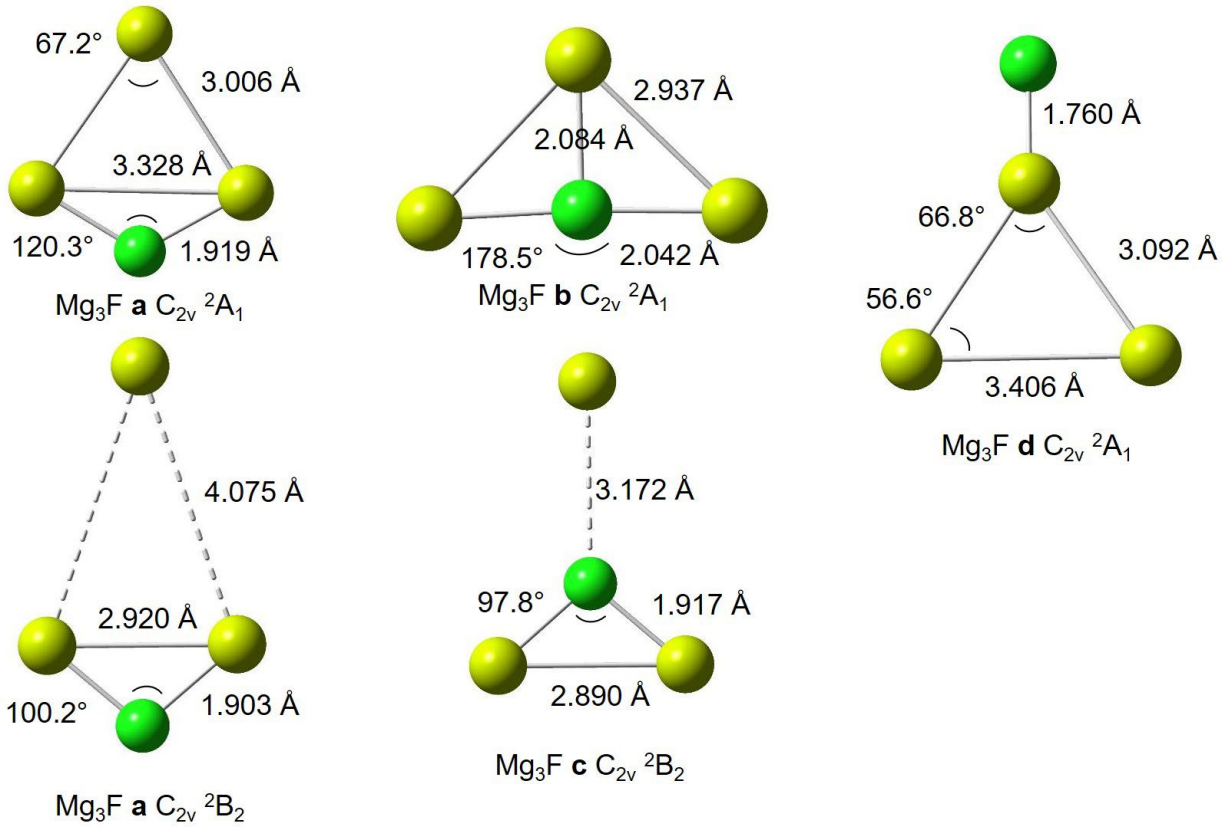

Figure 6.9. Molecular geometries for Mg_3F optimized at the CCSD(T)/awT level.

References

[1] Devore, T. C.; Gole, J. L. Oxidation of Small Metal Clusters. *High Temp. Sci.* **1989**, *27*, 49-59.

[2] Gole, J. L. The Unique Dynamics of Metal Cluster Oxidation and Complexation. *Advances in Metal and Semiconductor Clusters, Vol. I, Spectroscopy and Dynamics,* Duncan, M. A. (Ed.) JAI Press, Stamford, CT, 1993, pp. 159-209.

[3] Devore, T. C.; Brock, L.; Kahlscheuer, R.; Dulaney, K.; Gole, J. L. On the BiF Bond Dissociation Energy and an Evaluation of the BiF Red Emission Band Systems. *Chem. Phys.* **1991**, *155*, 423-433.

[4] Devore, T. C.; Gole, J. L. Formation of the Low-lying Electronic States of CrO in Highly Exothermic Reactive Oxidation. Assessment of New States and Partial Resolution of Previous Observations. *Chem. Phys.* **1989**, *133*, 95-102.

[5] Devore, T. C.; McQuaid, M.; Gole, J. L. Fluorination of Complexed Chromium Atoms and Molecules: Three New States of CrF and the Possible Observation of CrXF Emission Spectra. *High Temp. Sci.* **1990**, *29*, 1-15.

[6] Devore, T. C.; McQuaid, M.; Gole, J. L. Suggested Ground State Frequency and Bond Energy of NiF. *High Temp. Sci.* **1991**, *30*, 83-94.

[7] Woodward, R. W.; Le, P. N.; Temmen, M.; Gole, J. L. Potential Probes of Metal Cluster Oxide Quantum Levels. Optical Signatures for the Oxidation of Small Metal Clusters M_x (M= Cu, Ag, B, Mn). *J. Phys. Chem.* **1987**, *91*, 2637-2645.

[8] Devore, T. C.; Woodward, R. W.; Gole, J. L. Oxidation of Small Boron Agglomerates: Formation of and Chemiluminescent Emission from BBO. *J. Phys. Chem.* **1988**, *92*, 6919-1923.

[9] Devore, T. C.; Woodward, J. R.; Le, P. N.; Gole, J. L.; Dixon, D. A. Formation of Electronically Excited Ag_xO from the Oxidation of Small Silver Clusters. *J. Phys. Chem.* **1990**, *94*, 756-760.

[10] Devore, T. C.; Woodward, J. R.; Gole, J. L. Formation of Electronically Excited Mn_xO from the Oxidation of Small Manganese Clusters. *J. Phys. Chem.* **1989**, *93*, 4920-4923.

[11] Cobb, S. H.; Woodward, J. R.; Gole, J. L. A Chemical Process Producing a Continuous Laser Amplifier in the Visible Region. *Chem. Phys. Lett.* **1988**, *143*, 205-213.

[12] Cobb, S. H.; Woodward, J. R.; Gole, J. L. Continuous Chemical Amplification of Single- and Multi-mode Lasers in the Visible Region. *Chem. Phys. Lett.* **1989**, *156*, 197-203.

[13] Gole, J. L. Toward the Modeling of the Oxidation of Small Metal and Metalloid Molecules. in *Gas-Phase Metal Reactions*, Fontijn, A. (Ed.), North Holland, Amsterdam, 1992, pp. 573- 604.

[14] Gole, J. L.; Shen, K. K.; Woodward, J. R.; Cobb, S. H.; Doughty, J. R. Chemically Driven Pulsed and Continuous Visible Laser Amplifiers and Oscillators. *SPIE*, **1991**, *1397*, 125-135.

[15] Balfour, W. J.; Douglas, A. E. Absorption Spectrum of the Mg_2 Molecule. *Can. J. Phys.* **1970**, *48*, 901-914.

[16] Li, K. C.; Stwalley, W. C. Vibrational Levels Near Dissociation in Mg_2 and Long-Range Forces. *J. Chem. Phys.* **1973**, *59*, 4423-4427.

[17] Lee, T. J.; Rendell, A. P.; Taylor, P. R. Vibrations in Small Mg Clusters. *J. Chem. Phys.* **1990**, *93*, 6636-6641.

[18] Balfour, W. J.; Whitlock, R. F. Rotational Dependence of Franck–Condon Factors in the $A^1\Sigma_u^+ \leftarrow X^1\Sigma_g^+$ System of $^{24}Mg_2$. *Can. J. Phys.* **1972**, *50*, 1648-1651.

[19] Dixon, D. A.; Feller, D.; Peterson, K. A. A Practical Guide to Reliable First Principles Computational Thermochemistry Predictions Across the Periodic Table. In *Annual Reports in Computational Chemistry*, Wheeler, R. (Ed.), Elsevier, Amsterdam: **2012**; Vol. 8, pp 1-28.

[20] Peterson, K. A.; Feller, D.; Dixon, D. A. Chemical Accuracy in Ab Initio Thermochemistry and Spectroscopy: Current Strategies and Future Challenges. *Theor. Chem. Acc.* **2012**, *131*, 1079.

[21] Feller, D.; Peterson, K. A.; Dixon, D. A. Further Benchmarks of a Composite, Convergent, Statistically Calibrated Coupled Cluster Based Approach for Thermochemical and Spectroscopic Studies. *Mol. Phys.* **2012**, *110*, 2381-2399.

[22] Feller, D.; Peterson, K. A.; Dixon, D. A. The Impact of Larger Basis Sets and Explicitly Correlated Coupled Cluster Theory on the Feller-Peterson-Dixon Composite Method. In *Annual Reports in Computational Chemistry*, Vol. 12, Dixon, D. A. (Ed.), Elsevier, Amsterdam, 2016, pp. 47-78.

[23] McQuaid, M. J.; Morris, K.; Gole, J. L. Trends in the Optical Signatures for Transition Metal Oxide Carbonyl Complexes - Evaluation of Transition Metal Carbonyl $M(CO)_x$ (x=1,2) Binding Energies. *J. Am. Chem. Soc.* **1988**, *110*, 5280-5285.

[24] Grant, D. J.; Matus, M. H.; Switzer, J.; Dixon, D. A.; Francisco, J. S.; Christe, K.O. Bond Dissociation Energies in Second Row Compounds. *J. Phys Chem A.* **2008**, *112*, 3145-3156.

[25] Luo, Y.-R. *Comprehensive Handbook of Chemical Bond Energies*, CRC Press, Taylor and Francis Group, 2007.

[26] Becke, A. D. Density-Functional Thermochemistry. III. The Role of Exact Exchange. *J. Chem. Phys.* **1993**, *98*, 5648-5652.

[27] Lee, C.; Yang, W.; Parr, R. G. Accurate and Simple Analytic Representation of the Electron-Gas Correlation Energy. *Phys. Rev. B.* **1988**, *37*, 785-789.

[28] Dunning, T. H., Jr. Gaussian Basis Sets for Use in Correlated Molecular Calculations. I. The Atoms Boron Through Neon and Hydrogen. *J. Chem. Phys*. **1989**, *90*, 1007-1023.

[29] Kendall, R. A.; Dunning, T. H. Jr.; Harrison, R. J., Electron Affinities of the First Row Atoms Revisited. Systematic Basis Sets and Wave Functions. *J. Chem. Phys*. **1992**, *96*, 6796-6806.

[30] Prascher, B. P.; Peterson, K. A.; Woon, D. E.; Dunning, T. H., Jr.; Wilson, A. K . Gaussian Basis Sets for use in Correlated Molecular Calculations. VII. Valence, Core-Valence, and Scalar Relativistic Basis Sets for Li, Be, Na and Mg. *Theor. Chem. Acc.* ***2011***, *128*, 69-82.

[31] Frisch, M. J.; Trucks, G. W.; Schlegel, H. B.; Scuseria, G. E.; Robb, M. A.; Cheeseman, J. R.; Scalmani, G.; Barone, V.; Petersson, G. A.; Nakatsuji, H.; Li, X.; Caricato, M.; Marenich, A. V.; Bloino, J.; Janesko, B. G.; Gomperts, R.; Mennucci, B.; Hratchian, H. P.; Ortiz, J. V.; Izmaylov, A. F.; Sonnenberg, J. L.; Williams-Young, D.; Ding, F.; Lipparini, F.; Egidi, F.; Goings, J.; Peng, B.; Petrone, A.; Henderson, T.; Ranasinghe, D.; Zakrzewski, V. G.; Gao, J.; Rega, N.; Zheng, G.; Liang, W.; Hada, M.; Ehara, M.; Toyota, K.; Fukuda, R.; Hasegawa, J.; Ishida, M.; Nakajima, T.; Honda, Y.; Kitao, O.; Nakai, H.; Vreven, T.; Throssell, K.; Montgomery, J. A., Jr.; Peralta, J. E.; Ogliaro, F.; Bearpark, M. J.; Heyd, J. J.; Brothers, E. N.; Kudin, K. N.; Staroverov, V. N.; Keith, T. A.; Kobayashi, R.; Normand, J.; Raghavachari, K.; Rendell, A. P.; Burant, J. C.; Iyengar, S. S.; Tomasi, J.; Cossi, M.; Millam, J. M.; Klene, M.; Adamo, C.; Cammi, R.; Ochterski, J. W.; Martin, R. L.; Morokuma, K.; Farkas, O.; Foresman, J. B.; Fox, D. J. Gaussian 16, Revision A.03, Gaussian, Inc., Wallingford CT, 2016.

[32] Purvis, G. D., III; Bartlett, R. J. A Full Coupled Cluster Singles and Doubles Model: The Inclusion of Disconnected Triples. *J. Chem. Phys.* **1982**, *76*, 1910-1918.

[33] Raghavachari, K.; Truck, G.W.; Pople, J.A.; Head-Gordon, M. A Fifth-Order Perturbation Comparison of Electron Correlation Theories. *Chem. Phys. Lett*. **1989**, *157*, 479-483.

[34] Watts, J. D.; Gauss, J.; Bartlett, R. J. Coupled-Cluster Methods with Noniterative Triple Excitations for Restricted Open Shell Hartree-Fock and Other General Single Determinant Reference Functions. Energies and Analytical Gradients. *J. Chem. Phys.* **1993**, *98*, 8718-8733.

[35] Bartlett, R. J.; Musial, M. Coupled Cluster Theory in Quantum Chemistry. *Rev. Mod. Phys.* **2007**, *79*, 291-352.

[36] Knowles, P. J.; Hampel, C.; Werner, H.-J. Coupled Cluster Theory for High Spin, Open Shell Reference Wave Functions. *J. Chem. Phys*. **1993**, *99*, 5219-5227.

[37] Knowles, P. J.; Hampel, C.; Werner, H.-J. Erratum: Coupled Cluster Theory for High Spin, Open Shell Reference Wave Functions. *J. Chem. Phys*. **2000**, *112*, 3106-3107.

[38] Deegan, M. J. O.; Knowles, P. J. Perturbative Corrections to Account for Triple Excitations in Closed and Open Shell Coupled Cluster Theories. *Chem. Phys. Lett*. **1994**, *227*, 321-327.

[39] Woon, D. E.; Dunning, T. H. Jr. Gaussian Basis Sets for Use in Correlated Molecular Calculations. V. Core-Valence Basis Sets for Boron Through Neon. *J. Chem. Phys.* **1995**, *103*, 4572-4585.

[40] Peterson, K. A.; Dunning, T. H., Jr. Accurate Correlation Consistent Basis sets for Molecular core–valence Correlation Effects: The Second Row Atoms Al–Ar, and the First Row Atoms B–Ne Revisited *J. Chem. Phys.* **2002**, *117*, 10548-10560.

[41] Werner, H.-J.; Knowles, P. J.; Knizia, G.; Manby, F. R.; Schütz, M.; Celani, P.; Györffy, W.; Kats, D.; Korona, T.; Lindh, R.; Mitrushenkov, A.; Rauhut, G.; Shamasundar, K. R.; Adler, T. B.; Amos, R. D.; Bennie, S. J.; Bernhardsson, A.; Berning, A.; Cooper, D. L.; Deegan, M. J. O.; Dobbyn, A. J.; Eckert, F.; Goll, E.; Hampel, C.; Hesselmann, A.; Hetzer, G.; Hrenar, T.; Jansen, G.; Köppl, C.; Lee, S. J. R.; Liu, Y.; Lloyd, A. W.; Ma, Q.; Mata, R. A.; May, A. J.; McNicholas, S. J.; Meyer, W.; Miller III, T. F.; Mura, M. E.; Nicklass, A.; O'Neill, D. P.; Palmieri, P.; Peng, D.; Petrenko, T.; Pflüger, K.; Pitzer, R.; Reiher, M.; Shiozaki, T.; Stoll, H.; Stone, A. J.; Tarroni, R.; Thorsteinsson, T.; Wang, M.; Welborn, M. MOLPRO, Version 2018.1 , A Package of *ab initio* Programs, See https://www.molpro.net. Accessed October 6th, 2021.

[42] Werner, H.-J.; Knowles, P. J.; Knizia, G.; Manby, F. R.; Schütz, M. Molpro: A General-Purpose Quantum Chemistry Program Package. *WIREs Comput. Mol. Sci.* **2012**, *2*, 242-253.

[43] Werner, H-J.; Knowles, P. J.; Manby, F. R.; Black, J. A.; Doll, K.; Heßelmann, A.; Kats, D.; Köhn, A.; Korona, T.; Kreplin, D. A.; Ma, Q.; Miller III, T. F.; Mitrushchenkov, A.; Peterson, K. A.; Polyak, I.; Rauhut, G.; Sibaev, M. The Molpro Quantum Chemistry Package *J. Chem. Phys.* **2020**, *152*, 144107.

[44] Feller, D.; Peterson, K.A.; Hill, J. G. On the Effectiveness of CCSD(T) Complete Basis Set Extrapolations for Atomization Energies.*J. Chem. Phys.* **2011***, 135,* 044102.

[45] Peterson, K. A.; Woon, D. E.; Dunning, T. H. Benchmark Calculations with Correlated Molecular Wave Functions. IV. The Classical Barrier Height of the $H+H_2 \rightarrow H_2+H$ Reaction. *J. Chem. Phys.* **1994**, *100*, 7410-7415.

[46] Douglas, M.; Kroll, N. M. Quantum Electrodynamical Corrections to the Fine Structure of Helium. *Ann. Phys.* **1974**, *82*, 89-155.

[47] Hess, B. A. Applicability of the No-Pair Equation with Free-Particle Projection Operators to Atomic and Molecular Structure Calculations. *Phys. Rev. A.* **1985**, *32*, 756-763.

[48] Hess, B. A. Relativistic Electronic-Structure Calculations Employing a Two-Component No-Pair Formalism with External-Field Projection Operators. *Phys. Rev. A.* **1986**, *33*, 3742-3748.

[49] De Jong, W. A.; Harrison, R. J.; Dixon, D. A. Parallel Douglas-Kroll Energy and Gradients in NWChem: Estimating Scalar Relativistic Effects Using Douglas-Kroll Contracted Basis Sets. *J. Chem. Phys*. **2001**, *114*, 48-53.

[50] Moore, C. E. *Atomic Energy Levels As Derived from the Analysis of Optical Spectra*; *Vol. 1, H to V*. U.S. National Bureau of Standards Circular 467, COM-72-50282; U.S. Department of Commerce, National Technical Information Service: Washington, DC, 1949.

[51] https://atct.anl.gov/Thermochemical%20Data/version%201.122g/index.php accessed January 18, 2019.

[52] Ruscic, B.; Pinzon, R. E.; Morton, M. L.; von Laszewski, G.; Bittner, S.; Nijsure, S. G.; Amin, K. A.; Minkoff, M.; Wagner, A. F. Introduction to Active Thermochemical Tables: Several "Key" Enthalpies of Formation Revisited. *J. Phys. Chem. A* **2004**, *108*, 9979-9997.

[53] Changala, P. B.; Nguyen, T. L.; Baraban, J. H.; Ellison, G. B.; Stanton, J. F.; Bross, D. H.; Ruscic, B. Active Thermochemical Tables: The Adiabatic Ionization Energy of Hydrogen Peroxide. *J. Phys. Chem. A* **2017**, *121*, 8799-8806.

[54] Chase Jr., M.W. NIST-JANAF Themochemical Tables, Fourth Edition, J. Phys. Chem. Ref. Data, Monograph 9, 1998, 1-1951.

[55] Curtiss, L. A.; Raghavachari, K.; Redfern, P. C.; Pople, J. A. Assessment of Gaussian-2 and Density Functional Theories for the Computation of Enthalpies of Formation. *J. Chem. Phys.* **1997**, *106*, 1063-1079.

[56] Huber, K. P.; Herzberg, G. *Constants of Diatomic Molecules*, Van Nostrand and Company, 1979.

[57] Snelson, A. Infrared Spectra of Some Alkaline Earth Halides by the Matrix Isolation Technique. *J. Phys. Chem.* **1966**, *70*, 3208-3217.

[58] Calder, V.; Mann, D. E.; Seshadri, K. S.; Allevena, M.; White, D. Geometry and Vibrational Spectra of Alkaline-Earth Dihalides. II. CaF_2, SrF_2, and BaF_2. *J. Chem. Phys*. **1969**, *51*, 2093-2099.

[59] Hauge, R. H.; Margrave, J. L.; Kanaan, A. S. Infra-Red Spectra of Matrix-Isolated MgF_2. *J. Chem. Soc. Faraday Trans. II*, **1975**, *71*, 1082-1090.

[60] Hauge, R. H.; Margrave, J. L.; Kanaan, A. S. Infrared Spectra of Matrix-Isolated Species; Reaction Products of MgF_2 with Group–I and Group–II fluorides. *J. Chem. Soc. Faraday Trans. II*, **1976**, *72*, 1991-2000.

[61] Vasiliu, M.; Li, S.; Feller, D.; Gole, J. L.; Dixon, D. A. Structures and Heats of Formation of Simple Alkaline Earth Metal Compounds: Fluorides, Chlorides, Oxides, and Hydroxides for Be, Mg, and Ca. *J. Phys. Chem. A*, **2010**, *114,* 9349–9358.

[62] Engelke, F. Crossed-beám Chemiluminescence. II. Kinetics and Mechanisms for Reactions of Group IIA Metals in Ground and Metastable States with Fluorine. *Chem. Phys.* **1979**, *44*, 213-238.

[63] Gole, J. L. Non-Empirical LCAO-MO-SCF Studies of the Low-Lying States of BeF_2. *J. Chem. Phys.* **1973**, *58*, 869-875.

[64] Gole, J. L.; Siu, A. K. Q.; Hayes, E. F. Non-Empirical LCAO-MO-SCF Studies of the Group IIA Dihalides BeF_2, MgF_2 and CaF_2. *J. Chem. Phys.* **1973**, *58*, 857-868.

[65] DeKock, R. L.; Peterson, Michael A.; Timmer, Linda K.; Baerends, E. J.; Vernooijs, P. A Theoretical Study of the Linear Versus Bent Geometry for Several MX_2 Molecules: MgF_2, CaH_2, CaF_2, CeO_2 and $YbCl_2$. *Polyhedron* **1990**, *9*, 1919-1934.

[66] Lesiecki, M. L.; Nibler, J. W. Infrared and Raman Spectra and Structures of Matrix Isolated Magnesium Dihalides: MgF_2, $MgCl_2$, $MgBr_2$, and MgI_2. *J. Chem. Phys*. **1976**, *64*, 871-884.

[67] Chiles, R. A.; Dykstra, C. E.; Jordan, K. E. Bonding in the Mg_4 Cluster. An Example of Chemical Bonding Originating from Electron Correlation Effects, *J. Chem. Phys.* **1981**, *75*, 1044-1046.

[68] Köhn, A.; Weigend, F.; Ahlrichs, R. Theoretical Study on Clusters of Magnesium. *Phys. Chem. Chem. Phys.* **2001**, *3*, 711-719

[69] Kauffman, A.; Kornath, A.; Zoermer, A.; Ludwig, R. Small Magnesium Clusters: Between van der Waals and Valence Bonds. *Inorg. Chem.* **2010**, *49*, 3851–3856

[70] Lee, T.J.; Taylor, P. R. A Diagnostic for Determining the Quality of Single-Reference Electron Correlation Methods. *Int. J. Quantum Chem. Symp.* **1989**, *23*, 199-204.

[71] Yuwono, S. H.; Magoulas, I.; Piecuch, P. Quantum Computation Solves a Half-Century-Old Enigma: Elusive Vibrational States of Magnesium Dimer Found. *Sci. Adv.* **2020**, *6*, eaay4058.

[72] Knöckel, H.; Rühmann, S.; Tiemann, E. The $X^1\Sigma_g^+$ Ground State of Mg_2 Studied by Fourier-Transform Spectroscopy. *J. Chem. Phys.* **2013**, *138*, 094303.

[73] Knöckel, H.; Rühmann, S.; Tiemann, E. [Erratum]. The $X^1\Sigma_g^+$ Ground State of Mg_2 Studied by Fourier -transform Spectroscopy. *J. Chem. Phys.* **2013**, *138*, 189901.

[74] Knöckel, H.; Rühmann, S.; Tiemann, E. The $A^1\Sigma_u^+ + (1)^1\Pi_u$ System of Mg_2. *Eur. Phys. J. D* **2014**, *68*, 293.

[75] Lee, T. J.; Rendell, A. P.; Taylor, P. R. Theoretical Investigations of the Structures and Binding Energies of Be_n and Mg_n (n=3–5) Clusters. *J. Chem. Phys.* **1990**, *92*, 489-495.

[76] C. W. Bauschlicher, Jr. and H. Partridge, The Atomization Energy of Mg_4. *Chem. Phys. Lett.* **1999**, *300*, 364-368.

[77] Bauernschmitt, R.; Ahlrichs, R. Treatment of Electronic Excitations within the Adiabatic Approximation of Time Dependent Density Functional Theory. *Chem. Phys. Lett.* **1996**, *256*, 454-464.

[78] Casida, M. E.; Jamorski, C.; Casida, K. C.; Salahub, D. R. Molecular Excitation Energies to High-Lying Bound States from Time-Dependent Density-Functional Response Theory: Characterization and Correction of the Time-Dependent Local Density Approximation Ionization Threshold. *J. Chem. Phys.* **1998**, *108*, 4439-4449.

[79] Stratmann, R. E.; Scuseria, G. E.; Frisch, M. J. An Efficient Implementation of Time-Dependent Density-Functional Theory for the Calculation of Excitation Energies of Large Molecules. *J. Chem. Phys.* **1998**, *109*, 8218-8224.

[80] Tao, J. M.; Perdew, J. P.; Staroverov, V. N.; Scuseria, G. E. Climbing the Density Functional Ladder: Nonempirical Meta-Generalized Gradient Approximation Designed for Molecules and Solids. *Phys. Rev. Lett.* **2003**, *91*, 146401.

[81] Yanai, T.; Tew, D. P.; Handy, N. C. A New Hybrid Exchange-Correlation Functional Using the Coulomb-Attenuating Method (CAM-B3LYP). *Chem. Phys. Lett.* **204**, *393*, 51-57.

[82] Kowalski, A.; Menzinger, M. Electronic Energy Partitioning in the Reactions of $Mg^*(^3P)$ and $Ca^*(^3P, ^1D)$ with SF_6, TeF_6, and WF_6. *J. Phys. Chem.* **1988**, *92*, 4191-4196.

[83] Kramida, A., Ralchenko, Yu., Reader, J., and NIST ASD Team (2020). *NIST Atomic Spectra Database* (ver. 5.8), [Online]. Available: https://physics.nist.gov/asd [accessed October 28, 2021]. National Institute of Standards and Technology, Gaithersburg, MD. DOI: https://doi.org/10.18434/T4W30F

[84] Herzberg, G. *Electronic Spectra of Polyatomic Molecules*, Van Nostrand and Company, 1996

[85] Martin, T. P.; Bergmann, T.; Göhlich, H.; Lange, T. Evidence for Icosahedral Shell Structure in Large Magnesium Clusters. *Chem. Phys. Lett.* **1991**, *176*, 343-347.

[86] Levine R. D.; Bernstein, R. B. *Molecular Reaction Dynamics*, Oxford University Press, New York, 1974.

Appendix: Electronically Excited Complex Formation in Magnesium Cluster – Halogen Atom Reactions

Mg_2X_2

Mg_2F_2 has a ground state ^1A_g configuration with a triplet state less than 5 kcal/mol higher at the CCSD(T)/CBS level. The Mg-F bond distance is 1.908 Å and the Mg-Mg bond distance is 2.877 Å at the CCSD(T)/aug-pwCVTZ level. These are essentially the same bond distances as those predicted for Mg_2F. We considered the possibility that the emitter is Mg_2F_2 based on its calculated frequencies, but as described in the text, this does not match any thermodynamic or reactant constraints. For Mg_2F_2, the predicted symmetric stretch at 502 cm^{-1} is in reasonable agreement with the observed frequency of order 516 ± 10 cm^{-1} in the observed chemiluminescence spectrum. However, there are no low-lying frequencies to account for the observed 104 cm^{-1} transitions

Table A6.1. Heats of formation using the FPD approach at 0K and 298K in kcal/mol.

Molecule	Symmetry	State	$\Delta H_{f,0K}$	$\Delta H_{f,298K}$
Mg_2F_2	D_{2h}	$^3B_{1u}$	-154.0	-154.8
Mg_2F_4	D_{2h}	$^1A_{1g}$	-407.2	-408.3
Mg_2Cl_2	D_{2h}	$^1A_{1g}$	-111.8	-112.0
Mg_2Cl_2	D_{2h}	$^3B_{1u}$	-108.6	-108.9
Mg_2Cl_4	D_{2h}	$^1A_{1g}$	-230.1	-230.4

Table A6.2. Mg_2F_2 Cluster Decomposition Reaction energies at 0K and 298K in kcal/mol.

Reaction	$\Delta H_{r,0K}$	$\Delta H_{r,298K}$
$Mg_2F_2 \rightarrow Mg_2F + F$	142.5	144.0
$Mg_2F_2 \rightarrow MgF_2 + Mg$	18.7	20.3

Table A6.3. Frequencies (cm^{-1}) at the CCSD(T) level with the awD basis sets

Molecule	symmetry	υ
$^1Mg_2F_2$ D_{2h}	A_g	502.0
	A_g	308.9
	B_{3g}	400.7
	B_{1u}	462.7
	B_{2u}	448.4
	B_{3u}	148.2
$^1Mg_2F_4$ D_{2h}	A_g	787.5
	A_g	483.8
	A_g	254.2
	B_{2g}	132.6
	B_{3g}	440.4
	B_{3g}	145.3
	B_{1u}	763.2
	B_{1u}	456.8
	B_{2u}	500.5
	B_{2u}	101.1
	B_{3u}	261.1
	B_{3u}	52.6
$^1Mg_2Cl_2$ D_{2h}	A_g	317.1
	A_g	170.6
	B_{3g}	248.4
	B_{1u}	318.4
	B_{2u}	242.6
	B_{3u}	78.3
$^1Mg_2Cl_4$ D_{2h}	A_g	541.2
	A_g	281.8
	A_g	140.7
	B_{2g}	110.6
	B_{3g}	292.9
	B_{3g}	90.6
	B_{1u}	516.9
	B_{2u}	249.9
	B_{2u}	378.2
	B_{1u}	62.4
	B_{3u}	159.0
	B_{3u}	30.3

Mg_2F_2 has two possible absorptions that could be consistent with the observed chemiluminescence at 400 and 347 nm. The HOMO → LUMO transition is too far to the red. The HOMO is the doubly occupied (3s+3s) σ orbital for Mg_2^{2+} and the LUMO is the corresponding σ* orbital. The LUMO + 1 and LUMO + 3 are combinations of 3p orbitals on the Mg.

Table A6.4. Lowest lying intense transitions in Mg_2X_2 for X = F and Cl at the TPSS/aug-cc-pVTZ level

No.	eV	nm	f	Assignment
Mg_2F_2				
1	1.89	654.8	0.460	HOMO → LUMO
2	3.10	400.3	0.497	HOMO → LUMO+1
4	3.57	347.3	0.455	HOMO → LUMO+3
Mg_2Cl_2				
1	1.73	718.2	0.358	HOMO → LUMO
3	3.06	405.6	0.339	HOMO → LUMO+1
4	3.51	353.2	0.425	HOMO → LUMO+3

We also investigated the structure of Mg_2Cl_2. The ground state is the singlet again with the triplet 3.2 kcal/mol higher in energy at the CCSD(T) level. There are two possible transitions for Mg_2Cl_2 from the HOMO to the LUMO and LUMO+1 consistent with the chemiluminescence spectra.

Table A6.5. Geometry for Mg_2F C_{2v} $^2B_2$ at the CCSD(T) awD-DK and awT-DK levels.

	r(Mg-F)	<Mg-F-Mg
awD-DK	1.924	98.4
awT-DK	1.906	98.6

Table A6.6. Heats of formation using the FPD approach for Mg_2F C_{2v} optimized to at the CCSD(T) awT-DK level.

	$\Delta H_{f,0K}$	$\Delta H_{f,298K}$
Mg_2F C_{2v} $^2B_2$	-34.0	-34.2

Table A6.7. Electronic energy (Ee), zero-point energy (ZPE), thermal correction and Gibbs free energy correction for all the molecules at the B3LYP/aug-cc-pVTZ level.

B3LYP/aT	ZPE	Thermal correction at 298 K	Gibbs free energy correction	E electronic
Mg_2F C_{2v} $^2B_2$	0.002167	0.007249	-0.024932	-500.154095
Mg_2F $C_{\infty v}$ $^2\Sigma^+$	0.002195	0.007887	-0.025484	-500.141674
Mg_2F $D_{\infty h}$ $^2\Sigma_u^+$	0.001976	0.007687	-0.025930	-500.152936
Mg_2F_2 D_{2h}	0.004934	0.010956	-0.022271	-600.124010
Mg_2F_2 D_{2h} $^3B_{1u}$	0.005156	0.011042	-0.022813	-600.131344
Mg_2F_4 D_{2h}	0.009974	0.018743	-0.022143	-800.114415
Mg_3 D_{3h}	0.000615	0.006654	-0.028161	-600.297776
Mg_3 $D_{\infty h}$	0.000248	0.005205	-0.026566	-600.294651
Mg_2 $D_{\infty h}$	0.000103	0.004253	-0.023552	-400.196018
Mg_2^+ $D_{\infty h}$ $^2\Sigma_u^+$	0.000432	0.004314	-0.022350	-399.963087
Mg_3^+ $D_{\infty h}$ $^2\Sigma_g^+$	0.000948	0.007204	-0.028009	-600.088251
Mg_4 D_{4h}	0.000360	0.007565	-0.033604	-800.393121
Mg_4 T_d	0.001934	0.009661	-0.028037	-800.411940
Mg_3F **a** C_{2v} $^2A_1$	0.003027	0.010114	-0.027996	-700.258168
Mg_3F **b** C_{2v} $^2A_1$	0.002128	0.009770	-0.029918	-700.252081
Mg_3F **c** C_{2v} $^2B_2$	0.002225	0.009131	-0.032767	-700.251784
Mg_3F **d** C_{2v} $^2A_1$	0.002472	0.010231	-0.032211	-700.245176
Mg_2Cl C_{2v} $^2B_2$	0.001304	0.006838	-0.027439	-860.496004
Mg_2Cl $C_{\infty v}$ $^2\Sigma^+$	0.001586	0.007484	-0.027282	-860.502677
Mg_2Cl $D_{\infty h}$ $^2\Sigma_u^+$	0.001013	0.007214	-0.027373	-860.490375
Mg_2Cl_2 D_{2h}	0.003024	0.010043	-0.026986	-1320.812877
Mg_2Cl_2 D_{2h} $^3B_{1u}$	0.003150	0.010086	-0.027841	-1320.822769
Mg_2Cl_4 D_{2h}	0.006455	0.016799	-0.030503	-2241.525774

Table A6.8. Electronic energy (Hartrees) at the CCSD(T) level for diatomic Mg clusters using the 7-point fit with the awn-DK basis set (n = D, T, Q, 5) with the BSSE corrected.

Molecule	awD-DK	awT-DK	awQ-DK	aw5-DK	CBS
Mg_2 $D_{\infty h}$	-400.124013	-400.390063	-400.499104	-400.543666	-400.590419
Mg_2^+ $D_{\infty h}$ $^2\Sigma_u^+$	-399.890590	-400.156054	-400.264896	-400.309365	-400.356022

Table A6.9. Energy contribution to the total atomization energy in kcal/mol for diatomic Mg clusters using the 7-point fit with the awn-DK basis set (n = D, T, Q, 5) with the BSSE corrected.

Molecule	$\Delta E_{n=awD-DK}$	$\Delta E_{n= awT-DK}$	$\Delta E_{n= awQ-DK}$	$\Delta E_{n= aw5-DK}$	$\Delta E_{CBS-Q5-DK}$	ZPE	TC	$\sum D_{0,0K}$
Mg_2 $D_{\infty h}$	0.5	0.9	1.0	1.0	1.0	0.1	2.6	1.0
Mg_2^+ $D_{\infty h}$ $^2\Sigma_u^+$	-146.0	-146.0	-146.0	-146.0	-146.0	0.3	2.4	-146.4

Table A6.10. Electronic energy (Hartrees) at the CCSD(T) level for Mg clusters optimized to the awQ-DK basis set.

Molecule	awD-DK	awT-DK	awQ-DK	CBS
Mg_3 D_{3h}	-600.191401	-600.593223	-600.756128	-600.852364
Mg_3 $D_{\infty h}$	-600.187678	-600.587263	-600.750046	-600.846278
Mg_3^+ $D_{\infty h}$ $^2\Sigma_g^+$	-599.979761	-600.379279	-600.541211	-600.636870
Mg_4 T_d	-800.279327	-800.818470	-801.034886	-801.162548

Table A6.11. Energy contribution to the total atomization energy in kcal/mol for Mg clusters optimized to the awQ-DK basis set.

Molecule	$\Delta E_{n=awD-DK}$	$\Delta E_{n= awT-DK}$	$\Delta E_{n= awQ-DK}$	$\Delta E_{CBS-DTQ-DK}$	$\sum D_{0,0K}$
Mg_3 D_{3h}	4.1	6.4	6.2	5.9	5.4
Mg_3 $D_{\infty h}$	1.8	2.7	2.3	2.1	1.9
Mg_3^+ $^2D_{\infty h}$ $^2\Sigma_g^+$	-128.7	-127.8	-128.7	-129.3	-128.7
Mg_4 T_d	20.7	25.8	25.0	24.2	22.8

Table A6.12. Electronic energy (Hartrees) at the CCSD(T) level for Mg_2F, Mg_3F and Mg_2Cl optimized to the awT basis set.

Molecule	awD	awT	awQ	CBS	awT-DK
Mg_2F C_{2v} $^2B_2$	-499.257644	-499.604212	-499.736185	-499.813415	-500.303940
Mg_2F $C_{\infty v}$ $^2\Sigma^+$	-499.246173	-499.593286	-499.725325	-499.802580	-500.292978
Mg_2F $D_{\infty h}$ $^2\Sigma_u^+$	-499.247978	-499.595630	-499.726683	-499.803252	-500.295390
Mg_2F_2 D_{2h} $^1A_{1g}$	-599.038831	-599.465318	-599.621472	-599.712280	-600.251331
Mg_2F_2 D_{2h} $^3B_{1u}$	-599.032821	-599.459311	-599.615474	-599.706288	-600.245278
Mg_2F_4 D_{2h} $^1A_{1g}$ [a]	-798.600281	-799.189287	-799.393604	-799.511340	-800.148214
Mg_3F **a** C_{2v} $^2A_1$	-699.022974	-699.503837	-699.689533	-699.798437	-700.510139
Mg_3F **b** C_{2v} $^2A_1$	-699.016375	-699.495712	-699.680341	-699.788577	-700.502149
Mg_3F **a** C_{2v} $^2B_2$	-699.015194	-699.494712	-699.680592	-699.789669	
Mg_3F **c** C_{2v} $^2B_2$	-699.015035	-699.493735	-699.679214	-699.788046	
Mg_3F **d** C_{2v} $^2A_1$	-699.007412	-699.488609	-699.674469	-699.783473	
Mg_2Cl C_{2v} $^2B_2$	-859.400225	-859.860016	-860.038311	-860.142942	-861.883556
Mg_2Cl $C_{\infty v}$ $^2\Sigma^+$	-859.405264	-859.865851	-860.044106	-860.148682	-861.889237
Mg_2Cl $D_{\infty h}$ $^2\Sigma_u^+$	-859.382970	-859.842776	-860.020903	-860.125420	-861.866553
Mg_2Cl_2 D_{2h} $^1A_{1g}$	-1319.325954	-1319.979607	-1320.228478	-1320.374112	-1323.413129
Mg_2Cl_2 D_{2h} $^3B_{1u}$	-1319.320703	-1319.974560	-1320.223515	-1320.369198	-1323.408021
Mg_2Cl_4 D_{2h} $^1A_{1g}$ [a]	-2239.204631	-2240.248039	-2240.636834	-2240.863572	-2246.501702

[a] Mg_2F_4 and Mg_2Cl_4 were optimized at the CCSD(T)/awD level.

Table A6.13. Electronic energies for Mg atom with BSSE corrected for Mg clusters.

	awd-dk	awt-dk	awq-dk	aw5-dk	CBS[a]
Mg_2	-200.0617825	-200.1945245	-200.248815	-200.2710437	-200.294365
Mg for Mg_2^+	-200.062151	-200.194773	-200.248876	-200.2710685	-200.294352
Mg^+ for Mg_2^+	-199.7835123	-199.914593	-199.968179	-199.9901976	-200.013299
Mg_3 D_{3h}	-200.062219	-200.194941	-200.248920		-200.280823
Mg_4 T_d	-200.063096	-200.195523	-200.249045		-200.280649
Mg no BSSE	-200.061596	-200.194329	-200.248771	-200.2710287	-200.294381 (Q5) -200.280987 (DTQ)

[a] CBS(Q,5) for diatomics, and CBS(DTQ) for trimer and tetramer.

Table A6.14. FPD energy contributions to the total atomization energy in kcal/mol for Mg_2F, Mg_3F and Mg_2Cl optimized to the awT basis set.

Molecule	$\Delta E_{n=awD}$	$\Delta E_{n=awT}$	$\Delta E_{n=awQ}$	$\Delta E_{CBS-DTQ}$	ΔE_{SR}	ΔE_{ZPE}	ΔE_{SO}	$\Sigma D_{0,0K}$	ΔE_{TC}
Mg_2F C_{2v} $^2B_2$	118.3	122.1	123.6	124.5	-0.6	-1.5	-0.4	122.1	3.2
Mg_2F $C_{\infty v}$ $^2\Sigma^+$	111.1	115.3	116.8	117.7	-0.6	-1.5	-0.4	115.2	3.6
Mg_2F $D_{\infty h}$ $^2\Sigma_u^+$	112.2	116.7	117.7	118.2	-0.6	-1.0	-0.4	116.2	3.6
Mg_2F_2 D_{2h} $^1A_{1g}$	258.2	264.3	267.6	269.6	-1.1	-3.2	-0.8	264.6	3.8
Mg_2F_2 D_{2h} $^3B_{1u}$	254.4	260.5	263.8	265.8	-1.1	-3.3	-0.8	260.6	3.7
Mg_2F_4 D_{2h} $^1A_{1g}$ [a]	537.4	549.7	556.4	560.5	-1.8	-6.3	-1.6	550.9	5.5
Mg_3F **a** C_{2v} $^2A_1$	124.4	129.7	131.0	131.7	-0.8	-2.0	-0.4	128.5	4.4
Mg_3F **b** C_{2v} $^2A_1$	120.3	124.6	125.2	125.5	-0.7	-1.5	-0.4	123.0	4.8
Mg_3F **a** C_{2v} $^2B_2$	119.6	124.0	125.4	126.2					
Mg_3F **c** C_{2v} $^2B_2$	119.5	123.4	124.5	125.2					
Mg_3F **d** C_{2v} $^2A_1$	114.7	120.2	121.6	122.3					
Mg_2Cl C_{2v} $^2B_2$	77.0	81.8	83.8	85.0	-0.6	-0.9	-0.8	82.6	3.5
Mg_2Cl $C_{\infty v}$ $^2\Sigma^+$	80.2	85.5	87.4	88.6	-0.6	-1.1	-0.8	86.0	3.7
Mg_2Cl $D_{\infty h}$ $^2\Sigma_u^+$	66.2	71.0	72.9	74.0	-0.4	0.4	-0.8	73.1	3.9
Mg_2Cl_2 D_{2h} $^1A_{1g}$	177.0	185.4	189.6	192.2	-1.1	-2.0	-1.7	187.5	4.4
Mg_2Cl_2 D_{2h} $^3B_{1u}$	173.7	182.2	186.5	189.1	-1.1	-2.0	-1.7	184.3	4.4
Mg_2Cl_4 D_{2h} $^1A_{1g}$ [a]	393.9	410.9	418.8	423.6	-1.9	-4.1	-3.4	414.2	6.5

[a] Mg_2F_4 and Mg_2Cl_4 were optimized at the CCSD(T)/awD level.

Table A6.15. T_1 values at the CCSD(T) level with the awQ(-DK) basis set.

	awQ(-DK)[a]
Mg_2	0.011872
Mg_3 D_{3h}	0.011072
Mg_3 $D_{\infty h}$	0.010878
Mg_4 T_d	0.010858
Mg_2F C_{2v} $^2B_2$	0.013487
Mg_2F $D_{\infty h}$ $^2\Sigma_u^+$	0.014483
Mg_2F $C_{\infty v}$ $^2\Sigma^+$	0.020057
Mg_3F **a** C_{2v} $^2A_1$	0.024234
Mg_3F **a** $^2B_2$	0.012432
Mg_3F **b** C_{2v} $^2A_1$	0.022677
Mg_3F **c** $^2B_2$	0.013164
Mg_3F **d** $^2A_1$	0.011924
Mg_2Cl C_{2v} $^2B_2$	0.010514
Mg_2Cl $D_{\infty h}$ $^2\Sigma_u^+$	0.012771
Mg_2Cl $C_{\infty v}$ $^2\Sigma^+$	0.016655

[a] the awQ-DK basis sets were used for Mg clusters.

Table A6.16. Lowest lying intense transitions in Mg_2F at the CAM-B3LYP/aug-cc-pVTZ level and the B3LYP/aug-cc-pVTZ level.

No.	sym	eV	nm/cm^{-1}	f	assign
CAM-B3LYP					
4	B_2	2.54	488.0	0.292	SOMO → LUMO
6	B_2	3.71	334.6	0.413	SOMO → LUMO + 2 (+3 TPSS)
8	B_1	3.93	315.3	0.538	SOMO → LUMO + 4 (+2 TPSS) DOMO1 → LUMO+1
9	A_1	4.11	301.9	0.493	DOMO1 → LUMO
10	B_1	4.16	298.0	0.195	DOMO1 → LUMO+1
B3LYP					
3	B_2	2.45	506.5	0.282	SOMO → LUMO
8	B_2	3.53	351.6	0.412	SOMO → LUMO+3
10	B_1	3.97	312.2	0.669	DOMO1 → LUMO+1, SOMO → LUMO+2
11	A_1	3.98	311.8	0.116	highly mixed
12	A_1	4.03	307.6	0.313	DOMO1 → LUMO SOMO → LUMO+4(+2 TPSS)

Table A6.17. Lowest lying intense transitions in Mg_2^+ at the TPSS/aug-cc-pVTZ level, the CAM-B3LYP/aug-cc-pVTZ level and the B3LYP/aug-cc-pVTZ level.

No.	sym	eV	nm^{-1}	f	assign
TPSS					
6	Σ_u	3.64	341.1	0.883	SOMO → LUMO DOMO1 → SOMO
CAM-B3LYP					
6	Σ_u	3.61	343.0	0.922	SOMO → LUMO DOMO1 → SOMO
B3LYP					
6	Σ_u	3.62	342.4	0.924	SOMO → LUMO DOMO1 → SOMO

Table A6.18. Lowest lying intense transitions in Mg_2Cl at the CAM-B3LYP/aug-cc-pVTZ level and the B3LYP/aug-cc-pVTZ level.

No.	sym	eV	nm/cm^{-1}	f	assign
CAM-B3LYP					
6	Σ_g	3.45	359.6	0.582	SOMO → LUMO+2
15	?	4.87	254.7	0.375	DOMO1 → LUMO
B3LYP					
6	Σ_g	3.33	371.8	0.521	SOMO → LUMO+2
12	Σ_g	4.23	293.3	0.364	SOMO → LUMO+5 SOMO → LUMO+6

Table A6.19. Calculated r(Mg-Mg) in Å for Mg clusters at the B3LYP level and the CCSD(T) level.

Molecule	symmetry	r (Å)			
		B3LYP aT	CCSD(T) awD-DK	CCSD(T) awT-DK	CCSD(T) awQ-DK
Mg_2 [a]	$D_{\infty h}$	3.936	4.452	4.070	4.002
Mg_2^+ [a]	$D_{\infty h}$	3.064	3.052	3.023	3.016
Mg_3	D_{3h}	3.476	3.423	3.349	3.350
Mg_3	$D_{\infty h}$	3.815	4.122	3.840	3.840
Mg_3^+	$D_{\infty h}$	3.093	3.066	3.040	3.047
Mg_4	T_d	3.171	3.100	3.064	3.066

[a] At the CCSD(T) level, the diatomic Mg molecules were optimized by using 7-point fit with the BSSE corrected.

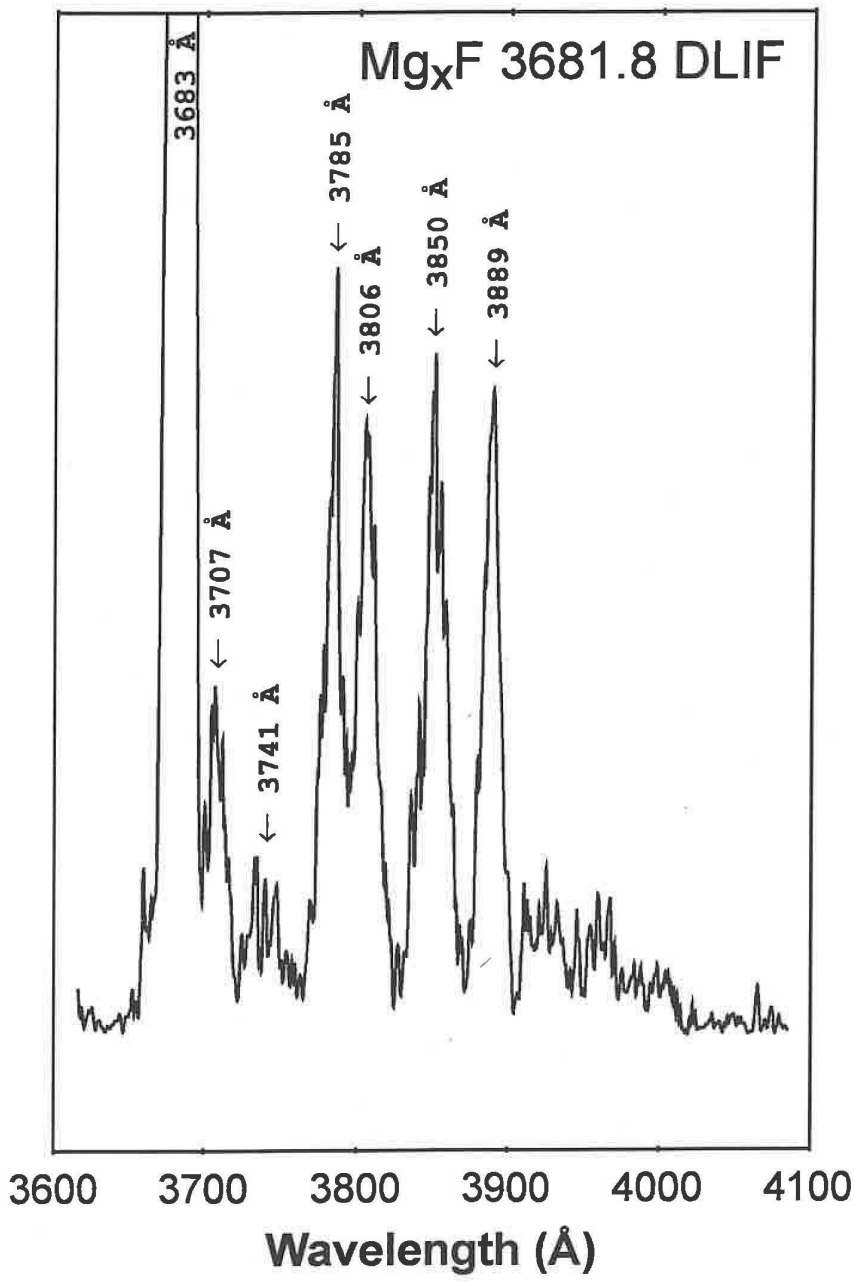
MgxF 3681.8 DLIF
3683 Å
3707 Å
3741 Å
3785 Å
3806 Å
3850 Å
3889 Å
3600
3700
3800
3900
4000
4100
Wavelength (Å)

Figure A6.1a

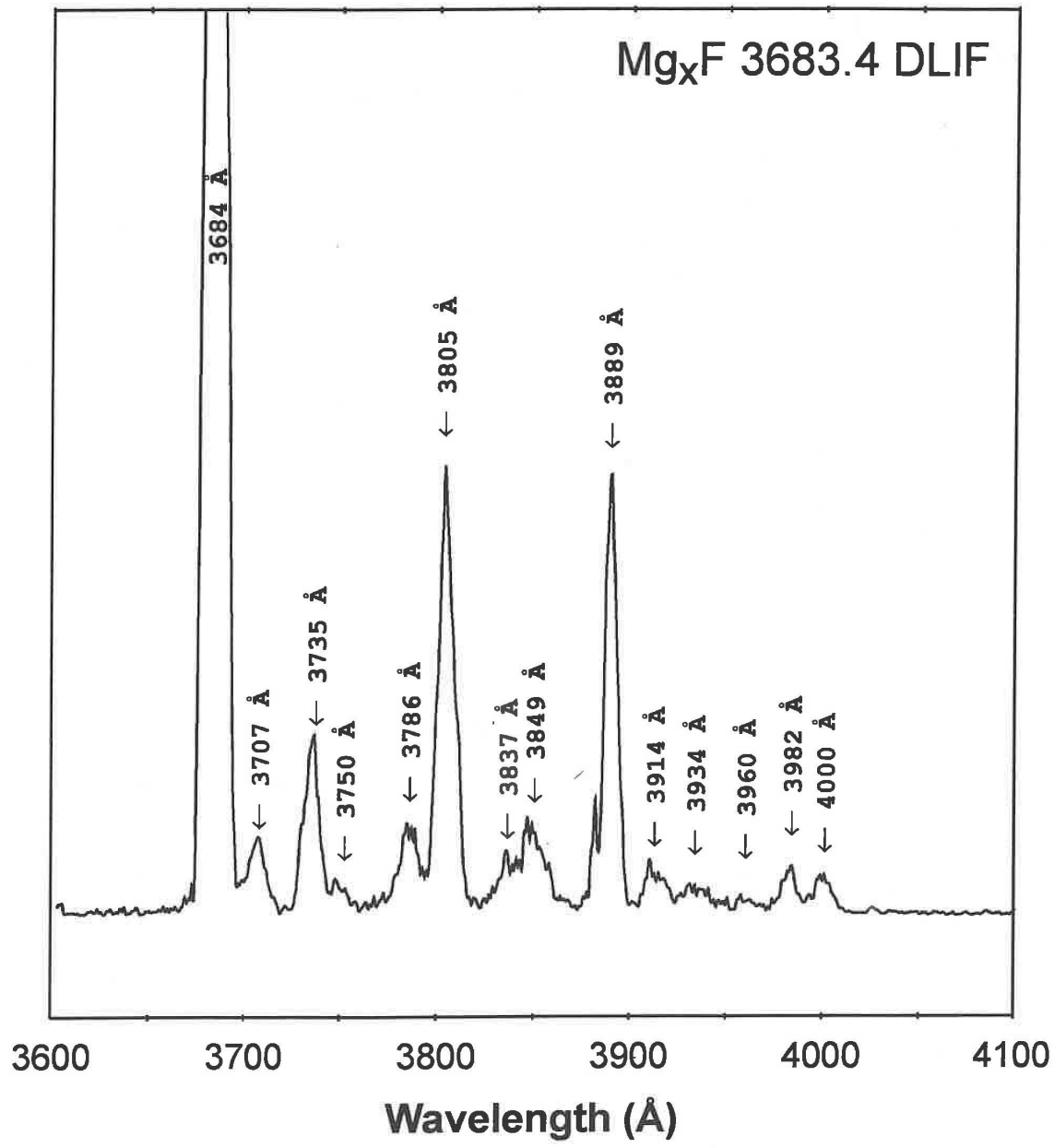
MgxF 3683.4 DLIF
3684 Å
3707 Å
3735 Å
3750 Å
3786 Å
3805 Å
3837 Å
3849 Å
3889 Å
3914 Å
3934 Å
3960 Å
3982 Å
4000 Å
3600
3700
3800
3900
4000
4100
Wavelength (Å)

Figure A6.1b

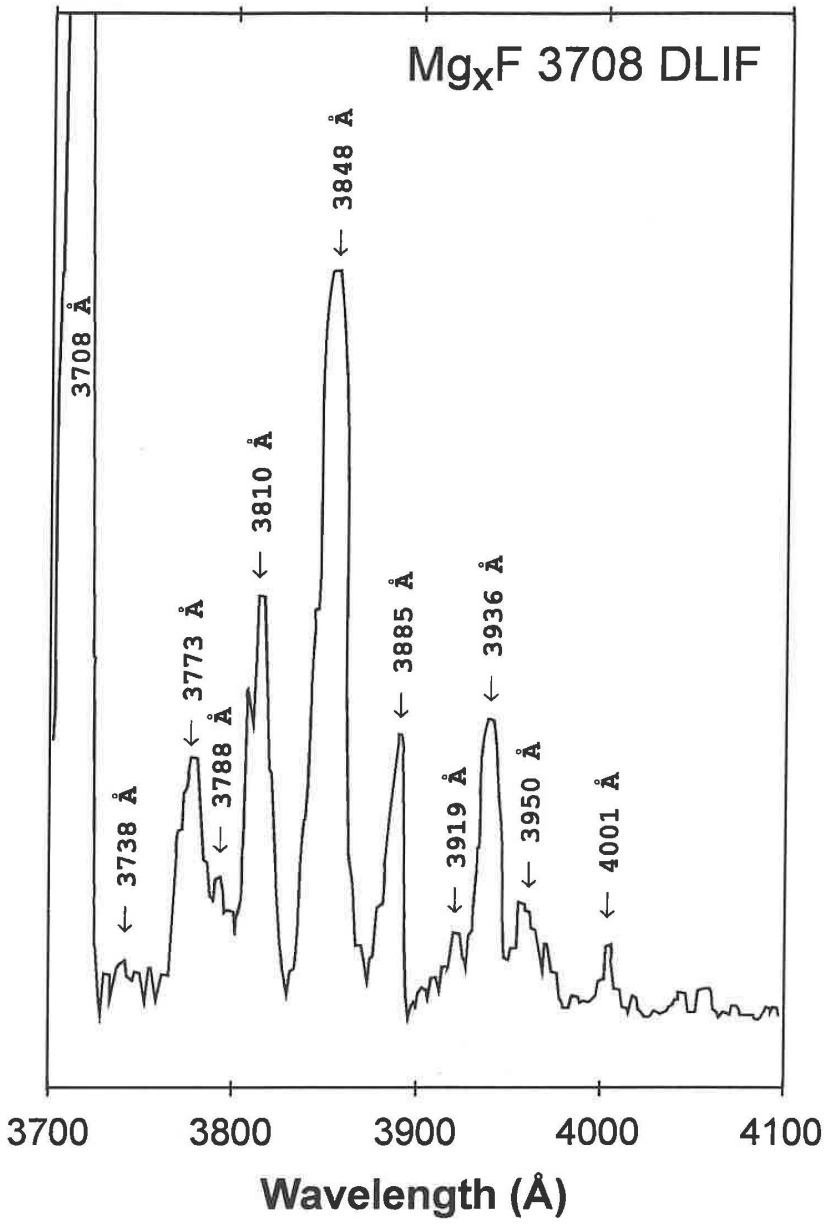
MgxF 3708 DLIF
3708 Å
3738 Å
3773 Å
3788 Å
3810 Å
3848 Å
3885 Å
3919 Å
3936 Å
3950 Å
4001 Å
3700
3800
3900
4000
4100
Wavelength (Å)

Figure A6.1c

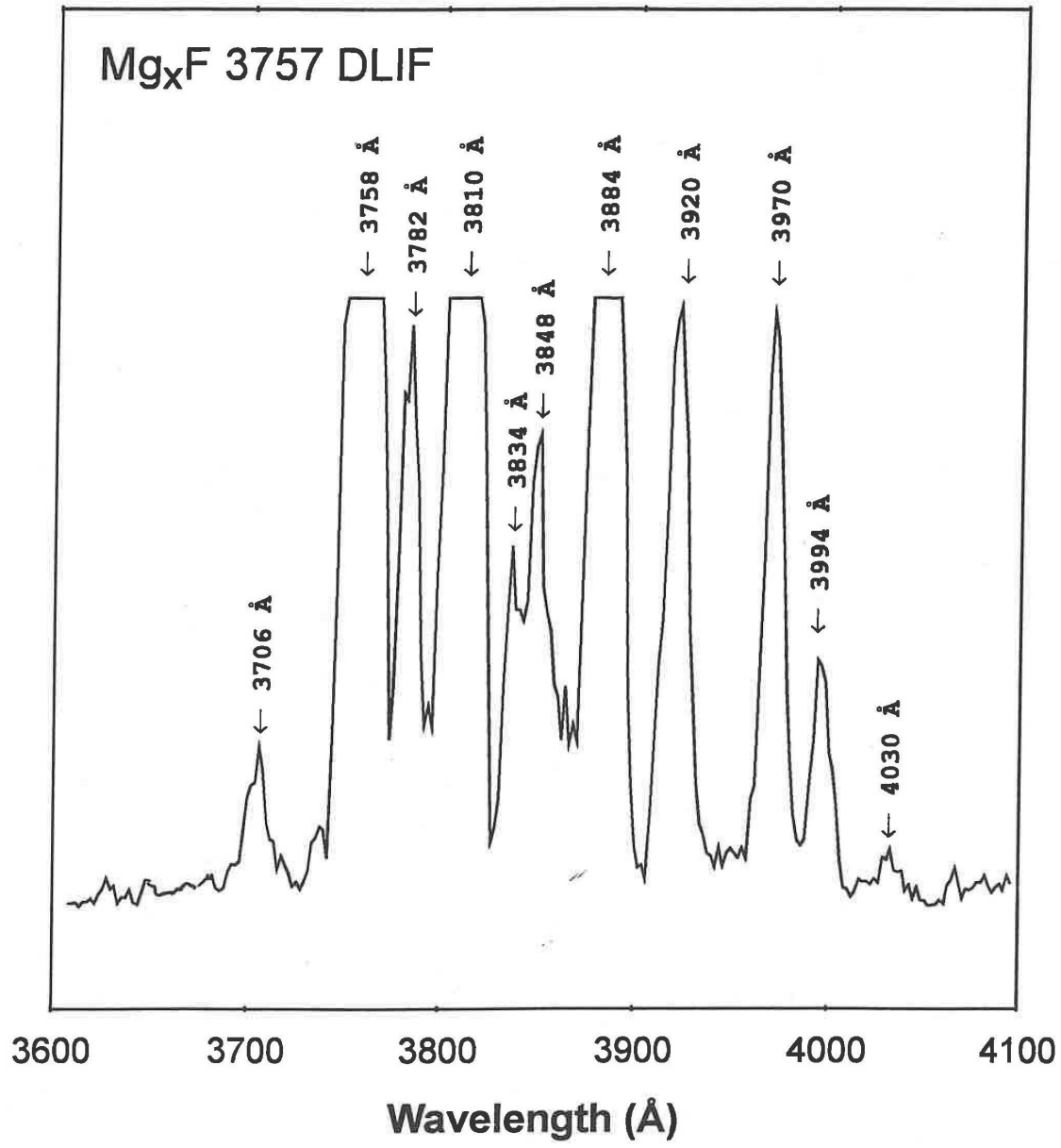
MgxF 3757 DLIF
3706 Å
3758 Å
3782 Å
3810 Å
3834 Å
3848 Å
3884 Å
3920 Å
3970 Å
3994 Å
4030 Å
3600
3700
3800
3900
4000
4100
Wavelength (Å)

Figure A6.1d

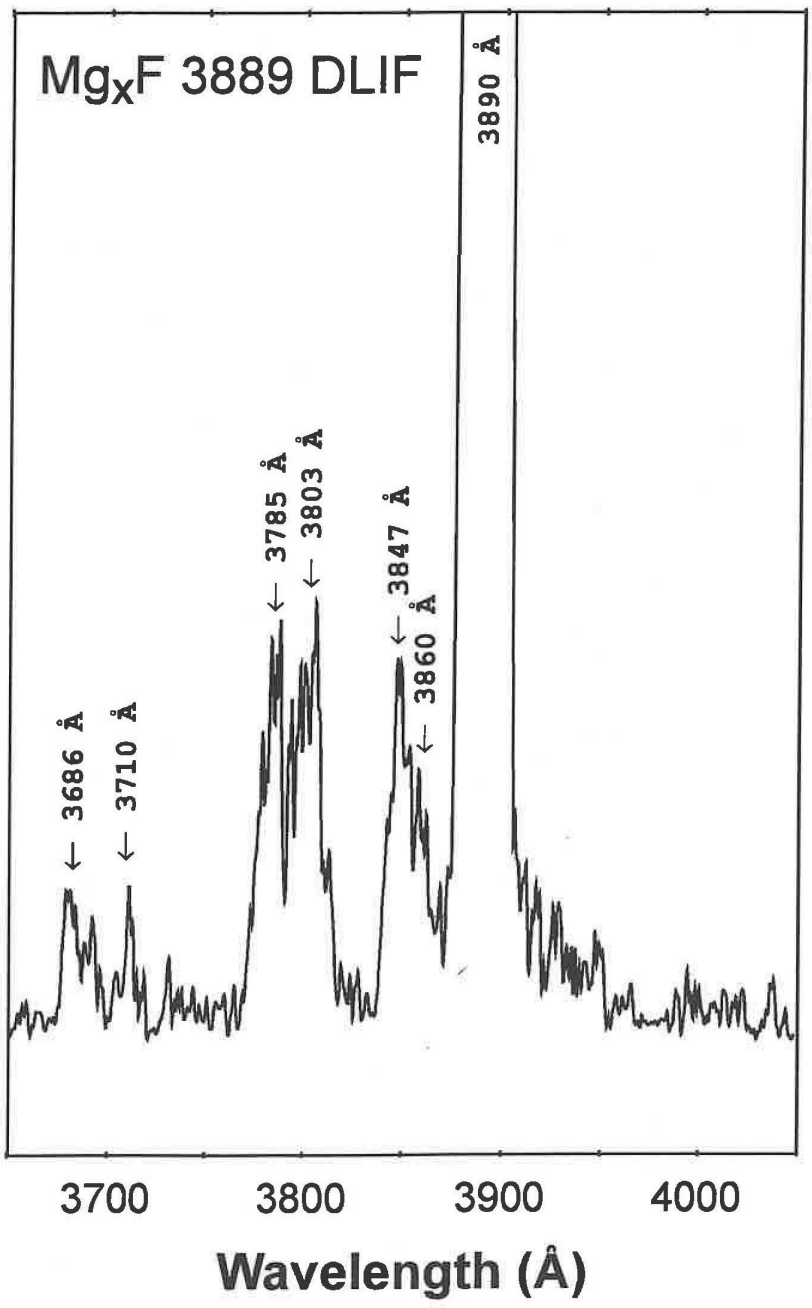

Figure A6.1e

Figure A6.1. Exemplary dispersed laser induced fluorescence spectra pumped at wavelengths (a) 3681.8Å, (b) 3683.4Å, (c) 3708Å, (d) 3757Å, and (e) 3889Å, as indicated in Figure 6.7 (text), grouped in some cases with ground and excited state bending coupled with Mg_2^+ stretching mode.

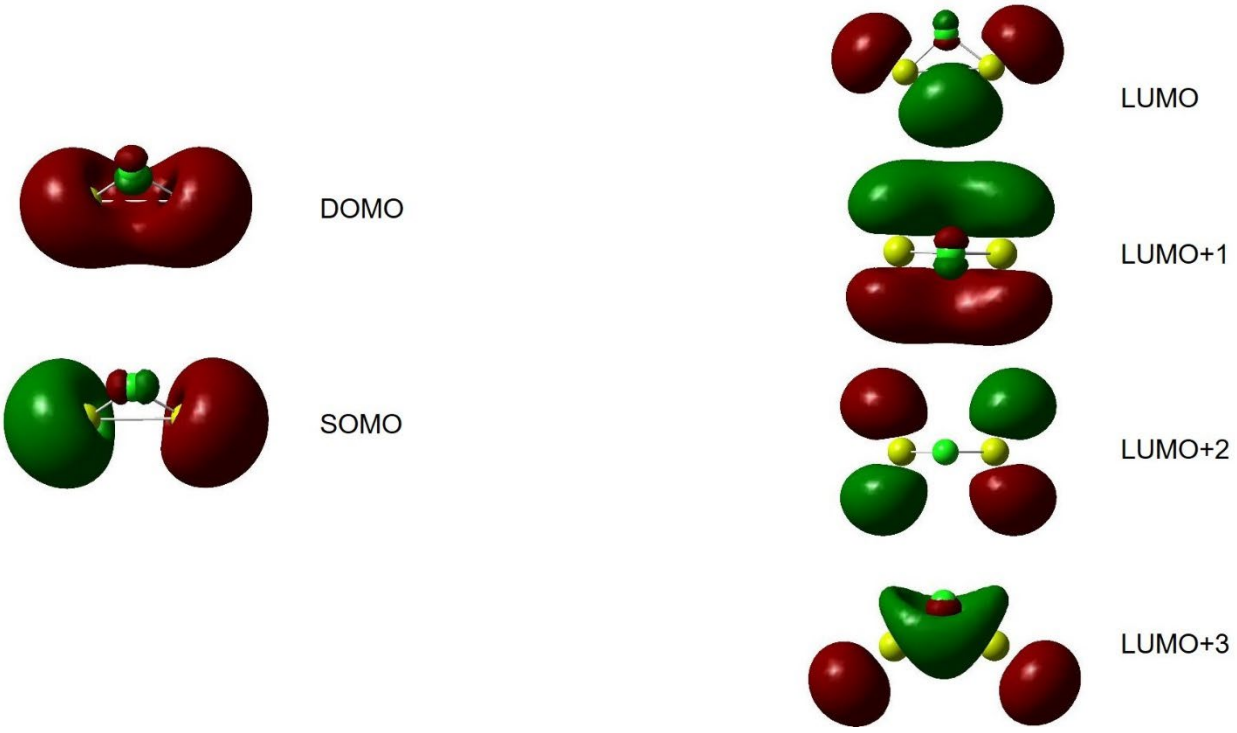

Figure A6.2. DOMO, SOMO and different LUMO in Mg_2F (C_{2v}) calculated at the TPSS/aug-cc-pVTZ level (isovalue = 0.03).

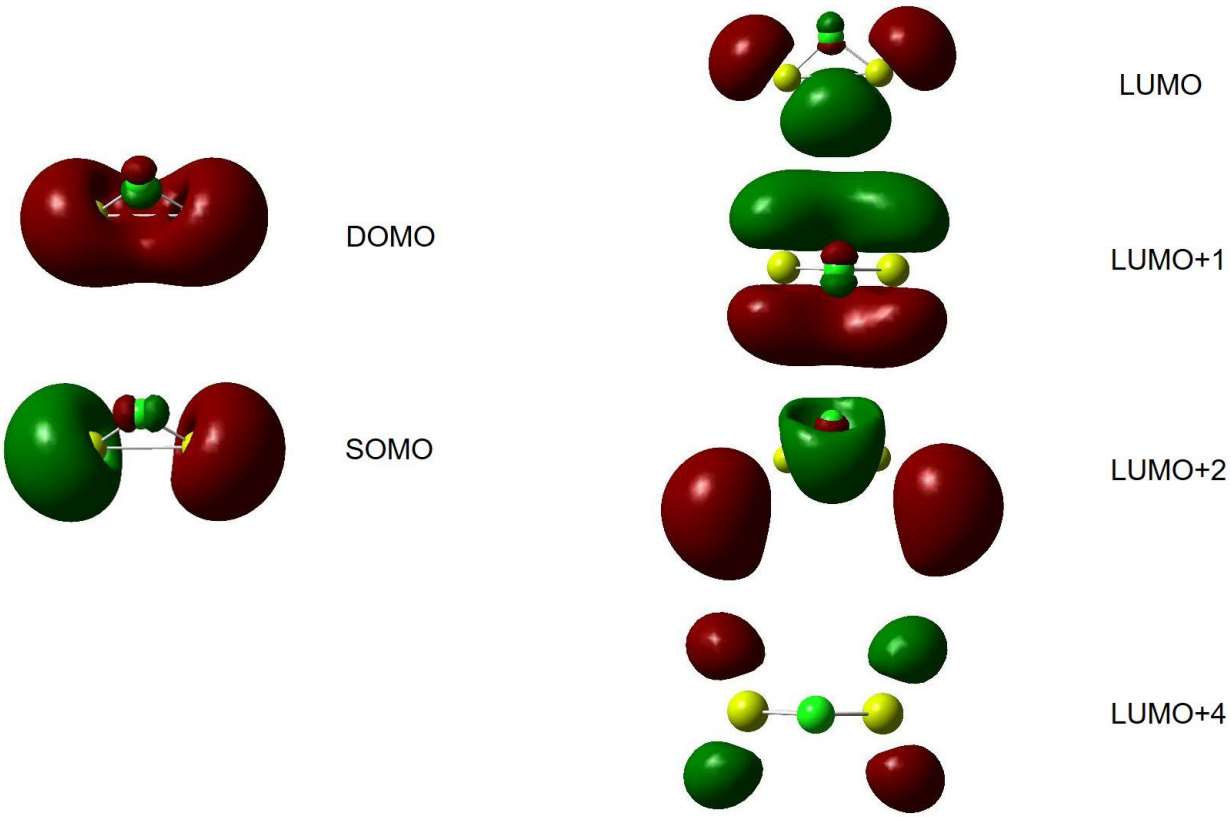

Figure A6.3. DOMO, SOMO and different LUMO in Mg_2F (C_{2v}) calculated at the CAM-B3LYP/aug-cc-pVTZ level (isovalue = 0.03, except 0.015 for LUMO+2).

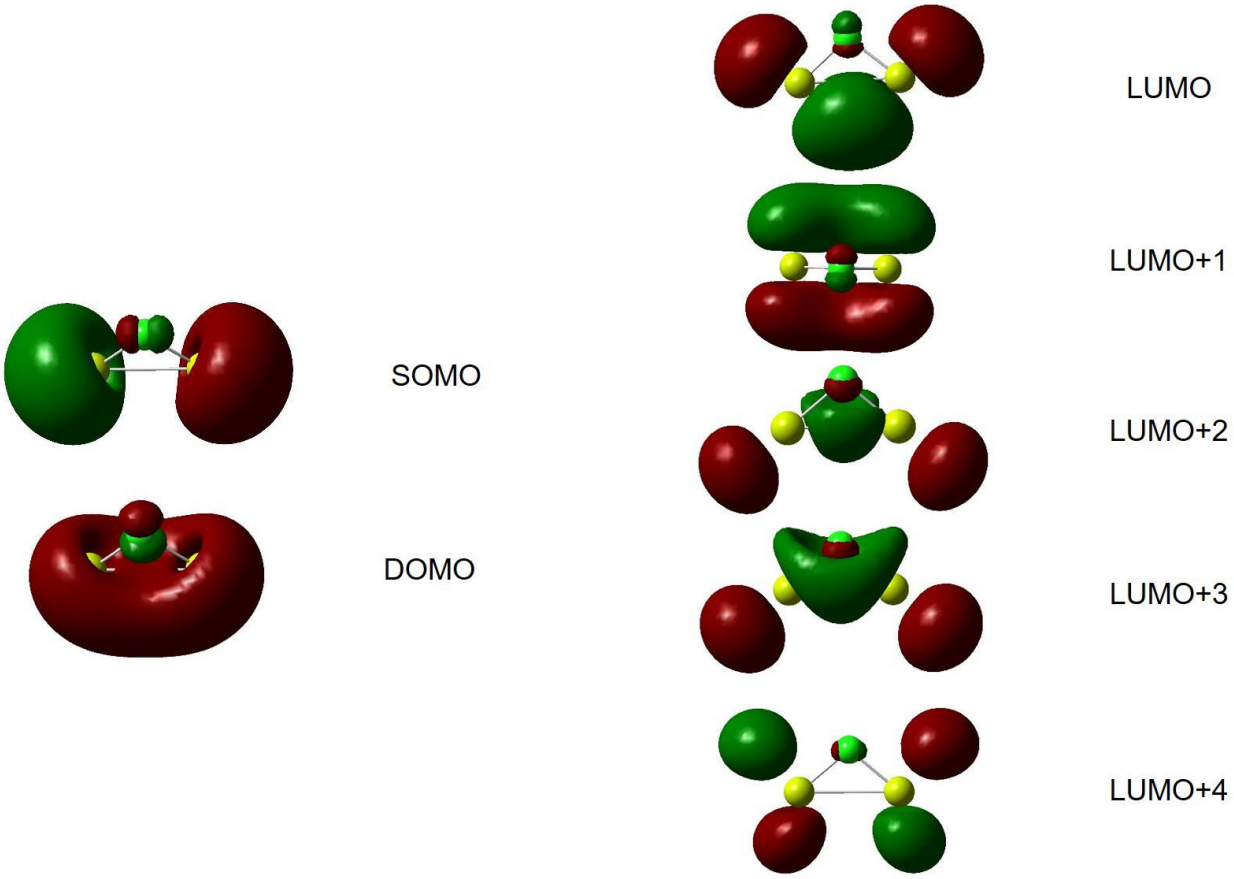

Figure A6.4. DOMO, SOMO and different LUMO in Mg_2F (C_{2v}) calculated at the B3LYP/aug-cc-pVTZ level (isovalue = 0.03).

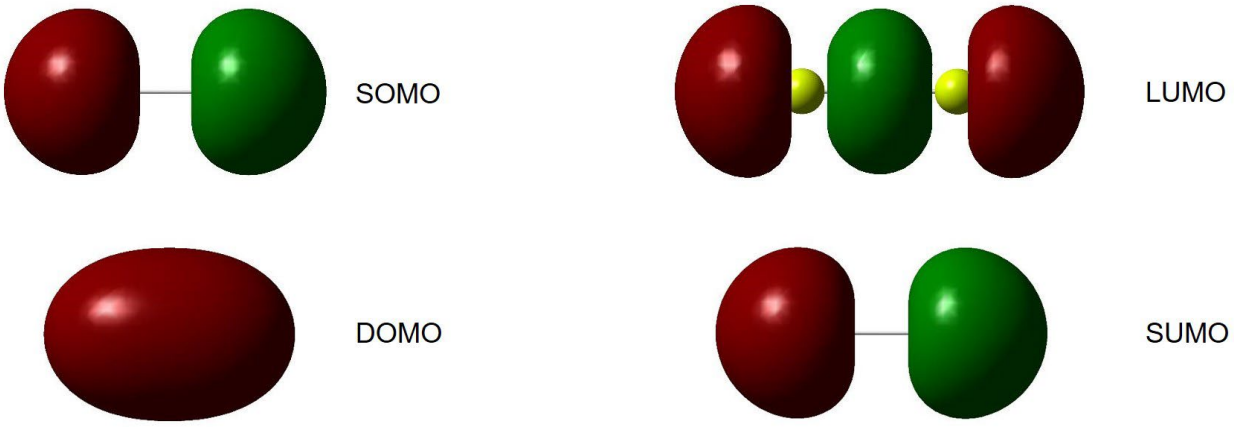

Figure A6.5. DOMO, SOMO and different LUMO in Mg_2^+ calculated at the TPSS/aug-cc-pVTZ level (isovalue = 0.03).

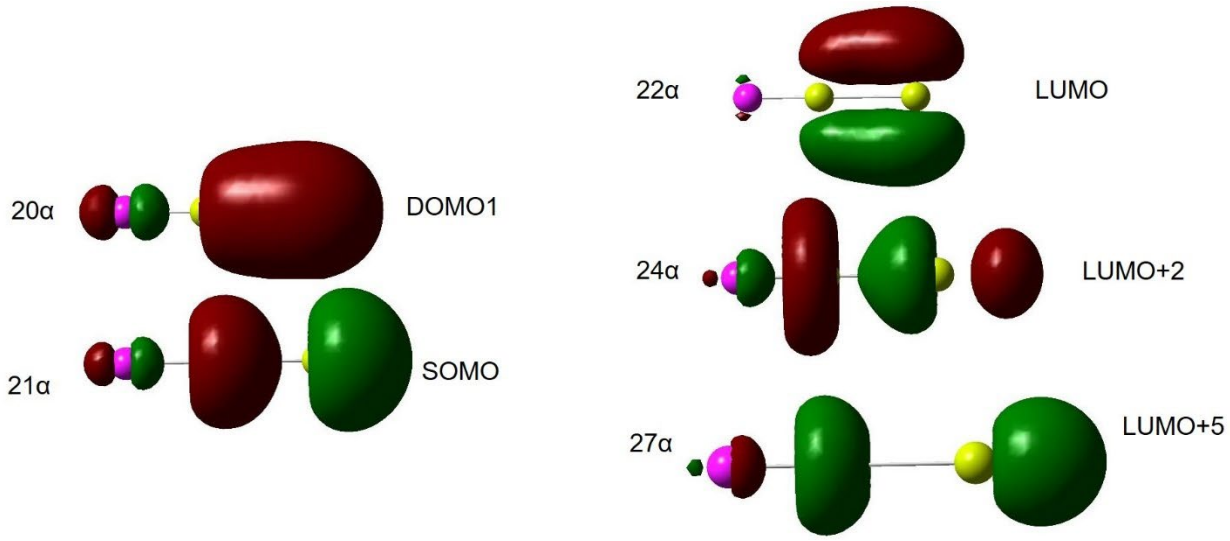

Figure A6.6. DOMO, SOMO and different LUMO in Mg_2Cl ($C_{\infty v}$) calculated at the TPSS/aug-cc-pVTZ level (isovalue = 0.03, except 0.02 for LUMO+5).

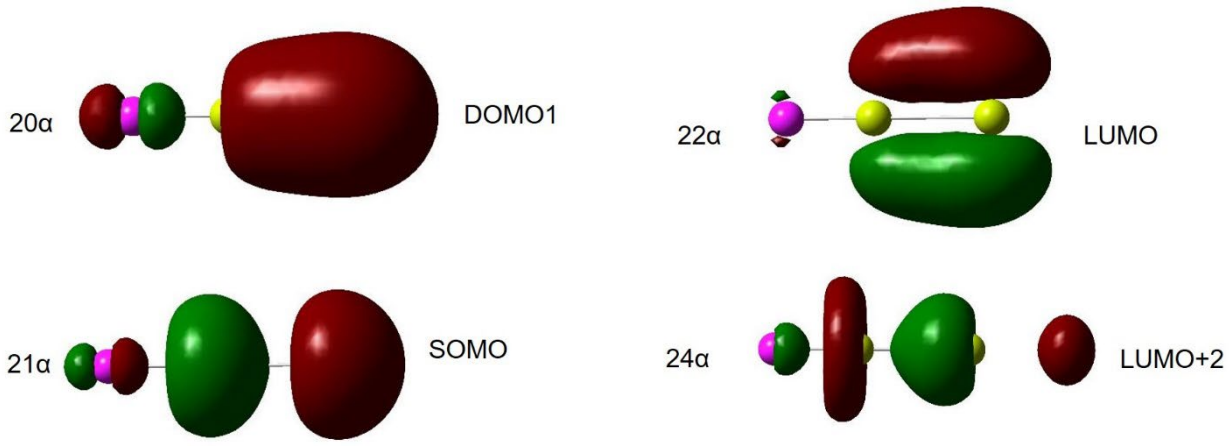

Figure A6.7. DOMO, SOMO and different LUMO in Mg_2Cl ($C_{\infty v}$) calculated at the CAM-B3LYP/aug-cc-pVTZ level (isovalue = 0.03, except 0.02 for LUMO+2).

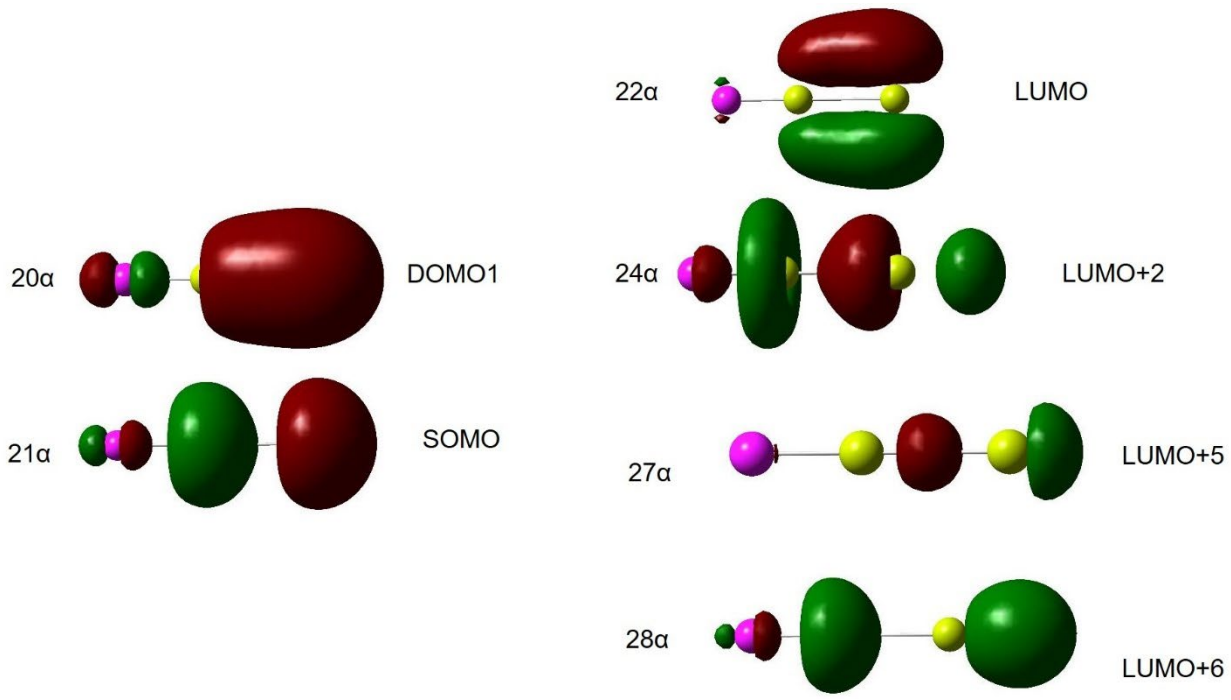

Figure A6.8. DOMO, SOMO and different LUMO in Mg_2Cl ($C_{\infty v}$) at the B3LYP/aug-cc-pVTZ level (isovalue = 0.03).

CHAPTER 7

CONCLUSIONS

The combustion of fossil fuels produces CO_2 which contributes to global warming. Capturing existing CO_2 either at the source or from air and exploiting alternative green energy technologies to replace the use of fossil fuel are both important to reducing CO_2 emissions. High level computational chemistry calculations have been performed to aid in the development of technologies for CO_2 capture and sequestration in the subsurface and the development of new catalysts focusing on biofuel conversion. In this dissertation, two chapters describe predictions of the thermodynamics of metal carbonates to develop approaches for predicting the properties of carbonate minerals. Two chapters are associated with the reactions of group IV transition metal oxides with CO_2 and for biofuel conversion. Chapter 6 provides the best energetics available for the formation of small Mg clusters with halogen atoms to interpret the observed chemiluminescence from reactions of magnesium clusters with halogen atoms.

Metal carbonates are important in a variety of geological processes, including providing paleoclimate information, biomineralization, and mineralization/dissolution processes relevant to CO_2 capture and sequestration in subsurface environments. In Chapter 2, the heats of formation of the carbonate, bicarbonate and bicarbonate/hydroxide metal complexes, including hydrates, of Mg^{2+}, Ca^{2+}, Fe^{2+}, and Cd^{2+}, and the oxides, dichlorides, and dihydroxides are predicted from atomization energies using correlated molecular orbital theory at the CCSD(T) level extrapolated to the complete basis set limit following the Feller-Peterson-Dixon (FPD) approach.

Using the calculated gas phase values and the available experimental solid state values, we predicted the cohesive energies of selective minerals. The gas phase decomposition energies into MO, CO_2 and H_2O follow the order Mg ~ Ca > Cd ~ Fe, and correlate with the hardness of the metal +2 ions. Gas phase hydration energies show that the order is Mg > Fe > Ca ~ Cd. There are a number of bulk hydrated Mg and Ca complexes that occur as minerals but there are few if any for Fe and Cd, suggesting that a number of factors are important in determining the stability of the bulk mineral hydrates. The FPD heats of formation were used to benchmark a range of density functional theory exchange-correlation functionals, including those commonly used in solid state mineral calculations. None of the functionals provided chemical accuracy agreement (± 1 kcal/mol) with the FPD results. The best agreement to the FPD results is predicted for ωB97X and ωB97X-D functionals with average unsigned errors of 10 kcal/mol. The worst functionals are PW91, BP86, and PBE with average unsigned errors of 32 to 36 kcal/mol.

In Chapter 3, the gas phase heats of formation of ground state MCO_3, $M(HCO_3)_2$ and $M(HCO_3)(OH)$, where M = Mn, Co, Ni, Cu and Zn, have been predicted using correlated molecular orbital theory at the CCSD(T) level extrapolated to the complete basis set limit using the FPD approach. Cohesive energies of the carbonates were predicted based on the calculated gas phase and experimental solid heats of formation. Coulombic dissociation energies (CDE) between metal cations and anions show a near linear correlation with Shannon metal cation atomic radii, yet no correlation is found with the hardness of these cations. The total reaction dissociation energies (TRDE) of transition metals are higher than their CDE in contrast to those for Mg and Ca based on our prior work. In addition to differences in the energies needed to prepare the transition metal dications, electron donation from the ligands to the 3d orbitals of open-shell transition metal dications from lone pairs of adjacent O atoms also plays a role. No

electron donation from the ligands to the fully occupied 3d orbitals of Zn and Cd were found. Decomposition energies for generating MO, CO_2 and/or H_2O were calculated. Gas phase metal exchange energies only partially correlate with the reduction potential ordering for M(s) → M^{2+}(aq). The FPD heats of formation were used to benchmark a range of density functional theory exchange−correlation functionals, including those commonly used in solid-state mineral calculations. None of the functionals provided chemical accuracy agreement (±1 kcal/mol) with the FPD results. The best agreement with the FPD results is predicted for the τ-HCTH functional with an average unsigned error of 8.3 kcal/mol.

The combustion of fossil fuels is leading to unacceptable levels of CO_2 in the atmosphere leading to global warming. As such, there is significant interest in the capture and conversion of CO_2 using a variety of species including metal oxides. Prior work[41,42] had incorrectly predicted the structures of CO_2 binding to TiO_2 nanoclusters. In Chapter 4, the chemisorption addition of CO_2 to M_3O_6 and $M_3O_6^-$ for M = Ti, Zr and Hf was examined using couple cluster CCSD(T) theory using density functional theory B3LYP geometries. For neutral $M_3O_6CO_2$, a bridge chemisorbed tridentate carbonate cluster is the lowest energy for Ti and Zr, and a terminal chemisorbed bidentate carbonate is the lowest energy for Hf. For anionic $M_3O_6CO_2^-$, the lowest energy structure is a terminal chemisorbed bidentate carbonate for all three metals. The use of correlation-consistent weighted core basis sets for the CCSD(T) calculations is shown to be necessary to obtain the correct energy ordering for the isomers. Only for $Ti_3O_6CO_2^-$, a center tridentate carbonate cluster is a low energy isomer. The electron affinities of $M_3O_6CO_2$ are ~ 0.2 eV larger than for M_3O_6. The CO_2 chemisorption binding energies increase slightly for $M_3O_6^-$ as compared to M_3O_6.

In Chapter 5, dehydration and dehydrogenation of one ethanol molecule on $(TiO_2)_n$ (n = 2 - 4) nanoclusters were studied using the correlated molecular orbital theory at the CCSD(T)/aug-cc-pVDZ(-PP(Ti)) level at density functional theory B3LYP/DZVP2 optimized geometries. Physisorption and chemisorption of ethanol at the bridge Ti on the trimer $(TiO_2)_3$ and tetramer $(TiO_2)_4$ is thermodynamically preferred over that at the terminal Ti=O. Two possible lowest energy pathways of dehydration were predicted for the dimer $(TiO_2)_2$ and trimer $(TiO_2)_3$ where the β hydrogen on ethanol transfers to the adjacent terminal oxygen, or to the adjacent bidentate oxygen. Only the latter pathway was predicted to be the lowest energy pathway on the tetramer $(TiO_2)_4$. Removal of the ethylene molecule from the $(TiO_2)_nOH_2$-C_2H_4 complex for n = 2 to 4 at 0 K requires 2 to 7 kcal/mol. For dehydrogenation, the pathway of transferring the α hydrogen to the adjacent Ti atom results in the lowest energy path by a proton coupled electron transfer (PCET) process. Removal of the acetaldehyde molecule requires 14 to 26 kcal/mol from the $(TiO_2)_nH_2$-C_2H_4O complex. Loss of H_2 from the $(TiO_2)_nH_2$ complex requires 5 to 8 kcal/mol. Dehydration and dehydrogenation of one ethanol occur below reactant asymptote for $(TiO_2)_n$, n = 2 to 4, whereas for $(WO_3)_3$ and $(MoO_3)_3$ two ethanols are required. Dehydration of one ethanol is thermodynamically preferred over dehydrogenation on $(TiO_2)_n$, n = 2 to 4. Physisorption and chemisorption of one ethanol molecule on $(TiO_2)_n$ (n = 2-4) nanoclusters are predicted to be more negative than physisorption and chemisorption of one methanol molecule on surface of rutile TiO_2(110). There is an approximate linear correlation of metal Lewis acidity with physisorption of one ethanol. A quadratic correlation is predicted between the chemisorption barrier of one ethanol and corresponding proton affinity of the oxygen to which it is being transferred. There are linear correlations between basicity of the oxygen site and the acidity of the OH group versus the energy to remove C_2H_4 from that site.

Metal cluster oxidation reactions can exhibit novel reaction dynamics including branching. A near ultraviolet transition of Mg_2F has been observed in emission from the reaction between magnesium clusters, most likely Mg_3, and fluorine atoms. Since there is little evidence for upper state internal excitation, the spectrum is assigned assuming the upper state is quenched to its lowest vibrational levels as shown in Chapter 6. Two of possibly three ground state vibrational frequencies, $\upsilon_1 = 516 \pm 10$ cm^{-1}, and $\upsilon_2 = 104 \pm 10$ cm^{-1} have been established. Dispersed laser induced fluorescence studies extrapolating on the observed chemiluminescence indicate an excited state symmetric stretch frequency of order 370 ± 30 cm^{-1}. Electronic structure calculations at the CCSD(T)/CBS level predict that the ground state of Mg_2F has C_{2v} symmetry and can be described as an $Mg_2^+F^-$ ion pair with two Mg-F bonds. Like the MgF A-X transition that is largely a transition between Mg orbitals, the observed transition in Mg_2F is largely between orbitals on the magnesium dimer ion. The asymmetric $C_{\infty v}$ $Mg_2^+F^-$ complex is also a minimum and is predicted to be 6.7 kcal/mol higher in energy. Calculated structures for the Mg_2Cl isomers are also presented and used to further interpret the experimental results for the reaction of Mg clusters with Cl atoms. In contrast to Mg_2F, the ground state of Mg_2Cl is a linear $C_{\infty v}$ MgMgCl structure with the C_{2v} and $D_{\infty h}$ isomers MgClMg slightly higher in energy.

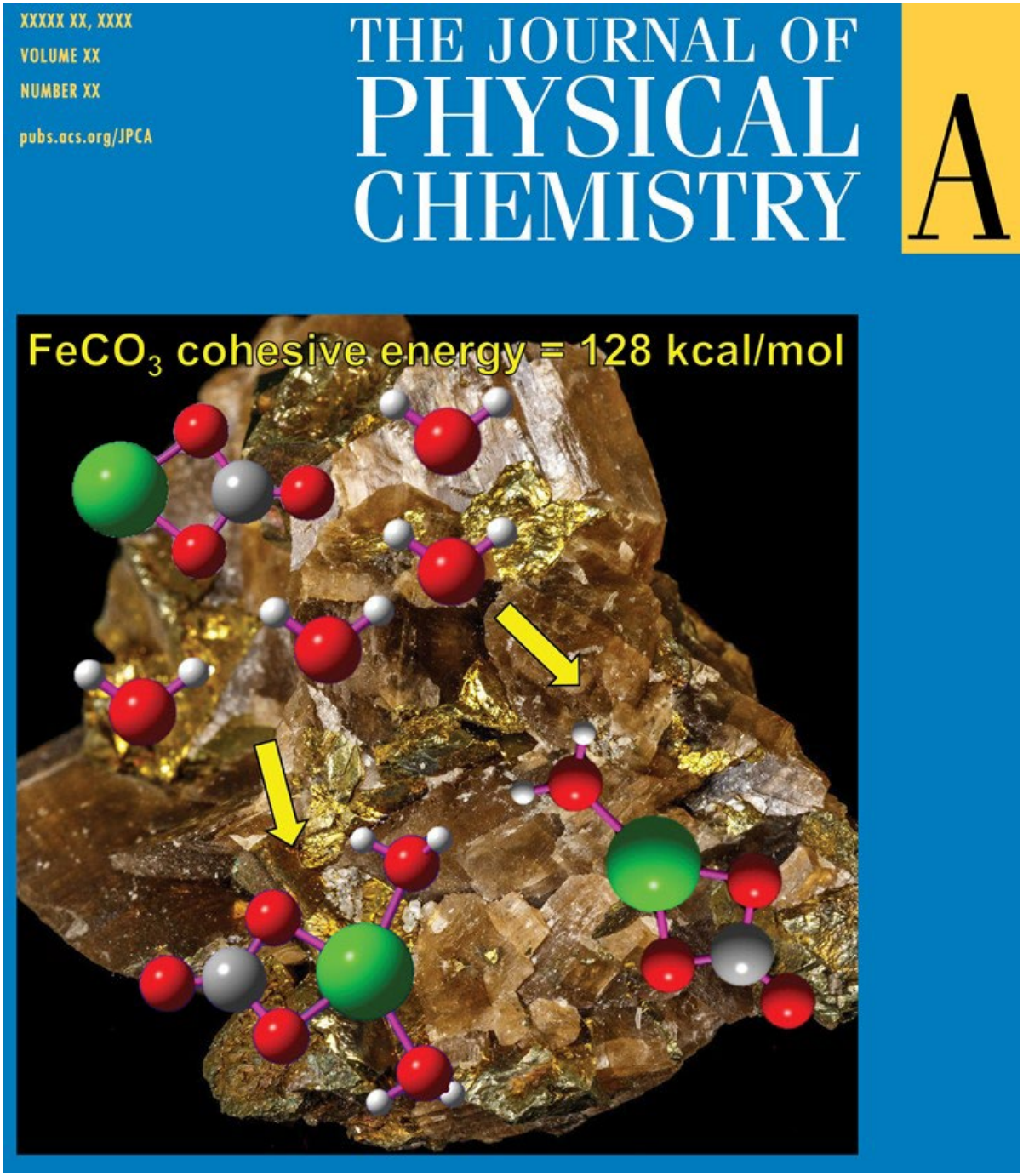

Figure 7.1. Cohesive energy of $FeCO_3$ at 298 K in kcal/mol and hydrated structures of $FeCO_3$. Green atoms = Fe, red atoms = O, grey atoms = C and white atoms = H.

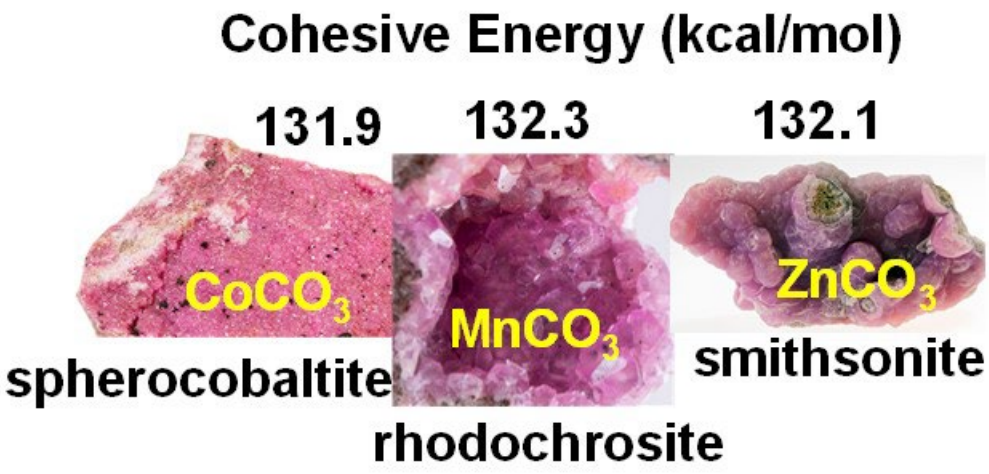

Figure 7.2. Cohesive energy of $CoCO_3$, $MnCO_3$ and $ZnCO_3$ at 298 K in kcal/mol.

Figure 7.3. CO_2 addition energies on $M_3O_6^-$ where M = Ti, Zr and Hf at 298 K in kcal/mol.

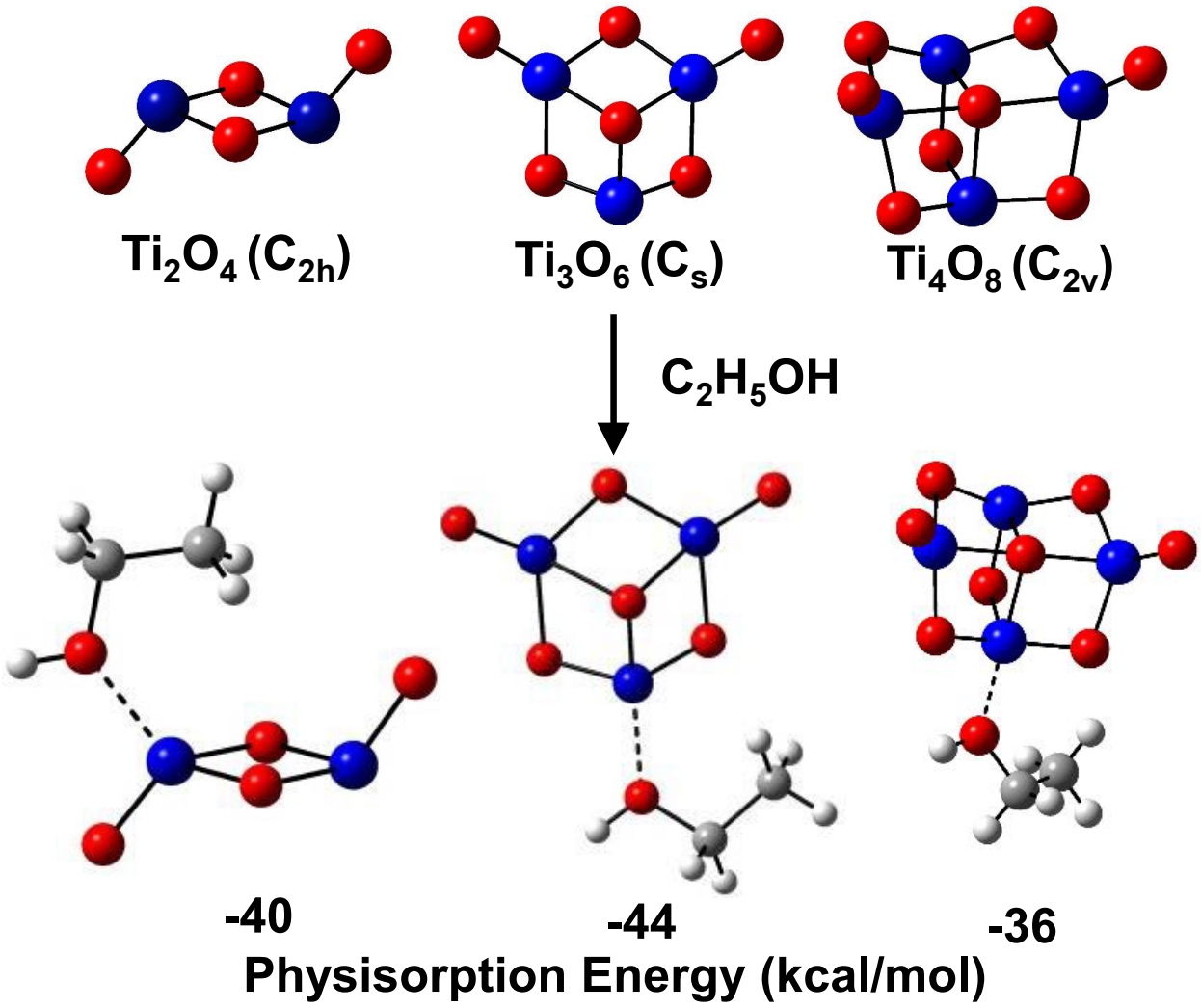

Figure 7.4. Physisorption energy of ethanol on $(TiO_2)_n$ nanoclusters, n = 2 to 4, at 0 K in kcal/mol.

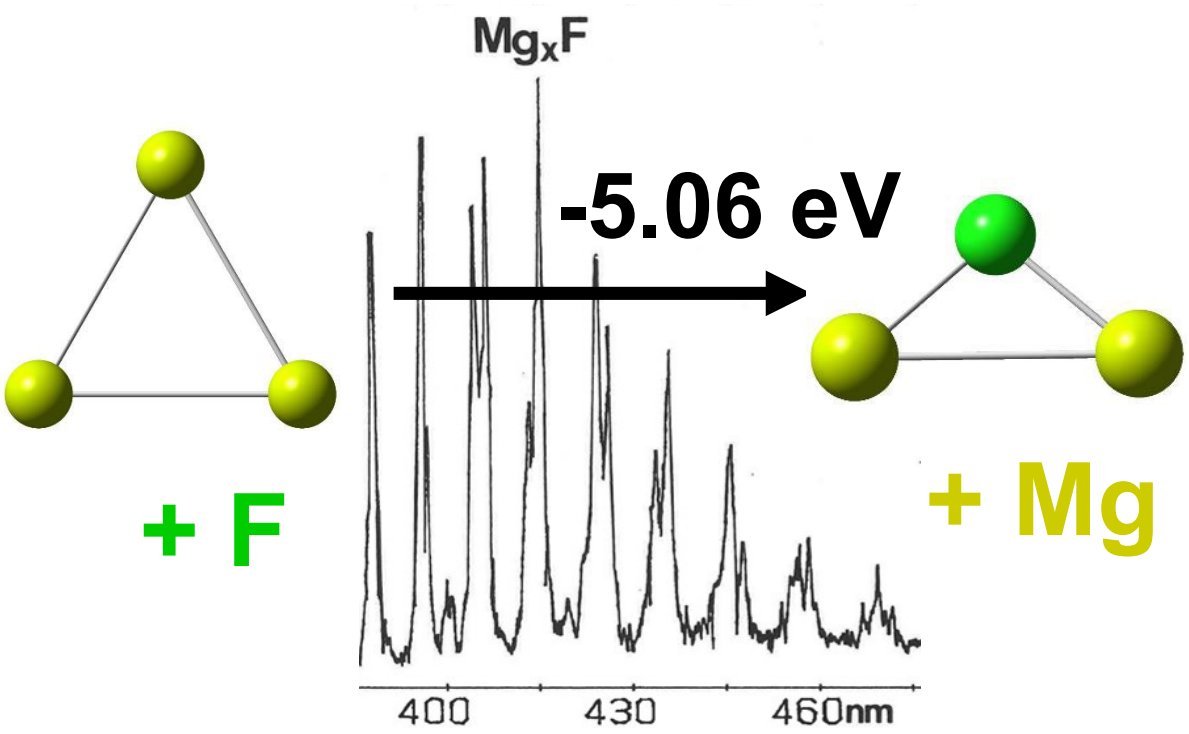

Figure 7.5. Reaction energy of $Mg_3 + F \rightarrow Mg_2F + Mg$ in eV at 298 K with part of chemiluminescent spectrum resulting from the reaction of a high flux of dry ice cooled, helium entrained, magnesium atoms and clusters (Mg_2, Mg_3) with helium entrained fluorine atoms and SF_x molecules.

REFERENCES

[1] https://www.esrl.noaa.gov/gmd/ccgg/trends/ (accessed February 6th,2023).

[2] Gupta, H.; Fan, L.-S. Carbonation-Calcination Cycle Using High Reactivity Calcium Oxide for Carbon Dioxide Separation from Flue Gas. *Ind. Eng. Chem. Res.* **2002**, *41*, 4035-4042.

[3] Yu, F.-C.; Phalak, N.; Sun, Z.; Fan, L.-S. Activation Strategies for Calcium-Based Sorbents for CO_2 Capture: A Perspective. *Ind. Eng. Chem. Res.* **2012**, *51*, 2133-2142.

[4] Chen, H.; Zhao, C.; Yu, W. Calcium-Based Sorbent Doped with Attapulgite for CO_2 Capture. *Appl. Energy* **2013**, *112*, 67-74.

[5] Chase, M. W., Jr. *NIST-JANAF Thermochemical Tables*, 4th ed. *J. Phys. Chem. Ref. Data.*, *Mono. 9*; American Institute of Physics: Woodbury, NY, 1998; Suppl 1.

[6] Yungman, V. S.; Glushko, V. P.; Medvedev, V. A.; Gurvich, L. V., Eds., *Thermal Constants of Substances*, 8 Vols., Wiley: New York, 1999.

[7] Wagman, D. D.; Evans, W. H.; Parker, V. B.; Schumm, R. H.; Halow, I.; Bailey, S. M.; Churney, K. L.; Nuttall, R. L. *J. Phys. Chem. Ref. Data* **1982**, *11* (Suppl. 2).

[8] Lackner, K. S.; Wendt, C. H.; Butt, D. P.; Joyce, E. L.; Sharp, D. H. Carbon Dioxide Disposal in Carbonate Minerals. *Energy* **1995***, 20,* 1153–1170.

[9] Chaka, A. M.; Felmy, A. R. Ab Initio Thermodynamic Model for Magnesium Carbonates and Hydrates. *J. Phys. Chem. A* **2014**, *118*, 7469−7488.

[10] Chaka, A. M. Ab Initio Thermodynamics of Hydrated Calcium Carbonates and Calcium Analogues of Magnesium Carbonates: Implications for Carbonate Crystallization Pathways. *ACS Earth Space Chem.* **2018**, *2*, 210−224.

[11] Chaka, A. M. Quantifying the Impact of Magnesium on the Stability and Water Binding Energy of Hydrated Calcium Carbonates by Ab Initio Thermodynamics. *J. Phys. Chem. A* **2019**, *123*, 2908−2923.

[12] Laugesen, J. L. Density Functional Calculations of Elastic Properties of Portlandite, $Ca(OH)_2$. *Cem. Concr. Res.* **2005**, *35*, 199−202.

[13] Chaka, A. M.; Felmy, A. R.; Qafoku, O. Ab initio Thermodynamics of Magnesium Carbonates and Hydrates in Water-Saturated Supercritical CO_2 and CO_2-rich Regions. *Chem. Geol.* **2016**, *434*, 1−11.

[14] Feller, D.; Dixon, D. A. Extended Benchmark Studies of Coupled Cluster Theory through Triple Excitations. *J. Chem. Phys.* **2001**, *115*, 3484–3496.

[15] Dixon, D. A.; Feller, D.; Peterson, K. A. Heats of Formation and Ionization Energies of NH_x, x=0-3. *J. Chem. Phys.* **2001**, *115*, 2576 – 2581.

[16] Ruscic, B.; Wagner, A. F.; Harding, L. B.; Asher, R. L.; Feller, D.; Dixon, D. A.; Peterson, K. A.; Song, Y.; Qian, X.; Ng, C.; Liu, J.; Chen, W.; Schwenke, D. W. On the Enthalpy of Formation of Hydroxyl Radical and Gas-Phase Bond Dissociation Energies of Water and Hydroxyl. *J. Phys. Chem. A* **2002**, *106*, 2727 – 2747.

[17] Pollack, L.; Windus, T. L.; de Jong, W. A.; Dixon, D. A. Thermodynamic Properties of the C_5, C_6, and C_8 *n*-Alkanes from Ab Initio Electronic Structure Theory. *J. Phys. Chem. A* **2005**, *109*, 6934 – 6938.

[18] Feller, D.; Peterson, K. A.; Dixon, D. A. A Survey of Factors Contributing to Accurate Theoretical Predictions of Atomization Energies and Molecular Structures. *J. Chem. Phys.* **2008**, *129*, 204015 – 204046.

[19] Peterson, K. A.; Feller, D.; Dixon, D. A. Chemical Accuracy in Ab Initio Thermochemistry and Spectroscopy: Current Strategies and Future Challenges. *Theor. Chem. Acc.* **2012**, *131*, 1 – 20.

[20] Feller, D.; Peterson, K. A.; Dixon, D. A. Further Benchmarks of a Composite, Convergent, Statistically Calibrated Coupled Cluster Based Approach for Thermochemical and Spectroscopic Studies. *Mol. Phys.* **2012**, *110*, 2381 – 2399.

[21] Dixon, D. A.; Feller, D.; Peterson, K. A. A Practical Guide to Reliable First Principles Computational Thermochemistry Predictions Across the Periodic Table. In *Annual Reports in Computational Chemistry*, Ralph, A. W., Ed.; Elsevier: 2012; Vol. 8, pp 1 – 28.

[22] Feller, D.; Peterson, K. A.; Dixon, D. A. The Impact of Larger Basis Sets and Explicitly Correlated Coupled Cluster Theory on the Feller-Peterson-Dixon Composite Method. In *Annual Reports in Computational Chemistry*, Vol. 12, Ed. D. A. Dixon, Elsevier, Amsterdam, 2016, pp 47 – 78.

[23] Chen, M.; Dyer, J. E.; Li, K.; Dixon, D. A. Prediction of Structures and Atomization Energies of Small Silver Clusters, $(Ag)_n$, n < 100. *J. Phys. Chem. A,* **2013**, *117*, 8298–8313.

[24] Chen, M.; Felmy, A. R.; Dixon, D. A. Structures and Stabilities of $(MgO)_n$ Nanoclusters. *J. Phys. Chem. A*, **2014**, *118*, 3136–3146.

[25] Chen, M.; Jackson, V. E.; Felmy, A. R.; Dixon, D. A. Structures and Energetics of $(MgCO_3)_n$ Clusters, n ≤ 16. *J. Phys. Chem. A*, **2015**, 119, 3419–3428.

[26] Chen, M.; Straatsma, T. P.; Fang, Z.; Dixon, D. A. A Structural and Electronic Property Study of $(ZnO)_n$, $n \leq 168$: The Transition from Zinc Oxide Molecular Clusters to Ultra-small Nanoparticles. *J. Phys. Chem. C*, **2016**, *120*, 20400–20418.

[27] Chen, M.; Dixon, D. A. Modeling the Formation of TiO_2 Ultra-Small Nanoparticles. *Nanoscale*, **2017**, *9*, 7143-7162.

[28] Chen, M.; Thanthiriwatte, K. S.; Dixon, D. A. Structures and Stabilities of $(CaO)_n$ Nanoclusters. *J. Phys. Chem. C*, **2017**, *121*, 23025–23038.

[29] Inoue, T.; Fujishima, A.; Konishi, S.; Honda, K. Photoelectrocatalytic Reduction of Carbon Dioxide in Aqueous Suspensions of Semiconductor Powders. *Nature* **1979**, *277*, 637 - 638.

[30] Tan, L.-L.; Ong, W.-J.; Chai, S.-P.; Mohamed, A. R. Band Gap Engineered, Oxygen-rich TiO_2 for Visible Light Induced Photocatalytic Reduction of CO_2. *Chem. Commun.* **2014**, *50*, 6923 - 6926.

[31] Ong, W.-J.; Tan, L.-L.; Chai, S.-P.; Yong, S.-T.; Mohamed, A. R. Self-Assembly of Nitrogen-Doped TiO_2 with Exposed (001) Facets on a Graphene Scaffold as Photo-Active Hybrid Nanostructures for Reduction of Carbon Dioxide to Methane. *Nano Res.* **2014**, *7*, 1528 - 1547.

[32] Ong, W.-J.; Tan, L.-L.; Chai, S.-P.; Yong, S.-T. Facet-Dependent Photocatalytic Properties of TiO_2-Based Composites for Energy Conversion and Environmental Remediation. *ChemSusChem* **2014**, *7*, 690 - 719.

[33] Yuan, L.; Han, C.; Pagliaro, M.; Xu, Y.-J. Origin of Enhancing the Photocatalytic Performance of TiO_2 for Artificial Photoreduction of CO_2 through a SiO_2 Coating Strategy. *J. Phys. Chem. C* **2016**, *120*, 265 - 273.

[34] Kohno, Y.; Tanaka, T.; Funabiki, T.; Yoshida, S. Photoreduction of Carbon Dioxide with Hydrogen over ZrO_2. *Chem. Commun.* **1997**, 841 - 842.

[35] Kohno, Y.; Tanaka, T.; Funabiki, T.; Yoshida, S. Identification and Reactivity of a Surface Intermediate in the Photoreduction of CO_2 with H_2 over ZrO_2. *J. Chem. Soc., Faraday Trans.* **1998**, *94*, 1875 - 1880.

[36] Kohno, Y.; Tanaka, T.; Funabiki, T.; Yoshida, S. Photoreduction of CO_2 with H_2 over ZrO_2. A Study of Interaction of Hydrogen with Photoexcited CO_2. *Phys. Chem. Chem. Phys.* **2000**, *2*, 2635 - 2639.

[37] Kohno, Y.; Tanaka, T.; Funabiki, T.; Yoshida, S. Reaction Mechanism in the Photoreduction of CO_2 with CH_4 Over ZrO_2. *Phys. Chem. Chem. Phys*. **2000**, *2*, 5302 - 5307.

[38] Chen, X.; Zhou, Y.; Liu, Q.; Li, Z.; Liu, J.; Zou, Z. Ultrathin, Single-Crystal WO_3 Nanosheets by Two-Dimensional Oriented Attachment Toward Enhanced Photocatalystic Reduction of CO_2 into Hydrocarbon Fuels Under Visible Light. *ACS Appl. Mater. Interfaces* **2012**, *4*, 3372 - 3377.

[39] Xie, S.; Zhang, Q.; Liu, G.; Wang, Y. Photocatalytic and Photoelectrocatalytic Reduction of CO_2 Using Heterogeneous Catalysts with Controlled, *Chem. Commun.* **2016**, *52*, 35 - 59.

[40] Flores, L. A.; Murphy, J. G.; Copeland, W. B.; Dixon, D. A. Reaction of CO_2 with Groups 4 and 6 Transition Metal Oxide Clusters. *J. Phys. Chem. A*, **2017**, *121*, 8719–8727

[41] Debnath, S.; Song, X.; Fagiani, M. R.; Weichman, M. L.; Gao, M.; Maeda, S.; Taketsugu, T.; Schöllkopf, W.; Lyalin, A.; Neumark, D. M.; et al. CO_2 Adsorption on $Ti_3O_6^-$: A Novel Carbonate Binding Motif. *J. Phys. Chem. C* **2019**, *123*, 8439−8446.

[42] Debnath, S.; Song, X.; Fagiani, M. R.; Weichman, M. L.; Gao, M.; Maeda, S.; Taketsugu, T.; Schöllkopf, W.; Lyalin, A.; Neumark, D. M.; et al. Correction to "CO_2 Adsorption on $Ti_3O_6^-$: A Novel Carbonate Binding Motif". *J. Phys. Chem. C* **2020**, *124*, 6952-6953.

[43] Li, Z.; Fang, Z.; Kelly, M. S.; Kay, B. D.; Rousseau, R.; Dohnalek, Z.; Dixon, D. A. Ethanol Conversion on Cyclic $(MO_3)_3$ (M = Mo, W) Clusters. *J. Phys. Chem. C* **2014**, *118*, 4869−4877.

[44] Rousseau, R.; Dixon, D. A.; Kay, B. D.; Dohnálek, Z. Dehydration, Dehydrogenation and Condensation of Alcohols on Supported Oxide Catalysts based on Cyclic $(WO_3)_3$ and $(MoO_3)_3$ Clusters. *Chem. Soc. Rev.*, **2014**, *43*, 7664.

[45] Fang, Z.; Li, Z.; Kelley, M. S.; Kay, B. D.; Li, S.; Hennigan, J. M.; Rousseau, R.; Dohnálek, Z.; Dixon, D. A. Oxidation, Reduction, and Condensation of Alcohols over $(MO_3)_3$ (M = Mo, W) Nanoclusters. *J. Phys. Chem. C* **2014**, *118*, 22620−22634.

[46] Kim, Y. K.; Kay, B. D.; White, J. M.; Dohnálek, Z. Alcohol Chemistry on Rutile TiO_2(110): The Influence of Alkyl Substituents on Reactivity and Selectivity. *J. Phys. Chem. C* **2007**, *111*, 18236-18242.

[47] Pang, C. L.; Lindsay, R.; Thornton, G. Structure of Clean and Adsorbate-Covered Single-Crystal Rutile TiO_2 Surfaces. *Chem. Rev.* **2013**, *113*, 3887−3948.

[48] Kim, Y. K.; Kay, B. D.; White, J. M.; Dohnálek, Z. Inductive Effect of Alkyl Chains on Alcohol Dehydration at Bridge-bonded Oxygen vacancies on TiO_2(110). *Catal. Lett.* **2007**, *119*, 1-4.

[49] Zhang, Z.; Bondarchuk, O.; White, J. M.; Kay, B. D.; Dohnálek, Z. Direct Visualization of 2-Butanol Adsorption and Dissociation on TiO_2(110). *J. Phys. Chem. C*, **2007**, *111*, 3021-3027.

[50] Henderson, M. A.; Otero-Tapia, S.; Castro, M. E. The Chemistry of Methanol on the TiO_2(110) Surface: The Influence of Vacancies and Coadsorbed Species. *Faraday Discuss.* **1999**, *114*, 313-329.

[51] Jensen, J. H. *Molecular Modeling Basics*; CRC Press: Boca Raton, FL, 2010; pp 25 – 76.

[52] Jensen, F. *Introduction to Computational Chemistry*, 2nd Ed; John Wiley & Sons, Ltd: West Sussex, England, 2007; pp 80 – 191.

[53] Born, M.; Oppenheimer, J. R. On the Quantum Theory of Molecules. *Ann Phys* **1927**, *389*, 457–484.

[54] Hartree, D. R. The Wave Mechanics of an Atom with a Non-Coulomb Central Field. *Math. Proc. Camb. Philos. Soc.* **1928**, *24*, 111-132.

[55] Slater, J. C. The Self Consistent Field and the Structure of Atoms. *Phys. Rev.* **1928**, *32*, 339–348.

[56] Gaunt, J. A. A Theory of Hartree's Atomic Fields. *Math. Proc. Camb. Philos. Soc.* **1928**, *24*, 328–342.

[57] Slater, J. C. Note on Hartree's Method. *Phys. Rev.* **1930**, *35*, 210–211.

[58] Fock, V. A. Näherungsmethode zur Lösung des quantenmechanischen Mehrkörperproblems. *Z. Phys.* **1930**, *61*, 126–148.

[59] Fock, V. A. "Selfconsistent field" mit Austausch für Natrium. *Z. Phys.* **1930**, *62*, 795–805.

[60] Hartree, D. R.; Hartree, W. Self-consistent field, with exchange, for beryllium. *Proc. R. Soc. Lond. A.* **1935**, *150*, 9-33.

[61] Slater, J. C. A Simplification of the Hartree-Fock Method. Phys. Rev. **1951**, *81*, 385–390.

[62] Pauli, W. Über den Zusammenhang des Abschlusses der Elektronengruppen im Atom mit der Komplexstruktur der Spektren. *Z Phys.* **1925**, *31*, 765–783.

[63] Dunning, T. H. Gaussian Basis Sets for Use in Correlated Molecular Calculations. I. The Atoms Boron through Neon and Hydrogen. *J. Chem. Phys*. **1989**, *90*, 1007 – 1023.

[64] Kendall, R. A.; Dunning, T. H.; Harrison, R. J. Electron Affinities of the First-Row Atoms Revisited. Systematic Basis Sets and Wave Functions. *J. Chem. Phys.* **1992**, *96*, 6796 - 6806.

[65] Godbout, N.; Salahub, D. R.; Andzelm, J.; Wimmer, E. Optimization of Gaussian-Type Basis Sets for Local Spin Density Functional Calculations Part I. Boron through Neon, Optimization Technique and Validation. *Can. J. Chem.* **1992**, *70*, 560 – 571.

[66] Sosa, C.; Andzelm, J.; Elkin, B. C.; Wimmer, E.; Dobbs, K. D.; Dixon, D.A. A Local Density Functional Study of the Structure and Vibrational Frequencies of Molecular Transition-Metal Compounds. *J. Phys. Chem.* **1992**, *96*, 6630 – 6636.

[67] Pople, J. A.; Krishnan, R.; Schlegel, H. B.; Binkley, J. S. Electron Correlation Theories and Their Application to the Study of Simple Reaction Potential Surfaces. *Int. J. Quantum Chem.* **1978**, *14*, 545 – 560.

[68] Purvis III, G. D.; Bartlett, R. J. A Full Coupled-Cluster Singles and Doubles Model: The Inclusion of Disconnected Triples. *J. Chem. Phys.* **1982**, *76*, 1910 – 1918.

[69] Raghavachari, K.; Trucks, G. W. Pople, J. A. Head-Gordon, M. A Fifth-order Perturbation Comparison of Electron Correlation Theories. *Chem. Phys. Lett.* **1989**, *157*, 479 – 483.

[70] Watts, J. D.; Gauss, J.; Bartlett, R. J. Coupled-Cluster Methods with Noniterative Triple Excitations for Restricted Open-Shell Hartree-Fock and other General Single Determinant Reference Functions. Energies and Analytical Gradients. *J. Chem. Phys.* **1993**, *98*, 8718 – 8733.

[71] Knowles, P. J.; Hampel, C.; Werner, H.-J. Coupled Cluster Theory for High Spin, Open Shell Reference Wave Functions. *J. Chem. Phys*. **1993**, *99*, 5219 – 5227.

[72] Deegan, M. J. O.; Knowles, P. J. Perturbative Corrections to Account for Triple Excitations in Closed and Open Shell Coupled Cluster Theories. *Chem. Phys. Lett*. **1994**, *227*, 321 – 327.

[73] Knowles, P. J.; Hampel, C.; Werner, H.-J. Erratum: Coupled Cluster Theory for High Spin, Open Shell Reference Wave Functions. *J. Chem. Phys*. **2000,** *112*, 3106 – 3107.

[74] Feller, D.; Peterson, K.A.; Hill, J. G. On the Effectiveness of CCSD(T) Complete Basis Set Extrapolations for Atomization Energies. *J. Chem. Phys.* **2011***, 135,* 044102 – 044102.

[75] Martin, J. M. L. Ab Initio Total Atomization Energies of Small Molecules-Towards the Basis Set Limit. *Chem. Phys. Lett.* **1996**, *259*, 669 – 678.

[76] Helgaker, T.; Klopper, W.; Koch, H.; Noga, J. Basis-Set Convergence of Correlated Calculations on Water. *J. Chem. Phys.* **1997**, *106*, 9639 – 9646.

[77] Halkier, A.; Helgaker, T.; Jørgensen, P.; Klopper, W.; Koch, H.; Olsen, J.; Wilson, A. L. Basis-Set Convergence in Correlated Calculations on Ne, N_2, and H_2O. *Chem. Phys. Lett.* **1998**, *286*, 243 – 252.

[78] Klopper, W.; Bak, K. L.; Jørgensen, P.; Olsen, J.; Helgaker, T. Highly Accurate Calculations of Molecular Electronic Structure. *J. Phys. B: At. Mol. Opt. Phys.* **1999**, *32*, R103 – R130.

[79] Hohenberg, P.; Kohn, W. Inhomogeneous Electron Gas. *Phys. Rev.* **1964**, *136*, B864 – B870.

[80] Kohn, W.; Sham, L. J. Self-Consistent Equations Including Exchange and Correlation Effects. *Phys. Rev.* **1965**, *140*, A1133 – A1138.

[81] Vosko, S. H.; Wilk, L.; Nusair, M. Accurate Spin-Dependent Electron Liquid Correlation Energies for Local Spin Density Calculations: A Critical Analysis. *Can. J. Phys.* **1980**, *58*, 1200 – 1211.

[82] Perdew, J. P.; Wang, Y. Accurate and Simple Analytic Representation of the Electron-Gas Correlation Energy. *Phys. Rev. B* **1992**, *45*, 13244 – 13249.

[83] Perdew, J. P; Chevary, J. A.; Vosko, S. H.; Jackson, K. A.; Pederson, M. R.; Singh, D. J.; Fiolhais, C. Atoms, Molecules, Solids, and Surfaces: Application of the Generalized Gradient Approximation for Exchange and Correlation. *Phys. Rev. B.* **1992**, *46*, 6671 – 6687.

[84] Becke, A. D. Density-Functional Exchange-Energy Approximation with Correct Asymptotic Behavior. *Phys. Rev. A* **1988**, 38, 3098 – 3100.

[85] Perdew, J. P.; Burke, K.; Ernzerhof, M. Generalized Gradient Approximation Made Simple. *Phys. Rev. Lett.* **1996**, *77*, 3865 – 3868.

[86] Becke, A. D. A New Mixing of Hartree-Fock and Local Density-Functional Theories. *J. Chem. Phys.* **1993**, *98*, 1372 – 1377.

[87] Becke, A. D. Density-Functional Theormochemistry. III. The role of exact exchange. *J. Chem. Phys.* **1993**, *98*, 5648 – 5652.

[88] Lee, C.; Yang, W.; Parr, R. G. Development of the Colle-Salvetti Correlation-Energy Formula into a Functional of the Electron Density. *Physical Review B.* **1988**, *37*, 785 – 789.

[89] Cohen, A. J.; Mori-Sanchez, P.; Yang, W. Challenges for Density Functional Theory. *Chem. Rev.* **2012**, *112*, 289 – 320.

[90] Moore, C. E. *Atomic Energy Levels As Derived from the Analysis of Optical Spectra*; U.S. National Bureau of Standards Circular 467, COM-72-50282; U.S. Department of Commerce, National Technical Information Service: Washington, DC, 1949; Vol. *1*, H to V.

[91] Douglas, M.; Kroll, N. M. Quantum Electrodynamical Corrections to the Fine Structure of Helium. *Ann. Phys.* **1974**, *82*, 89 – 155.

[92] Hess, B. A. Applicability of the No-Pair Equation with Free-Particle Projection Operators to Atomic and Molecular Structure Calculations. *Phys. Rev. A.* **1985**, *32*, 756 – 763.

[93] Hess, B. A. Relativistic Electronic-Structure Calculations Employing a Two-Component No-Pair Formalism with External-Field Projection Operators. *Phys. Rev. A.* **1986**, *33*, 3742 – 3748.

[94] de Jong, W. A.; Harrison, R. J.; Dixon, D. A. Parallel Douglas-Kroll energy and gradients in NWChem. Estimating scalar relativistic effects using Douglas-Kroll contracted basis sets. *J. Chem. Phys*., **2001**, 114, 48 - 53.

[95] Curtiss, L. A.; Raghavachari, K.; Redfern, P. C.; Pople, J. A. Assessment of Gaussian-2 and Density Functional Theories for the Computation of Enthalpies of Formation. *J. Chem. Phys.* **1997**, *106*, 1063 – 1079.

[96] Atkins, P.; de Paula, J. *Atkins' Physical Chemistry*, 8th ed.; W. H. Freeman and Company, NY, 2006.

[97] Heisenberg, W. Über den anschaulichen Inhalt der quantentheoretischen Kinematik und Mechanik. *Z. Phys.* **1927**, *43*, 172 – 198.

[98] McQuarrie, D. A. *Statistical Mechanics*. University Science Books: Sausalito, CA, **2000**.

[99] Hu, Y.; Vasiliu, M.; Thanthiriwatte, K. S.; Jackson, V. E.; Chaka, A. M.; Dixon, D. A. Thermodynamics of Metal Carbonates and Bicarbonates and Their Hydrates for Mg, Ca, Fe, and Cd Relevant to Mineral Energetics. *J. Phys. Chem. A* **2020**, *124*, 1829−1840.

[100] Hu, Y.; Chaka, A. M.; Dixon, D. A. Thermodynamics of the Metal Carbonates and Bicarbonates of Mn, Co, Ni, Cu, and Zn Relevant to Mineral Energetics. *J. Phys. Chem. A* **2022**, *126*, 7874−7887.

[101]Chen, C.; Dixon, D. A. Structure and Stability of Hydrolysis Reaction Products of MgO Nanoparticles Leading to the Formation of Brucite. *J. Phys. Chem. C* **2017**, *121*, 21750-21762.

[102] Chen, M.; McNeill, A. S.; Hu, Y.; Dixon, D. A. Elucidation of Bottom-Up Growth of $CaCO_3$ Involving Prenucleation Clusters from Structure Predictions and Decomposition of Globally Optimized $(CaCO_3)_n$ Nanoclusters. *ACS Nano*, **2020**, *14*, 4153-4165.

[103] Hu, Y.; Persaud, R. R.; Vasiliu, M.; Dixon, D. A. Different Carbonate Isomers Formed by the Addition of CO_2 to $M_3O_6^-$ for M = Ti, Zr, and Hf. *J. Phys. Chem. A* **2020**, *124*, 5402−5407.

[104] Devore, T. C.; Wang, H.; Winstead, C. B.; Gole, J. L.; Hu, Y.; Dixon, D. A. Electronically Excited Complex Formation in Magnesium Cluster−Halogen Atom Reactions. *J. Phys. Chem. A* **2022**, *126*, 1848−1860.